The University of Sheffield

Novel Dual-rotor Counter-rotating PM Machines with Radial and Axial Configurations

Zhitong Ran

A thesis submitted for the degree of Doctor of Philosophy

Department of Electronic and Electrical Engineering

The University of Sheffield

Mappin Street, Sheffield, S1 3JD, UK

June 2024

ABSTRACT

This thesis systematically investigates radial-flux dual-rotor (DR) permanent magnet (PM) (DRPM) machines with (a) different slot/pole number combinations, (b) magnetic fluxes produced by two rotors in both series and parallel, and (c) two rotors operating at either the same or different speeds. All the investigations are carried out by analytical analyses and/or finite element analysis (FEA), together with experimental verification.

In the scenario that two rotors of DRPM machines operate at the same speed, the DRPM machines with series (S) and parallel (P) magnetic circuits (SDRPM and PDRPM machines) are compared. The analysis indicates that SDRPM machines generally exhibit higher torque. Moreover, the outer rotor of the DRPM machine contributes most to the total torque, which also shows the single rotor permanent magnet (SRPM) machine has a potentially higher torque than the DRPM machine. Therefore, the SDRPM machine is selected to compare with the SRPM. It reveals that the SDRPM machines have higher overload capabilities but lower torque density and less efficient PM utilisation than the SRPM machines.

Although with lower torque density and PM utilisation, DRPM machines inherently have two rotors compared to SRPM machines. Thus, DRPM machines can be employed in applications that require two rotors, thereby replacing two SRPM motors. The counter-rotating (CR) operation is selected for further analysis as a special case in a scenario with different rotational speed rotors since the CR operation systems are widely used in industrial applications, such as underwater vehicles, wind power turbines, household appliances, etc. Therefore, a yokeless counter-rotating dual-rotor PM (YCDRPM) machine, which features series magnetic circuits, is introduced and analysed. This YCDRPM machine has the synergies of a magnetic gear and a PM machine to achieve dual-rotor CR operation, significantly reducing the cost and saving the space compared to using two SRPM machines. However, the sandwiched stator of the YCDRPM machine results in a complex mechanical structure, and its radial flux configuration makes the torques of two rotors more challenging to adjust. Therefore, a novel counter-rotating single-stator dual-internal-rotor PM (CSDPM) machine is proposed. The CSDPM machine design includes a single shared winding set, one shared stator, and two robust rotors. Different from conventional radially arranged radial-flux magnetic geared machines, axially arranged radial-flux rotors of CSDPM machines allow for easier assembly and can modify the torque split of two rotors. The proposed CR operation system with the CSDPM machine shows higher torque than the conventional CR system using two SRPM machines.

ACKNOWLEDGEMENTS

Foremost, I extend my deepest gratitude to my supervisor, Prof. Zi-Qiang Zhu, who has provided invaluable guidance not only in my academic endeavours but also in my life. His continuous support and mentorship in my research have been crucial, and his teachings on life, philosophy, and art have broadened my horizons.

I am profoundly grateful to Tula Technology Company and Midea Group for their generous support throughout my research. Special thanks go to Dr. Zhiqian Chen, Dr. Matthew Younkins, Dr. Philippe Farah, Dr. Yanjian Zhou, Dr. Liang Chen, Dr. Lei Yang, and Dr. Huan Qu for their invaluable supervision, advice, and assistance with my projects.

I would like to thank Dr. Yafeng Zhang, Dr. Dawei Liang, Dr. Fangrui Wei, Dr. Luocheng Yan, Dr. Ji Qi, Dr. Fan Xu, Dr. Shensheng Wang, Dr. Yan Jia, Dr. Dong Xiang, Mr. Yinzhao Zheng, Mr. Yang Chen, Mr. Jun Yan, Mr. Hai Xu, et al, in the Electrical Machines and Drives Research Group at the University of Sheffield for their technical discussions and support. I will never forget the time we spent together, particularly during the period of COVID-19.

I would also like to thank all my friends at Sheffield. Your presence in my life is truly a blessing.

Finally, I would like to express my deepest gratitude to my parents for their unconditional love and constant encouragement. Your support has been the cornerstone of my journey.

CONTENTS

NOMENCLATURES

Symbol	Description	Unit
A_{Ik}	Amplitude of the kth order harmonic of F_I	AT
A_{Ok}	Amplitude of the kth order harmonic of F_O	AT
B_a	Flux density generated by armature reaction	T
B_r	Air gap flux density in radial direction generated by PM	T
B_I	Inner air gap flux density	T
B_{IIPM}	Air gap flux density in inner air gap produced by inner rotor PM	T
$B_{I\text{-}load}$	Inner air gap flux density at on-load condition	T
B_{IOPM}	Air gap flux density in inner air gap produced by outer rotor PM	T
B_O	Outer air gap flux density	T
B_{OIPM}	Air gap flux density in outer air gap produced by inner rotor PM	T
$B_{O\text{-}load}$	Outer air gap flux density at on-load condition	T
B_{OOPM}	Air gap flux density in outer air gap produced by outer rotor PM	T
b_{is}	Stator inner slot opening	mm
b_{os}	Stator outer slot opening	mm
b_s	Stator slot opening	mm
C_T	Cogging torque factor	-
e_A	Phase-A back EMF	V
e_B	Phase-B back EMF	V
e_C	Phase-C back EMF	V
e_{IA}	Phase-A back EMF induced by inner PMs	V
e_{IB}	Phase-B back EMF induced by inner PMs	V
e_{IC}	Phase-C back EMF induced by inner PMs	V

e_{OA}	Phase-A back EMF induced by outer PMs	V
e_{OB}	Phase-B back EMF induced by outer PMs	V
e_{OC}	Phase-C back EMF induced by outer PMs	V
f	Frequency of supply	HZ
F_a	MMF generated by armature reaction	AT
F_I	MMF generated by inner PM	AT
F_{im}	MMF generated by inner PM	AT
F_O	MMF generated by outer PM	AT
F_{om}	MMF generated by outer PM	AT
F_{PM}	MMF generated by PMs	AT
F_{PMi}	Amplitude of the i-th harmonic component of F_{PM}	AT
G_r	Gearing ratio	-
h_{is}	Inner tooth-tip height	mm
h_{os}	Outer tooth-tip height	mm
h_{sy}	Stator yoke height	mm
I_{ph}	Amplitude of phase current	A
i_A	Phase-A current	A
i_B	Phase-B current	A
i_C	Phase-C current	A
K_{IC}	Carter's coefficients of inner air gap	-
K_{IOC}	Carter's coefficients of inner and outer air gaps	-
K_{OC}	Carter's coefficients of outer air gap	-
k_{wm}	Winding factor of the m-th harmonic order	-
l_{end}	End-winding length	mm
L_g	Air gap length	mm

L_{gap}	Axial gap length between two rotors	mm
L_{IE}	Effective inner air gap	mm
L_{IOE}	Effective inner and outer air gap	mm
L_{OE}	Effective outer air gap	mm
L_{im}	Inner PM thickness	mm
L_{om}	Outer PM thickness	mm
L_{stk}	Stack length	mm
m	Number of phases	-
N	Number of turns of stator winding	-
N_A	Phase-A winding function	-
N_B	Phase-B winding function	-
N_C	Phase-C winding function	-
n_h	Rotational speed of high pole number rotor	r/min
n_I	Rotational speed of inner rotor	r/min
n_l	Rotational speed of low pole number rotor	r/min
n_O	Rotational speed of outer rotor	r/min
N_m	Amplitude of the m-th harmonic order of winding function	-
N_{ph}	Number of turns per phase	-
N_s	Number of stator slot (or number of modular stator segments)	-
p	Number of rotor pole pairs	-
P_I	Inner air gap permeance	H/m
P_{I0}	Fundamental amplitude of inner air gap permeance	H/m
P_{Ij}	Amplitude of the jth order harmonic of inner air gap permeance	H/m
P_{IO}	Inner and outer air gaps permeance	H/m
P_{IO0}	Fundamental amplitude of inner and outer air gaps permeance	H/m

P_{IOj}	Amplitude of the *j*th order harmonic of inner and outer air gaps permeance	H/m
P_O	Outer air gap permeance	H/m
P_{O0}	Fundamental amplitude of outer air gap permeance	H/m
P_{Oj}	Amplitude of the *j*th order harmonic of outer air gap permeance	H/m
p_h	Pole pair number of high pole number rotor	-
p_I	Pole pair number of inner rotor	-
p_l	Pole pair number of low pole number rotor	-
p_O	Pole pair number of outer rotor	-
p_r	Pole pair number	-
P_{loss}	Total loss in machine	W
q	Number of slots per pole per phase	-
R_g	Reluctance of airgap over one pole pitch	H^{-1}
r_{Ig}	Inner air gap radius	mm
r_{Og}	Outer air gap radius	mm
R_{si}	Stator inner radius	mm
R_{so}	Stator outer radius	mm
S_g	Surface area of airgap per pole	mm^2
S_{im}	Surface area of inner PM per pole	mm^2
S_{om}	Surface area of outer PM per pole	mm^2
T_{avg}	Average torque	Nm
T_E	Electromagnetic torque	Nm
T_{IE}	Inner electromagnetic torque	Nm
T_{IEavg}	Average inner electromagnetic torque	Nm
T_{OE}	Outer electromagnetic torque	Nm
T_{OEavg}	Average outer electromagnetic torque	Nm

t_s	Slot pitch	mm
V_{PM}	PM volume	cm^3
w_{st}	Stator tooth width	mm
Λ_{im}	Inner PM permeance	H/m
Λ_{om}	Outer PM permeance	H/m
Λ_a	Air gap permeance	H/m
Λ_{a0}	Fundamental amplitude of air gap permeance	H/m
η	Efficiency of machine	%
δ	Relative angle between two rotors	rad
θ	Air gap circumferential position	rad
θ_I	Mechanical axis angle of inner rotor	rad
θ_O	Mechanical axis angle of outer rotor	rad
θ_{im}	Inner PM pole arc	rad
θ_{om}	Outer PM pole arc	rad
μ_0	Vacuum permeability	H/m
μ_r	Relative permeability	-
$\rho_{\text{Toruqe/PM}}$	PM utilisation	Nm/cm^3
Φ_1	Resultant flux of SDRPM machine	Wb
Φ_2	Resultant flux of ER PM machine	Wb
Φ_{im}	Inner PM equivalent magnetic flux	Wb
Φ_{om}	Outer PM equivalent magnetic flux	Wb
ψ	Flux linkage	Wb
ω	Electrical velocity of rotor	r/min
ω_I	Electrical velocity of inner rotor	r/min
ω_O	Electrical velocity of outer rotor	r/min

ABBREVIATIONS

CDR	Counter-rotating DR
CR	Counter rotating
CSDPM	Counter-rotating single-stator dual-internal-rotor permanent magnet
CSDPM-FR	CSDPM machine with fixed rotor stack length
CSDPM-FS	CSDPM machine with fixed stator stack length
CW	Concentrated winding
DR	Dual rotor
DRPM	Dual rotor permanent magnet
DW	Distributed winding
EMF	Electromotive force
ER	External rotor
ERSPM	External rotor surface-mounted permanent magnet
FEA	Finite element analysis
FRPM	Flux reversal permanent magnet
FS	Fractional slot
FSCW	Fractional slot concentrated winding
InS	Inner stator
IPM	Interior permanent magnet
IR	Internal rotor
IRSPM	Internal rotor surface-mounted permanent magnet
IS	Integer slot
ISDW	Integer slot distributed winding
MMF	Magnetomotive force

Non-OW	Non-overlapping winding
OS	Outer stator
OW	Overlapping winding
PDRPM	DRPM machine with parallel magnetic circuits
PM	Permanent magnet
PMSM	Permanent magnet synchronous machine
SDRPM	DRPM machine with series magnetic circuits
SFPM	Switched flux permanent magnet
SPM	Surface-mounted permanent magnet
SR	Single rotor
TC	Tooth coil
TW	Toroidal winding
YASA	Yokeless and segmented armature
YCDRPM	Yokeless counter-rotating dual-rotor permanent magnet

CHAPTER 1

GENERAL INTRODUCTION

1.1 Introduction

Since Michael Faraday discovered electromagnetic induction, which led to the development of the first electrical generator [FAR21] [FAR31], electrical machines have been developed over hundreds of years. Electrical machines play a crucial role in converting electrical energy into mechanical energy or vice versa, and are widely used in transportation, aerospace, household appliances, and other fields.

There are three ways to generate magnetic fields in electrical machines. The magnetic field can be generated by the current flowing through the field windings, such as the electrically excited machines, in which the brushes/commutator are often required for the power supply. However, electrical machines that employ commutators and brushes have a limited service life due to friction and sparks generated by the brushes/commutator. The brushless machine, such as the induction machine, can generate magnetic fields through electromagnetic induction. In this type of machine, the current in the rotor needed to generate torque is obtained through electromagnetic induction of the magnetic field of the stator winding. The magnetic field in the brushless machine can also be generated by permanent magnets (PMs). PM materials and PM machines have been developed for several decades. Compared with other machines, the PM machine shows high torque density, high efficiency, simple structure, and easy control. Moreover, PM brushless machines do not require any external power supply or winding structures for excitation, which reduces manufacturing costs and makes them easy to assemble [ZHU07].

Among all the different types of electrical machines, the single-rotor electrical machines are extensively employed in industry due to their simple mechanical structure and ease of assembly [CHA08]. In order to further enhance electrical machine performance and consider more different working conditions, the dual-rotor electrical machines have been proposed [KEL69] [QU03a]. This innovation provides additional insights into electrical machine structural design, aiming to improve performance and adapt to various operational scenarios. Therefore, this thesis focuses on the PM machines with dual rotors, i.e., dual-rotor PM (DRPM) machines. This chapter systematically introduces the single-rotor (SR) and DRPM machines, as shown in Fig. 1.1. Section 1.2 introduces the general SR PM machines from aspects of winding and PM topologies. In order to meet various application requirements, which require dual rotors to operate at the same or different rotational speeds, DRPM

machines with the same or different rotor speeds are proposed. DRPM machines with the same or different rotor speeds are divided into two groups, i.e., DRPM machines with parallel and series magnetic circuits, as will be introduced in Sections 1.3 and 1.4, respectively.

Moreover, specific applications, such as underwater vehicles, wind turbines, and household appliances, require counter-rotating (CR) operation. The CR DRPM machine is proposed to achieve CR operation without the redundancy of multiple machines or additional mechanical systems like bevel-planetary gearboxes. The CR DRPM machine aims to simplify the mechanical configuration and enhance CR system efficiency, which will be introduced in Section 1.5 in detail. Finally, the scope and contributions of this thesis will be shown in Section1.6.

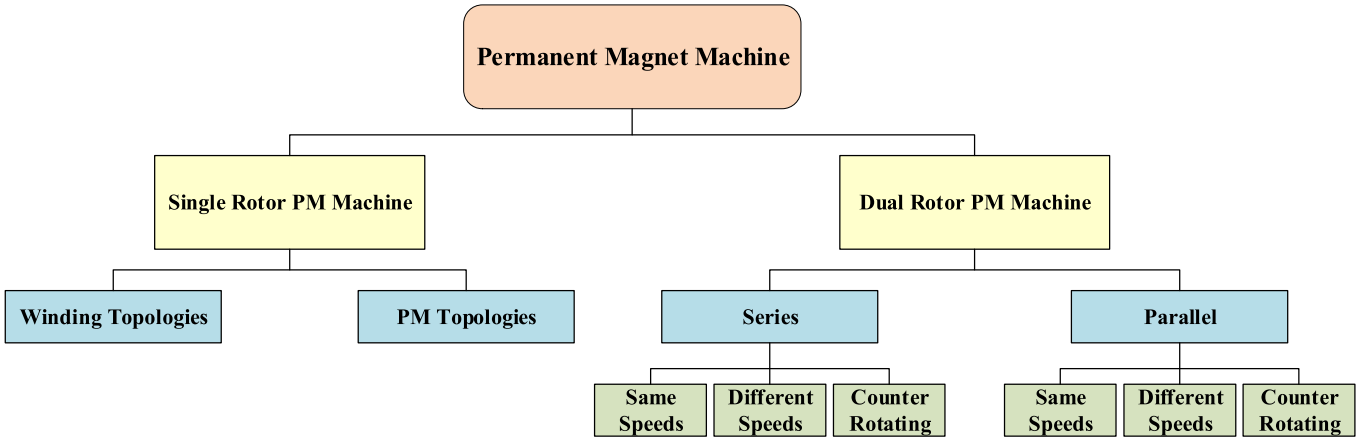

Fig. 1.1. Outline of introduction.

1.2 Single Rotor PM Machines

Due to their simple mechanical structures, single-rotor PM machines are commonly used. They can be classified as either rotor PM or stator PM machines. Figs. 1.2 (a) and (b) illustrate the rotor surface-mounted PM (SPM) and interior PM (IPM) machines, respectively. These two types of machines have high power density, efficiency, and reliability. They are the most popular types of rotor PM machines used. Figs. 1.2 (c) and (d) show typical stator PM machines, i.e., switched flux PM (SFPM) and flux reversal PM (FRPM) machines. Compared to rotor PM machines, stator PM machines locate the PM on the stator together with the stator winding. This causes poor thermal management capability as the stator winding temperature increases. Moreover, the manufacture of stator PM machines is difficult and costly due to their complex stator structure. Thus, this thesis focuses on the rotor PM machines for further investigation. In addition, the single rotor PM machine can be categorized by the rotor position. Figs. 1.2 (a)-(d) show the rotor located inside the stator, which is also called an internal rotor (IR) machine. In contrast, the external rotor (ER) machine locates the rotor outside the stator. The ER SPM machine is shown in Fig. 1.2 (e). The PM machines can also be classified by the direction of the magnetic flux. In

addition to the radial-flux PM machines mentioned above, Fig. 1.2 (f) shows an axial-flux PM machine.

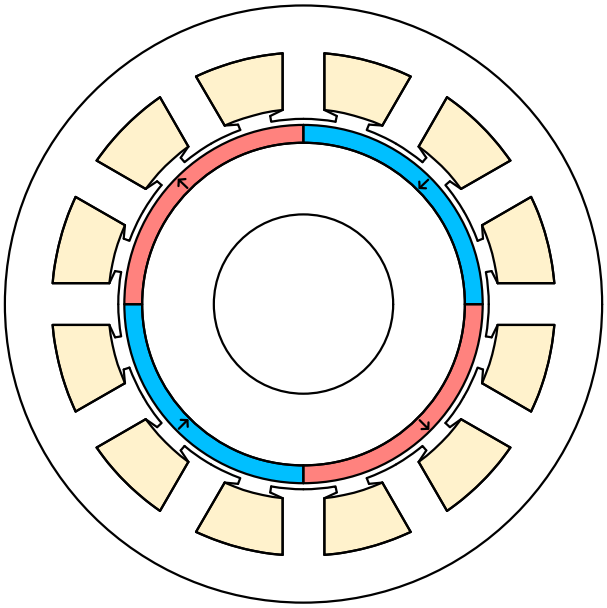

(a) SPM

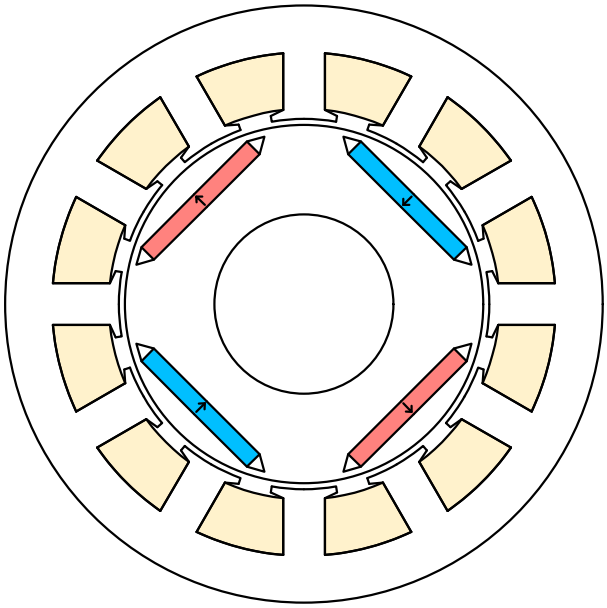

(b) IPM

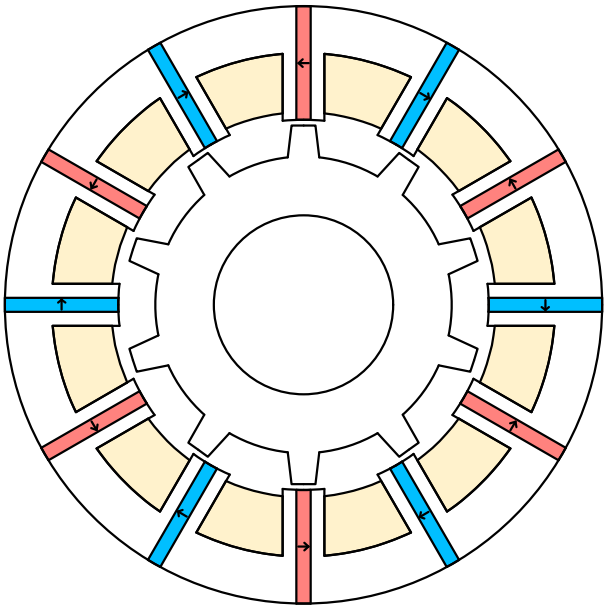

(c) SFPM

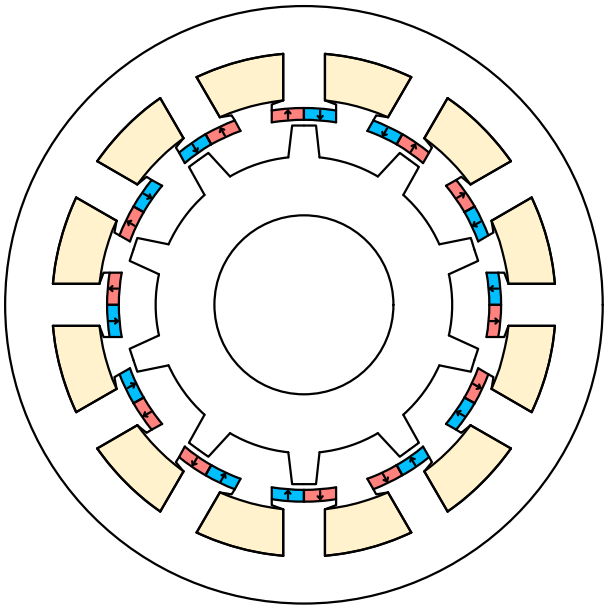

(d) FRPM

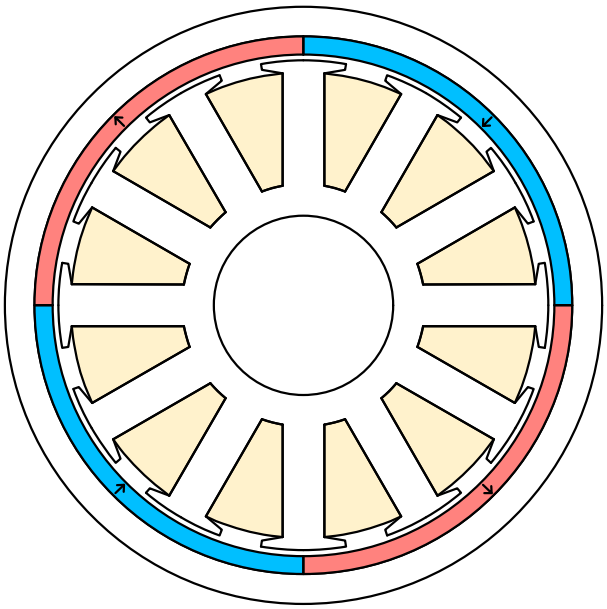

(e) ER SPM

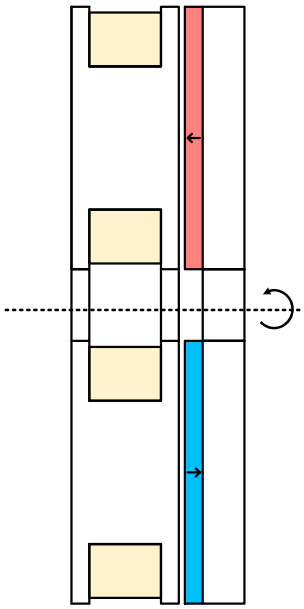

(f) Axial-flux PM machine

Fig. 1.2. General brushless PM electrical machines.

1.2.1 Winding topologies

Fig. 1.2 shows the stator structure of the PM machines with the slots to accommodate windings. The stator windings can be categorized into two types: overlapping winding (OW) and non-overlapping winding (non-OW), which usually depend on the number of slots per pole per phase (q). OW is typically used in integer slot (IS) machines, $q \geq 1$, and it includes two types of winding - concentrated winding (CW) and distributed winding (DW), as depicted in Figs. 1.3 (a) and (b), respectively. Figs. 1.3 (c) and (d) show typical configurations of non-overlapping winding, which include tooth coil (TC) and toroidal winding (TW). It is worth noting that the TC is always a CW. Compared with non-OW, OW has a higher winding factor, and the OW machines have the potential to utilise the reluctance torque. However, OW usually shows a significantly longer end-winding length than non-OW. Thus, the OW machines have higher copper loss and longer axial length, which result in low power density. TC non-OW, generally used in fractional slot (FS) machines, $q < 1$, tends to achieve a high winding factor. TW has the same winding factor as the OW but potentially a shorter end-winding axial length, which may increase the torque density of the OW machine. However, the outside conductors of toroidal windings in single rotor PM machines cannot produce back-EMF, but they contribute to the end-winding length and increase copper loss.

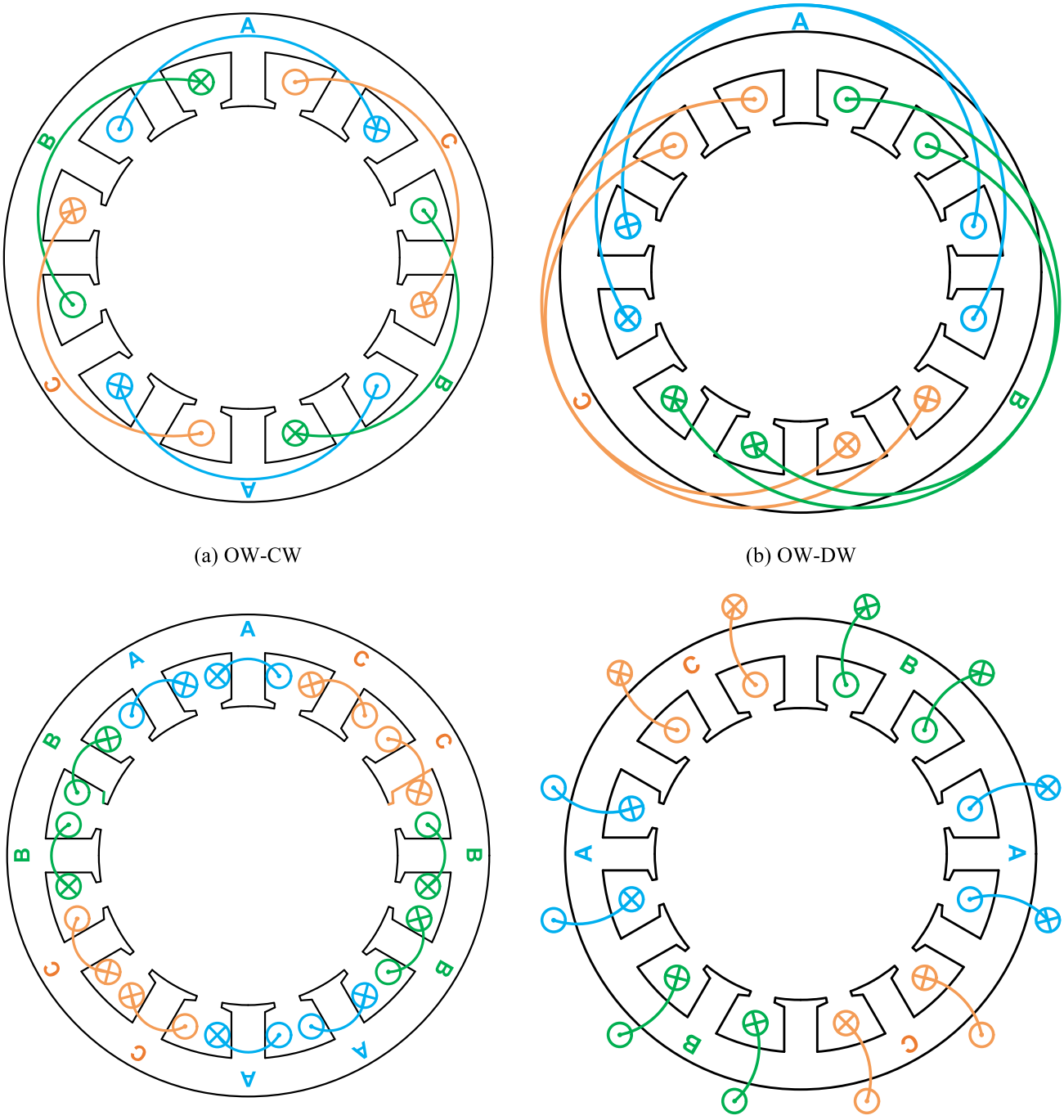

(a) OW-CW (b) OW-DW

(c) Non-OW-TC (d) Non-OW-TW

Fig. 1.3. Winding configurations in PM machines.

1.2.2 PM topologies

This section introduces the PM topologies of the rotor and stator PM machines separately. ER PM machines have become popular in some applications such as wind power, in-wheel drive, etc. since the ER PM machines have larger space utilisation ratios and torque density. However, the ER structure also causes complex mechanical and cooling issues compared to the internal rotor (IR) PM machine. IR and ER PM machines only have rotor position differences, and the torque production mechanism and analysis

method are the same. Thus, this section only discusses IR PM machines.

A. Surface PM rotor

Generally, surface PM rotors have three common structures, i.e., surface-mounted PM, surface-inset PM, and Halbach PM, as shown in Fig. 1.4. The SPM rotor is known for its simple structure and ease of manufacturing. It is considered a non-salient rotor since the permeance of rare-earth PMs is similar to that of the air, which eliminates reluctance torque. Therefore, the torque per PM volume of the SPM machine is relatively lower. The surface-inset PM rotor has iron salience between PMs, which provides a slot for easily fixing PMs, and the rotor saliency can generate reluctance torque. However, the iron saliency also provides a flux path to the PM leakage and takes up the space of the PM arc width, reducing the average torque of the machine. Halbach PM increases PM flux. It consists of magnets that are magnetized in the direction of the flux path. As the Halbach PM provides the magnetic flux path, the amount of rotor iron can be reduced, thereby reducing the overall weight of the Halbach PM rotor.

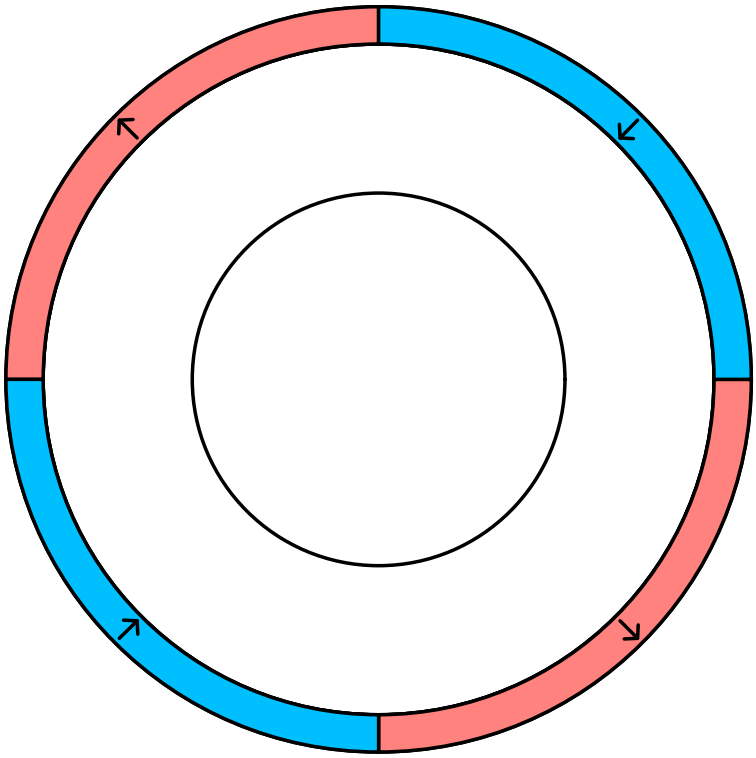

(a) Surface-mounted PM

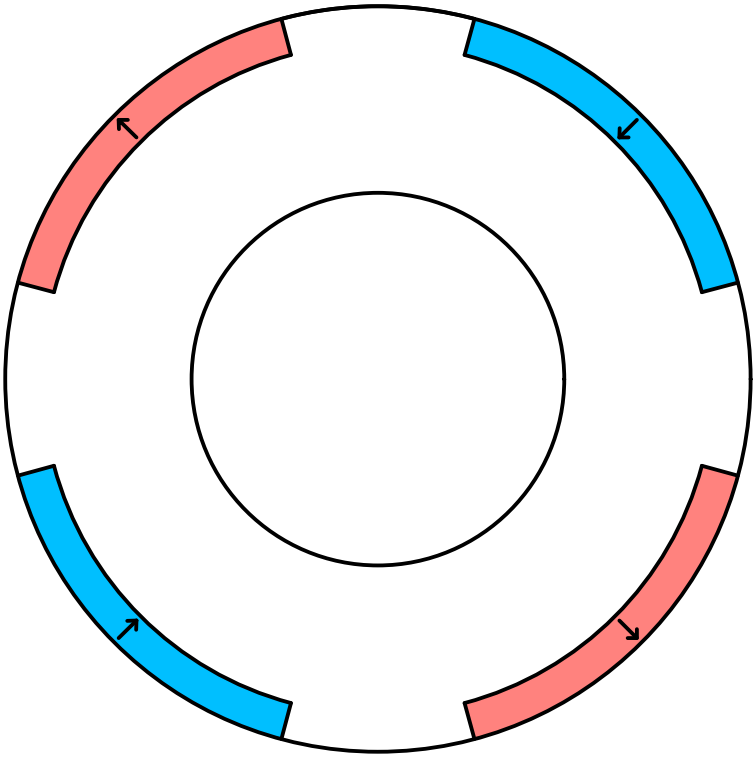

(b) Surface-inset PM

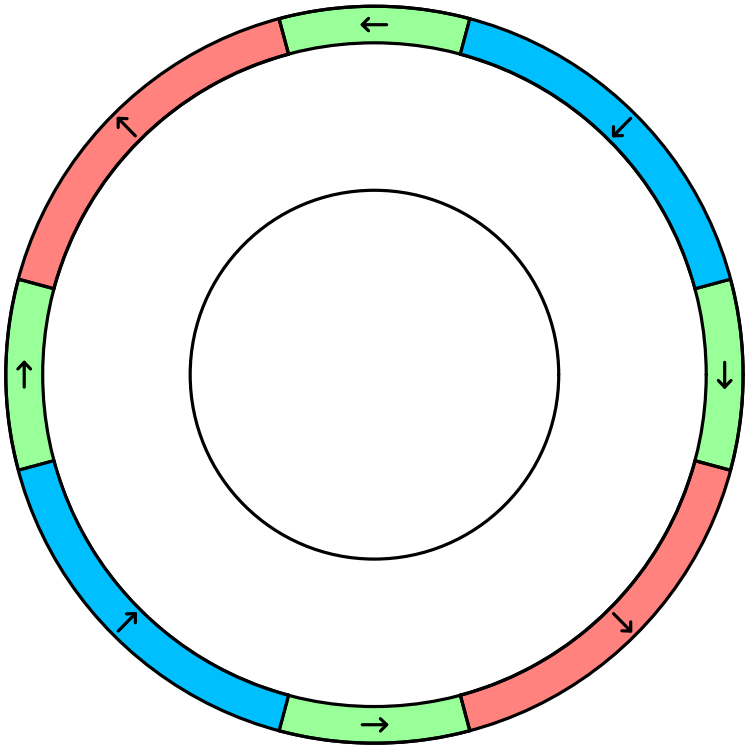

(c) Halbach PM

Fig. 1.4. Surface PM rotor topologies.

B. Interior PM rotor

The PMs are embedded in the iron core of the IPM rotor. Similar to surface-inset PM rotor, the IPM rotor is a salient rotor that can generate reluctance torque to increase torque density and power density especially under flux weakening operation.

Typically, the IPM rotor can be categorized by different PM arrangements into I-type, V-type, U-type, Δ-type, and spoke-type, as shown in Fig. 1.5. For the I-type IPM rotor, PMs are inserted into the rotor iron core in a shape resembling the letter "I". This design aims to optimise the magnetic flux distribution within the rotor. The magnets in an I-type rotor are buried within the rotor core, which helps them withstand high rotational speeds and mechanical stresses. This design is commonly used in applications requiring high torque and good flux-weakening performance. The V-type IPM rotor has PMs arranged in a "V" pattern. Due to the flux-focusing effect, the V-type and spoke-type structures can improve torque performance compared to the I-type IPM rotor. As shown in Figs. 1.5 (c) and (d), the hybrid-type IPM rotors, such as U-type and Δ-type rotors, are designed as a V-type combined with I-type configurations. This topology combines the advantages of V-type and I-type rotors, which utilise the flux-focusing effect and have a low leakage coefficient. However, the complexity of the rotor structure results in difficulty in manufacturing and high cost.

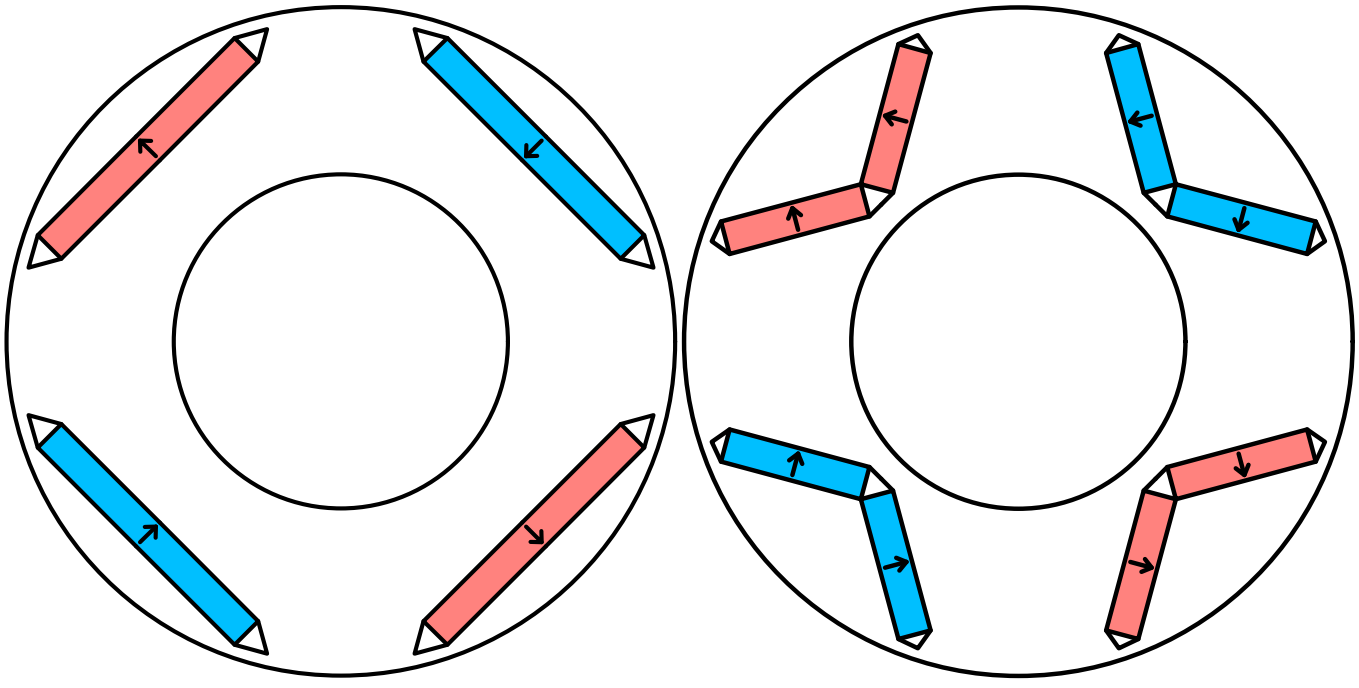

(a) I-type (b) V-type

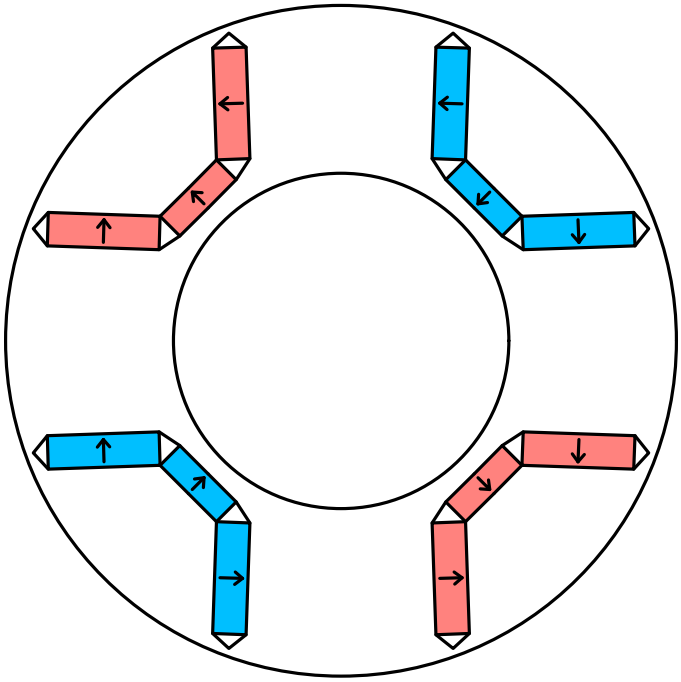

(c) U-type

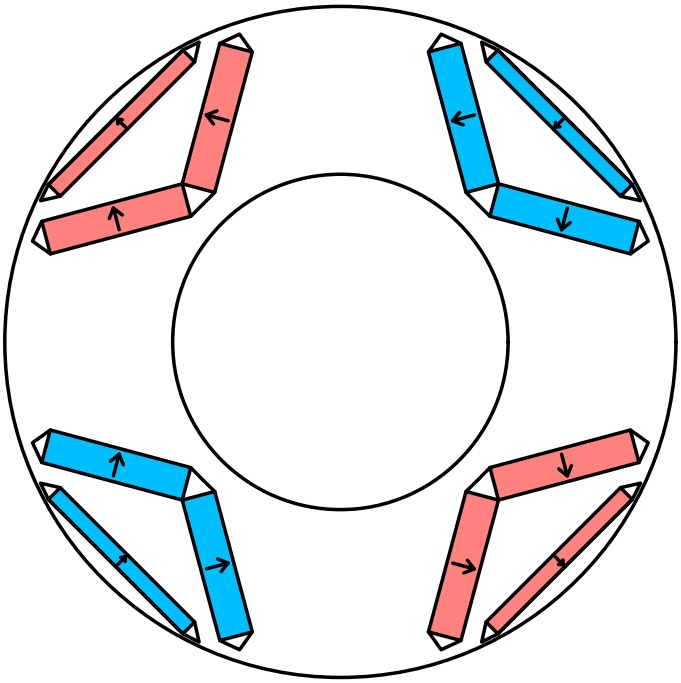

(d) Δ-type

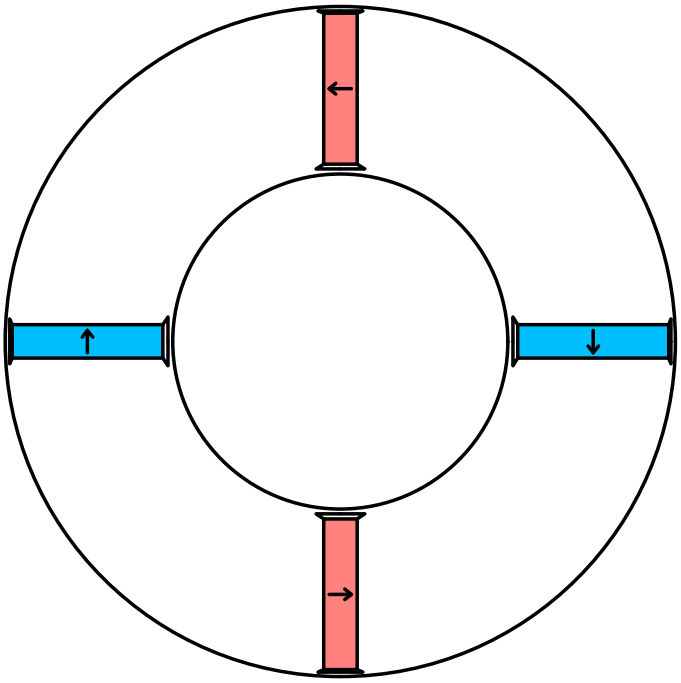

(e) Spoke-type

Fig. 1.5. Interior PM rotor topologies.

C. Stator PM

The stator PM can also be categorised by surface and interior PM configurations. Fig. 1.6 shows the typical stator PM topologies. In the FRPM machine, PMs are mounted on the surface of the inner side of the stator teeth. In the SFPM machines, PMs are embedded in the stator teeth. Usually, stator PM machines utilise field modulation to improve torque density. However, as mentioned in Section 1.2.1, the PMs of stator PM machines are located near the stator winding, which limits their thermal management capability.

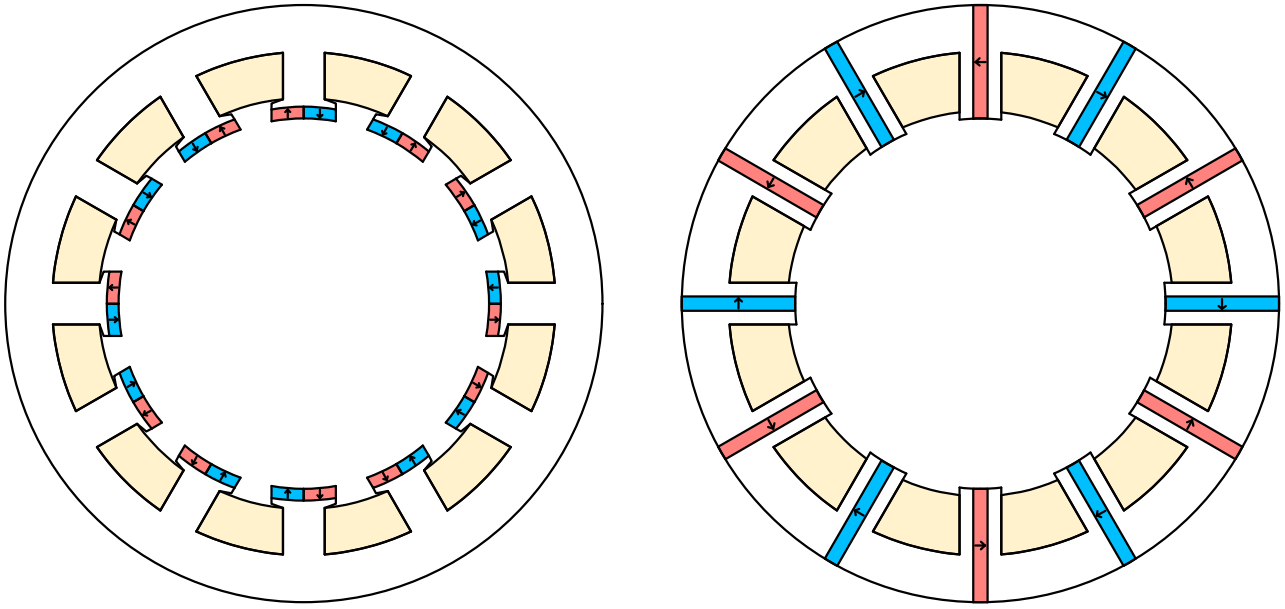

(a) (b)

Fig. 1.6. Stator PM topologies.

1.3 Dual Rotor PM Machines with Parallel Magnetic Circuits

DRPM machines are proposed further to improve the torque density of SR PM machines. The first induction machine with a dual-rotor structure was utilised in 1969 [KEL69]. For the axial-flux PM machines, in 1988, the axial-flux DRPM machine with TW configuration, which is known as the TOURUS machine, was proposed in [SPO88]. The magnetic fluxes generated by two rotors of the TOURUS machine are in parallel [SPO90]. The shared stator yoke is necessary for the TOURUS machine to provide the path for the parallel fluxes, as shown in Fig. 1.7 (a). In [WOO07], the PM patterns of two rotors of the TOURUS machine are changed to the N-N pattern from the N-S pattern, and thus, two rotor PMs generate fluxes in series. In this case, the stator yoke can be completely removed to achieve a yokeless and segmented armature (YASA) structure, as shown in Fig. 1.7 (b).

For the radial-flux PM machine, in 2003, the radial-flux DRPM machine with a shared stator is

proposed in [QU03a] to enhance the torque density (Considering the space requirement of the machine in applications, the torque density in this Thesis is defined by Electromagnetic Torque/Machine Volume, Nm/m³). Similarly, the radial-flux DRPM machine can be divided into two groups based on the magnetic circuits of two rotors in parallel or series. In this thesis, the DRPM machine with parallel magnetic circuits is called the PDRPM machine, in which the magnetic fluxes generated by each rotor are in parallel, as shown in Fig. 1.7 (c). The PDRPM machine can be designed as a combination of two single-rotor PM machines, and the two rotors do not interact with each other. The DRPM machine with series magnetic circuits is called the SDRPM machine. The magnetic fluxes generated by two rotors in the SDRPM machine are in series, in which two rotors are interacted, as shown in Fig. 1.7 (d). The corresponding two rotors can operate at the same or different speeds for all types of DRPM machines. The radial-flux DRPM machine has a slightly lower torque density and efficiency compared to the axial-flux DRPM machine [Qu03b]. However, the axial-flux DRPM machine has several inherent disadvantages, i.e., difficulty in manufacturing, particularly on the steel lamination, high cost, and imbalance of magnetic force between the stator and rotor. Thus, this thesis focuses on the radial-flux DRPM machine for further investigation. To introduce DRPM machines, refer to the flow chart in Fig. 1.8. This section provides an overview of PDRPM machines, while SDRPM machines will be discussed in the following section.

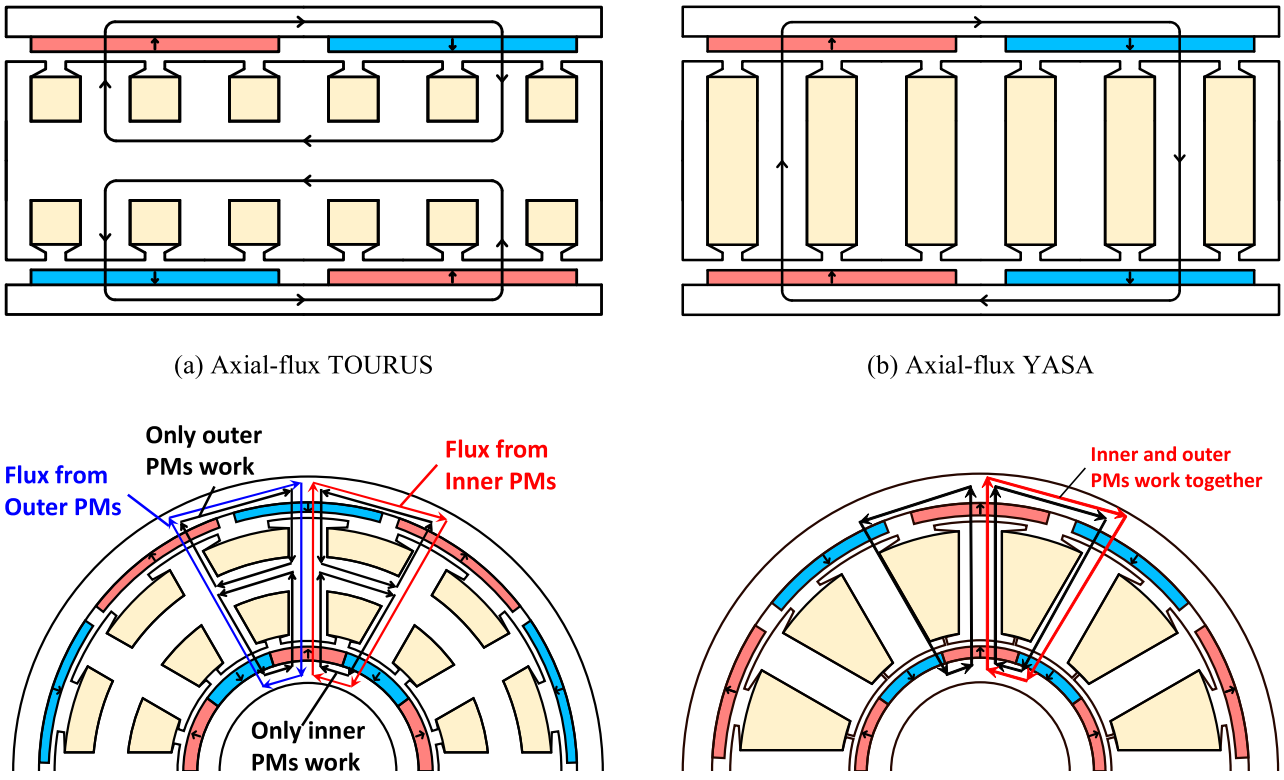

(a) Axial-flux TOURUS

(b) Axial-flux YASA

(c) Radial-flux PDRPM

(d) Radial-flux SDRPM

Fig. 1.7. General DRPM machines.

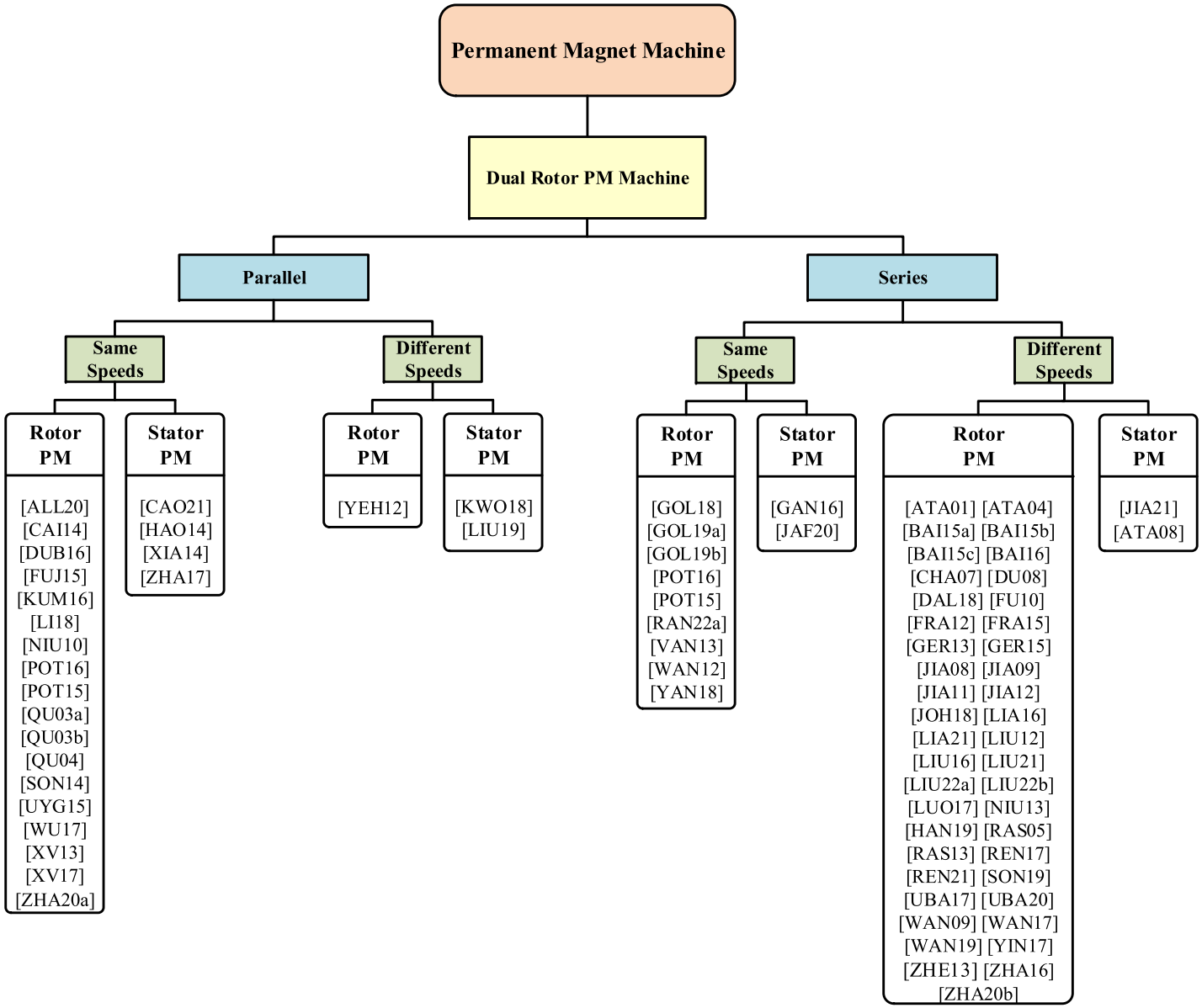

Fig. 1.8. Classification of DRPM machines.

1.3.1 Same rotor speed

The PDRPM machine with two SPM rotors has received extensive attention and research due to its easy manufacturing. [QU03a] first proposed the PDRPM machine with two different rotor combinations, i.e., hybrid-PM and surface-PM rotors, as shown in Figs. 1.9. The output torque is directly related to the air gap surface area for constant electrical and magnetic loadings. Thus, the torque density can be enhanced by increasing the air gap volume from doubled air gaps. The PDRPM machine proposed in [QU03a] uses the non-OW TW. It utilises both working surfaces of the stator core, allowing the conductors of TW on both sides to generate back EMF and significantly shortening the end-winding length. This design enables the machine to use a much higher percentage of the stator winding to produce torque than conventional machines, resulting in improved machine efficiency [QU04]. Two rotors have the same pole number and rotational speeds and are connected by an end disc for easy assembly. However, the sandwiched stator shows poor heat dissipation capacity. [XU13] uses the PDRPM machine for wind power generation and investigates the influence of slot pole number combinations on machine performance [XU17]. Since the magnetic fluxes generated by inner and outer PMs are parallel, the PDRPM machine can be designed equivalently by splitting into an IR PM machine and an ER PM machine for simplicity [UYG15] [SON14]. The same rotor speed DR machines have two rotors of the same rotational speed. Thus, two rotors are fixed on one end disk and mounted on one shaft. This type of machine has only one output despite having two rotors. Therefore, the same-rotor-speed DR machine can be treated as a single-rotor machine, but it splits one rotor into two parts and arranges it on two sides of the stator.

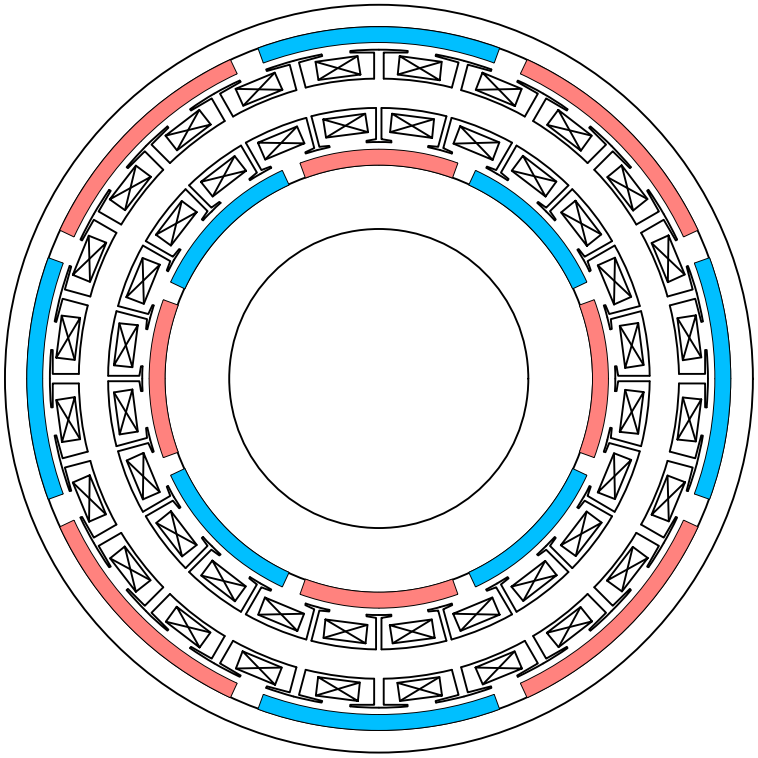

Fig. 1.9. PDRPM machine topologies [QU03a].

Vernier PM machines typically have high coil pitch stator winding configurations, resulting in a long end-winding. The PDRPM machine structure is designed to produce back EMF on both side conductors of the TW and effectively shorten the end-winding length. As a result, the vernier PDRPM machine with TW configuration, as proposed in [NIU10], aims to enhance torque density and reduce copper loss. Additionally, the open stator slot structure is considered to improve the field modulation effect in the vernier PM machine. Based on this topology, the vernier PDRPM machine with the consequent pole is proposed in [ALL20]. The consequent pole configuration increases the torque per PM volume of the vernier PDRPM machine and reduces the cost, as shown in Fig. 1.10.

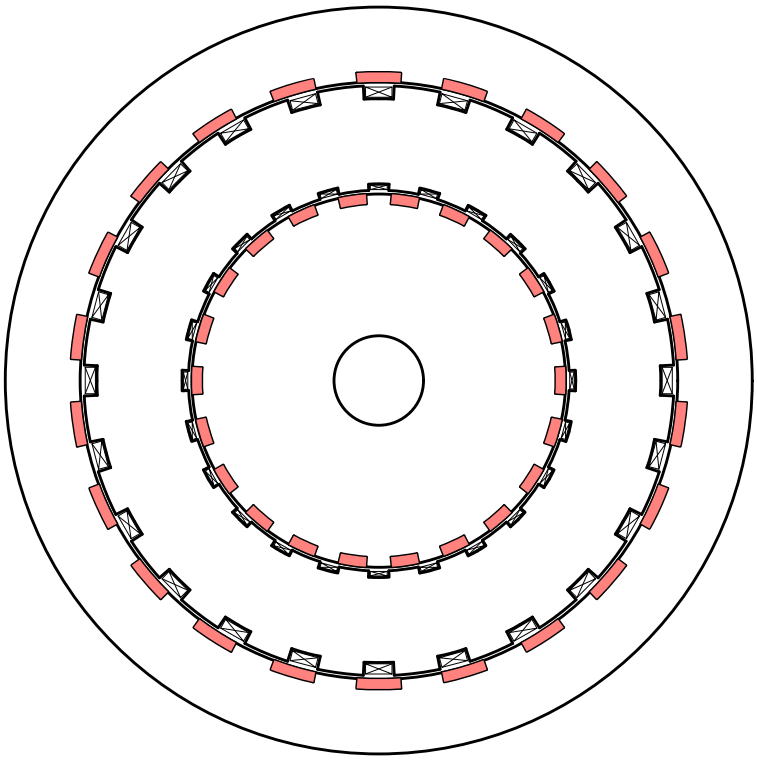

Fig. 1.10. Dual-rotor PMVM with consequent pole [ALL20].

To discuss the different rotor types of the PDRPM machine, [FUJ15] investigates the influence of different rotor types on PDRPM machines. It compares the SPM, surface-inset PM, I-type IPM, and V-type IPM rotors PDRPM machines, as shown in Fig. 1.11. The 3rd-generation Toyota Prius IPM machine is selected as a baseline. The dual surface-inset PM rotors PDRPM machine shows the highest torque among all PDRPM machines, slightly higher than the dual I-type IPM rotors PDRPM machine. In order to use the PDRPM machine in automotive applications, the inner rotor is considered to be an I-type rotor to prevent scattering of the PMs when the inner rotor rotates at high speed and uses the surface-inset PM outer rotor, called dual-SI PDRPM machine, as shown in Fig. 1.11 (e). This machine still shows significantly lower torque than the 3rd-generation Toyota Prius IPM machine with the same PM volume, machine outer diameter and stack length. However, the TW configuration reduces the copper loss due to the short end-winding length, which results in high efficiency. In addition, low back EMF causes low torque and increases the flux weakening speed. Thus, the maximum power of the dual-SI PDRPM machine is higher than that of the 3rd-generation Toyota Prius IPM machine.

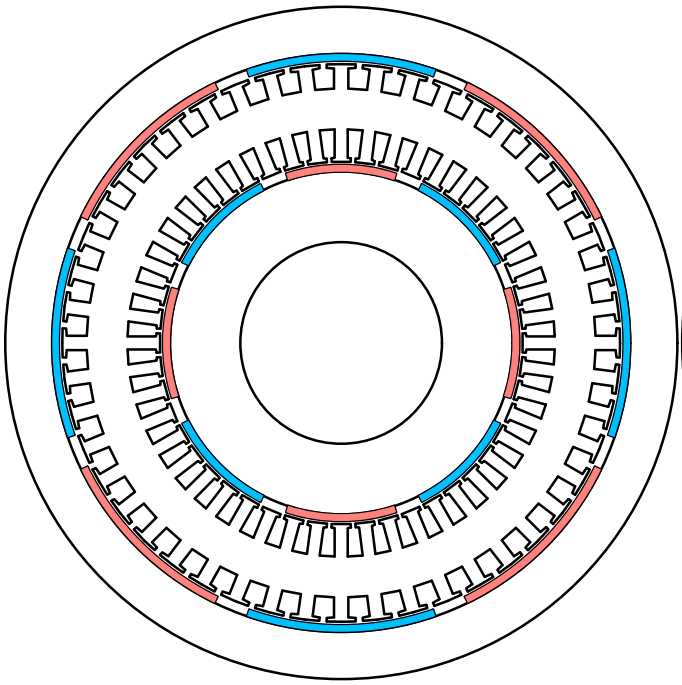

(a) Dual SPM

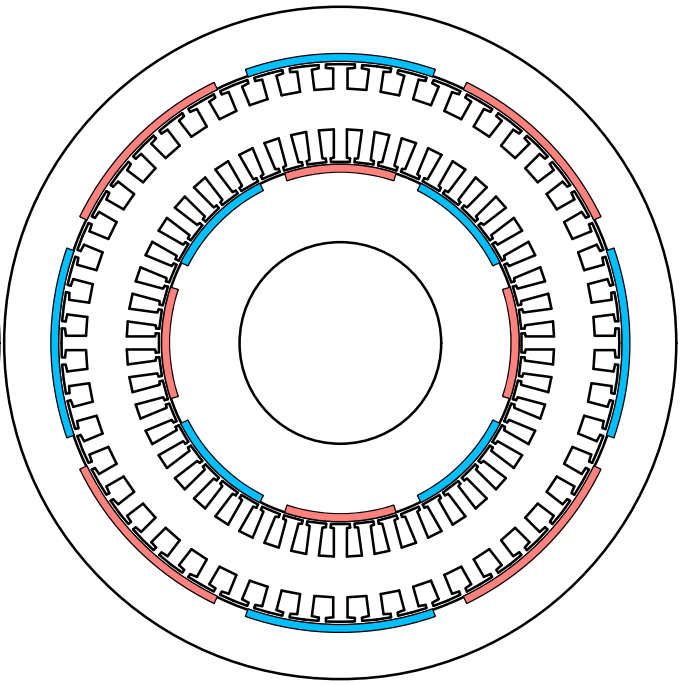

(b) Dual surface-inset PM

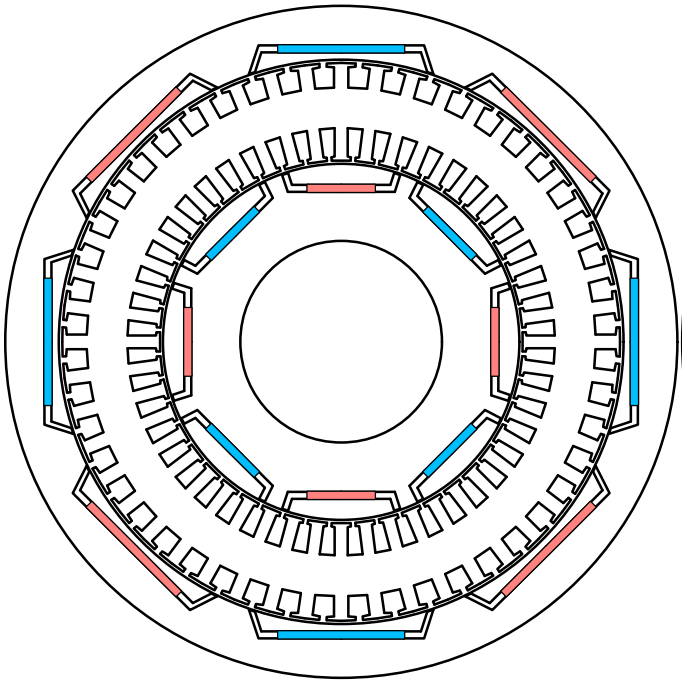

(c) Dual I-type

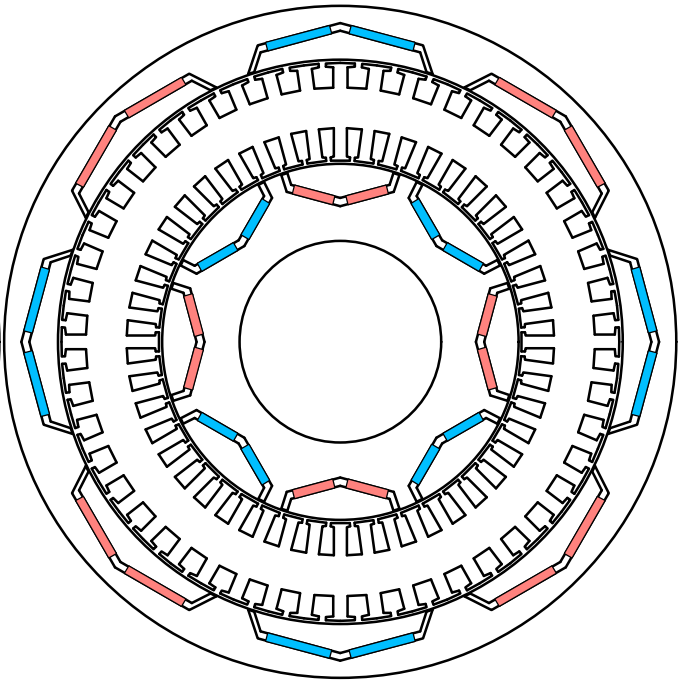

(d) Dual V-type

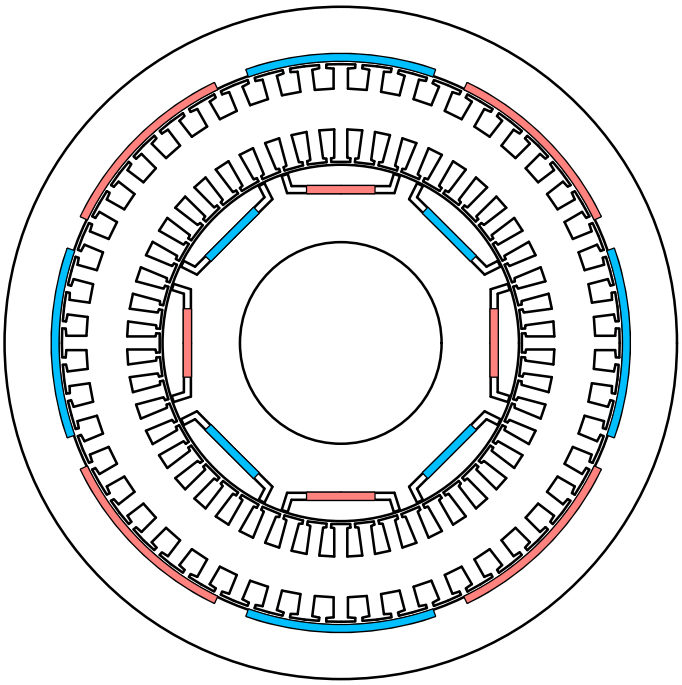

(e) Dual-SI

Fig. 1.11. PDRPM machines with different rotor types [FUJ15].

The Halbach PM arrangement is considered to further increase the torque of the PDRPM machine. The Halbach PM provides the flux path that reduces the amount of rotor iron core. The PDRPM machine has two rotors, and the Halbach PM arrangement significantly reduces the rotor weight, increasing the torque per weight of the PDRPM machine [KUM16] [WU17]. The consequent pole is employed in the PDRPM machine to significantly reduce the PM volume and enhance the torque per PM volume [ZHA20a].

The PM-assisted synchronous reluctance machine has many attractive features for traction application, including the possibility of using low-cost ferrite PMs, high reluctance torque, and optimal flux weakening capability [CAI14]. The DR structure is considered to achieve the PM-assisted synchronous reluctance machine. [LI18] proposed a dual-rotor hybrid machine that integrates the synchronous reluctance rotor and the SPM rotor into a PDRPM machine, which is shown in Fig. 1.12. It shows that the torque of the proposed machine is close to that of the Toyota Prius machine even using the ferrite PM. However, to achieve the maximum torques of both rotors with one set of the shared stator winding, the optimal offset angle between two rotors requires change for different loading conditions, which is inconvenient in automotive applications.

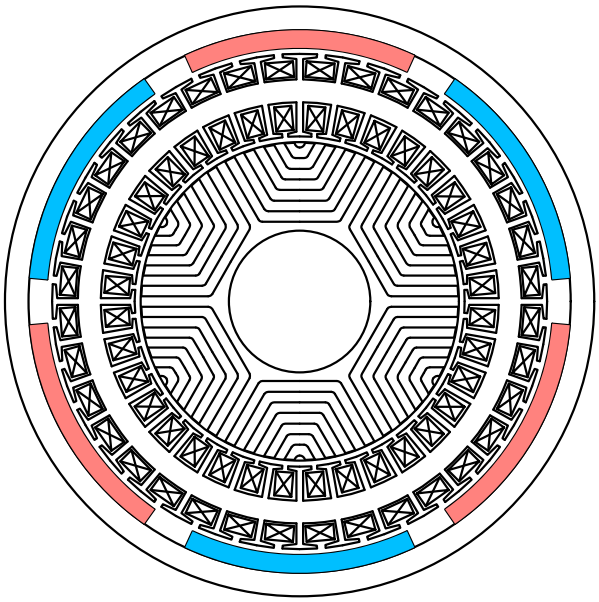

Fig. 1.12. SPM ER and reluctance IR PM-assisted synchronous reluctance machine [LI18].

In addition to the rotor PM PDRPM machine mentioned above, the stator PM switched flux PDRPM machine is proposed in [HAO14] [ZHA17]. The switched flux PDRPM machine shows comprehensive advantages in high torque/power density, efficiency, low cogging torque, and torque ripple [XIA18]. To produce different torques of two rotors of a switched flux PDRPM machine, [CAO21] introduces one set of magnetic coupling winding on the stator to regulate the PM fields in two side air gaps, as shown in Fig. 1.13. However, the PMs and several sets of windings are located on the stator, which causes the temperature rise of the winding which affects the PM performance. As a result, the thermal management capacity of the machine is significantly reduced, and the sandwiched stator makes heat dissipation more difficult.

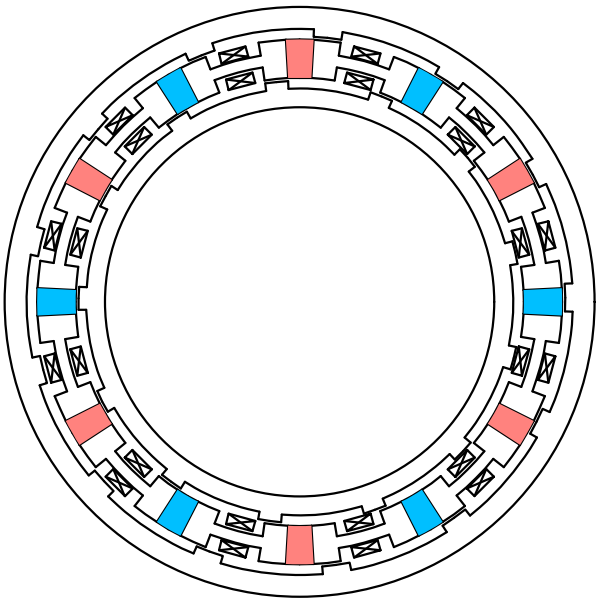

Fig. 1.13. Dual-rotor FSPM machine [ZHA17].

1.3.2 Different rotor speeds

As discussed in the pervious section, the same speed inner and outer rotors of the DRPM machine are fixed on the same shaft, resulting in a single output port despite having two rotors. The concept of dual-mechanical ports in electrical machines was initially introduced by [XU05], as shown in Fig. 1.14. This method allows the DRPM machine to set two rotors on separate shafts, accommodating different operational requirements [XV09]. This configuration offers a space and cost-efficient alternative to utilising two PM machines, as the DRPM machine can operate as two independent outputs when two rotors operate at different speeds.

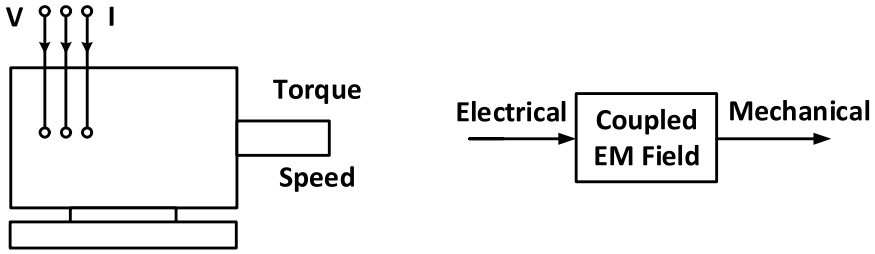

(a) Conventional electrical machine

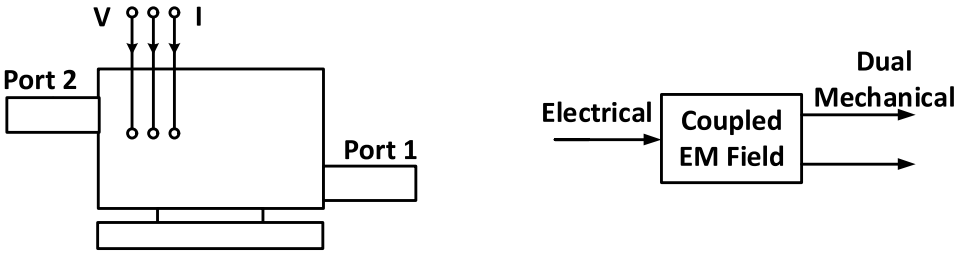

(b) Dual-mechanical-port electrical machines

Fig. 1.14. Dual-mechanical-port electrical machines [XU05].

In the application described in [YEH12], the PDRPM machine with two different-speed rotors is used in air conditioning systems. Two different-speed rotors are mounted on different shafts. The machine achieves various operational modes for each rotor by configuring different stator winding groups for the corresponding rotor, enabling them to operate separately as condensers and evaporators, as shown in Fig. 1.15 (a). Furthermore, [KWO18] proposes integrating vernier and flux-reversal PM machines into a PDRPM machine for washing machines. This integration allows the PDRPM machine to transition between washing and dehydrating modes, each requiring different operating conditions. There is a non-magnetic barrier between the sandwiched stator, which was designed to eliminate magnetic coupling of the inner and outer parts [KWO18]. The outer machine is a Vernier FRPM machine. A consequent-pole type was used on the stator. The inner machine is a conventional FRPM machine. Without the barrier, the machine would experience magnetic flux coupling, causing back EMF distortion and unwanted torque

generation on the unintended part. The outer machine is designed for the washing mode with high torque and low-speed requirements. The inner machine is designed for dehydrating mode with low torque and high-speed requirements. These configurations require two sets of stator windings and inverters to control two rotors separately.

For the stator PM PDRPM machine with different-speed rotors, [LIU19] proposed a switched flux PDRPM machine with different pole number rotors, as shown in Fig. 1.15 (c). The optimised machine increases the sinusoidal degree of the waveform of no-load back EMF and reduces the cogging torque.

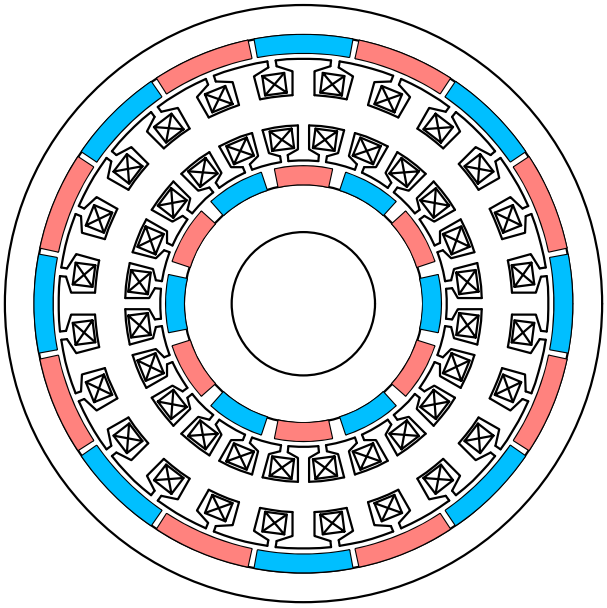

(a) [YEH12]

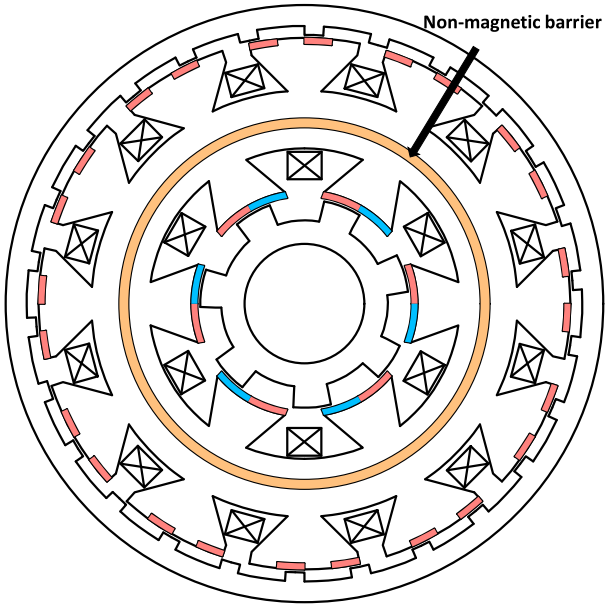

(b) [KWO18]

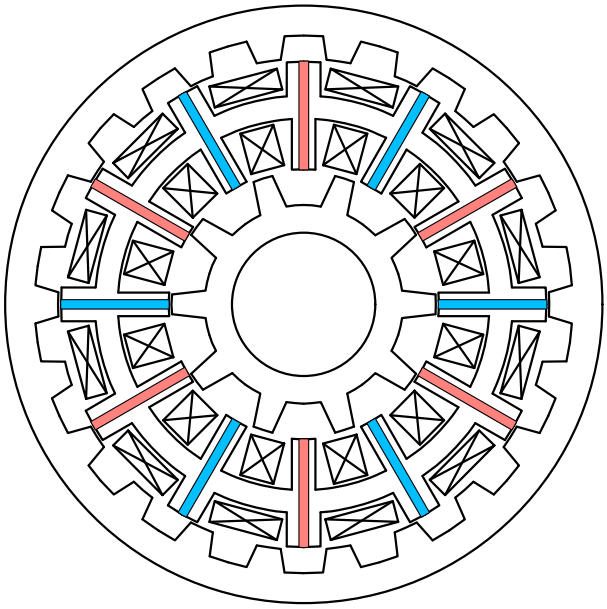

(c) [LIU19]

Fig. 1.15. PDRPM machine with different-speed rotors.

1.4 Dual Rotor PM Machines with Series Magnetic Circuits

1.4.1 Same rotor speed

In contrast to the PDRPM machine, the magnetic circuits of the two rotors of the SDRPM machine are in series. The PDRPM machine integrates the features of both IR and ER PM machines by connecting the inner and outer magnetic circuits in parallel. However, this design necessitates a shared stator yoke, which increases iron losses and reduces slot areas. Moreover, the fluxes generated by PMs on each rotor are superimposed on the stator yoke. Thus, the thick stator yoke is required to avoid severe magnetic saturation, further reducing the stator slot area. To address this issue, the radial-flux yokeless SDRPM machine is proposed in [VAN13], as illustrated in Fig. 1.16. Different from the PDRPM machine, the SDRPM machine maintains the same flux pattern for inner and outer PMs, aligning the flux directions and the polarities of the MMFs in the inner and outer air gaps. Thus, the fluxes generated by PMs flow through two air gaps and rotor yokes [WAN12]. This design allows to remove the stator yoke, significantly reducing weight and iron losses. The yokeless SDRPM machine employs FSCW TC [VAN13]. This configuration offers a large slot area, allowing the copper wire to be wound directly onto the stator cores, thus improving the slot fill factor and reducing the weight of the machine.

The SDRPM machine utilises the Halbach PM arrangement [GOL18] [GOL19a] [GOL19b] to further increase torque density. The proposed SDRPM machine with Halbach PM shows high power and torque densities. Eliminating the stator yoke provides a large slot area for inserting cooling channels into the stator slot, which improves heat dissipation [GOL19a]. The Halbach PM arrangement provides the flux path, allowing the two rotors of the SDRPM machine to reduce the amount of iron core, significantly reducing the weight of the machine. Comparison in [GOL18] shows that the Halbach PM SDRPM machine has the highest torque density due to having the lowest active mass weight compared to IR, ER, and dual-stator Halbach PM machines. A sub-domain model for the SDRPM machine was developed by [GOL19b], which demonstrates good agreement with finite element analysis (FEA) results, making it useful for the initial design stages of the SDRPM machine.

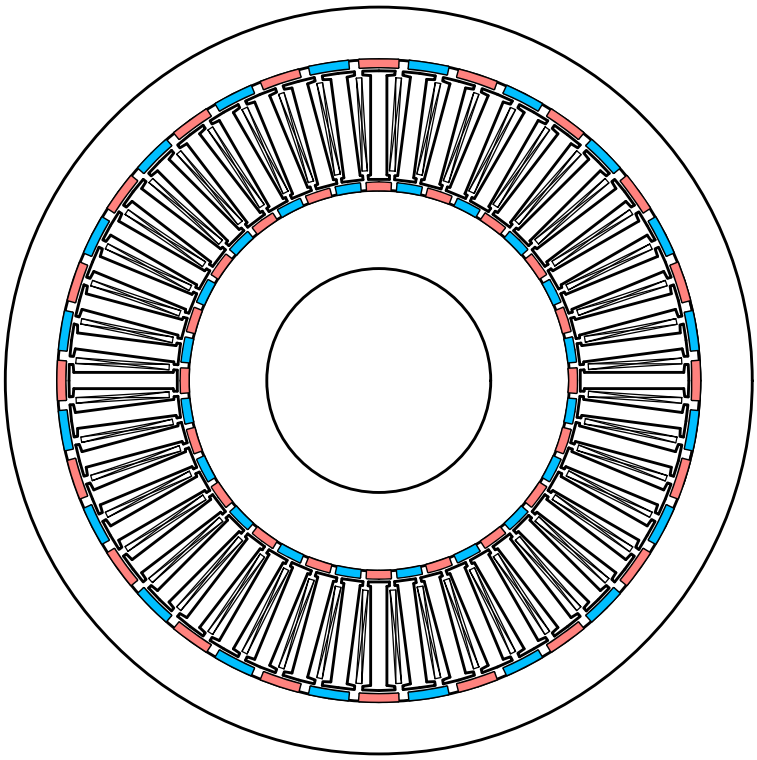

Fig. 1.16. Yokeless SDRPM machine [VAN13].

When comparing IS PDRPM machines and IS SDRPM machines, the IS TW PDRPM machines demonstrate superior performance in megawatt-scale wind power generation applications compared to IS TC SDRPM machines [POT16]. This advantage is due to the TW configuration in IS TW PDRPM machines, which reduces the length of end-windings. Consequently, for high-power applications, the copper loss and active mass of end-windings in IS TC SDRPM machines are significantly higher than those in IS TW PDRPM machines [POT15]. In contrast, FS TC SDRPM machines show higher torque than FS TC PDRPM machines in low-power applications since the yokeless modular structure offers a larger slot area, allowing for higher input current under the same copper loss conditions [RAN22a].

In addition to the rotor PM SDRPM machine mentioned above, stator PM switched flux SDRPM machines are proposed in [GAN16] [JAF20], as shown in Fig. 1.17. The stator PM provides the flux path to connect the inner and outer rotors. Two same-speed rotors of the stator PM switched flux SDRPM machine are displaced by half a pole pitch to maintain symmetry for flux flow. The stator PM switched flux SDRPM machine achieves higher saturation limits as the effective airgap is twice that of the conventional machine. In [JAF20], the split-tooth stator is employed, and the PM is located in the middle of two stator sides to provide a flux path, as shown in Fig 1.17 (b). The windings are wrapped on the stator parts toroidally. The cogging torque ripple of the proposed machine is less than that of the SFPM machine. However, the torque of the stator PM switched flux SDRPM is lower in the case of the same current density compared with the conventional SFPM machine.

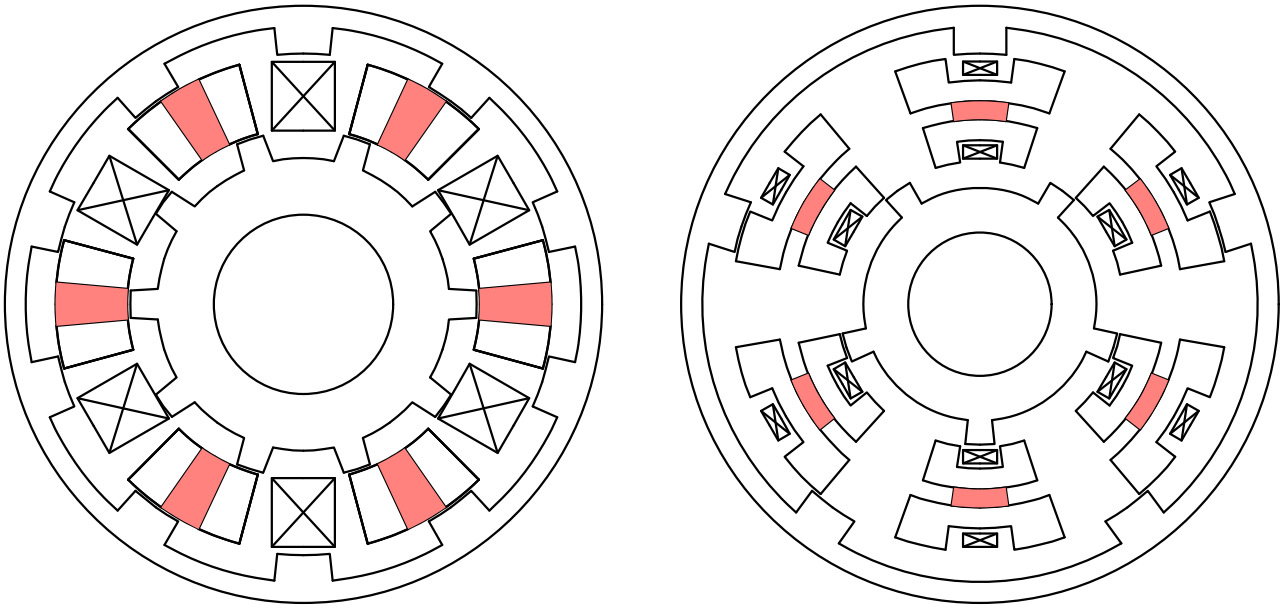

(a) [GAN16] (b) [JAF20]

Fig. 1.17. Switched flux SDRPM machines.

1.4.2 Different rotor speeds

In contrast to the PDRPM machine, the magnetic circuits of the two rotors in the SDRPM machine are series, resulting in magnetic interaction between the rotors. Two different-speed rotors of the SDRPM machine must employ field modulation to achieve torque transmission.

[ATA01] first proposed a novel high-performance magnetic gear for efficient energy transmission, as shown in Fig. 1.18. The magnetic gear is constructed by a lower number of poles in the inner SPM rotor, a higher number of poles in the outer SPM rotor, and sandwiched stator modulating segments. The harmonic order of flux density produced by either the high or low number of poles rotor PMs is given by [ATA04] [ATA06] [RAS05] [JIA09]:

$$p_{m,k} = |mp \pm kN_s|$$

$$m = 1,3,5, \ldots$$

$$k = 0,1,2,3, \ldots \tag{1.1}$$

where N_s is the number of stator modulating segments, and p is the number of PM pairs of the rotor. In addition, the rotational speed of magnetic field generated by PM can be calculated as:

$$\omega_{m,k} = \frac{mp}{mp \pm kN_s}\omega_r \tag{1.2}$$

where ω_r is the rotational speed of the PM rotor. Thus, in order to transmit the torque between two different pole rotors at different speeds. The pole pair number of the other PM rotor must be equal to the

harmonic order when $k \neq 0$, and the corresponding gearing ratio G_r with the fixed stator modulating segments can be expressed as:

$$G_r = \frac{mp}{|mp \pm kN_s|} \tag{1.3}$$

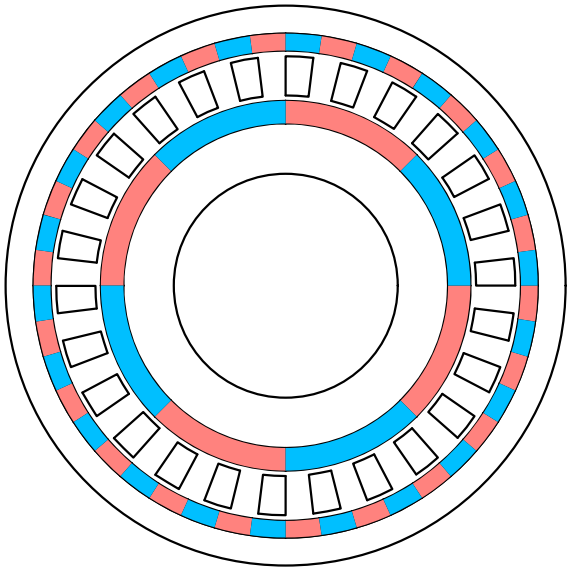

Fig. 1.18. A novel high-performance magnetic gear [ATA01].

Based on the magnetic gear, [CHA07] introduced an inner stator (InS) magnetic-geared PM machine, as depicted in Fig. 1.19 (a). This machine utilises field modulation to reduce speed or increase torque by seven times. Additionally, if the load torque exceeds the peak torque transmission capacity, the magnetic gear will slip instead of experiencing mechanical breakage. This machine has been comprehensively analysed in [JIA08] [DU08] [RAS13] [FRA12] [FRA15] [GER13] [GER15]. [JIA09] applied this InS magnetic-geared PM machine in wind power, yielding several benefits:

- The low-speed ER design allows direct coupling with wind blades for efficient power capture.
- The integration of a coaxial magnetic gear enables the PM brushless generator to operate at high speeds, achieving high power density.
- The magnetic gear provides physical isolation between the inner and outer rotors, reducing maintenance costs and acoustic noise.

Despite these advantages, the mechanical structure of the machine is complex, involving four coaxial components, two sets of PM arrays, and three layers of air gaps. This complexity results in low reliability, too much use of PMs, challenging manufacturing processes, and high costs. Then, [ATA08] proposed an outer stator (OS) magnetic-geared PM machine that integrates a magnetic gear and a PM machine, as shown in Fig. 1.19 (b). Compared with the machine shown in Fig. 1.19 (a), this machine sets the modulation pole pieces as a rotational part. The outer PMs of the magnetic gear are mounted on the stator

to save an air gap, which is more conducive to manufacturing realisation. The stator is located on the outermost side, which is more conducive to the heat dissipation of the armature winding. To simplify the mechanical structure of the magnetic-geared machine, [JIA11] [JIA12] directly wound the stator winding on the stationary modulation ring to realise the intermediate stator magnetic-geared machine, as shown in Fig. 1.19 (c). However, the intermediate segmented modulation ring employs the DW, making the assembly more difficult. Moreover, the intermediate stator has poor heat dissipation capability compared with the Ins and OS structure [DAL18]. Therefore, InS and OS magnetic-geared PM machines are the most popular types among all magnetic-geared machines.

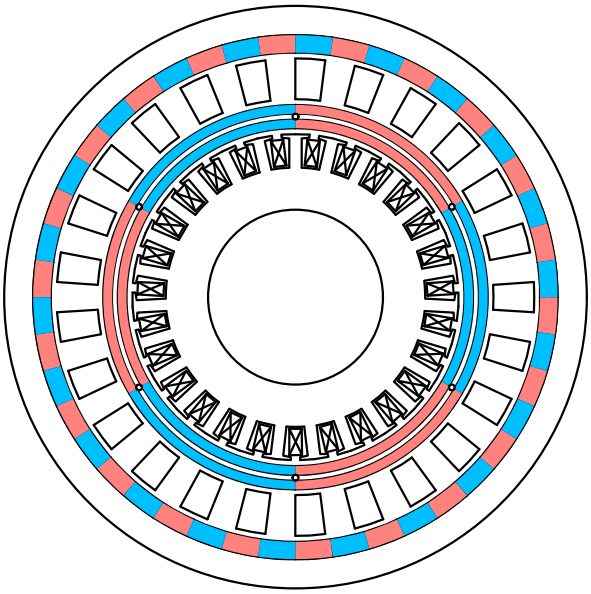

(a) InS magnetic-geared machine [CHA07]

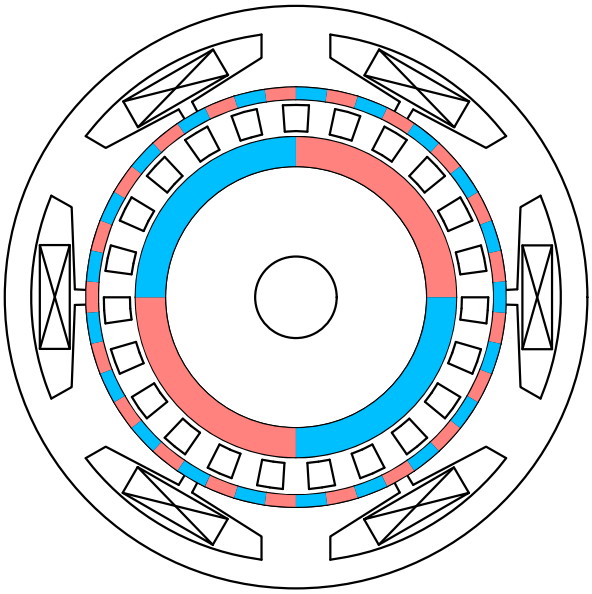

(b) OS magnetic-geared machine [ATA08]

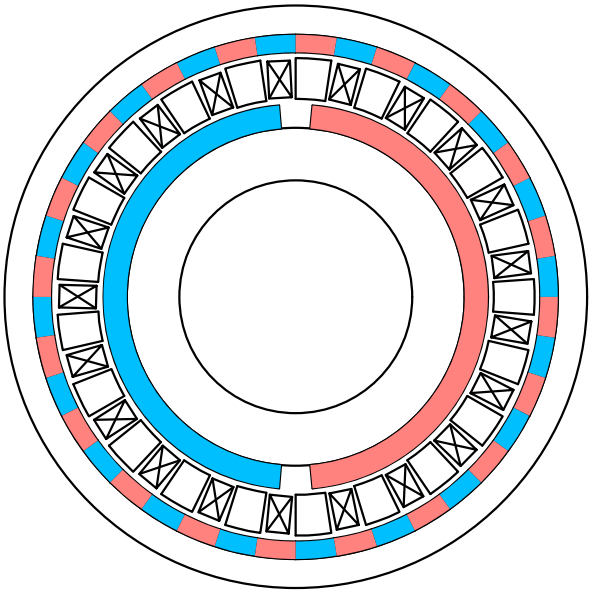

(c) Intermediate stator magnetic-geared machine [JIA11]

Fig. 1.19. Magnetic-geared PM machines.

For the InS magnetic-geared machine, [WAN09] removes the inner rotor, and the inner magnetic field is only generated by the armature reaction, as shown in Fig. 1.20. This design reduces costs and simplifies the mechanical structure by saving an air gap, one rotor, and one set of PMs. Extensive research has been conducted on this machine [FU10] [UBA17] [UBA20] [WAN17a] [LIU12] [ZHA20b]. However, compared to the OS magnetic-geared machine, the InS magnetic-geared machine presents challenges in assembling the ER and rotational modulation ring with the inner stator.

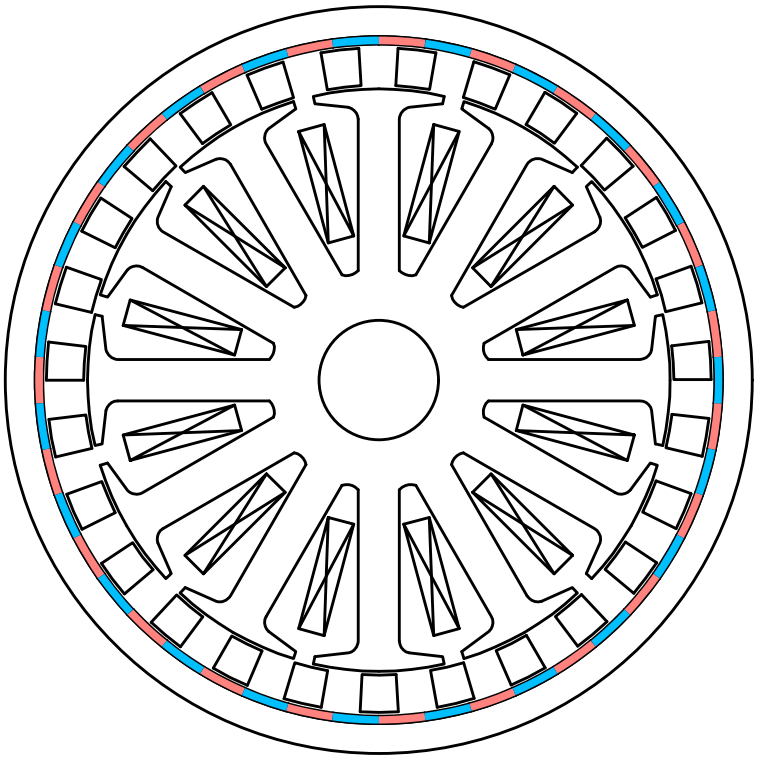

Fig. 1.20. InS magnetic-geared machine [WAN09].

Similarly, for the OS magnetic-geared machine, [ZHE13] remove the PM on the stator of the OS magnetic-geared machine in [ATA08], and the outer magnetic field is only generated by the armature reaction [BAI15a] [BAI15b] [BAI15c] [BAI16] [LIU21], as shown in Fig. 1.21. This machine is proposed in [ZHE13] and comprehensively analysed in [BAI15a]. The analytical modelling of this machine is developed in [YIN17]. The consequent pole rotor is employed to reduce the PM amount [BAI15b]. [BAI15c] replaces the steel modulation ring with PM, and the inner rotor can be salient rotor to enhance the rotor mechanical strength. [BAI16] inserts the nonmagnetic metal bar into the modulation ring to enhance the mechanical strength of the modulation ring. [LIU21] employs one more modulation winding on the stator to improve the field modulation effect to increase the torque.

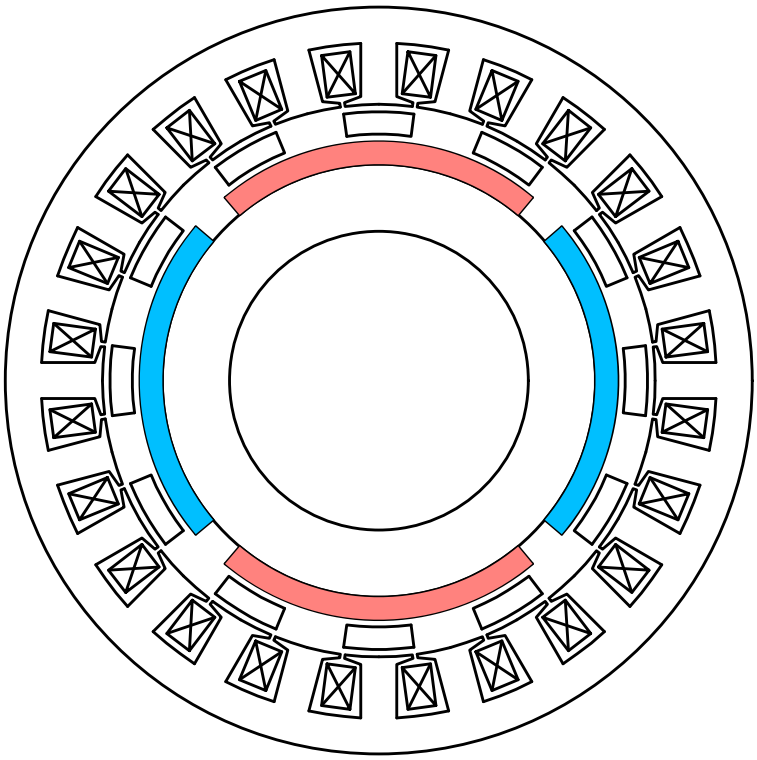

Fig. 1.21. OS magnetic-geared machine [ZHE13].

In [Niu13], a consequent pole OS magnetic-geared machine is developed, which features the consequent poles on both the inner rotor and the modulation ring [NIU13] [LUO17] [LIU16] [WAN19]. This machine utilises two sets of stator windings to enhance the field modulation effect, as illustrated in Fig. 1.22. It is applied in electrical continuously variable transmission systems [NIU13] and wind energy conversion systems [LIU16] [WAN19] [LUO17]. The proposed machine with the doubly bidirectional flux-modulation effect increases torque density. Additionally, it enables various-speed constant-amplitude voltage operation over a wide speed range, providing stable DC power with a simple uncontrolled diode rectifier. The main advantages include a simple structure without requiring a gearbox and brush system.

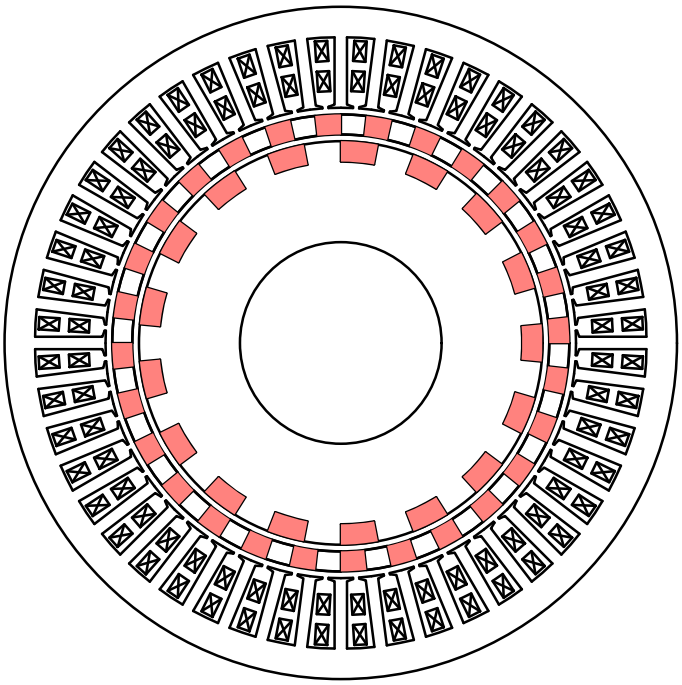

Fig. 1.22. OS magnetic-geared machine with consequent pole [NIU13].

The spoke PM array is employed in magnetic-geared IR PM machine to increase the torque density [LIA21] [REN17] [HAN19] [REN21] [LIU22a] [LIU22b] [LI16a]. This magnetic-geared IR PM machine with spoke PM is shown in Fig. 1.23. Spoke PMs are located on the modulation ring to utilise the flux focusing, and two sets of stator windings are employed to utilise doubly bidirectional flux-modulation effect. Thus, this type of machine shows significantly high torque and power densities. Generally, the topologies evolution of the magnetic-geared machines is shown in Fig. 1.24.

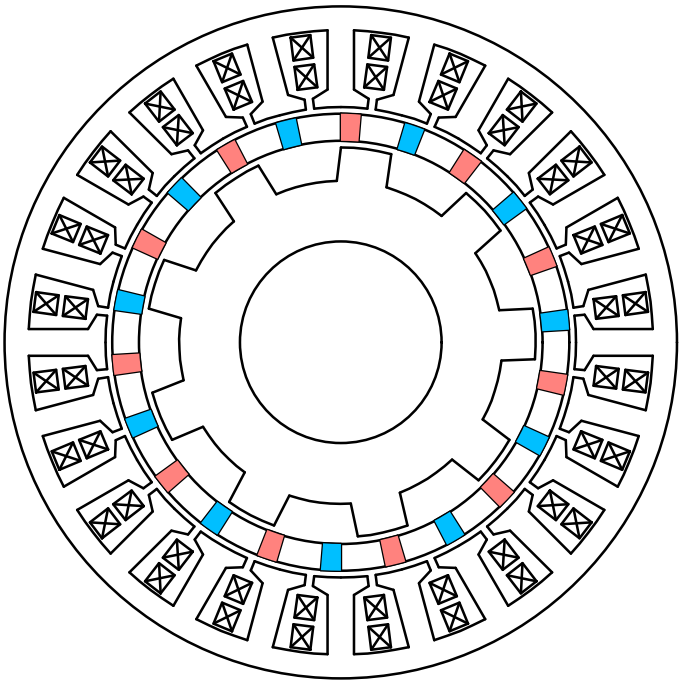

Fig. 1.23. OS magnetic-geared machine with spoke PM [REN21].

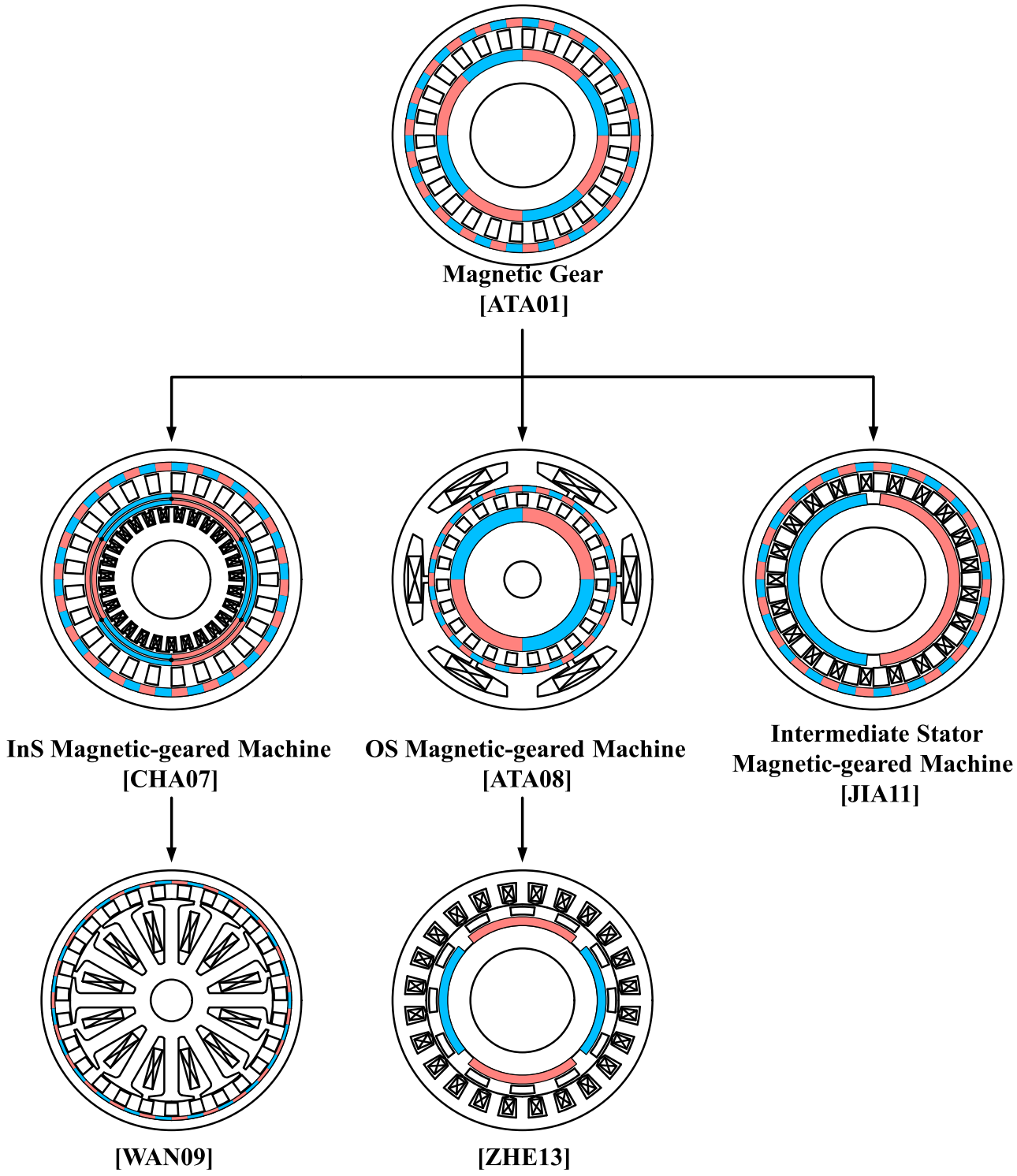

Fig. 1.24. Topologies evolution from magnetic gear to some other magnetically-geared machines.

1.5 Counter-Rotating Dual Rotor PM Machines

Counter-rotating (CR) machines are extensively utilised to enhance the performance of specialised industrial applications, including underwater vehicles, wind turbines, and household appliances. [HOL94] introduced a CR ring thruster for underwater vehicles, where two thruster rings rotate in opposite

directions to mitigate roll motion during underwater propulsion. It has been optimised in [SAS98], as shown in Fig. 1.24. This CR propulsion system prevents single-direction rotational water flow, which can cause underwater vehicles to yaw in one direction [LIU18]. The counteracting torques generated by the two CR propellers enable precise and straight movement of the vehicle [SHI20]. Additionally, in axially arranged CR propellers, the aft propeller recovers rotational energy losses from the fore propeller, resulting in an efficient propulsion system [HOU18]. Propulsion efficiency is further improved when the fore propeller rotates faster than the aft propeller, as compared to both propellers rotating at the same speed [MAL13] [YAN96]. Traditionally, CR underwater vehicle propulsion is driven by either two separate machines or a single machine integrated with a bevel-planetary mechanical gearbox, as shown in Fig. 1.25. This setup is costly, heavy, and space-consuming, and its complex mechanical structure necessitates frequent maintenance.

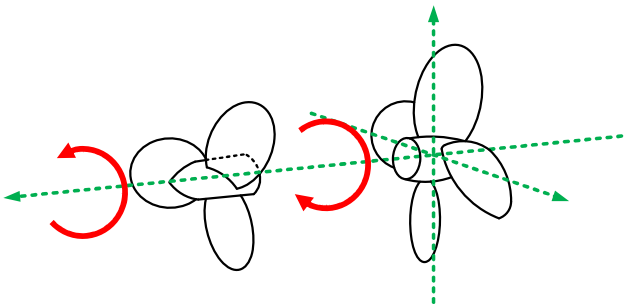

Fig. 1.24. Counter-rotating propellers for underwater propulsion [SAS98].

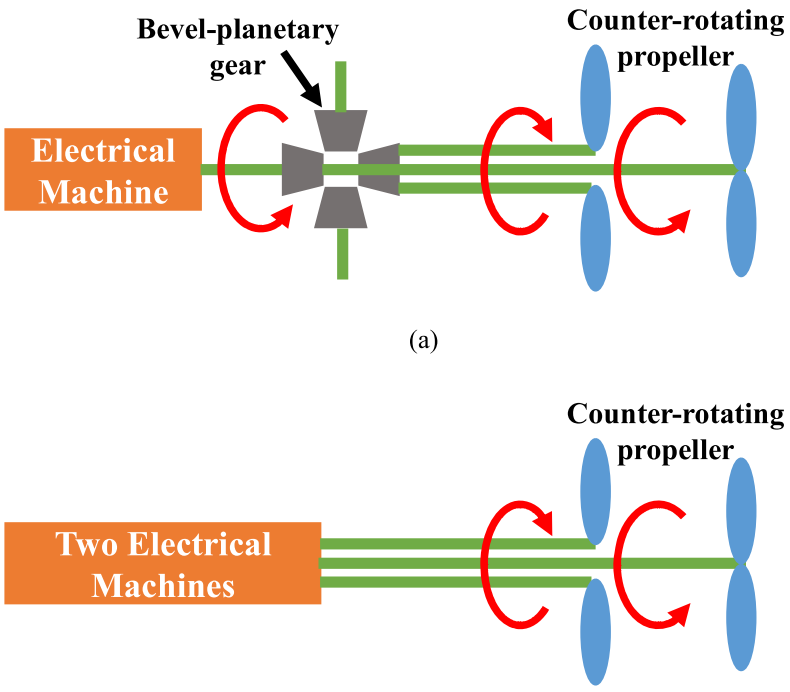

Fig. 1.25. Typical system of counter rotating propellers.

In the field of wind power turbines, [SHI98] was the first to patent a CR wind turbine system. Subsequently, [JUN05] developed a 30kW CR wind turbine system featuring a smaller auxiliary rotor placed upwind of the main rotor to capture additional wind energy and compensate for the dead zone of the main rotor, as shown in Fig. 1.26. This configuration enhances the aerodynamic efficiency and power output compared to conventional single-blade wind turbines [SAN13]. The smaller blade length of the auxiliary rotor allows for higher tip speeds, further increasing power output. However, similar to underwater propulsion, CR wind turbine systems usually incorporate a bevel-planetary mechanical gear, leading to mechanical complexity, maintenance issues, noise, low reliability, and high costs. To circumvent these problems, [BOO10] used slip rings in the stator armature winding to design the stator as a rotating part, achieving CR operation without a mechanical gearbox. Nevertheless, this approach also suffers from reliability issues and slip ring maintenance requirements.

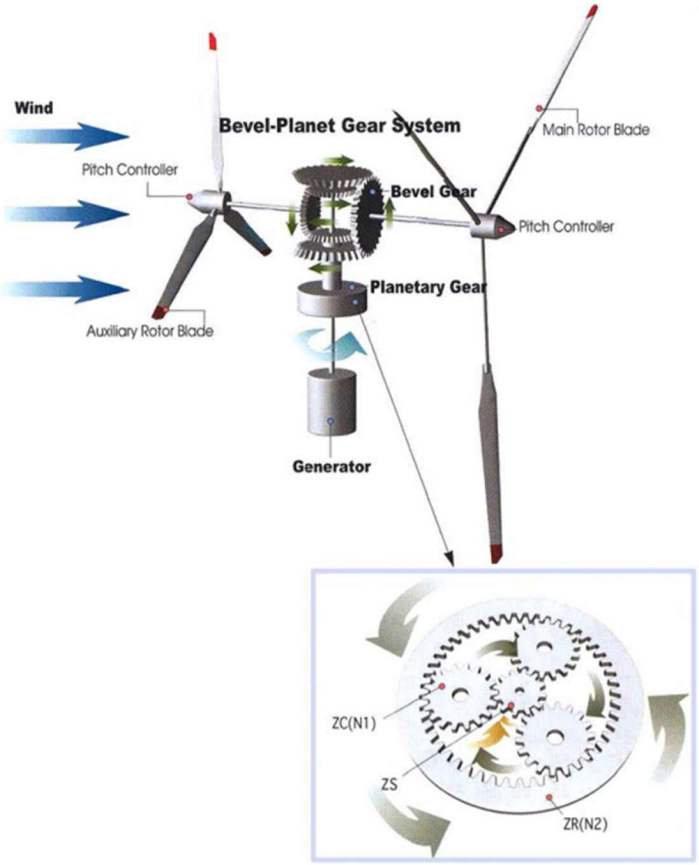

Fig. 1.26. Planetary gear system-based counter-rotating system [JUN05].

In the field of aerospace, Henry Bright patented the first CR propellers for a helicopter in 1859 [HAY52], as shown in Fig. 1.27. Based on this topology, coaxial CR propellers for helicopters evolved into fully operational models recognised in aviation [LEI06] [COL97] [HOL04]. CR propellers are developed to improve aircraft performance and address aerodynamic challenges associated with propellers rotating in a single direction, which utilise a dual-blade system on the same axis but rotate

oppositely to balance the forces involved [SCH12] [WEI22].

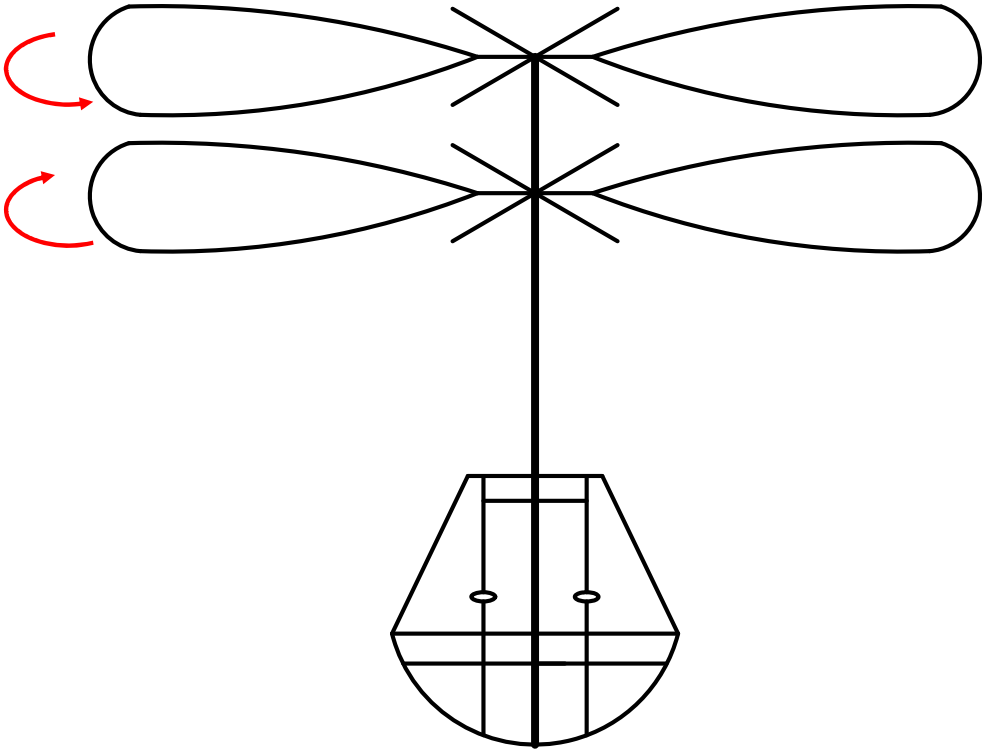

Fig. 1.27. CR propellers [HAY52].

CR propellers mitigate the aerodynamic issue of asymmetry of lift, a phenomenon occurring in rotorcraft during forward flight, where rotor blades alternately advance and retreat relative to the direction of flight. The advancing blades encounter more airspeed and generate more lift compared to the retreating blades [WAT04] [REH22] [LEI06]. By employing two rotors that rotate in opposite directions, CR propellers save a tail rotor and maintain balanced lift on both sides, enhancing stability during takeoffs, landings, and manoeuvres [SIN21]. In hover, CR propeller rotors show a 13% higher performance merit than single-rotor configurations, and the lack of a tail rotor enhances overall efficiency by avoiding power losses, thereby offering a 20% higher efficiency for coaxial CR propeller helicopters [BOU97] [BOU99].

Additionally, in CR propeller systems where the propellers are axially aligned, the aft propeller captures rotational energy lost by the forward propeller, enhancing overall propulsion efficiency [COR22]. This configuration saves 8% fuel compared to turbofan engines [STR82] [HAG88].

Generally, the CR propeller rotor in aircraft is driven by a single engine integrated with a complex mechanical gearbox. This conventional setup is often costly, heavy, and consumes substantial space within the airframe.

Therefore, CR DR electrical machines are proposed to achieve CR operation, improve reliability, and reduce weight, cost, and space requirements. The DRPM machine, utilising high-energy PM material, is

the most popular topology due to its high torque density and efficiency. The CR DRPM machine can also be categorised into two groups by magnetic circuits of two rotors in series or parallel, as shown in Fig. 1.28.

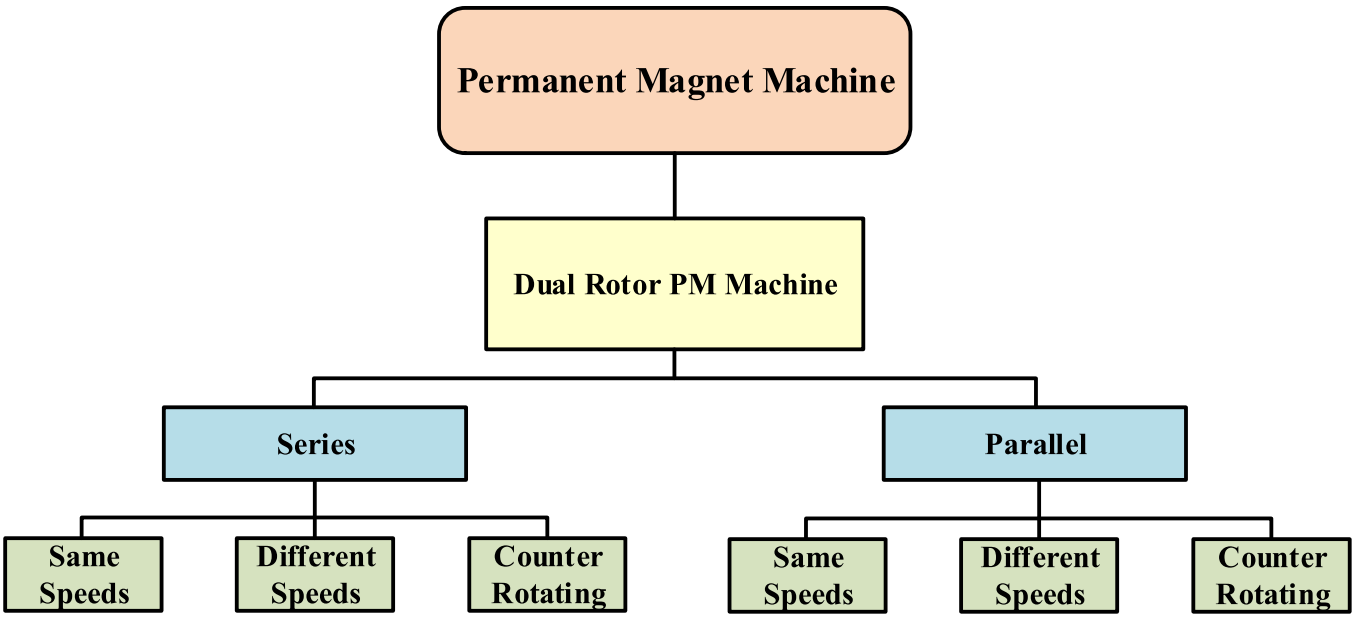

Fig. 1.28. Categorisation of CR DRPM machine.

1.5.1 Parallel magnetic circuits

In Section 1.3.2, [YEH12] introduced a DRPM machine that fixes two rotors on separate shafts, enabling independent rotor operation. Similarly, [ZHA14] [ZHA07] [CHE11] also proposed DRPM machines with shared armature winding sets and two same pole number rotors, achieving CR operation by altering the phase sequences for the corresponding rotors, as illustrated in Fig. 1.29 (a). For the stator PM CR DRPM machine, the CR switched flux PM machine is proposed in [ULL22a] [ULL22b] [MIR21], as shown in Fig. 1.29 (b). In this machine, stator PMs produce opposite polarities MMFs in two air gaps, and the armature reaction produces the same polarities MMFs in two air gaps, allowing two rotors to achieve CR operation. However, these types of CR DRPM machines have only one set of stator winding and the same pole number rotors. Thus, the rotational speeds of the two rotors should be the same, but only the directions are different.

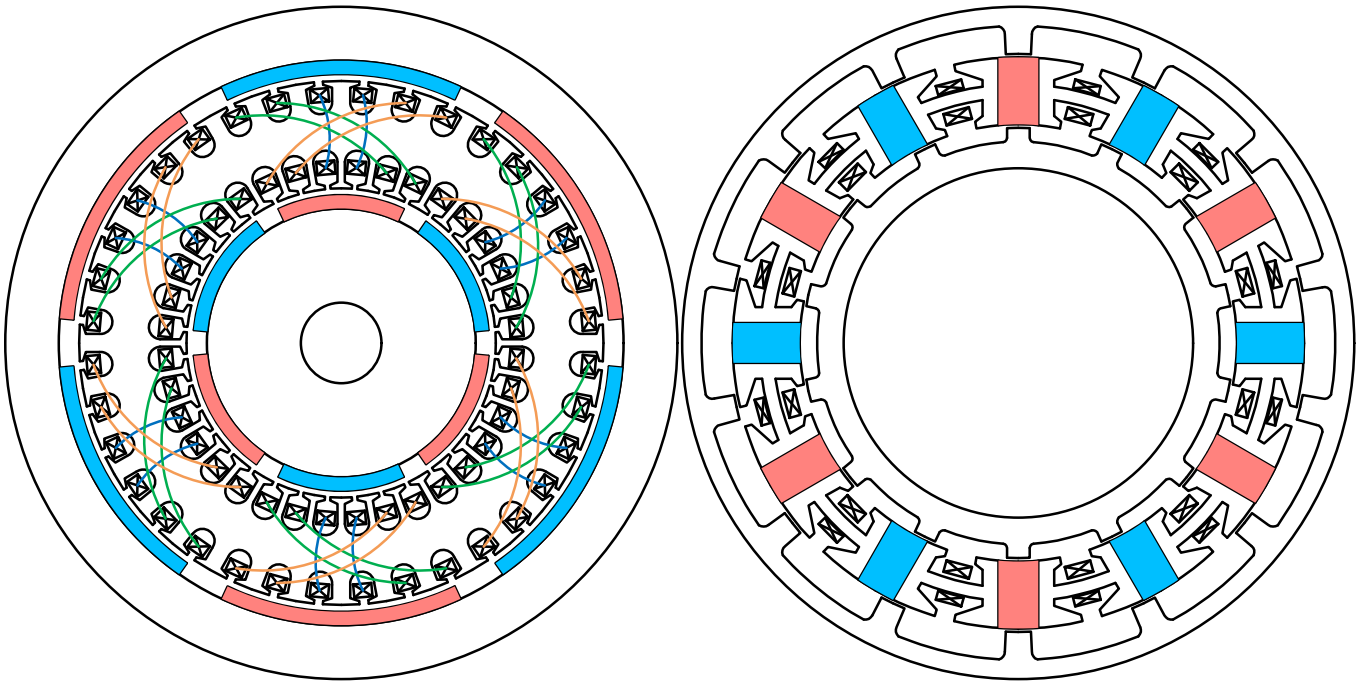

(a) [ZHA14] (b) [ULL22a]

Fig. 1.29. CR DRPM machines with parallel magnetic circuits.

1.5.2 Series magnetic circuits

For the CR DRPM machine with series magnetic circuits, magnetic-geared machines are the most popular type, which can utilise field modulation to achieve CR operation. [WAN17b] [LUO17] [CHE21] proposed magnetic-geared CR DRPM machines that use two winding sets interacting with a rotor and a modulation ring, employing dual field modulation to achieve CR operation and enhance torque density, as shown in Fig. 1.30. However, the modulation ring typically has inadequate mechanical strength to serve as an output rotor. The sandwiched modular stator magnetically geared DRPM machine addresses this by using a modular stator between the two rotors as the modulation ring, providing a robust rotor structure [JIA12]. Nevertheless, the sandwiched stator assembly with dual-mechanical ports introduces mechanical complexity and manufacturing challenges.

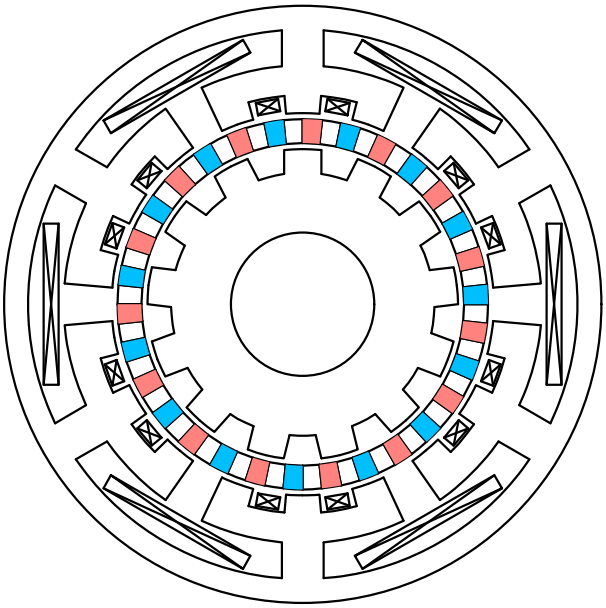

Fig. 1.30. CR DRPM machines with series magnetic circuits [CHE21].

These methods for achieving CR operation can also be applied to axial flux DRPM machines [HUA24] [ZHU18a] [HAS20] [XIA23]. As mentioned in Section 1.3, the conventional YASA machine has two rotors with the same pole number and rotates at the same speed, as shown in Fig. 1.31 (a). In [ZHU18a] [KHA18b], the axial-flux YASA machine employs two different pole number rotors to utilise the field modulation in the FS CW machine to achieve CR operation [ZHU18b], as shown in Fig. 1.31 (b). Then, [HAS20] utilises the same method on the conventional TOURUS machine (Fig. 1.31 (c)). The TW configuration is employed on the common stator yoke, as shown in Fig. 1.31 (d). However, axial flux machines face inherent drawbacks in lamination manufacturing and axial magnetic attraction forces between the rotor and stator.

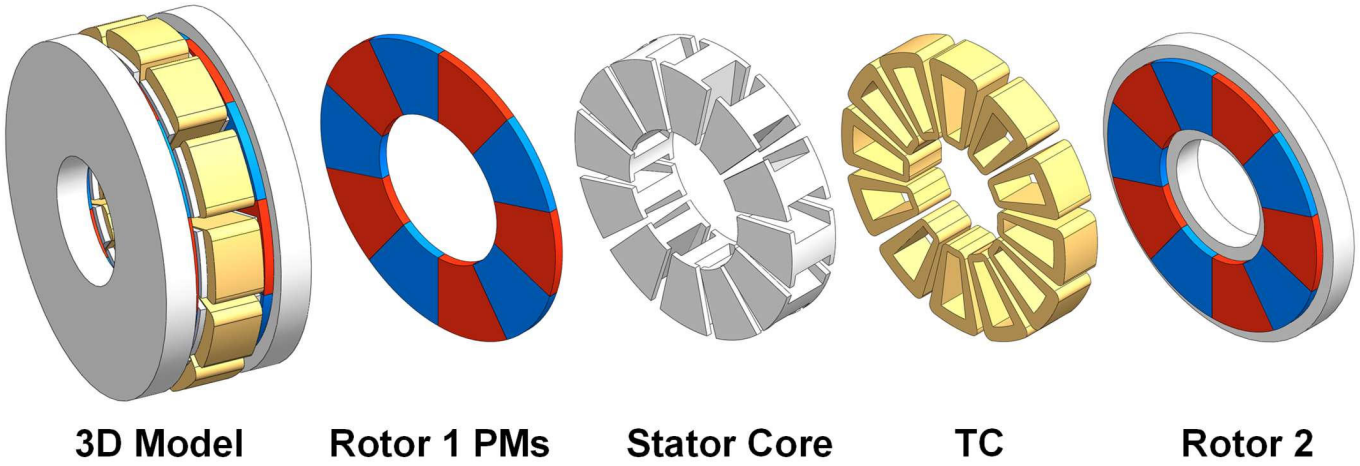

(a) Conventional YASA

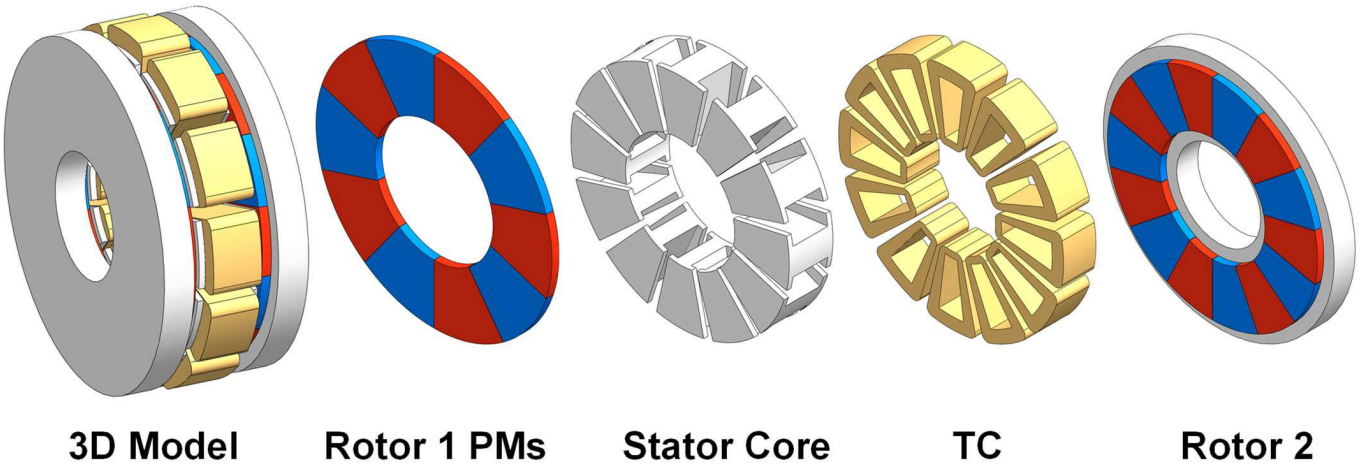

(b) [ZHU18a]

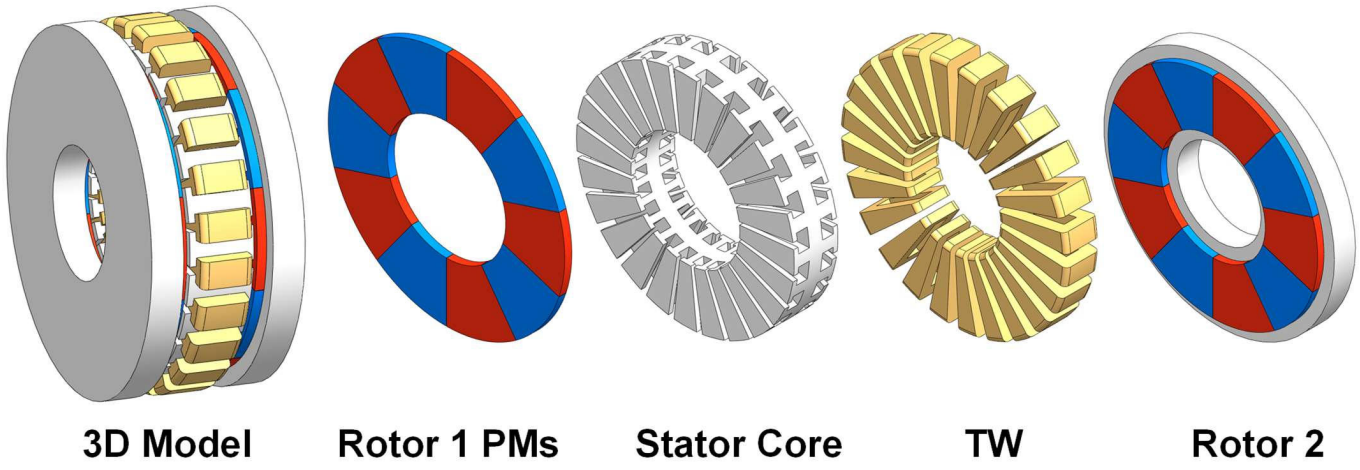

(c) Conventional TOURUS

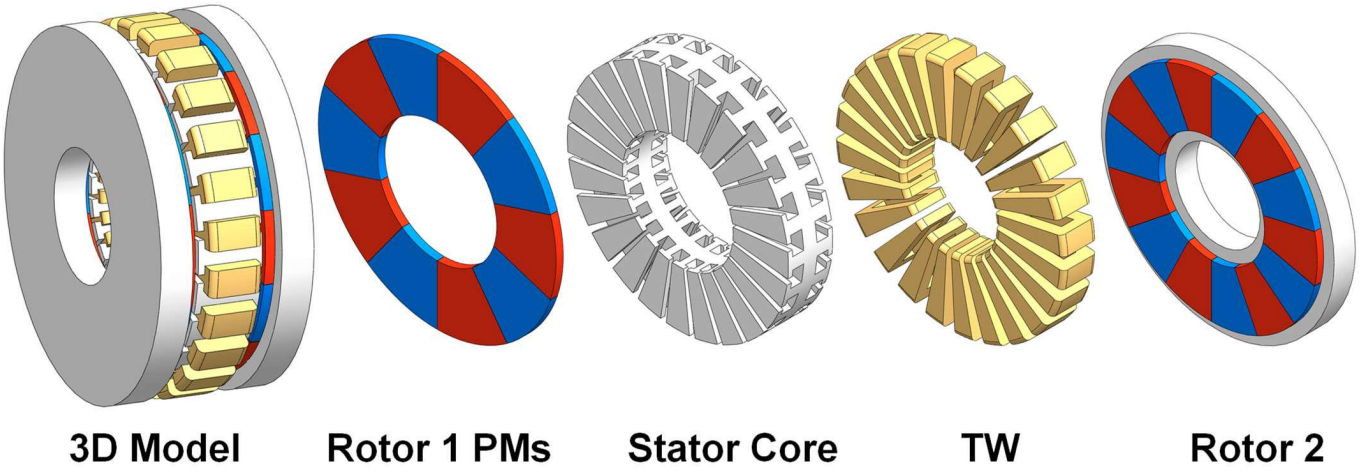

(d) [HAS20]

Fig. 1.31. Axial-flux DRPM machines.

1.6 Scope and Contributions of Thesis

This thesis focuses on the DRPM machines. Comparative studies are conducted on PDRPM, SDRPM, and SR SPM machines to analyse the performance of DRPM machines under the same speed scenario. The counter-rotating operations of DRPM machines are investigated as a particular case of different speed scenarios. The counter-rotating SDRPM machine is investigated, and a novel counter-rotating PDRPM machine is proposed. The research scope and analysed machines in each chapter are shown in Figs. 1. 32 and 1.33 with the detailed contents described as follows:

Chapter 1

PM machine topologies, including both single and dual-rotor, are introduced. With particular attention paid to the DRPM machines, the topologies are reviewed based on the same speeds, different speeds, and counter-rotating operations.

Chapter 2

In order to analyse the electromagnetic performances of DRPM machines under the same speed scenario, the radial-flux PDRPM and SDRPM machines with non-OW TC and TW, and OW DW configurations are comprehensively compared, accounting for different slot/pole number combinations, stator winding configurations, and machine sizes. The designs of all machines are optimised using the finite element analysis based on a genetic algorithm. FEA predictions are validated by experiments.

Chapter 3

The comparison of SDRPM and PDRPM machines reveals that the external rotor of the PDRPM machine with TC winding configuration contributes the majority of torque to the total torque, which is even higher than the total torques of the TW PDRPM machine and the TC SDRPM machine under the same speed scenario. The single external-rotor machine potentially has even higher torque than the dual-rotor machine. Thus, the comparative analysis of the electromagnetic performances of radial flux DR SPM machines with FS non-OW, with reference to external- and internal-rotor SPM machines. The SDRPM machine is selected to compare with the single-rotor machines since the SDRPM machine shows higher torque than the PDRPM machine in Chapter 2. All machines are optimised by genetic algorithm using finite element analysis under various design optimisation scenarios, together with the equivalent magnetic circuit analysis. In addition, the influence of air gap length, PM volume, machine inner bore radius, and pole number is investigated. The measured results validate the FEA results.

Chapter 4

Under the same speed scenario, the DRPM machine has lower torque than the single-rotor PM

machine. However, dual-rotor machines inherently have an extra rotor compared with single-rotor machines. When the two rotors of the dual-rotor machine operate in different working conditions, the dual-rotor machine can replace two single-rotor machines to meet the requirements of some special applications that require two rotors to reduce the cost and save space. Thus, the counter-rotating operations of DRPM machines are investigated as a special case of different speed scenarios. Radial-flux FSCW yokeless counter-rotating dual-rotor permanent magnet (YCDRPM) machines are investigated. The magnetic circuits of two rotors of YCDRPM machines are in series. Based on the magnetic field modulation theory, a YCDRPM machine combines magnetic gear and PM machine to realise dual-rotor counter-rotating operation for special applications, such as washing machines, counter-rotating wind power generators, and underwater vehicles. The operation principle and three feasible slot/pole number combinations are investigated under different operation modes. The YCDRPM machine is analysed using an analytical method and validated by FEA and experiments.

Chapter 5

The sandwiched modular stator of the YCDRPM machine results in a complex mechanical structure that makes manufacturing and assembly difficult. Thus, a novel counter-rotating single-stator dual-internal-rotor permanent magnet (CSDPM) machine is proposed. The magnetic circuits of two rotors of the CSDPM machine are in parallel. This machine utilises magnetic field modulation in the FSCW PM and vernier PM machines to realise the counter-rotating operation for some special applications. The magnetic field modulation principle and the relationship between two rotors and the armature reaction are analysed. The electromagnetic performance of the CSDPM machine is comprehensively investigated. Experiments on a prototype CSDPM machine validate the results.

Chapter 6

General conclusions are described based on the previous chapters. Also, potential future works are proposed.

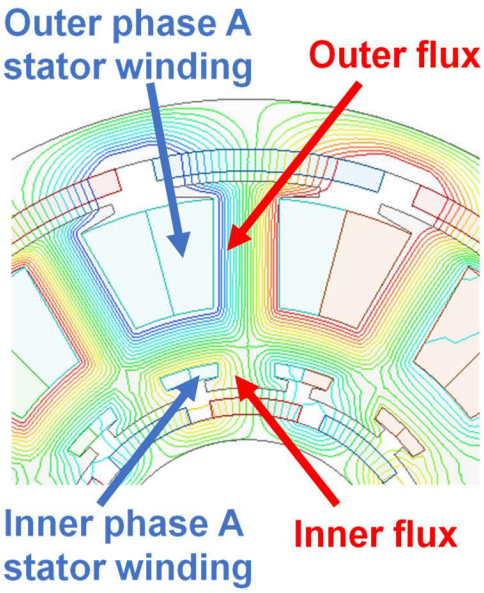

(a) TC-SDRPM.

(b) TC-PDRPM.

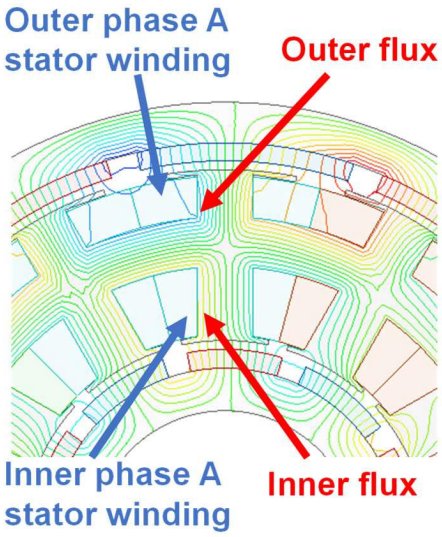

(c) TW-PDRPM.

Fig. 2.6. Open circuit flux line linked with phase A stator winding of optimised 12s10p machines (Rotor position at 0 deg).

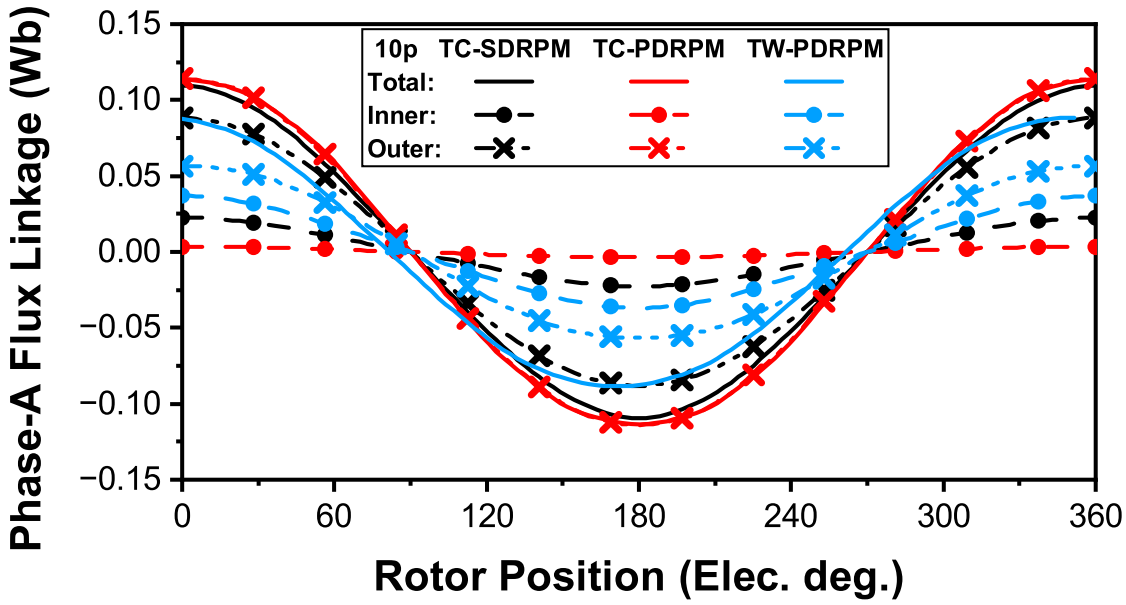

(a) Waveforms.

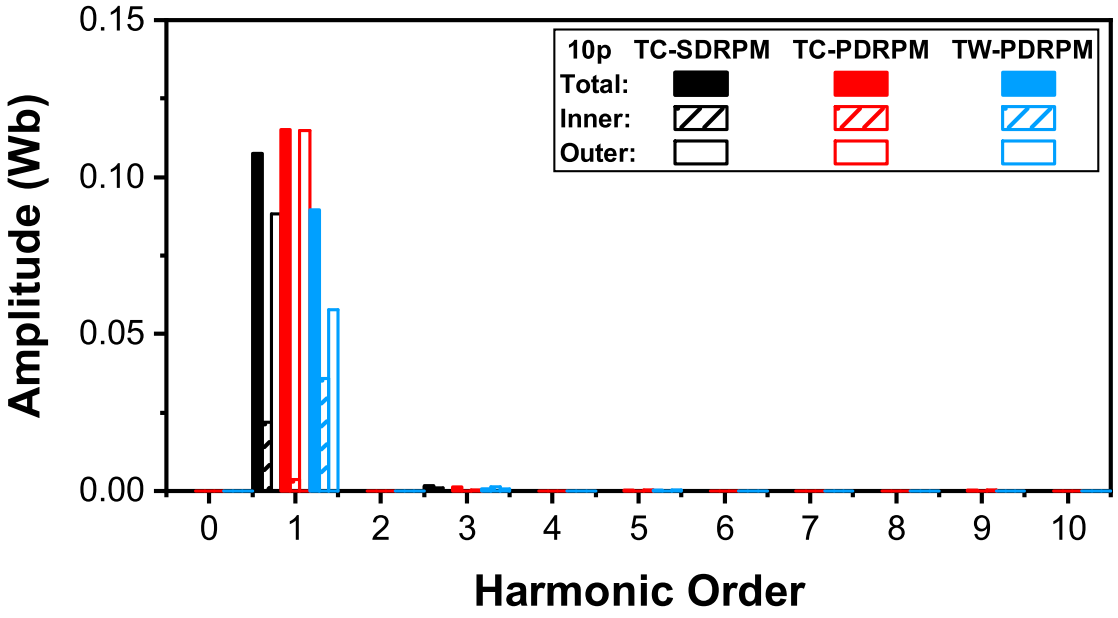

(b) Spectra.

Fig. 2.7. Comparison of phase flux linkages of 12s10p machines.

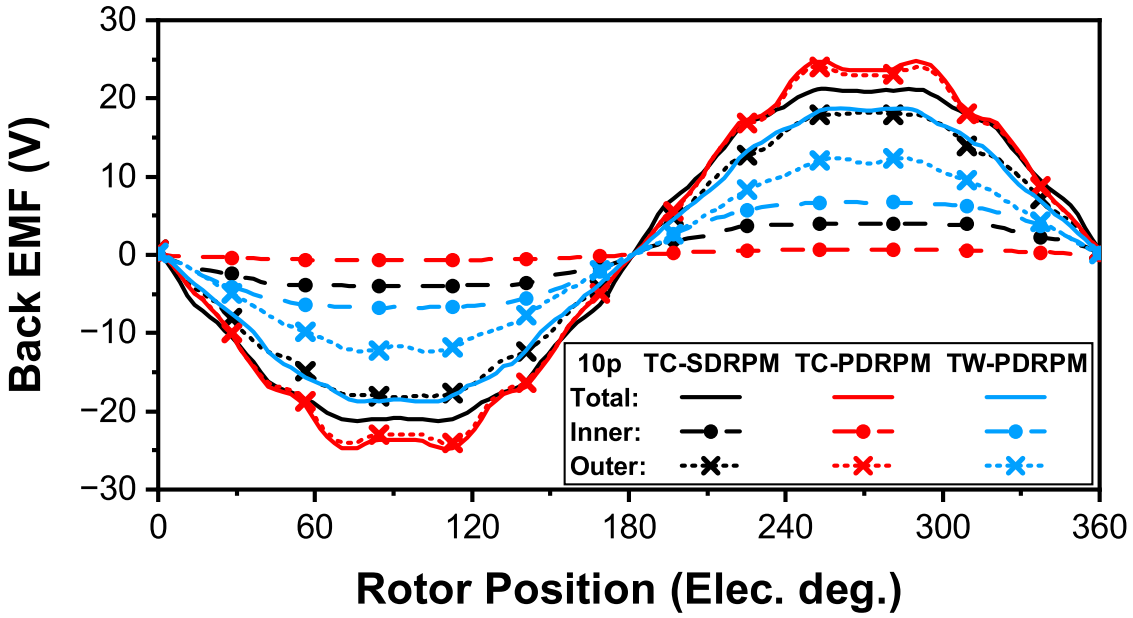

(a) Waveforms.

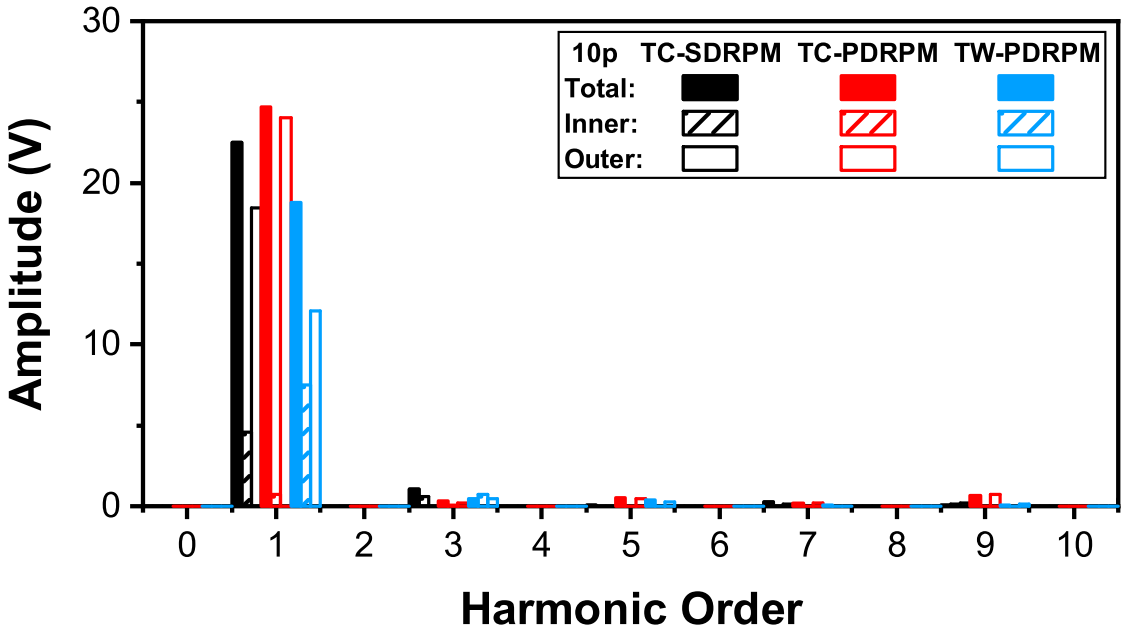

(b) Spectra.

Fig. 2.8. Comparison of phase-A back EMFs of 12s10p machines (Rated speed=400 r/min).

2.4.3 Torques, PM utilisations, and overload capabilities

The on-load torques of all optimised 12s10p machines under 30W copper loss with zero d-axis current control are shown in Fig. 2.9. The TC-PDRPM machine has the highest torque, 4.3 Nm, due to its highest back EMF. In contrast, the TW-PDRPM machine has the lowest torque, 3.2Nm. Since the TW-PDRPM not only has the lowest back EMF but also the stator yoke design in the PDRPM machines further reduces the slot area compared with the yokeless structure of the TC-SDRPM machine, leading to an even lower

input current in the PDRPM machines under the same copper loss condition (Table 2.3).

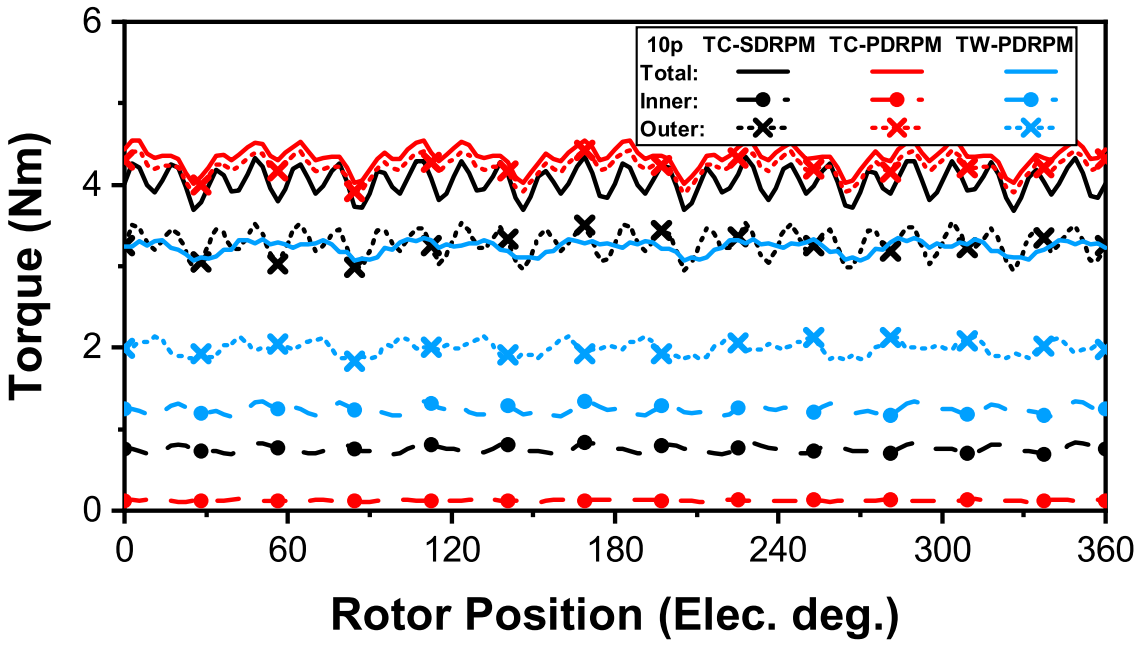

(a) Waveforms.

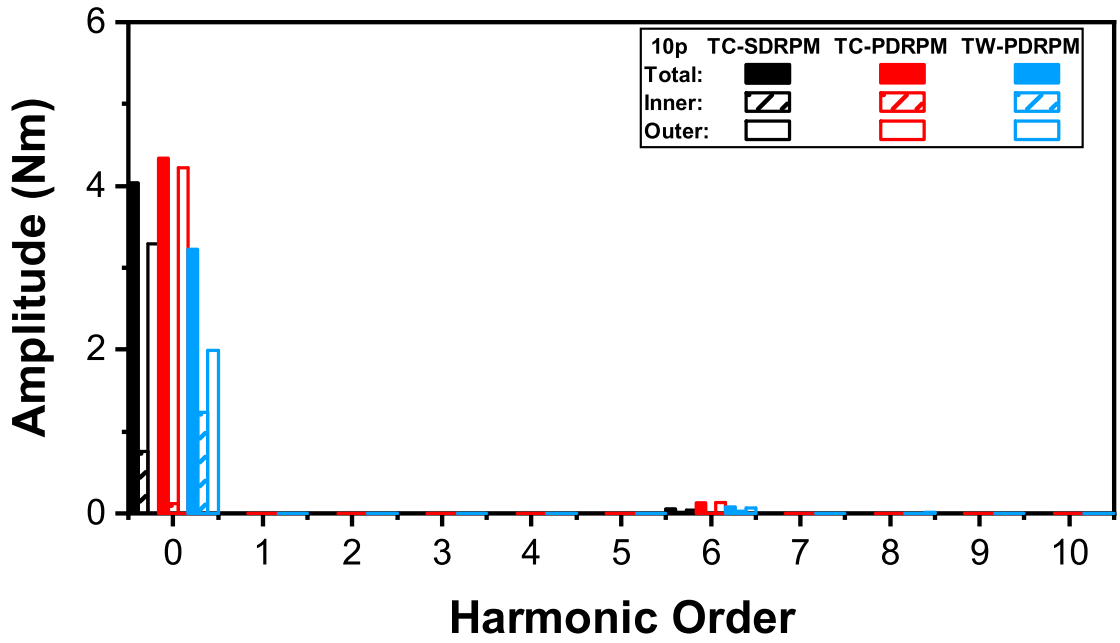

(b) Spectra.

Fig. 2.9. Comparison of torques of 12s10p machines.

The original optimisation objective has only considered the optimal torque and not set the limitation of PM volume. Thus, the PM utilisation of all machines are compared in Fig. 2.10. The PM utilisation is the ratio of average torque and PM volume, it can be defined as:

$$\rho_{\text{Torque/PM}} = \frac{T_{avg}}{V_{PM}} \tag{2.2}$$

where T_{avg} is the average torque, and V_{PM} is the PM volume. It can be seen that the TC-PDRPM machine has the highest outer PM utilisation, while the TW-PDRPM machine has the highest inner PM utilisation.

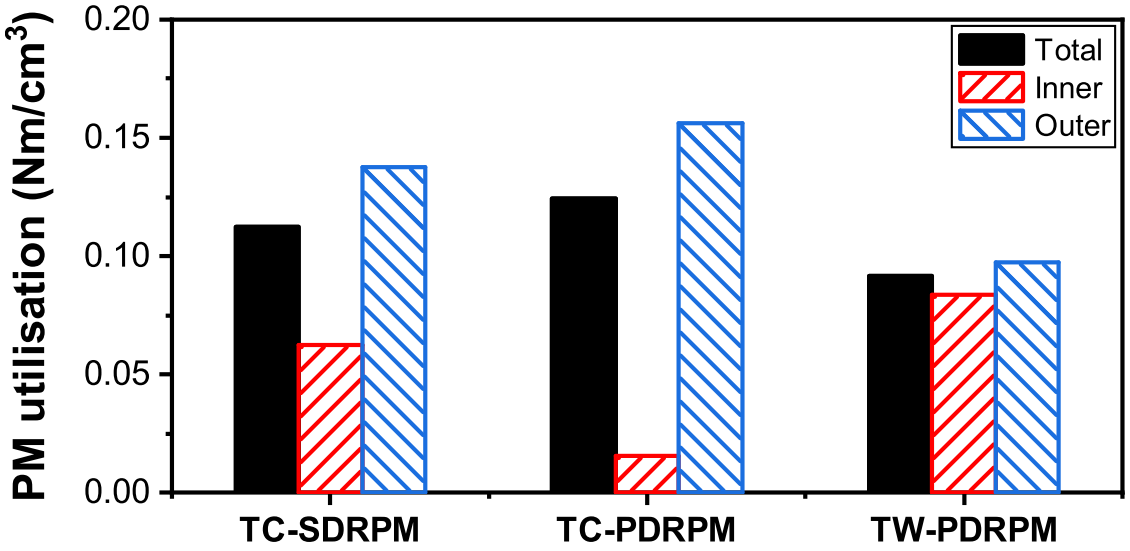

Fig. 2.10. Comparison of PM utilisation of 12s10p machines.

The overload capabilities of all 12s10p machines are shown in Fig. 2.11. It can be seen that the TC-SDRPM and TC-PDRPM machines have the same overload capabilities. However, the TC-PDRPM machine always produces higher torque than the TC-SDRPM machine at different copper losses. In contrast, the TW-PDRPM machine has the weakest overload capability.

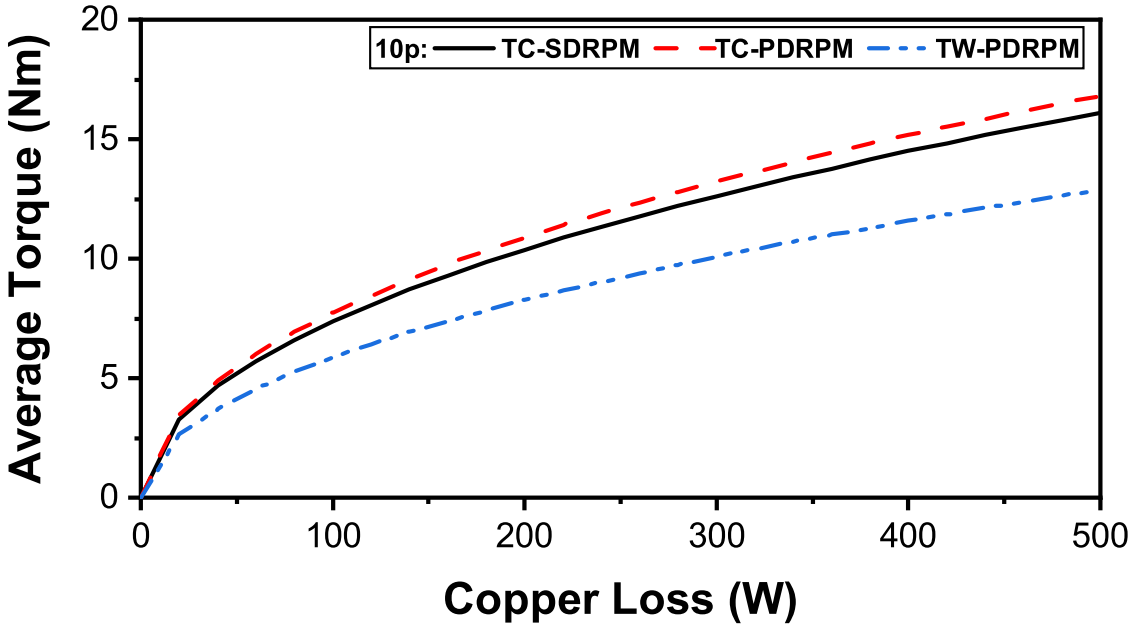

Fig. 2.11. Torques versus copper loss of optimised 12s10p machines with zero d-axis current.

2.4.4 Losses and efficiencies

The PM eddy current, iron, and copper losses of all optimised 12s10p machines at the rated load are shown in Fig. 2.12. As can be seen, the TC-SDRPM machine has the lowest iron loss due to its yokeless stator structure.

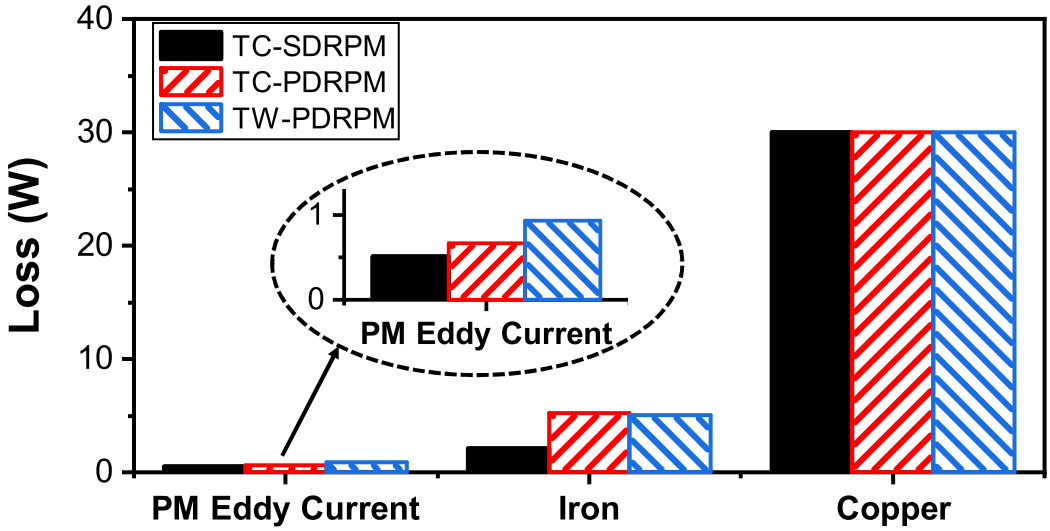

Fig. 2.12. Losses of optimised 12s10p machines at rated load (Rated speed=400 r/min).

Furthermore, the efficiencies (2.3) of all three machines are calculated and compared in Fig. 2.13. Clearly, the 12s10p TC-SDRPM machine has the highest efficiency due to the low PM eddy current and iron losses.

$$\eta = \frac{T_{avg}\omega}{T_{avg}\omega + P_{loss}} \tag{2.3}$$

where ω is the machine rotating speed and P_{loss} is the total loss in the machine.

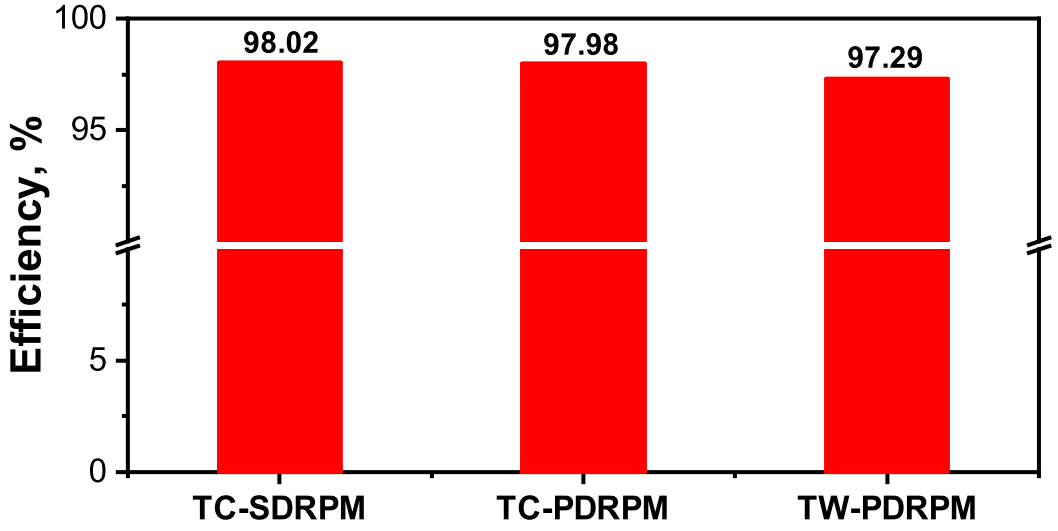

Fig. 2.13. Efficiencies of optimised 12s10p machines.

2.5 Influence of Slot/Pole Number Combinations of TW-SDRPM, TW-PDRPM, and TOW-PDRPM machines

The influence of slot/pole number combinations of TC-SDRPM, TC-PDRPM, and TW-PDRPM machines are investigated in this chapter, i.e., 12s10p FS machines, 12 slots 20 poles (12s20p), and 12 slots 22 poles (12s22p) IS machines. Their winding connections and corresponding coil EMF phasors are shown in Fig. 2.14. The number of slots per pole per phase q can be calculated by:

$$q = \frac{N_s}{2mp} \tag{2.4}$$

where N_s is the number of the stator slot, m is the number of the phase, p is the number of the rotor pole pairs.

It should be noted that the pole pair numbers of 12s20p and 12s22p combinations in formula (2.4) are the pole pair numbers of the armature windings as 2 and 1, respectively. Thus, q of 12s10p machines is 2/5. The q of the 12s20p and 12s22p IS machines are 1 and 2, respectively.

For all machines with different slot/pole number combinations, the winding connected for the highest winding factors. Therefore, the optimal coil pitches of 12s10p, 12s20p, and 12s22p SDRPM machines are 1, 3, and 5, respectively. All machines with different slot/pole number combinations are globally optimised with the same condition as Chapter 2.3 to maximise the torque. The optimised parameters are listed in Table 2.4.

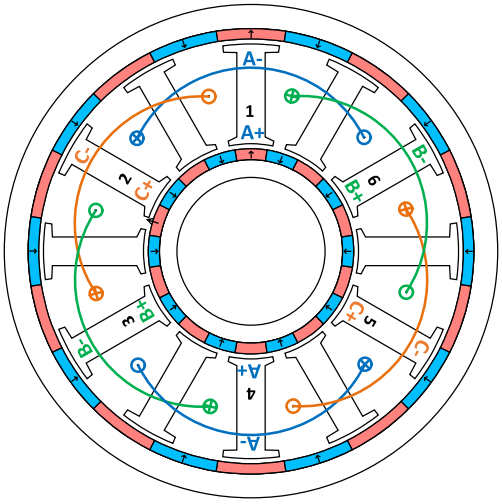

I. (a)

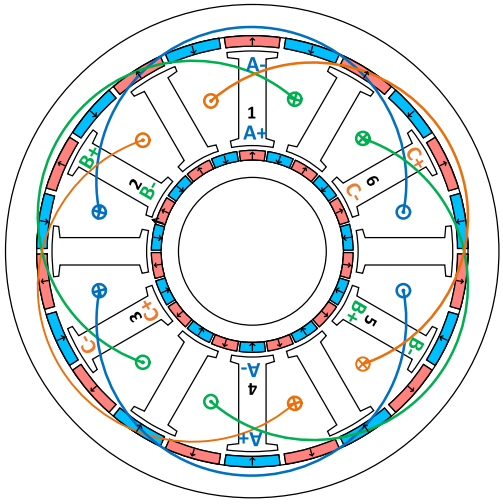

II. (a)

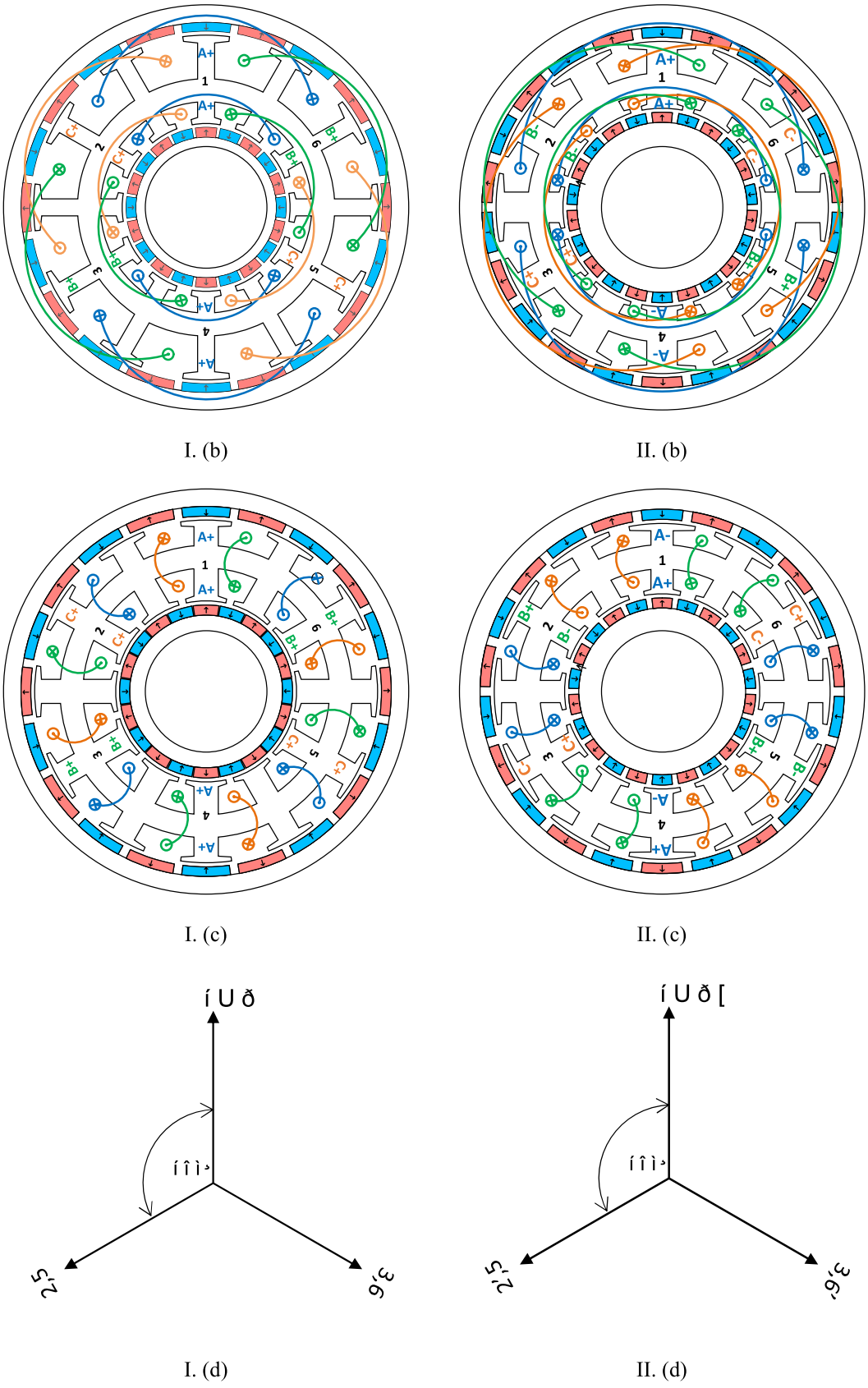

Fig. 2.14. Cross-sections of machines with different slot/pole number combinations and corresponding coil EMF phasors. I. 12s20p. II. 12s22p (a) TC-SDRPM. (b) TC-PDRPM. (c) TW-PDRPM. (d) Corresponding coil EMF phasors.

TABLE 2.4
PARAMETERS OF OPTIMISED OF TC-SDRPM, TC- AND TW-PDRPM MACHINES WITH DIFFERENT SLOT/POLE NUMBER COMBINATIONS

Symbols	TC-SDRPM		TC-PDRPM		TW-PDRPM	
N_s/p	12/20	12/22	12/20	12/22	12/20	12/22
w_{ist}/w_{ost}	3.8	4	2/4.2	2.4/4.8	2.7/5.3	2.6/5.6
R_s/R_7	-	-	*0.51*	*0.55*	*0.66*	*0.67*
h_{sy}	-	-	*5.6*	*6.4*	*5.7*	*6*
R_2/R_7	*0.405*	*0.42*	*0.38*	*0.4*	*0.45*	*0.47*
R_4/R_7	*0.86*	*0.83*	*0.85*	*0.82*	*0.85*	*0.84*
bis	*3.2*	*3.7*	*5.3*	*6.2*	*6*	*4*
b_{os}	10.4	12.3	12.8	8.2	9.4	5.2
h_{is}	1	1.3	1.3	1.5	1	1
h_{os}	1.3	1.1	1.2	1.1	1	1
α_{is}	15	6.1	9.5	15	9.7	5
α_{os}	17	12.7	10.5	10	12	11.4
R_2-R_1	2.2	1.9	2.3	1.9	2.2	2.2
R_6-R_5	2.3	2	2	1.9	2.1	2.3
θ_{im}	180	164	15.3	15.4	17.2	14.2
θ_{om}	180	163	16.5	11.9	15.2	11.8
V_{im}	13.4	11.2	11.1	10.7	14.5	13.7
V_{om}	31.9	25.9	26	19.1	25	22.7
V_{PM}	45.3	37.1	37.1	29.8	39.5	36.4
I_{amp}	5.3	3.8	4.7	3.5	4.9	4.5

2.5.1 Air gap flux densities

Fig. 2.15 shows the open circuit flux lines and magnetic flux density distributions of all optimised machines. With the increase of pole number, the pole pitch decreases, and the magnetic saturations on the stator and rotor are less.

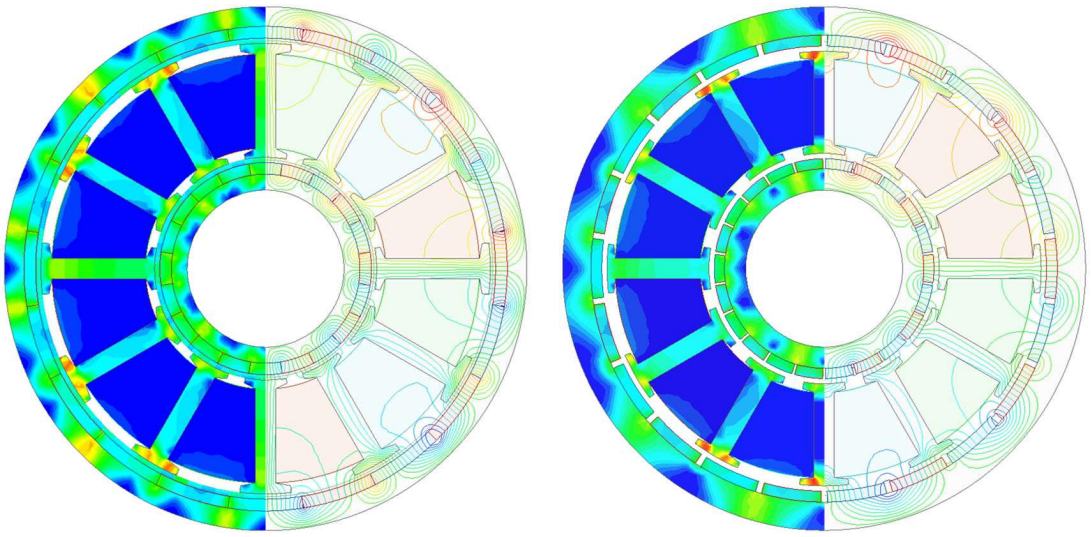

I. (a) II. (a)

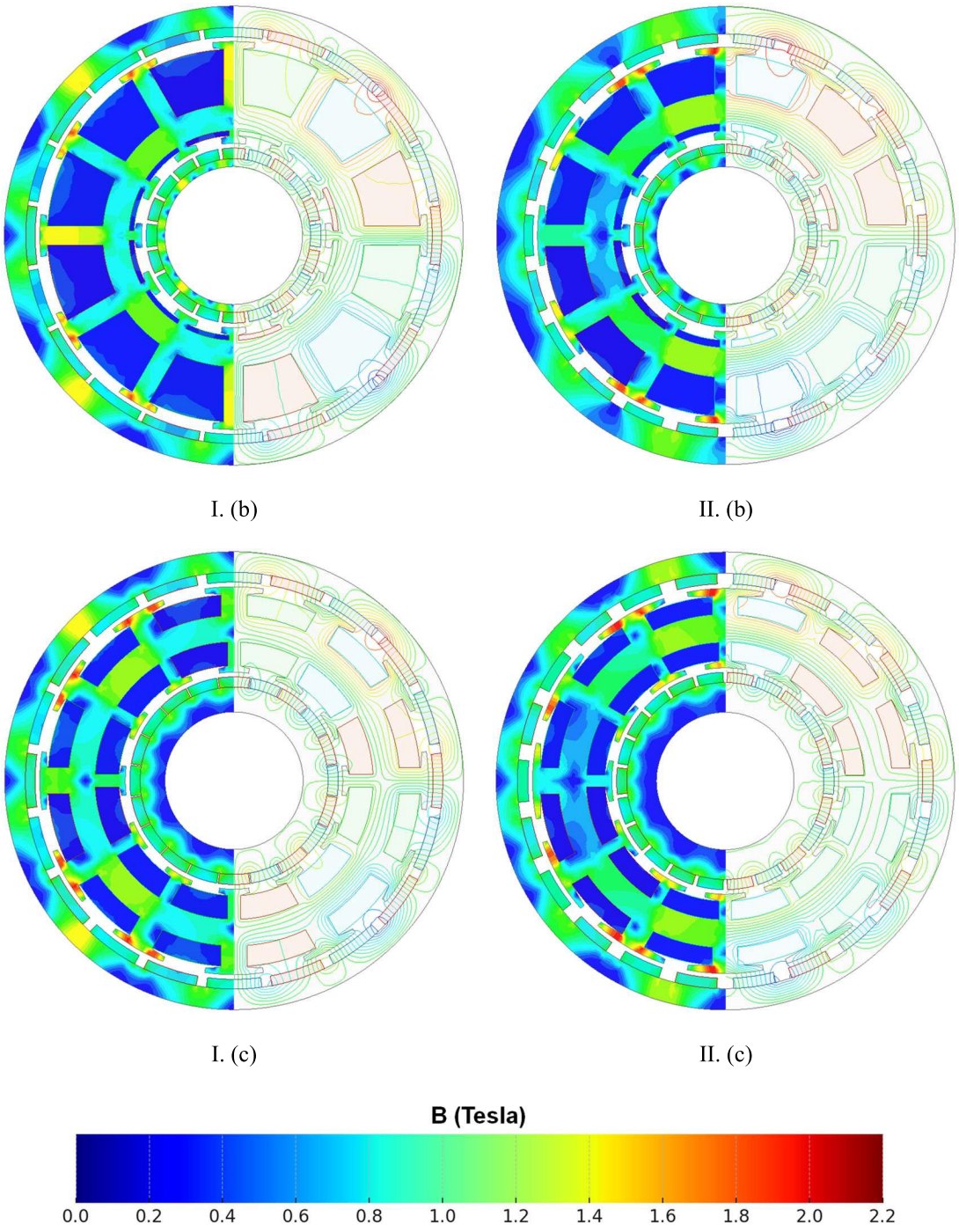

Fig. 2.15. Open circuit flux density distributions and flux lines of optimised machines with different slot/pole number combinations. I. 12s20p. II. 12s22p (a) TC-SDRPM. (b) TC-PDRPM. (c) TW-PDRPM.

Fig. 2.16 shows the variations of inner and outer air gap flux densities of all machines with pole numbers. The inner and outer fluxes of the TC-SDRPM machine interact. Thus, the outer air gap flux density decreases with the inner air gap flux density as the pole number increases in the TC-SDRPM machine. As mentioned in Chapter 2.4, the inner rotor contributes minimally to the TC-PDRPM machine. Therefore, the inner air gap flux density of the TC-PDRPM machine is the smallest among all machines

with different slot/pole number combinations. The waveforms and spectra of air gap flux densities of all machines are shown in Fig. 2.17.

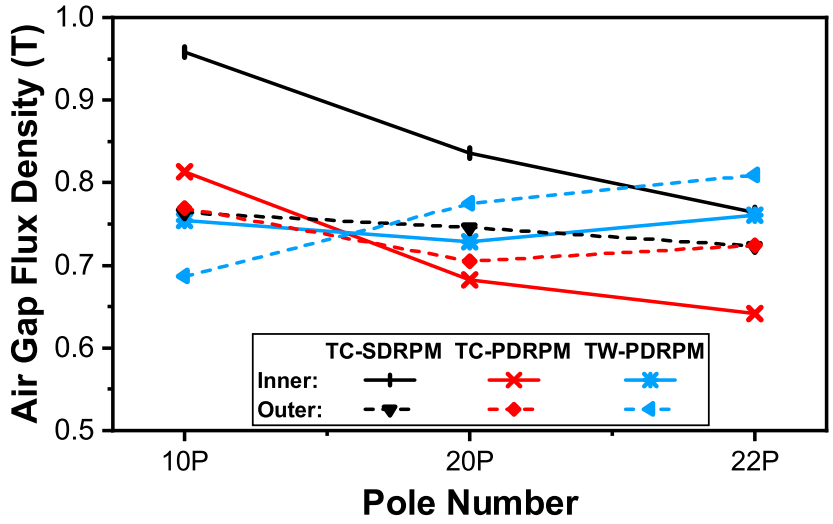

Fig. 2.16. Inner and outer air gaps flux densities versus pole numbers.

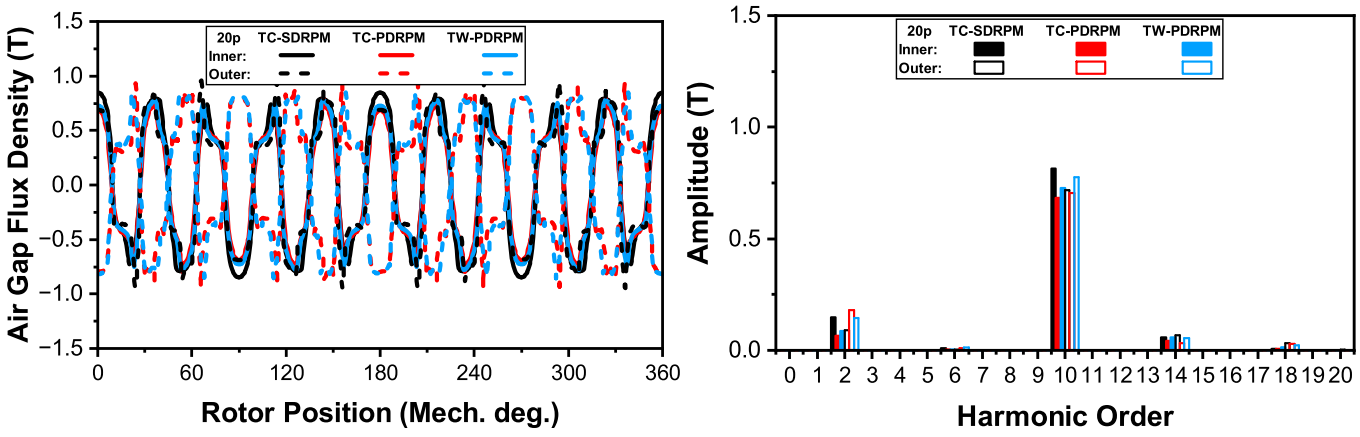

(a) 12s20p.

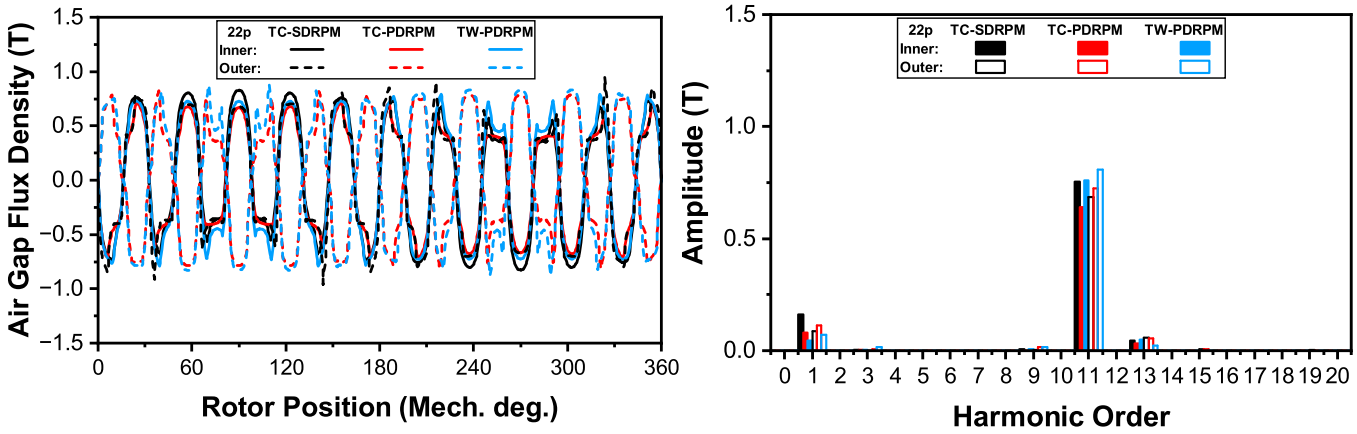

(b) 12s22p.

Fig. 2.17. Inner and outer air gap flux densities of TC-SDRPM, TC- and TW-PDRPM machines.

2.5.2 Flux linkages and back EMFs

Fig. 2.18 shows the phase A flux linkages of all machines with different pole numbers. In TC-PDRPM machines with different pole numbers, the flux linkage generated by the inner rotor is negligible. However, the outer rotor radius is significantly larger than that of the inner rotor, and the outer PM generates higher flux due to the larger PM width. As a result, the outer rotor generates significantly higher flux linkage. Thus, TC-PDRPM machines with different slot/pole number combinations have the highest total flux linkages among all machines. The total flux linkages of the 10p and 22p TC-SDRPM machines are higher than those of the corresponding TW-PDRPM machines. The outer flux linkages of the 20p TW-PDRPM and TC-SDRPM machines are similar, but the inner flux linkage of the TC-SDRPM machine is lower than that of the TW-PDRPM machine. Therefore, the total flux linkage of the 20P TW-PDRPM machine is higher than that of the 20p TC-SDRPM machine. The back EMFs and flux linkages of all machines under different pole numbers with similar relationships are shown in Fig. 2.19. The waveforms and spectra of phase-A flux linkages and back EMFs of all machines are shown in Fig. 2.20 and Fig. 2.21, respectively.

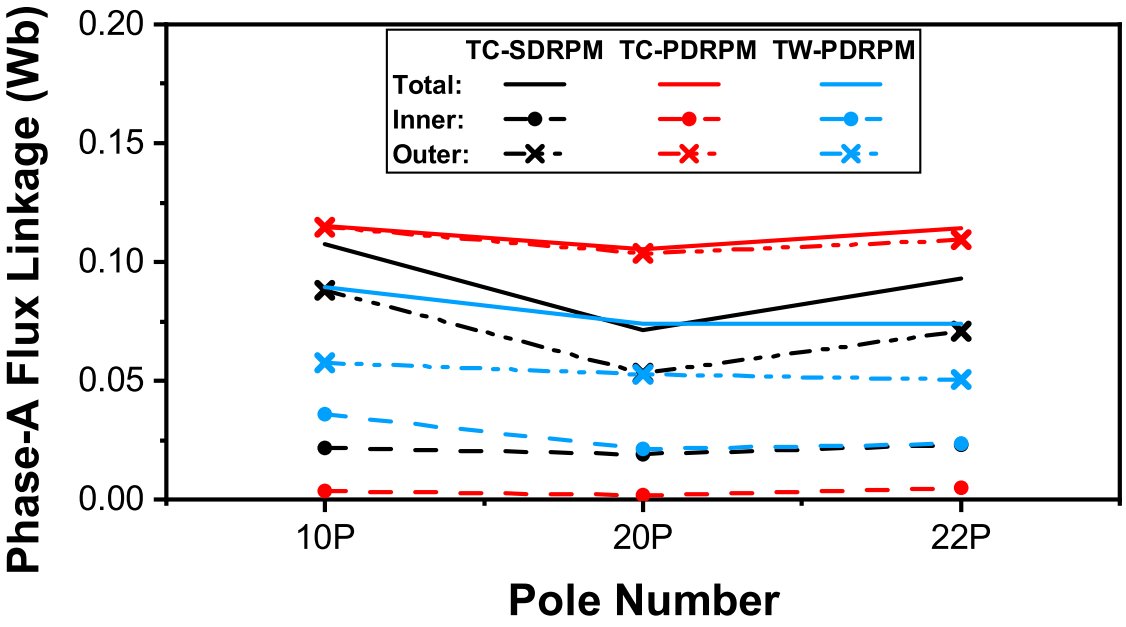

Fig. 2.18. Phase A flux linkages versus pole numbers.

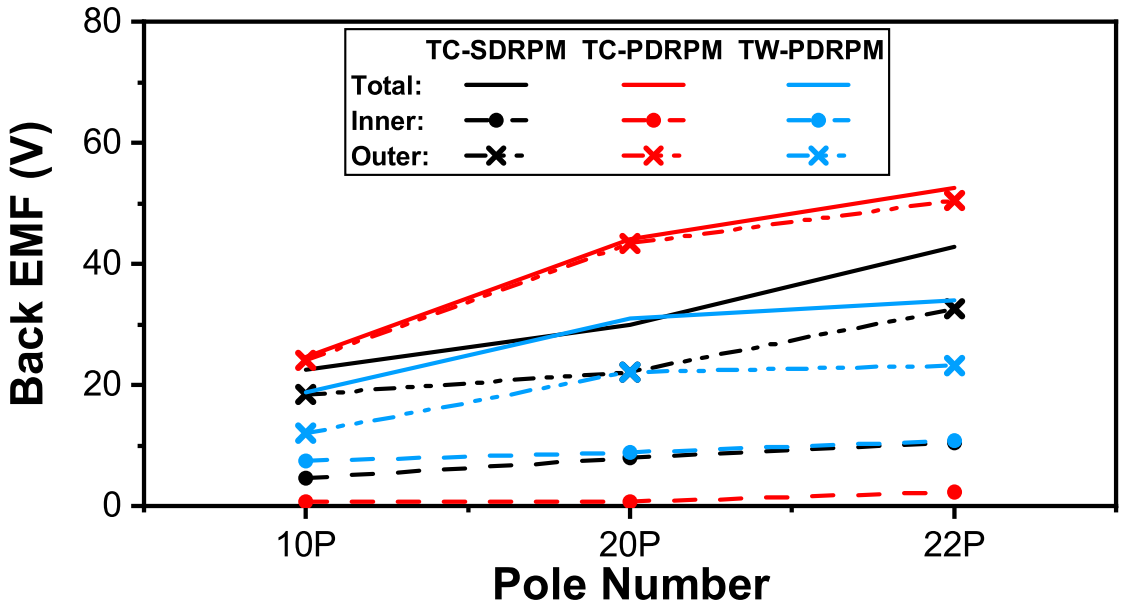

Fig. 2.19. Back EMFs versus pole numbers (Rated speed=400 r/min).

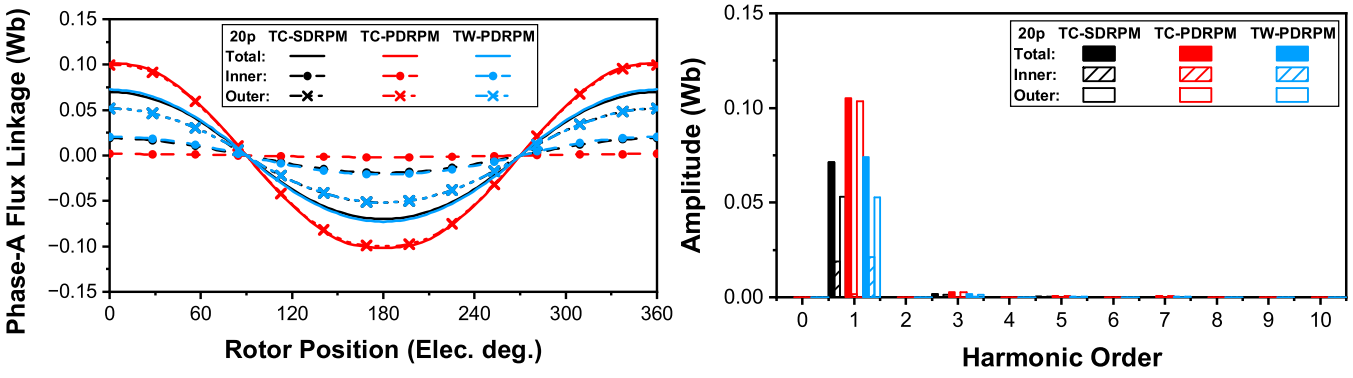

(a) 12s20p.

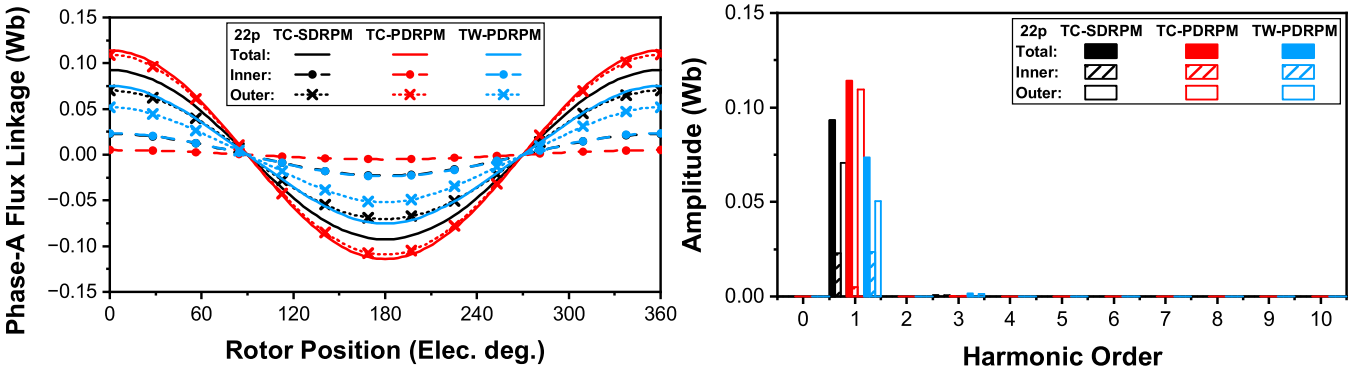

(b) 12s22p.

Fig. 2.20. Phase-A flux linkages of TC-SDRPM, TC- and TW-PDRPM machines.

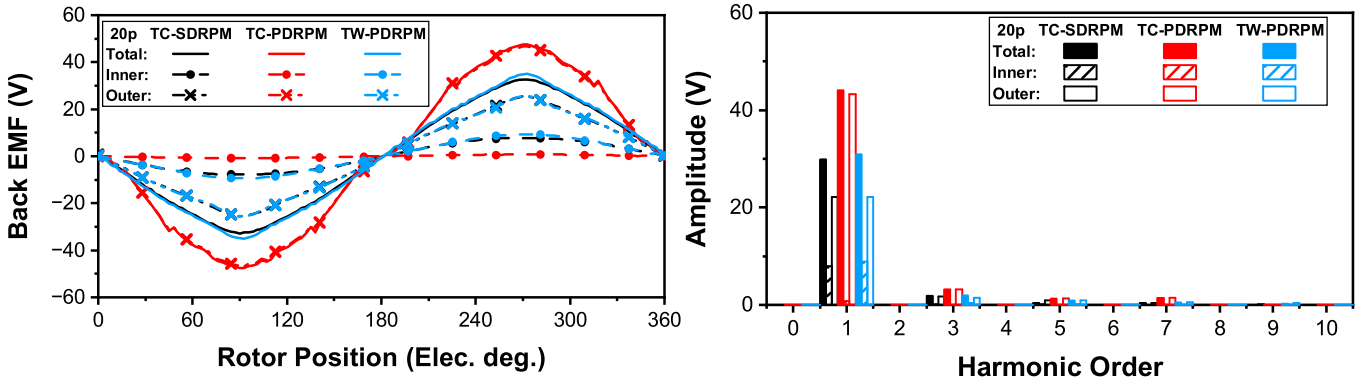

(a) 12s20p.

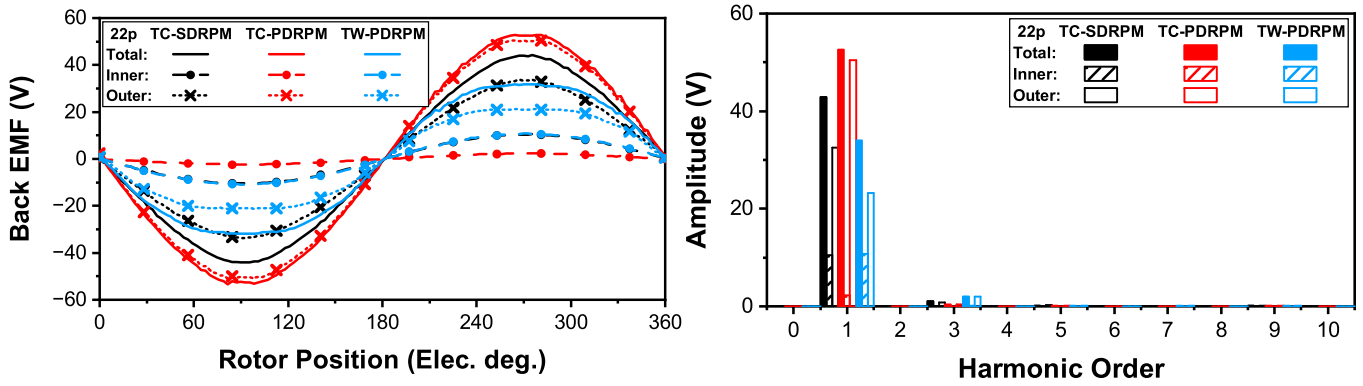

(b) 12s22p.

Fig. 2.21. Back EMFs of TC-SDRPM, TC- and TW-PDRPM machines (Rated speed=400 r/min).

2.5.3 Torques, PM utilisations, and overload capabilities

The torques and PM utilisations of TC-SDRPM, TC- and TW-PDRPM machines with different numbers of slot/pole number combinations are shown in Figs. 2.22 and 2.23, respectively. The TC-PDRPM machines with different slot/pole number combinations and all winding configurations show the highest torque due to their highest back EMF. Moreover, the total PM utilisations of the TC-PDRPM machines are higher than other types of machines. On the other hand, the torques of TW-PDRPM machines with different slot/pole number combinations are the lowest. Although the TW configuration has shorter end-winding length than the TC configuration, the yokeless modular stator structure provides a big slot area for the TC-SDRPM machines. The 10p and 20p TC-SDRPM machines allow higher input current than TW-PDRPM machines, even when considering the end-winding length under the same copper loss condition. For the 22p machines, the back EMF of the TC-SDRPM machine is significantly higher than that of the TW-PDRPM machine. Additionally, the 22p machine has a strong 2 pole stator armature reaction. The 22p TW-PDRPM machine faces severe magnetic saturation in the stator yoke, as shown in Fig. 2.24. Therefore, despite having a higher input current, the torque of the 22p TC-SDRPM machine is higher than that of the 22p TW-PDRPM machine. The waveforms and spectra of torques of

TC-SDRPM, TC-PDRPM and TW-PDRPM machines are shown in Fig. 2.25.

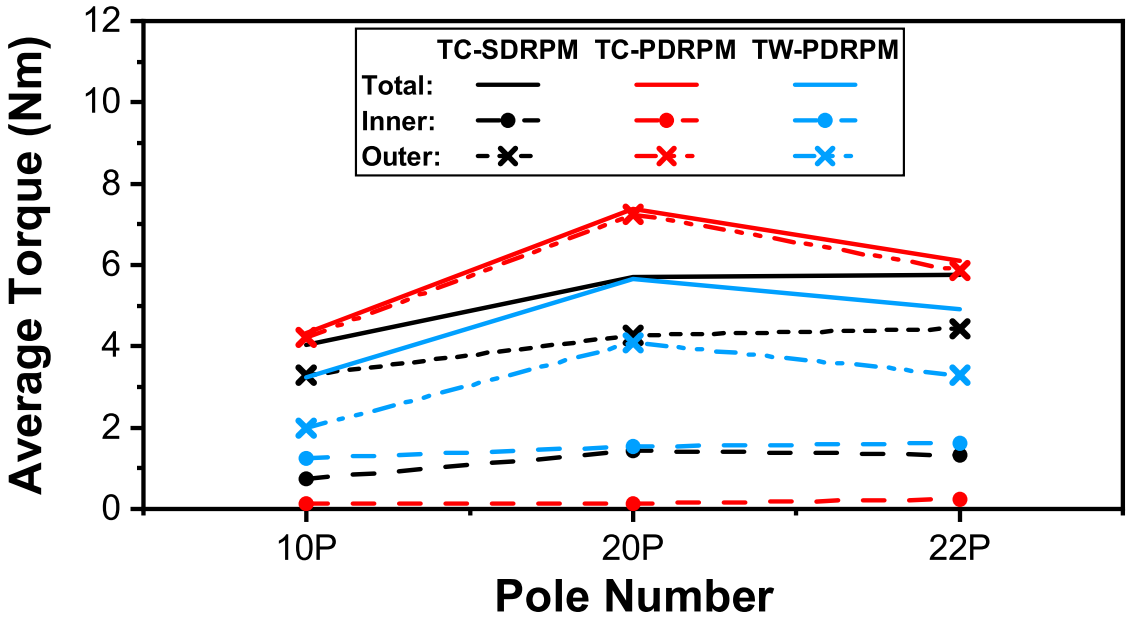

Fig. 2.22. Torques versus pole numbers.

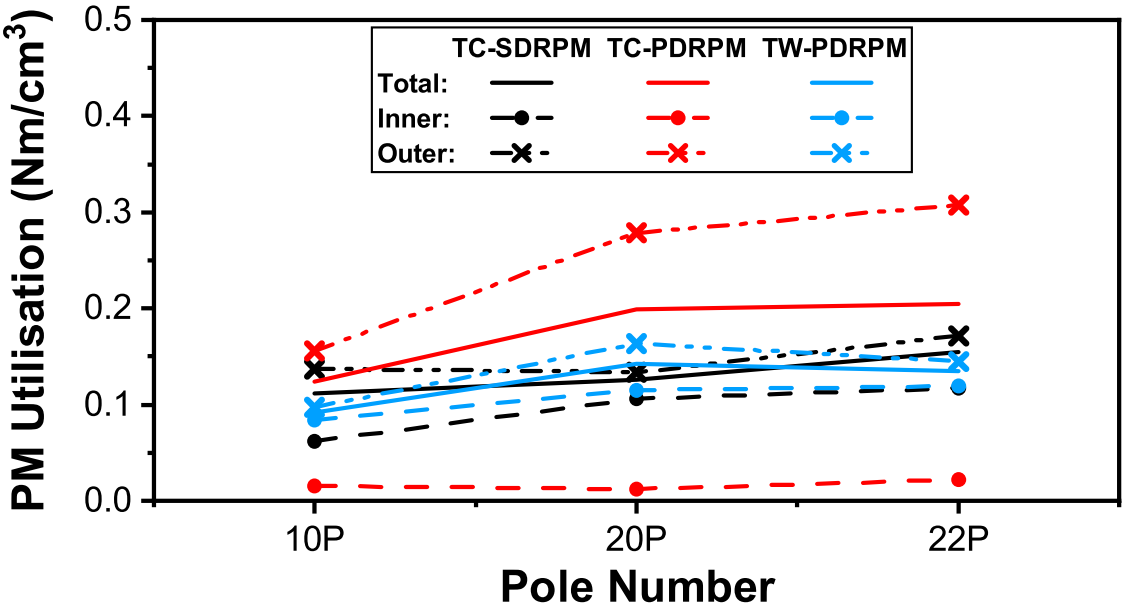

Fig. 2.23. PM utilisations versus pole numbers.

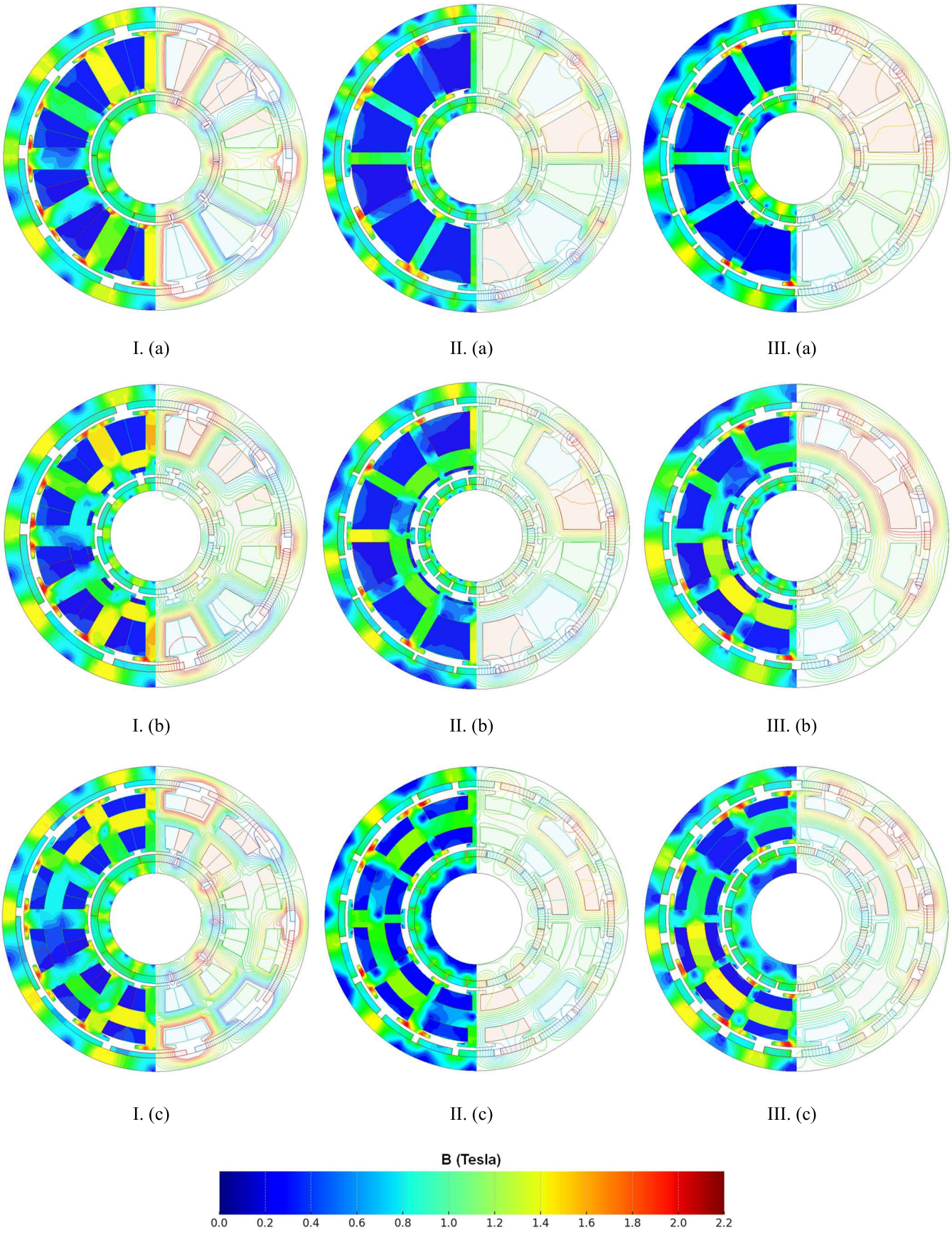

Fig. 2.24. Flux density distributions and flux lines at rated load. I. 12s10p. II. 12s20p. III. 12s22p. (a) TC-SDRPM. (b) TC-PDRPM. (c) TW-PDRPM.

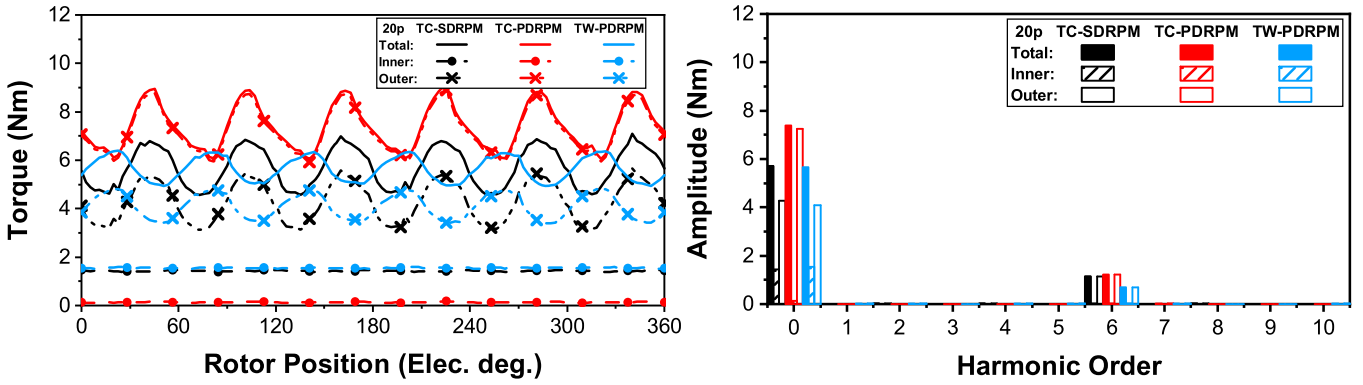

(a) 12s20p.

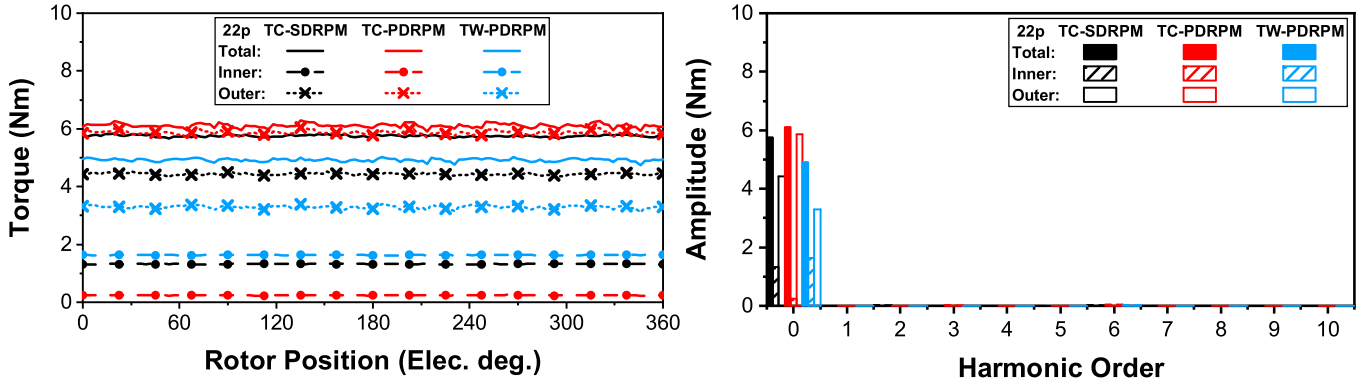

(b) 12s22p.

Fig. 2.25. Torques of TC-SDRPM, TC- and TW-PDRPM machines.

Fig. 2.26 shows the average torques of all machines under different copper losses. The machine 22p TW-PDRPM exhibits the weakest overload capability due to the strong armature reaction. On the other hand, the TC-SDRPM machines have stronger overload capability compared to other types of machines with the same pole number. This is because the series connection of TC-SDRPM machines leads to almost double the equivalent airgap length, i.e. 2×(PM thickness + airgap).

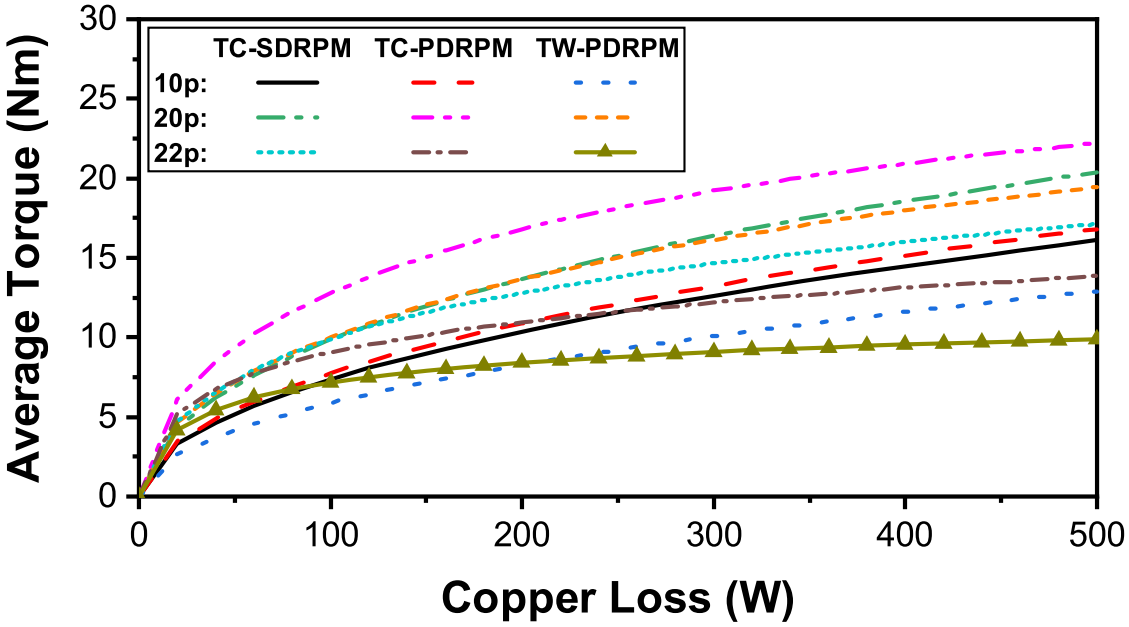

Fig. 2.26. Average torques versus copper loss of TC-SDRPM, TC- and TW-PDRPM machines with different slot-pole number combinations with zero d-axis current.

2.5.4 Losses and efficiencies

The PM eddy current and iron losses of all optimised machines with different slot/pole number combinations are shown in Fig. 2.27. The copper loss for all machines is the same at 30W. The TC-SDRPM machines have the lowest iron loss with different pole numbers because of the yokeless stator structure. Fig. 2.28 illustrates the efficiencies of all machines. It is observed that all types of machines achieve relatively higher efficiency with the 12s20p slot/pole number combination. The 12s20p TC-PDRPM machine has the highest efficiency compared to all other machines since it has the highest torque.

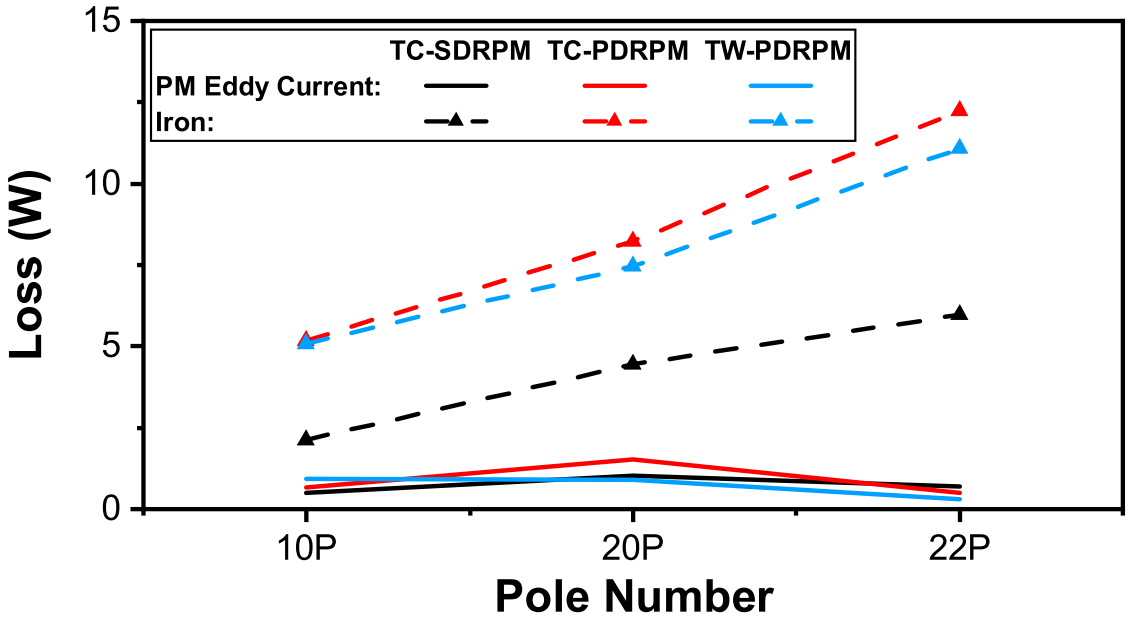

Fig. 2.27. Losses of TC-SDRPM, TC- and TW-PDRPM machines with different slot-pole number combinations at rated load (Rated speed=400 r/min).

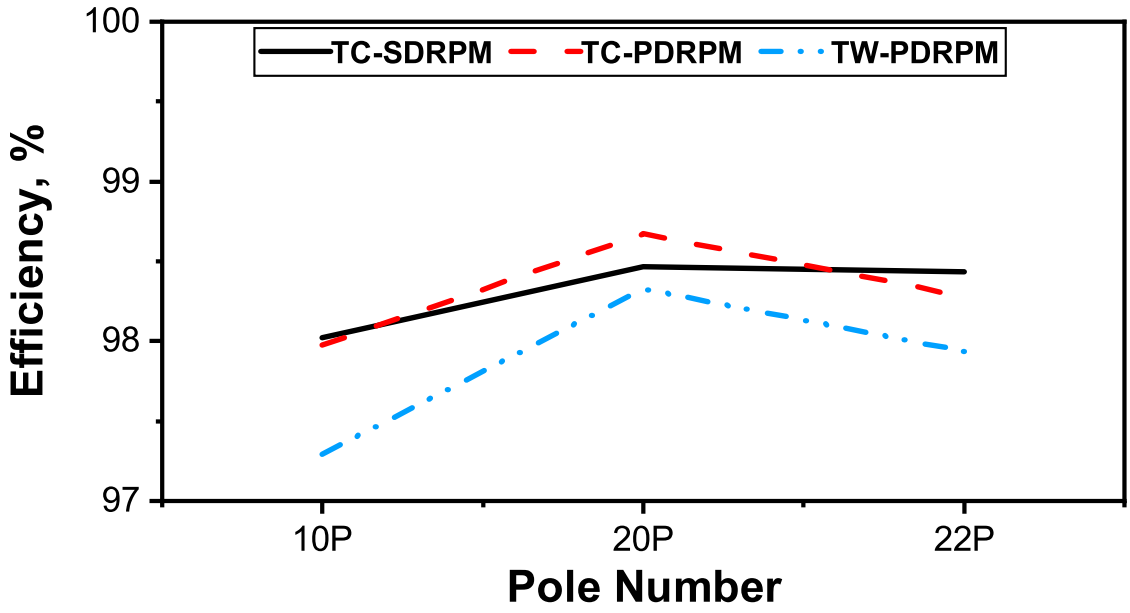

Fig. 2.28. Efficiencies of TC-SDRPM, TC- and TW-PDRPM machines with different slot-pole number combinations at rated load.

2.6 Influence of Machine Size

Compared to the IS SDRPM machine, it was reported [POT16] that the PDRPM machine performs better in MW wind power generation applications. However, different machine sizes with different slot/pole number combinations should be discussed for different applications. Therefore, this chapter investigates the influence of the machine size for TC-SDRPM and TC- and TW-PDRPM machines with

different numbers of slot/pole number combinations. The scaling-up analysis is conducted in three distinct directions, as illustrated in Fig. 2.29. The red arrow K_r presents the machine only scaling up in the radial direction but keeping other parameters the same in the axial direction. The blue arrow K_a shows the machine only scaling up in the axial direction but keeping other parameters the same in the radial direction.

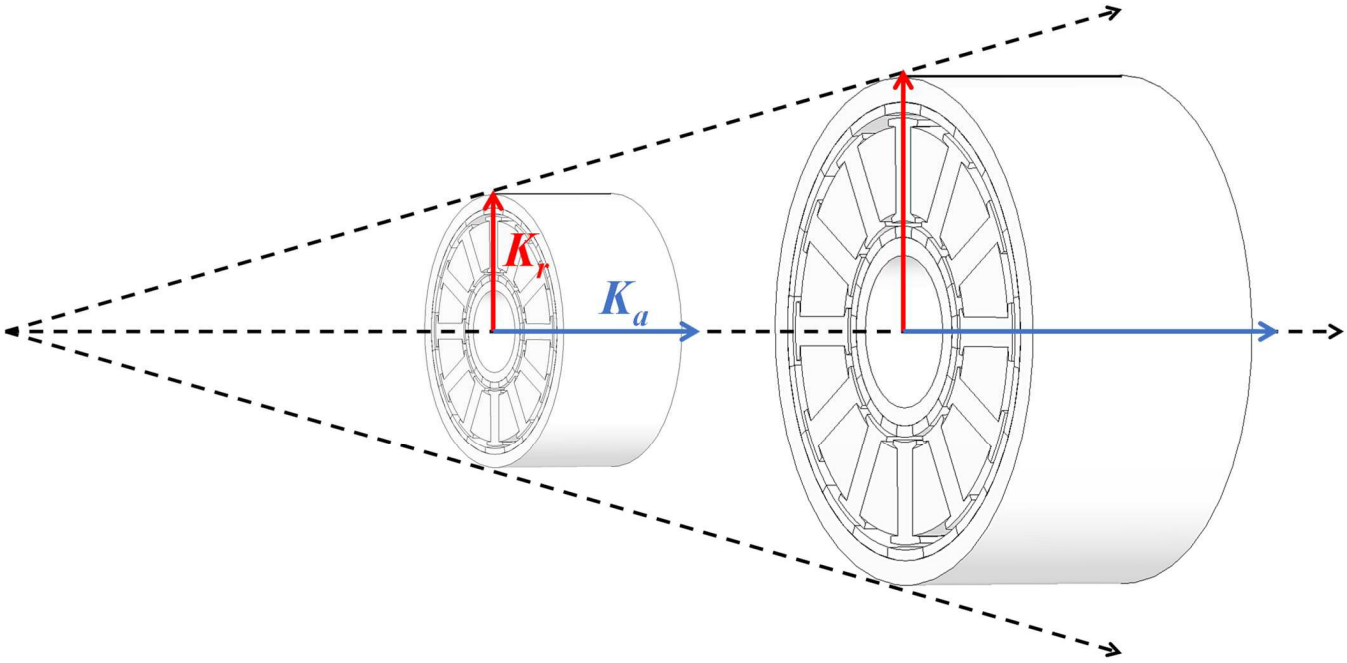

Fig. 2.29. Scale up method of machine.

2.6.1 Scale-up in radial direction

In the radial direction, the copper loss scales up as K_r^2. The end-winding length is influenced significantly by the radially scaling up. The stator armature winding input current with zero *d*-axis current control and the torque of all machines varied with the K_r are shown in Fig. 2.30.

In this case, the torque of the 12s20p TW-PDRPM machine increases to the highest with the increase in K_r. The TW configuration gives the IS TW-PDRPM machines an advantage of their shorter end-winding length. Thus, the 12s20p and 12s22p TW-PDRPM machines have higher input current with increased K_r. However, the strong 2 pole stator armature reaction in the 12s22p TW-PDRPM machine leads to severe magnetic oversaturation, which results in the torque of the 12s22p TW-PDRPM machine increasing slowly with K_r.

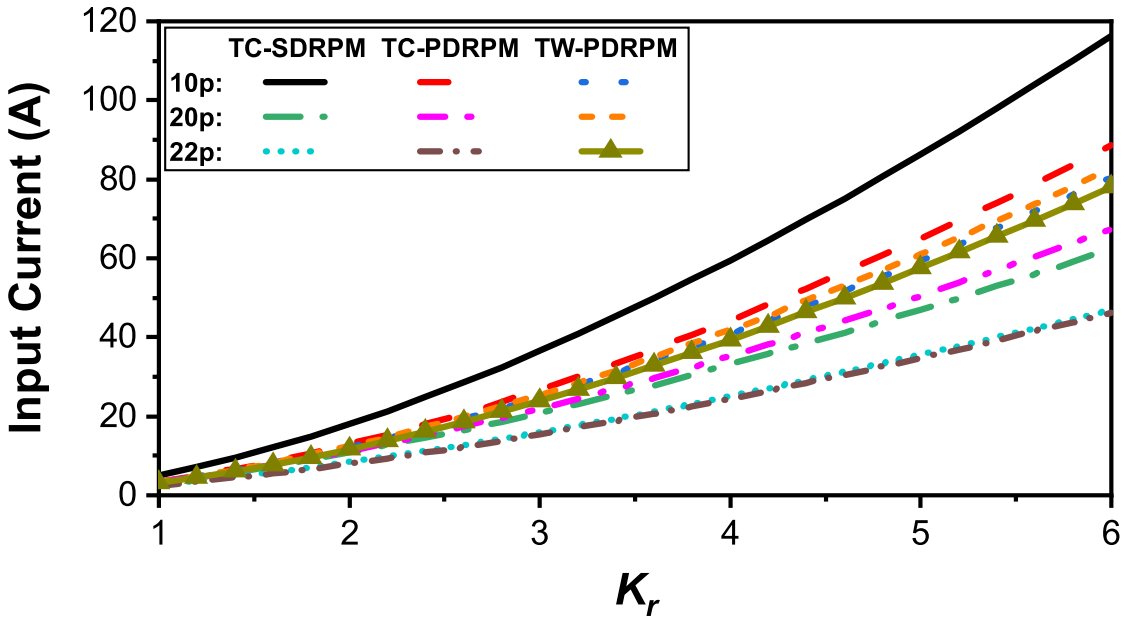

(a)

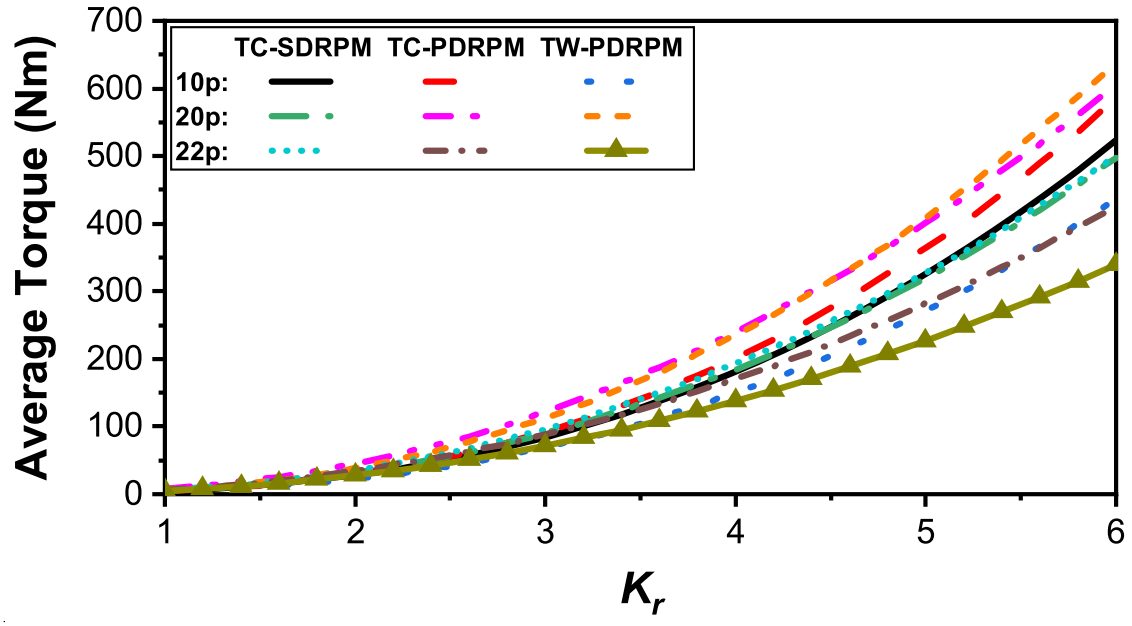

(b)

Fig. 2.30. Variation of average torque and stator q-axis input current with K_r. (a) Input current. (b) Average torque.

2.6.2 Scale-up in axial direction

In the axial direction, copper loss increases in proportion to K_a. Fig. 2.31 shows the input currents and torques of all machines vary with K_a. With axial scaling, the effect of end-winding length becomes negligible gradually. Therefore, the input currents in TC-SDRPM and TC-PDRPM machines increase more with Ka than in TW-PDRPM machines. This leads to a more significant increase in the torque of TC-SDRPM and TC-PDRPM machines compared to TW-PDRPM machines.

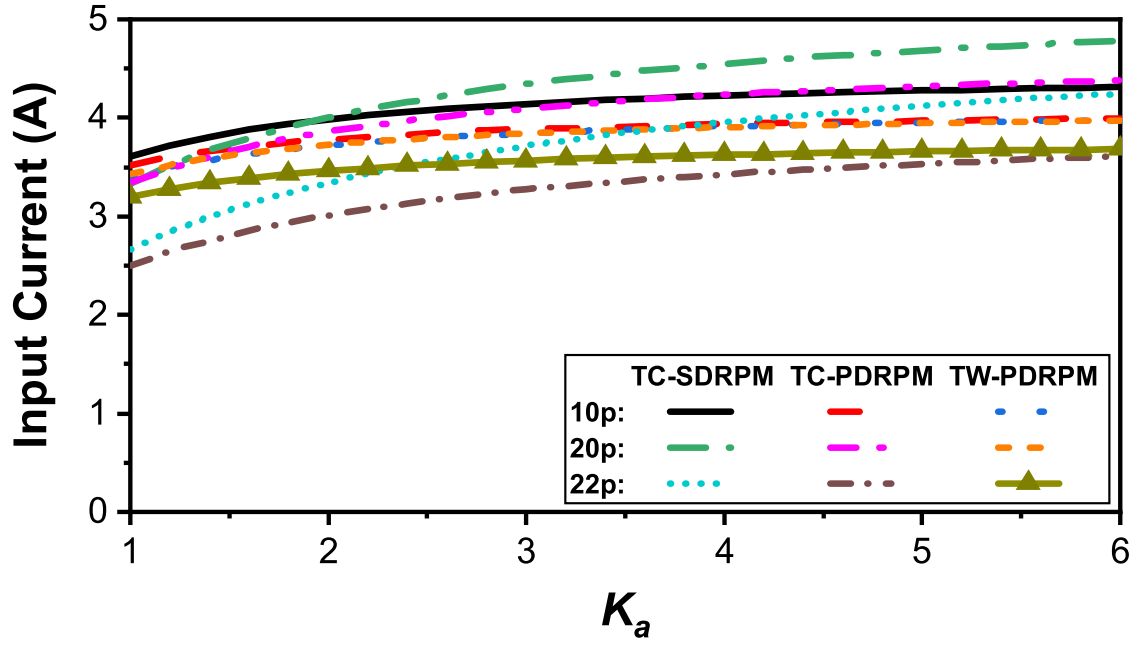

(a)

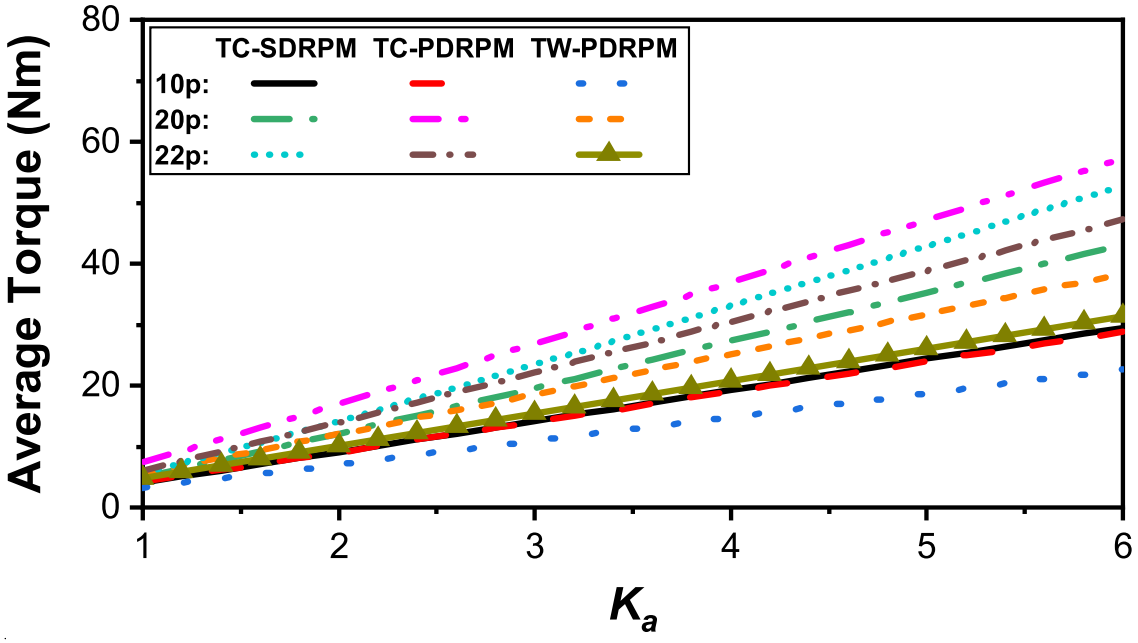

(b)

Fig. 2.31. Variation of average torque and stator q-axis input current with K_a. (a) Input current. (b) Average torque.

2.6.3 Scale-up in radial and axial directions

When both radial and axial directions are scaled up, the volume of the machine is scaled up. The copper loss scales up as $K_a \times K_r^2$. Fig. 2.32 shows the relationships between the torque of all machines with K_a and K_r.

As mentioned in Chapter 2.6.1, the IS TW-PDRPM machines have higher stator q-axis input currents

than IS TC-SDRPM and TC-PDRPM machines due to their short end-winding length. However, when the axial direction is considered. The stator q-axis input current difference is insignificant compared to only the radial direction scales up. Therefore, the advantage of the short end-winding in TW-PDRPM machines is less. The TC-SDRPM machine performs well with different slot pole number combinations when both radial and axial lengths increase.

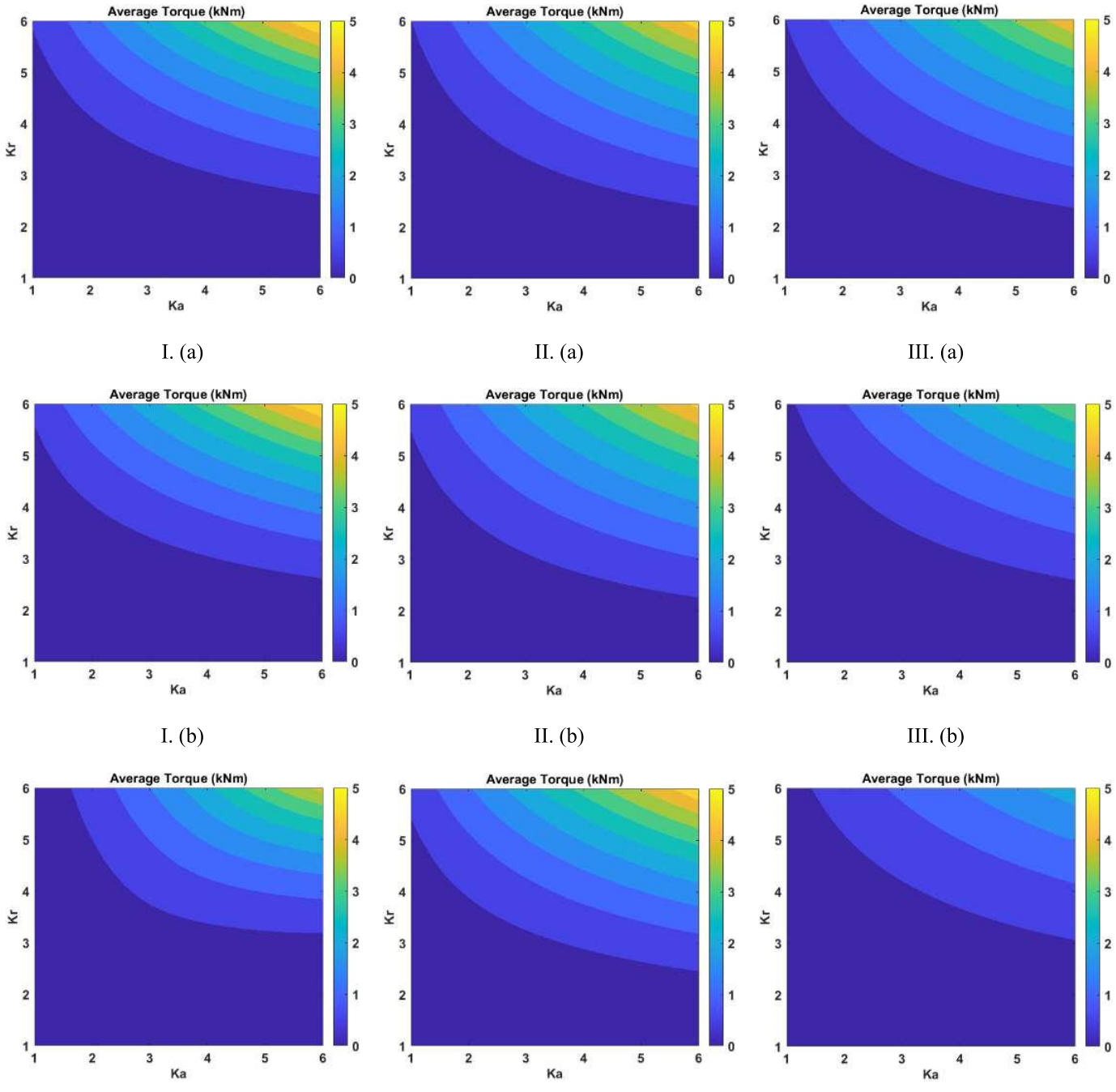

Fig. 2.32. Variation of average torque with K_r and K_a. I. 12s10p. II. 12s20p. III. 12s22p. (a) TC-SDRPM. (b) TC-PDRPM. (c) TW-PDRPM.

2.6.4 Summary

The TC-SDRPM, TC- and TW-PDRPM machines with different slot/pole number combinations and machine sizes are discussed in this chapter. Fig. 2.33 shows the recommended machine type for different machine sizes. The discussion on the applicability of different machine types in different dimensions only considered the electromagnetic torque of the machines. It can be concluded that the TW-PDRPM machine is better for the large radius and small axial length application due to the short end-winding length of the TW configuration. On the other hand, the TC-PDRPM machine is suitable for large axial length and small radius applications due to its relatively higher torque, and the end-winding length becomes gradually negligible with the increasing axial length. The TC-SDRPM machine always performs well when both radial and axial lengths increase.

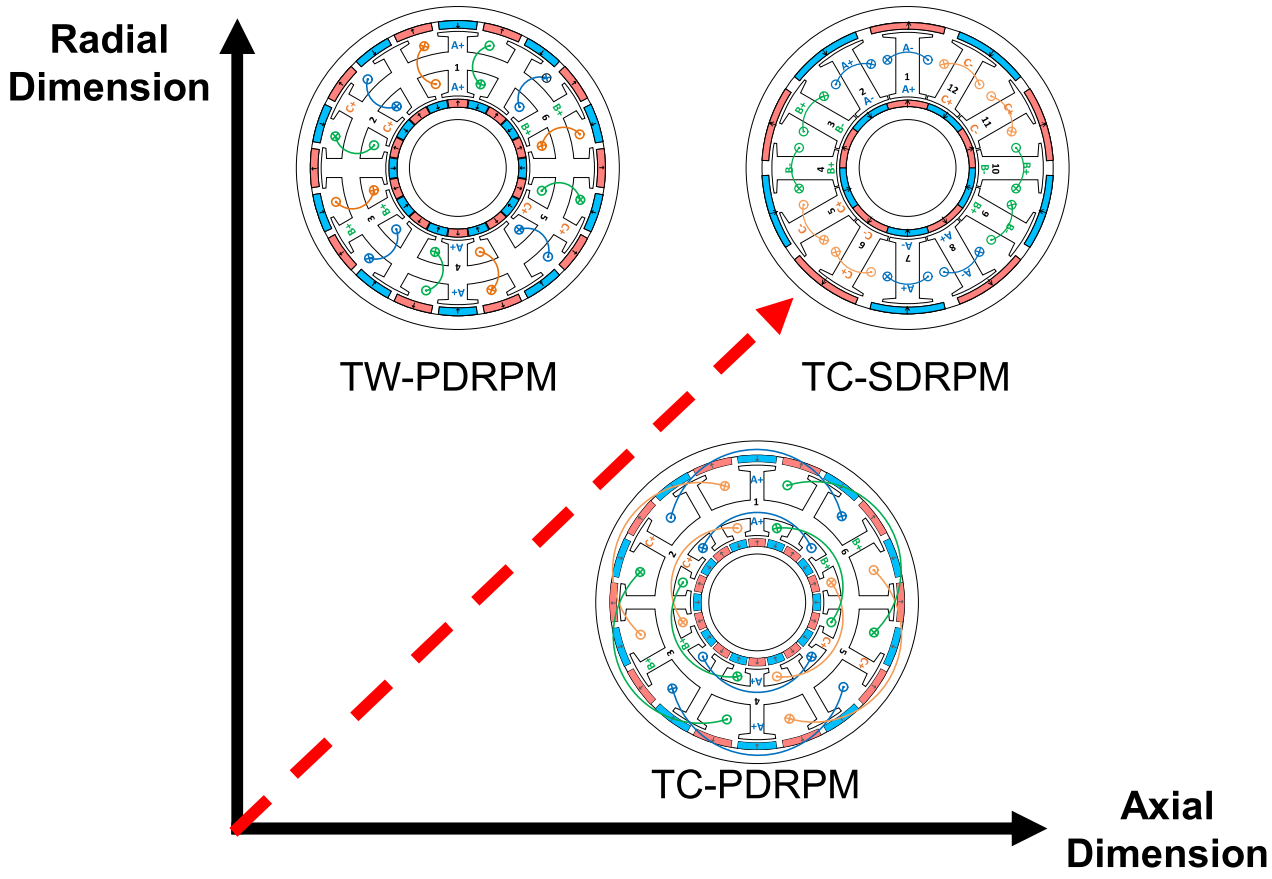

Fig. 2.33. Recommended machine type for different machine sizes.

2.7 Experimental Validation

The 12s10p TW-PDRPM and TC-SDRPM machines, Fig. 2.34, are prototyped and tested to validate the FEA results. The design parameters are listed in Tables 2.2 and 2.3.

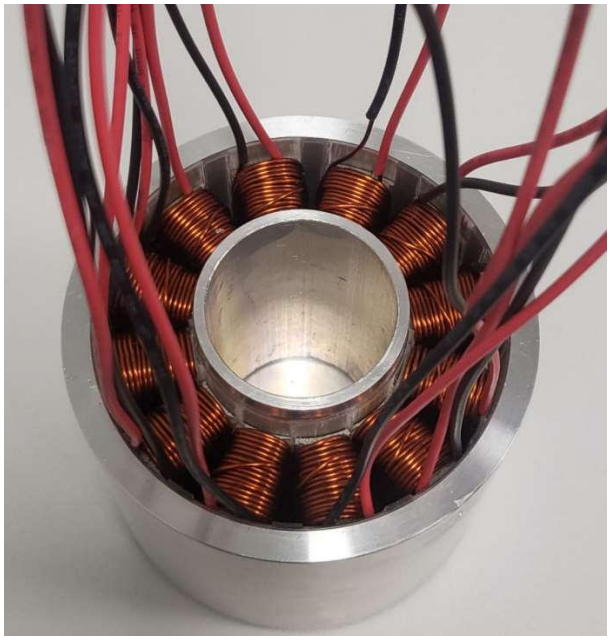

(I.a)

(II.a)

(I.b)

(II.b)

Fig. 2.34. 12s10p machine prototypes. I. TC-SDRPM. II. TW-PDRPM. (a) Stator. (b) Rotor.

The cogging torques and static torques of 12s10p TC-SDRPM and TW-PDRPM machines are measured by using the test method in [ZHU09] and the test rig shown in Fig. 2.35. The phase-back EMFs of two machines are obtained at 800 r/min. The FEA predicted and measured results of cogging torques

and back EMFs of the two machines are shown in Figs. 2.36 and 2.37, respectively. Although the amplitudes and waveforms exhibit some differences, it is worth mentioning that both FEA and experiments confirm the small cogging torques in the prototype machines. The differences between the measured and the predicted torque and EMF amplitudes are mainly attributed to the manufacturing imperfection. Overall, for both back-EMF and cogging torque, the FEA predictions are well validated by experiments.

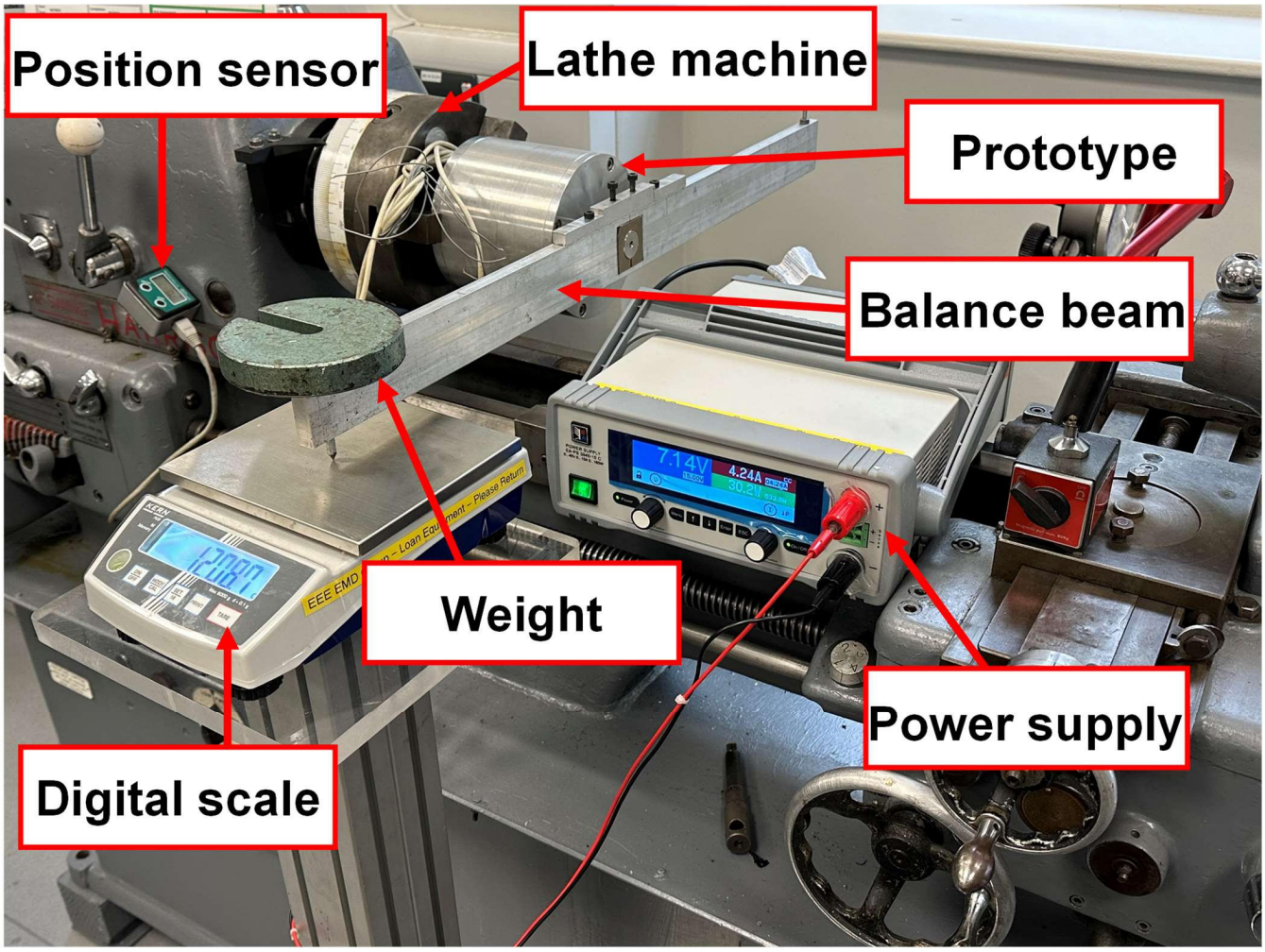

Fig. 2.35. Test rig for static torque measurement.

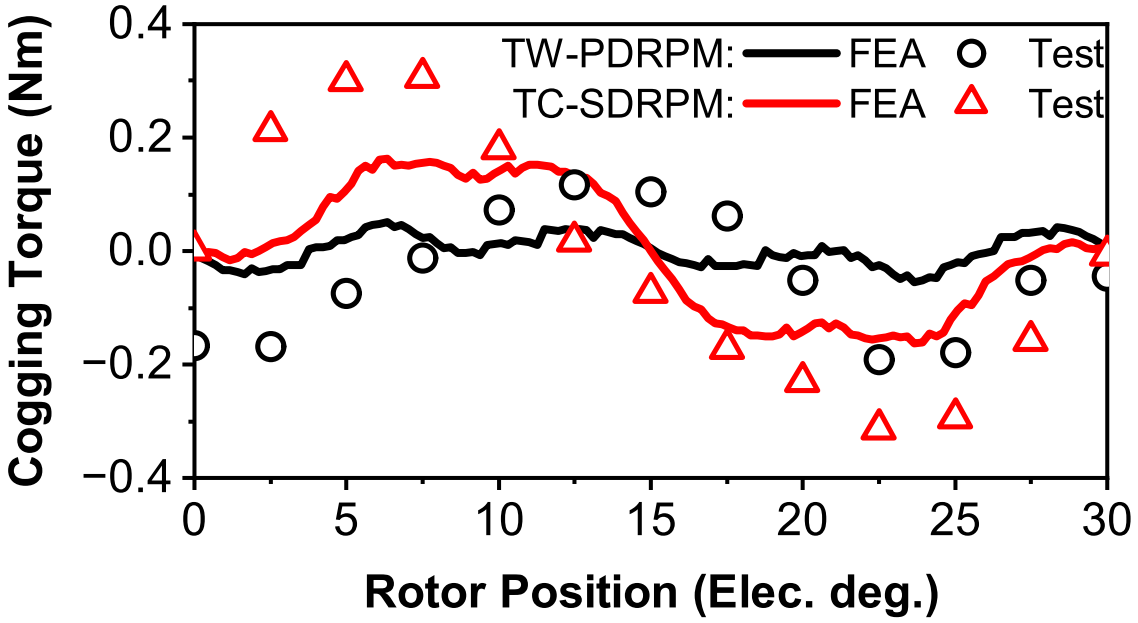

(a) Waveforms.

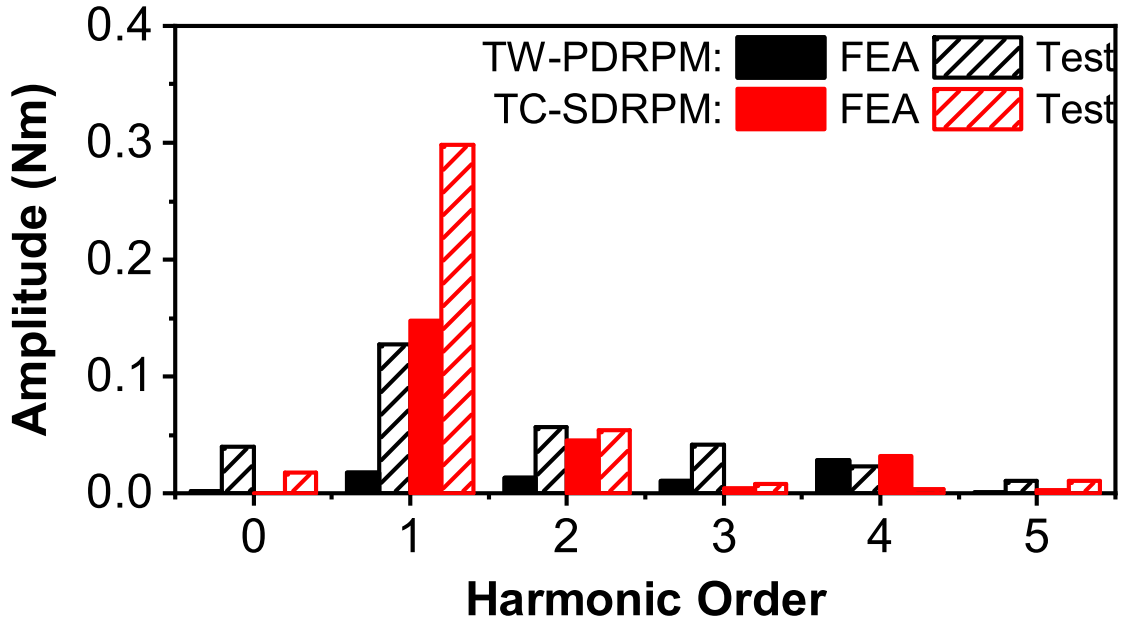

(b) Spectra.

Fig. 2.36. FEA predicted and measured cogging torques.

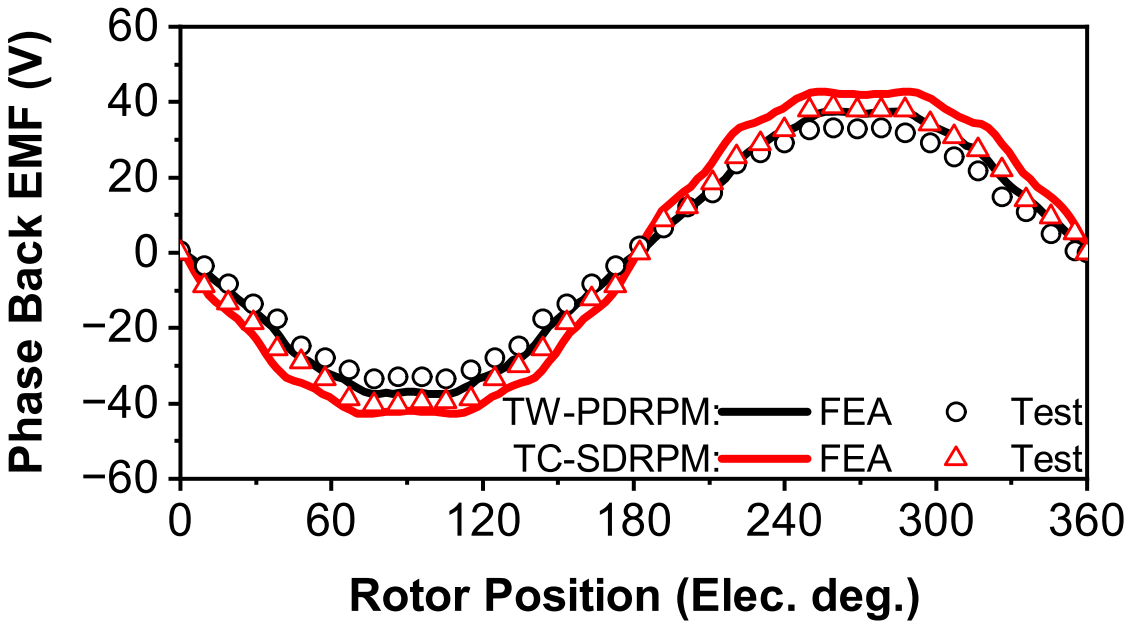

(a) Waveforms.

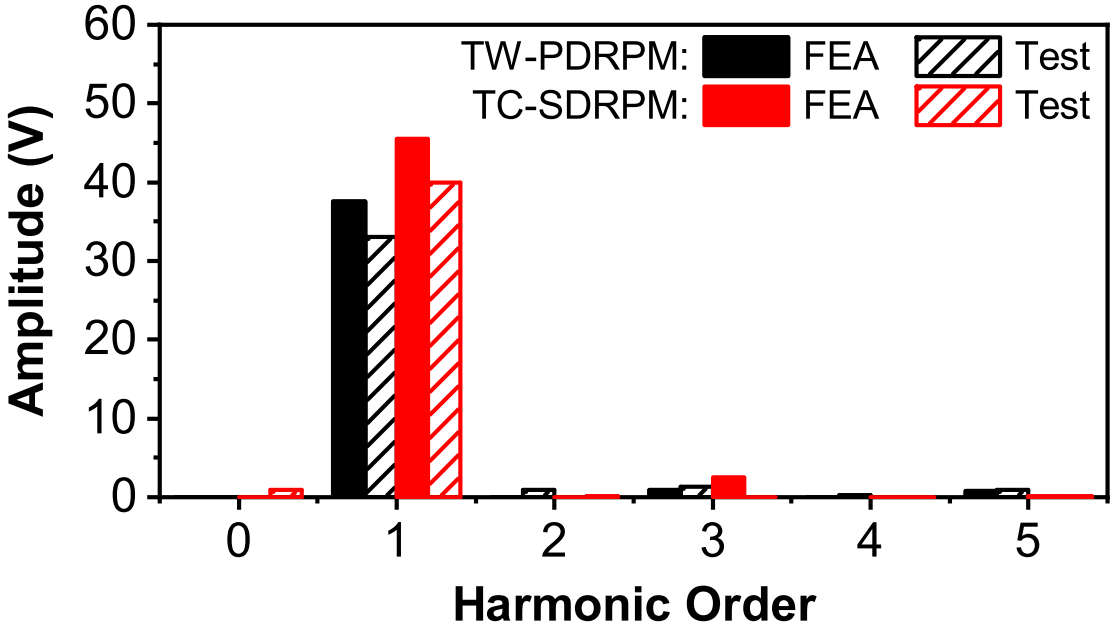

(b) Spectra.

Fig. 2.37. FEA predicted and measured phase back EMFs.

The full and half load static torques of TW-SDRPM and TC-PDRPM machines are measured by injecting a range of DC ($I_A = -2I_B = -2I_C = I_{DC}$), and the full load current I_{rated} corresponds to the copper loss of 30 W, as shown in Fig. 2.38 (a). Fig. 2.38 (b) shows the variation of average torque with current. The measured torques match well with the FEA results, and as expected, the TC-SDRPM machine has a higher torque compared to the TC-SDRPM machine.

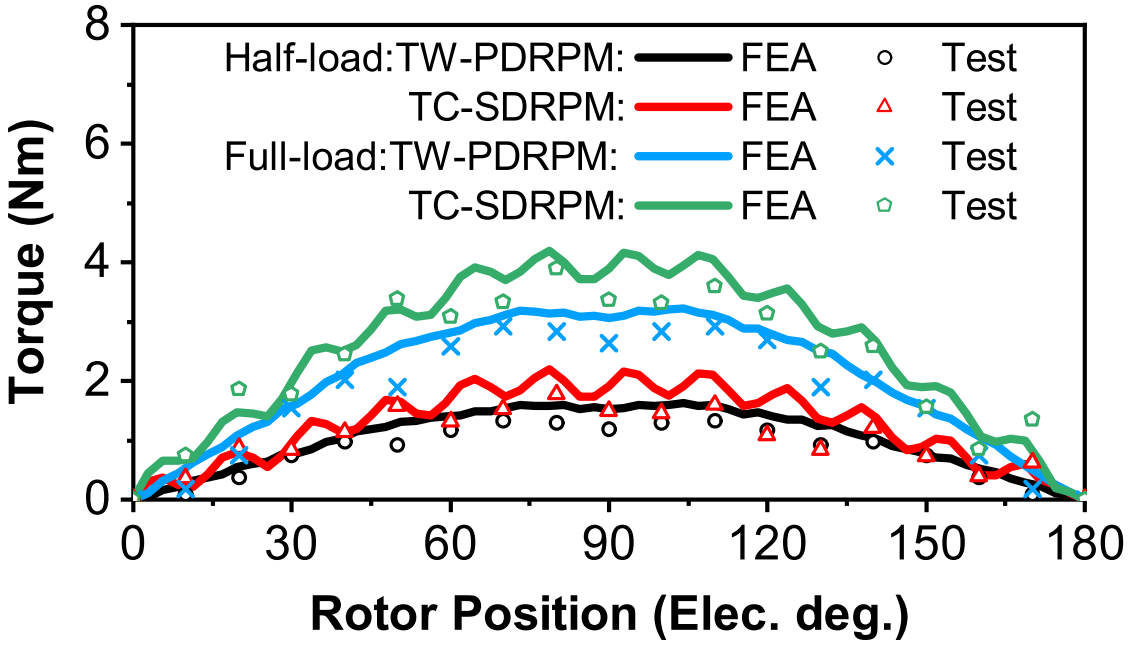

(a) Static torques at full and half-load conditions.

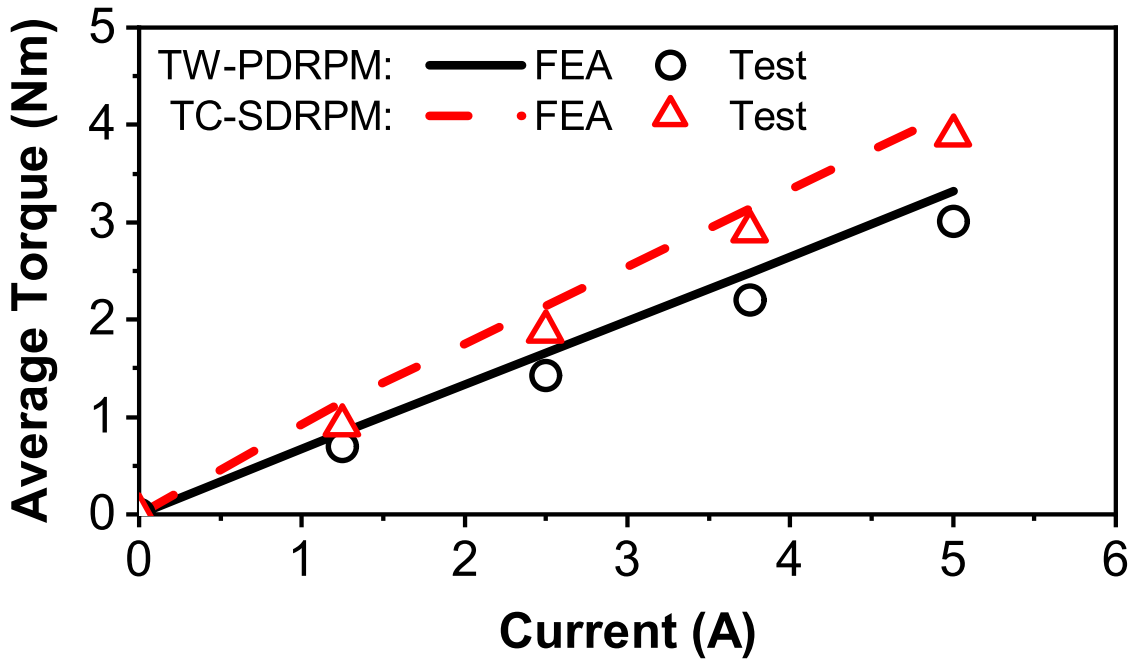

(b) Variation of average torques with currents.

Fig. 2.38. FEA and measured torques.

2.8 Conclusion

This chapter has presented a comparative study of radial flux TC-SDRPM, TC-PDRPM, and TW-PDRPM machines with different slot/pole number combinations and machine sizes. All machines are optimised by the FEA genetic algorithm.

Some conclusions can be drawn as follows.

1. In a radial structure machine, the outer rotor inherently has a larger radius than the inner rotor, resulting in a larger pole arc for the outer rotor PM, producing higher flux. The TC-PDRPM machine has the highest utilisation of the outer rotor PM. Thus, the TC-PDRPM machine has the highest PM utilisation among all types of machines with different slot/pole number combinations.

2. In terms of machine size scaling effects, the 12s20p TW-PDRPM machine shows the highest torque when scaling up radially, which is attributed to its short end-winding. The 12s20p TC-PDRPM machine performs better in axial scaling up since the TC-PDRPM machine has the highest torque, and the end-winding length is negligible with the axial length increase. The TC-SDRPM machine has the best performance when the machine scales up in both axial and radial directions.

The 12s10p TW-PDRPM and TC-SDRPM machines have been prototyped for validation. The experimental results have good agreement with the FEA.

CHAPTER 3

DUAL- AND SINGLE-ROTOR RADIAL-FLUX FRACTIONAL-SLOT PERMANENT MAGNET MACHINES

In Chapter 2, the comparison of dual-rotor PM machines with series and parallel magnetic circuits (SDRPM and PDRPM machines) reveals that the external rotor of the PDRPM machine with tooth coil winding configuration contributes the majority of torque to the total torque, which is even higher than the total torques of the toroidal winding-PDRPM machine and the tooth coil-SDRPM machine. It shows that the single external-rotor machine potentially has even higher torque than the dual-rotor machine. Thus, this chapter presents a comparative analysis of the electromagnetic performance of radial flux dual-rotor surface-mounted permanent magnet (SPM) machines with fractional slot non-overlapping windings, with reference to external- and internal-rotor SPM machines. The SDRPM machine is selected to compare with the single-rotor machines since the SDRPM machine shows higher torque than the PDRPM machine in Chapter 2. All machines are optimised by genetic algorithm using finite element analysis under various design optimisation scenarios, together with the equivalent magnetic circuit analysis. In addition, the influence of air gap length, PM volume, machine inner bore radius, and pole number is investigated. The results have revealed that the dual rotor SPM machine has lower torque but higher overload capability than the single rotor SPM machines. The SDRPM machine is prototyped and tested to validate the results.

This chapter is published in the 2022 International Conference on Electrical Machines (ICEM) (ICEM) [RAN22b], and submitted to IEEE access:

Z. T. Ran, Z. Q. Zhu, F. R. Wei and E. Cetin, "Comparative study of yokeless dual-rotor and external-rotor radial-flux fractional-slot PM machines," *2022 International Conference on Electrical Machines (ICEM)*, Valencia, Spain, pp. 1913-1919, 2022.

Z.T. Ran and Z.Q. Zhu, “Comparative study of dual- and single-rotor radial-flux fractional-slot permanent magnet machines,” IEEE Access.

3.1 Introduction

High torque density electrical machines are widely used in industry, such as aerospace, robotics, electric vehicles, and wind power generators, etc. Permanent magnet (PM) synchronous machines (PMSMs) using high-energy PM materials are arguably the most popular electrical machine technology

due to high torque density and high efficiency [ZHU14]. To further improve the torque density of PMSMs, many researchers have strived to develop new machine topologies, of which dual-rotor (DR) PM machines have received widespread interest [RAN22b] [ZHA17] [JAF20] [GAN16] [LIU19].

The radial flux DRPM machine was proposed in [QU03a]. The machine is constructed by a sandwiched stator with inner and outer surface-mounted PM (SPM) rotors. Since the inner and outer rotors have the same pole number, two rotors are mounted on the same shaft with the same rotating speed. The magnetic fluxes generated by inner and outer PMs are in parallel and superimposed in the stator yoke [QU04]. Thus, the machine can be simply designed as an internal rotor PM machine combined with an external rotor PM machine [SON14] [ALL20].

In order to further enhance the torque of the DRPM machine. Various PM arrangements of inner and outer rotors are investigated. Compared to a SPM rotor, an interior PM (IPM) inner rotor utilises the internal space of the DRPM machine to increase torque due to flux focusing [FUJ15]. Moreover, a Halbach-array PM configuration helps the DRPM machine significantly to reduce the weight of two rotors, and thus, the torque density of the machine is increased [KUM16]. However, the DRPM machine exhibits the issue of high PM amount requirement due to two rotors. Thus, a consequent pole DRPM machine is proposed to reduce the PM amount and cost [ZHA20a]. The current harmonic injection method is also considered to increase the torque of the DRPM machine. However, the severe magnetic saturation in the stator yoke caused by the current harmonic injection reduced the torque [WAN12].

Since the inner and outer PMs have the opposite magnetisation directions, the fluxes superimposed in the stator yoke of a conventional DRPM machine lead to a thick stator yoke. This influences the slot area and the machine weight. Therefore, in order to further improve the electromagnetic performance of the conventional DRPM machine. The yokeless series magnetic circuits DRPM (SDRPM) machine is proposed in [VAN13]. The inner and outer PMs have the same magnetisation direction, and the fluxes generated by the inner and outer PMs are in series in the SDRPM machine. Thus, the stator yoke can be completely removed. This yokeless structure provides a large slot area, and the copper wire can be wound directly onto the modular stator cores to enhance the slot fill factor and reduce the weight of the conventional DRPM machine [WAN12].

In the SDRPM machine, the Halbach-array PMs are used to increase the torque and reduce the machine weight further [GOL19a]. The yokeless structure and Halbach-array PM significantly reduced the weight the SDRPM machine compared to the internal-rotor SPM (IRSPM) and external-rotor SPM (ERSPM) machines. Thus, the Halbach-array PM SDRPM machine shows higher torque density compared to single-rotor SPM (SRSPM) machines which is better for aerospace applications [GOL19b]. The current harmonic injection method is more effective in the SDRPM machine to increase the torque

compared to the conventional DRPM machine due to yokeless structure [GOL18].

[POT16] compares the SDRPM and conventional DRPM machines. In general, the SDRPM machine shows higher torque than the DRPM machine under the same thermal condition because the yokeless structure provides a larger slot area to the SDRPM machine. Only under the large machine size and high coil pitch condition, the conventional DRPM machine shows higher torque than the SDRPM machine, since the conventional DRPM machine can employ toroidal winding on the stator yoke to reduce the end-winding length significantly.

In order to further analyse the electromagnetic performance of the DRPM machine. It is necessary to compare the DRPM machine with the conventional SRSPM machines. [DUB16] compared the SDRPM machine with the SRSPM machines in aerospace applications. The SDRPM machine shows efficiency similar to the conventional ERSPM machine but with poor heat dissipation capacity. Therefore, to discuss the electromagnetic performance of the DR structure machines. In this chapter, the higher torque SDRPM machine is selected to compare with the IR and ER SPM machines. The SPM machine with fractional-slot concentrated winding is widely used due to its high efficiency, short end-winding, and good fault-tolerance capability [EL10] [ZHU11]. Thus, the fractional slot concentrated winding (FSCW) SDRPM and SRSPM machines are considered.

This chapter comprehensively analyses and compares the electromagnetic performances of ERSPM, IRSPM, and SDRPM machines by using finite element analysis (FEA). The results are further explained by equivalent magnetic circuit theory. Section 3.2 describes the topologies of the SDRPM machine and conventional ERSPM and IRSPM machines. Section 3.3 describes the global optimisation of all machines via the FEA-based genetic algorithm. Section 3.4 compares their electromagnetic performances, which are further explained by the equivalent magnetic circuit in section 3.5. Section 3.6 investigates the influence of air gap length, PM volume, machine inner bore radius, and pole number on the electromagnetic performance of SDRPM and SRSPM machines. Section 3.7 shows the experimental validation. Finally, the conclusion is given in section 3.8.

3.2 Machine Topologies

Among the FSCW PM machines with different slot/pole number combinations, the 12-slot/10-pole machine has lower cogging torque and better electromagnetic performance [EL10] [ZHU11], and thus, is firstly investigated and the influence of slot/pole number combinations will be given later in section 3.6. The radial flux 12-slot/10-pole SDRPM machine is shown in Fig. 3.1(a), together with the winding arrangement and the magnetising direction of PMs. It has the following features:

- Both rotors are SPM.

- The inner and outer rotors are mounted on the same shaft rotating with the same speed.
- The magnetic poles of the two rotors are aligned and have the same pole numbers and also the same magnetisation polarities.
- The magnetic circuits of inner and outer rotors are in series.
- The sandwiched single stator is yokeless.
- The fractional slot concentrated tooth-coil winding is used.

For the modular stator, the concentrated winding can improve slot fill factor and make assembling easier, and meanwhile, have short end-winding and high fault tolerance, etc.

To make a comprehensive comparative study between SDRPM and SRSPM machines, the IRSPM and ERSPM machines are selected for comparison, as shown in Fig. 3.1(b) and (c). The SDRPM and SRSPM machines have the same slot/pole number combination and winding topology, as well as the same lamination and PM materials. The coil back-EMF phasors are the same for all machines, as depicted in Fig. 3.2.

TABLE 3.1
BASIC DESIGN PARAMETERS

Parameters	Values
Outer radius of outer rotor	50mm
Lamination stack length	50mm
Number of outer rotor poles	10
Number of inner rotor poles	10
Number of stator slots	12
PM remanence	1.2T
PM relative permeability	1.05
Rated speed	400 r/min
Number of series turns per phase	192
PM grade	N35SH
Lamination grade	M300

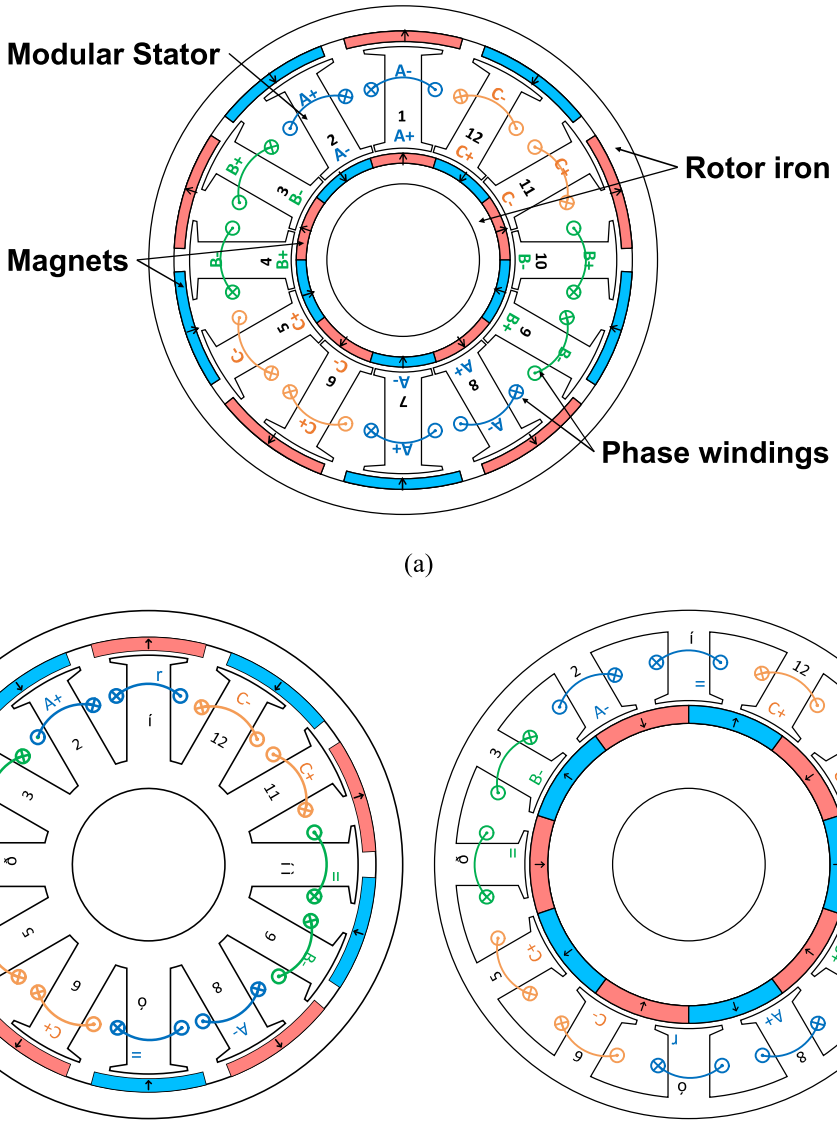

(a)

(b) (c)

Fig. 3.1. Topologies of 12-slot/10-pole machines. (a) SDRPM. (b) ERSPM. (c) IRSPM.

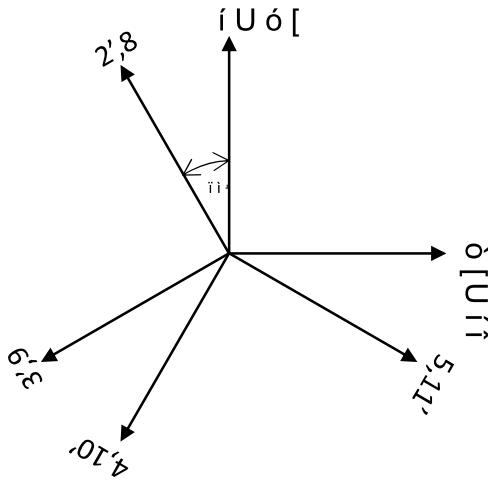

Fig. 3.2. Coil EMF phasors of 12-slot/10-pole SDRPM, ERSPM, and IRSPM machines.

3.3 Design Optimisation

To make a fair comparison, all machines are globally optimised by the genetic algorithm using the FEA. The global optimisation objective is maximum torque under a fixed 30 W copper loss. During the optimisation, other fixed and variable parameters are listed in Table 3.2 and Table 3.3, respectively. Furthermore, to avoid the magnetic flux density over-saturation on the iron core, the magnetic flux density in stator and rotor cores of all machines are constrained under 1.7T during the optimisation.

TABLE 3.2
FIXED PARAMETERS

Parameters	
Outer radius of outer rotor	50mm
Lamination stack length	50mm
Shaft radius	15mm
Copper loss	30W
Airgap length	1mm
Max iron core magnetic flux density	1.7T

TABLE 3.3
VARIABLE PARAMETERS

Parameters	Symbol
Outer PM thickness	L_{om}
Inner PM thickness	L_{im}
Outer PM pole arc	θ_{om}
Inner PM pole arc	θ_{im}
Stator outer radius	R_{so}
Stator inner radius	R_{si}
Stator outer slot opening	b_{os}
Stator inner slot opening	b_{is}
Outer tooth-tip height	h_{os}
Inner tooth-tip height	h_{is}
Outer tooth-tip slope	α_{os}
Inner tooth-tip slope	α_{is}
Stator tooth width	w_{st}
Stator yoke height	h_{sy}

All design parameters are illustrated in Fig. 3.3. All machines are optimised, and the optimised parameters are shown in Table 3.4. The open-circuit flux density distributions and flux lines are shown in Fig. 3.4. It should be noted that the volume of PM is not fixed in the optimisation but will be investigated later in section 3.5.

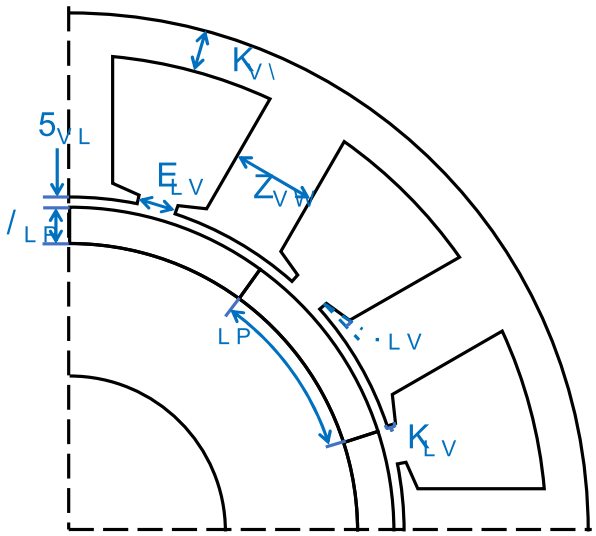

(a)

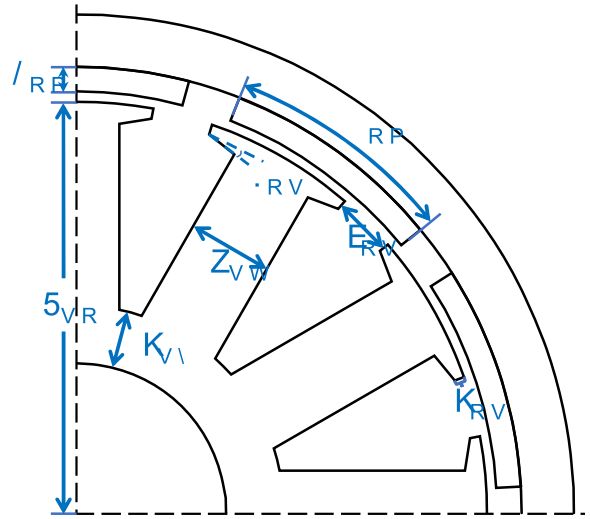

(b)

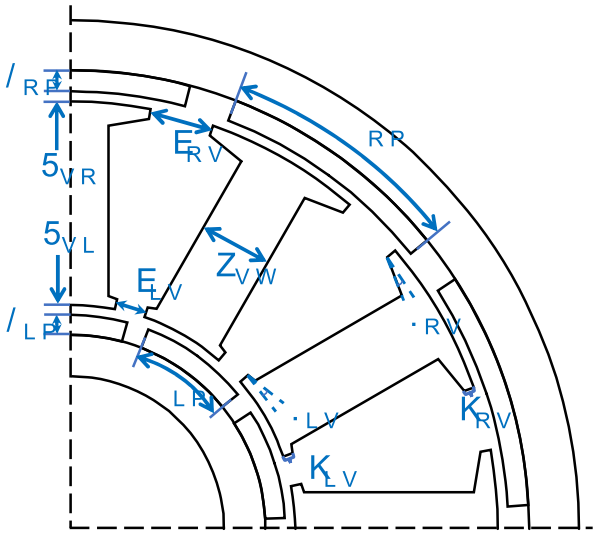

(c)

Fig. 3.3. Dimensional parameters. (a) ERSPM. (b) IRSPM. (c) SDRPM.

TABLE 3.4
PARAMETERS OF OPTIMISED MACHINES

Parameters	ERSPM	IRSPM	SDRPM
Outer PM thickness (mm)	2.5	-	2.0
Inner PM thickness (mm)	-	3.5	2.0
Outer PM pole arc (°elec.)	145	-	150
Inner PM pole arc (°elec.)	-	180	178.5
PM volume (cm^3)	27.5	32.4	36
Stator outer radius (mm)	41	-	42
Stator inner radius (mm)	-	32.3	22
Stator outer slot opening (mm)	6.2	-	6.4
Stator inner slot opening (mm)	-	3.8	0.4
Outer tooth-tip height (mm)	0.7	-	0.7
Inner tooth-tip height (mm)	-	0.8	1.3
Outer tooth-tip slope (deg.)	19	-	14
Inner tooth-tip slope (deg.)	-	12	0
Stator tooth width (mm)	8.6	8.3	7.2
Stator yoke height (mm)	5.4	4	-
Slot area (mm^2)	144	156	172

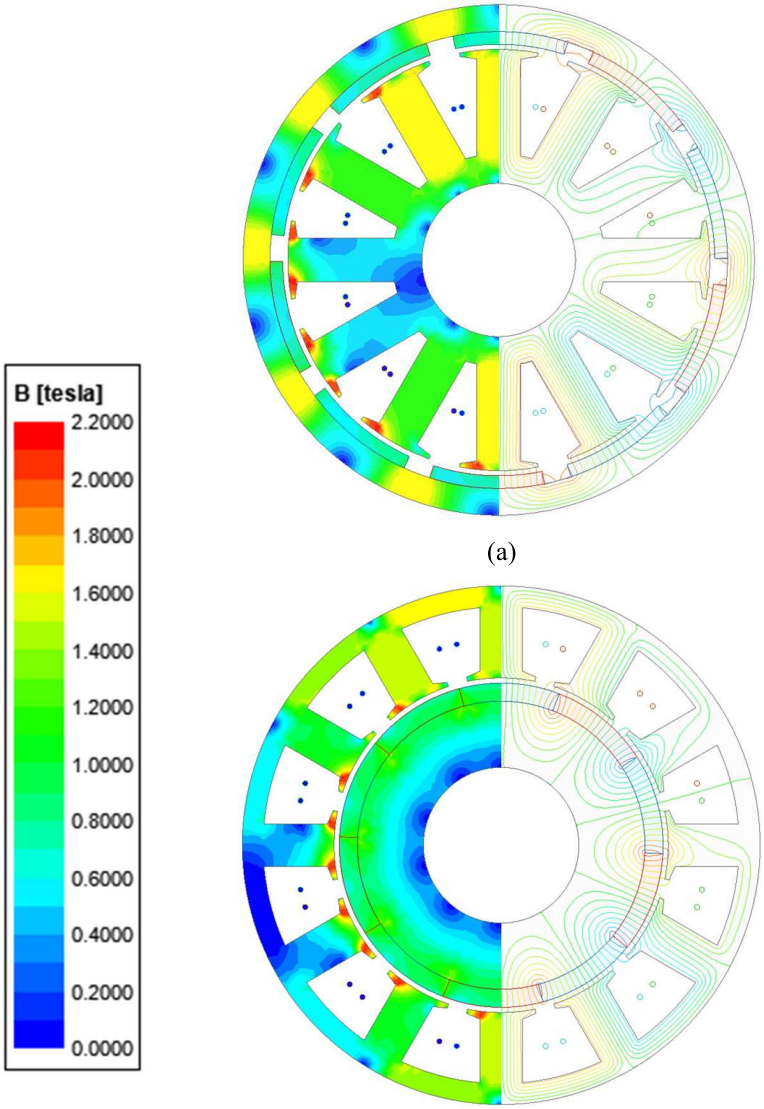

(a)

(b)

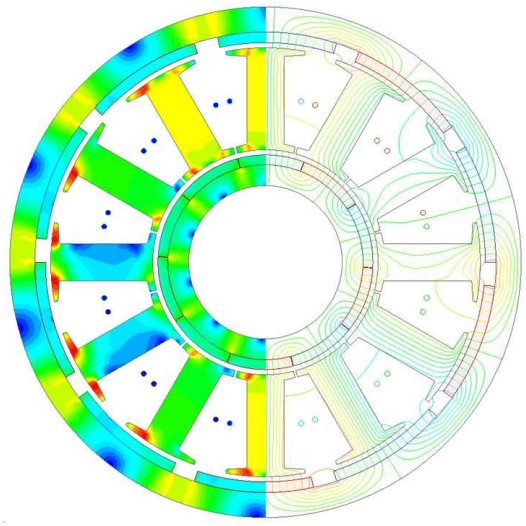

(c)

Fig. 3.4. Open circuit flux density distributions and flux lines. (a) ERSPM. (b) IRSPM. (c) SDRPM.

3.4 Comparison of Electromagnetic Performances of SRSPM and SDRPM Machines

In this section, the electromagnetic performances of all machines will be compared.

Fig. 3.5 shows the air-gap flux densities of the IRSPM, ERSPM, and SDRPM machines. For the optimised SDRPM machine, as shown in Table 3.5, the tooth fluxes collected at the outer and inner airgaps are very similar. Since the radius and area of outer airgap are larger than those of inner airgap, the flux density in the inner airgap of SDRPM machine is larger than that in the outer airgap, as shown in Fig. 3.5(b). The outer airgap flux density of the ERSPM machine is larger than that of the SDRPM machine, since, with a similar outer airgap area, the magnetic flux of the outer airgap of the ERSPM machine is larger than the SDRPM machine. The main reason is that for the radial-flux SDRPM machine, the inner and outer magnetic circuits are connected in series, but the PMs of the inner and outer rotors cannot generate the same magnetic flux due to the different radii of the two rotors. Therefore, the resultant magnetic flux of the SDRPM machine is decreased, which will be further discussed in Section 3.5 by using equivalent magnetic circuits.

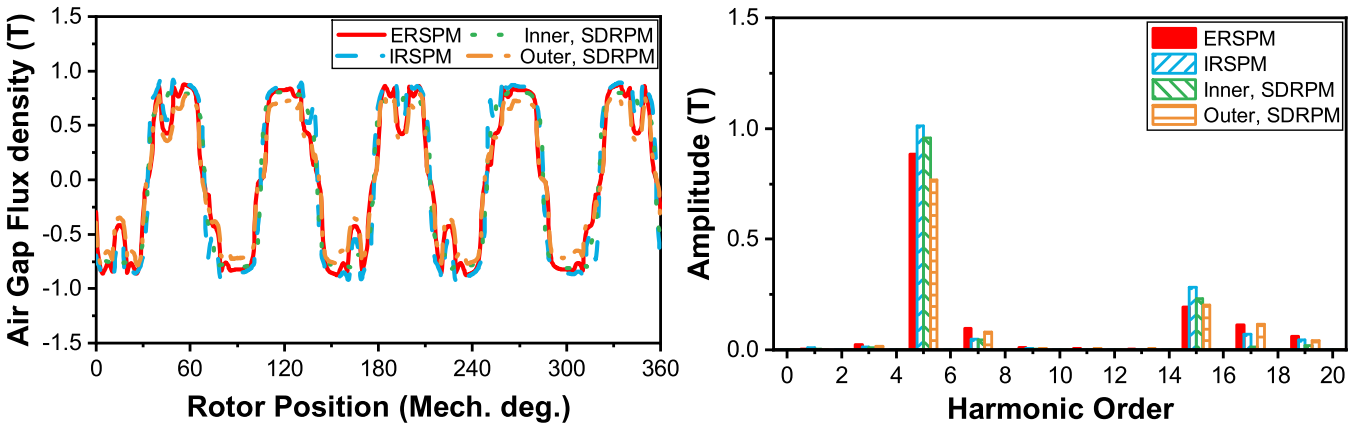

(a) Waveforms. (b) Spectra.

Fig. 3.5. Comparison of inner and outer airgap flux densities of ERSPM, IRSPM, and SDRPM machines.

TABLE 3.5
AIRGAP CHARACTERISTICS OF SRSPM AND SDRPM MACHINES

Outer/Inner airgaps	ERSPM	IRSPM	SDRPM
Airgap flux density (T)	0.88/-	-/1.0	0.77/0.96
Airgap radius (mm)	41/-	-/31	42/21
Airgap area (mm^2)	261/-	-/198	267/135
Coil flux linkage (mWb)	0.674/-	-/0.656	0.598/0.533

Fig. 3.6 compares the phase A flux linkages of three machines. The fundamental component of the phase flux linkage of the ERSPM machine is the largest, 0.125Wb. The fundamental component of the phase flux linkage of the SDRPM machine is the smallest, 0.107Wb. This means the magnetic fluxes linking with the coils of the SDRPM machines is smaller than that of the IRSPM and ERSPM machines, even if the SDRPM machines employ more PM material.

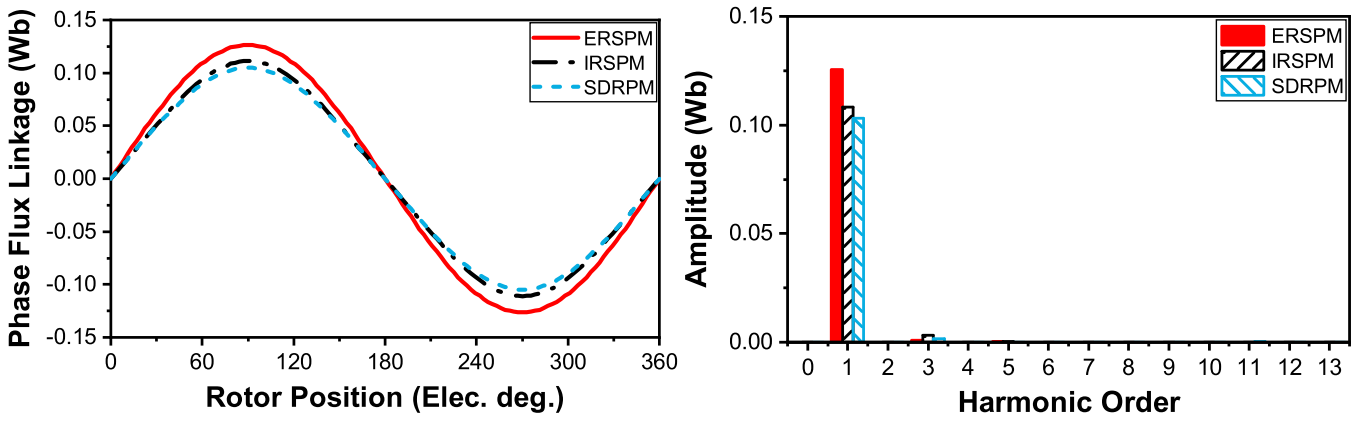

(a) Waveforms. (b) Spectra.

Fig. 3.6. Comparison of phase-A flux linkages ERSPM, IRSPM, and SDRPM machines.

Since the phase A flux linkage of the ERSPM machine is the highest, its back EMF is also the largest. As can be seen from Fig. 3.7(b), the fundamental component of the back EMF of the ERSPM machine is 26.3V, and that of the SDRPM machine is the lowest, 22.5V.

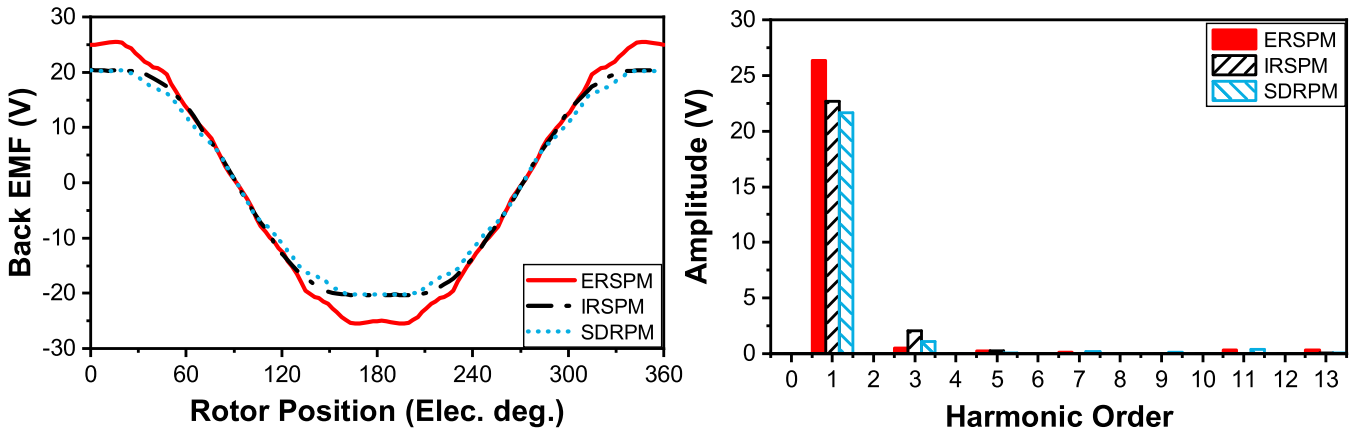

(a) Waveforms. (b) Spectra.

Fig. 3.7. Comparison of phase-A back EMFs of ERSPM, IRSPM, and SDRPM machines (400 r/min).

The torques of the SRSPM and SDRPM machines are compared in Fig. 3.8. The globally optimized SDRPM machine has the largest slot area compared to other machines due to the yokeless structure, allowing for the highest input current under the same copper loss condition. The ERSPM machine exhibits the highest back EMF, with an average torque of 5.9Nm, higher than the SDRPM machine by 10.2%. Although the back EMF of the IRSPM machine is slightly larger than that of the SDRPM machine, the input current of the SDRPM machine is higher, resulting in similar torque outputs for both the IRSPM and SDRPM machines.

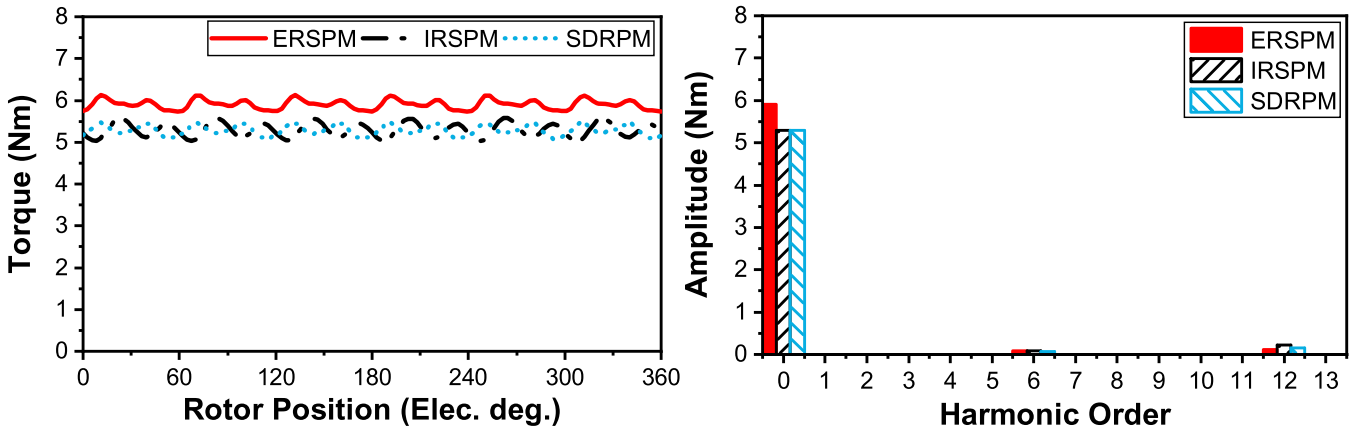

(a) Waveforms. (b) Spectra.

Fig. 3.8. Comparison of torques of ERSPM, IRSPM, and SDRPM machines under 30 W copper loss.

In order to compare the overload capacity of the ERSPM, IRSPM, and SDRPM machines, the variation of average torque with current is shown in Fig. 3.9. The average torque of the ERSPM machine is higher than that of the SDRPM machines before the current is increased to 60A. Then, the ERSPM machine is saturated magnetically, Fig. 3.10. Moreover, the torques of the SDRPM and IRSPM machines continue to increase linearly and exceed the ERSPM machine.

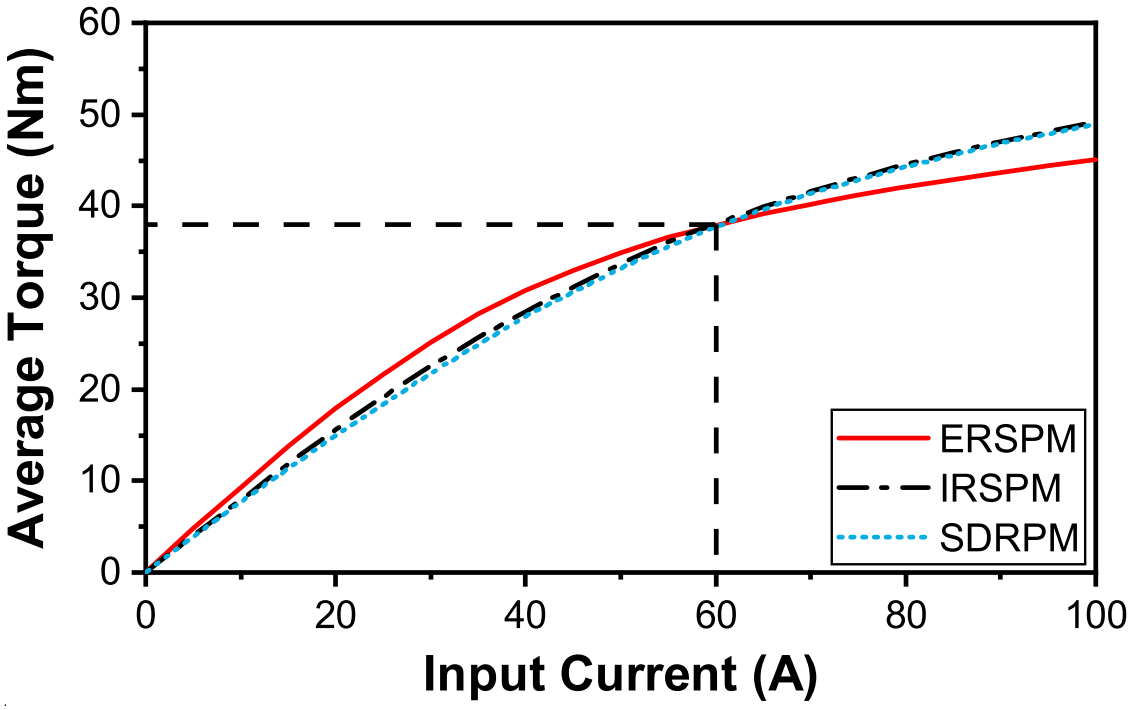

Fig. 3.9. Torque versus current of ERSPM, IRSPM, and SDRPM machines.

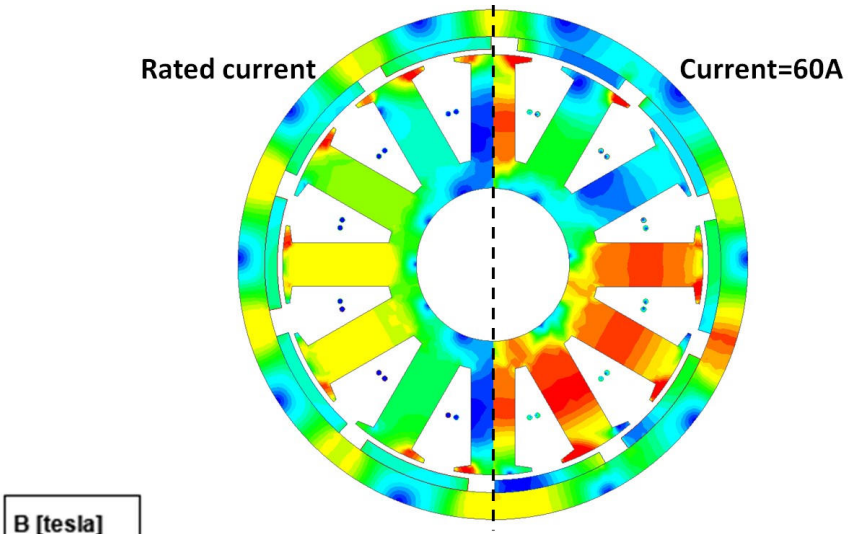

(a) ERSPM.

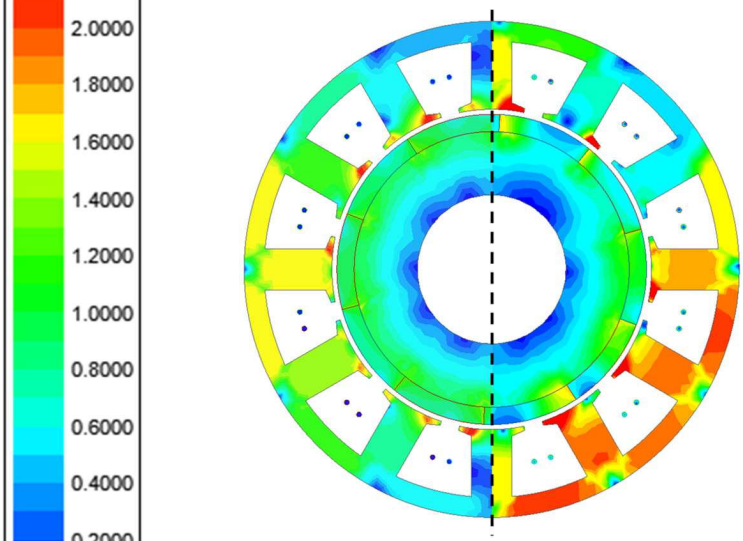

(b) IRSPM.

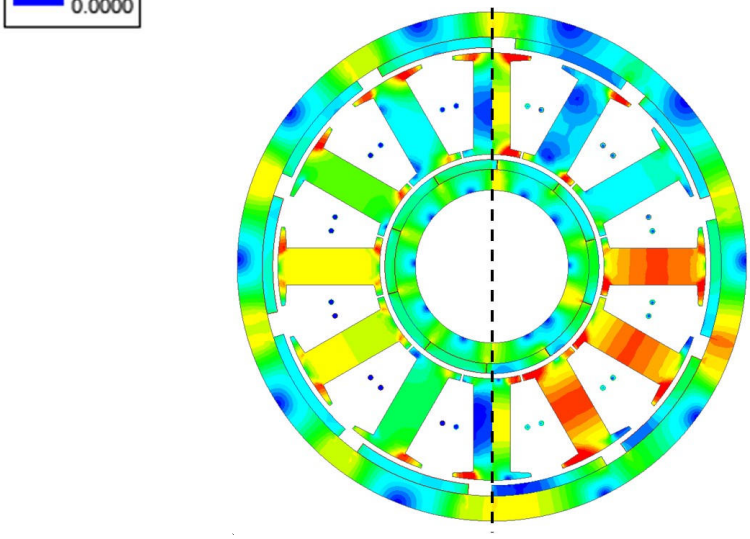

(c) SDRPM.

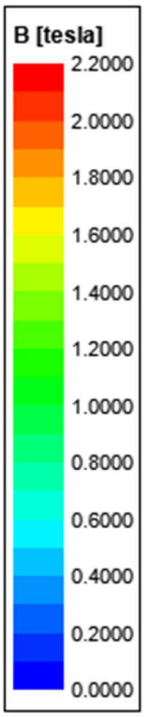

Fig. 3.10. Flux density distributions and flux lines at rated current (left) and current=60A (right).

Since the PM volume is not fixed during the optimisation, in order to compare the torque per of PM volume between these machines, $\rho_{\text{Torque/PM}}$, is defined as:

$$\rho_{\text{Torque/PM}} = \frac{T}{V_{PM}} \tag{3.1}$$

where T is the electromagnetic torque, and V_{PM} is the PM volume.

The values of $\rho_{\text{Torque/PM}}$ of all machines are listed in Table 3.6 As can be seen, the conventional ERSPM machine has the highest $\rho_{\text{Torque/PM}}$. The IRSPM machine has the same torque as the SDRPM machine. However, the SDRPM machine has two rotors that employ more PM material. Thus, $\rho_{\text{Torque/PM}}$ of the IRSPM machine is also higher than that of the SDRPM machine.

TABLE 3.6
TORQUE CHARACTERISTICS OF SRSPM AND SDRPM MACHINES

Parameters	ERSPM	IRSPM	SDRPM
T (Nm)	5.9	5.3	5.3
PM volume (cm^3)	27.5	32.4	36
$\rho_{\text{Torque/PM}}$ (Nm/cm^3)	0.215	0.164	0.147

As can be seen from Table 3.6, the conventional ERSPM machine can achieve higher torque than the SDRPM machines, even with a lower PM volume. The conventional IRSPM machine can achieve the same torque as the SDRPM machine by using less PM volume. This means that compared with the conventional SRSPM machine, the SDRPM machines have no advantage in terms of the torque, the torque density, and the cost, which is not as expected as the axial field yokeless and segmented armature DRPM machine [TAR22] and the linear machine [EGU20], which will be further investigated in the next section.

3.5 Further Analysis by Equivalent Magnetic Circuit

In the following equivalent magnetic circuit analysis, the globally optimised SDRPM machine is selected to explain why the resultant flux linkage in the SDRPM machine is low.

Neglecting the flux leakages, the magnetic flux path and the corresponding equivalent magnetic circuit are shown in Fig. 3.11 and Fig. 3.12, respectively. R_g is the reluctance of airgap over one pole pitch. The permeability of the core material is assumed to be infinite, and thus, the reluctances of the stator and rotor cores can be neglected.

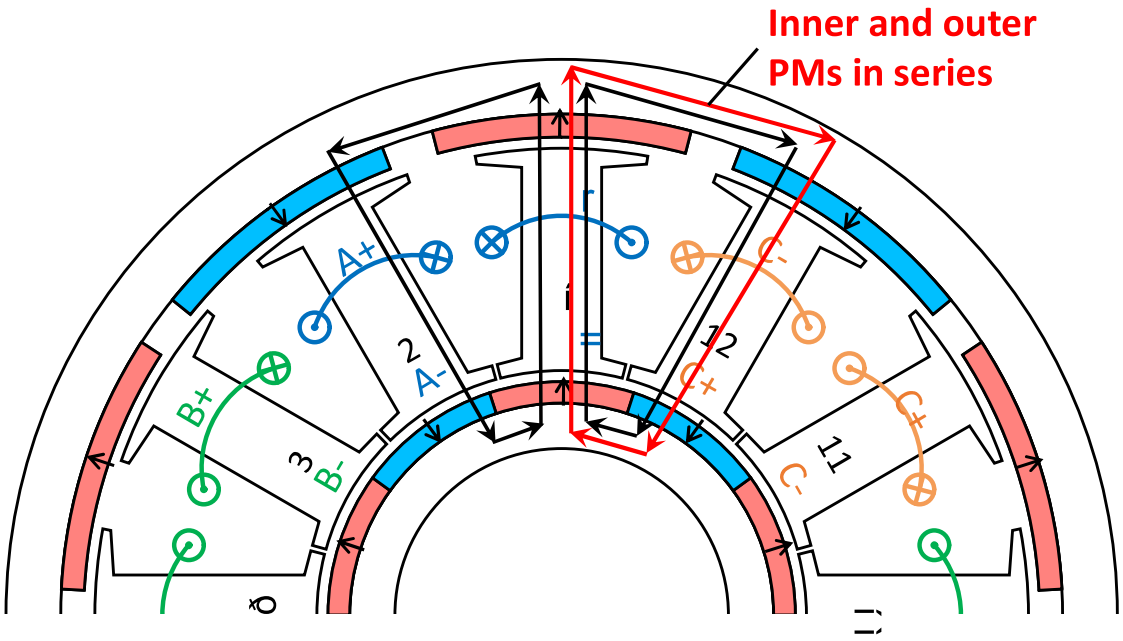

Fig. 3.11. Magnetic flux path of SDRPM machine.

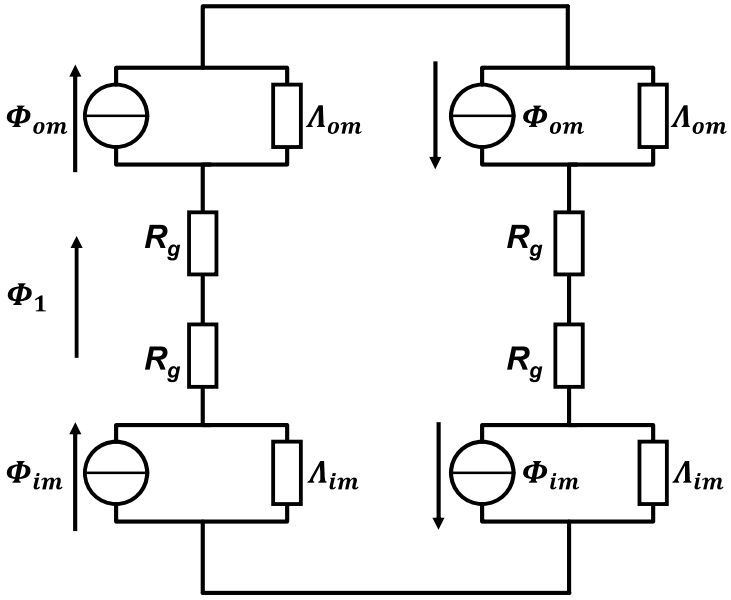

Fig. 3.12. Equivalent magnetic circuit of SDRPM machine.

In the equivalent magnetic circuit, the PMs act as flux sources with permeance in parallel and the airgap equivalent reluctance can be expressed as:

$$\Phi_{om} = B_r S_{om} \tag{3.2}$$

$$\Phi_{im} = B_r S_{im} \tag{3.3}$$

$$\Lambda_{om} = \frac{\mu_r \mu_0 S_{om}}{L_{om}} \tag{3.4}$$

$$\Lambda_{im} = \frac{\mu_r \mu_0 S_{im}}{L_{im}} \tag{3.5}$$

$$R_g = \frac{L_g}{\mu_0 S_g} \tag{3.6}$$

where Φ_{om} and Φ_{im} are the outer and inner PM equivalent fluxes, respectively. B_r is the remanence of the PM, and L_g, L_{om}, and L_{im} are the airgap, outer and inner PM thicknesses, respectively. Λ_{om} and Λ_{im} refer to the permeance of inner and outer PMs, respectively. S_g, $S_{om,}$ and S_{im} are the magnetic fluxes flow through the surface area of airgap, outer and inner PMs per pole. μ_r and μ_0 are the relative permeability and the permeability of free air space, respectively.

For the radial-flux SDRPM machine, the inner rotor radius is inherently smaller than the outer rotor:

$$S_{om} \gg S_{im} \tag{3.7}$$

Thus,

$$\Phi_{om} \gg \Phi_{im} \tag{3.8}$$

Therefore, the flux through a stator tooth Φ_1 can be expressed as:

$$\Phi_1 = \frac{1/\Lambda_{om}\Phi_{om} + 1/\Lambda_{im}\Phi_{im}}{2R_g + 1/\Lambda_{om} + 1/\Lambda_{im}} < \frac{\Phi_{om} + \Phi_{im}\frac{1/\Lambda_{im}}{1/\Lambda_{om}}}{1 + \frac{1/\Lambda_{im}}{1/\Lambda_{om}}} < \Phi_{om} \tag{3.9}$$

The magnetic circuit of the IRSPM machine is the same as that of the ERSPM machine. For a comparative analysis between the SDRPM and the SRSPM machines, the ERSPM machine is selected as the benchmark for the equivalent magnetic circuit study. After completely removing the inner rotor part and inner airgap from the SDRPM machine, it transforms into an ERSPM machine. The equivalent magnetic circuit of the ERSPM machine is shown in Fig. 3.13.

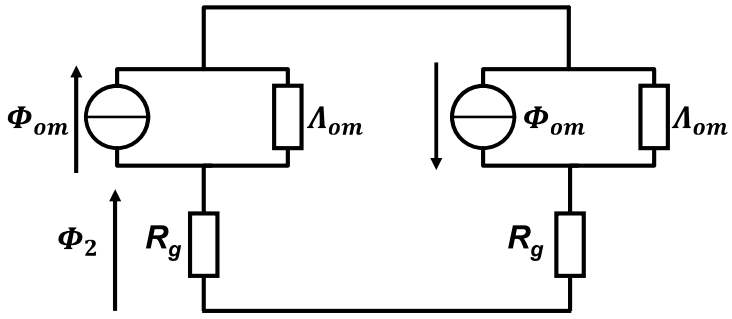

Fig. 3.13. Equivalent magnetic circuit of ERSPM machine.

In this case, the magnetic flux Φ_2 can be expressed as:

$$\Phi_2 = \frac{1/\Lambda_{om}\Phi_{om}}{R_g + 1/\Lambda_{om}} \tag{3.10}$$

Thus,

$$\Phi_2 - \Phi_1 = \frac{\frac{1}{\Lambda_{om}}\Phi_{om}}{R_g + \frac{1}{\Lambda_{om}}} - \frac{\frac{1}{\Lambda_{om}}\Phi_{om} + \frac{1}{\Lambda_{im}}\Phi_{im}}{2R_g + \frac{1}{\Lambda_{om}} + \frac{1}{\Lambda_{im}}} = \frac{K_1 + K_2}{\left(R_g + \frac{1}{\Lambda_{om}}\right)\left(2R_g + \frac{1}{\Lambda_{om}} + \frac{1}{\Lambda_{im}}\right)} \tag{3.11}$$

where K_1 and K_2 are defined as:

$$K_1 = \frac{(\Phi_{om} - \Phi_{im})}{\Lambda_{im}\Lambda_{om}} > 0 \tag{3.12}$$

$$K_2 = R_g(\frac{1}{\Lambda_{om}}\Phi_{om} - \frac{1}{\Lambda_{im}}\Phi_{im}) \tag{3.13}$$

and

$$1/\Lambda_{om}\Phi_{om} = F_{om} = HL_{om} \tag{3.14}$$

$$1/\Lambda_{im}\Phi_{im} = F_{im} = HL_{im} \tag{3.15}$$

where F_{om} and F_{im} are the outer and inner PMs equivalent MMFs, respectively. H is the magnetizing force.

From the optimised parameters of the SDRPM machine:

$$L_{om} = L_{im} \tag{3.16}$$

and

$$F_{om} = F_{im} \tag{3.17}$$

Thus,

$$\Phi_2 - \Phi_1 > 0 \tag{3.18}$$

Therefore, for the radial-flux SDRPM machine, since the inner and outer PMs magnetic circuits are connected in series, the inner PM cannot (or is very difficult to) generate the same magnetic flux as the outer PM, the resultant magnetic flux of the machine will be decreased. Consequently, although more PMs are used, the flux linkage is lower, and the corresponding output torque is also smaller. Compared with the SRSPM machine, such as the ERSPM machine, in which one of the rotor parts of the SDRPM machine is removed, the main magnetic flux and consequently the phase flux linkage become higher. Thus, the output torque of the SRSPM machine is higher while the PM volume is much smaller.

3.6 Influence of Design Parameters in SDRPM and SRSPM Machines under Different Critical Parameter Conditions

The analysis of the magnetic circuit in the SDRPM machine reveals that due to different radii of outer and inner airgaps, the inner and outer PMs produce different magnetic fluxes, which results in the resultant coil flux linkage smaller than that produced by the outer PMs. The larger the difference between the magnetic fluxes produced by the outer and inner PMs, the more the reduction. In other words, the inner PMs have a detrimental effect on the magnetic flux produced by the outer PMs.

Additionally, the SDRPM machine exhibits increased magnetic reluctance for the outer PMs, the inner PMs and airgap are equivalent to an extra air gap for the outer PMs compared to the SRSPM machine. Therefore, in this section, a comprehensive comparative study of the electromagnetic performance of dual- and single-rotor SPM machines is carried out, and the influence of air gap length, PM volume, machine inner bore radius, and pole numbers is investigated.

3.6.1 Air gap length

Compared with the SRSPM machines, although there is another PM excitation the SDRPM machine has an extra air gap which leads to a higher magnetic reluctance in the main flux circuit. The influences of the inner and outer air gap lengths on the electromagnetic torque of the SDRPM machine are shown in Fig. 3.14. The inner and outer rotor radii of the SDRPM machine are fixed when the inner and outer air gap lengths are varied. Only the inner and outer radii of the modular stator are changed with the corresponding air gap. Since the air gap length in the SRSPM machine is 1mm, the variation range of the inner and outer air gap lengths of the SDRPM machine is 0.5 mm to 1.0 mm. When the inner and outer air gap lengths are both 0.5mm, the resultant air gap of the SDRPM machine is 1mm.

Fig. 3.14 shows the variation of torque of the SDRPM machine with the inner and outer air gap lengths. The inner rotor torque of the SDRPM machine increases with both inner and outer air gap lengths decreasing due to the inverse relationship between the length and magnetic reluctance of the air gap. The outer rotor torque increases with a decrease in the outer air gap length and increases with an increase in the inner air gap length. This can be explained according to formula (3.9), which means that the magnetic flux generated by the outer PM is reduced by the flux produced by the inner PM. Therefore, when the inner air gap reluctance increases with the inner air gap length, The flux generated by inner PM is reduced. The outer rotor flux has increased.

The total torque of the SDRPM machine is increased with both inner and outer air gap lengths decreased. When the inner and outer air gap lengths of the SDRPM machine are 0.5mm, the total air gap

length of the SDRPM machine is the same as the SRSPM machine. In this case, the torque of the SDRPM machine can achieve 6Nm, which is only slightly higher than 5.9Nm for the ERSPM machine and higher than 5.3Nm for the IRSPM machine. The torque per PM volume of the SDRPM machine is 0.166 Nm/cm^3, which is higher than that of the IRSPM machine, 0.164 Nm/cm^3, but still lower than that of the ERSPM machine, 0.215 Nm/cm^3. When the inner and outer air gap lengths of the SDRPM machine are 1mm, the single air gap length of the SDRPM machine is the same as the SRSPM machine. The torque of the SDRPM machine is only 5.3Nm, which is the same as that of the IRSPM machine but much lower than that of the ERSPM machine. In this case, the torque per PM volume of the SDRPM machine is only 0.147 Nm/cm^3, which is lower than those of the ERSPM and IRSPM machines. The torque comparison of SDRPM and SRSPM machines with different air gap length conditions is listed in Table 3.7. Considering the SDRPM machine has a more complex mechanical structure than the SRSPM machines. In the rest of the research of this chapter, the inner and outer air gap lengths of the SDRPM machine are both fixed at 1mm, the same as the air gap length of the SRSPM machines.

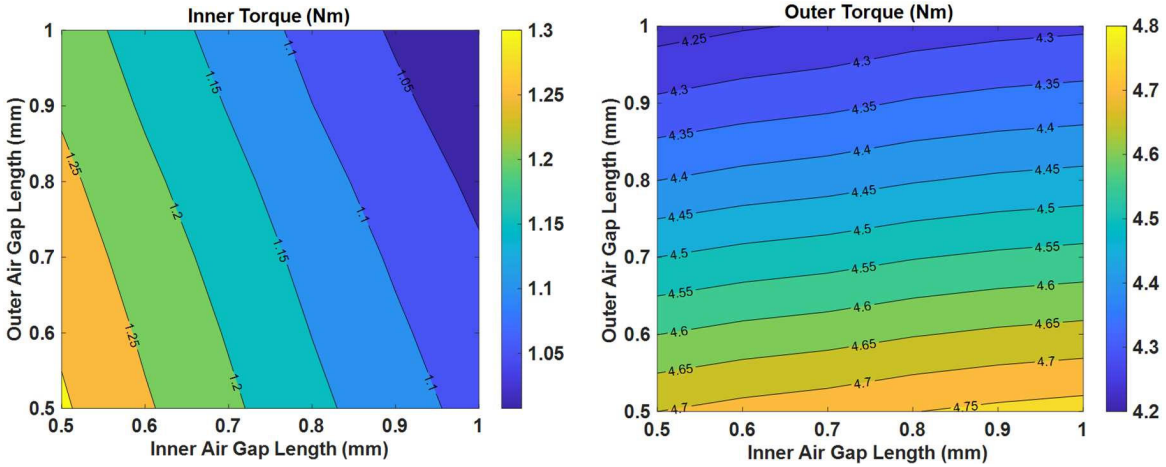

(a) Inner torque.

(b) Outer torque.

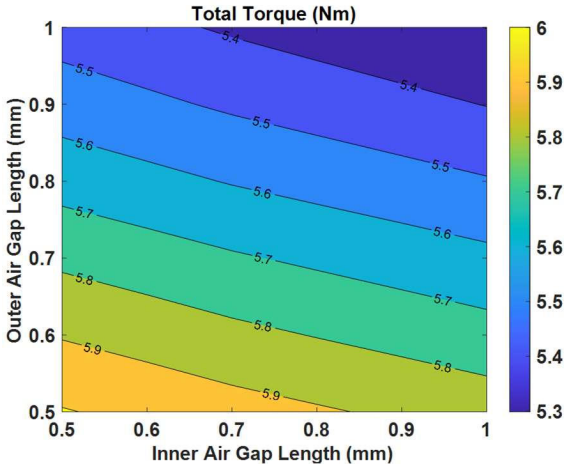

(c) Total torque.

Fig. 3.14. Average torque of SDRPM machine with different inner and outer air gap lengths.

TABLE 3.7
TORQUE CHARACTERISTICS OF SRSPM AND SDRPM MACHINES

Parameters	ERSPM	IRSPM	SDRPM	
Air gap length (mm)	1	1	0.5/0.5	1/1
T (Nm)	5.9	5.3	6.0	5.3
PM volume (cm^3)	27.5	32.4	36	36
$\rho_{\mathrm{Torque/PM}}$ (Nm/cm^3)	0.215	0.164	0.166	0.147

3.6.2 PM volume

In the previous sections, in order to reach the maximum torque of all machine types under different scenarios. All optimisations are considered the PM amount unrestricted. Thus, the influence of PM volume is investigated in this section. There are two scenarios: the PM volume is fixed either as that of the SDRPM or SRSPM machines during the optimisations, which will be discussed as follows separately.

A. PM volume fixed as same as SDRPM machine

In this sub-section, the same optimization procedure and design constraints for SDRPM machines in Section 3.3 are employed for the SDRPM machines, except that the PM volume is now fixed at $36cm^3$, as the optimised SDRPM machine. The optimised parameters are listed in Table 3.8. Fig. 3.15 illustrates the corresponding open circuit flux line and flux density distributions.

TABLE 3.8
PARAMETERS OF OPTIMISED MACHINES

Parameters	ERSPM	IRSPM	SDRPM
Slot/pole number combination		12-slot/10-pole	
Outer PM thickness (mm)	3.2	-	2.0
Inner PM thickness (mm)	-	5	2.0
Outer PM pole arc (°elec.)	152.5	-	150
Inner PM pole arc (°elec.)	-	164	178.5
PM volume (cm^3)	36	36	36
Stator outer radius (mm)	40.2	-	42
Stator inner radius (mm)	-	28.7	22
Stator outer slot opening (mm)	8.5	-	6.4
Stator inner slot opening (mm)	-	2.8	0.4
Outer tooth-tip height (mm)	0.6	-	0.7
Inner tooth-tip height (mm)	-	1.2	1.3
Outer tooth-tip slope (deg.)	4	-	14
Inner tooth-tip slope (deg.)	-	4.8	0
Stator tooth width (mm)	8.5	7	7.2
Stator yoke height (mm)	4.5	3.7	-
Slot area (mm^2)	140	209	172

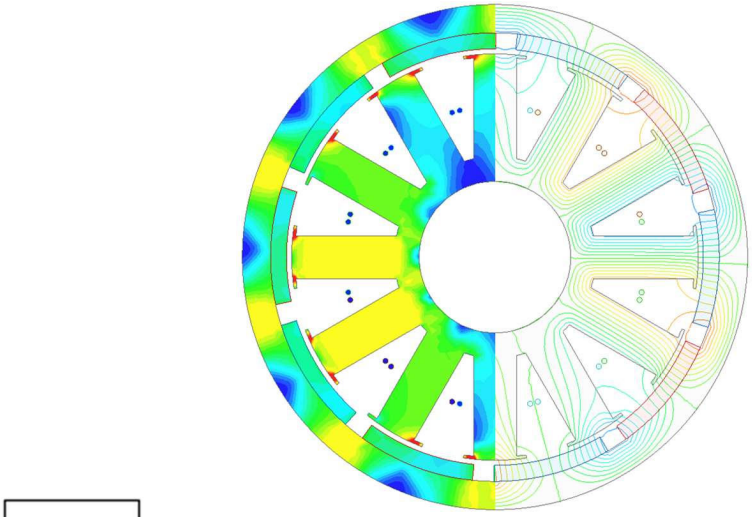

(a) ERSPM.

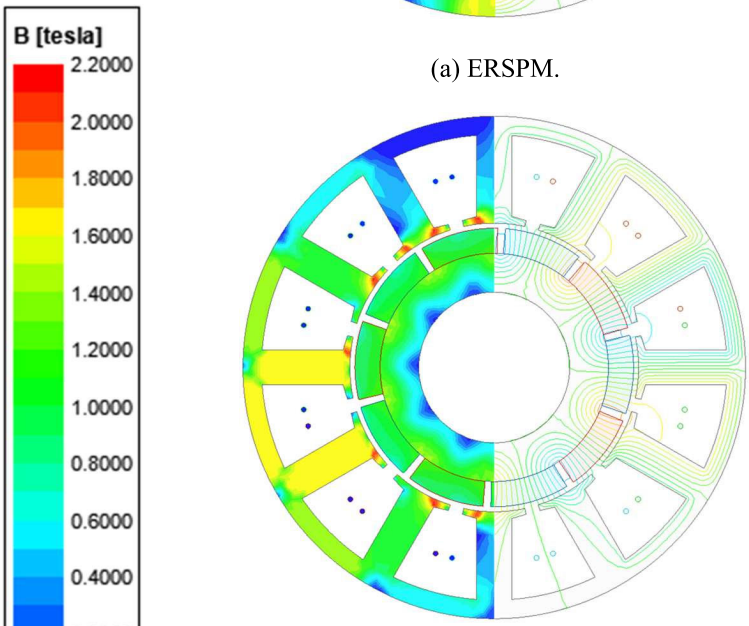

(b) IRSPM.

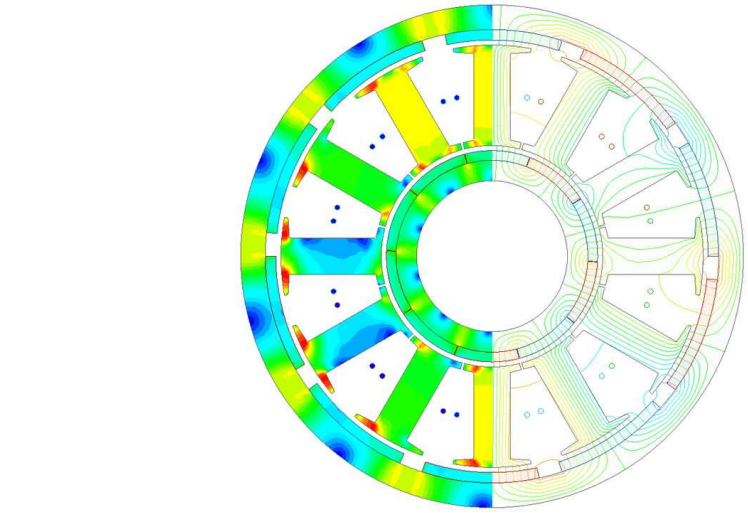

(c) SDRPM.

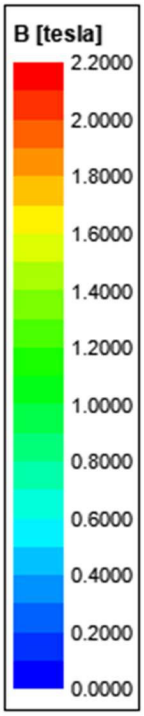

Fig. 3.15. Open circuit flux density distributions and flux lines. (PM volume fixed to 36cm³)

Fig. 3.16a shows the air gap flux densities of the optimised ERSPM, IRSPM, and SDRPM machines, all set with a fixed PM volume of 36cm³. In this scenario, the single rotor of the SRSPM machines employed the same PM volume as the sum of two rotors of the SDRPM machine. Thus, the fundamental component of the air gap flux density of the ERSPM machine is higher than the outer air gap flux density of the SDRPM machine. Similarly, the air gap flux density in the IRSPM machine exceeds the inner air gap flux density of the SDRPM machine. The flux linkages of all machines are shown in Fig. 3.16b. In this scenario, the fundamental component of the flux linkage of the SDRPM machine is slightly higher than that of the IRSPM machine but still significantly lower than that of the ERSPM machine. The back EMFs of all machines have the same trend, as shown in Fig. 3.16c.

The torques of the ERSPM, IRSPM and SDRPM machines are optimised under the same PM volume shown in Fig. 3.16d. The IRSPM machine has a larger slot area, which allows higher input current compared to the SDRPM machine for the same copper loss. Thus, compared with the SDRPM machine, although the back EMF of the IRSPM machine is slightly lower, the torque is still higher.

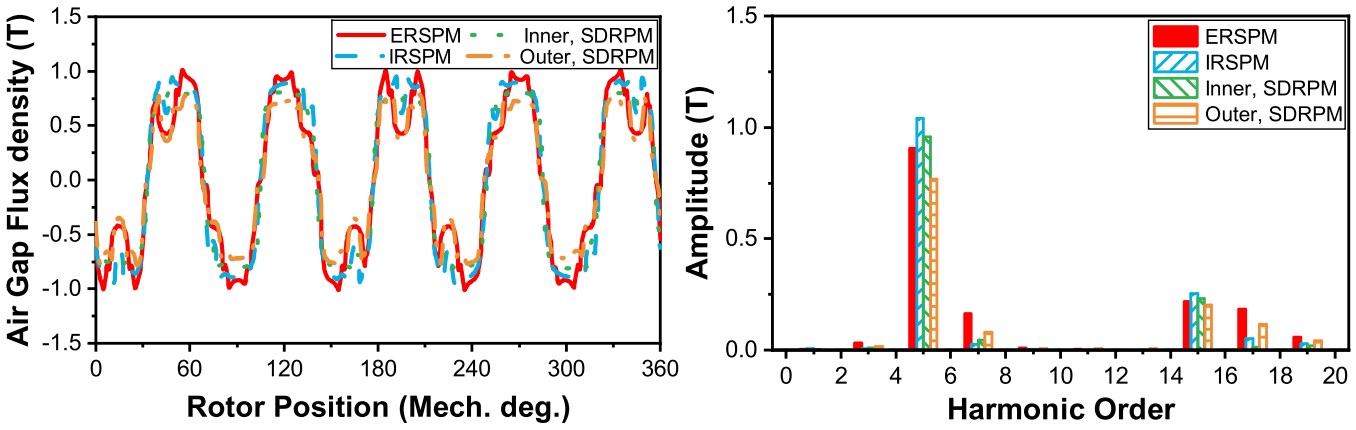

(a) Air gap flux densities.

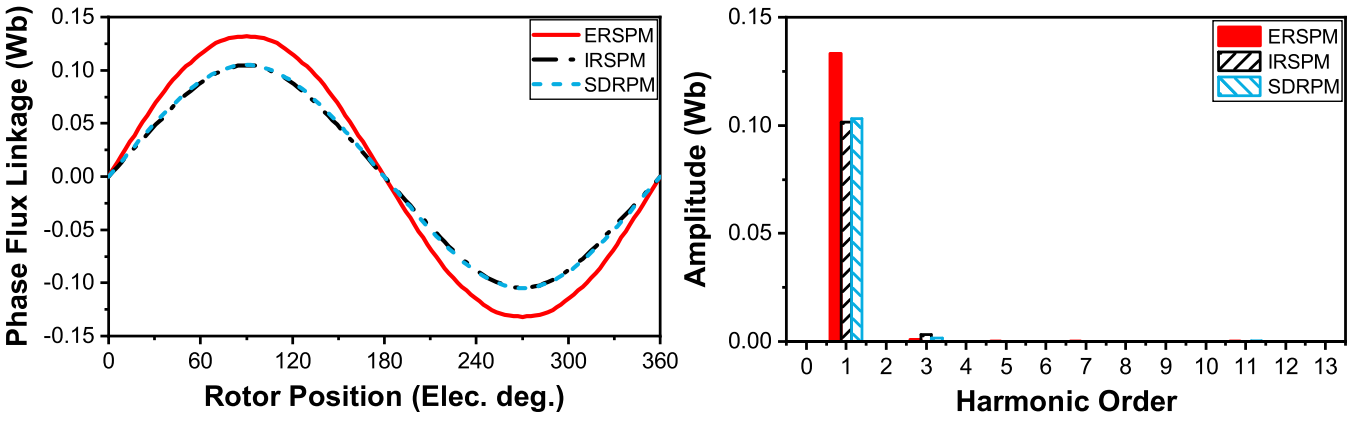

(b)) Flux linkages.

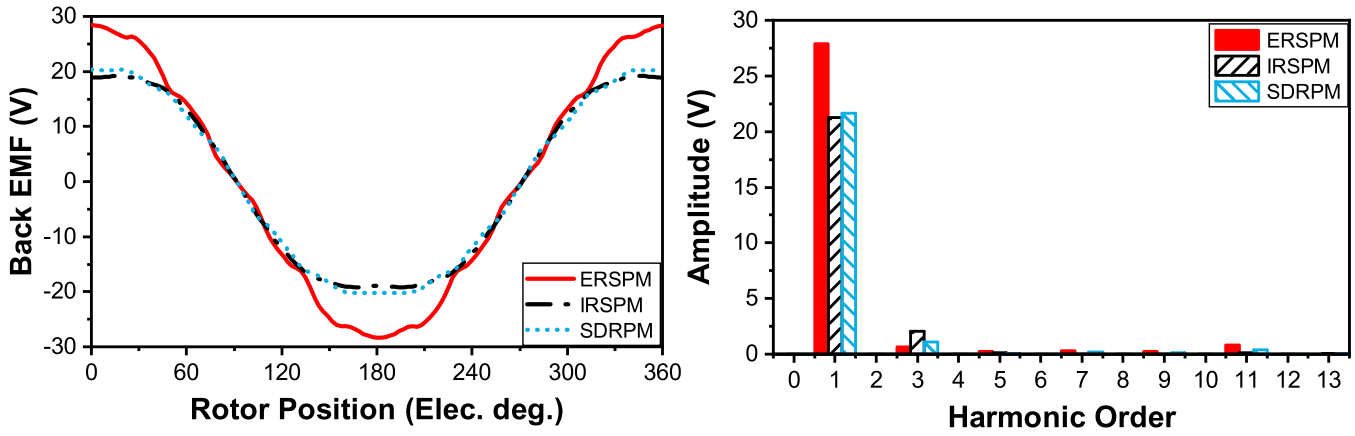

(c) Back EMFs.

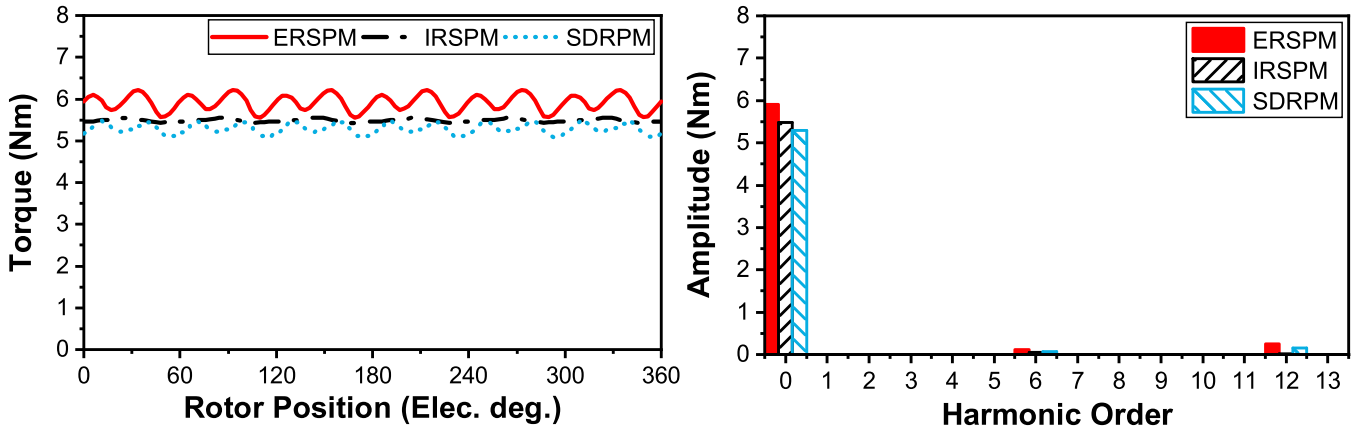

(d) Torques.

Fig. 3.16. Comparisons of ERSPM, IRSPM, and SDRPM machines (400 r/min PM volume fixed to 36cm³).

B. PM amount fixed as same as SRSPM machine

In this scenario, during the optimization, the PM volumes of IRSPM and SDRPM machines are fixed as the same PM volume of the optimised ERSPM machine in Section 3.3, i.e., 27.5 cm^3. The optimised parameters are listed in Table 3.9 and the corresponding open circuit flux line and flux density distributions are shown in Fig. 3.17.

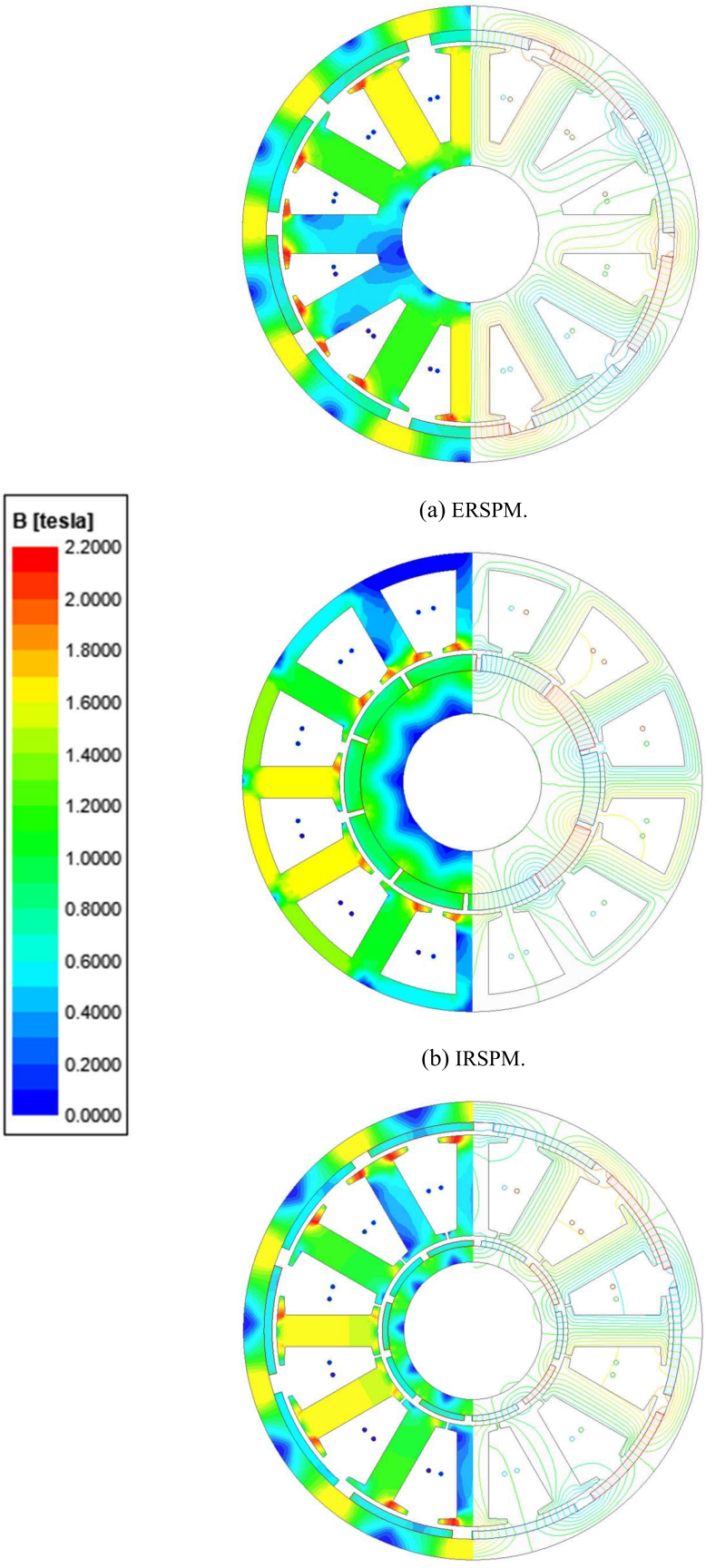

(a) ERSPM.

(b) IRSPM.

(c) SDRPM.

Fig. 3.17. Open circuit flux density distributions and flux lines. (PM volume fixed to 27.5 cm^3)

TABLE 3.9
PARAMETERS OF OPTIMISED MACHINES

Parameters	ERSPM	IRSPM	SDRPM
Slot/pole number combination		12-slot/10-pole	
Outer PM thickness (mm)	2.5	-	1.7
Inner PM thickness (mm)	-	3.6	1.3
Outer PM pole arc (°elec.)	145	-	153
Inner PM pole arc (°elec.)	-	168	155
PM volume (cm^3)	27.5	27.5	27.5
Stator outer radius (mm)	41	-	42.7
Stator inner radius (mm)	-	29	20.7
Stator outer slot opening (mm)	6.2	-	7
Stator inner slot opening (mm)	-	2.5	0.5
Outer tooth-tip height (mm)	0.7	-	1
Inner tooth-tip height (mm)	-	0.9	1.4
Outer tooth-tip slope (deg.)	19	-	13
Inner tooth-tip slope (deg.)	-	11.5	2.7
Stator tooth width (mm)	8.6	7	7
Stator yoke height (mm)	5.4	3.6	-
Slot area (mm^2)	144	207	180

In this scenario, the SDRPM machine has the same PM volume as the SRSPM machines. However, the SDRPM machine has an extra rotor compared to the SRSPM machines, resulting in relatively thinner PM thicknesses for its inner and outer rotors. The air gap flux densities, flux linkages, back EMFs, and torques are shown in Fig. 3.18, respectively. It can be observed that the flux densities and torques in both external and internal rotor SRSPM machines are higher than those in the SDRPM machine.

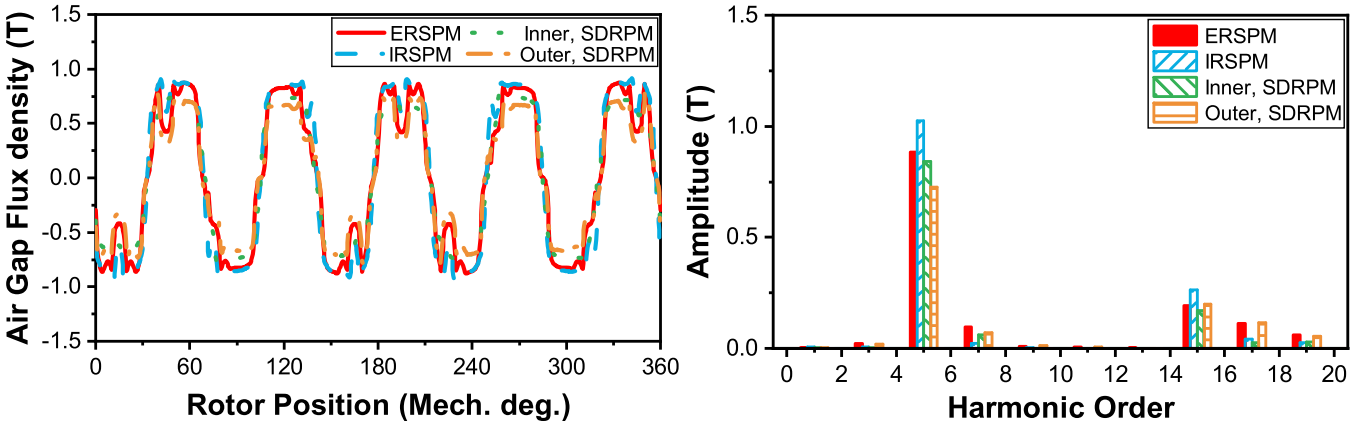

(a) Air gap flux densities.

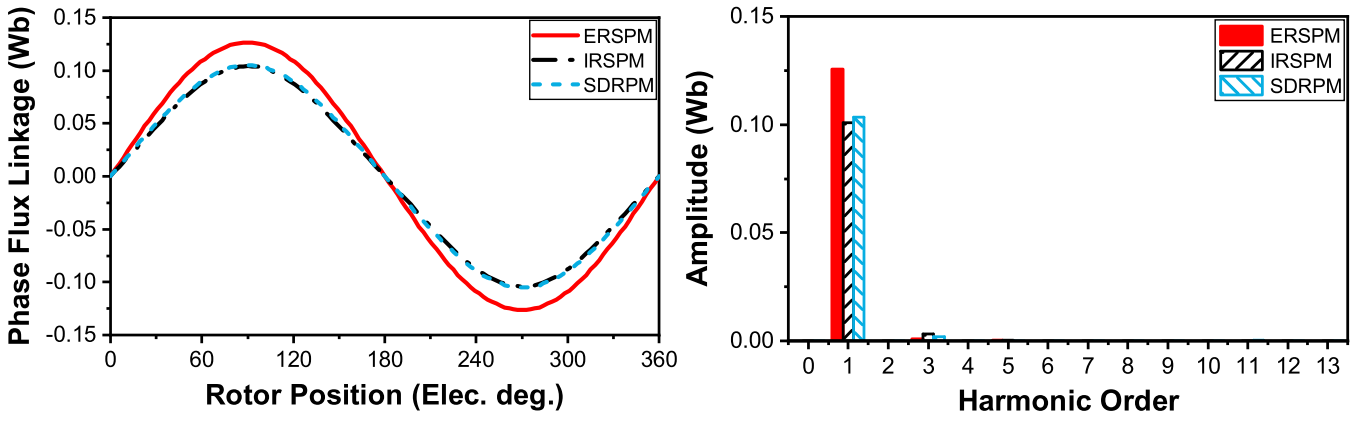

(b) Flux linkages.

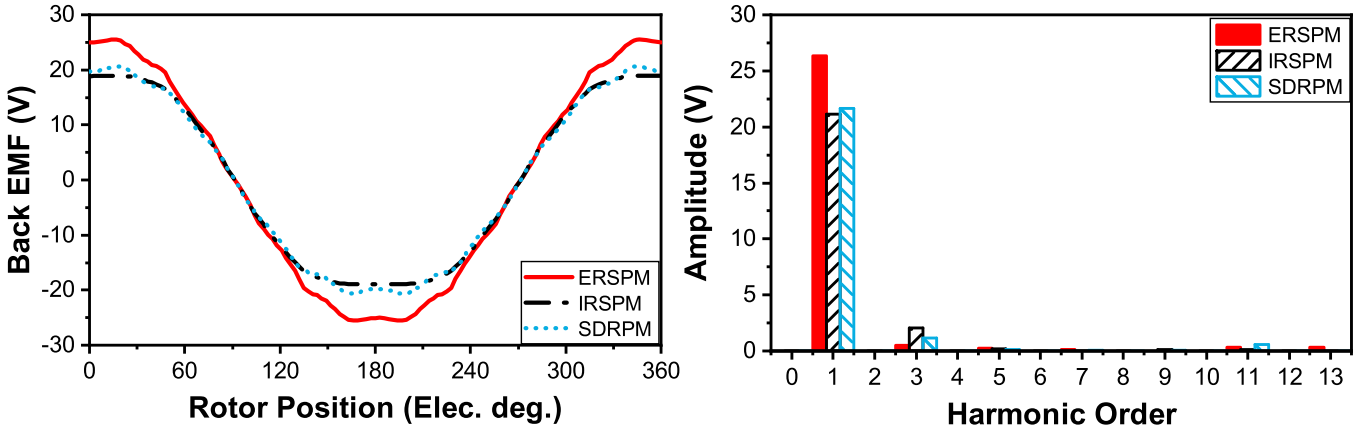

(c) Back EMFs.

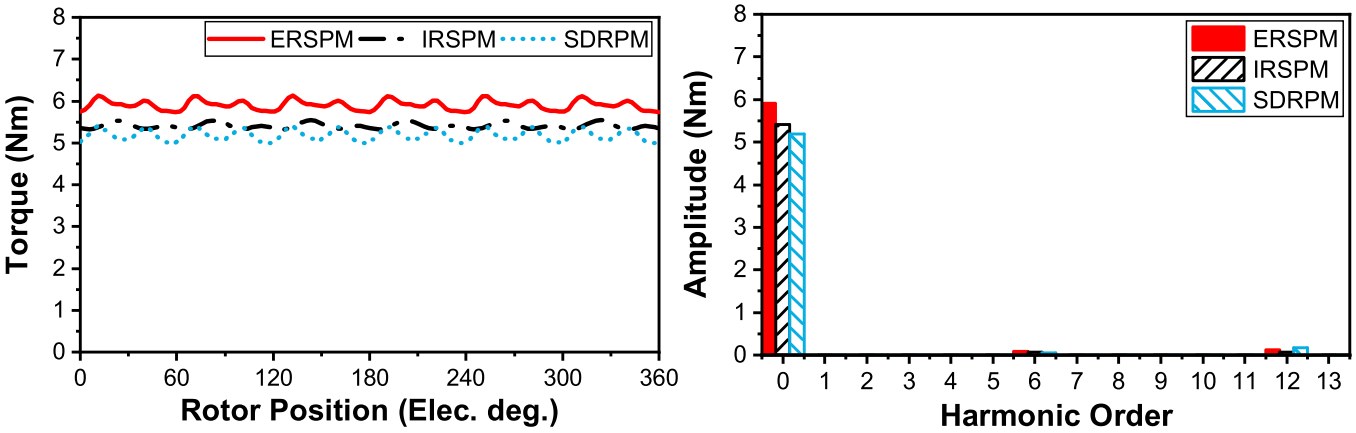

(d) Torques.

Fig. 3.18. Comparisons of ERSPM, IRSPM, and SDRPM machines (400 r/min PM volume fixed to 27.5 cm^3).

3.6.3 Inner bore radius

A. Without machine inner bore radius restriction

Compared with the SRSPM machine, the SDRPM machine requires more active space to accommodate two rotors. Therefore, this section considers an optimisation scenario without restriction on the machine inner bore radius.

In this section, all machines are optimized by FEA to maximise the torque. The copper loss is maintained at 30W, and the machine outer radius is set at 50mm. The PM volume and the machine inner bore radius are optimised without any constraints. The optimised design parameters of all machines are listed in Table 3.10, while the corresponding open circuit flux density distributions and flux lines are shown in Fig. 3.19.

TABLE 3.10
PARAMETERS OF OPTIMISED MACHINES

Parameters	ERSPM	IRSPM	SDRPM
Slot/pole number combination		12-slot/10-pole	
Inner bore radius (mm)	10.7	12	9.7
Outer PM thickness (mm)	2.7	-	2
Inner PM thickness (mm)	-	3.7	2
Outer PM pole arc (°elec.)	138	-	169
Inner PM pole arc (°elec.)	-	180	167
PM volume (cm^3)	28.1	30.3	34.7
Stator outer radius (mm)	41	-	42
Stator inner radius (mm)	-	29	18
Stator outer slot opening (mm)	5.4	-	8
Stator inner slot opening (mm)	-	2	0.5
Outer tooth-tip height (mm)	0.8	-	1
Inner tooth-tip height (mm)	-	1	1
Outer tooth-tip slope (deg.)	15	-	13.5
Inner tooth-tip slope (deg.)	-	7	15
Stator tooth width (mm)	9	8	7
Stator yoke height (mm)	8	3.8	-
Slot area (mm^2)	134	189	176

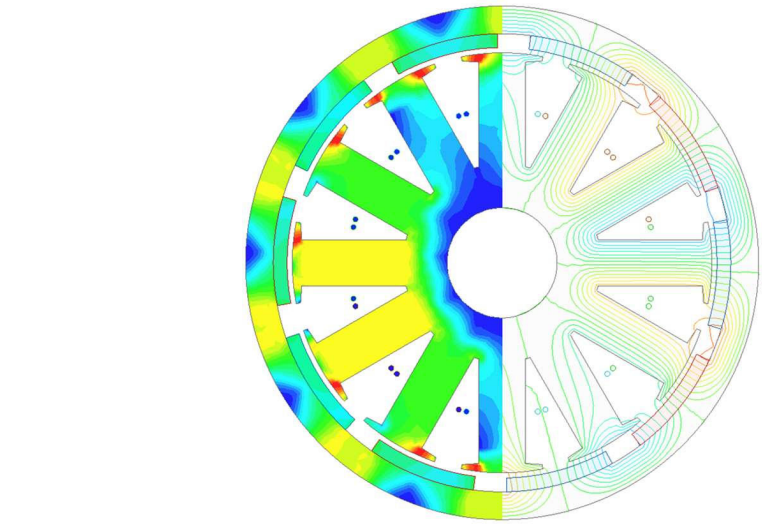

(a) ERSPM.

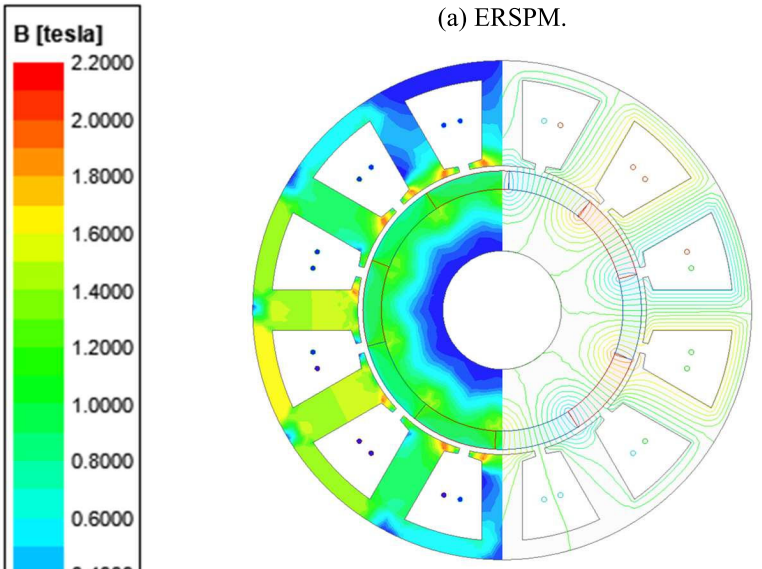

(b) IRSPM.

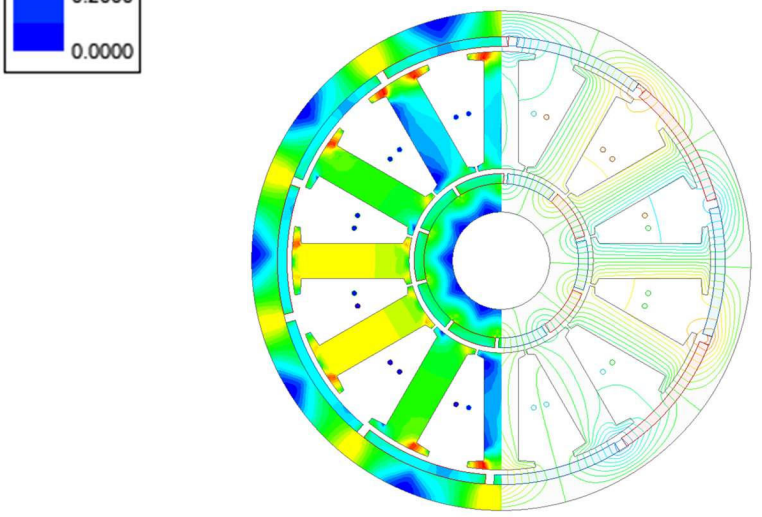

(c) SDRPM.

Fig. 3.19. Open circuit flux density distributions and flux lines. (without machine inner bore radius restriction)

The variations of the torque with the machine inner bore radius of all machines during the optimisation are shown in Fig. 3.20. It reveals that the ERSPM machine achieves higher torque with an inner bore radius of approximately 10mm. A small inner bore radius provides a large slot area for a higher input current. However, a further reduction in the machine inner bore radius restricts the stator yoke thickness and stator tooth width, leading to a decrease in torque. The SDRPM machine shows a similar trend as the ERSPM machine. Reducing the SDRPM machine inner bore radius enlarges the slot area and the torque of the outer rotor, meanwhile sacrifices the torque of the inner rotor, but the total torque is increased. In contrast, the torque of the IRSPM machine is relatively unaffected by changes in the machine inner bore radius.

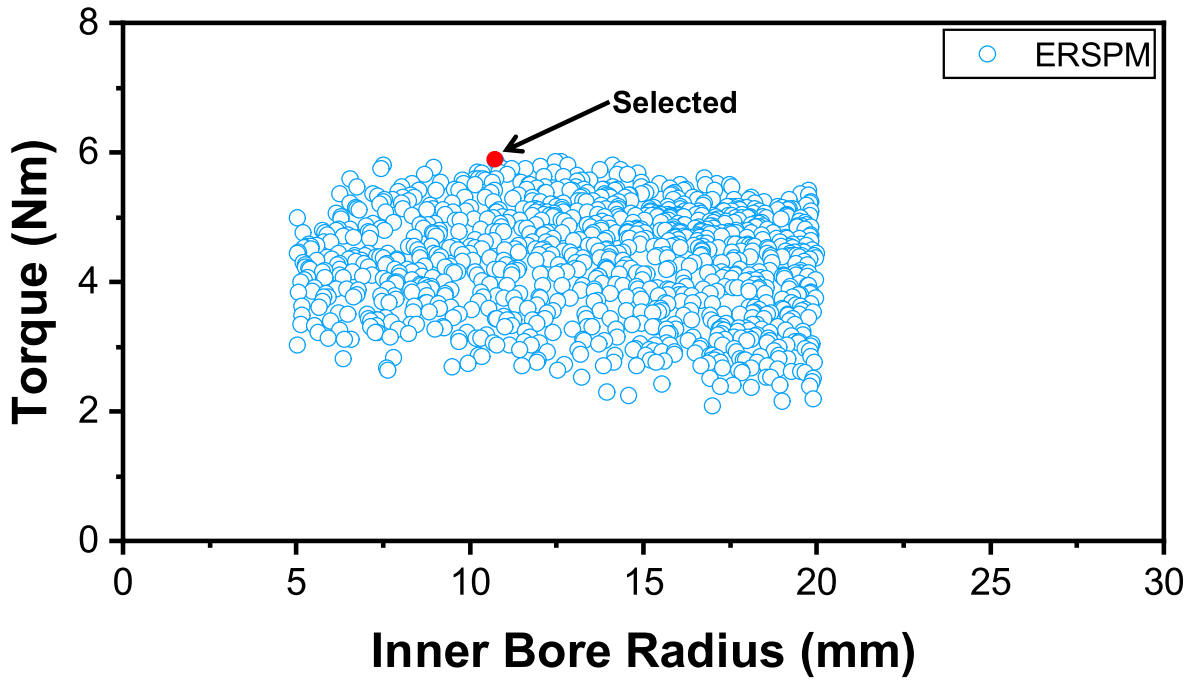

(a) ERSPM.

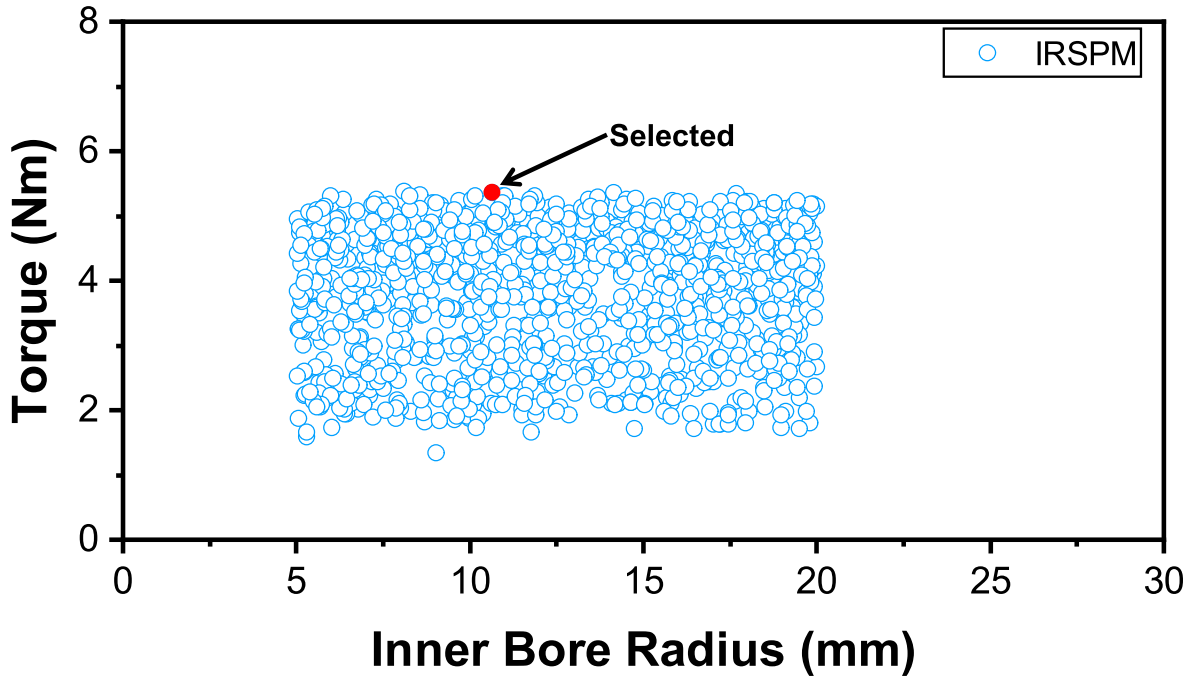

(b) IRSPM.

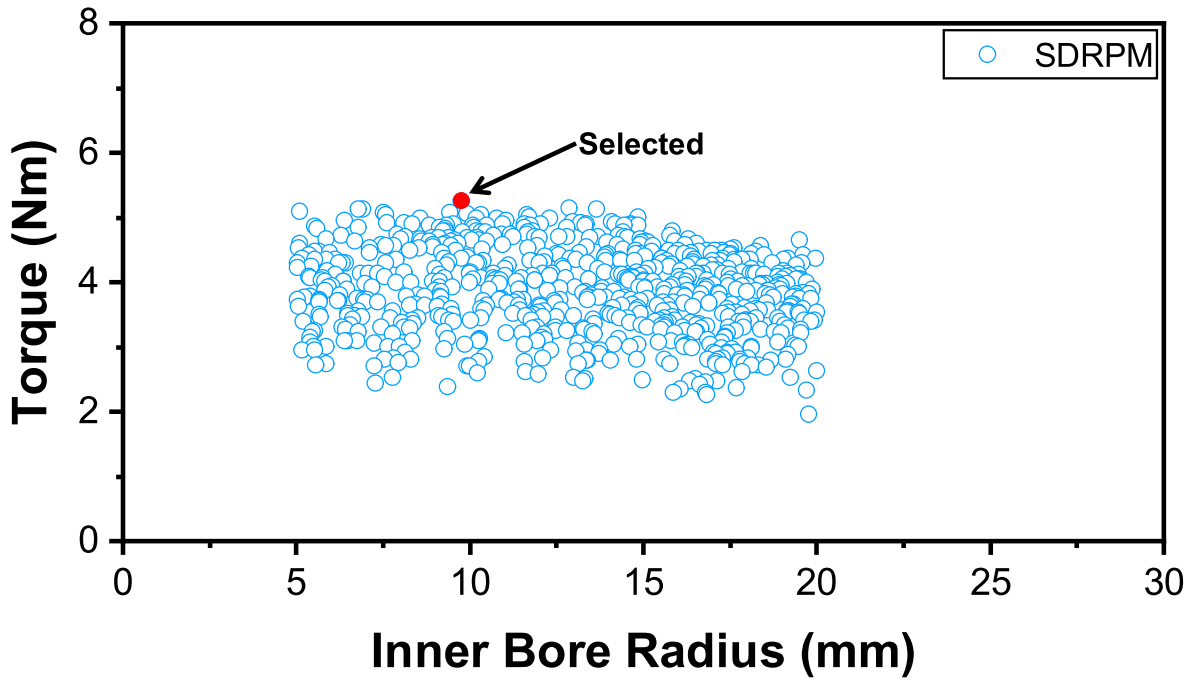

(c) SDRPM.

Fig. 3.20. Variation of torque with inner bore radius during optimisation.

For the ERSPM machine, the optimisation tends to utilise more PM material to enhance the flux linkage. Decreasing the inner stator bore radius of the ERSPM machine results in the increase the stator

yoke thickness, thereby improving magnetic saturation even with an increased PM volume.

For the IRSPM machine, as the rotor inner bore radius reduces, the stator slot area is increased, being the largest among all machines. Therefore, the IRSPM machine allows the highest input current of all machines for the same copper loss.

The optimised SDRPM machine has the smallest optimised inner bore radius since it needs more active space for an extra rotor compared to the SRSPM machines. However, further increasing the inner active space cannot compensate for the resultant flux reduction due to difference in the fluxes generated by inner and outer PMs of the SDRPM machine. Therefore, as shown in Figs. 3.21, the conclusions for ERSPM, IRSPM, and SDRPM machines are the same with/without the restriction of the inner bore radius.

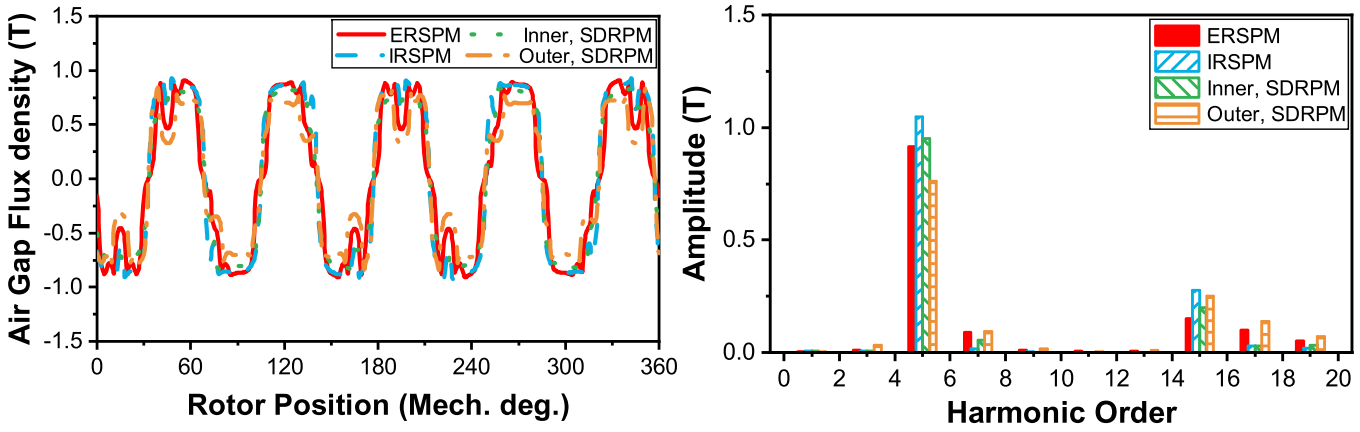

(a) Air gap flux densities.

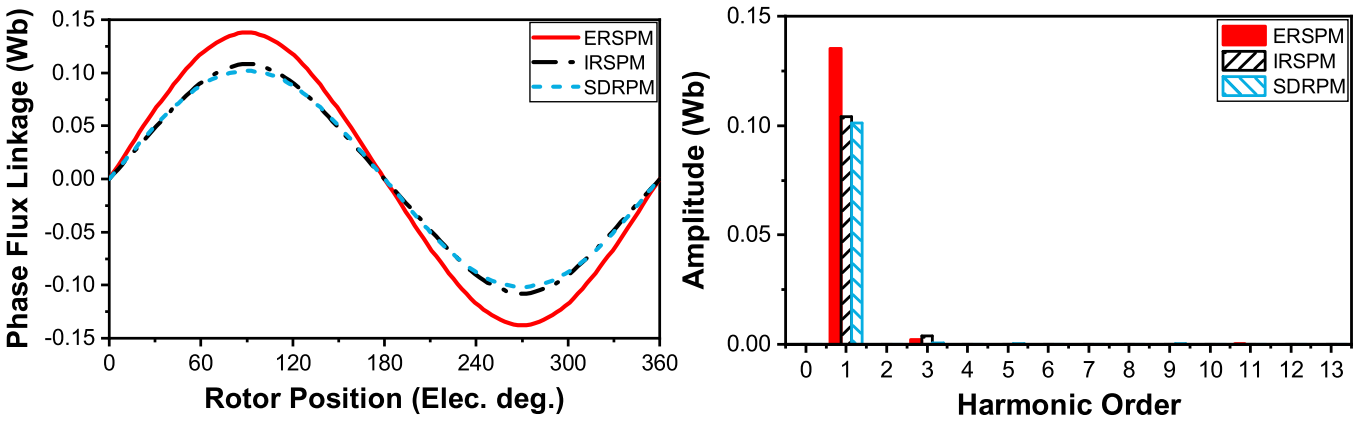

(b) Flux linkages.

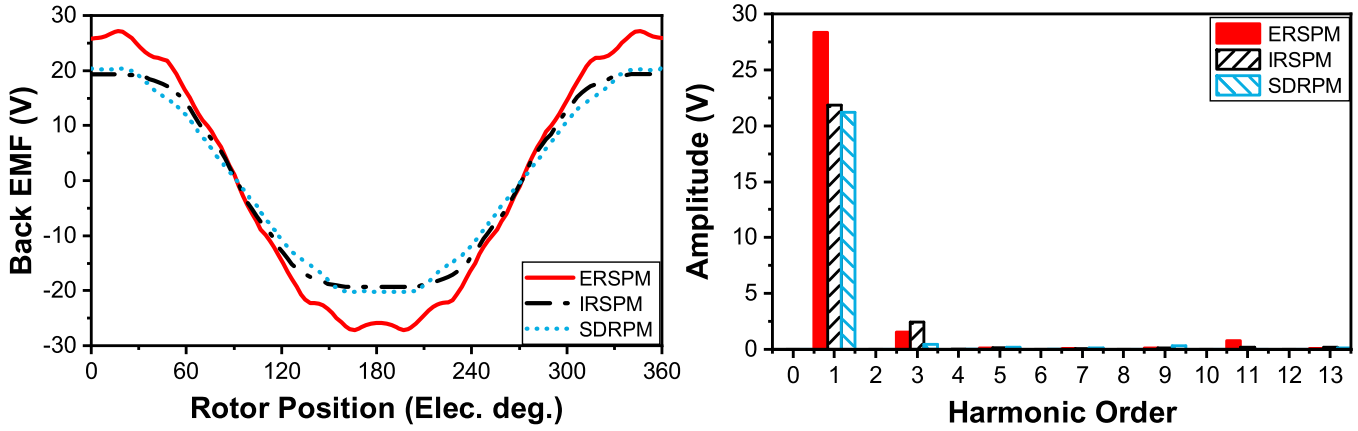

(c) Back EMFs.

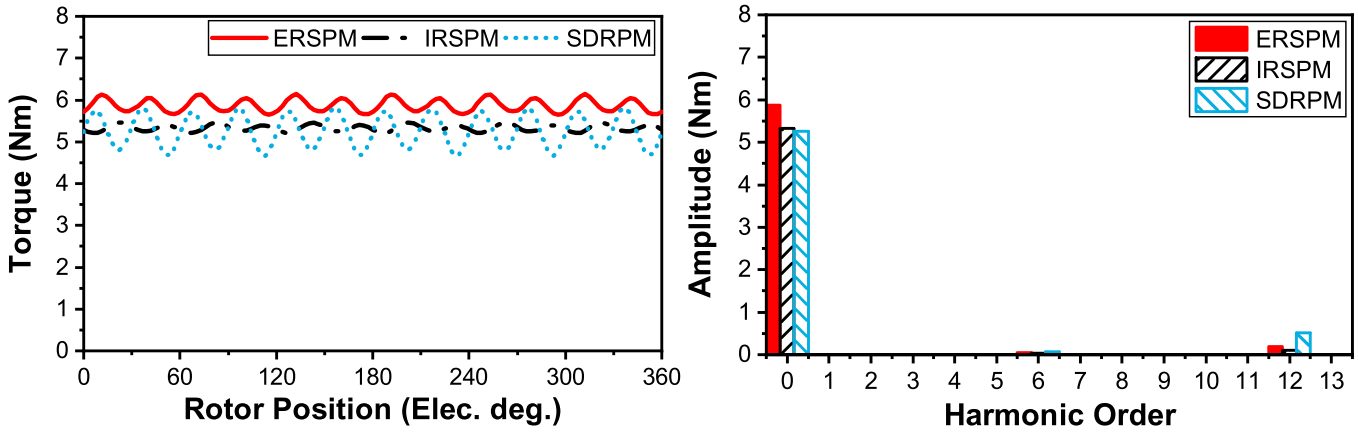

(d) Torques.

Fig. 3.21. Comparisons of ERSPM, IRSPM, and SDRPM machines without inner bore radius restriction (400 r/min).

B. With large inner bore radius

Since when the inner bore radius is small (15mm), the inner and outer PMs of the SDRPM machine hardly generate the same magnetic fluxes, resulting in deteriorated resultant torque performance. Therefore, in this sub-section, the scenario with a large inner bore radius (35mm) and hence a small difference between the inner and outer PM rotors in SDRPM machine is considered.

All machines are globally optimised with the same condition as section 3.3, but the inner bore radius is fixed to 35mm, as listed in Table 3.11.

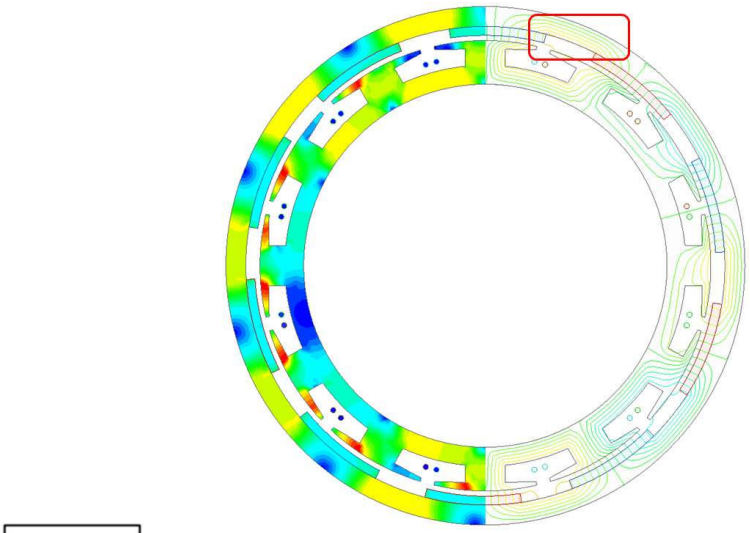

(a) ERSPM.

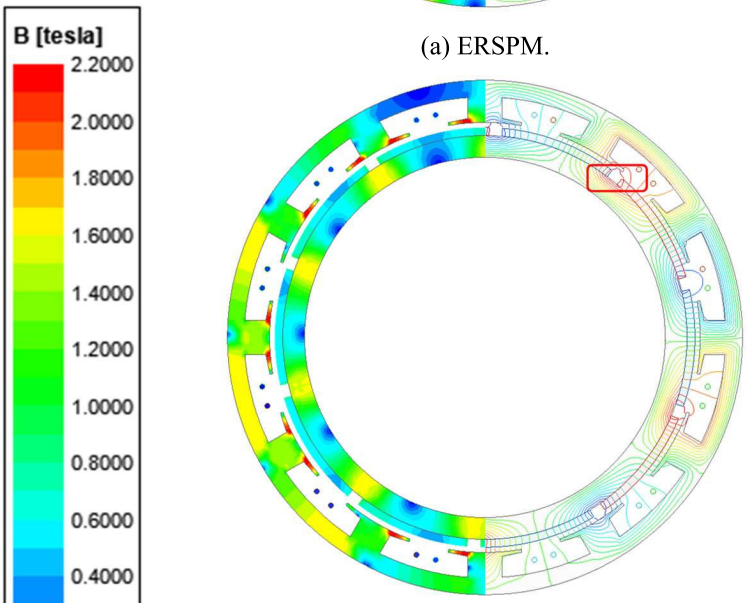

(b) IRSPM.

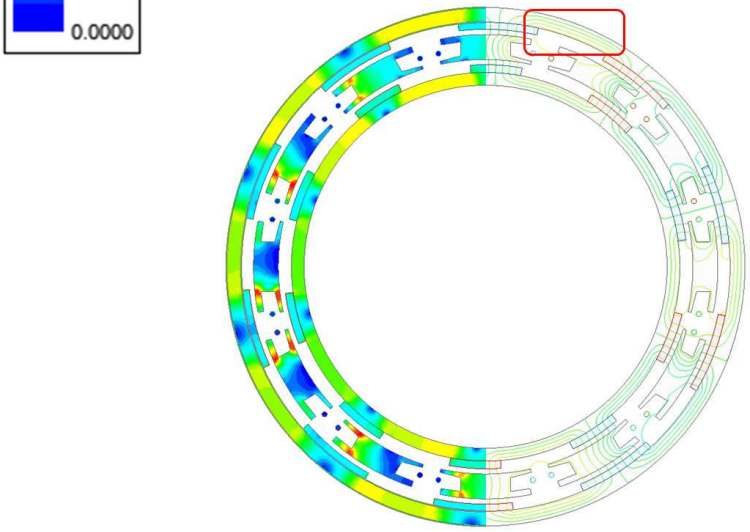

(c) SDRPM.

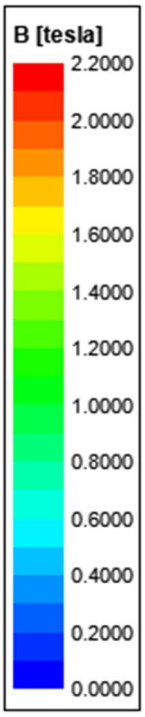

Fig. 3.22. Open circuit flux density distributions and flux lines. (inner bore radius=35mm)

TABLE 3.11
PARAMETERS OF OPTIMISED MACHINES

Parameters	ERSPM	IRSPM	SDRPM
Slot/pole number combination		12-slot/10-pole	
Inner bore radius (mm)	35	35	35
Outer PM thickness (mm)	1.7	-	1.4
Inner PM thickness (mm)	-	1.5	1.5
Outer PM pole arc (°elec.)	117	-	95
Inner PM pole arc (°elec.)	-	162	75
PM volume (cm^3)	15.8	17.5	18
Stator outer radius (mm)	43.4	-	44.8
Stator inner radius (mm)	-	40.8	40
Stator outer slot opening (mm)	2.8	-	5.6
Stator inner slot opening (mm)	-	7.73	3.4
Outer tooth-tip height (mm)	0.7	-	1.1
Inner tooth-tip height (mm)	-	0.6	0.6
Outer tooth-tip slope (deg.)	12	-	3
Inner tooth-tip slope (deg.)	-	2.6	2
Stator tooth width (mm)	7.7	6.6	9.7
Stator yoke height (mm)	3.5	3.3	-
Slot area (mm^2)	46.4	67.5	33

The open circuit flux lines and flux density distributions of the optimised machines are shown in Fig. 3.22. Since the pole arc ratio is small, the magnetic loadings of all machines are low, and the back EMF waveforms of all machines are not sinusoidal, Fig. 3.23. Therefore, in order to analyse the influence of the large inner bore radius and improve the magnetic loadings of all machines. All machines with different slot/pole number combinations based on the large inner bore radius are analysed in the next section.

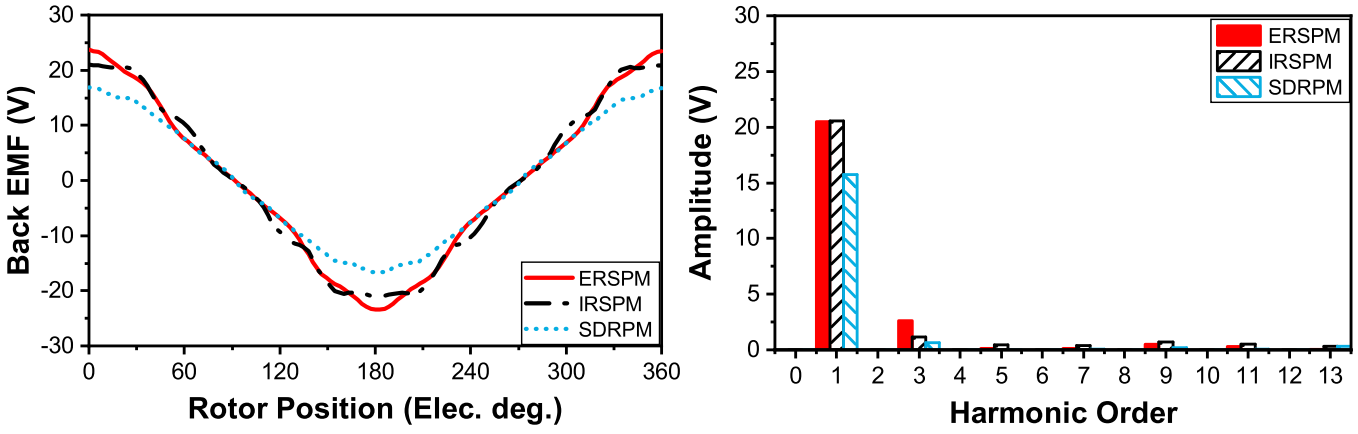

(a) Waveforms.

(b) Spectra.

Fig. 3.23. Comparison of phase-A back EMFs of 12-slot/10-pole ERSPM, IRSPM, and SDRPM machines (400 r/min, inner bore radius=35mm).

3.6.4 Pole number

Based on the equivalent magnetic circuit analysis, the pole arcs of the inner and outer PMs are critical parameters in output performance. Thus, the influence of the pole number is investigated in this section.

In order to enhance the output performance of the SDRPM machine by minimising the difference between the inner and outer PM arcs, the machine with different pole numbers is analysed based on the large inner bore radius (35mm) to further reduce the difference between the inner and outer PMs.

Based on the previous section, to avoid the magnetic saturation on the lamination of all machines with a 35mm inner bore radius while improving the magnetic loadings. The high rotor pole numbers are considered for all machines. Since the SDRPM machine has a yokeless modular stator, only the FSCW machines are considered in this section and the slot number is doubled, being increased from 12 slots to 24 slots. The influence of pole number on the electromagnetic performance of 24-slot machines is investigated. Therefore, the EDRPM, IRSPM, and ERSPM machines with the same 24 slots and different pole numbers, i.e., 20-pole, 22-pole, 26-pole, 28-pole and 32-pole, are globally optimised with the same condition as section 3.3. The ERSPM, IRSPM, and SDRPM machines have 35mm inner bore radius with the same 24-slot and different pole numbers, i.e., 20-pole, 22-pole, 26-pole, 28-pole, and 32-pole, as shown in Fig. 3.24. The corresponding coil phasors are shown in Fig. 3.25. All machines are globally optimised with the same condition as section 3.3, i.e., maximum average torque and minimum torque ripple. The optimised parameters of all machines are listed in Table 3.13. The inner bore radius is fixed at 35mm. The open circuit flux line and flux density distributions of optimised machines are depicted in Fig. 3.26.

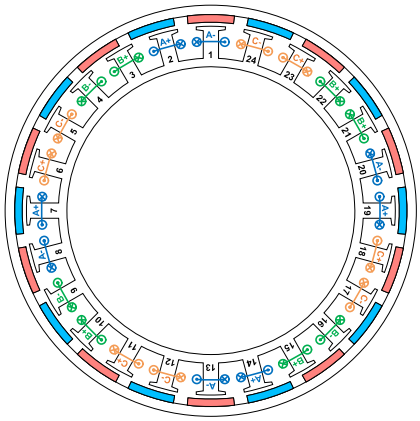

I. (a) ERSPM.

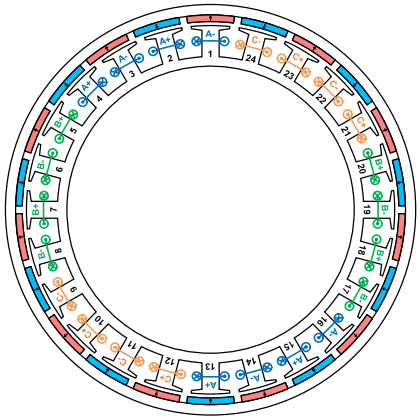

II. (a) ERSPM.

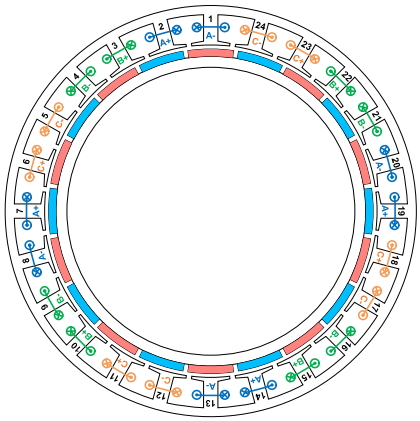

I. (b) IRSPM.

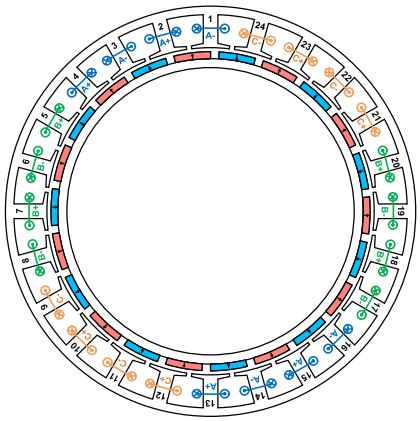

II. (b) IRSPM.

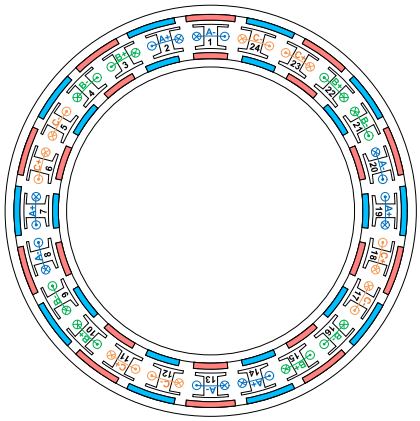

I. (c) SDRPM.

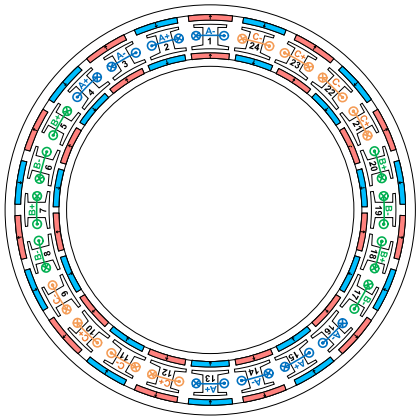

II. (c) SDRPM.

I. 24-slot/20-pole

II. 24-slot/22-pole

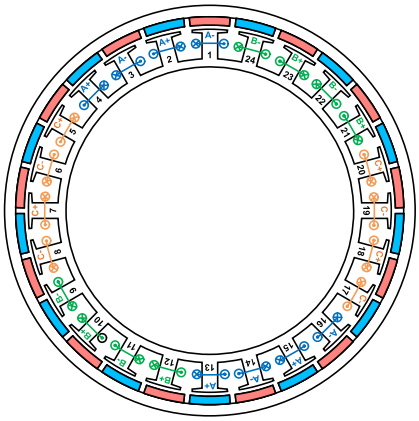

III. (a) ERSPM.

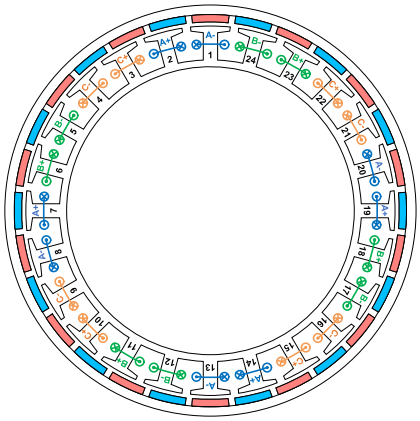

IV. (a) ERSPM.

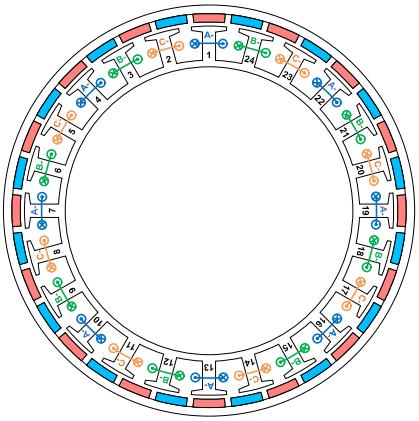

V. (a) ERSPM.

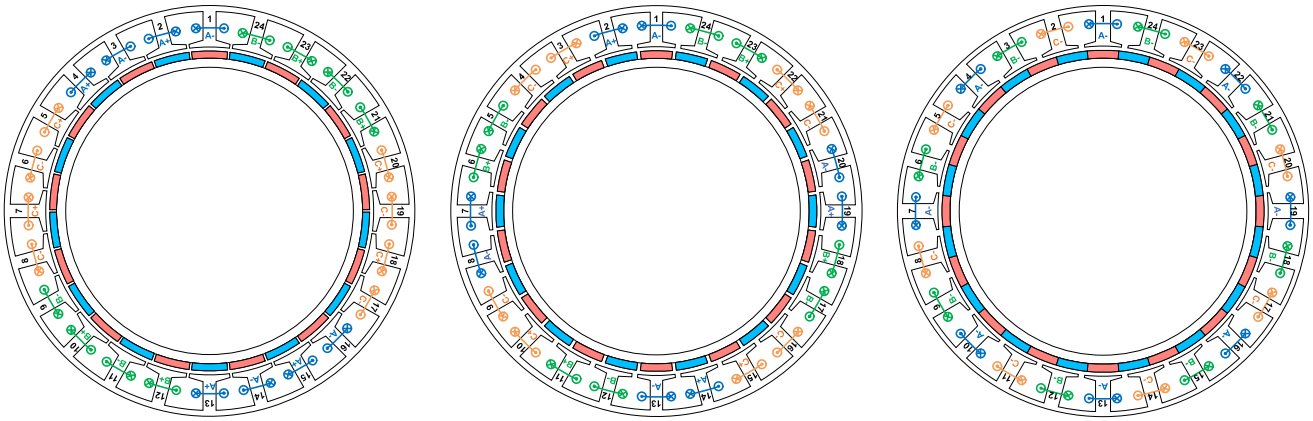

III. (b) IRSPM. IV. (b) IRSPM. V. (b) IRSPM.

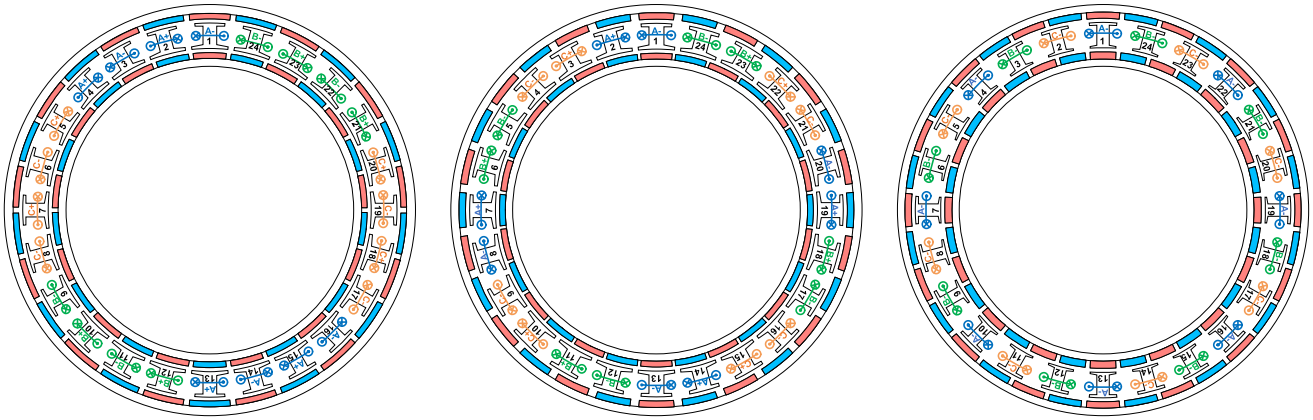

III. (c) SDRPM. IV. (c) SDRPM. V. (c) SDRPM.

III. 24-slot/26-pole IV. 24-slot/28-pole V. 24-slot/32-pole

Fig. 3.24. Cross-sections. I. 24-slot/20-pole. II. 24-slot/22-pole. III. 24-slot/26-pole. IV. 24-slot/28-pole. V. 24-slot/32-pole. (inner bore radius=35mm)

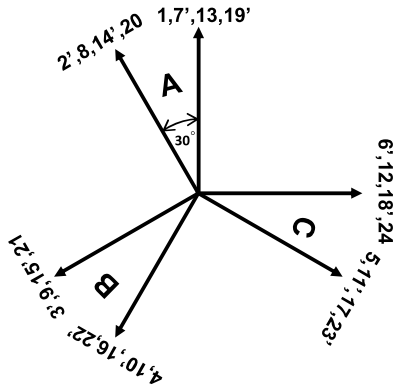

(a) 24-slot/20-pole.

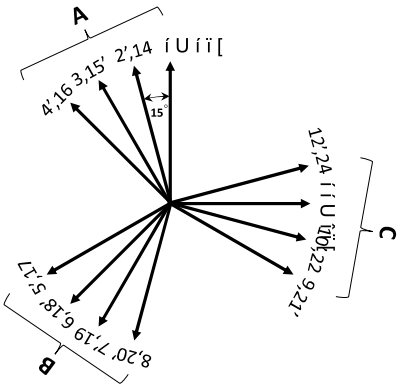

(b) 24-slot/22-pole.

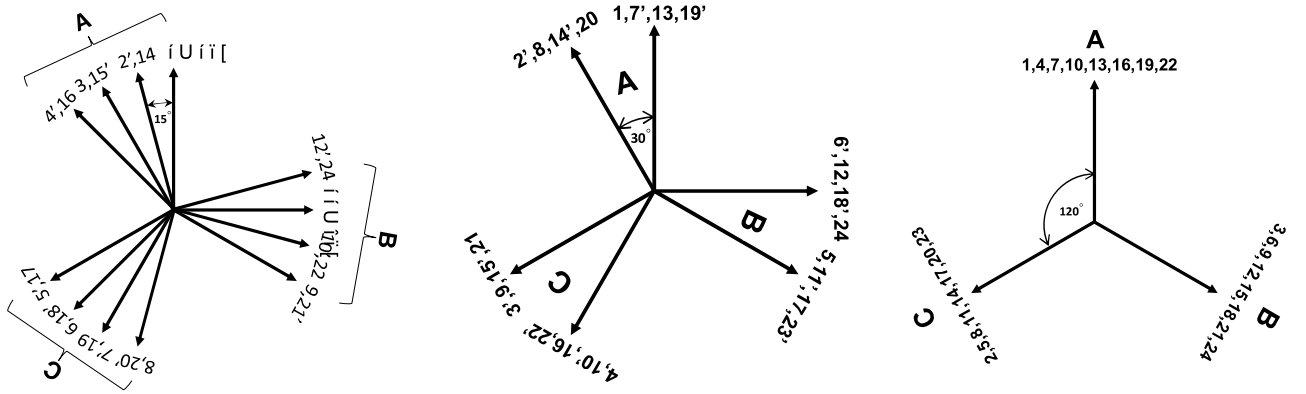

(c) 24-slot/26-pole. (d) 24-slot/28-pole. (e) 24-slot/32-pole.

Fig. 3.25. Coil EMF phasors of ERSPM, IRSPM, and SDRPM machines.

TABLE 3.13
PARAMETERS OF OPTIMISED MACHINES

Ns/2p	24-slot/20-pole			24-slot/22-pole			24-slot/26-pole			24-slot/28-pole			24-slot/32-pole		
Machine	ER	IR	DR	ER	IR	DR	ER	IR	DR	ER	IR	DR	ER	IR	DR
L_{om} (mm)	1.8	-	1.4	1.6	-	1.4	2	-	1.4	1.8	-	1.6	2	-	1.5
L_{im} (mm)	-	1.7	1.4	-	1.7	1.4	-	1.7	1.4	-	1.8	1.4	-	1.9	1.7
θ_{om} (elec. deg.)	138	-	145	154.2	-	143	156.8	-	156.8	151.8	-	142.8	148.6	-	155
θ_{im} (elec. deg.)	-	162	125	-	146.4	153.2	-	167.4	156.8	-	160	161	-	180	151
$R_{so.}$ (mm)	20.5	19	28.5	45	-	45.2	44.2	-	45.5	44.9	-	45.4	45	-	45.6
R_{si} (mm)	45	-	45.5	-	38.9	38.3	-	38.9	38.3	-	39	38.2	-	40	39.5
b_{os} (mm)	-	40.4	39.5	2.3	-	3.8	2.9	-	4.6	2.1	-	4.4	3.2	-	2.6
b_{is} (mm)	2.3	-	1.5	-	1.2	1.5	-	0.68	1.5	-	1.4	1.4	-	1.6	2.1
h_{os} (mm)	-	1.3	1.6	0.57	-	0.58	0.57	-	0.58	1	-	0.7	0.85	-	0.6
h_{is} (mm)	0.7	-	0.6	-	0.67	0.69	-	0.96	0.69	-	0.8	0.7	-	0.6	0.4
α_{os} (deg.)	-	0.6	0.6	14	-	5.9	9.8	-	5.9	14.4	-	5.4	14	-	3.4
α_{is} (deg.)	12.5	-	0.8	-	5.2	3.8	-	9.1	3.8	-	5.9	4.7	-	10	7
w_{st} (mm)	-	4.7	4.1	4.1	3.6	3.6	3.8	3.2	3.3	3.4	3	3.6	3.2	3.6	3
h_{sy} (mm)	3.7	3.5	3.3	2.3	2	-	1.9	1.4	-	1.7	1.5	-	1.57	1.2	-
V_{PM} (cm^3)	2	2.2	-	19.7	16	29.4	25.8	18.7	31.4	22.1	19.4	33.2	24.4	23	36.6
A_{slot} (mm^2)	42.5	53	35.3	39.5	56.7	31.5	38.7	60.1	35	44.5	63.3	33.1	47.2	61.1	39.5
I_{amp} (A)	4.8	5.1	4.4	4.5	5.3	4	4.4	5.5	4.2	4.7	5.6	4.1	4.9	5.5	4.5

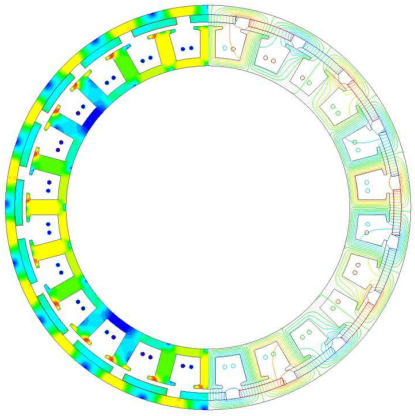

I. (a) ERSPM.

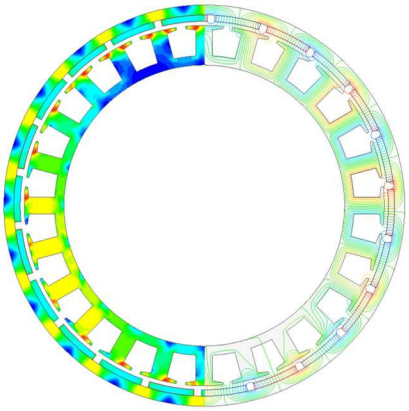

II. (a) ERSPM.

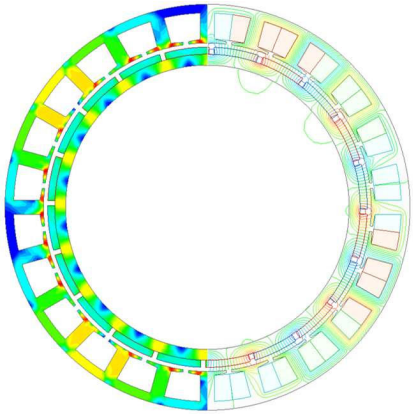

I. (b) IRSPM.

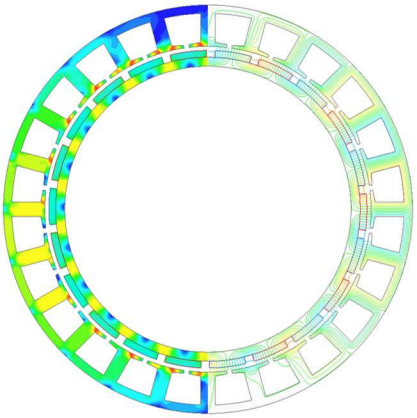

II. (b) IRSPM.

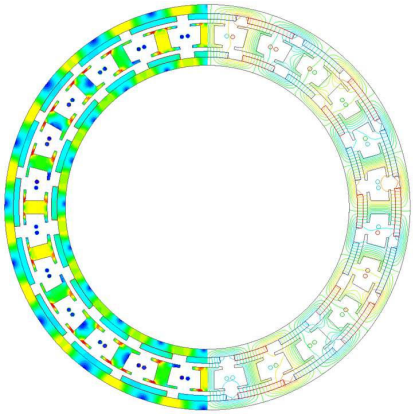

I. (c) SDRPM.

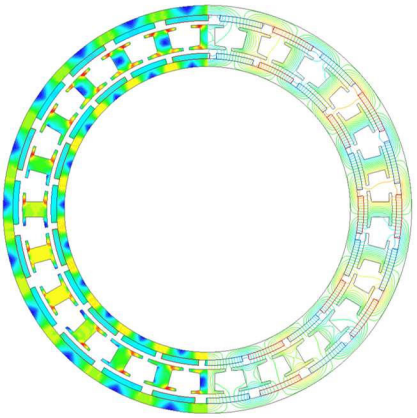

II. (c) SDRPM.

I. 24-slot/20-pole

II. 24-slot/22-pole

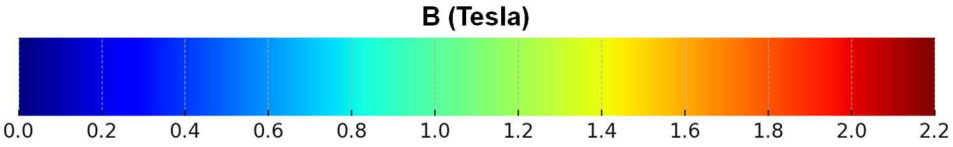

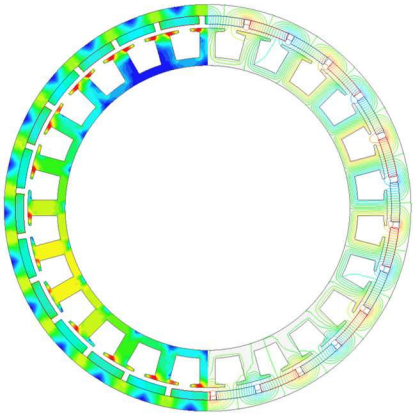

III. (a) ERSPM.

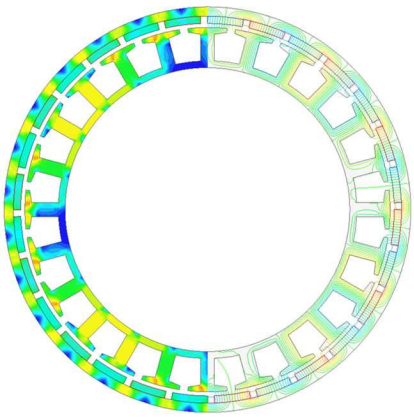

IV. (a) ERSPM.

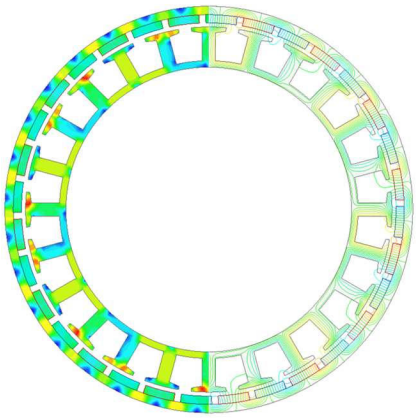

V. (a) ERSPM.

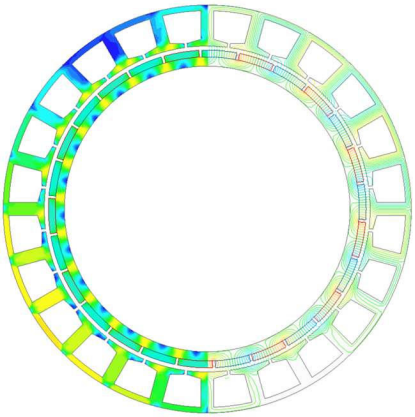

III. (b) IRSPM.

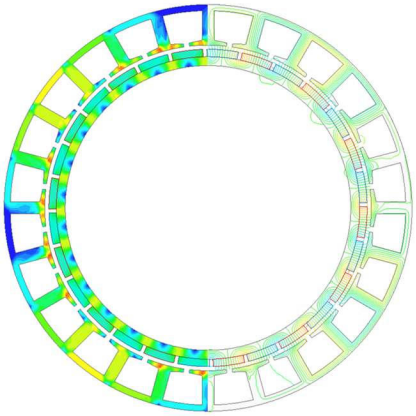

IV. (b) IRSPM.

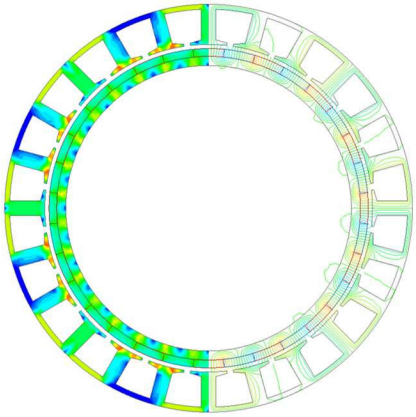

V. (b) IRSPM.

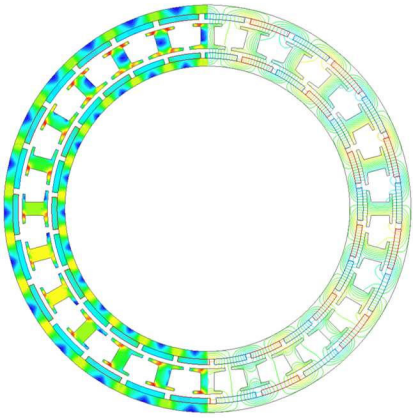

III. (c) SDRPM.

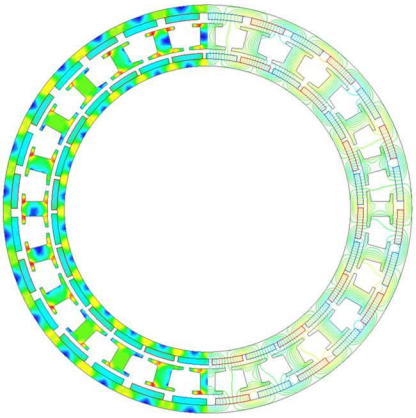

IV. (c) SDRPM.

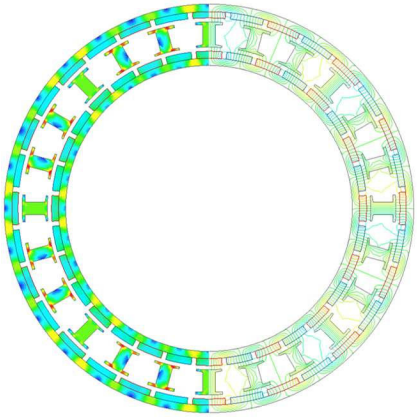

V. (c) SDRPM.

III. 24-slot/26-pole

IV. 24-slot/28-pole

V. 24-slot/32-pole

Fig. 3.26. Open circuit flux density and equal potential distributions. I. 24-slot/20-pole. II. 24-slot/22-pole. III. 24-slot/26-pole. IV. 24-slot/28-pole. V. 24-slot/32-pole. (inner bore radius=35mm)

Fig. 3.27a shows the average torques of optimised ERSPM, IRSPM, and SDRPM machines with different pole numbers. The torques of the ERSPM and IRSPM machines are increased with pole numbers and achieve the highest average torque at 28 poles. Then, the torque decreased with further increased pole numbers because the flux leakage between PMs increased (Fig. 3.26). For the SDRPM machine, although the flux leakage between PMs increased with the pole numbers, the difference of pole arcs between inner and outer PMs is diminished. The average torque of the SDRPM machine increased with pole numbers constantly. However, the increase in torque of the SDRPM machine is small. The torque of the SDRPM machine still cannot exceed that of the SRSPM machines, which can only approach the SRSPM machine. This is because diminishing the difference between inner and outer PMs only ensures that the resultant magnetic flux would not decrease. The variations of the torque per PM volume of optimised machines with different pole numbers are shown in Fig. 3.27b. It can be seen that $\rho_{\mathrm{Torque/PM}}$ of the SDRPM machine is maintained around 0.12 Nm/cm^3 and almost only half of those of the SRSPM machines.

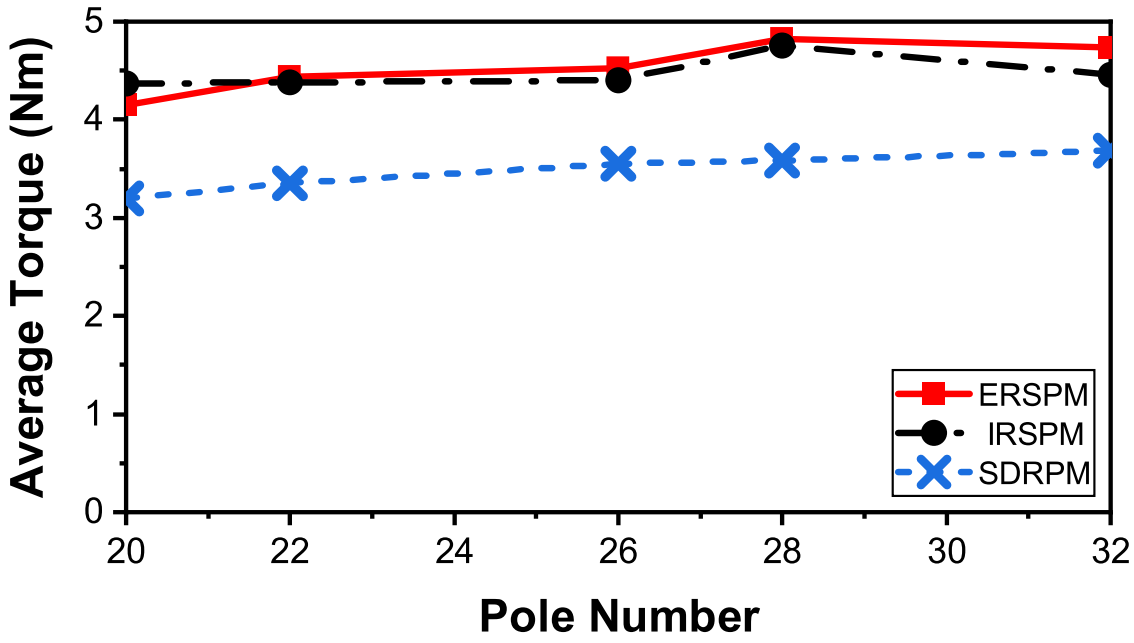

(a) Average torque.

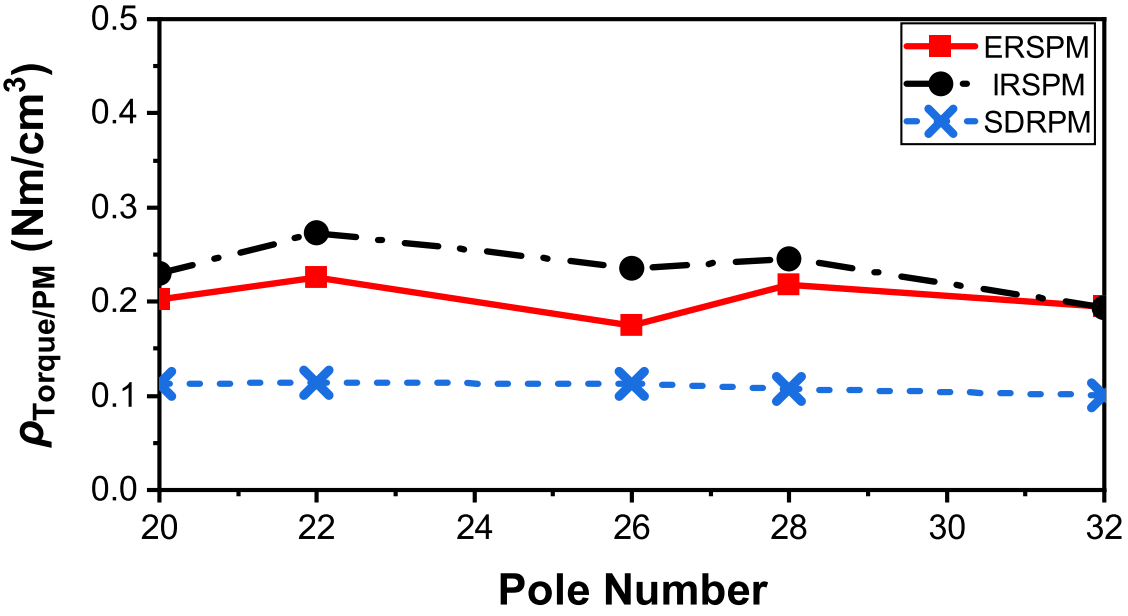

(b) $\rho_{\mathrm{Torque/PM}}$.

Fig. 3.27. Average torque and $\rho_{\mathrm{Torque/PM}}$ of optimised ERSPM, IRSPM, and SDRPM machines with different pole numbers.

The electromagnetic performances of the ERSPM, IRSPM, and SDRPM machines have 35mm inner bore radius with the same 24-slot and different pole numbers, i.e., 20-pole, 22-pole, 26-pole, 28-pole, and 32-pole will be compared.

Fig. 3.28 shows the air-gap flux densities of the ERSPM, IRSPM, and SDRPM machines with a 35mm inner bore radius with different slot/pole number combinations. All the fundamental components of air gap flux densities of SDRPM machines with different slot/pole number combinations are smaller than those of the ERSPM and IRSPM machines with the same slot/pole number combinations.

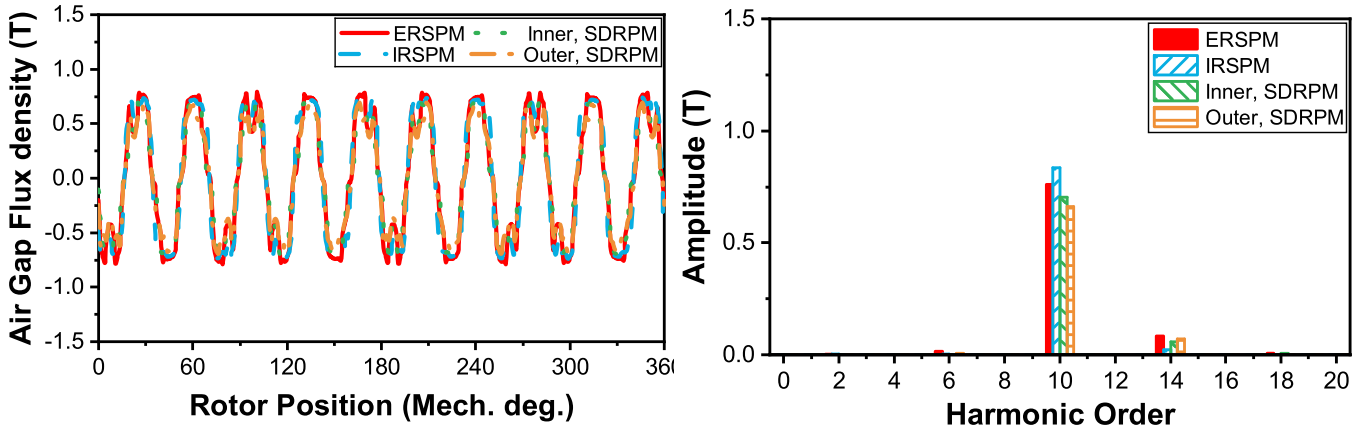

(a) 24-slot/20-pole.

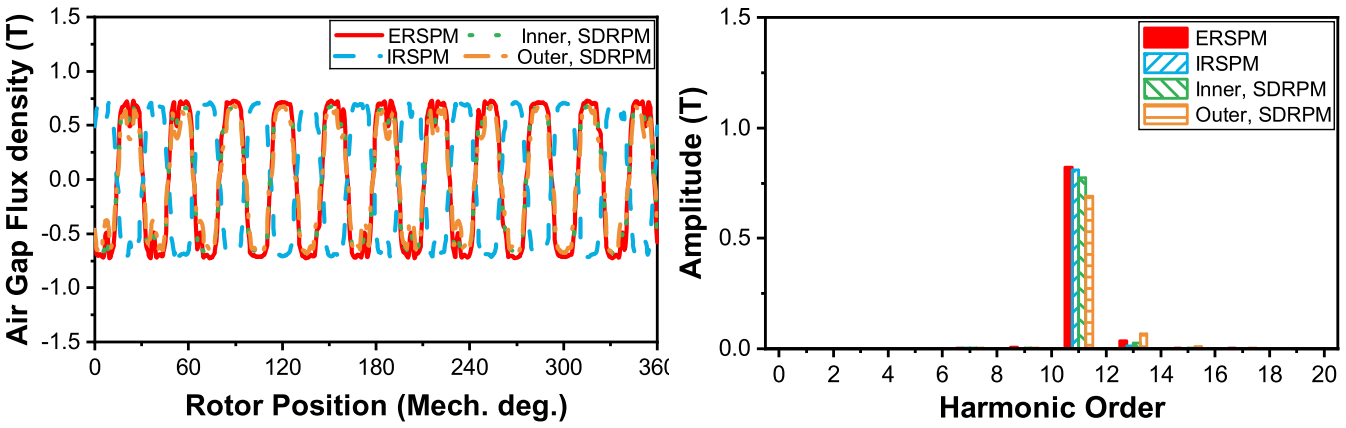

(b) 24-slot/22-pole.

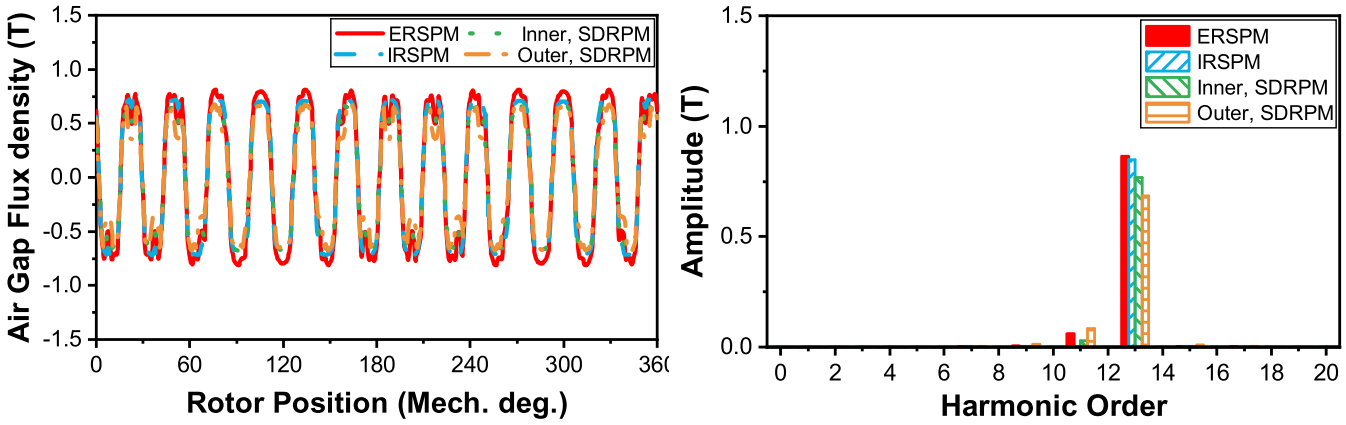

(c) 24-slot/26-pole.

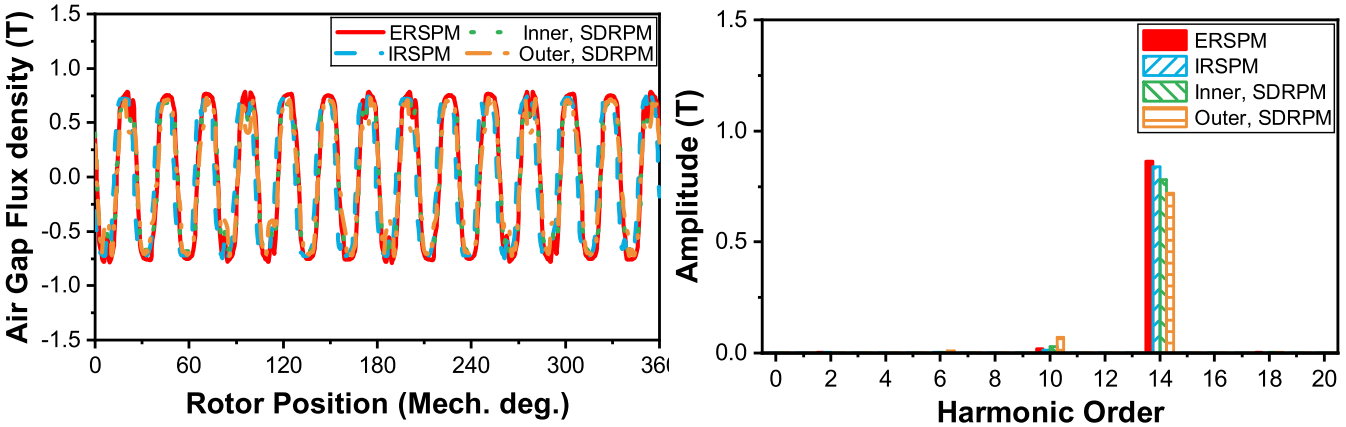

(d) 24-slot/28-pole.

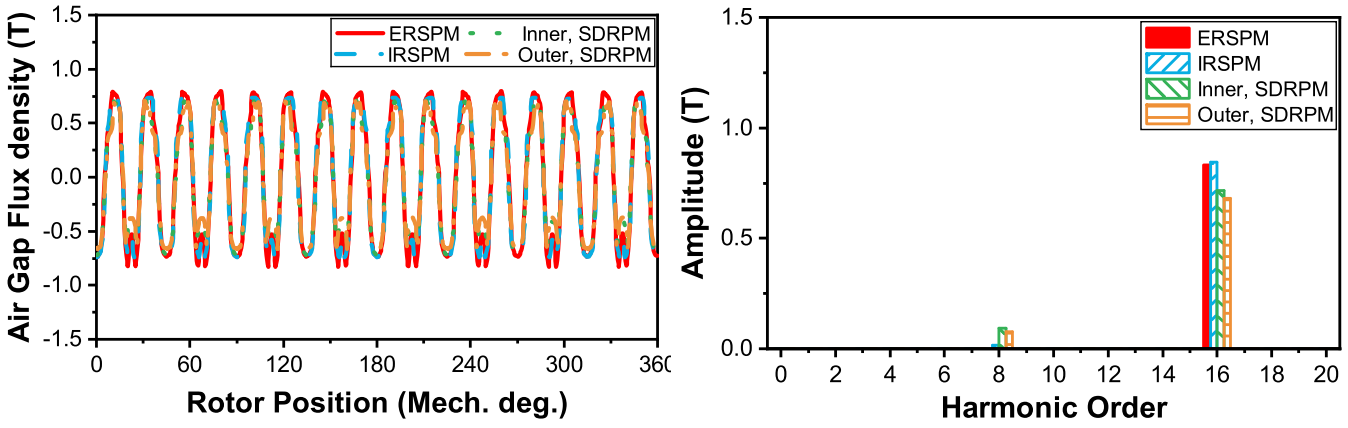

(e) 24-slot/32-pole.

Fig. 3.28. Comparison of inner and outer airgap flux densities of ERSPM, IRSPM, and SDRPM machines.

Fig. 3.29 compares the phase A flux linkages of all machines. The fundamental components of the phase flux linkages of the ERSPM machines with different slot/pole number combinations are higher than those of SDRPM machines with the same slot/pole number combination.

Comparing all the SDRPM machines with the IRSPM machines with the same slot/pole number combination, the fundamental component of the phase flux linkage of the 20-pole SDRPM machine is lower than that of the IRSPM machine. As the pole number increases, the fundamental components of the phase flux linkages of the 22-pole and 26-pole SDRPM machines are the same as the corresponding IRSPM machines. Further increasing the pole number, the fundamental components of the phase flux linkages of the 28-pole and 32-pole SDRPM machines exceed the corresponding IRSPM machines. The corresponding back EMFs of all machines show the same trend as the phase flux linkages, as shown in Fig. 3.30.

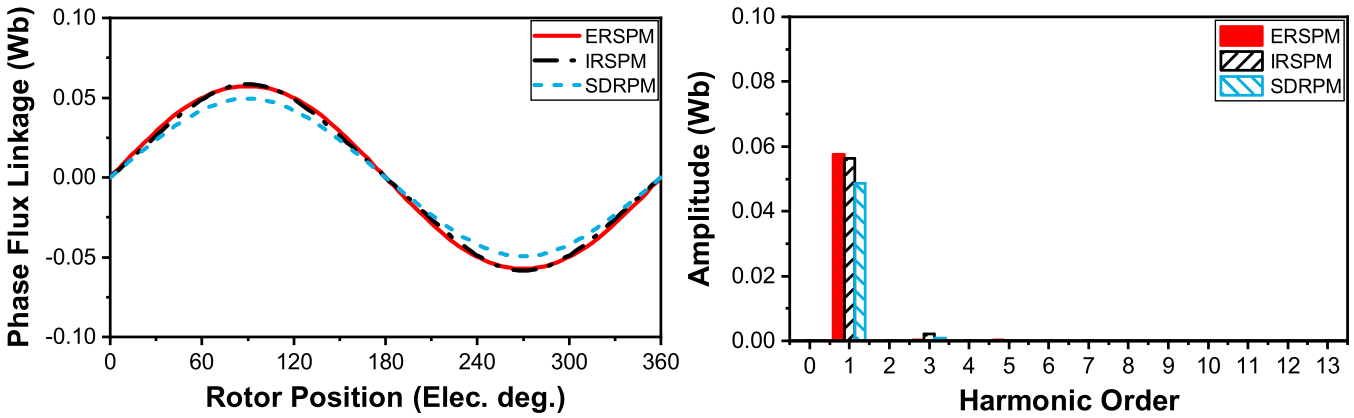

(a) 24-slot/20-pole.

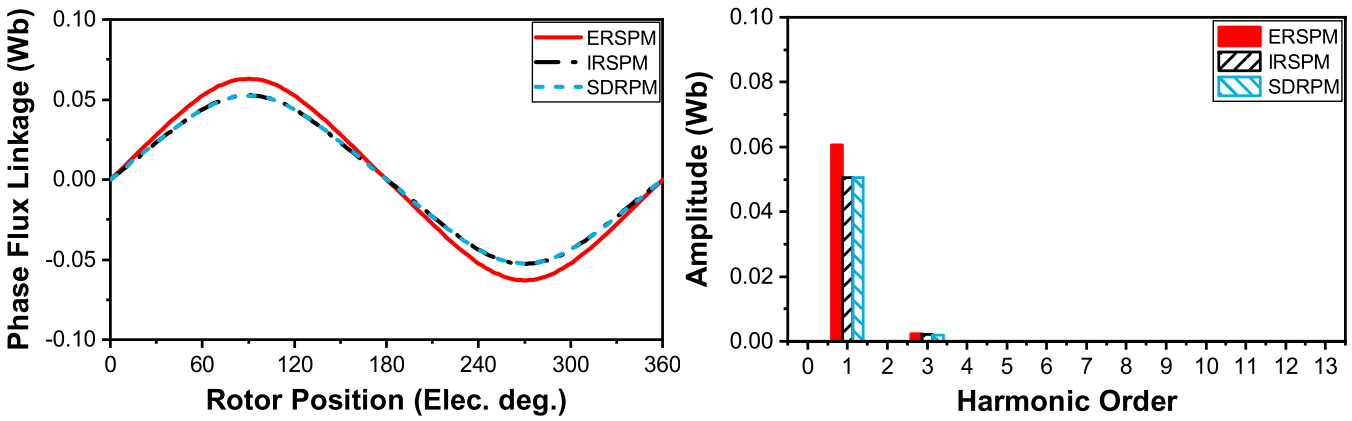

(b) 24-slot/22-pole.

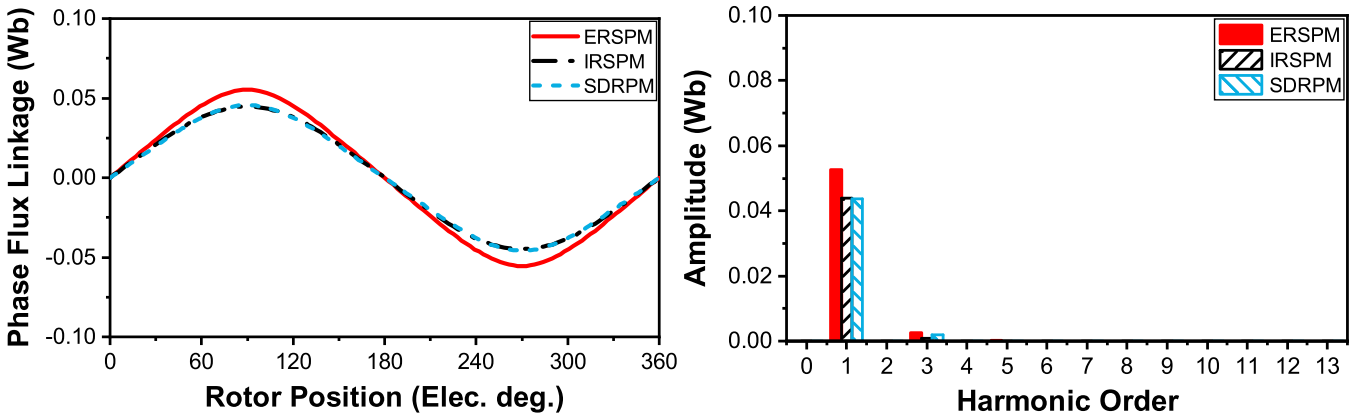

(c) 24-slot/26-pole.

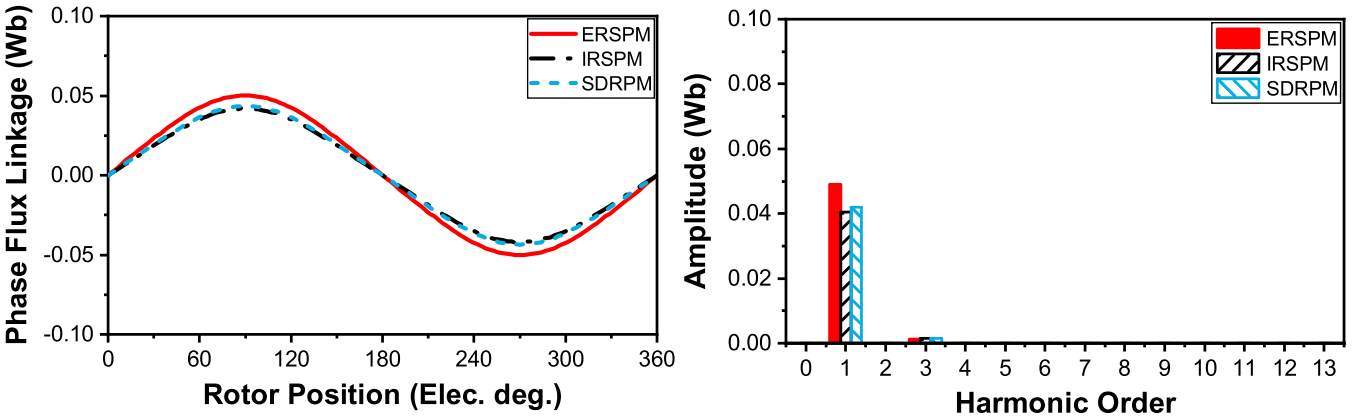

(d) 24-slot/28-pole.

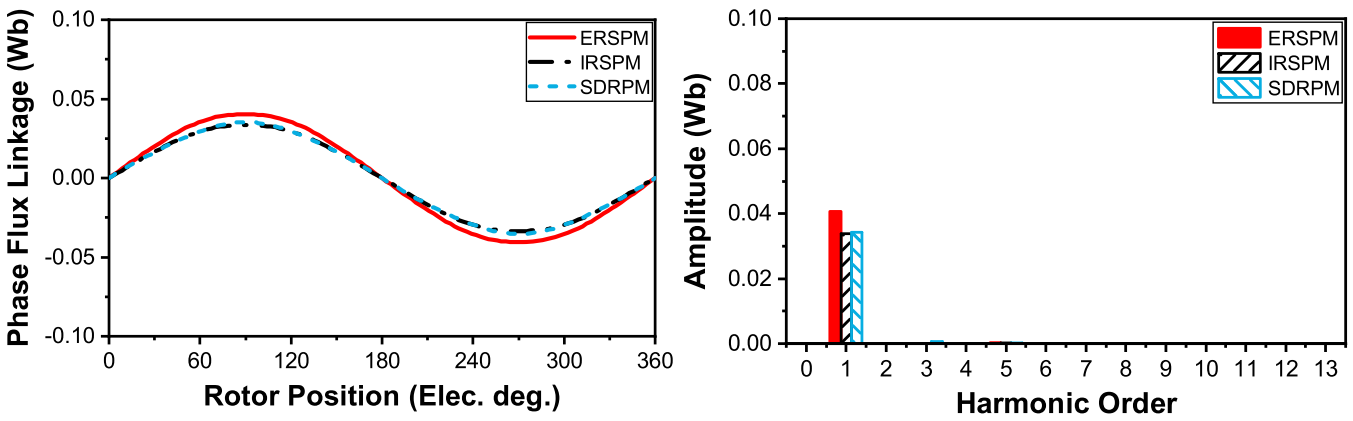

(e) 24-slot/32-pole.

Fig. 3.29. Comparison of phase-A flux linkages of ERSPM, IRSPM, and SDRPM machines.

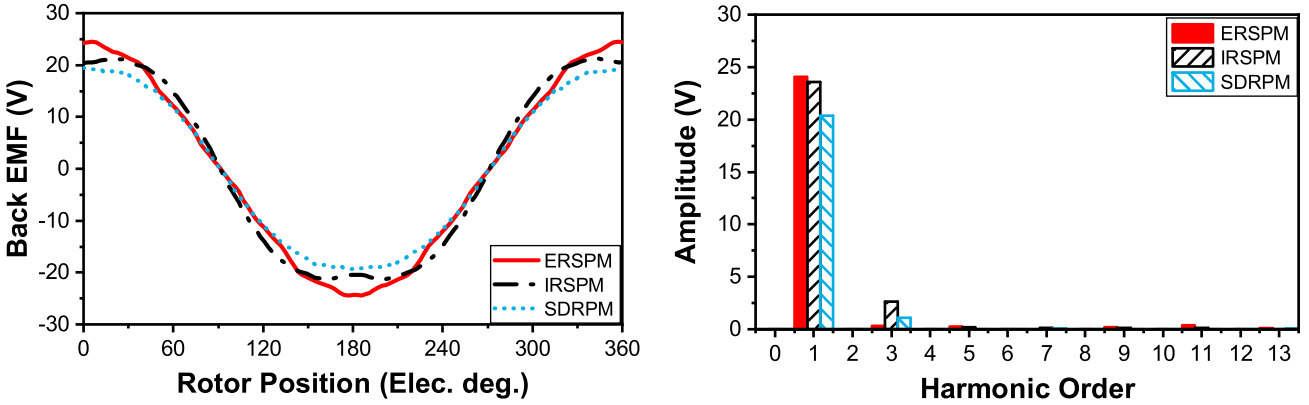

(a) 24-slot/20-pole.

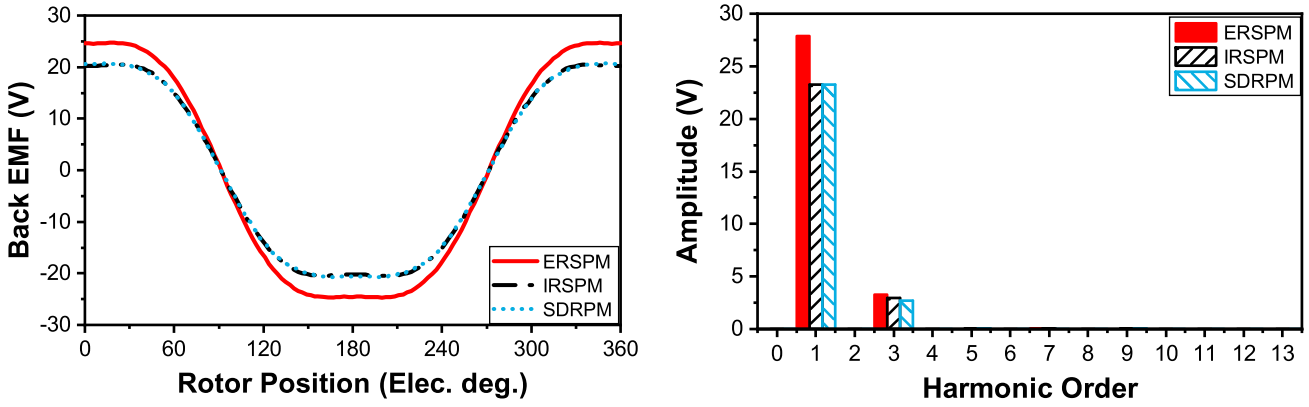

(b) 24-slot/22-pole.

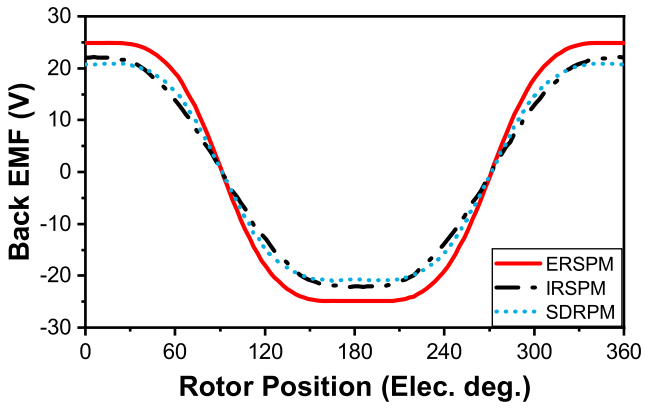

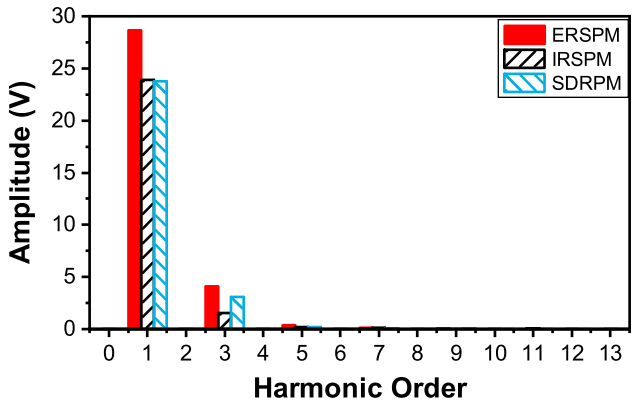

(c) 24-slot/26-pole.

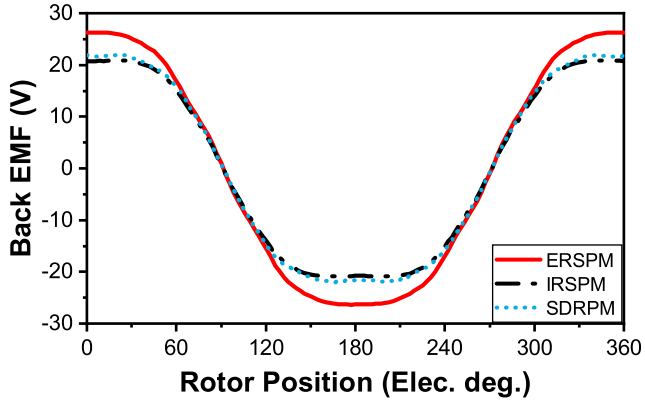

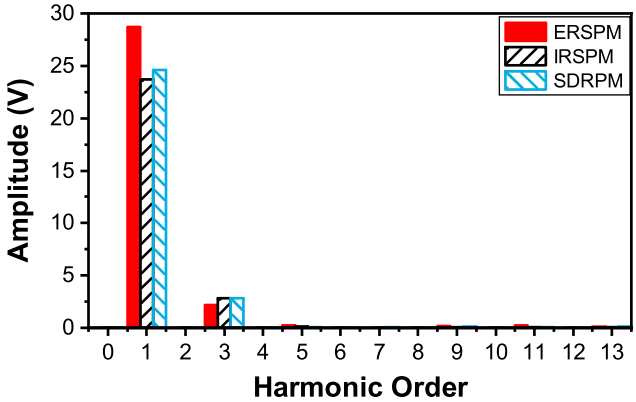

(d) 24-slot/28-pole.

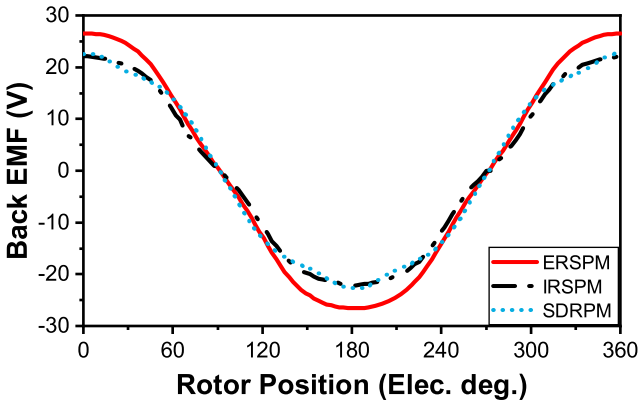

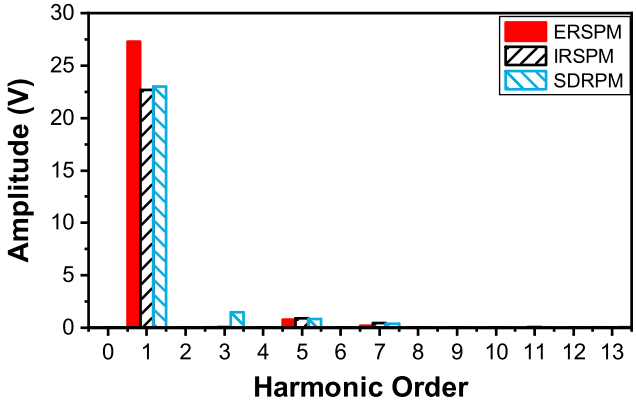

(e) 24-slot/32-pole.

Fig. 3.30. Comparison of phase-A back EMFs of ERSPM, IRSPM, and SDRPM machines, 400 r/min.

The electromagnetic torques of the ERSPM, IRSPM, and SDRPM machines with a 35mm inner bore radius with different slot/pole number combinations are shown in Fig. 3.31. All machines have the same 30 W copper loss, and the corresponding amplitudes of the input current I_{amp} for each machine are listed in Table 3.13. The torques of the globally optimised SDRPM machines with different slot/pole number combinations are always lower than those of the corresponding ERSPM and IRSPM machines.

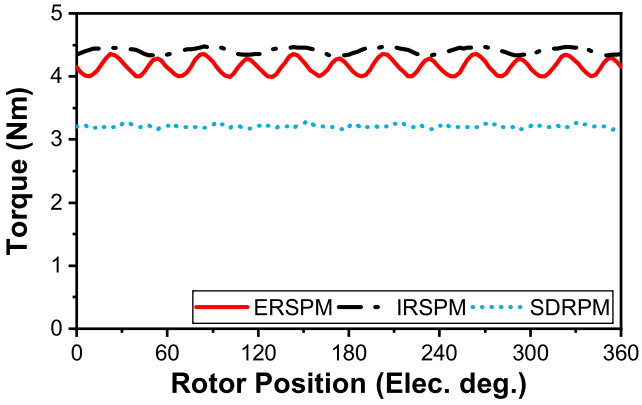

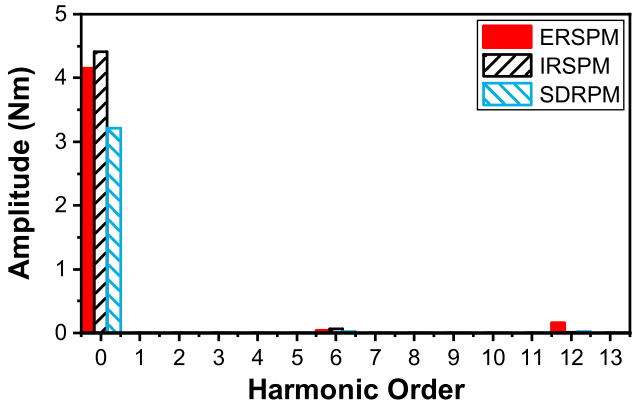

(a) 24-slot/20-pole.

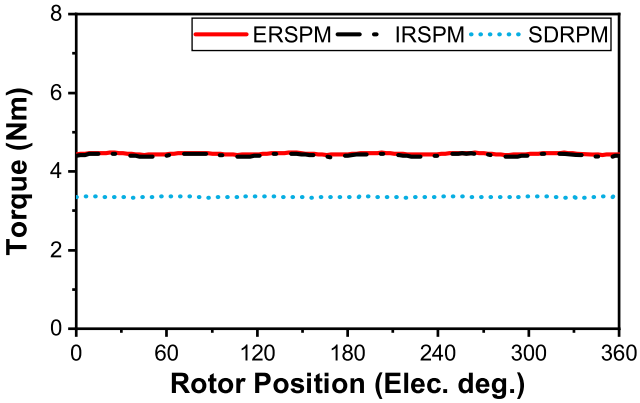

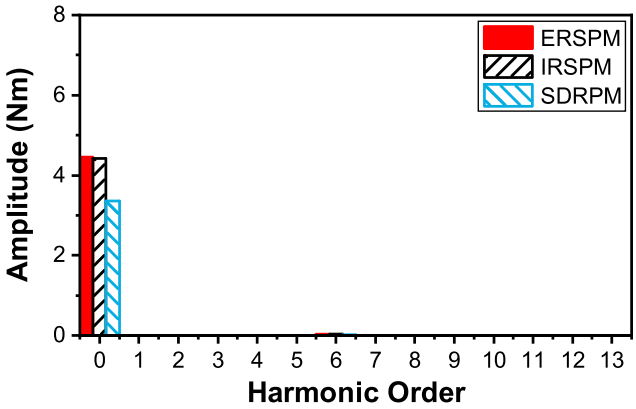

(b) 24-slot/22-pole.

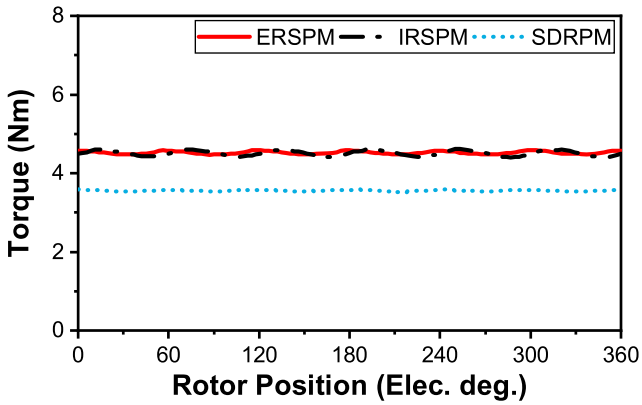

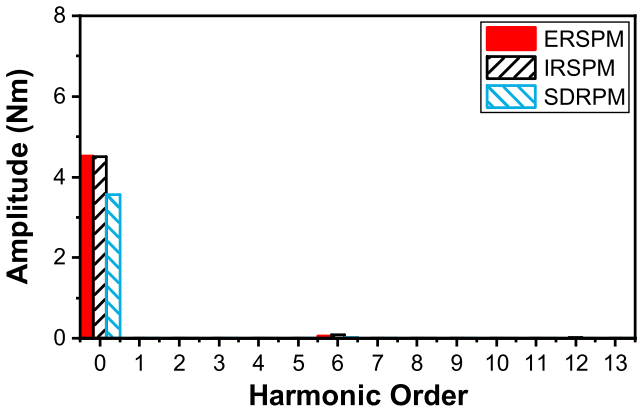

(c) 24-slot/26-pole.

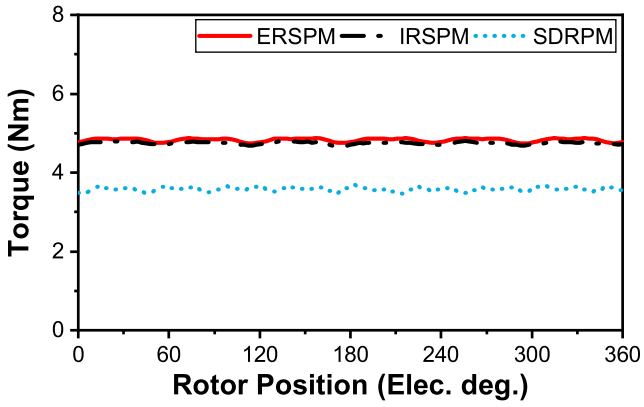

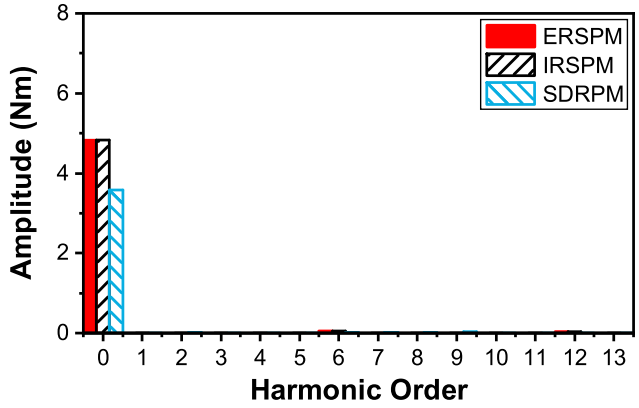

(d) 24-slot/28-pole.

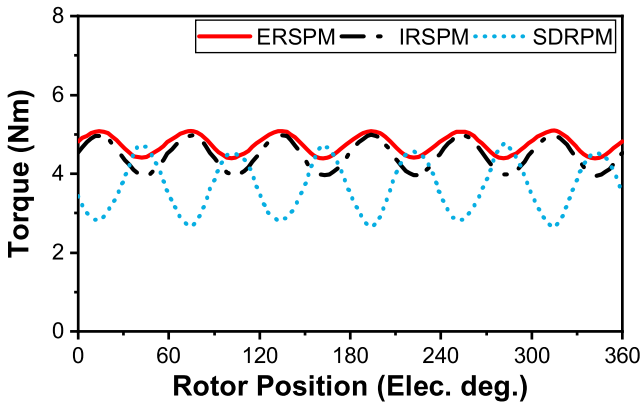

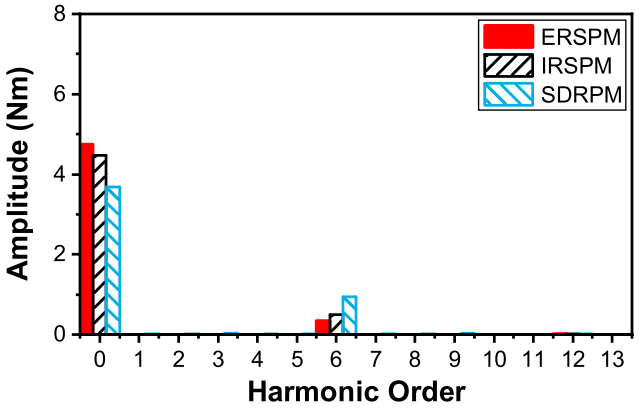

(e) 24-slot/32-pole.

Fig. 3.31. Comparison of torques of ERSPM, IRSPM, and SDRPM machines.

3.7 Experimental Validation

The 12-slot/10-pole YDRPM machine is prototyped and tested to validate the FEA results, as shown in Fig. 3.32. The machine parameters are listed in Tables 3.1 and 3.3. The cogging torque, back EMF, static torque at full and half load conditions, and average torques vs. currents are tested to verify the FEA results. The dynamic test platform is used to test the back EMF, as shown in Fig. 3.33 (a). The cogging torque and static torque are tested by the method in [ZHU09], and the test rig is shown in Fig. 3.33 (b).

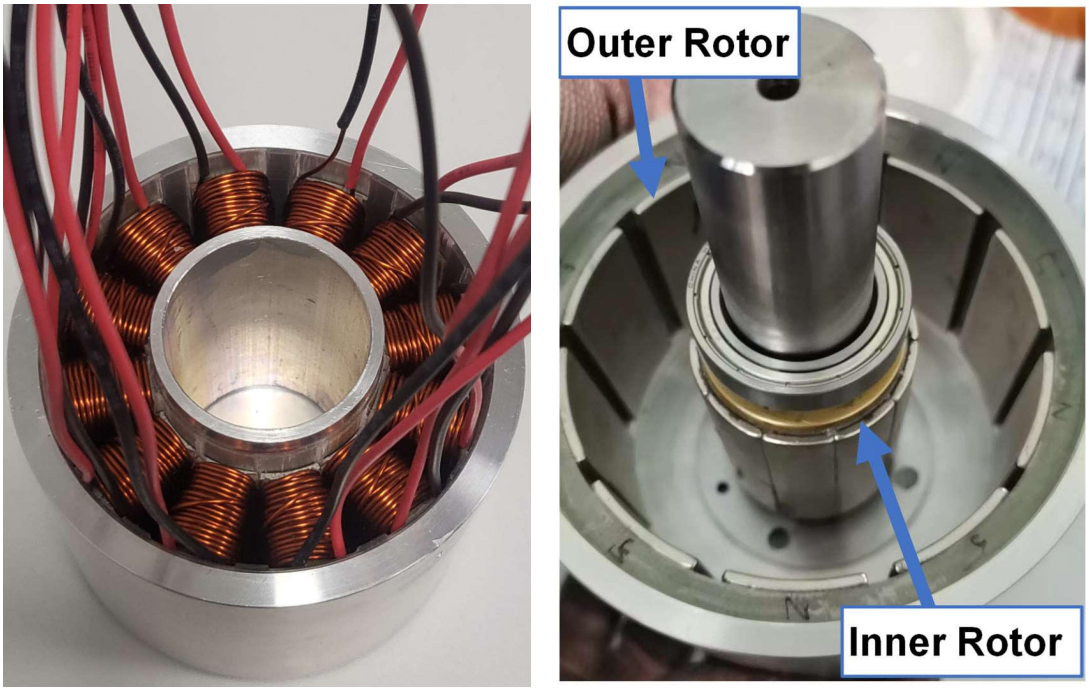

(a) Stator (b) Rotor

Fig. 3.32. 12-slot/10-pole SDRPM prototype.

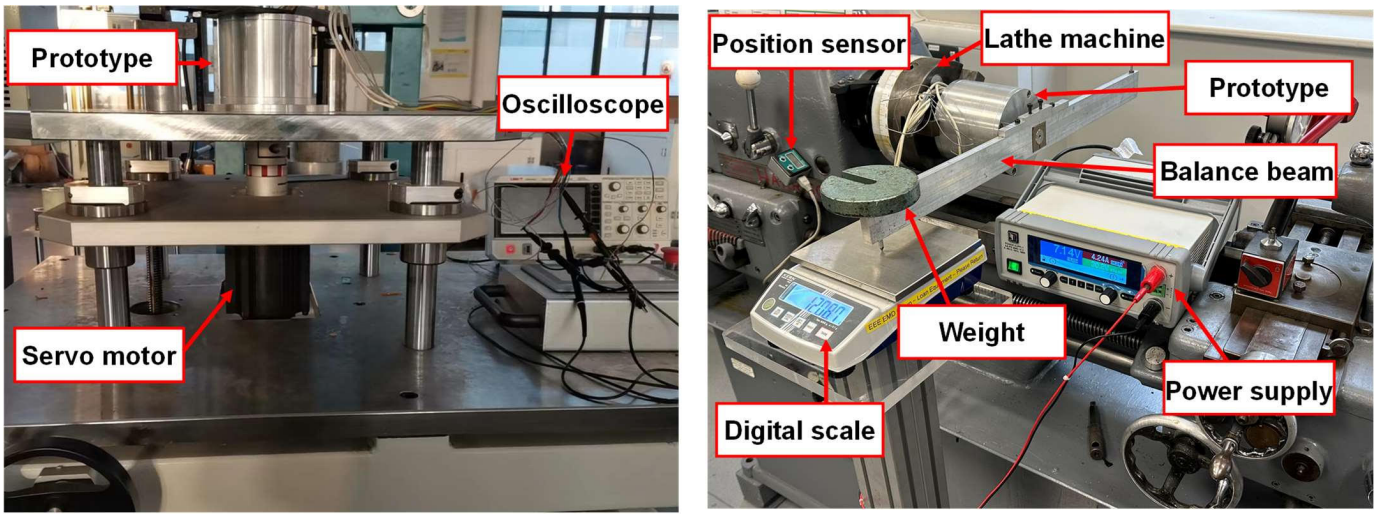

(a) Dynamic test platform. (b) Static test platform.

Fig. 3.33. Test rigs.

Fig. 3.34 shows the measured and FEA predicted results of the cogging torque and phase back EMF of the 12-slot/10-pole YDRPM machine. The phase-back EMF of the machine is obtained at 800 r/min. Although the amplitudes and waveforms exhibit some differences, it is worth noting that both FEA predicted and measured results confirm the low cogging torque in the prototype machine. The

discrepancies between the tested and predicted amplitudes of cogging torque and EMF are principally attributed to manufacturing imperfections. The resin injection has been used to join all stator modules together during assembly to position the stator modules and facilitate assembly since the modular stator structure of the machine. This process increases the manufacturing tolerance of the prototype, resulting in discrepancies between the prototype and the FEA model. Overall, the experimental results corroborate the FEA predictions for both back-EMF and cogging torque.

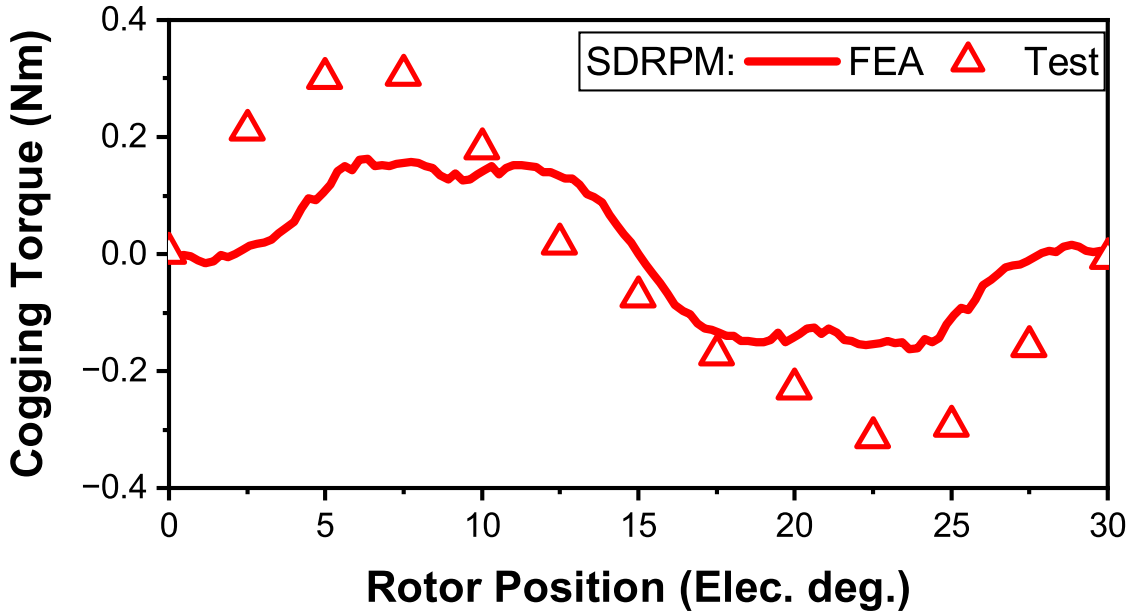

(a) Cogging torque waveforms.

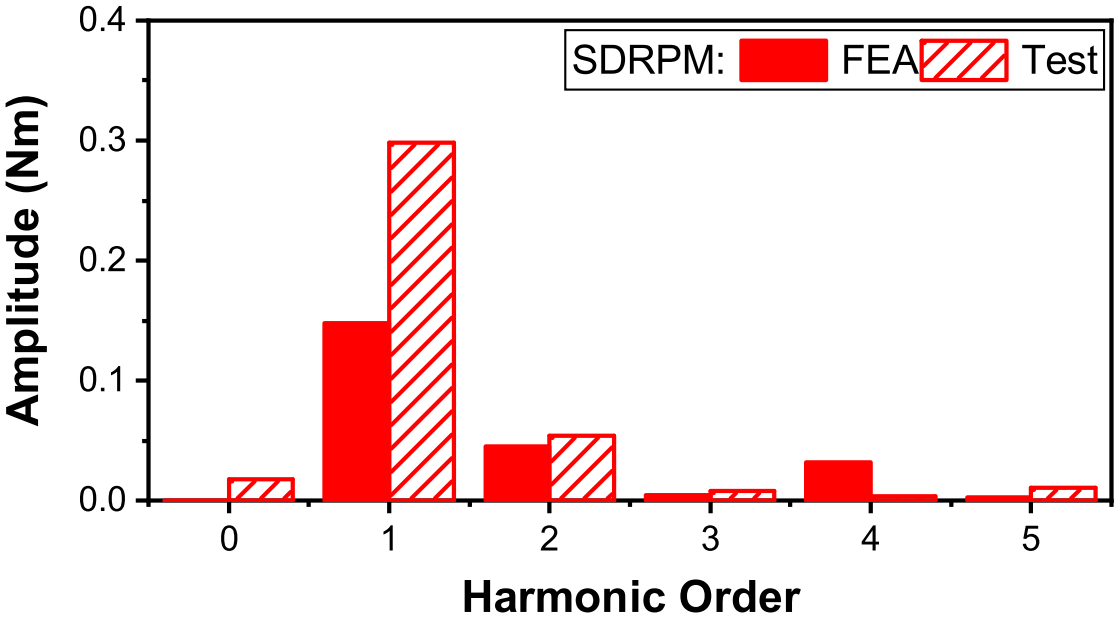

(b) Cogging torque spectra.

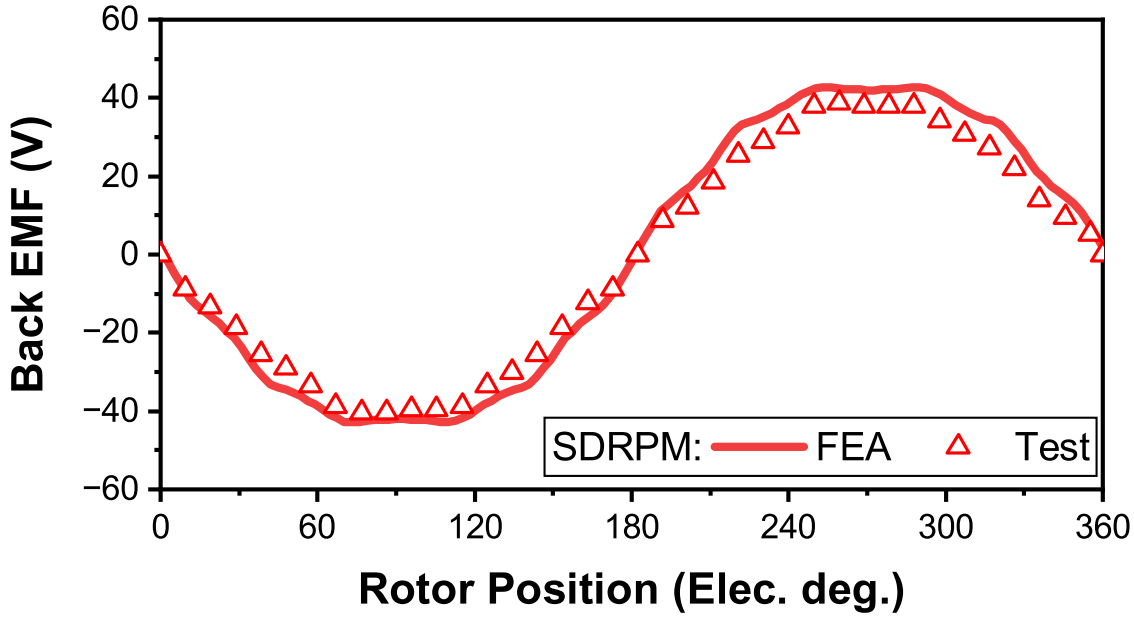

(c) Phase back EMF waveforms.

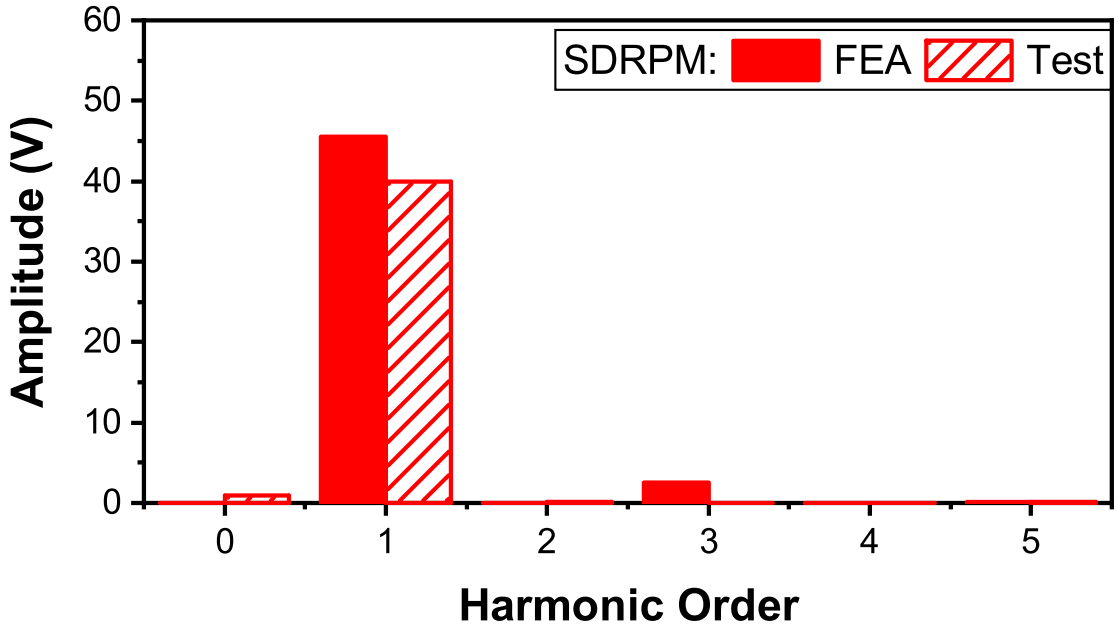

(d) Phase back EMF spectra.

Fig. 3.34. FEA predicted and measured results.

The static torques at full and half loads for the SDRPM machine are measured by supplying a range of DC currents ($I_A = -2I_B = -2I_C = I_{DC}$), and the full-load current corresponding to a copper loss of 30 W, as depicted in Fig. 3.35 (a). Fig. 3.35 (b) shows the variation of average torque with current. The measured torques align closely with the FEA predictions.

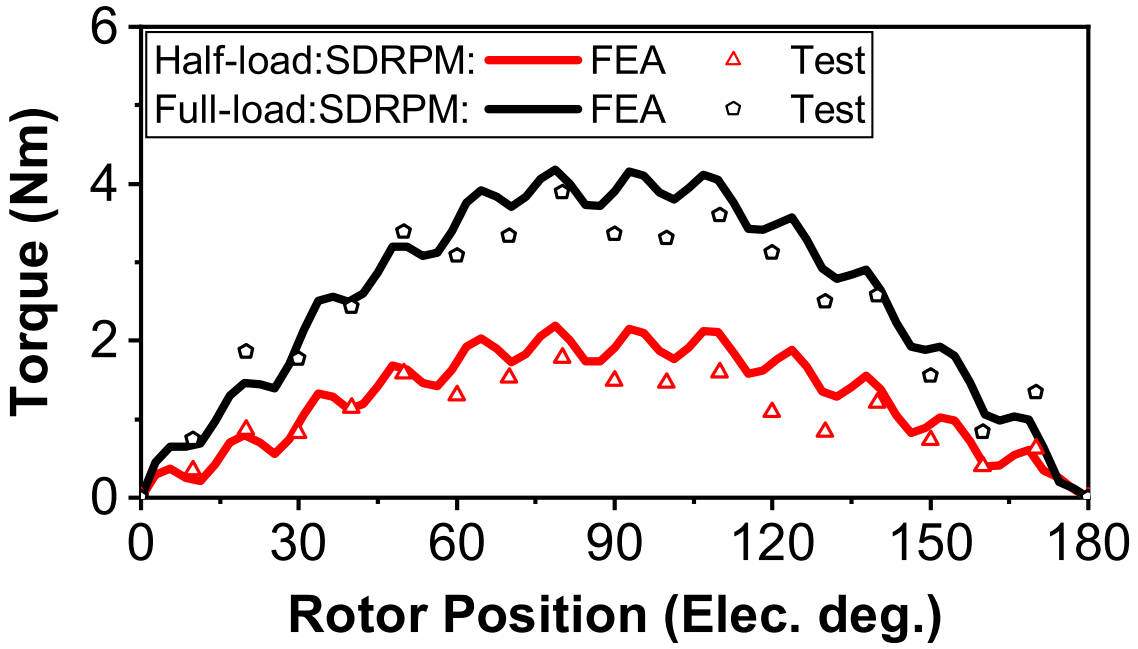

(a) Static torques at full and half-load conditions.

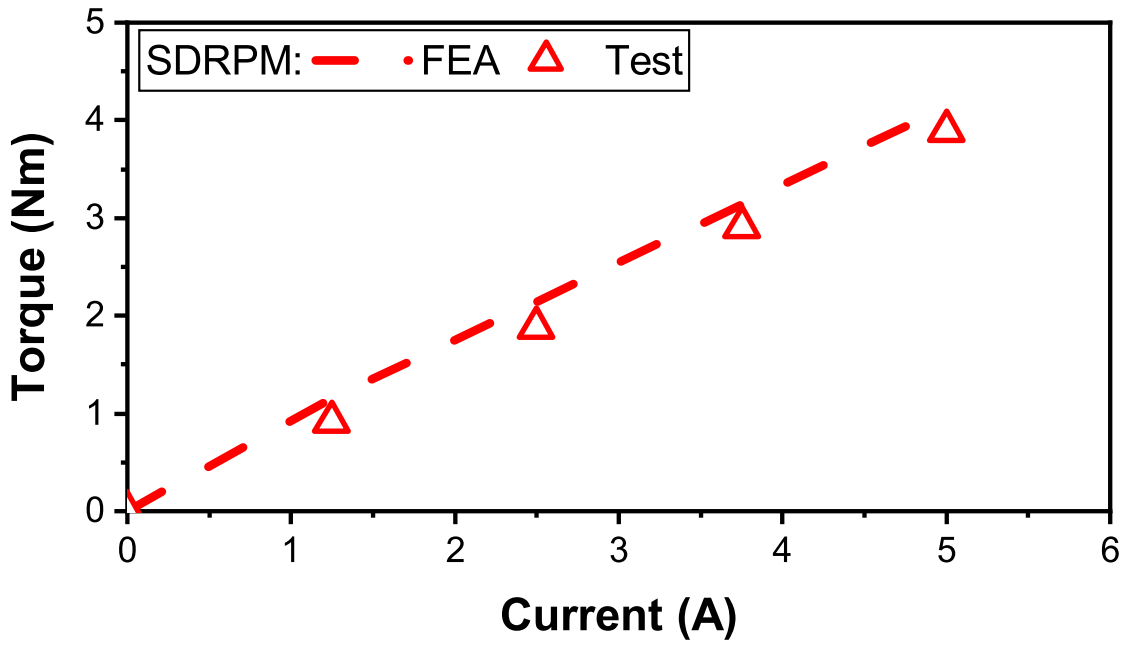

(b) Variation of average torques with currents.

Fig. 3.35. FEA and measured torques.

3.8 Conclusion

This chapter has compared the electromagnetic performances of the radial-flux FSCW SDRPM machine and the conventional ERSPM and IRSPM machines under different conditions. All machines are optimised and analysed by the FEA, and the results are theoretically explained using the equivalent magnetic circuit.

For the radial-flux SDRPM machine, the radii of inner and outer SPM rotors are different. As a result, the inner and outer PMs hardly generate the same magnetic flux, thus, the series connected magnetic circuits decreases the resultant magnetic flux. This has been explained in this chapter for the first time. In addition, based on the comparative studies under different critical parameter conditions. The SDRPM machine only has a higher torque than the SRSPM machines when they have the same total air gap length. However, under different scenarios in inner bore radius, pole numbers and PM volumes, it is revealed that compared with the conventional SRSPM machines, the radial-flux SDRPM machine has a complex structure, lower torque, higher cost, and lower torque per PM volume.

CHAPTER 4

INVESTIGATION OF YOKELESS COUNTER-ROTATING DUAL-ROTOR PERMANENT MAGNET MACHINES

Chapter 3 compares the electromagnetic performance of dual-rotor and single-rotor PM machines. It reveals that the dual-rotor PM machine, with the same pole number and rotational speed of two rotors, has lower torque than the single-rotor PM machine. However, dual-rotor machines inherently have an extra rotor compared with single-rotor machines. When the two rotors of the dual-rotor machine operate in different working conditions, the dual-rotor machine can replace two single-rotor machines to meet the requirements of some special applications that require two rotors to reduce the cost and save space. Radial-flux fractional slot concentrated winding (FSCW) yokeless counter-rotating dual-rotor permanent magnet (YCDRPM) machines are investigated in this chapter. Based on the magnetic field modulation theory, a YCDRPM machine combines magnetic gear and PM machine to realise dual-rotor counter-rotating operation for special applications, such as washing machines, counter-rotating wind power generators, and underwater vehicles. The operation principle and three feasible slot/pole number combinations are investigated under different operation modes. All YDCRPM machines are optimised and analysed by finite element analysis (FEA). The YCDRPM machine not only operates as a counter-rotating DRPM machine but also can utilise the magnetic gearing effect to enhance the output torque. The results are validated by experiments on a prototype YCDRPM machine.

This chapter is submitted to IEEE Transactions on Transportation Electrifications:
Z.T. Ran, Z.Q. Zhu, Hai Xu, Y.J. Zhou, L. Chen, and L. Yang, “Investigation of yokeless counter-rotating dual-rotor permanent magnet machines,” submitted to IEEE Transactions on Transportation Electrifications. (under review)

4.1 Introduction

In recent years, the technologies of dual-rotor permanent magnet (DRPM) machines have developed significantly, as they can be used to improve the torque density of the PM machines.

The dual-rotor topology for the induction machine was first proposed in [KEL69]. Based on that topology, [QU03a] [QU03b] proposed the surface-mounted PM (SPM) radial-flux toroidal wound DRPM

machine, the inner and outer rotors with the same pole numbers are fixed on the same shaft to enhance the torque density of the PM machine. Thus, the high torque density DRPM machine is considered for wind power generation [XU13] [POT15] [POT16]. The different PM arrangements on the two rotors were discussed in [FUJ15], and the consequent pole was employed in [ZHA20a] to significantly reduce the PM volume and enhance the torque density. Since the DRPM machine contains two rotors, the Halbach-array PM is employed to reduce the weight of both rotors [KUM16]. Moreover, the different slot/pole number combinations were discussed in [XU17]. The vernier DRPM machine utilises the short end-winding of toroidal winding and the magnetic field modulation of both air gaps to improve the torque density [NIU10] [ALL20].

In order to further improve the electromagnetic performance of the DRPM machine, [WAN12] connected the inner and outer magnetic circuits in series in the DRPM machine, in which the stator yoke is not the main path of the resultant flux. Thus, the harmonic injection method was used to enhance the output torque without increasing the stator yoke thickness. Since the fluxes generated by inner and outer PMs are connected in series, [VAN13] proposed the radial flux yokeless and segmented armature DPM (YDRPM) machine. The removed stator yoke offers a large slot area, low weight and iron loss. Furthermore, since the modular stator significantly improves the winding fill factor, the SDPM machine has received great attention from researchers.

[GOL18] compared the Halbach-array YDRPM machine with the single rotor PM machines. The Halbach-array YDRPM machine shows the highest torque density since both rotors employ the Halbach-array PMs, and the active weight is significantly reduced [GOL19a] [GOL19b].

However, since the inner and outer rotors share the same stator, the outer rotor is insufficiently utilised [LIU18], and the different fluxes generated by inner and outer PMs may decrease the torque of DRPM machines [RAN22]. Furthermore, the inner and outer rotors are fixed on the same shaft, and the DRPM machine contains two rotors but has only one output port. [XU05] first proposed the dual-mechanical ports employed on the electrical machine. Two rotors of the DRPM machine can be fixed on the different shafts for different working conditions. Thus, compared with using two different PM machines for specific applications, the DRPM machine can save space and cost since the two rotors of the DRPM machine can be considered as two separate outputs.

[YEH12] uses the DRPM machine in the air conditioner. The two rotors with the same pole numbers are fixed on different shafts, and the different working conditions of rotors are achieved by arranging the different stator winding groups to control each rotor. Thus, two rotors work as the condenser and evaporator separately. Moreover, [KWO18] integrates vernier and flux-reversal PM machines under different working conditions into a single machine in the washing machine, since the washing and

dehydrating modes require the electrical machine to operate under different conditions. In order to further improve the torque density of the DRPM machine, the magnetically geared DRPM machine employs two different pole number rotors, with the benefits of magnetic gearing effect between two rotors [JIA12] [ZHU18a]. Moreover, the modulation ring of the magnetically geared machine can be designed as a rotor for the output [BAI15a]. However, the modulation ring has low mechanical strength as an output rotor [BAI16].

In addition, counter-rotating operation machines are required for some special applications. [SHI98] proposed a counter-rotating DR (CDR) wind turbine, and [JUN05] analysed and compared the CDR wind turbine with the single rotor wind turbine. It shows that the CDR wind turbine significantly increases the power conversion efficiency since the auxiliary counter-rotating rotor compensates for the dead zone in the main rotor area and generates additional torque. Moreover, the different direction moments of inertia also are beneficial to low noise and vibration [BOO10]. Thus, the CDRPM machines are proposed for the CDR wind power generation [ULL22a] [ULL22b] [MIR21]. The outer stator magnetically geared CDRPM machine proposed in [WAN17b] utilises the magnetic gearing effect between the rotor, modulation ring, and stator winding to achieve counter-rotating operation. Its control strategy is investigated in [LUO17]. Furthermore, [CHE22] replaces the inner PM rotor with the salient pole rotor, which reduces the PM volume. The split stator teeth are also employed to form a vernier machine to enhance the torque.

The underwater vehicles required counter-rotating operation machines as well. The counter-rotating propeller for the underwater vehicle is reported in [HOL94], which shows that the ring thrusters are essentially two motors with a large hollow rotor. Moreover, two counter-rotating rotors offer different direction moments of inertia to solve the yawing and spinning problem during travelling through a guided route [LIU18]. Furthermore, since the aft propeller can utilise the rotation flow from the forward propeller, the propulsion efficiency of the contra-rotating propellers is superior to other propeller types [SAS98]. In addition, the propulsion with a higher rotating speed aft propeller than the forward propeller has higher efficiency than the propulsion with the same rotating speed aft and forward propellers [SHI20]. [CHE11] proposed the CDRPM machine for the underwater vehicle by employing toroidal winding and changing the inner and outer phase sequence on the shared stator for different rotors. The counter-rotating operation in the machine is realised by the twisted stator windings changing the corresponding inner and outer phase sequences, which generate the same speed and different rotating direction magnetic field for the inner and outer air gaps.

This chapter proposes a novel radial-flux yokeless CDRPM (YCDRPM) machine. The counter-rotating operation is achieved by utilising the magnetic gearing effect between two rotors and the

sandwiched modular stator. Since the modular stator is employed for a higher slot fill factor and larger slot area, the fractional slot concentrated winding (FSCW) is considered. The electromagnetic performances of different slot/pole number combinations of the YCDRPM machines are investigated and compared by finite element analysis (FEA). Section 4.2 introduces the topologies of the YCDRPM machines with different slot/pole number combinations. Section 4.3 elaborates on the operation principle of the YCDRPM machine. Section 4.4 globally optimises the YCDRPM machine by FEA genetic algorithm to maximise the output torque under a fixed copper loss. In section 4.5, the electromagnetic performances of the YCDRPM machines are compared under different operation modes. The prototype and experimental results are given in Section 4.6. Finally, the conclusion is given in section 4.7.

4.2 Machine Topologies

Based on the radial flux yokeless DRPM machine [VAN13] and the magnetic gear [ATA01], the sandwiched stationary modulation ring can be wounded the windings as a stator, and the counter-rotating magnetic field working harmonics can realize a YCDRPM machine. For underwater vehicle applications, the electromagnetic torques of two rotors need to be equal or similar for underwater vehicle applications [ZHA14]. The two rotors of the radial-flux DRPM machine proposed in this chapter are inherently different. Thus, the large inner bore radius is selected to sufficiently utilise the outer rotor and make two rotors have similar electromagnetic torques. The 12 slots-10/14 poles (12s-10p/14p) YCDRPM machine with different inner bore radii is analysed in Appendix C.

Fig. 4.1 shows the 24 slots stator with different pole number rotors of YCDRPM machines and the related coil back-EMF phasors. They are constructed by a lower number of poles inner SPM rotor, a higher number of poles outer SPM rotor, and a sandwiched yokeless stator. Since the outer rotor inherently has a larger radius in the radial-flux machine, which is better to be as a higher pole number rotor. The basic design parameters are listed in Table 4.1. Based on the electromagnetic theory, to ensure the synchronous operation of the motor, the following relationship should be satisfied:

$$p_I \pm p_O = N_s \tag{4.1}$$

where N_s is the number of stator modulating segments, p_I is the number of PM pairs of inner rotor, p_O is the number of PM pairs of outer rotor.

The corresponding gearing ratio G_r with the fixed stator modulating segments can be expressed as:

$$G_r = \frac{p_O}{p_I} \tag{4.2}$$

where n_I and n_O are the rotation speed of the inner and outer rotors, respectively.

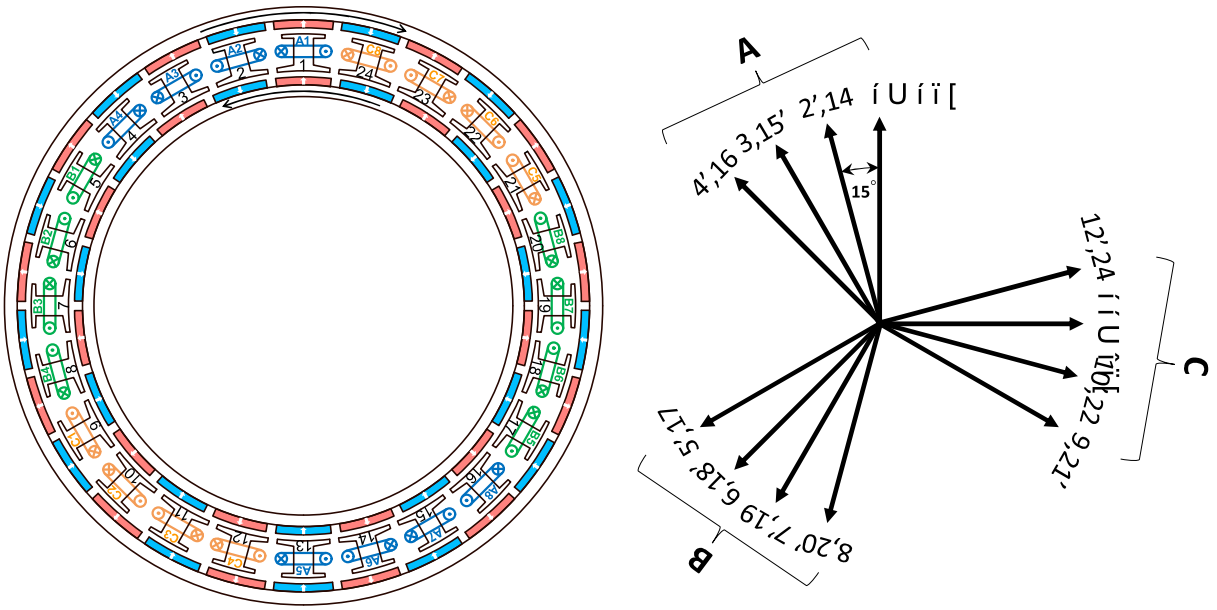

(a) 24 slots-26/22 poles.

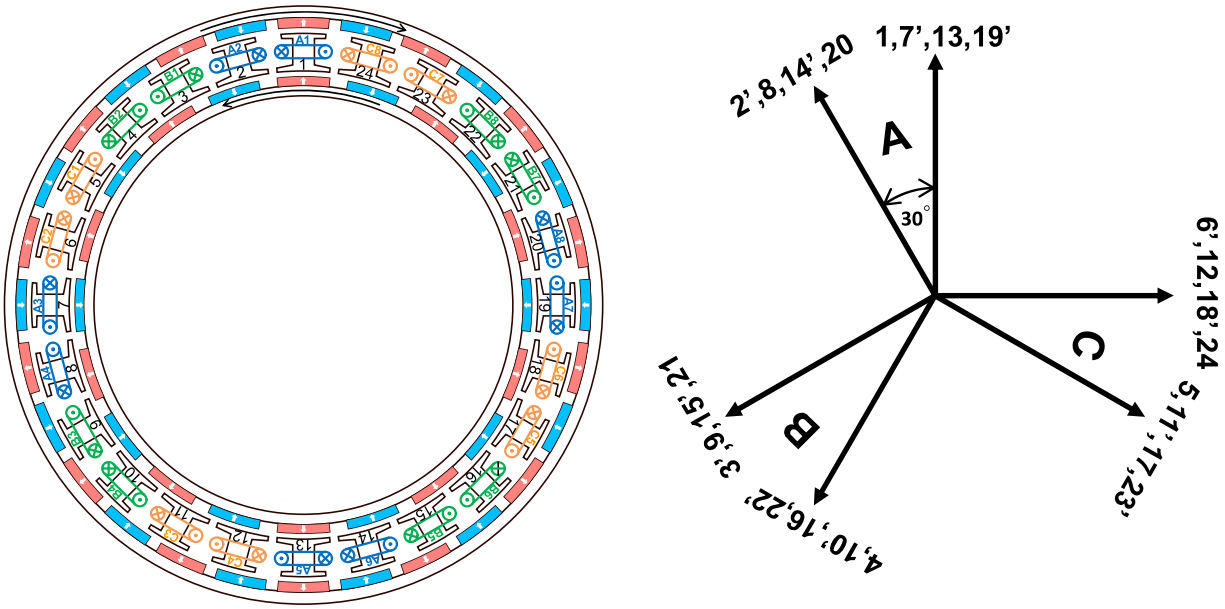

(b) 24 slots-28/20 poles.

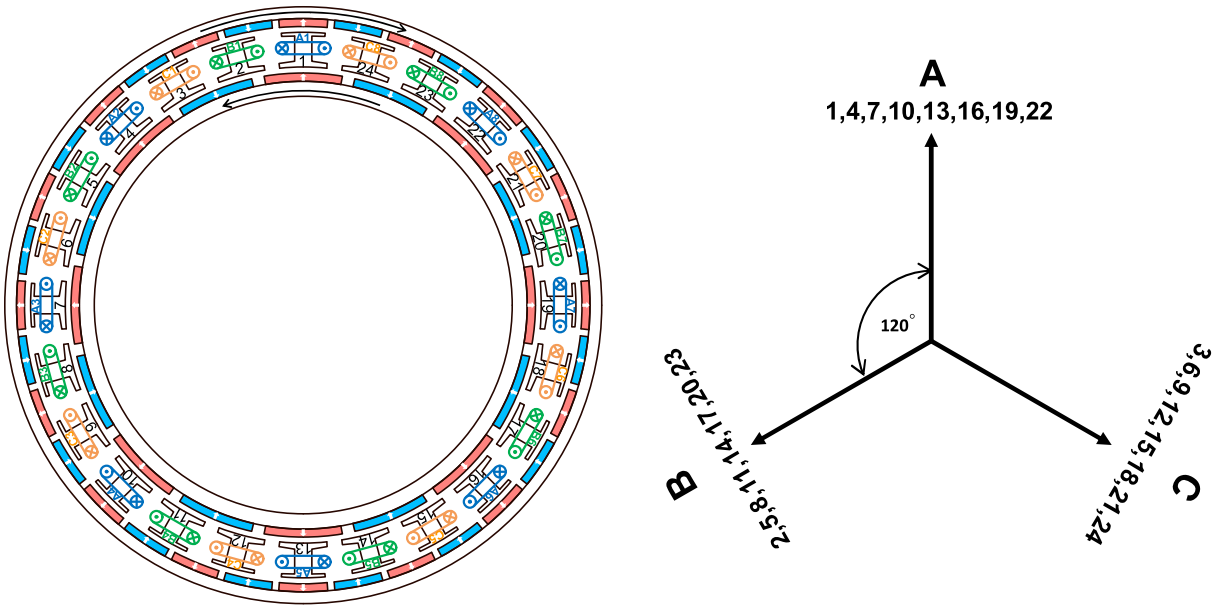

(c) 24 slots-32/16 poles.

Fig. 4.1. Topologies and coil back EMF phasors of YCDRPM machines with different slot/pole number combinations.

TABLE 4.1
BASIC DESIGN PARAMETERS

Parameters	Values
Number of stator slots	24
Remanence of PM	1.2 T
Magnet relative permeability	1.05
Frequency of stator flux	100/3 Hz
Turns per phase	192
PM grade	N35SH
Lamination grade	M300

4.3 Operation Principle

The proposed YCDRPM machine operates as a magnetic gear combined with an electrical machine. This section discusses the operation principle of the YCDRPM machine and explains it from the magnetic gearing effect, armature reaction, and torque production.

The proposed YCDRPM machine operates as a magnetic gear combined with an electrical machine. This section discusses the operation principle of the YCDRPM machine. In addition, since the proposed machine has two mechanical ports, the different operation modes of the machine are also discussed in this section. The discussions are based on the following condition:

1) This section considers the simplified machine structure. The corresponding definitions of parameters are illustrated in Fig. 4.2.

2) Only the radial component of the air gap magnetic field is discussed. The tangential component of the air gap magnetic field is neglected for simplified analysis.

3) The magnetic saturation in the steel lamination is not considered.

4) The relative permeability of the modular stator (modulation ring) is infinite, and the permeance of the air is considered 1.

5) The flux leakage and end effect are neglected for simplified analysis.

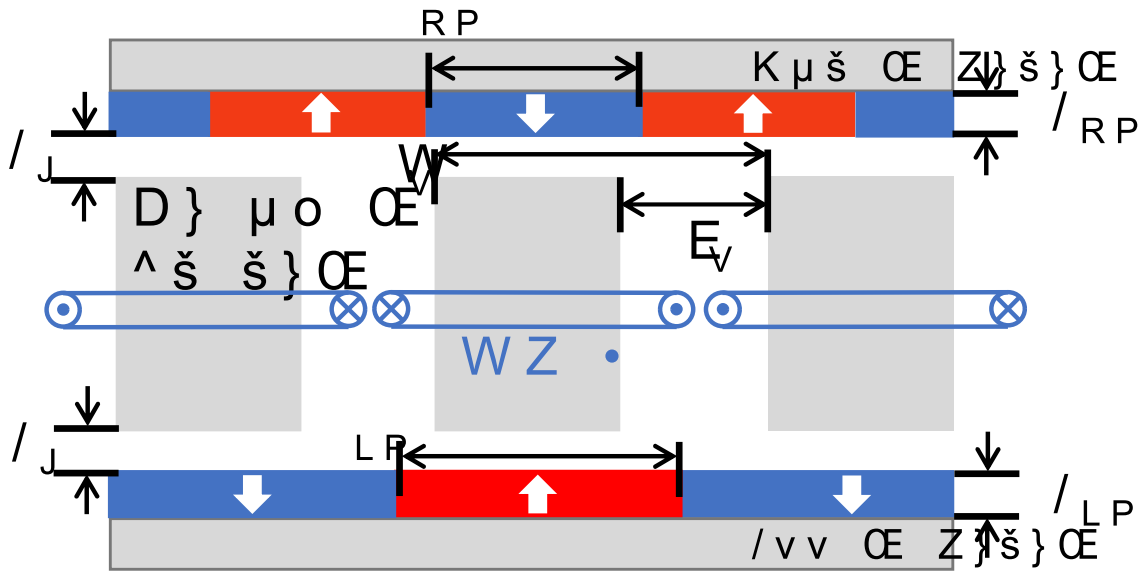

Fig. 4.2. Definitions of parameters of simplified machine structure.

4.3.1 Air gap flux density generated by PMs

The modular stator teeth are considered in the stationary modulation ring when the proposed machine works under open-circuit conditions. The YCDRPM machine works as a counter-rotating magnetic gear.

The magnetic motive forces (MMFs) are generated by the inner and outer PMs, $F_I(\theta)$ and $F_O(\theta)$, and their Fourier series expansions are expressed as:

$$\begin{cases} F_I(\theta,t) = \sum_{k=1,3,5\ldots}^{\infty} A_{Ik}\cos(kp_I\theta - k\omega_I t) \\ A_{Ik} = \dfrac{4B_r L_{im}}{k\pi\mu_0\mu_r}\sin\left(\dfrac{kp_I\theta_{im}}{2}\right) \end{cases} \tag{4.3}$$

$$\begin{cases} F_O(\theta,t) = \sum_{k=1,3,5\ldots}^{\infty} A_{Ok}\cos\left(kp_O\theta - k\omega_O t\right) \\ A_{Ok} = \dfrac{4B_r L_{om}}{k\pi\mu_0\mu_r}\sin\left(\dfrac{kp_O\theta_{om}}{2}\right) \end{cases} \tag{4.4}$$

where k is a positive odd integer, A_{Ik} and A_{Ok} are the inner and outer amplitudes of the kth order harmonic, θ is the air gap circumferential position, B_r is the PM remanence, L_{im} and L_{om} are the thicknesses of the inner and outer PMs, θ_{im} and θ_{om} are the angles of the width of the inner and outer PMs, μ_r is the PM relative permeability, μ_0 is the vacuum permeability, and ω_I and ω_O are the electrical velocities of inner and outer rotors.

The inner and outer air gap permeances considering the modular stator slotting effect can be calculated as:

$$P_I(\theta) = P_{I0} - \sum_{j=1,2,3\ldots}^{\infty} P_{Ij}\cos(jN_s\theta) \tag{4.5}$$

$$P_O(\theta) = P_{O0} - \sum_{j=1,2,3\ldots}^{\infty} P_{Oj}\cos(jN_s\theta) \tag{4.6}$$

where N_s is the number of the modular stator teeth, j are the harmonic orders. The coefficients of the permeance function can be calculated as [ZHU93] [XU24]:

$$P_{I0} = \frac{\mu_0}{K_{IC}L_{IE}}\left(1 - 1.6\beta_I\frac{b_s}{t_s}\right) \tag{4.7}$$

$$L_{IE} = L_g + \frac{L_{im}}{\mu_r} \tag{4.8}$$

$$P_{Ij} = \frac{4\mu_0\beta_I}{j\pi L_{IE}}\left[0.5 + \frac{\left(j\frac{b_s}{t_s}\right)^2}{0.78125 - 2\left(j\frac{b_s}{t_s}\right)^2}\right]\sin\left(1.6j\pi\frac{b_s}{t_s}\right) \tag{4.9}$$

$$K_{IC} = \left[1 - \frac{2}{\pi}\frac{b_s}{t_s}\left\{\tan^{-1}\left(\frac{b_s}{L_{IE}}\right) - \frac{L_{IE}}{b_s}\ln\left[1 + \frac{1}{4}\left(\frac{b_s}{L_{IE}}\right)\right]\right\}\right]^{-1} \tag{4.10}$$

$$\beta_I = \frac{1}{2} - \frac{1}{2\sqrt{1 + \left(\frac{b_s}{2L_{IE}}\right)^2}} \tag{4.11}$$

$$P_{O0} = \frac{\mu_0}{K_{OC} L_{OE}} \left(1 - 1.6\beta_O \frac{b_s}{t_s}\right) \tag{4.12}$$

$$L_{OE} = L_g + \frac{L_{om}}{\mu_r} \tag{4.13}$$

$$P_{Oj} = \frac{4\mu_0 \beta_O}{j\pi L_{OE}} \left[0.5 + \frac{\left(j\frac{b_s}{t_s}\right)^2}{0.78125 - 2\left(j\frac{b_s}{t_s}\right)^2}\right] \sin\left(1.6j\pi \frac{b_s}{t_s}\right) \tag{4.14}$$

$$K_{OC} = \left[1 - \frac{2}{\pi}\frac{b_s}{t_s}\left\{\tan^{-1}\left(\frac{b_s}{L_{OE}}\right) - \frac{L_{OE}}{b_s}\ln\left[1 + \frac{1}{4}\left(\frac{b_s}{L_{OE}}\right)\right]\right\}\right]^{-1} \tag{4.15}$$

$$\beta_O = \frac{1}{2} - \frac{1}{2\sqrt{1 + \left(\frac{b_s}{2L_{OE}}\right)^2}} \tag{4.16}$$

where b_s is the slot opening length, t_s is the slot pitch, L_g is the air gap length, L_{IE} and L_{OE} are the inner and outer effective air gaps, and K_{IC} and K_{OC} are the Carter's coefficients of the inner and outer air gaps.

Therefore, the air gap flux density in the inner air gap produced by the inner rotor PM can be calculated by:

$$B_{IIPM}(\theta, t) = F_I(\theta, t) P_I(\theta)$$

$$= \sum_{k=1,3,5\ldots}^{\infty} A_{Ik} P_{I0} \cos(kp_I\theta - k\omega_I t) + \frac{1}{2}\sum_{k=1,3,5\ldots}^{\infty}\sum_{j=1,2,3\ldots}^{\infty} A_{Ik} P_{Ij} \cos[(jN_s - kp_I)\theta + k\omega_I t]$$

$$+ \frac{1}{2}\sum_{k=1,3,5\ldots}^{\infty}\sum_{j=1,2,3\ldots}^{\infty} A_{Ik} P_{Ij} \cos[(jN_s + kp_I)\theta - k\omega_I t] \tag{4.17}$$

For the air gap flux density in the outer air gap produced by the outer rotor PM as:

$$B_{OOPM}(\theta, t) = F_O(\theta, t) P_O(\theta)$$

$$= \sum_{k=1,3,5\ldots}^{\infty} A_{Ok} P_{O0} \cos(kp_O\theta - k\omega_O t) + \frac{1}{2}\sum_{k=1,3,5\ldots}^{\infty}\sum_{j=1,2,3\ldots}^{\infty} A_{Ok} P_{Oj} \cos[(jN_s - kp_O)\theta + k\omega_O t]$$

$$+ \frac{1}{2}\sum_{k=1,3,5\ldots}^{\infty}\sum_{j=1,2,3\ldots}^{\infty} A_{Ok} P_{Oj} \cos[(jN_s + kp_O)\theta - k\omega_O t] \tag{4.18}$$

Since the fluxes generated by the inner and outer PMs are in series, the air gap flux density in the inner and outer air gaps contains the flux generated by the PMs of opposite rotors. The flux crosses two air

gaps, and the permeance function of the inner and outer air gaps can be expressed by:

$$P_{IO}(\theta) = P_{IO} - \sum_{j=1,2,3\ldots}^{\infty} P_{IOj}\cos(jN_s\theta) \tag{4.19}$$

$$P_{IO} = \frac{\mu_0}{K_{IOC}L_{IOE}}\left(1 - 1.6\beta_{IO}\frac{b_s}{t_s}\right) \tag{4.20}$$

$$L_{IOE} = 2L_g + \frac{L_{im}}{\mu_r} + \frac{L_{om}}{\mu_r} \tag{4.21}$$

$$P_{IOj} = \frac{4\mu_0\beta_{IO}}{j\pi L_{IOE}}\left[0.5 + \frac{\left(j\frac{b_s}{t_s}\right)^2}{0.78125 - 2\left(j\frac{b_s}{t_s}\right)^2}\right]\sin\left(1.6j\pi\frac{b_s}{t_s}\right) \tag{4.22}$$

$$K_{IOC} = \left[1 - \frac{2}{\pi}\frac{b_s}{t_s}\left\{\tan^{-1}\left(\frac{b_s}{L_{IOE}}\right) - \frac{L_{IOE}}{b_s}\ln\left[1 + \frac{1}{4}\left(\frac{b_s}{L_{IOE}}\right)\right]\right\}\right]^{-1} \tag{4.23}$$

$$\beta_{IO} = \frac{1}{2} - \frac{1}{2\sqrt{1 + \left(\frac{b_s}{2L_{IOE}}\right)^2}} \tag{4.24}$$

Thus, the air gap flux density in the inner air gap produced by the outer rotor PM can be calculated by:

$$B_{IOPM}(\theta,t) = F_O(\theta,t)P_{IO}(\theta)$$

$$= \sum_{k=1,3,5\ldots}^{\infty} A_{Ok}P_{IO}\cos(kp_O\theta - k\omega_O t) + \frac{1}{2}\sum_{k=1,3,5\ldots}^{\infty}\sum_{j=1,2,3\ldots}^{\infty} A_{Ok}P_{IOj}\cos[(jN_s - kp_O)\theta + k\omega_O t]$$

$$+\frac{1}{2}\sum_{k=1,3,5\ldots}^{\infty}\sum_{j=1,2,3\ldots}^{\infty} A_{Ok}P_{IOj}\cos[(jN_s + kp_O)\theta - k\omega_O t] \tag{4.25}$$

Similarly, the air gap flux density in the outer air gap produced by the inner rotor PM can be calculated by:

$$B_{OIPM}(\theta,t) = F_I(\theta,t)P_{IO}(\theta)$$

$$= \sum_{k=1,3,5\ldots}^{\infty} A_{Ik}P_{IO}\cos(kp_I\theta - k\omega_I t) + \frac{1}{2}\sum_{k=1,3,5\ldots}^{\infty}\sum_{j=1,2,3\ldots}^{\infty} A_{Ik}P_{IOj}\cos[(jN_s - kp_I)\theta + k\omega_I t]$$

$$+\frac{1}{2}\sum_{k=1,3,5\ldots}^{\infty}\sum_{j=1,2,3\ldots}^{\infty} A_{Ik}P_{IOj}\cos[(jN_s + kp_I)\theta - k\omega_I t] \tag{4.26}$$

Thus, after the interaction between inner and outer air gap flux densities, the air gap flux densities in the inner and outer air gaps can be obtained as:

$$B_I(\theta,t) = B_{IIPM}(\theta,t) + B_{IOPM}(\theta,t)$$

$$= \sum_{k=1,3,5\ldots}^{\infty} A_{Ik}P_{I0}\cos(kp_I\theta - k\omega_I t) + \sum_{k=1,3,5\ldots}^{\infty} A_{Ok}P_{IO}\ \cos(kp_O\theta - k\omega_O t)$$

$$+\frac{1}{2}\sum_{k=1,3,5\ldots}^{\infty}\sum_{j=1,2,3\ldots}^{\infty} A_{Ik}P_{Ij}\cos[(jN_s - kp_I)\theta + k\omega_I t]$$

$$+\frac{1}{2}\sum_{k=1,3,5\ldots}^{\infty}\sum_{j=1,2,3\ldots}^{\infty} A_{Ik}P_{Ij}\cos[(jN_s + kp_I)\theta - k\omega_I t]$$

$$+\frac{1}{2}\sum_{k=1,3,5\ldots}^{\infty}\sum_{j=1,2,3\ldots}^{\infty} A_{Ok}P_{IOj}\cos[(jN_s - kp_O)\theta + k\omega_O t]$$

$$+\frac{1}{2}\sum_{k=1,3,5\ldots}^{\infty}\sum_{j=1,2,3\ldots}^{\infty} A_{Ok}P_{IOj}\cos[(jN_s + kp_O)\theta - k\omega_O t] \quad (4.27)$$

$$B_O(\theta,t) = B_{OOPM}(\theta,t) + B_{OIPM}(\theta,t)$$

$$= \sum_{k=1,3,5\ldots}^{\infty} A_{Ok}P_{O0}\cos(kp_O\theta - k\omega_O t) + \sum_{k=1,3,5\ldots}^{\infty} A_{Ik}P_{IO0}\cos(kp_I\theta - k\omega_I t)$$

$$+\frac{1}{2}\sum_{k=1,3,5\ldots}^{\infty}\sum_{j=1,2,3\ldots}^{\infty} A_{Ok}P_{Oj}\cos[(jN_s - kp_O)\theta + k\omega_O t]$$

$$+\frac{1}{2}\sum_{k=1,3,5\ldots}^{\infty}\sum_{j=1,2,3\ldots}^{\infty} A_{Ok}P_{Oj}\cos[(jN_s + kp_O)\theta - k\omega_O t]$$

$$+\frac{1}{2}\sum_{k=1,3,5\ldots}^{\infty}\sum_{j=1,2,3\ldots}^{\infty} A_{Ik}P_{IOj}\cos[(jN_s - kp_I)\theta + k\omega_I t]$$

$$+\frac{1}{2}\sum_{k=1,3,5\ldots}^{\infty}\sum_{j=1,2,3\ldots}^{\infty} A_{Ik}P_{IOj}\cos[(jN_s + kp_I)\theta - k\omega_I t] \quad (4.28)$$

Therefore, the harmonic orders in the inner and outer air gaps are the same (listed in formula (4.29)) but with different amplitudes. The 24 slots-26/22 poles (24s-26p/22p) YCDRPM machine with the simplified model (Fig. 4.2) is selected as an example, and its inner and outer air gap flux densities are

shown in Fig. 4.3. The comparison of FEA and analytical results is shown in Fig. 4.4.

$$\begin{cases} |j_1 N_s \pm k_1 p_I|, \; k_1 = 1,3,5,\ldots; \; j_1 = 0,1,2,\ldots \\ |j_2 N_s \pm k_2 p_O|, \; k_2 = 1,3,5,\ldots; \; j_2 = 0,1,2,\ldots \end{cases} \tag{4.29}$$

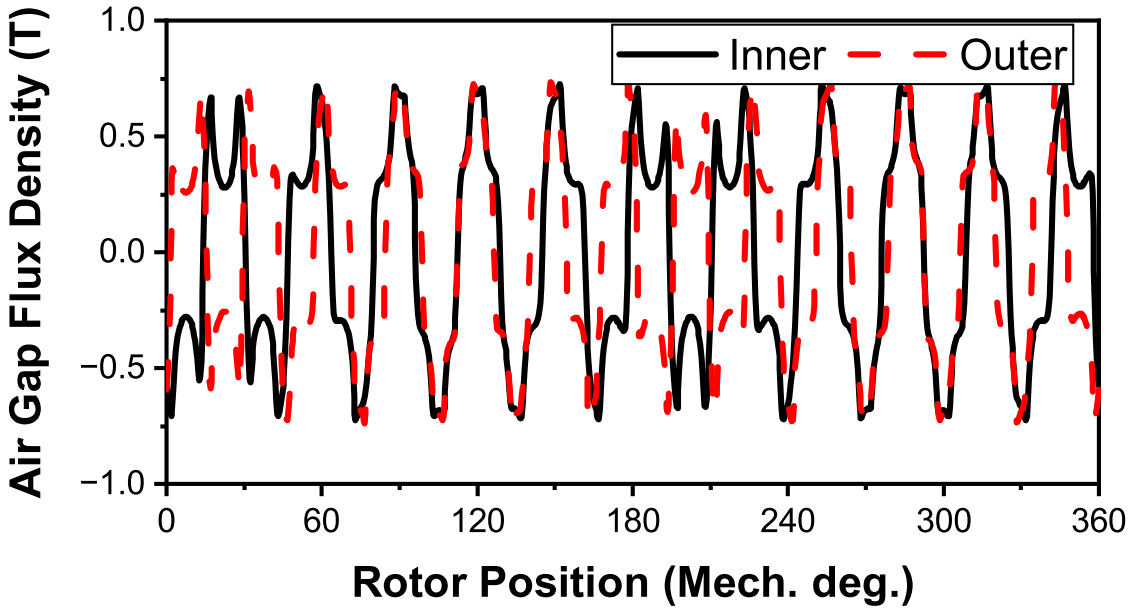

(a) Waveforms.

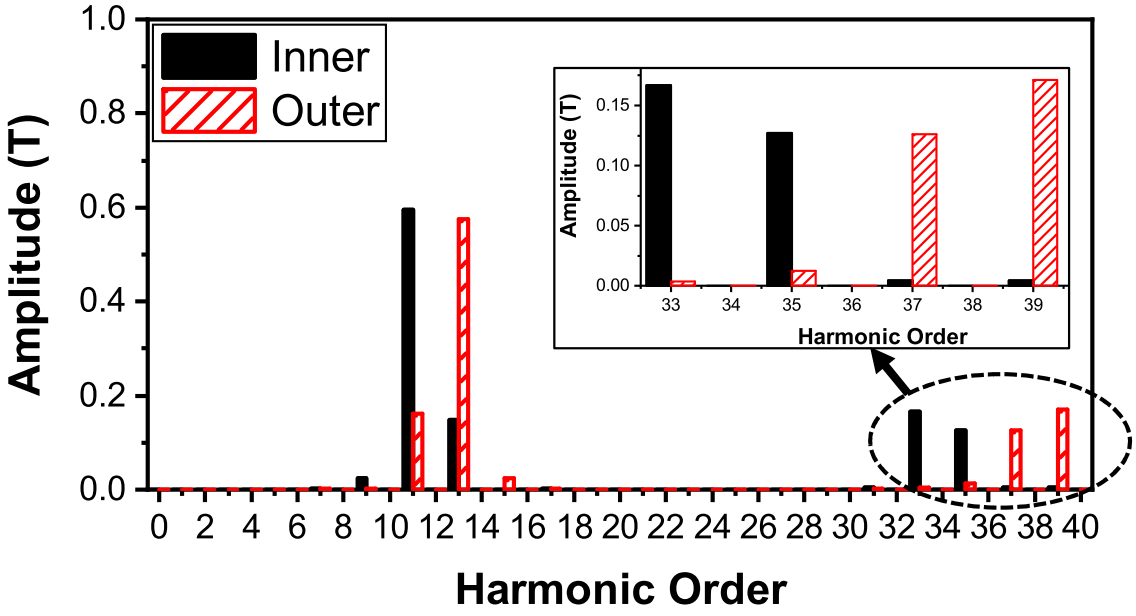

(b) Spectra.

Fig. 4.3. Air gap flux densities generated by PMs of 24s-26p/22p YCDRPM machine with the simplified model.

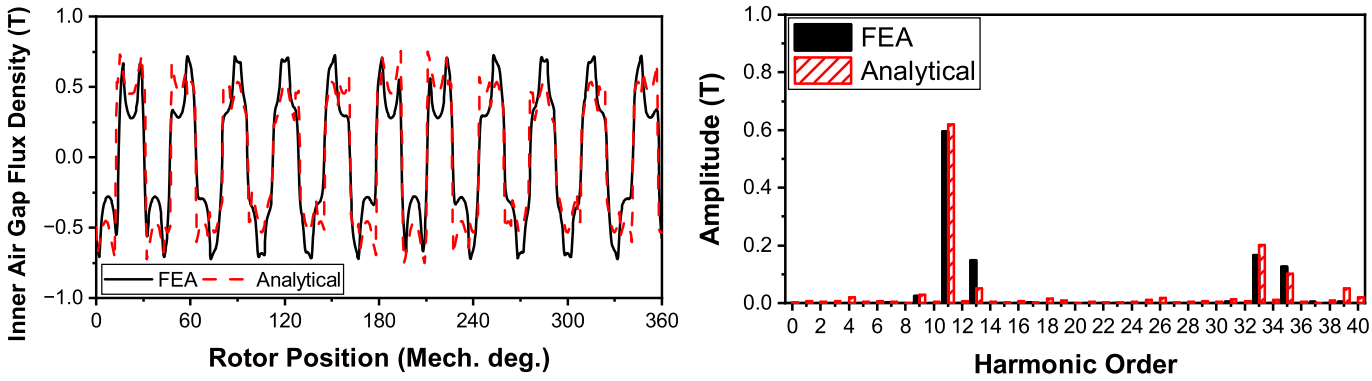

(a) Inner air gap.

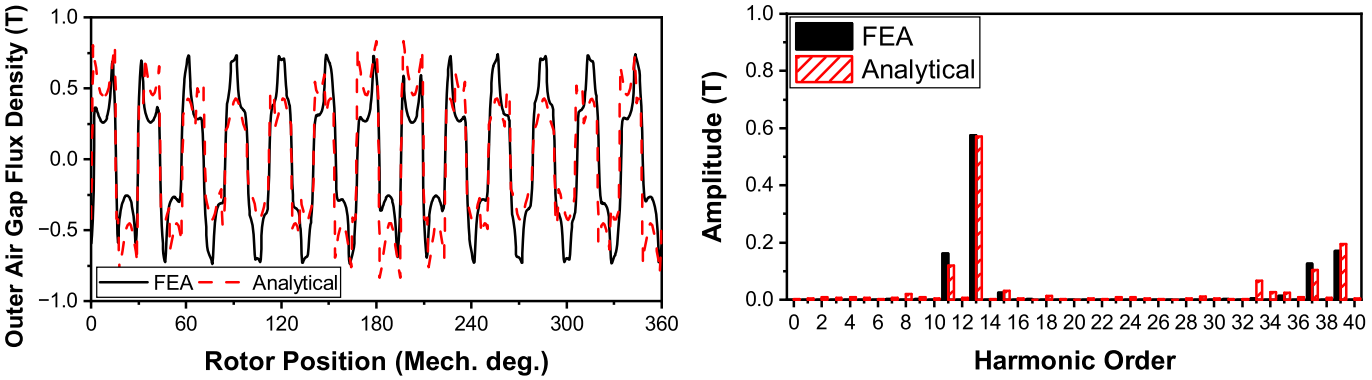

(b) Outer air gap.

Fig. 4.4. Comparison of FEA and analytical results of air gap flux densities generated by PMs of 24s-26p/22p YCDRPM machine with the simplified model.

4.3.2 Air gap flux density generated by armature reaction

According to [LI13] [LIP08], the Fourier series expansion of the three-phase machine winding function is given as:

$$\begin{cases} N_A(\theta) = \sum_{m=1,3,5\ldots}^{\infty} N_m \cos(m\theta) \\ N_B(\theta) = \sum_{m=1,3,5\ldots}^{\infty} N_m \cos\left(m\theta - m\frac{2}{3}\pi\right) \\ N_C(\theta) = \sum_{m=1,3,5\ldots}^{\infty} N_m \cos\left(m\theta + m\frac{2}{3}\pi\right) \\ N_m = \frac{2}{m\pi} N_{ph} k_{wm} \end{cases} \tag{4.30}$$

where N_m is the amplitude of the m-th harmonic order, N_{ph} is the number of turns per phase, and k_{wm} is the winding factor of the m-th harmonic order. The winding factor of the 24s-26p/22p YCDRPM machine is shown in Fig. 4.5.

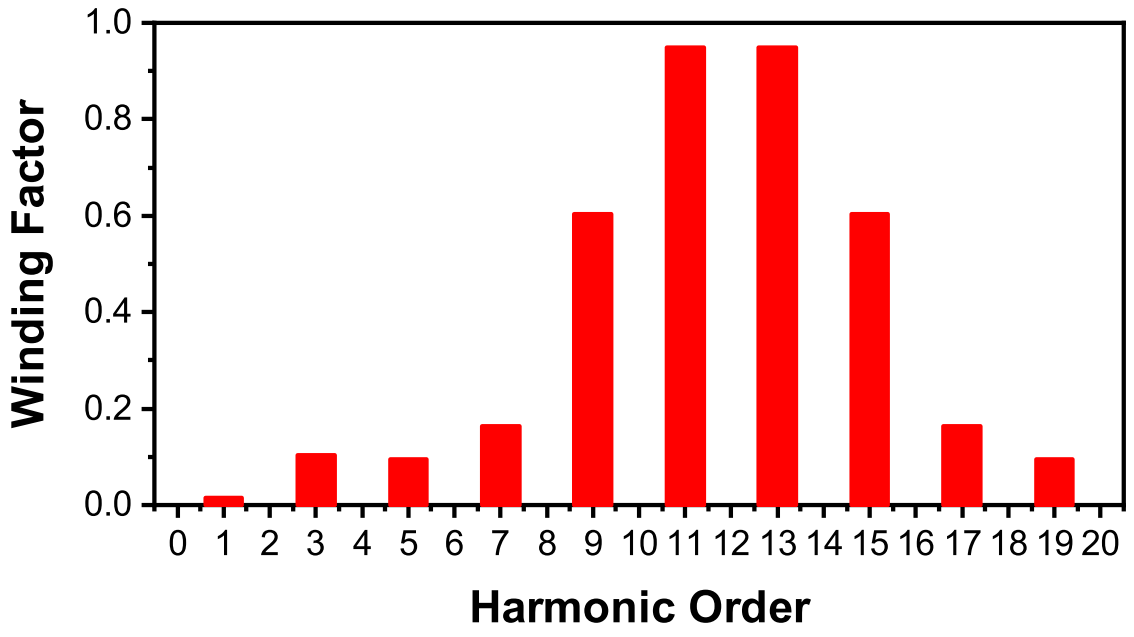

Fig. 4.5. Winding factor of 24s-26p/22p YCDRPM machine.

The input three-phase currents can be expressed as:

$$\begin{cases} i_A(t) = I_{max}cos(\omega_s t) \\ i_B(t) = I_{max}cos(\omega_s t - \frac{2}{3}\pi) \\ i_C(t) = I_{max}cos(\omega_s t + \frac{2}{3}\pi) \end{cases} \tag{4.31}$$

where I_{max} is the amplitude of phase current, and ω_s is the electrical rotating speed. Thus, the MMF generated by the armature reaction can be expressed as:

$$F_a(\theta,t) = N_A(\theta)i_A(t) + N_B(\theta)i_B(t) + N_C(\theta)i_C(t) = \sum_{m=1,3,5\ldots}^{\infty} N_m I_{max}\cos(k\theta \pm \omega_s t) \tag{4.32}$$

The flux generated by the armature reaction crosses both inner and outer equivalent air gaps simultaneously. Thus, the inner and outer flux densities generated by the armature reaction are the same, which can be calculated as:

$$B_a(\theta,t) = F_a(\theta,t)P_{IO}(\theta)$$

$$= \sum_{m=1,3,5\ldots}^{\infty} N_m I_{max}P_{IO}\ \cos(m\theta \pm k\omega_s t) + \frac{1}{2}\sum_{m=1,3,5\ldots}^{\infty}\sum_{j=1,2,3\ldots}^{\infty} N_m I_{max}P_{IOj}\cos[(m+jN_s)\theta \pm \omega_s t]$$

$$+\frac{1}{2}\sum_{m=1,3,5\ldots}^{\infty}\sum_{j=1,2,3\ldots}^{\infty} N_m I_{max}P_{IOj}\cos[(m-jN_s)\theta \pm \omega_s t] \tag{4.33}$$

Fig. 4.6 compares the FEA and analytical results of the air gap flux densities generated by armature

reaction of the 24s-26p/22p YCDRPM machine with the simplified model.

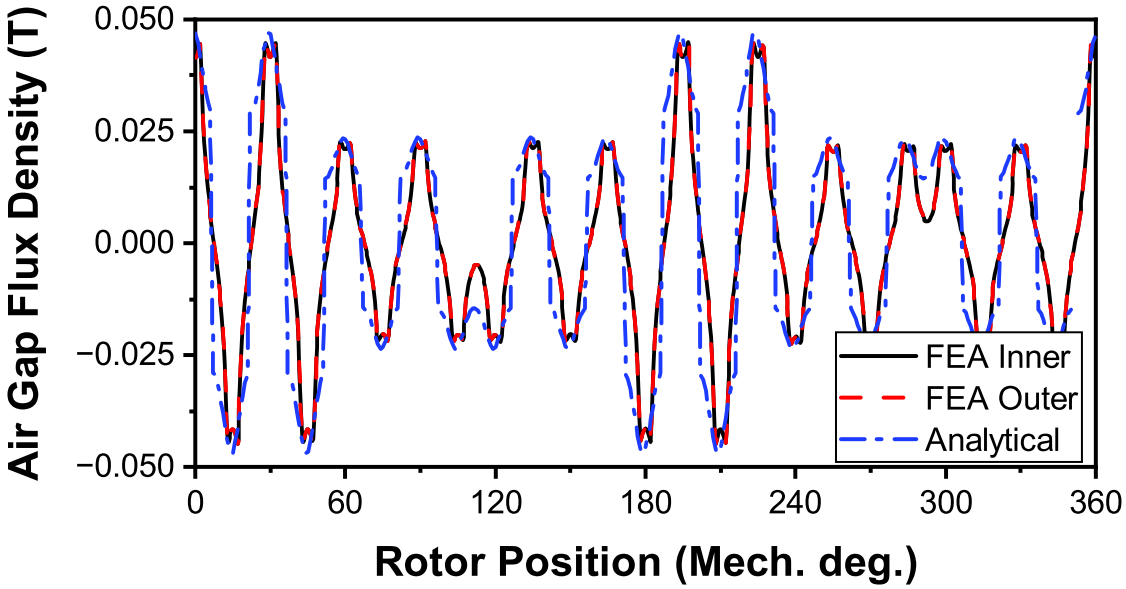

(a) Waveforms.

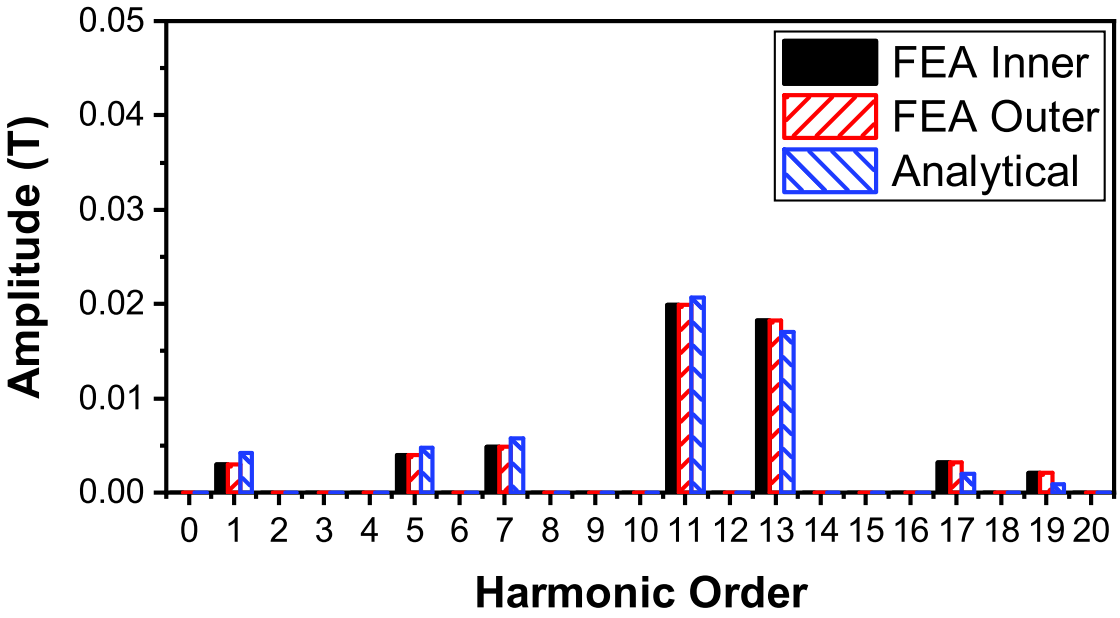

(b) Spectra.

Fig. 4.6. Comparison of FEA and analytical results of air gap flux densities generated by armature reaction of 24s-26p/22p YCDRPM machine with the simplified model.

Thus, the inner and outer air gap flux densities at on-load condition can be expressed as:

$$B_{I-load}(\theta,t) = B_I(\theta,t) + B_a(\theta,t) \tag{4.34}$$

$$B_{O-load}(\theta,t) = B_O(\theta,t) + B_a(\theta,t) \tag{4.35}$$

From (4.33), The harmonic order generated by the armature reaction in the inner and outer air gaps can

be listed as:

$$|m \pm j_3 N_s|,\ j_3 = 0,1,2,\ldots \tag{4.36}$$

4.3.3 Criteria for pole numbers and speeds:

Since the pole numbers and speeds of armature reaction field and rotor should be the same to generate torque, the armature reaction drives the inner rotor should satisfy the relationship as follows:

$$\begin{cases} |m \pm j_3 N_s| = |j_1 N_s \pm k_1 p_I| \\ \dfrac{\omega_s}{|m \pm j_3 N_s|} = \dfrac{k_1 \omega_I}{|j_1 N_s \pm k_1 p_I|} \end{cases} \tag{4.37}$$

According to the operation principle of magnetic gear, the pole pair numbers of two rotors and the number of modular stator teeth should be:

$$\begin{cases} k_2 p_O = |k_1 p_I \pm j N_s| \\ \omega_I = \dfrac{k_1 p_I \pm j N_s}{k_1 p_I} \omega_O \end{cases} \tag{4.38}$$

Thus, the armature reaction and outer rotor also meet the relationship as:

$$\begin{cases} |m \pm j_3 N_s| = |j_2 N_s \pm k_2 p_O| \\ \dfrac{\omega_s}{|m \pm j_3 N_s|} = \dfrac{k_2 \omega_O}{|j_2 N_s \pm k_2 p_O|} \end{cases} \tag{4.39}$$

Consequently, when the armature reaction can drive the inner rotor, the same armature reaction can operate the outer rotor.

The proposed YCDRPM machine satisfies a special condition in (4.37), which is as follows:

$$p_I - N_s = -p_O \tag{4.40}$$

Thus, the relationship of rotational speeds between the inner and outer rotor is:

$$\omega_I = -\omega_O = n_I p_I \frac{2\pi}{60} = -n_O p_O \frac{2\pi}{60} \tag{4.41}$$

where n_I and n_O are the mechanical rotational speeds of inner and outer rotors. The negative value indicates that two rotors always rotate in opposite directions to achieve the counter-rotating. Thus, the frequency of the stator flux f, n_I, and n_O can be calculated by:

$$f = \frac{n_I p_I}{60} = \frac{n_O p_O}{60} \tag{4.42}$$

4.3.4 Back EMF

The phase back EMF induced by no-load inner and outer air gap flux densities can be expressed as [LI16b]:

$$
\begin{cases}
e_{IA}(t) = -\frac{d}{dt}\left\{r_{Ig}L_{stk}\int_0^{2\pi} B_I(\theta,t)N_A(\theta)d\theta\right\} \\
= \sum_{k=1,3,5\ldots}^{\infty} r_{Ig}L_{stk} \\
\times\left\{\begin{matrix}\omega_I A_{Ik}\left[\begin{matrix}2N_{ph}k_{\omega kp_I}P_{I0}\sin(k\omega_I t) \\ +\sum_{j=1,2,3\ldots}^{\infty}\frac{kp_I}{jN_s\pm kp_I}N_{ph}k_{\omega(jN_s\pm kp_I)}P_{Ij}\sin(k\omega_I t)\end{matrix}\right] \\ +\omega_O A_{Ok}\left[\begin{matrix}2N_{ph}k_{\omega kp_O}P_{I00}\sin(k\omega_O t) \\ +\sum_{j=1,2,3\ldots}^{\infty}\frac{kp_O}{jN_s\pm kp_O}N_{ph}k_{\omega(jN_s\pm kp_O)}P_{IOj}\sin(k\omega_O t)\end{matrix}\right]\end{matrix}\right\} \\
e_{IB}(t) = -\frac{d}{dt}\left\{r_{Ig}L_{stk}\int_0^{2\pi} B_I(\theta,t)N_B(\theta)d\theta\right\} \\
= \sum_{k=1,3,5\ldots}^{\infty} r_{Ig}L_{stk} \\
\times\left\{\begin{matrix}\omega_I A_{Ik}\left[\begin{matrix}2N_{ph}k_{\omega kp_I}P_{I0}\sin\left(k\omega_I t - k\frac{2}{3}\pi\right) \\ +\sum_{j=1,2,3\ldots}^{\infty}\frac{kp_I}{jN_s\pm kp_I}N_{ph}k_{\omega(jN_s\pm kp_I)}P_{Ij}\sin\left(k\omega_I t - k\frac{2}{3}\pi\right)\end{matrix}\right] \\ +\omega_O A_{Ok}\left[\begin{matrix}2N_{ph}k_{\omega kp_O}P_{IO}\ \sin\left(k\omega_O t - k\frac{2}{3}\pi\right) \\ +\sum_{j=1,2,3\ldots}^{\infty}\frac{kp_O}{jN_s\pm kp_O}N_{ph}k_{\omega(jN_s\pm kp_O)}P_{IOj}\sin\left(k\omega_O t - k\frac{2}{3}\pi\right)\end{matrix}\right]\end{matrix}\right\} \\
e_{IC}(t) = -\frac{d}{dt}\left\{r_{Ig}L_{stk}\int_0^{2\pi} B_I(\theta,t)N_C(\theta)d\theta\right\} \\
= \sum_{k=1,3,5\ldots}^{\infty} r_{Ig}L_{stk} \\
\times\left\{\begin{matrix}\omega_I A_{Ik}\left[\begin{matrix}2N_{ph}k_{\omega kp_I}P_{I0}\sin\left(k\omega_I t + k\frac{2}{3}\pi\right) \\ +\sum_{j=1,2,3\ldots}^{\infty}\frac{kp_I}{jN_s\pm kp_I}N_{ph}k_{\omega(jN_s\pm kp_I)}P_{Ij}\sin\left(k\omega_I t + k\frac{2}{3}\pi\right)\end{matrix}\right] \\ +\omega_O A_{Ok}\left[\begin{matrix}2N_{ph}k_{\omega kp_O}P_{IO0}\sin\left(k\omega_O t + k\frac{2}{3}\pi\right) \\ +\sum_{j=1,2,3\ldots}^{\infty}\frac{kp_O}{jN_s\pm kp_O}N_{ph}k_{\omega(jN_s\pm kp_O)}P_{IOj}\sin\left(k\omega_O t + k\frac{2}{3}\pi\right)\end{matrix}\right]\end{matrix}\right\}
\end{cases}
\tag{4.43}
$$

$$
\begin{cases}
e_{OA}(t) = -\frac{d}{dt}\left\{r_{Og}L_{stk}\int_0^{2\pi} B_O(\theta,t)N_A(\theta)d\theta\right\} \\
= \sum_{k=1,3,5\ldots}^{\infty} r_{Og}L_{stk} \\
\times \left\{\begin{array}{l} \omega_O A_{Ok}\left[\begin{array}{c} 2N_{ph}k_{\omega kp_O}P_{O0}\sin(k\omega_O t) \\ +\sum_{j=1,2,3\ldots}^{\infty}\frac{kp_O}{jN_s\pm kp_O}N_{ph}k_{\omega(jN_s\pm kp_O)}P_{Ij}\sin(k\omega_O t)\end{array}\right] \\ +\omega_I A_{Ik}\left[\begin{array}{c} 2N_{ph}k_{\omega kp_I}P_{IO0}\sin(k\omega_I t) \\ +\sum_{j=1,2,3\ldots}^{\infty}\frac{kp_I}{jN_s\pm kp_I}N_{ph}k_{\omega(jN_s\pm kp_I)}P_{IOj}\sin(k\omega_I t)\end{array}\right]\end{array}\right\} \\
e_{OB}(t) = -\frac{d}{dt}\left\{r_{Og}L_{stk}\int_0^{2\pi} B_O(\theta,t)N_B(\theta)d\theta\right\} \\
= \sum_{k=1,3,5\ldots}^{\infty} r_{Og}L_{stk} \\
\times \left\{\begin{array}{l} \omega_O A_{Ok}\left[\begin{array}{c} 2N_{ph}k_{\omega kp_O}P_{O0}\sin\left(k\omega_O t - k\frac{2}{3}\pi\right) \\ +\sum_{j=1,2,3\ldots}^{\infty}\frac{kp_O}{jN_s\pm kp_O}N_{ph}k_{\omega(jN_s\pm kp_O)}P_{Oj}\sin\left(k\omega_O t - k\frac{2}{3}\pi\right)\end{array}\right] \\ +\omega_I A_{Ik}\left[\begin{array}{c} 2N_{ph}k_{\omega kp_I}P_{IO0}\sin\left(k\omega_I t - k\frac{2}{3}\pi\right) \\ +\sum_{j=1,2,3\ldots}^{\infty}\frac{kp_I}{jN_s\pm kp_I}N_{ph}k_{\omega(jN_s\pm kp_I)}P_{IOj}\sin\left(k\omega_I t - k\frac{2}{3}\pi\right)\end{array}\right]\end{array}\right\} \\
e_{OC}(t) = -\frac{d}{dt}\left\{r_{Og}L_{stk}\int_0^{2\pi} B_O(\theta,t)N_C(\theta)d\theta\right\} \\
= \sum_{k=1,3,5\ldots}^{\infty} r_{Og}L_{stk} \\
\times \left\{\begin{array}{l} \omega_O A_{Ok}\left[\begin{array}{c} 2N_{ph}k_{\omega kp_O}P_{O0}\sin\left(k\omega_O t + k\frac{2}{3}\pi\right) \\ +\sum_{j=1,2,3\ldots}^{\infty}\frac{kp_O}{jN_s\pm kp_O}N_{ph}k_{\omega(jN_s\pm kp_O)}P_{Oj}\sin\left(k\omega_O t + k\frac{2}{3}\pi\right)\end{array}\right] \\ +\omega_I A_{Ik}\left[\begin{array}{c} 2N_{ph}k_{\omega kp_I}P_{IO}\ \sin\left(k\omega_I t + k\frac{2}{3}\pi\right) \\ +\sum_{j=1,2,3\ldots}^{\infty}\frac{kp_I}{jN_s\pm kp_I}N_{ph}k_{\omega(jN_s\pm kp_I)}P_{IOj}\sin\left(k\omega_I t + k\frac{2}{3}\pi\right)\end{array}\right]\end{array}\right\}
\end{cases}
\tag{4.44}
$$

where r_{Ig} and r_{Og} are the inner and outer air gap radii, and L_{stk} is the stack length. The FEA and analytical results of the back EMFs induced by the inner and outer rotors are shown in Fig. 4.7.

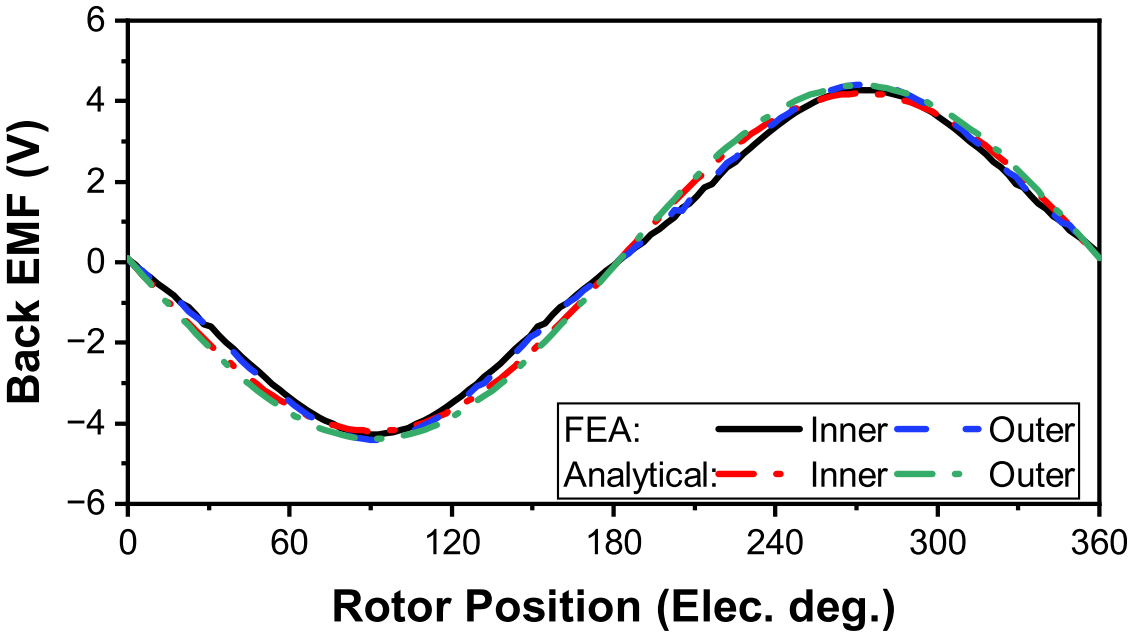

(a) Waveforms.

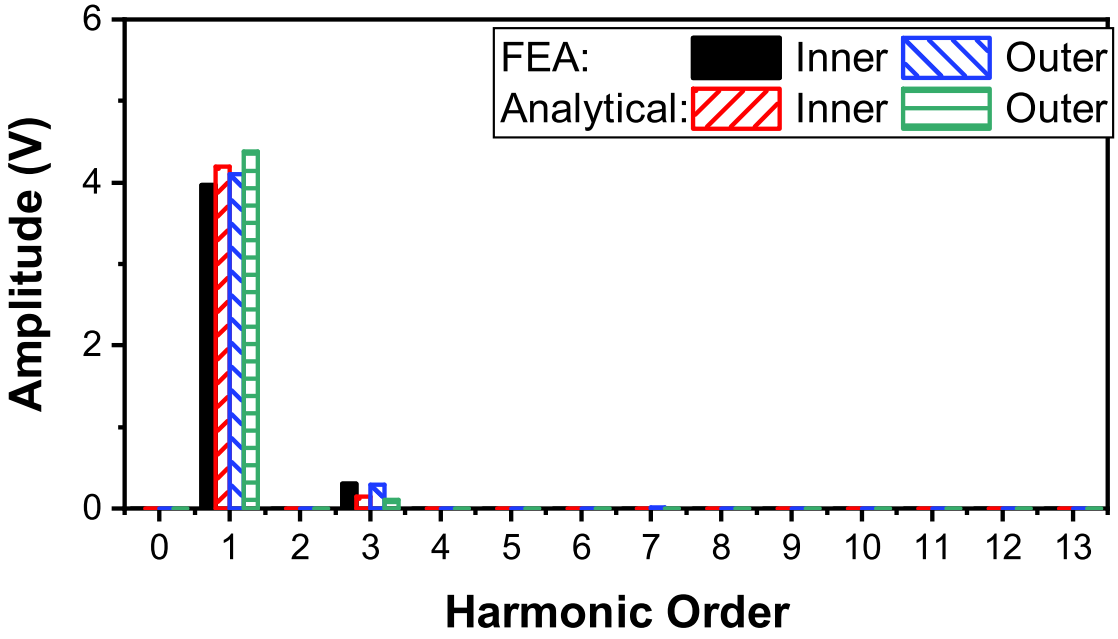

(b) Spectra.

Fig. 4.7. Comparison of FEA and analytical results of back EMFs generated of 24s-26p/22p YCDRPM machine with the simplified model. (n_I=2000/11 rpm, n_O=2000/13 rpm)

4.3.5 Torque production

The reluctance torque of the surface-mounted PM machines can be neglected, the inner and outer electromagnetic torques can be obtained by:

$$T_{IE}(t) = \frac{e_{IA}(t)i_A(t) + e_{IB}(t)i_B(t) + e_{IC}(t)i_C(t)}{n_I \cdot \frac{2\pi}{60}} \tag{4.45}$$

$$T_{OE}(t) = \frac{e_{OA}(t)i_A(t) + e_{OB}(t)i_B(t) + e_{OC}(t)i_C(t)}{n_O \cdot \frac{2\pi}{60}} \tag{4.46}$$

where i_A, i_B and i_C are the phase-A, -B and -C currents. Thus, the average torques of the inner and outer rotors can be obtained as:

$$T_{IEavg} = 1.5 r_{Ig} L_{stk} I_{max} \left\{ \begin{array}{l} A_{I1} \left[\dfrac{2N_{ph} k_{\omega p_I} P_{I0}}{} + \displaystyle\sum_{j=1,2,3\ldots}^{\infty} \frac{p_I}{jN_s \pm p_I} N_{ph} k_{\omega(jN_s \pm p_I)} P_{Ij} \right] \\ +A_{O1} \left[\dfrac{2N_{ph} k_{\omega p_O} P_{IO}}{} + \displaystyle\sum_{j=1,2,3\ldots}^{\infty} \frac{p_O}{jN_s \pm p_O} N_{ph} k_{\omega(jN_s \pm p_O)} P_{IOj} \right] \end{array} \right\} \tag{4.47}$$

$$T_{OEavg} = 1.5 r_{Og} L_{stk} I_{max} \left\{ \begin{array}{l} A_{O1} \left[\dfrac{2N_{ph} k_{\omega p_O} P_{O0}}{} + \displaystyle\sum_{j=1,2,3\ldots}^{\infty} \frac{p_O}{jN_s \pm p_O} N_{ph} k_{\omega(jN_s \pm p_O)} P_{Oj} \right] \\ +A_{I1} \left[\dfrac{2N_{ph} k_{\omega p_I} P_{IO0}}{} + \displaystyle\sum_{j=1,2,3\ldots}^{\infty} \frac{p_I}{jN_s \pm p_I} N_{ph} k_{\omega(jN_s \pm p_I)} P_{IOj} \right] \end{array} \right\} \tag{4.48}$$

The FEA and analytical results of the torques of the inner and outer rotors are shown in Fig. 4.8. The analytical results are slightly higher than the FEA results since the magnetic saturation effect is not considered in the analytical method.

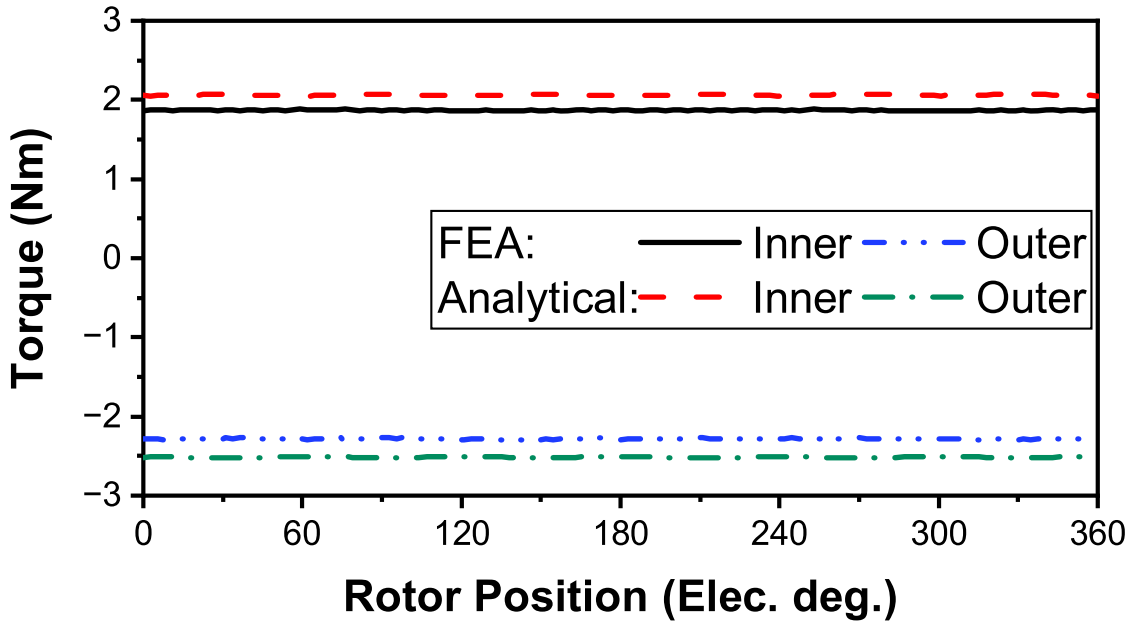

(a) Waveforms.

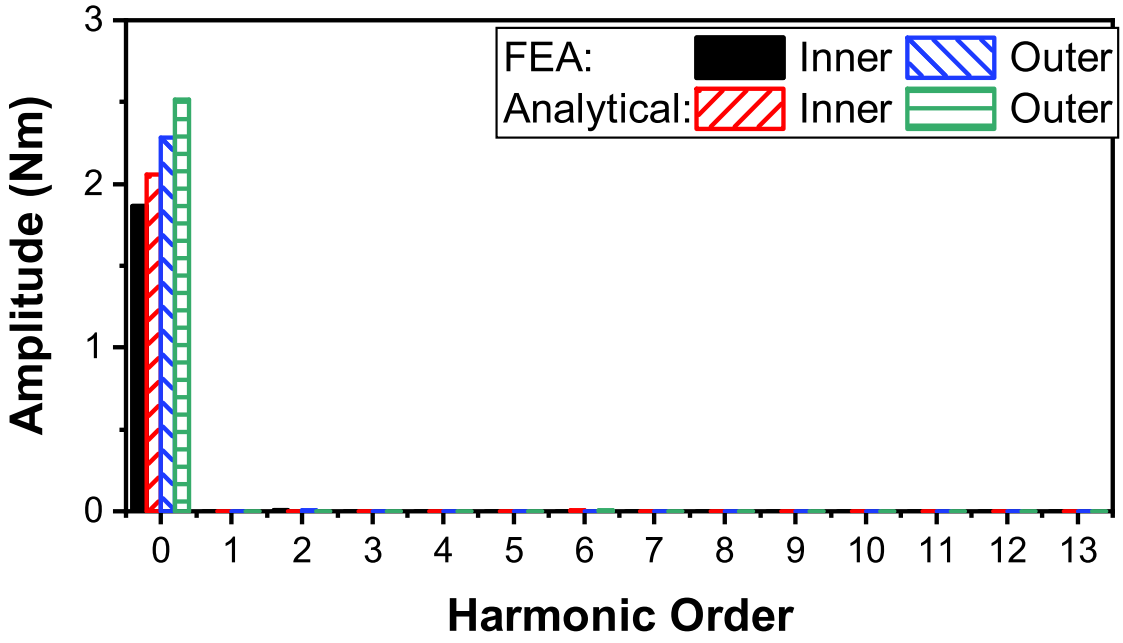

(b) Spectra.

Fig. 4.8. Comparison of FEA and analytical results of torques of 24s-26p/22p YCDRPM machine with the simplified model.

4.3.6 Torque transmission

The proposed YCDRPM machine can be operated as a magnetic gear, it will be further discussed in Section 4.3.7. In this operation mode, according to the working principle of magnetic gears, when mechanical torque is applied to one rotor of the YCDRPM machine, the torque transmits to the corresponding other rotor. The gear will slip if the load is increased beyond the stall torque. The relationship of torque transmission can be expressed similar to those of magnetic gears and magnetically

geared machines [CHA07] [ATA08] [WAN14]:

$$\frac{T_{OE}}{T_{IE}} = \frac{p_O}{p_I} = G_r \tag{4.49}$$

4.3.7 Operation modes

The proposed YCDRPM machine consists of two mechanical ports and two rotors working in different directions with the magnetic gearing effect. Thus, in Fig. 4.9, four different operation modes of the machine are considered as follows:

1) Power split mode: In this scenario, both the inner and outer rotors are connected to the load, with torque transfer occurring due to the magnetic gearing effect. Simultaneously, the machine functions as a generator, and the input mechanical power induces electromotive force (EMF) in the windings.

2) Magnetic geared motor mode: One rotor inputs the mechanical torque to utilize the magnetic gearing effect to transmit the torque. The stator windings are also injected with the rated current. Thus, the output rotor benefits from electric and mechanical powers. In this mode, the magnetic gearing effect enhances the output torque, and the electromagnetic torque is compromised to increase the output torque. The machine can be used for high torque and low-speed applications.

3) Pure electric motor mode: In this mode, the initial relative angle between two rotors is zero. The machine works as a PM machine, the rated current is injected into the stator windings, and both rotors produce output torque.

4) Pure generator mode: In this mode, mechanical torque is applied to both rotors, inducing EMF in the stator windings. This allows the machine to function as a generator. Owing to its counter-rotating characteristics, the machine is well-suited for use in counter-rotating wind turbines.

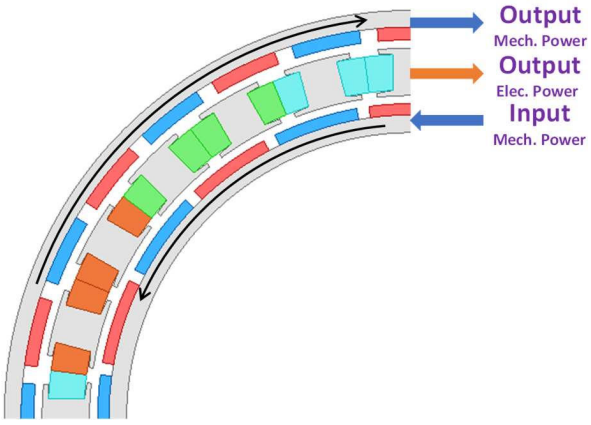

(a) Power split.

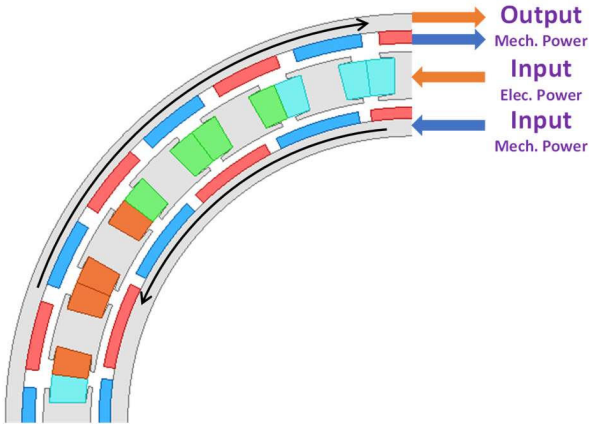

(b) Magnetic geared motor.

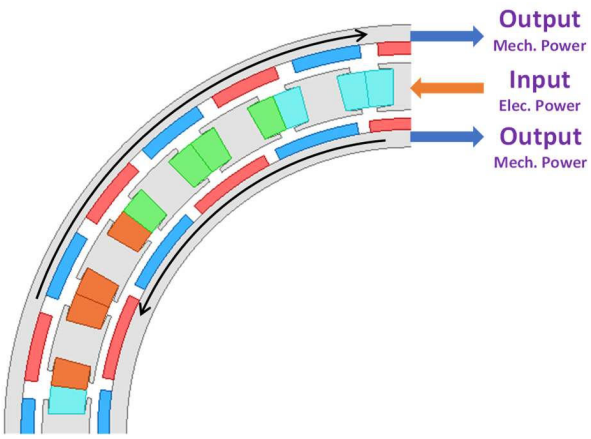

(c) Pure electric motor.

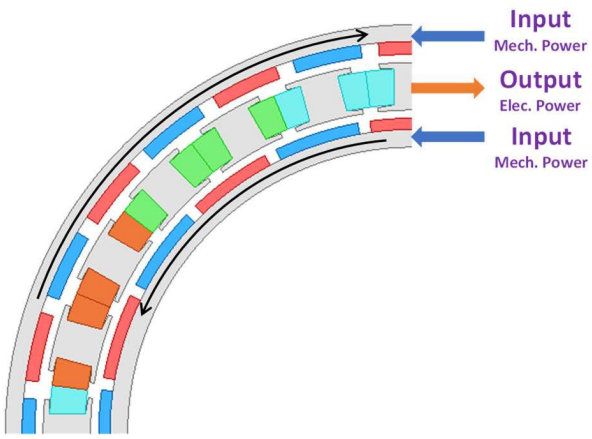

(d) Pure generator.

Fig. 4.9. Proposed machine operating modes.

4.4 Design Optimisation

All the YCDRPM machines with different slot pole number combinations, i.e., 24s-26p/22p, 24 slots-28/20 poles (24s-28p/20p), and 24 slots-32/16 poles (24s-32p/16p), are globally optimised by the genetic algorithm using the FEA to analyse the electromagnetic performance. Since the machine has a relatively large radius inner bore compared with the outer diameter of the machine, the radii of inner and outer rotors are similar. Thus, the optimisation objective is to maximise the total torque (the sum of torques of inner and outer rotors) of the YCDRPM machine. The optimised machine achieves maximum torque with both rotors exhibiting similar torque values. Furthermore, optimal designs are sought under a 1.7 T magnetic flux density constraint for the iron cores, ensuring that no severe magnetic saturation occurs within the laminations of the optimised machines. The fixed and variable parameters can be found in Table 4.2 and Table 4.3, respectively. The associated variables are depicted in Fig. 4.10. Moreover, the design parameters of optimised machines are shown in Table 4.4. The corresponding open-circuit flux density distributions and flux lines are shown in Fig. 4.11.

TABLE 4.2
FIXED PARAMETERS

Parameter	Values
Outer radius of outer rotor (mm)	50
Stack length (mm)	50
Copper loss (W)	30
Inner and outer air gap lengths (mm)	1
Max iron core flux density (T)	1.7
Radius of shaft (mm)	35

TABLE 4.3
VARIABLE PARAMETERS

Parameter	Symbols
Outer PM thickness	L_{om}
Inner PM thickness	L_{im}
Outer PM pole arc	θ_{om}
Inner PM pole arc	θ_{im}
Stator outer radius	R_{so}
Stator inner radius	R_{si}
Stator outer slot opening	b_{os}
Stator inner slot opening	b_{is}
Outer tooth-tip height	h_{os}
Inner tooth-tip height	h_{is}
Outer tooth-tip slope	α_{os}
Inner tooth-tip slope	α_{is}
Stator tooth width	w_{st}

TABLE 4.4
DESIGNS OF OPTIMISED MACHINES

Parameter	24s-26p/22p	24s-28p/20p	24s-32p/16p
Outer PM thickness (mm)	1.35	1.6	1.34
Inner PM thickness (mm)	1.35	1.4	1.4
Outer PM pole arc (°elec.)	156	143	160
Inner PM pole arc (°elec.)	154	130	152
PM volume (cm^3)	31	30.5	31.5
Stator outer radius (mm)	45.5	45.5	45.5
Stator inner radius (mm)	39.3	39.2	40
Stator outer slot opening (mm)	4.6	4.4	4.6
Stator inner slot opening (mm)	1.5	1.5	2.6
Outer tooth-tip height (mm)	0.6	0.7	0.5
Inner tooth-tip height (mm)	0.7	0.7	0.8
Outer tooth-tip slope (deg.)	6	5.4	2.6
Inner tooth-tip slope (deg.)	4	4.7	3.4
Stator tooth width (mm)	3.4	3.6	3
Slot area (mm^2)	35	33	35

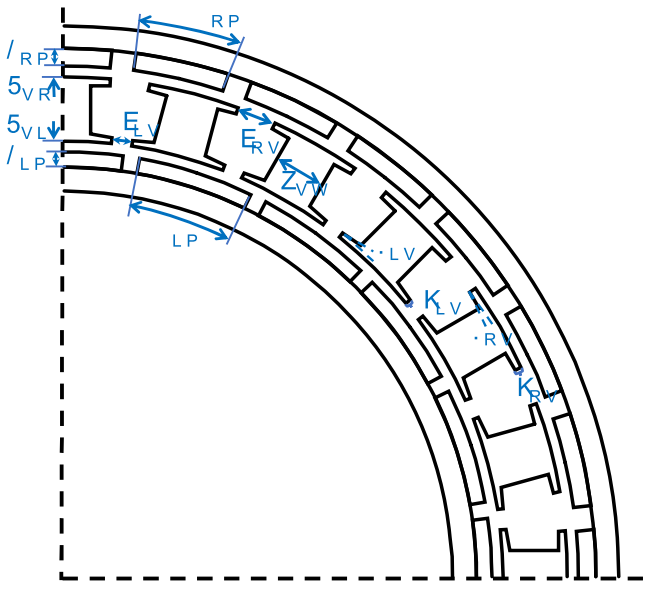

Fig. 4.10. Variable parameters of YCDRPM machine.

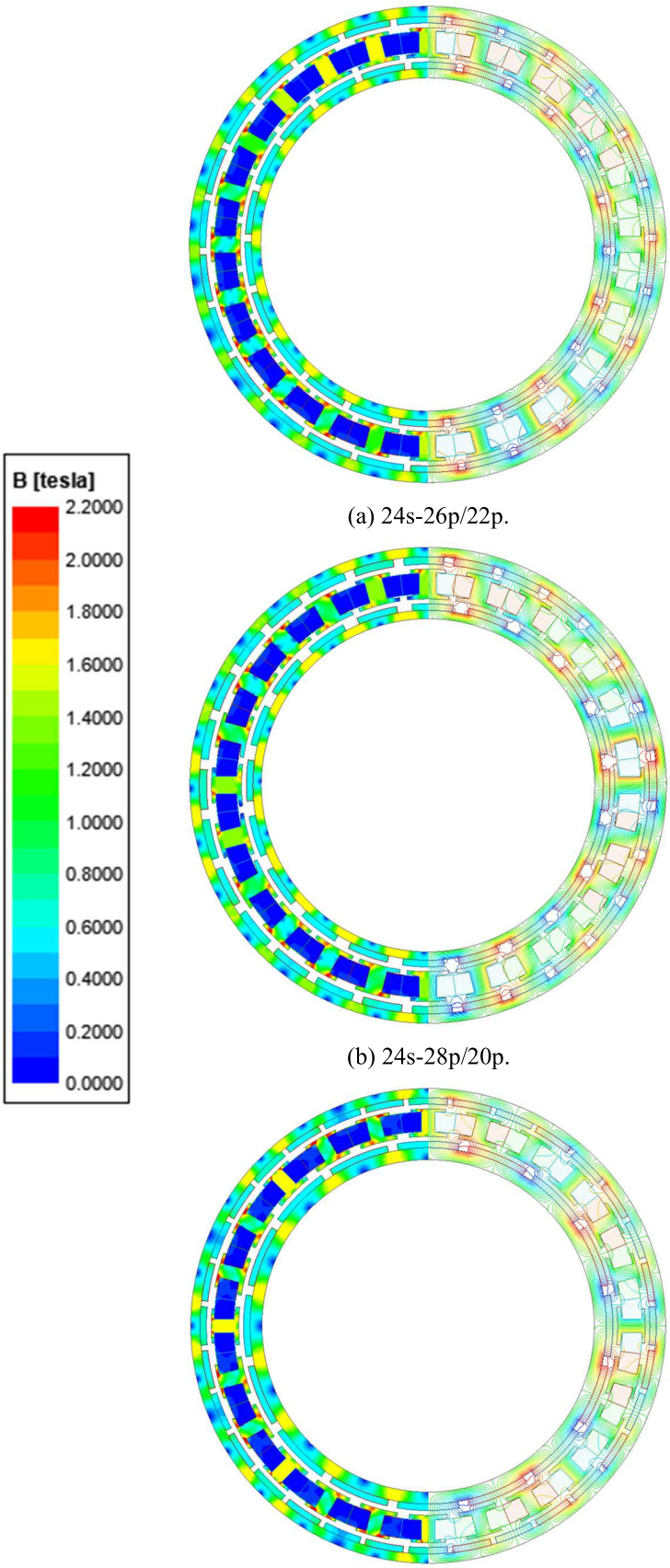

(a) 24s-26p/22p.

(b) 24s-28p/20p.

(c) 24s-32p/16p.

Fig. 4.11. Open circuit flux density distributions and flux lines of YCDRPM machines.

4.5 Analysis of Electromagnetic Performance of YCDRPM Machine

In the following, the positive and negative torques represent the output and input torques, respectively. The machine has different operation modes depending on the initial position of the inner and outer rotors. Thus, the relative angle δ between two rotors can be expressed as:

$$\delta = p_I\theta_I - p_O\theta_O \tag{4.50}$$

where θ_I and θ_O are the mechanical axis angles of the inner and outer rotors, respectively. The maximum relative angle is 180 electrical degrees, found in Fig. 4.12.

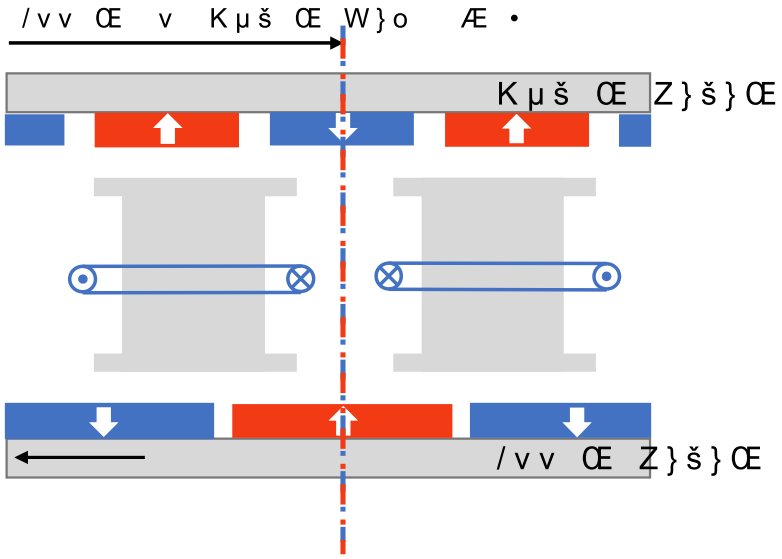

(a) Minimum relative angle. (0 elec. deg.)

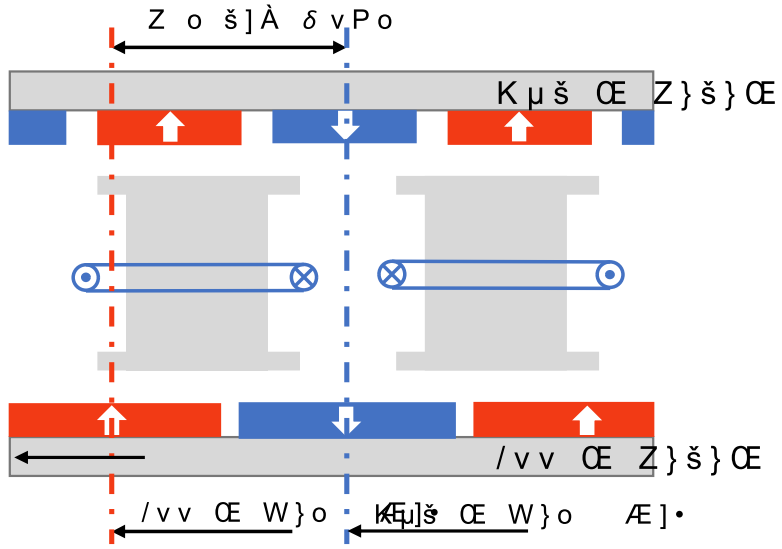

(b) Maximum relative angle. (180 elec.deg.)

Fig. 4.12. Relative angle between inner and outer rotors.

Therefore, under no-load condition, the magnetic gearing effect between two rotors can be obtained by fixing the outer rotor at zero position and rotating the inner rotor only. The magnetic gear torque-rotor position characteristics for the proposed machines are shown in Fig. 4.13. The curve is asymmetric in that the maximum torque is not obtained at 90 electric degrees. It is caused by the magnetic saturation on the steel lamination.

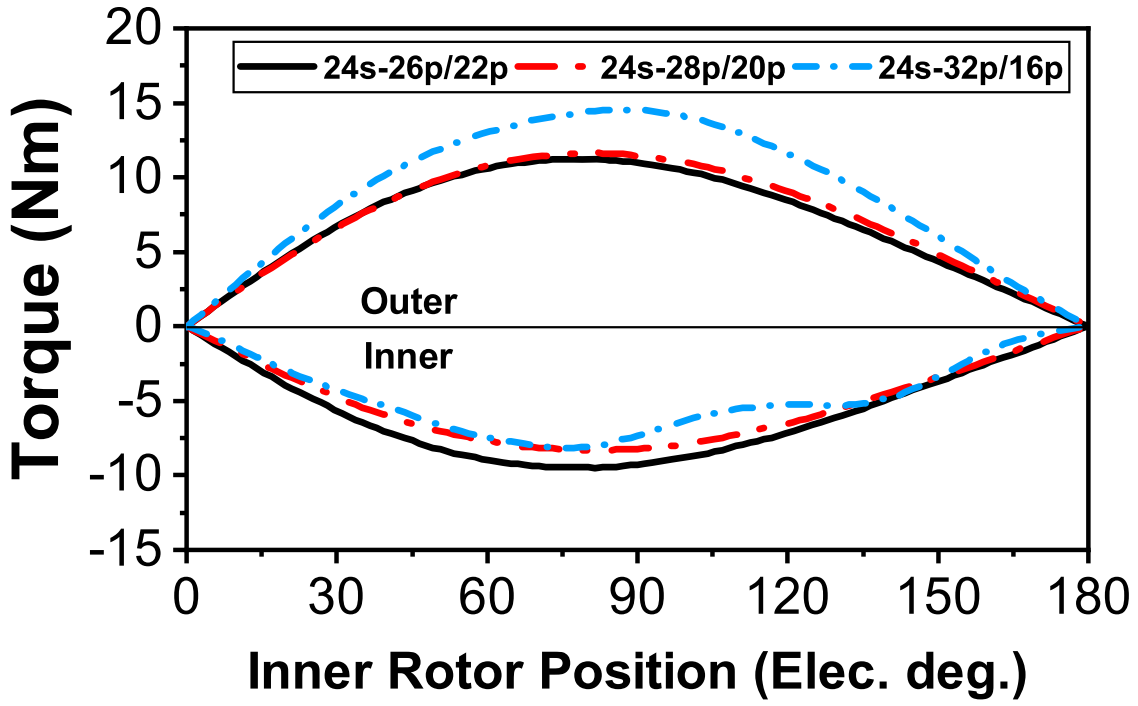

Fig. 4.13. Magnetic gearing effect torque vs. inner rotor angle characteristics.

4.5.1 Pure electric motor mode

In Fig. 4.13, when the inner rotor pole axis is aligned with the outer rotor pole axis (δ=0°). The YCDRPM machines work on the pure electric motor mode, without magnetic gearing torque between inner and outer rotors. Both rotors work as output ports, and only stator windings are injected current as input.

Under this operation mode, the inner air gap flux densities of the proposed machines are compared in Fig. 4.14. Since the 24s-26p/22p YCDRPM machine has a similar pole number of the inner and outer rotors, the inner and outer PMs pole arc are similar. Therefore, the inner PM of the 24s-26p/22p machine has minimal impact on the resultant flux. As a result, the flux of the inner air gap of the 24s-26p/22p machine is the largest, as shown in Fig. 4.14b.

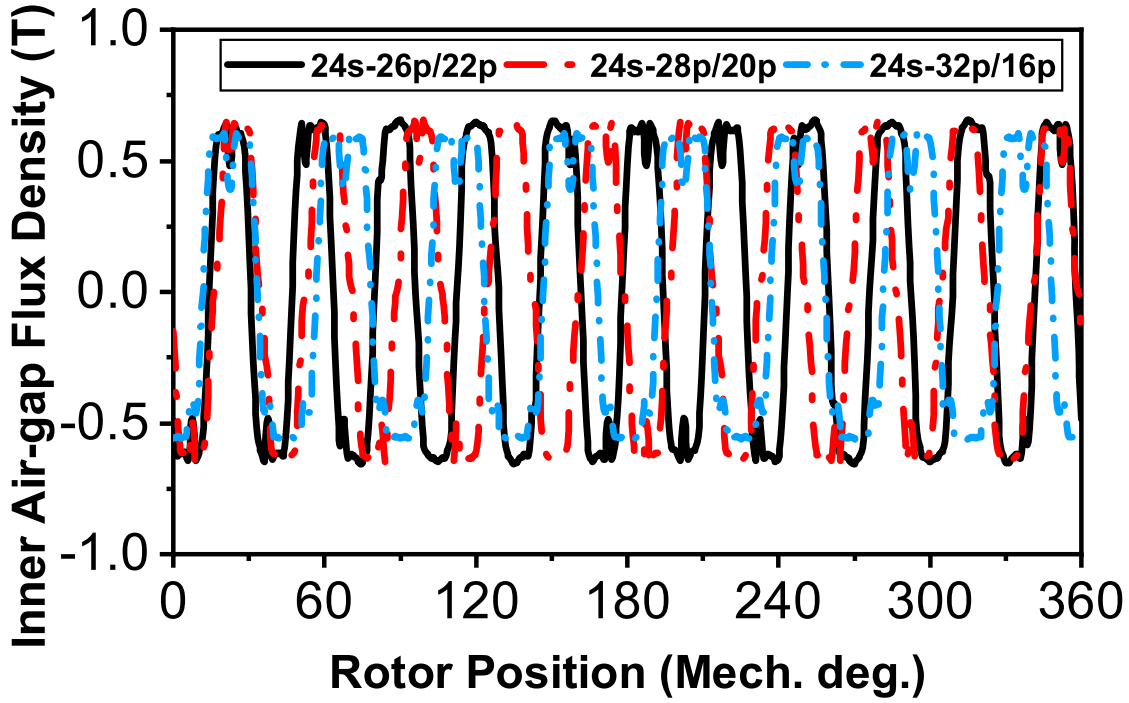

(a) Waveforms.

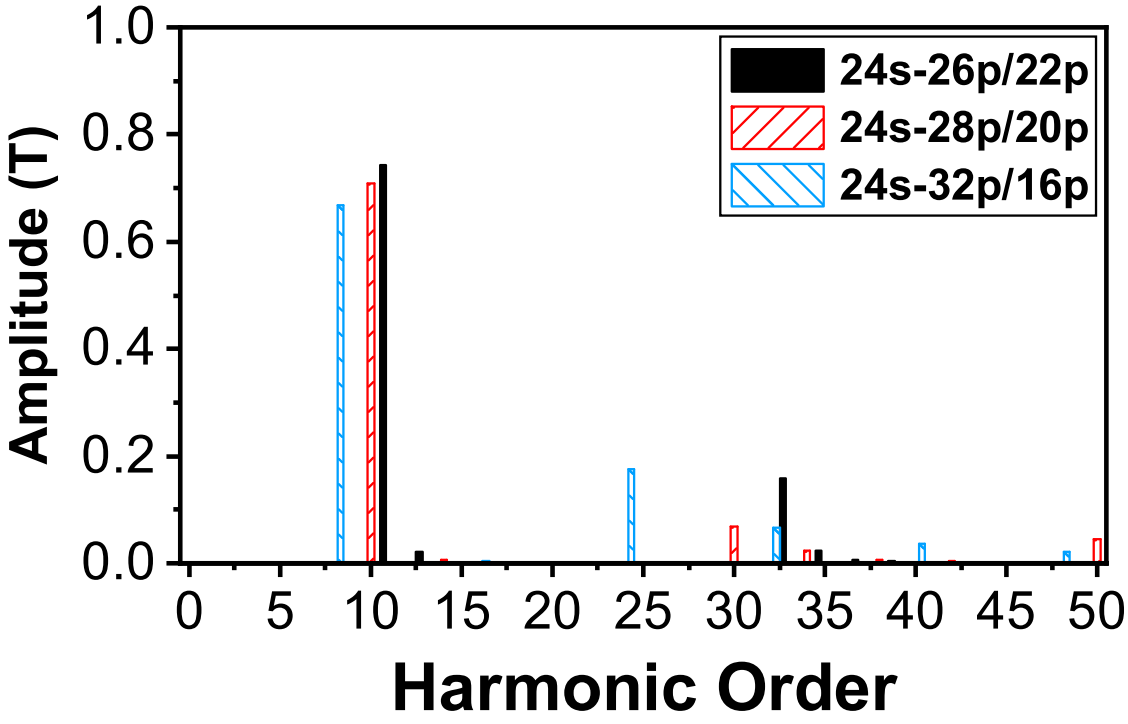

(b) Spectra.

Fig. 4.14. Comparison of inner air gap flux densities of YCDRPM machines.

The comparison of the outer air gap flux densities of the YCDRPM machines is shown in Fig. 4.15. The outer PM of the 24s-28p/20p machine is the thickest, and the outer air gap flux generated by the outer PM is the largest. Thus, the outer air gap flux density of the 24s-28p/20p machine is the largest, Fig.

4.15b.

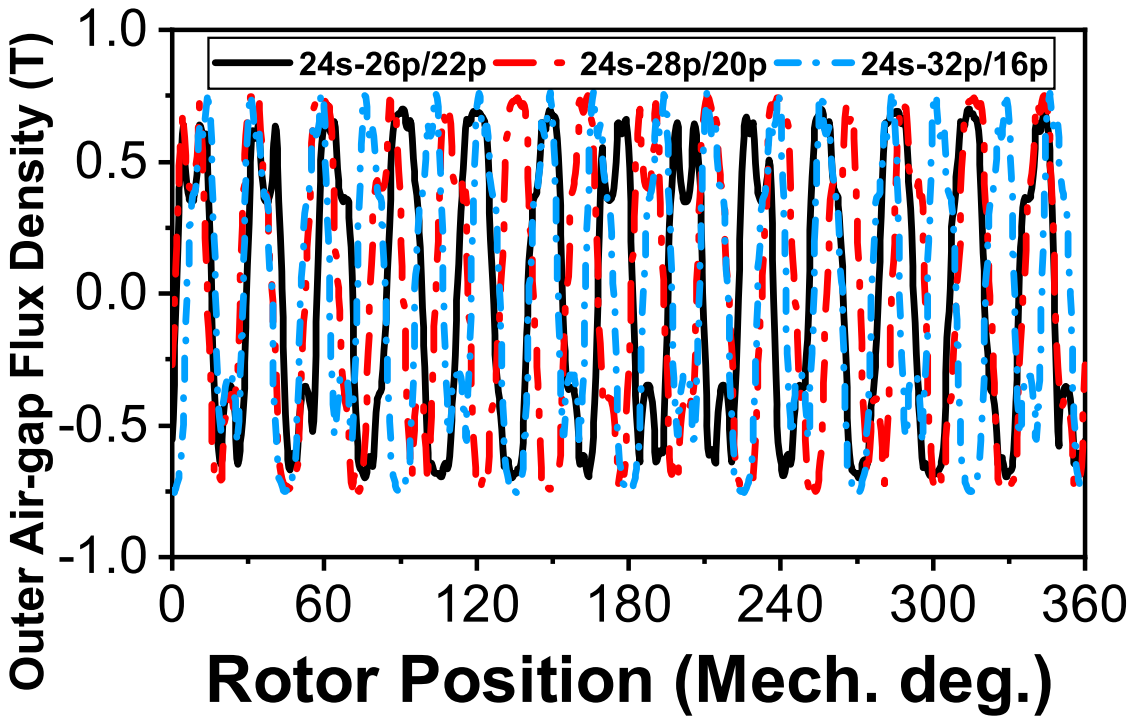

(a) Waveforms.

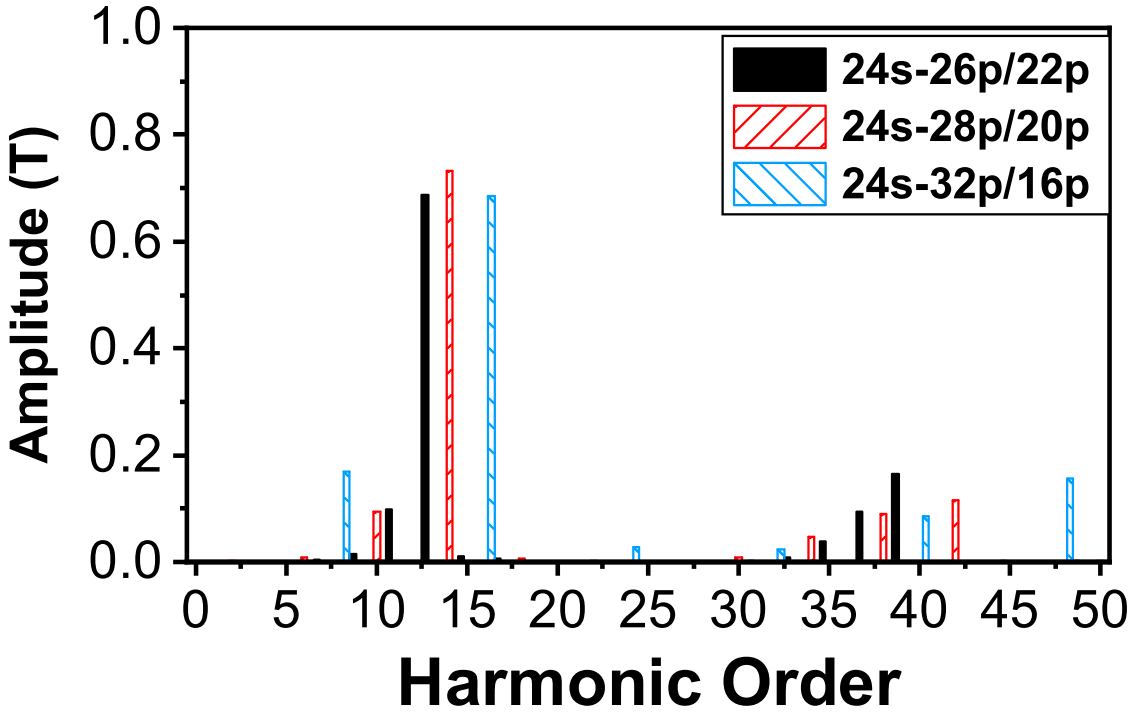

(b) Spectra.

Fig. 4.15. Comparison of outer air gap flux densities of YCDRPM machines.

As the stator flux frequency remains constant at 100/3 Hz for all machines, despite the varying rotation speeds of the rotors, the frequency of the flux linkages and the back electromotive forces (EMFs)

generated in the stator windings remain consistent. Fig. 4.16 compares the phase-A flux linkage of the YCDRPM machines, which share a similar fundamental component value of 0.045 Wb for the flux linkage. Consequently, the fundamental components of the back EMFs for all YCDRPM machines are approximately 9.6 V, as depicted in Fig. 4.17(b). Moreover, when operating in pure generator mode, the induced voltage in the stator winding is represented as back EMF.

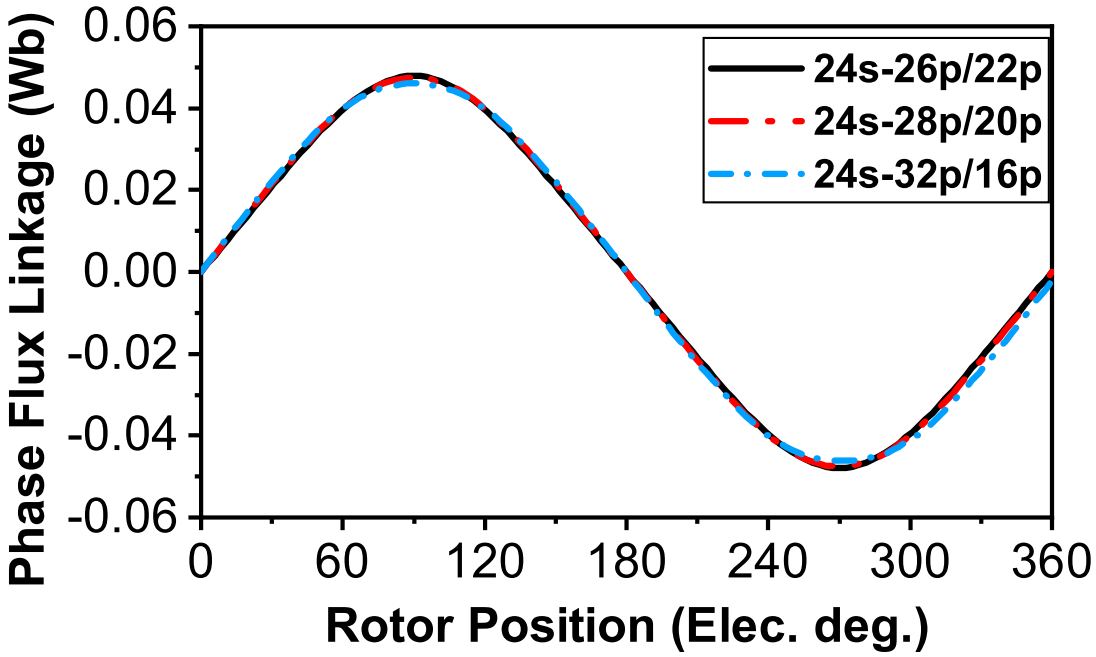

(a) Waveforms.

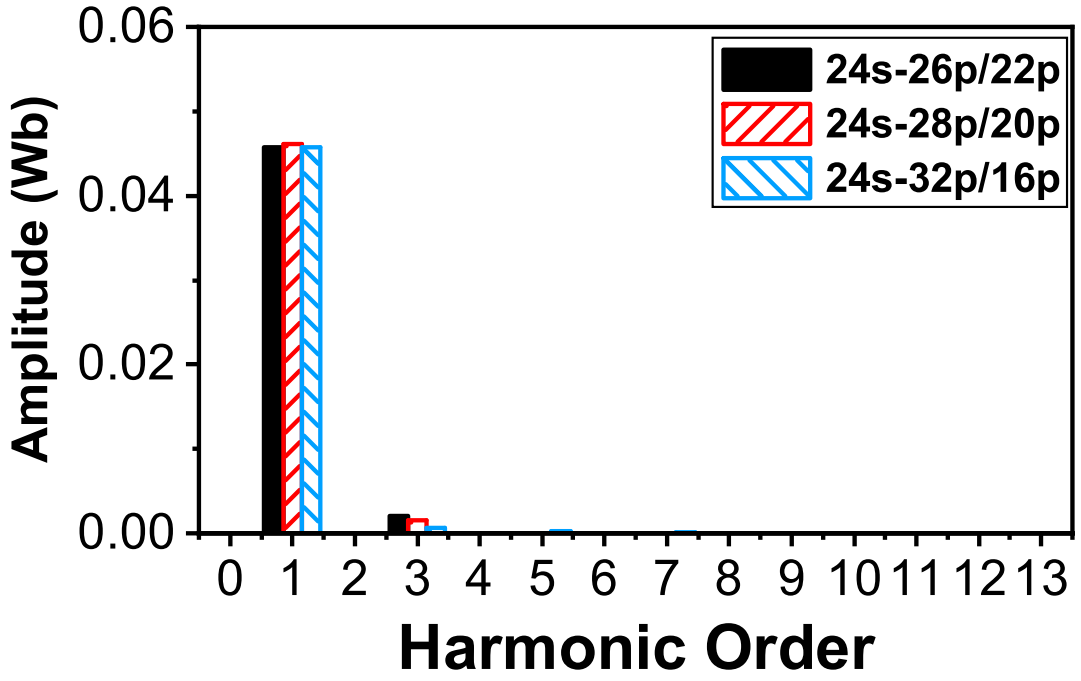

(b) Spectra.

Fig. 4.16. Comparison of phase-A flux linkages of YCDRPM machines.

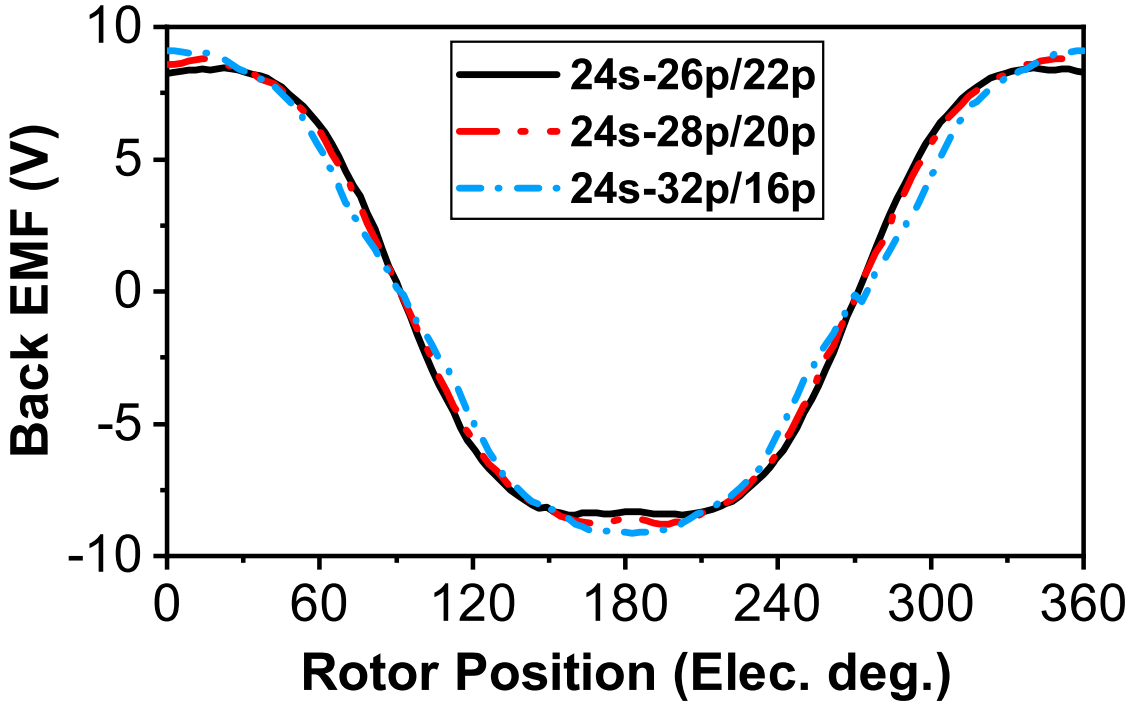

(a) Waveforms.

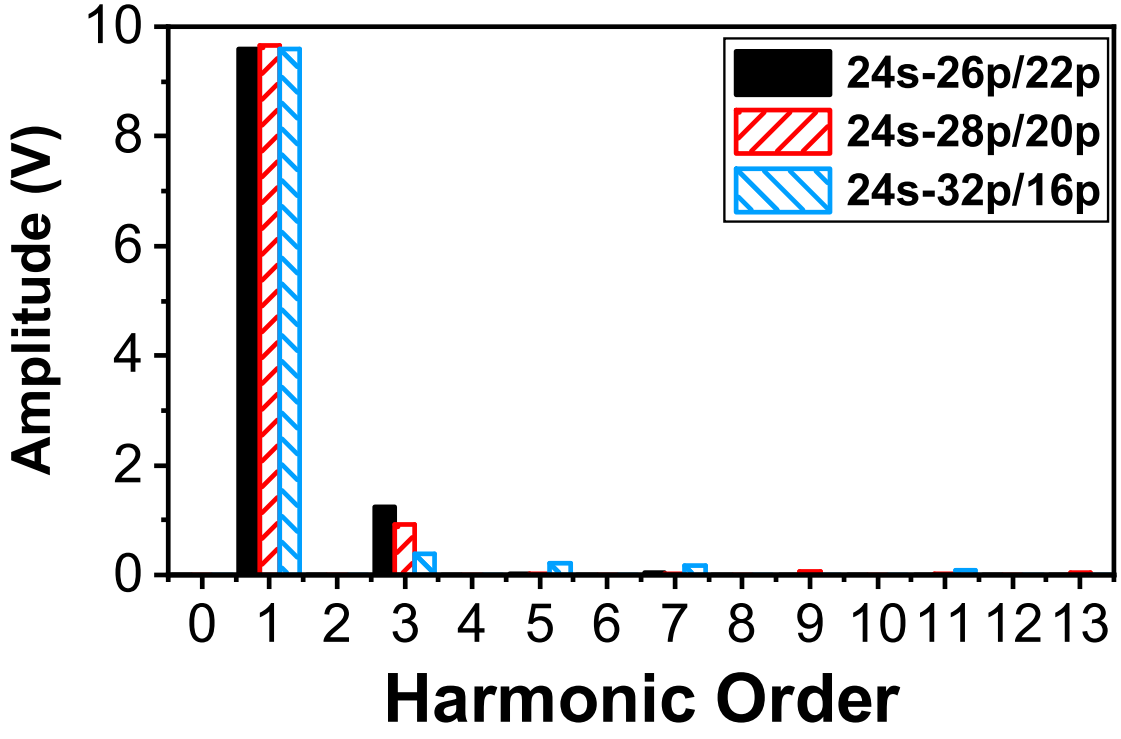

(b) Spectra.

Fig. 4.17. Comparison of phase-A back EMFs of YCDRPM machines (Stator frequency=100/3 Hz).

Due to the small slot area, the input currents of the proposed machines are small under the 30W copper loss condition. The 26p/22p machine has the largest average inner rotor torque because of the highest number of the inner pole pair. The 28p/20p machine has the highest average outer rotor torque reaching

2.4Nm. The average outer rotor torque of the 32p/16p machine is only 2.1 Nm. It is because the increased pole number causes significant flux leakage between PMs.

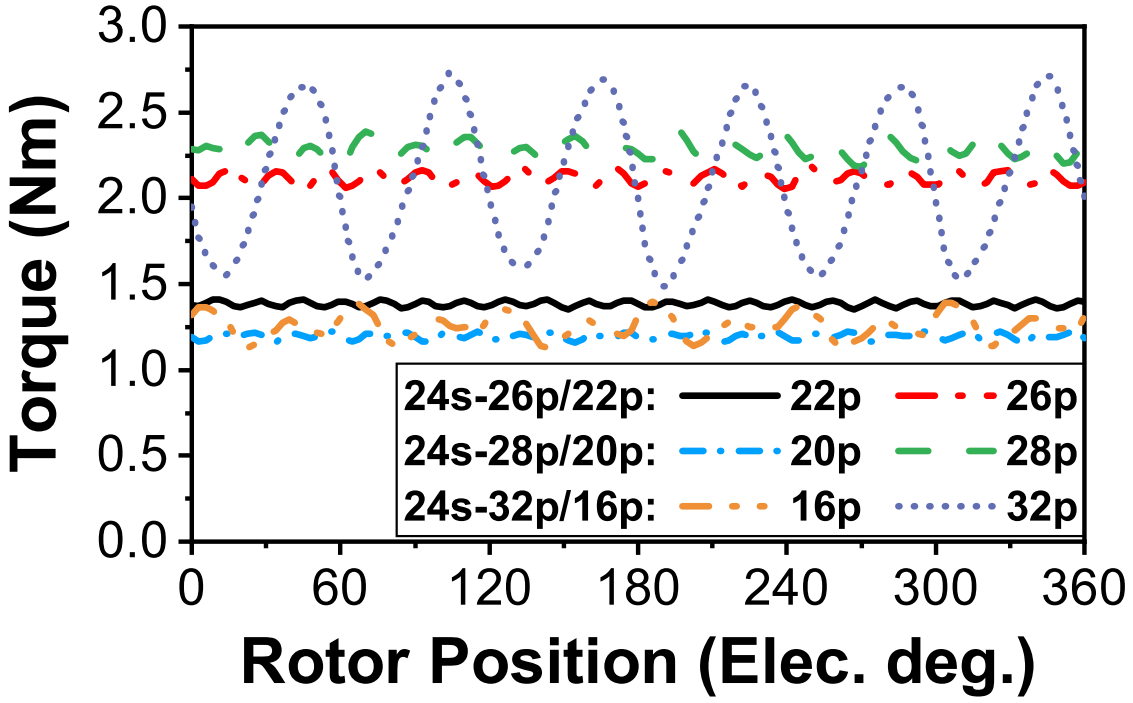

(a) Waveforms.

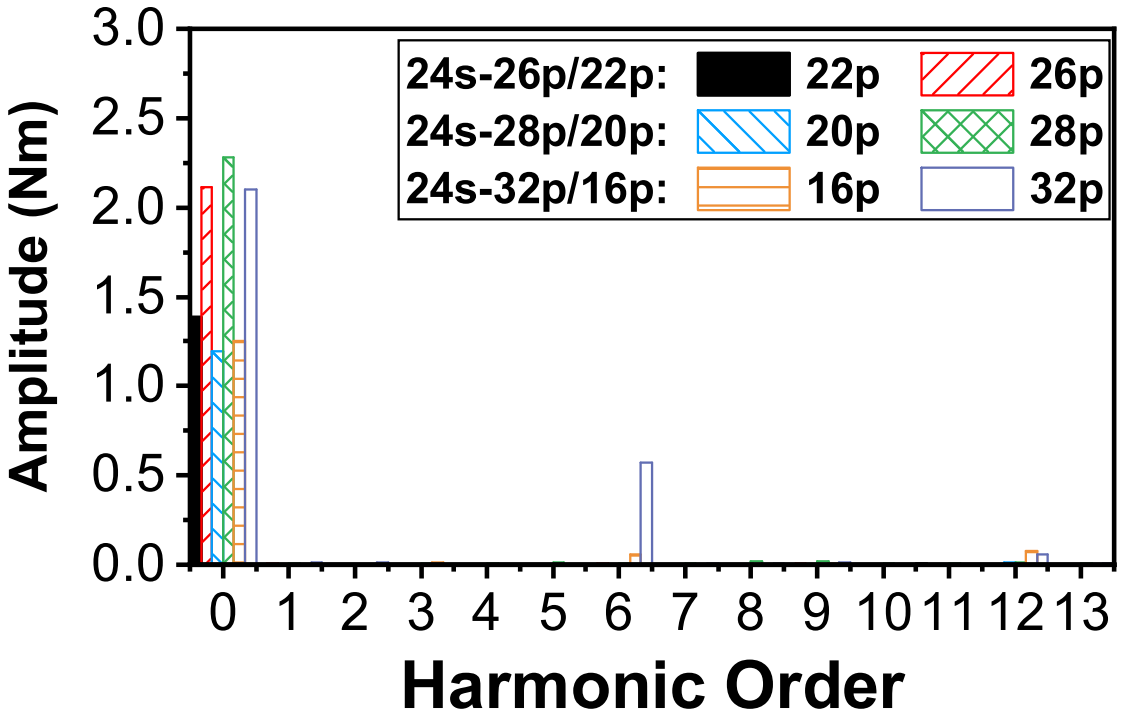

(b) Spectra.

Fig. 4.18. Comparison of output torques of YCDRPM machines.

The 26p/22p machine has the smallest torque ripple of both rotors, and the 32p/16p machine has the largest torque ripple. The phenomenon can be predicted by the cogging torque factor C_T, which is proposed in [Zhu00]:

$$C_T = \frac{2pN_s}{LCM(2p, N_s)} \tag{4.51}$$

where p is the pole pair number, LCM($2p$, N_s) is the least common multiple between the number of stator teeth and inner or outer rotors poles. The higher value of C_T represents the higher cogging torque. Thus, the value of C_T can be calculated, and the 26p/22p machine has the smallest C_T=2 for both rotors. The cogging torque factor of both rotors of the 32p/16p machine is the largest C_T=8.

Therefore, the 24s-26p/22p YCDRPM machine has the lowest torque ripple and most similar torques between the inner and outer rotors, which is better for the requirement of the counter-rotate applications.

4.5.2 Magnetic geared motor mode

The outer rotor achieves the maximum output torque in this mode, and the inner rotor and the stator winding injected current are both inputs. In Fig. 4.13, the initial relative angle δ between inner and outer rotors can be obtained to maximise the torque of the outer rotor. In practice, the relative angle δ is determined by the applied load. The relative angle is zero when the inner or outer rotor has no load applied on the shaft. However, with the increase of the applied load, the relative angle is increased until the inner or outer rotor reaches maximum torque. Moreover, both rotors would slip when the inner or outer rotor applied load exceeds the maximum torque value.

It can be found that the relative angle δ of the 24s-26p/22p machine is 79 electric degrees, for the 24s-28p/20p machine is 82 electric degrees, and 88 electric degrees for 24s-32p/16p machine. Thus, the initial relative mechanical angles between the inner and outer rotors of 24s-26p/22p, 24s-28p/20p, and 24s-32p/16p YCDRPM machines are 7.2°, 8.2° and 11°, respectively. In order to obtain the maximum torque of the outer rotor, the d-axis of the outer rotor is aligned with phasor A, and the rotating inner rotor sets the initial relative angle. The 24s-26p/22p YCDRPM machine is shown in Fig. 4.19 as the example.

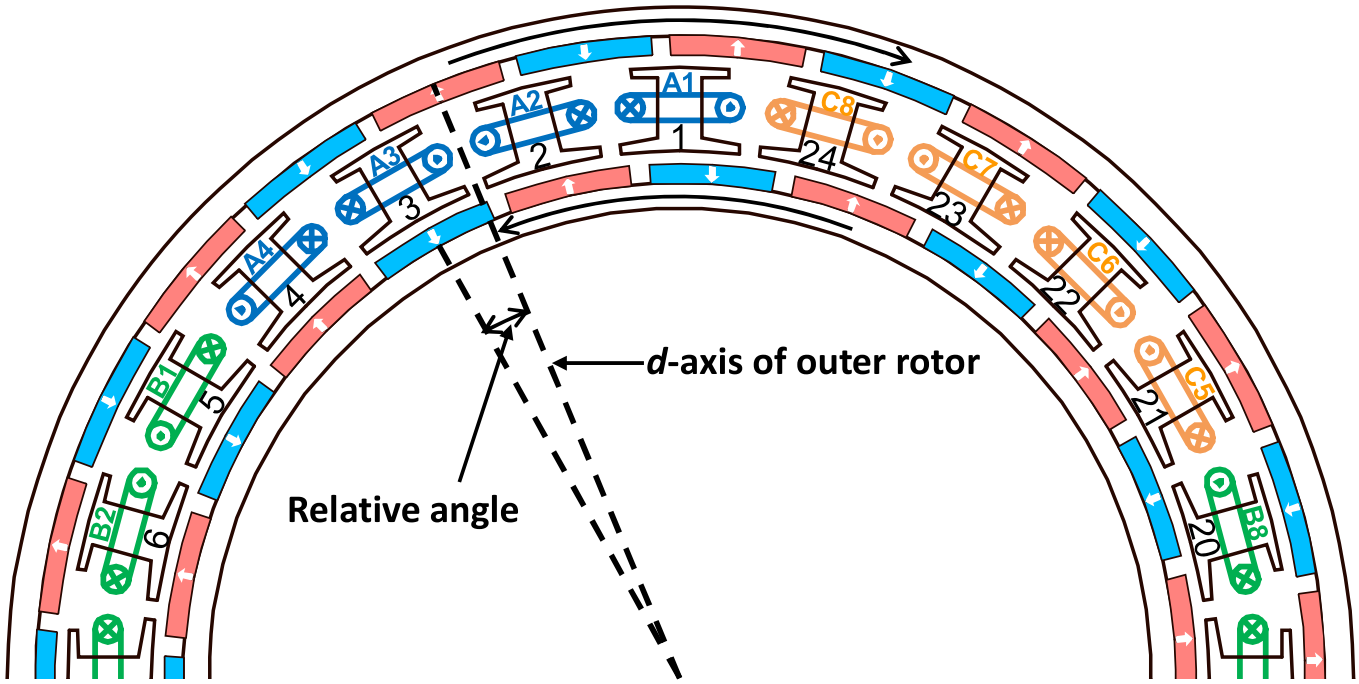

Fig. 4.19. Initial positions of inner and outer rotors of 24-26/22 YCDRPM machine.

Under the open circuit condition, the magnetic gearing torque of the inner and outer rotors of all the machines is shown in Fig. 4.20. The average torque of the inner rotor of the 24s-26p/22p machine is 9.8Nm, and the outer rotor torque is 11.6Nm, which satisfies the gear ratio of 13:11 between the inner and outer rotors. The gear ratio of the 24s-28p/20p machine is 7:5, and the average magnetic gearing torques of the inner and outer rotors are 8.2Nm and 11.5Nm, respectively. The 24s-32p/16p machine has the largest magnetic gearing torque of the outer rotor. Because of the largest gear ratio of 2:1 between the inner and outer rotors, the average magnetic gearing torque of the outer rotor reaches 15Nm.

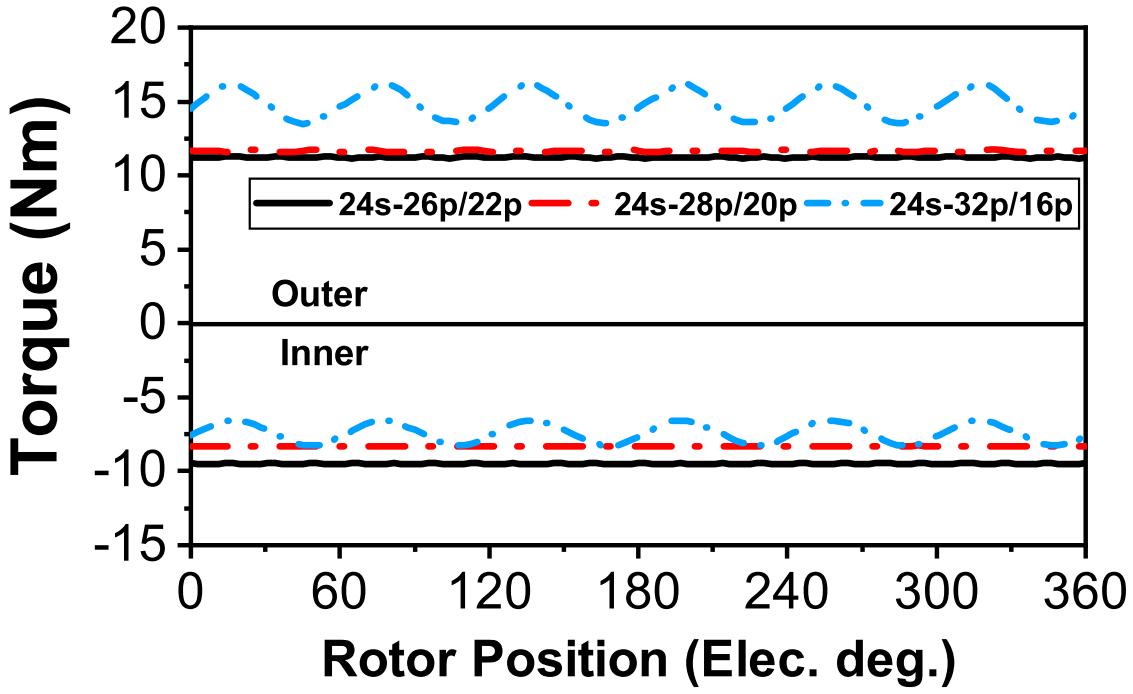

(a) Waveforms.

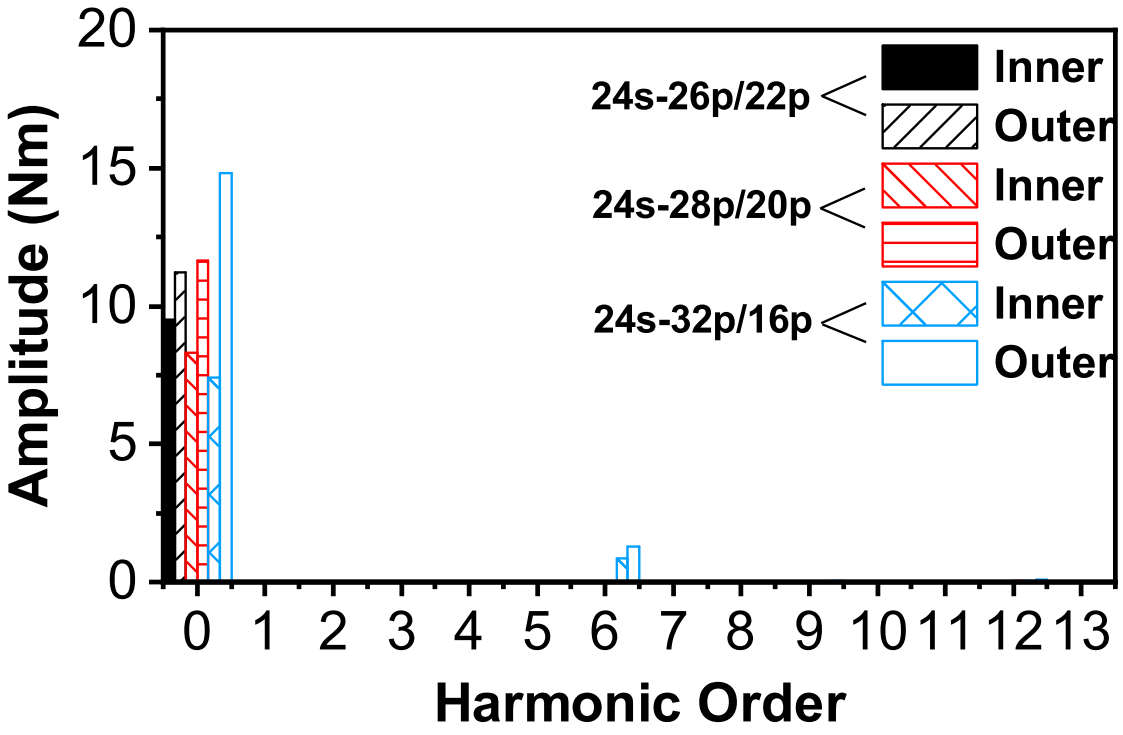

(b) Spectra.

Fig. 4.20. Comparison of magnetic gearing torques of YCDRPM machines.

After the currents injected in the stator windings, the outer rotor torques of all the machines are increased, as shown in Fig. 4.21. The 24s-32p/16p YCDRPM machine has the highest torque of the outer rotor, 17Nm. On the other hand, the torque of the outer rotor of the 24s-26p/22p YCDRPM machine is

the lowest due to the low gear ratio.

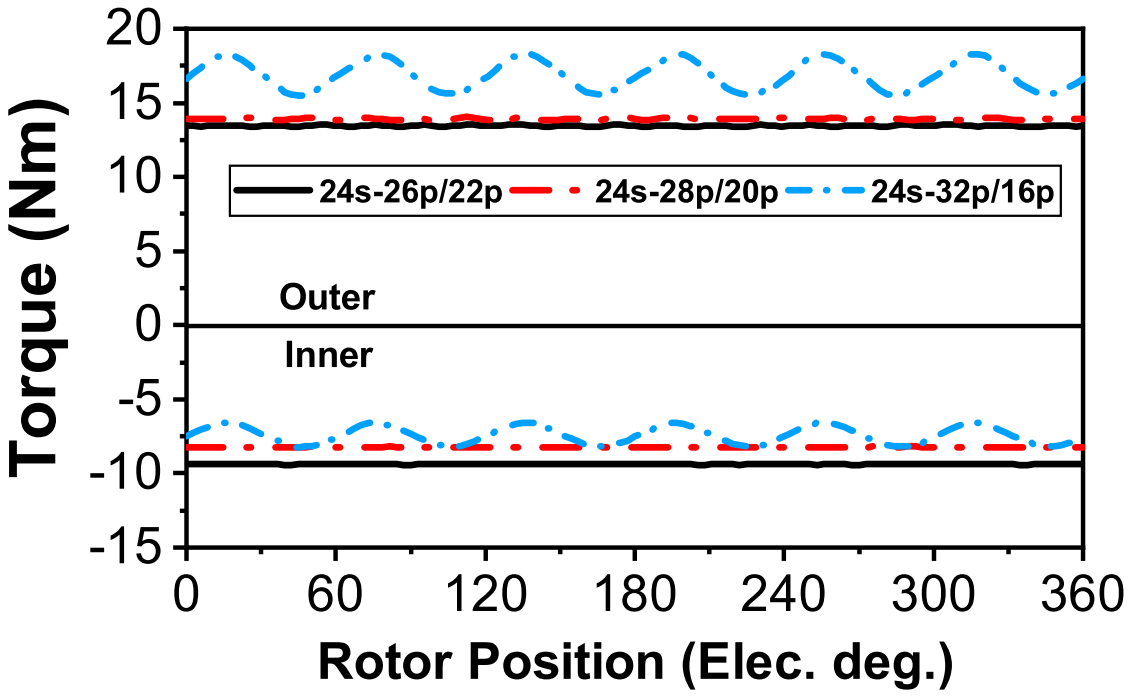

(a) Waveforms.

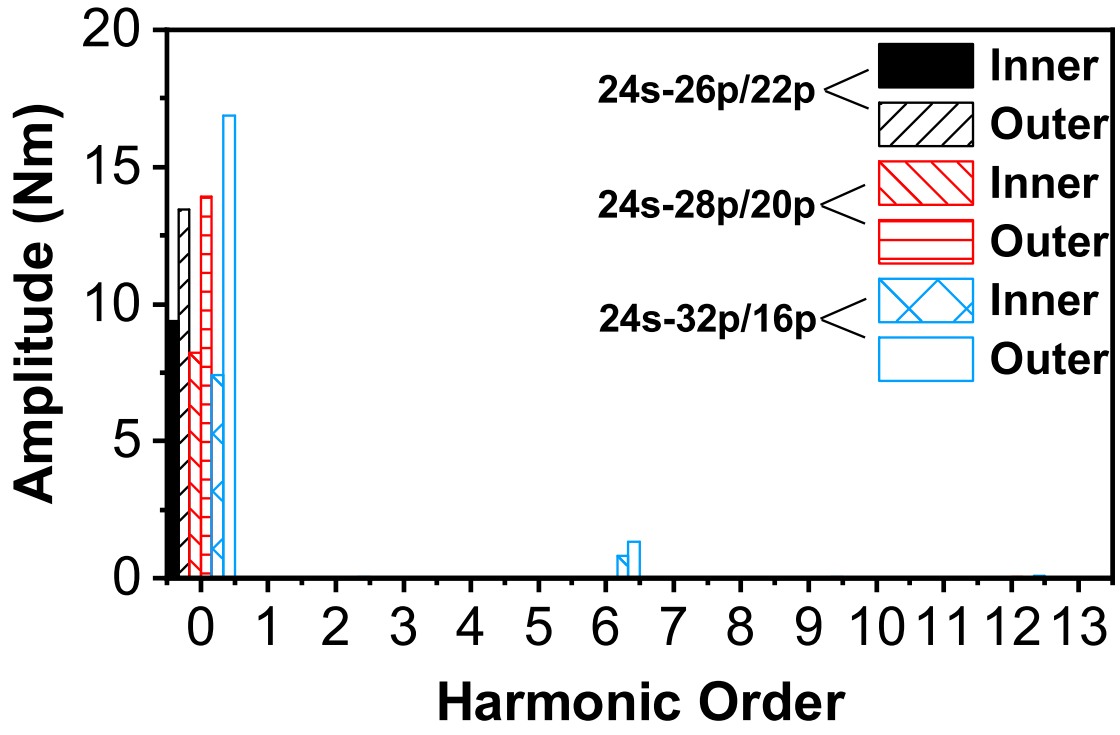

(b) Spectra.

Fig. 4.21. Comparison of inner and outer torques of YCDRPM machines at full load.

In this scenario, the characteristics of the torque-current angle curve of all the machines are shown in Fig. 4.22. The armature reaction causes the difference between the output torque and gearing effect

torque. Thus, the torque produced by the armature reaction can be split between the inner and outer rotors by changing the current angle.

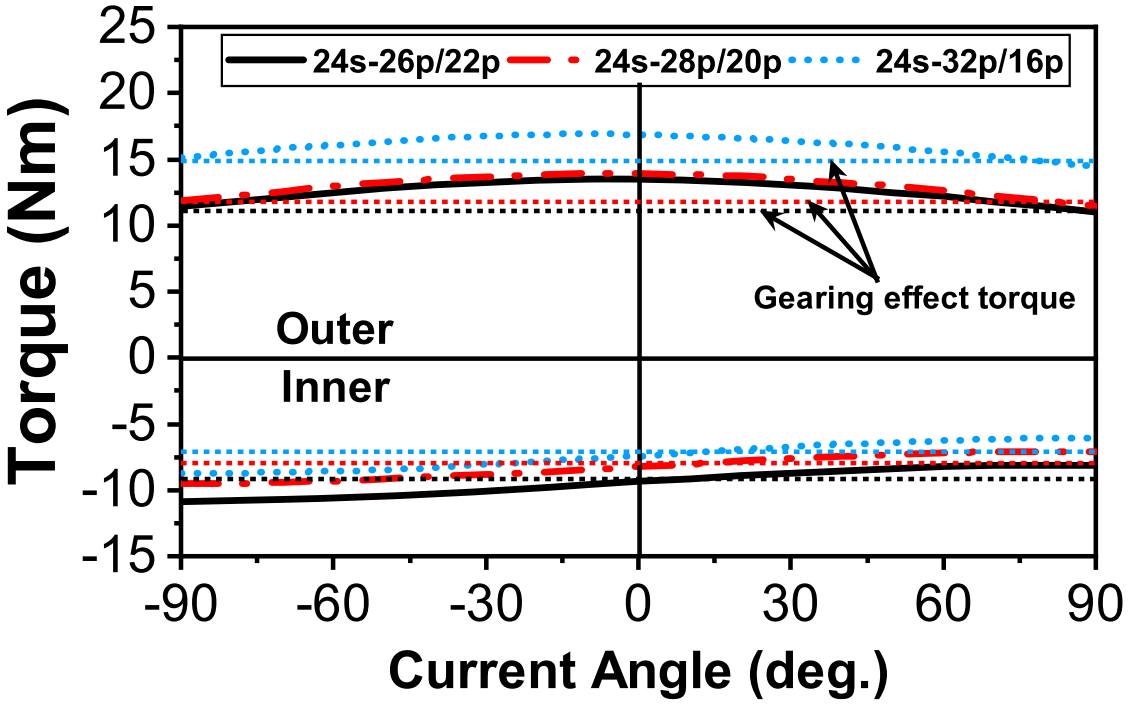

Fig. 4.22. Torque-current angle curves at maximum magnetic gearing torque.

4.6 Experimental Validation

In order to validate the analytical derivation and FEA predictions, a 24s-26p/22p YCDRPM machine is prototyped and tested. The parameters of prototype machine are listed in Tables 4.1 and 4.4. The prototype machine and test rigs are shown in Figs. 4.23 and 4.24, respectively. The dynamic test platform is used to measure the waveforms of back-EMF, and the static test platform is used to measure the cogging torques and on-load static torques.

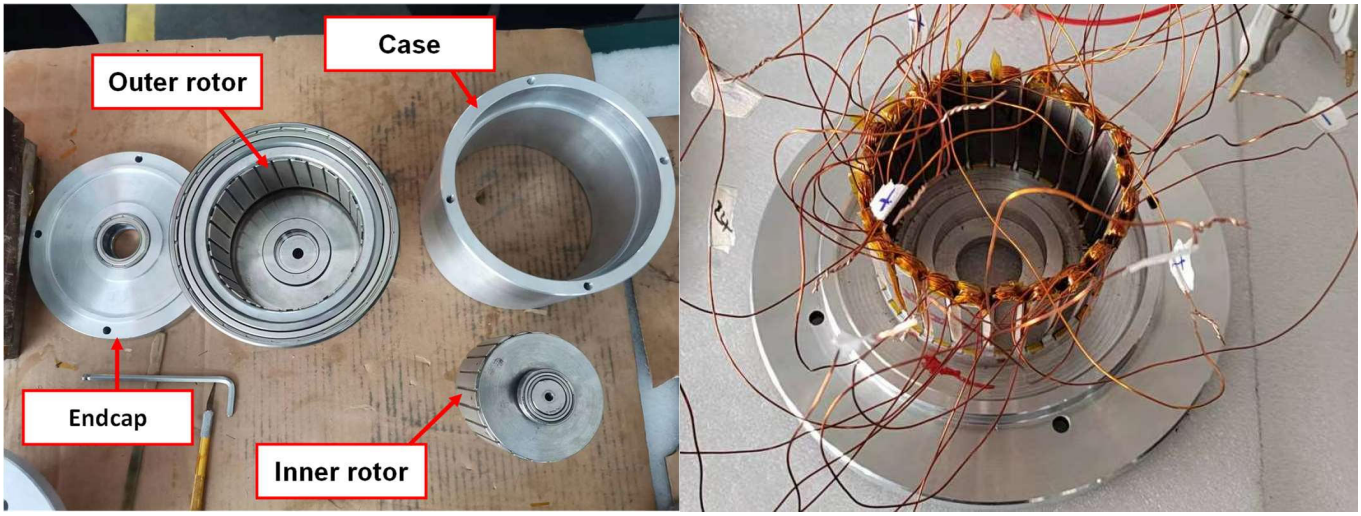

(a) Rotor. (b) Stator.

Fig. 4.23. 24s-26p/22p YCDRPM prototype.

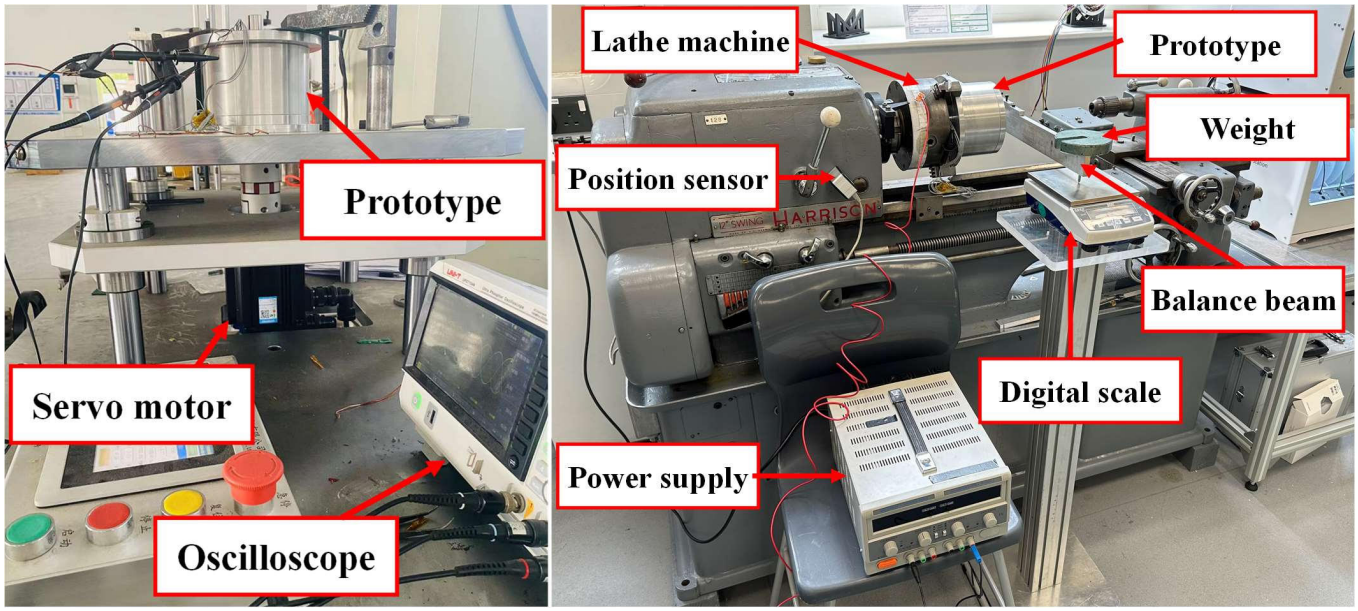

(a) Dynamic test platform. (b) Static test platform.

Fig. 4.24. Test rigs.

The cogging torques of the inner and outer rotors of the YCDRPM machine are measured using the method in [ZHU09]. For measurements, one rotor shaft is connected to a balance beam linked to a digital weight scale to measure the force produced by the prototype while the other rotor rotates freely. The stator is fixed to a lathe machine and can be rotated to adjust the rotor positions. Fig. 4.25 shows the measured and FEA-predicted cogging torques of the YCDRPM machine. The measured results match the FEA predictions well and exhibit the low cogging torques as expected.

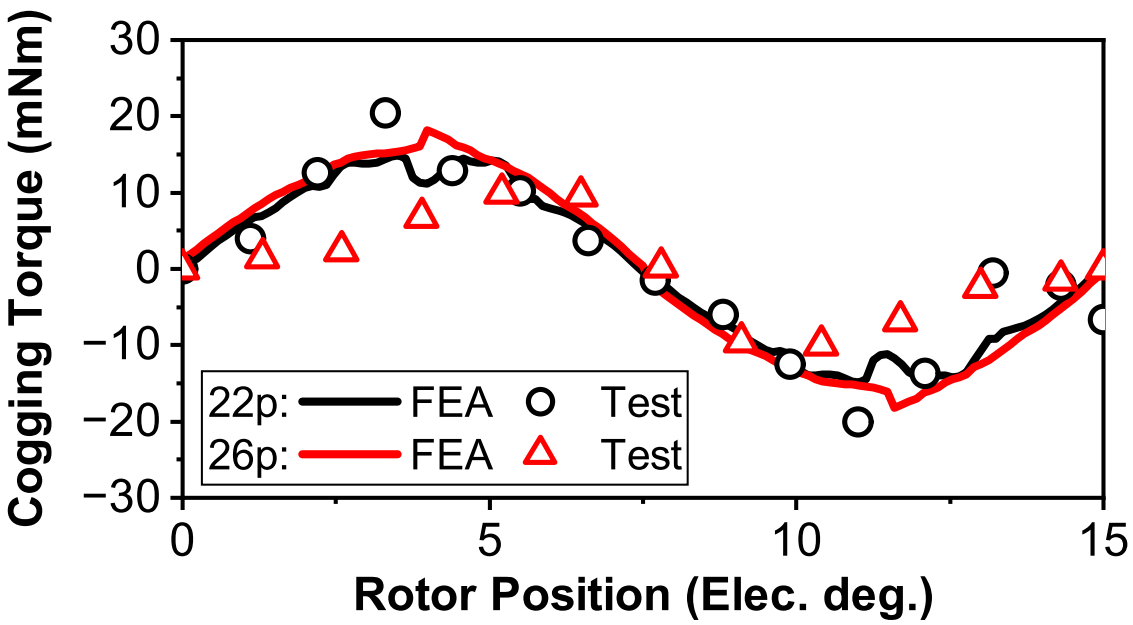

(a) Waveforms.

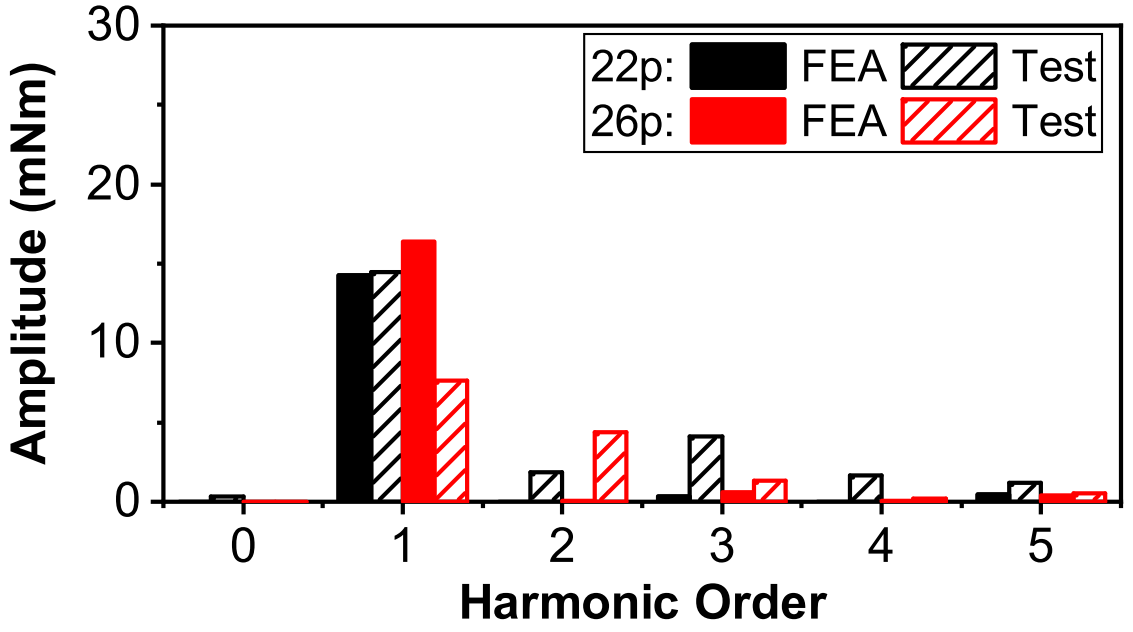

(b) Spectra.

Fig. 4.25. FEA predicted and measured cogging torques.

Fig. 4.26 shows the measured and predicted phase back EMFs. The 400 r/min servo motor drives the inner rotor. Thus, the outer rotor rotates in the opposite direction at 338 r/min. The results show good agreement between the measured and FEA-predicted back EMFs.

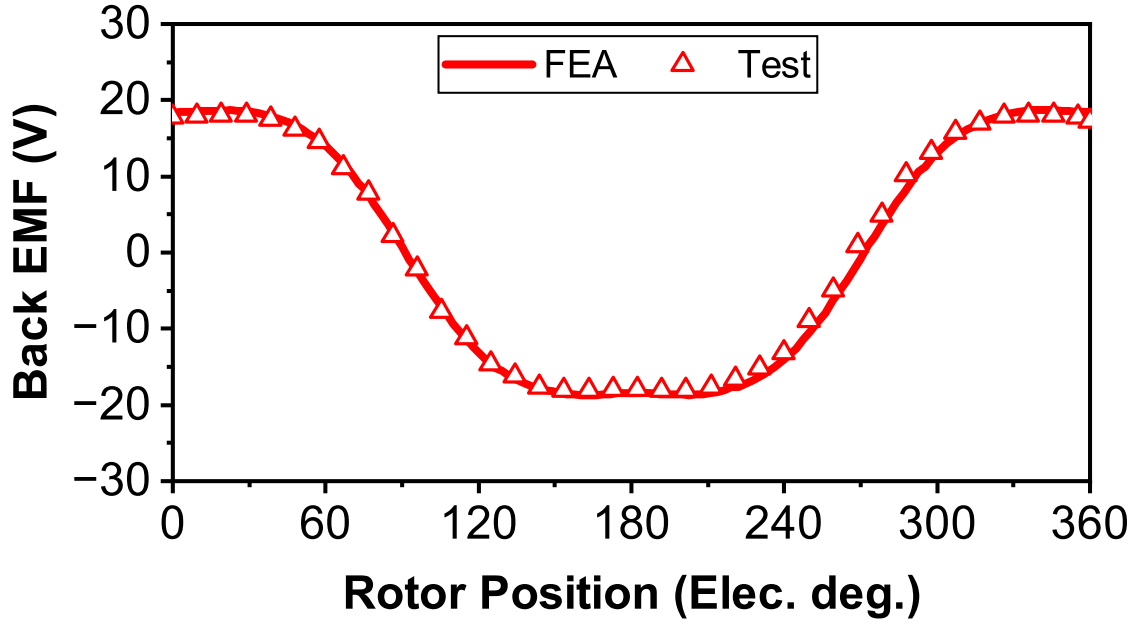

(a) Waveforms.

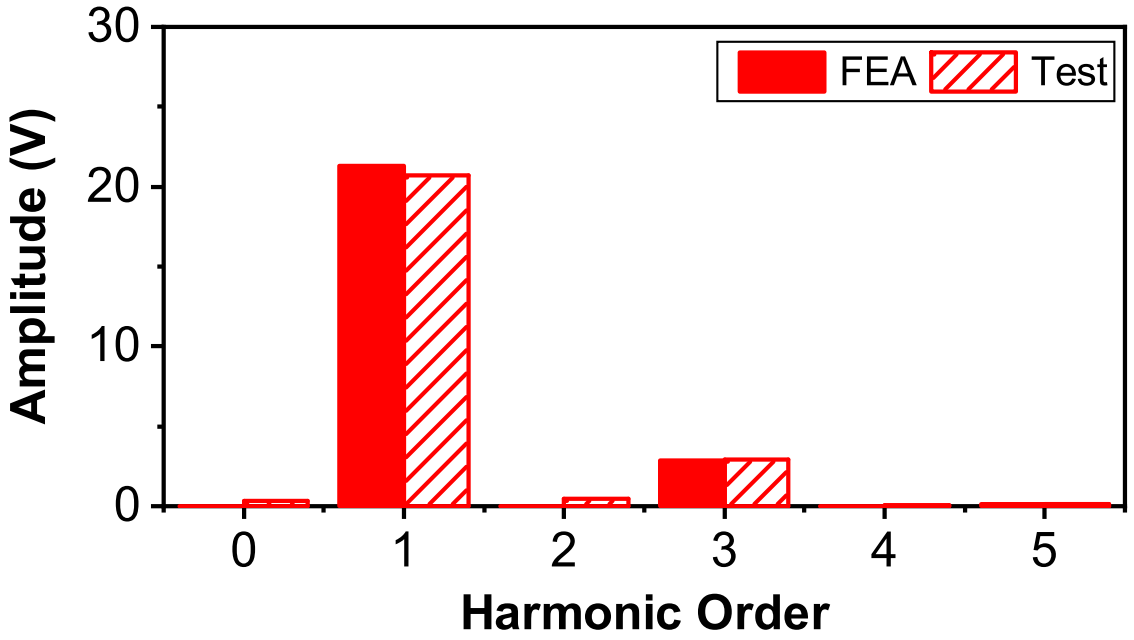

(b) Spectra.

Fig. 4.26. Measured and FEA-predicted phase back EMFs.

As mentioned in Section 4.5, when two rotors rotate freely without applying load to the rotors, the YCDRPM machine operates in pure electric motor mode. The static torques of two rotors of the YCDRPM machine at half and full loads in pure electric motor mode can be measured by supplying a range of DC currents ($I_A = -2I_B = -2I_C = I_{DC}$), the full-load current corresponding to a copper loss of 30 W, as shown in Fig. 4.27 (a). Fig. 4.27 (b) shows the variation of average torque with current. The measured torques match well with the FEA predictions.

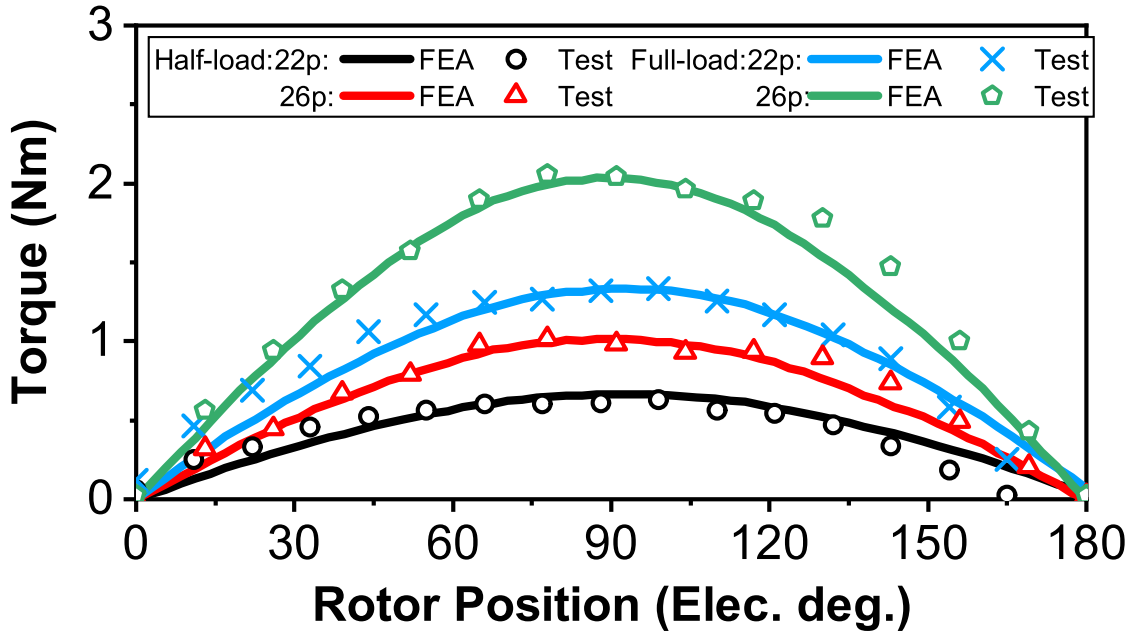

(a) Static torques at full and half-load conditions.

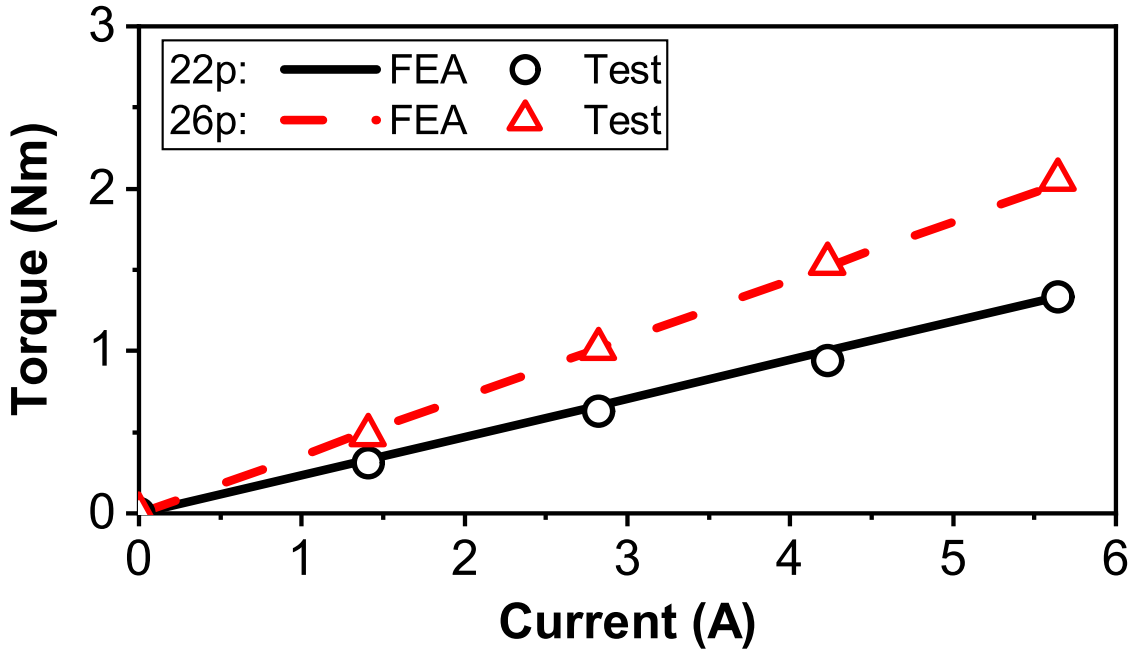

(b) Variation of average torques with currents.

Fig. 4.27. FEA and measured torques.

4.7 Conclusion

A radial-flux yokeless counter-rotating dual-rotor permanent magnet (YCDRPM) machine is presented and investigated in this chapter. The YCDRPM machine combines a magnetic gear and a PM machine. The stator winding is wound on the modulation ring of the magnetic gear, which avoids the low

mechanical strength of the modulation ring as a rotor. Since the FSCW is employed for the yokeless structure, the armature reaction generates a counter-rotating MMF for different sides to achieve the counter-rotating operation. Furthermore, the different operation modes of the YCDRPM machine are discussed. The YCDRPM machine benefits from the magnetic gear effect. When the YCDRPM machine works under the magnetic geared motor mode, the output torque is significantly increased by the transferred magnetic gearing effect and armature reaction. The performance comparisons of the different slot/pole number combinations of the YCDRPM machine show that the 24s-26p/22p combination shows better electromagnetic performance in terms of the output torque and torque ripple.

CHAPTER 5

A NOVEL COUNTER-ROTATING SINGLE-STATOR DUAL-INTERNAL-ROTOR PERMANENT MAGNET MACHINE

Chapter 4 investigates the counter-rotating (CR) magnetic geared dual-rotor machine. However, its sandwiched modular stator results in a complex mechanical structure that makes manufacturing and assembly difficult. This chapter proposes a novel counter-rotating single-stator dual-internal-rotor permanent magnet (CSDPM) machine. This machine utilises magnetic field modulation in the fractional slot concentrated winding permanent magnet (PM) and vernier PM machines to realise the counter-rotating operation for some special applications, such as underwater vehicles, wind power turbines, household appliances, etc. This machine has only one set of stator armature winding with easy manufacturing and robust structure, which greatly reduces the cost, weight, and space requirement compared with the conventional counter-rotating (CR) system. The magnetic field modulation principle and the relationship between two rotors and the armature reaction are analysed. The electromagnetic performance of the CSDPM machine is comprehensively investigated. It shows that the proposed CR system with the CSDPM machine has higher torque than the conventional CR system by using two single-rotor PM machines. There is no magnetic coupling effect between the two rotors in the CSDRPM machine. The torque split of two rotors can be easily changed with the corresponding rotor stack length. The results are validated by experiments on a prototype CSDPM machine.

This chapter is submitted to IEEE Transactions on Transportation Electrifications:
Z.T. Ran, Z.Q. Zhu, Y.J. Zhou, L. Chen, and L. Yang, “A novel counter-rotating single-stator dual-internal-rotor permanent magnet machine,” submitted to IEEE Transactions on Transactions on Transportation Electrifications. (under review)

5.1 Introduction

Counter-rotating (CR) machines are widely used to improve the performance of some special industrial applications, such as underwater vehicles, wind power turbines, and household appliances, etc.

[HOL94] proposed a CR ring thruster for underwater vehicles. Two thruster rings rotate in opposite directions to eliminate the roll motion when the propulsion operates underwater. Compared with the

conventional single-direction rotating propulsion, the CR underwater propulsion can avoid the single-direction rotational water flow to make the underwater vehicle yaw in one direction [LIU18]. Meanwhile, the rotational torques produced by two CR propellers cancel each other out to help the underwater vehicle move straight and accurately [SHI20]. In addition, for the axially arranged CR propellers, the aft propeller recovers the rotating energy loss from the fore propeller, resulting in a highly efficient propulsion system [HOU18]. Compared with two propellers rotating at the same speed, the fore propeller which rotates faster than the aft propeller can improve the propulsion efficiency [MAL13] [YAN96] [SAS98]. Generally, the conventional CR underwater vehicle propulsion is controlled by two electrical machines separately or one electrical machine integrated with a bevel-planetary mechanical gearbox, as shown in Fig. 5.1, which causes high cost, heavy weight, and large space. The complex mechanical structure also needs more regular maintenances.

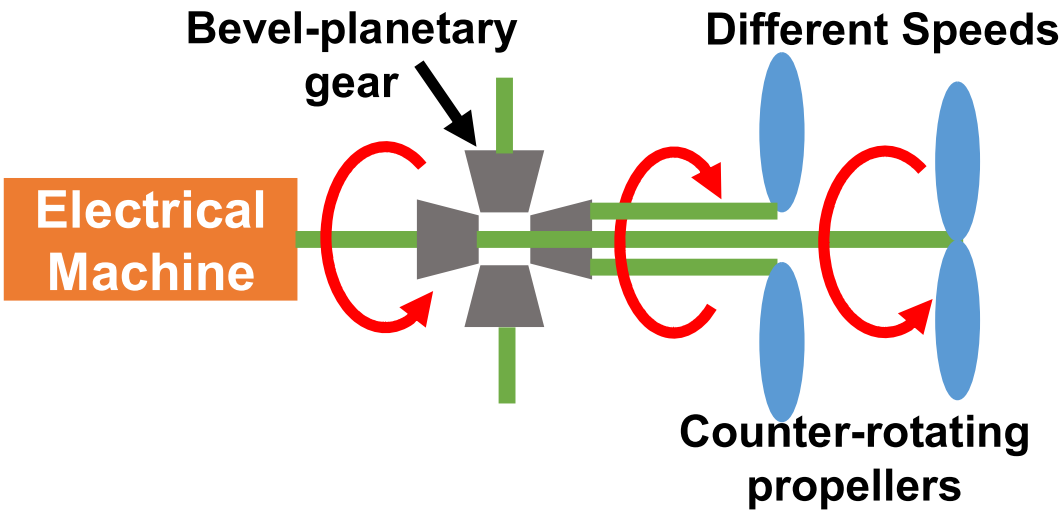

(a) One electrical machine with mechanical gearbox.

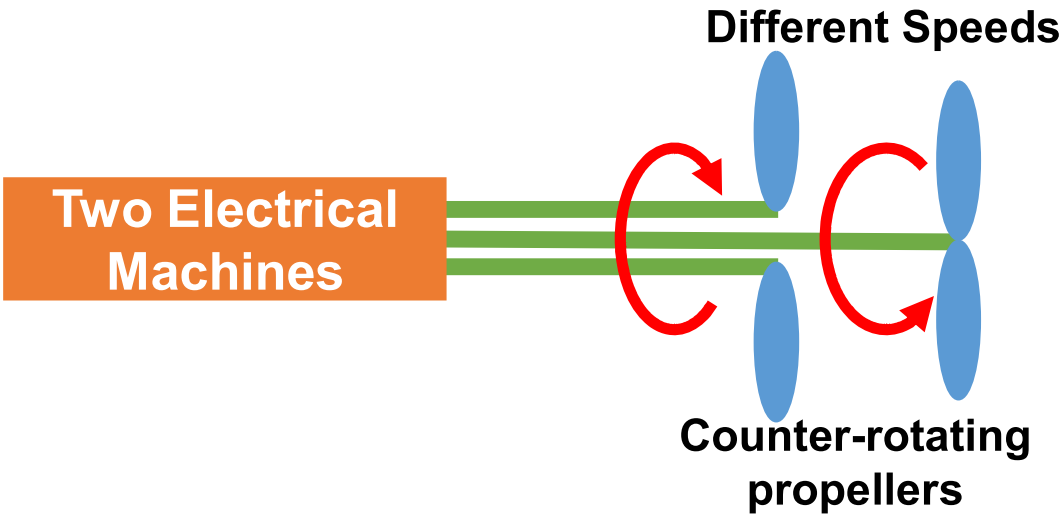

(b) Two electrical machines.

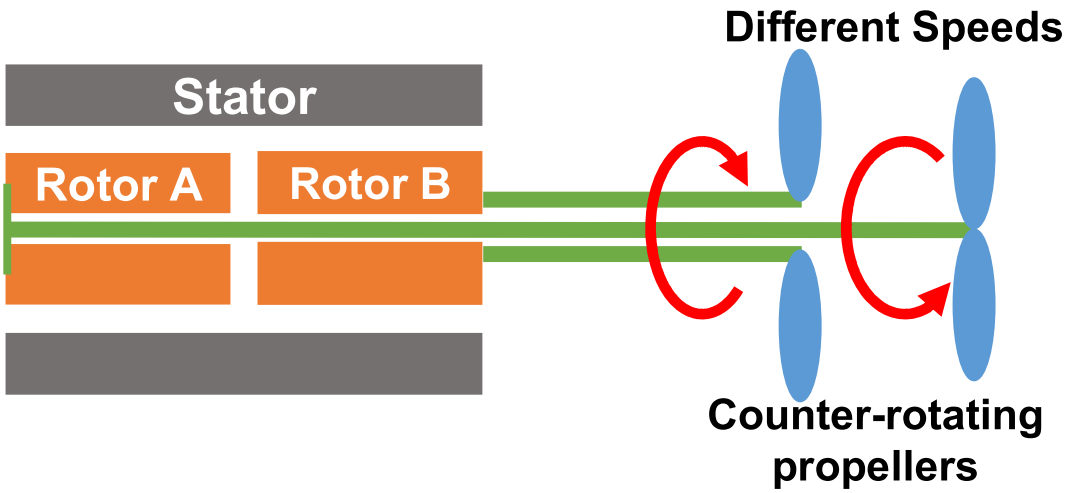

(c) Proposed CSDPM machine.

Fig. 5.1. Counter-rotating operation systems.

For wind power turbines, [SHI98] first patented the CR wind turbine system. Then, [JUN05] developed a 30kW CR wind turbine consisting of an upwind auxiliary rotor rotating at 300 rpm and a downwind main rotor rotating in a different direction at 150 rpm. It introduced a smaller auxiliary rotor placed upwind of the main rotor to capture additional wind energy and compensate for the dead zone of the main rotor area. This configuration increases the power output of the wind turbine system by improving the aerodynamic efficiency compared with the conventional single-blade wind power turbine [SAN13]. In addition, the smaller blade length of the auxiliary rotor allows for higher tip speeds, resulting in higher power output. [SHE07] indicates a counter-rotating wind turbine with different rotational speeds rotors operated on the island of Sprogø, Denmark; it can produce 43.5 % more annual energy than a single-rotor turbine. Similarly, the CR wind turbine system is usually achieved by one electrical machine integrated with the bevel-planetary mechanical gear, which has a complex mechanical structure and suffers from maintenance requirements, noise, low reliability, and high cost, etc. [BOO10] employs the slip rings for the stator armature winding for an electrical machine to design the stator as a rotational part to achieve the CR wind turbine system without a mechanical gearbox. However, it also causes low reliability and introduces maintenance requirements of slip rings.

Therefore, dual-rotor (DR) electrical machines are considered to achieve CR operation while improving reliability and reducing the weight, cost, and space requirements. The DR permanent magnet (DRPM) machine using high-energy PM material is the most popular topology due to high torque density and high efficiency.

The conventional DRPM machine only considered one mechanical port, where two rotors with the same pole number are fixed on the same shaft and rotate at the same speed [QU03a] [QU04] [VAN13].

Thus, two rotors in the conventional DRPM machine cannot rotate separately. The DRPM machines are considered to operate two rotors freely in different working conditions after multi-mechanical ports utilised in the electrical machine are proposed in [XU05].

[YEH12] proposed a DRPM machine in which two rotors have the same pole number but are set on different shafts. This DRPM machine employs two sets of stator armature windings to control two rotors working separately. In [ZHA14] [ZHA07] [CHE11], the DRPM machine has two armature winding sets and two rotors with the same pole numbers to achieve the CR operation by changing the phase sequences for the corresponding controlled rotors. The magnetically geared machine utilises field modulation to realise CR operation. [WAN17b] [LUO17] [CHE22] proposed the magnetically geared CR DRPM machine. This type of machine employs two winding sets that interact with a rotor and a modulation ring to utilise the dual field modulation to realise the CR operation and improve the torque density. However, the modulation ring usually shows poor mechanical strength to be an output rotor. The sandwiched modular stator magnetic geared DRPM machine uses the modular stator between two rotors to be the modulation ring, which shows a robust rotor structure [JIA12]. However, the sandwiched stator assembly with dual-mechanical ports also causes a complex mechanical structure and manufacturing challenges. This similar problem is also shown in flux switching CR DRPM machines [ULL22a] [ULL22b] [MIR21]. The same approaches to achieve the CR operation can also be applied in the axial flux DRPM machines [HUA24] [ZHU18a] [HAS20] [XIA23]. However, the axial flux machine has inherent disadvantages in lamination manufacturing and axial magnetic attraction force between the rotor and stator.

This chapter proposes a novel counter-rotating single-stator dual-internal-rotor PM (CSDPM) machine. The CSDPM machine realises the CR operation by utilising magnetic field modulation in the fractional slot concentrated winding (FSCW) PM machine and integral slot distributed winding (ISDW) vernier PM (VPM) machine [ZHU18b] [LIU19]. The proposed CR operation system with the CSDPM machine is shown in Fig. 5.1c. In this chapter, the machine topology and operation principle are illustrated in Section 5.2 and Section 5.3, respectively. Section 5.4 describes the global optimisation design of the CSDPM machine via the genetic algorithm based on the finite element analysis (FEA). Then, the electromagnetic performance of the CSDPM machine is comprehensively analysed in Section 5.5. The CSDPM machines with different slot pole number combinations are investigated in Section 5.6. Section 5.7 is the experimental validation, and Section 5.8 concludes this chapter.

5.2 Machine Topologies

The CSDPM machine realises the CR operation by utilising magnetic field modulation in the FSCW PM and ISDW VPM machines, which can be treated as a combination of a single FSCW or ISDW stator

producing two counter-rotating magnetic fields with different pole numbers and two counter-rotating PM rotors with different pole numbers but corresponding to those of the stator magnetic fields, respectively. This chapter selects the slot-pole number combinations of FSCW 12 slots-10 poles (12s10p) and 12 slots-14 poles (12s14p) SRPM machines for further investigation in this section. Other feasible slot-pole number combinations based on the magnetic field modulation theory are discussed in Section 5.3 and analysed in Section 5.6. Fig. 5.2 shows the topologies of the FSCW 12s10p and 12s14p SRPM machines, along with their corresponding coil back EMF phasors. The CSDPM machine is constructed by one shared stator of 12 slots, one stator armature winding set, and 10p and 14p rotors, as shown in Fig. 5.3.

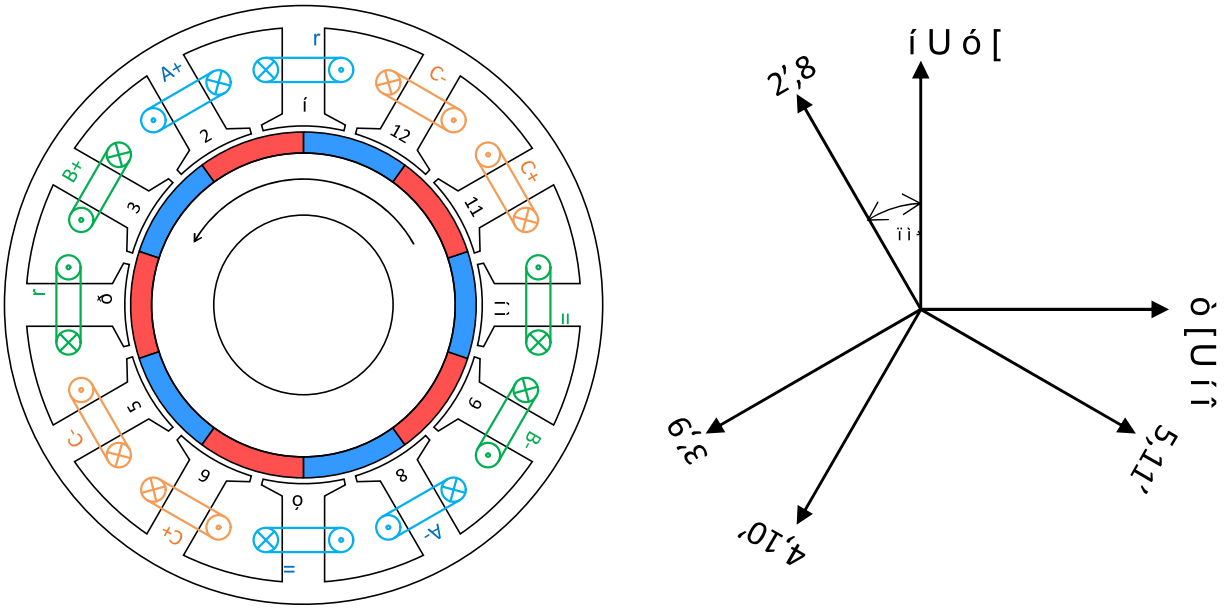

(a) 12s10p.

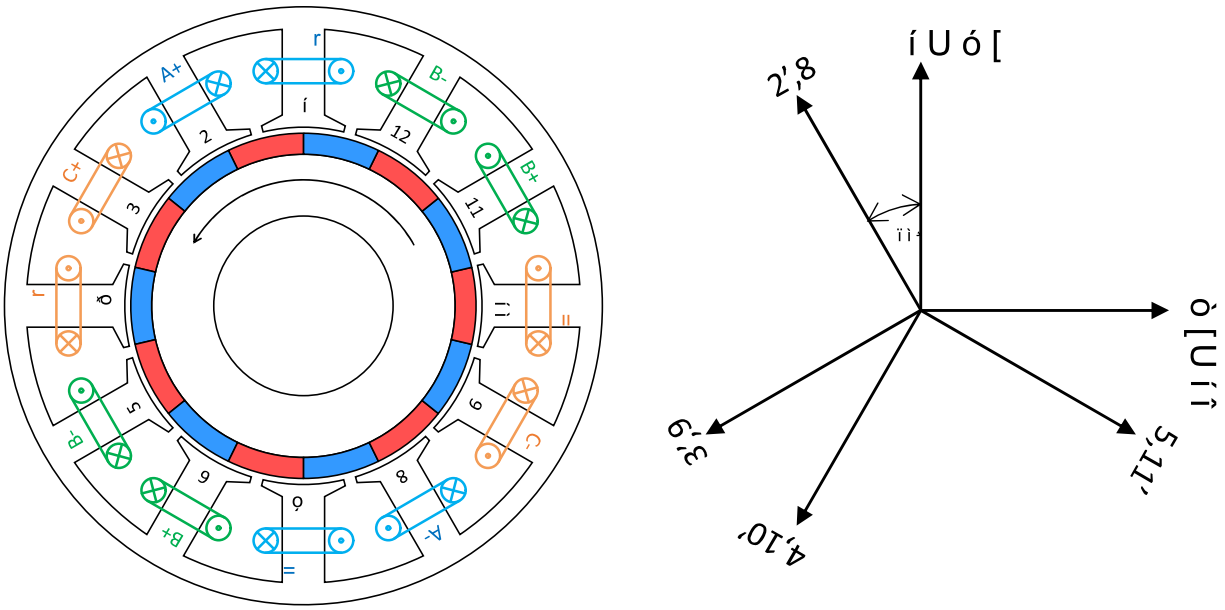

(b) 12s14p.

Fig. 5.2. Topologies and coil back EMF phasors of SRPM machines with different slot-pole number combinations.

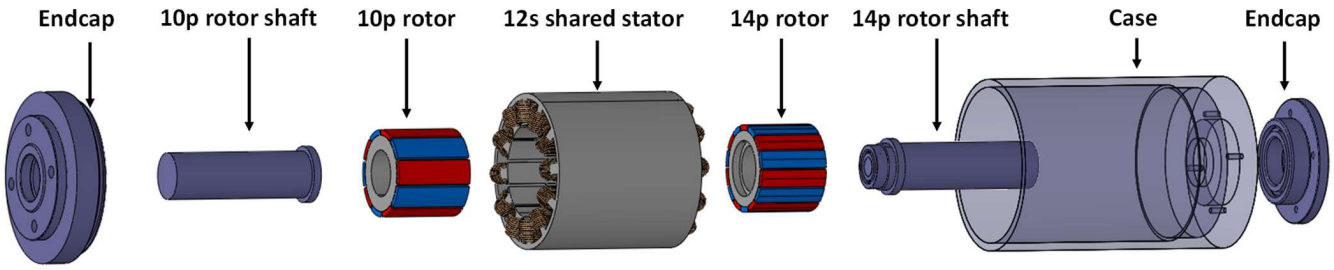

Fig. 5.3. Proposed CSDPM machine mechanical structure.

5.3 Operation Principle

The operational principle of the CSDPM machine is based on the magnetic field modulation concept [ATA06] [ATA01]. The analysis of the magnetic field in the air gap in the CSDPM machine can be separated into magnetic fields generated by the PM and armature reaction. This section mainly discusses the magnetic field modulation principle in the CSDPM machine rather than computing the actual magnetic fluxes. Therefore, for simplification, the following assumptions are considered in this study:

1) The permeance of laminations is considered infinite, and the magnetic saturation of the lamination is neglected.
2) The tangential component of the air-gap magnetic field is neglected.
3) Leakage flux and the end effect are neglected.
4) The relative permeability of PMs is assumed to be equivalent to that of air.

5.3.1 Air gap flux density generated by rotor PM

In the CSDPM machine, the magnetic motive force (MMF) generated by the rotor PM is shown in Fig. 5.4. It can be formulated as:

$$F_{PM}(\theta,t)=\sum_{i=1,3,5\ldots}^{\infty}F_{PMi}\cos\left[ip_r(\omega_r t-\theta)\right] \tag{5.1}$$

where p_r is the number of pole pairs, ω_r is the rotor mechanical rotating speed, F_{PMi} is the amplitude of the i-th harmonic component of the MMF generated by PM, and θ is the air gap circumferential position.

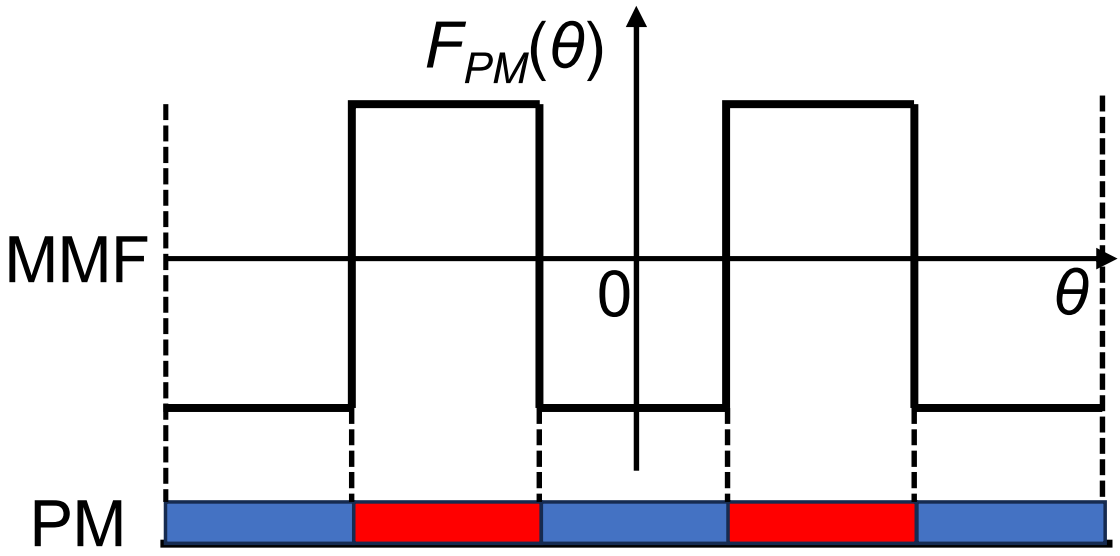

Fig. 5.4. MMF generated by rotor PM.

The air gap flux density distribution is affected by the stator teeth. The stator teeth can be treated as modulation modular, and the magnetic permeance function is formulated as:

$$\Lambda_s(\theta) = \Lambda_{s0} - \sum_{j=1,2,3\ldots}^{\infty} \Lambda_{sj} \cos(jN_s\theta) \tag{5.2}$$

where Λ_{s0} is the fundamental amplitude of the air gap permeance, Λ_{sj} is the j-th amplitude of the air gap permeance, N_s is the number of the stator tooth. Therefore, the magnetic flux density generated by PM in the radial direction is modulated by stator teeth in the air gap and can be obtained as:

$$\begin{aligned} B_r &= F_{PM}\Lambda_s \\ &= \sum_{i=1,3,5\ldots}^{\infty} F_{PMi}\Lambda_{s0}\cos(ip_r\theta - ip_r\omega_r t) + \frac{1}{2}\sum_{i=1,3,5\ldots}^{\infty}\sum_{j=1,2,3\ldots}^{\infty} F_{PMi}\Lambda_{sj}\cos[(ip_r + jN_s)\theta - jp_r\omega_r t] \\ &\quad + \frac{1}{2}\sum_{i=1,3,5\ldots}^{\infty}\sum_{j=1,2,3\ldots}^{\infty} F_{PMi}\Lambda_{sj}\cos[(ip_r - jN_s)\theta - jp_r\omega_r t] \end{aligned} \tag{5.3}$$

Thus, in order to produce the synchronous torque, the order of the working harmonic is $ip_r \pm jN_s$. The positive and negative values represent the rotor rotating in the same or counter directions.

5.3.2 Air gap flux density generated by stator armature reaction

According to [LI13] [LIP08], the Fourier series expansion of the three-phase machine winding function is given as:

$$\begin{cases} N_A(\theta) = \sum_{k=1,3,5\ldots}^{\infty} N_k cos(k\theta) \\ N_B(\theta) = \sum_{k=1,3,5\ldots}^{\infty} N_k cos(k\theta - k\frac{2}{3}\pi) \\ N_C(\theta) = \sum_{k=1,3,5\ldots}^{\infty} N_k \cos\left(k\theta - k\frac{4}{3}\pi\right) \\ N_k = \frac{2}{k\pi} N_{ph} k_{wk} \end{cases} \tag{5.4}$$

where N_k is the amplitude of the k-th order harmonic, and k_{wk} is the winding factor of the k-th order harmonic.

Set the three-phase current as:

$$\begin{cases} i_A(t) = I_{ph} cos(\omega_s t) \\ i_B(t) = I_{ph} cos(\omega_s t - \frac{2}{3}\pi) \\ i_C(t) = I_{ph} cos(\omega_s t - \frac{4}{3}\pi) \end{cases} \tag{5.5}$$

where ω_s is the electrical rotating speed, I_{ph} is the amplitude of the winding current. Thus, based on the set phase current in (4.5), the MMF generated by stator winding can be formulated as:

$$F_s(\theta, t) = N_A(\theta) i_A(t) + N_B(\theta) i_B(\omega_s t) + N_C(\theta) i_C(t) = \sum_{K=1,3,5\ldots}^{\infty} N_k I_{ph} \cos(k\theta \pm \omega_s t) \tag{5.6}$$

Then, the magnetic flux density generated by armature reaction in the radial direction is modulated by stator teeth in the air gap also can be obtained as:

$$\begin{aligned} B_s &= F_s \Lambda_s \\ &= \sum_{k=1,3,5\ldots}^{\infty} N_k I_{ph} \Lambda_{s0} \cos(k\theta \pm \omega_s t) + \frac{1}{2} \sum_{k=1,3,5\ldots}^{\infty} \sum_{j=1,2,3\ldots}^{\infty} N_k I_{ph} \Lambda_{sj} \cos[(k + jN_s)\theta \pm \omega_s t] \\ &\quad + \frac{1}{2} \sum_{k=1,3,5\ldots}^{\infty} \sum_{j=1,2,3\ldots}^{\infty} N_k I_{ph} \Lambda_{sj} \cos[(k - jN_s)\theta \pm \omega_s t] \end{aligned} \tag{5.7}$$

Thus, the modulated harmonics from armature reaction with the order of $k \pm jN_s$. The positive and negative values represent the rotor rotating in the same or reversed directions.

Therefore, two rotors with different pole pair numbers p_1 and p_2 realise the CR operation by a shared stator armature winding has to meet the relationship as:

$$p_1 - jN_s = -p_2 \tag{5.8}$$

In this case, two working harmonic orders always rotate in opposite directions after the magnetic field modulation. The 12s10p and 12s14p slot pole number combinations are taken as an example. Fig. 5.5a shows the air gap flux density generated by the stator winding of the 12s10p and 12s14p SRPM machines (Fig. 5.2). The corresponding working harmonic order is shown in Fig. 5.5b.

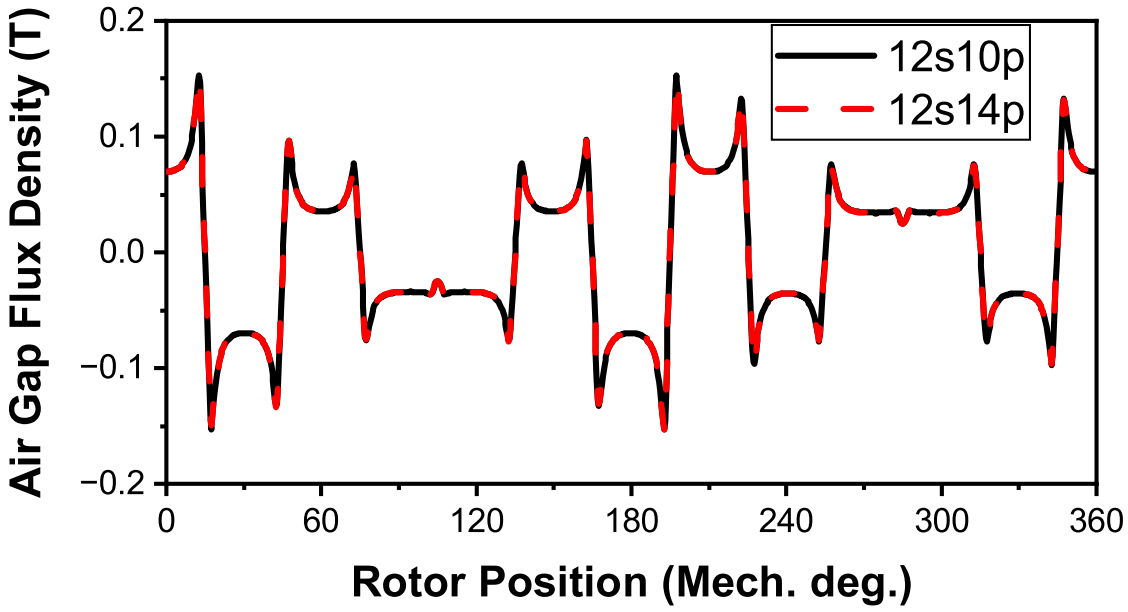

(a) Waveform.

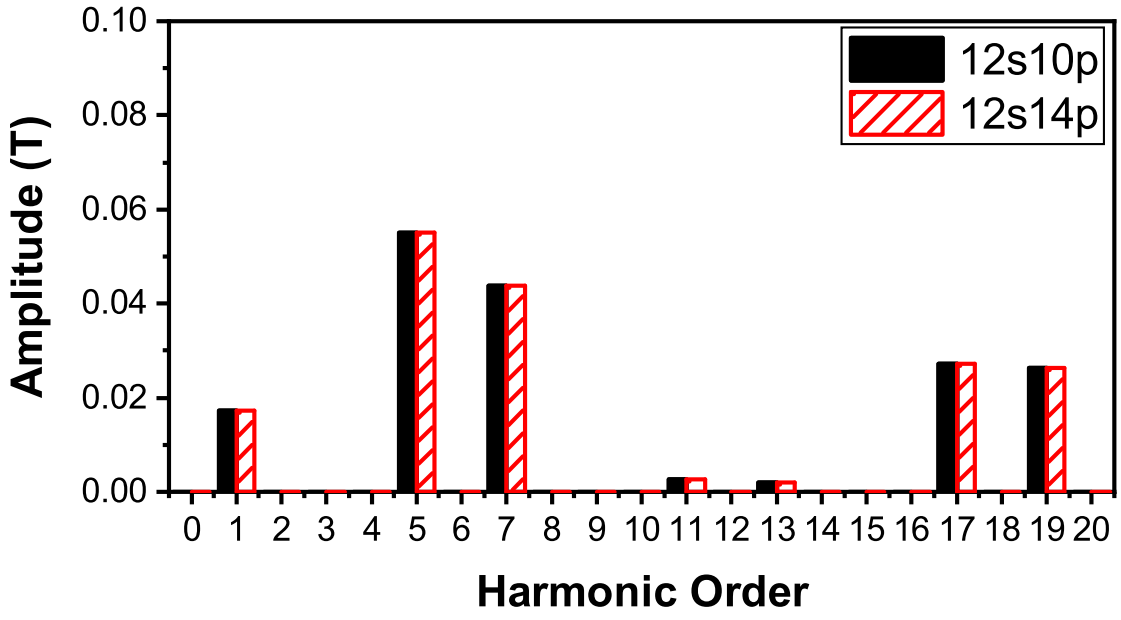

(b) Spectra.

Fig. 5. Air gap flux density generated by armature reaction of 12s10p and 12s14p SRPM machines.

From formula (5.3), the working harmonic order generated by the rotor PM from 10p rotor is:

$$Working\ Harmonic\ Order = 5i \pm 12j = \begin{cases} 5, 17, \dots \\ -7, -19, \dots \end{cases} \tag{5.9}$$

The 7th-order harmonic is counter-rotating with the 5th-order harmonic. As Fig. 5.5 shows, the armature reaction of the stator winding arrangements of 12s10p and 12s14p machines can drive both 10p and 14p rotors, but only rotational directions are different. Therefore, in the CSDPM machine, two rotors rotate in counter directions when the 14p and 10p rotors have a shared stator and are controlled by one shared stator winding set.

5.3.3 Rotational speeds of two rotors

Since the CSDPM machine has a shared single stator and one set of stator armature winding for two rotors with different pole numbers, the rotational speeds of two rotors are determined by the frequency f of the no-load and on-load stator fluxes as follows:

$$\begin{cases} p_l = jN_s - p_h \\ n_l = -\dfrac{n_h p_h}{jN_s - p_h} \\ f = \dfrac{n_l p_l}{60} = -\dfrac{n_h p_h}{60} \end{cases} \tag{5.10}$$

where n_l is the rotational speed of the low pole number rotor, n_h is the rotational speed of the high pole number rotor, p_l is the pole pair number of the low pole number rotor, and p_h is the pole pair number of the high pole number rotor. Two rotors always rotate in counter directions.

5.3.4 Torque production

The reluctance torque of the SPM machine is neglected, and the electromagnetic torque can be calculated by:

$$T_E = \frac{3E_{ph}I_{ph}}{2\omega_r} \tag{5.11}$$

where the phase back EMF E_{ph} induced by air gap flux density generated by rotor PM can be expressed as [LI16b]:

$$
\begin{cases}
e_A(t) = -\dfrac{d}{dt}\left[r_g L_{stk}\displaystyle\int_0^{2\pi} B_r(\theta,t)N_A(\theta)d\theta\right] \\
= \displaystyle\sum_{i=1,3,5\ldots}^{\infty} \omega_r F_{PMi} r_g L_{stk}\left[\begin{array}{c} 2N_{ph}k_{\omega ip_r}\Lambda_{s0}\sin(ip_r\omega_r t) \\ + \displaystyle\sum_{j=1,2,3\ldots}^{\infty} \frac{ip_r}{jN_s \pm ip_r} N_{ph}k_{\omega(jN_s\pm ip_r)}\Lambda_{sj}\sin(ip_r\omega_r t)\end{array}\right] \\
e_B(t) = -\dfrac{d}{dt}\left[r_g L_{stk}\displaystyle\int_0^{2\pi} B_r(\theta,t)N_B(\theta)d\theta\right] \\
= \displaystyle\sum_{i=1,3,5\ldots}^{\infty} \omega_r F_{PMi} r_g L_{stk}\left[\begin{array}{c} 2N_{ph}k_{\omega ip_r}\Lambda_{s0}\sin\left(ip_r\omega_r t - k\dfrac{2\pi}{3}\right) \\ + \displaystyle\sum_{j=1,2,3\ldots}^{\infty} \frac{ip_r}{jN_s \pm ip_r} N_{ph}k_{\omega(jN_s\pm ip_r)}\Lambda_{sj}\sin\left(ip_r\omega_r t \pm k\dfrac{2\pi}{3}\right)\end{array}\right] \\
e_C(t) = -\dfrac{d}{dt}\left[r_g L_{stk}\displaystyle\int_0^{2\pi} B_r(\theta,t)N_C(\theta)d\theta\right] \\
= \displaystyle\sum_{i=1,3,5\ldots}^{\infty} \omega_r F_{PMi} r_g L_{stk}\left[\begin{array}{c} 2N_{ph}k_{\omega ip_r}\Lambda_{s0}\sin\left(ip_r\omega_r t + k\dfrac{2\pi}{3}\right) \\ + \displaystyle\sum_{j=1,2,3\ldots}^{\infty} \frac{ip_r}{jN_s \pm ip_r} N_{ph}k_{\omega(jN_s\pm ip_r)}\Lambda_{sj}\sin\left(ip_r\omega_r t \mp k\dfrac{2\pi}{3}\right)\end{array}\right]
\end{cases}
\tag{5.12}
$$

where r_g is the air gap radius, and L_{stk} is the stack length. Therefore, the average torque can be obtained by:

$$
T_{avg} = \frac{3}{2} r_g L_{stk} I_{ph} F_{PM1}\left[2N_{ph}k_{\omega p_r}\Lambda_{s0} + \sum_{j=1,2,3\ldots}^{\infty} \frac{p_r}{jN_s \pm p_r} N_{ph}k_{\omega(jN_s\pm p_r)}\Lambda_{sj}\right] \tag{5.13}
$$

where I_{ph} is the amplitude of phase current. It can be seen that both the inner and outer air gap flux densities are contributing to the electromagnetic torque.

Thus, the p_r-th and ($N_s \pm p_r$)-th order harmonics can generate electromagnetic torque. In this chapter, two rotors of the proposed machine with $p_l = N_s - p_h$, which both can generate the torque under the same armature reaction.

5.4 Design Optimisation

The CSDPM machine can be treated as a 12s10p SRPM machine combined with a 12s14p SRPM machine. Thus, to simplify the three-dimensional optimisation of the CSDPM machine, this section optimises 12s10p and 12s14p SRPM machines to maximise torque based on the two-dimensional model in FEA. The shared stator in the CSDPM machine is designed for both 10p and 14p rotors. As the pole number increases, the pole pitch is decreased. Thus, in the 12s14p SRPM machine, both the width of the stator teeth and the height of the stator yoke are thinner than those in the 12s10p SRPM machine. Thus, if

the stator is optimised for a 14p rotor but paired with a 10p rotor, the stator will encounter severe magnetic saturation issues. Therefore, for simplicity, in this section, the 12s10p SRPM machine is optimised to maximise the torque in advance. Then, the 12s14p SRPM machine only optimises the rotor structure with the stator structure of the optimised 12s10p SRPM machine. Tables 5.1 and 5.2 list the fixed and variable parameters in the optimisation process. Fig. 5.6 shows these parameters, distinguishing between variables (marked with blue symbols) and fixed parameters (marked with red symbols).

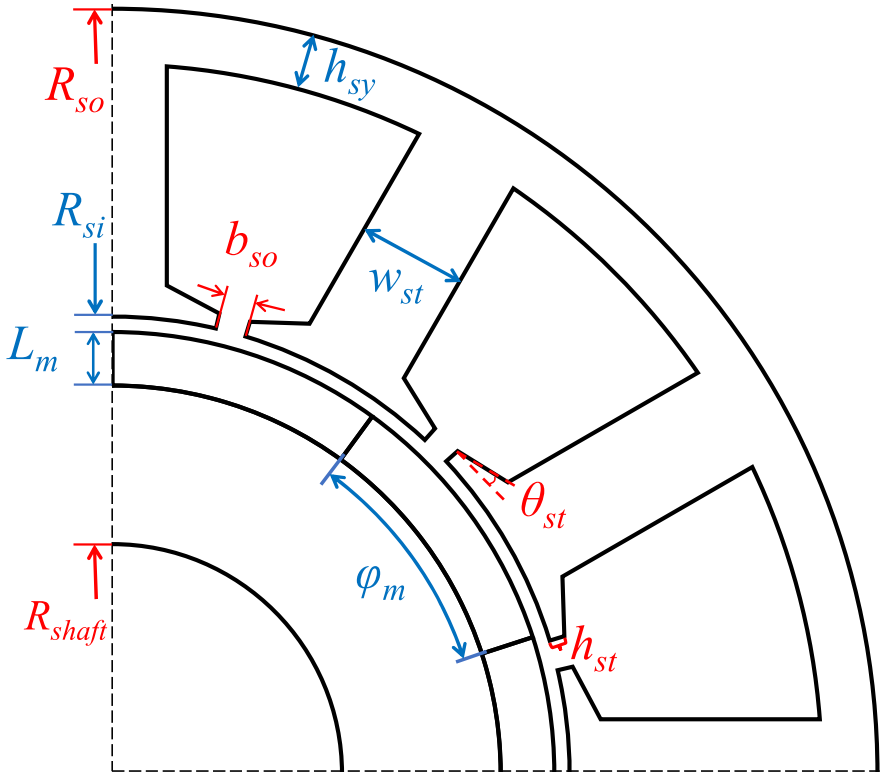

Fig. 5.6. Design parameters of internal-rotor SRPM machine. (Variable: Blue; Fixed: Red).

TABLE 5.1 FIXED PARAMETERS

Parameter	Values
Copper loss (W)	30
Slot fill factor %	35
Machine outer radius (mm)	50
Stack length (mm)	50
Tooth-tip slope (deg.)	15
Tooth-tip height (mm)	1
Stator slot opening (mm)	2
Air gap length (mm)	1
Shaft radius (mm)	15
Remanence of PM	1.2 T
Magnet relative permeability	1.05
Lamination material	M300
PM material	NdFe35

TABLE 5.2 VARIABLE PARAMETERS

Parameter	Symbols
PM thickness	L_m
PM pole arc	φ_m
Split ratio	k_s
Stator yoke height	h_{sy}
Stator tooth width	w_{st}

In addition, the end-winding length is considered during the optimisation. The end-winding configuration of double-layer FSCW SRPM machines is built by quarter-circles and straight lines [ZHU22], as shown in Fig. 5.7.

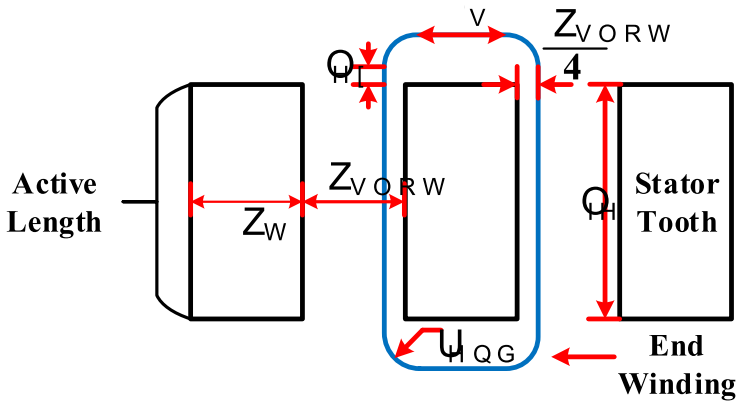

Fig. 5.7. Simplified end-winding model.

Thus, the per-turn end-winding length l_{end} can be calculated by:

$$l_{end} = 2\pi r_{end} + 4l_{ex} + 2l_s \tag{5.11}$$

The optimised parameters for both machines are listed in Table 5.3. Fig. 5.8 shows the open-circuit flux density distributions and flux lines for both machines. Since the 12s14p machine uses the same stator structure as the optimised 12s10p machine. The magnetic saturation on the stator of the 12s14p machine is less.

TABLE 5.3 Designs of Optimised Machines

Parameter	12s10p	12s14p
PM thickness (mm)	3.5	3.5
PM pole arc (elec. deg.)	180	180
Split ratio	0.58	
Stator tooth width (mm)	7.2	
Stator yoke thickness (mm)	3.6	
PM volume (mm^3)	30	
Input current (A)	5.2	

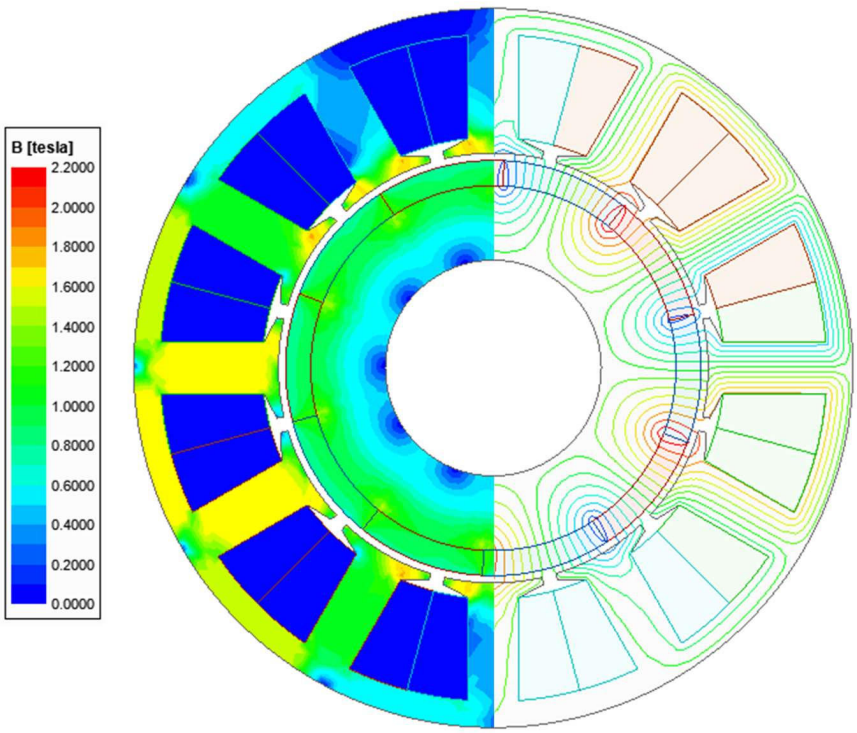

(a) 12s10p.

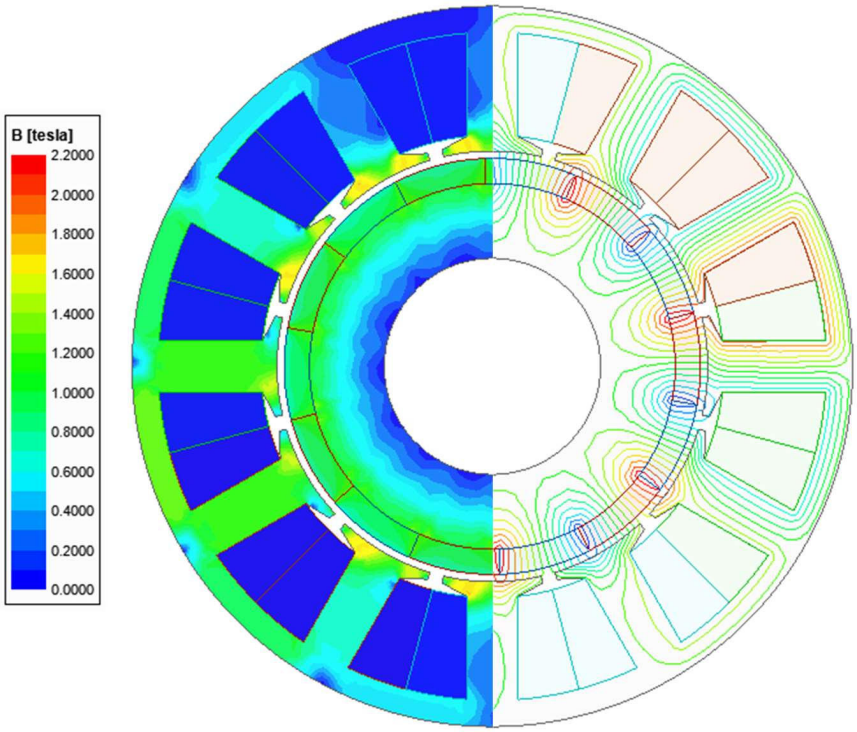

(b) 12s14p.

Fig. 5.8. Open circuit flux density and flux line distributions of SRPM machines.

Then, the CSDPM machine is assemblied by using the optimised 12s10p and 12s14p machines. The two rotors of the CSDPM machine rotate in different directions and speeds, so they are fixed on different shafts. Bearings 1 and 3 are fixed on two endcaps separately to support the corresponding rotor. Bearing 2

is embedded in shaft 1 to connect two shafts to avoid eccentricity and enhance the mechanical strength of the machine. The radial magnetic forces on the rotors are balanced, and thus, one rotor is not affected by another rotor by the shaft connection. To avoid the frictional contact between two rotors which rotate in opposite directions, an additional air gap is introduced between the 10p and 14p rotors, as shown in Fig. 5.9. The stack lengths of two rotors can be equal or unequal. In the next section, the case of equal stack lengths of two rotors is investigated first, and then the effect of the stack length on torque split is analysed.

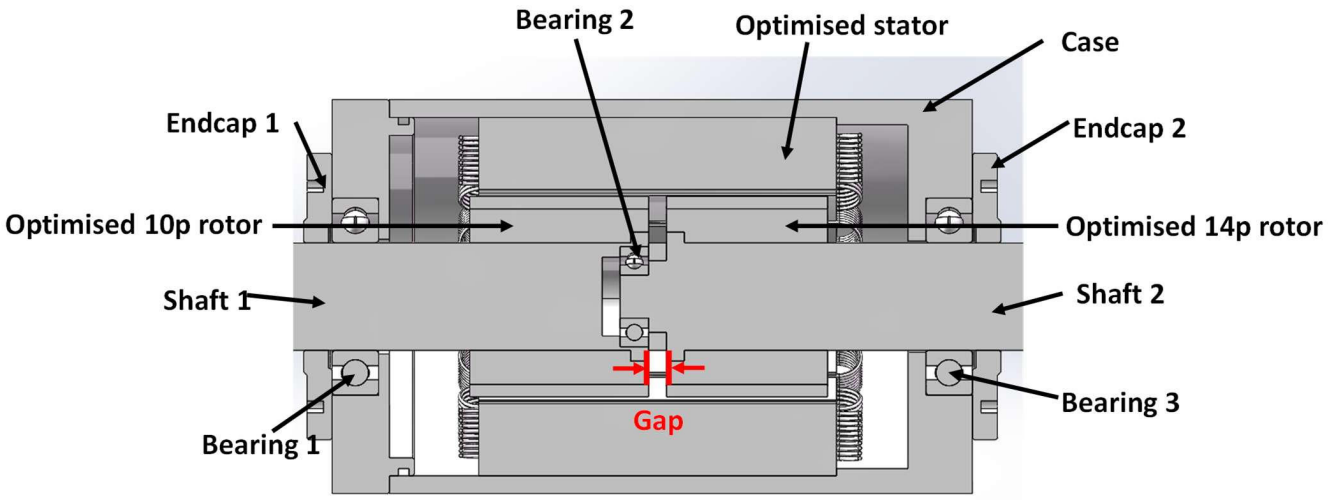

Fig. 5.9. Assembly structure of CSDPM machine.

Therefore, two designs are considered when the gap is introduced between two rotors.

1) In the first design, referred to as the CSDPM-FS machine, the additional gap between two rotors is accommodated by reducing the stack lengths of both rotors equally, with the stator stack length fixed at 100mm.

2) In the second design, referred to as the CSDPM-FR machine, the additional gap between two rotors is accommodated by extending the stator stack length, with each rotor stack length fixed at 50mm.

The design parameters of the CSDPM machines are listed in Table 5.4. The gap between two rotors in two design scenarios is considered the same at 5mm for further analysis. The open-circuit flux density distributions of CSDPM-FS and -FR machines are shown in Fig. 5.10.

TABLE 5.4
DESIGN PARAMETERS

Parameter	CSDPM-FS	CSDPM-FR
Stator stack length (mm)	100	105
Two rotors stack length (mm)	47.5	50
Gap length between two rotors (mm)	5	
Machine outer radius (mm)	50	
Two rotors PM thickness (mm)	3.5	
Two rotors PM pole arc (elec. deg.)	180	
Split ratio	0.58	
Stator tooth width (mm)	7.2	
Stator yoke thickness (mm)	3.6	
Tooth-tip slope (deg.)	15	
Tooth-tip height (mm)	1	
Stator slot opening (mm)	2	
Air gap length (mm)	1	
Shaft radius (mm)	15	

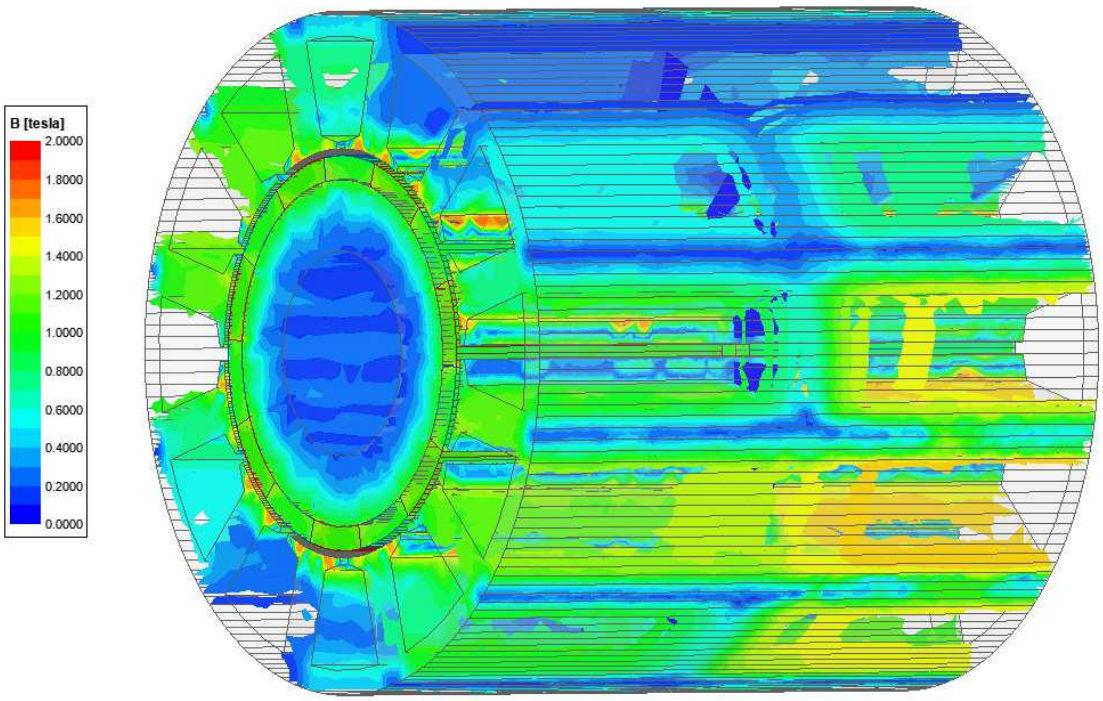

(a) CSDPM-FS.

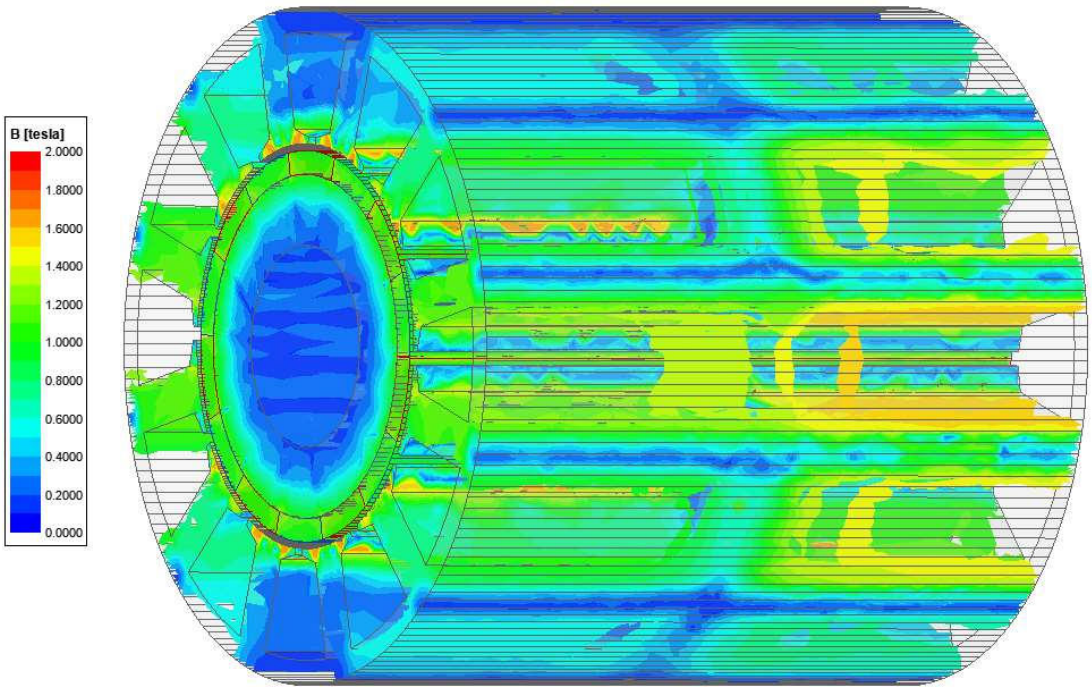

(b) CSDPM-FR.

Fig. 5.10. Open circuit flux density distributions of CSDPM machines.

5.5 Comprehensive Analysis of Electromagnetic Performance of CSDPM Machines

The electromagnetic performances of CSDPM-FS and -FR are investigated and compared in this section based on the three-dimensional FEA.

5.5.1 No-load

Fig. 5.11 shows the air gap flux densities of the CSDPM-FS and -FR machines. The scanning of air gap flux densities of the CSDPM-FS and -FR machines are shown in Fig. 5.12 and 5.13, respectively. This can be seen from radial, tangential, and axial air gap flux density components. The flux density almost dropped to zero in the position of the gap between the two rotors of both CSDPM-FS and -FR machines.

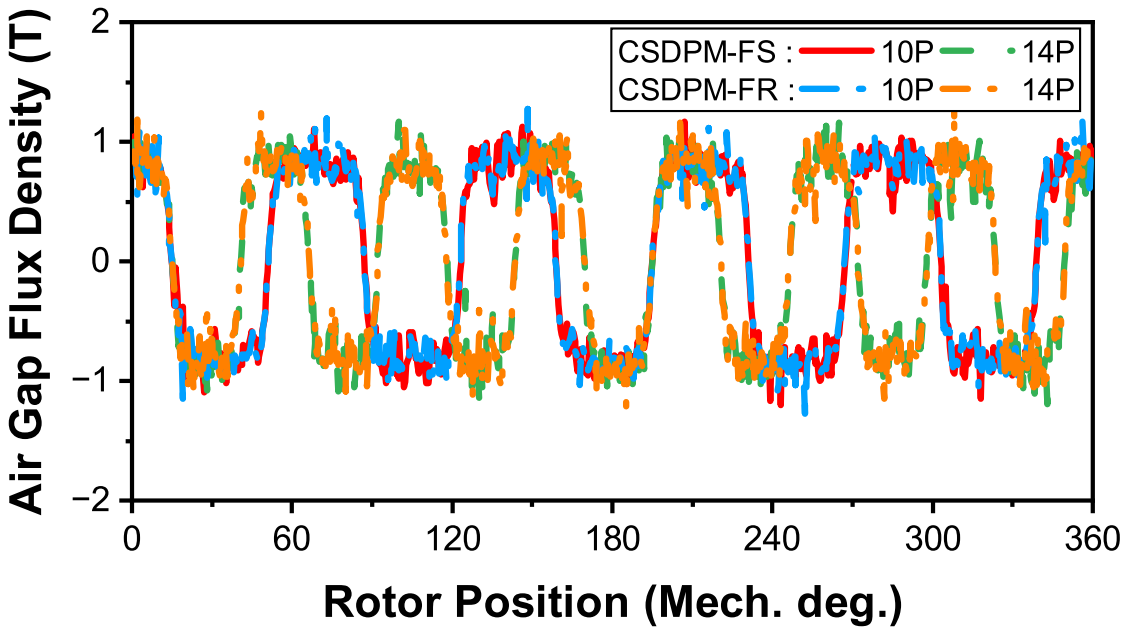

(a) Waveforms.

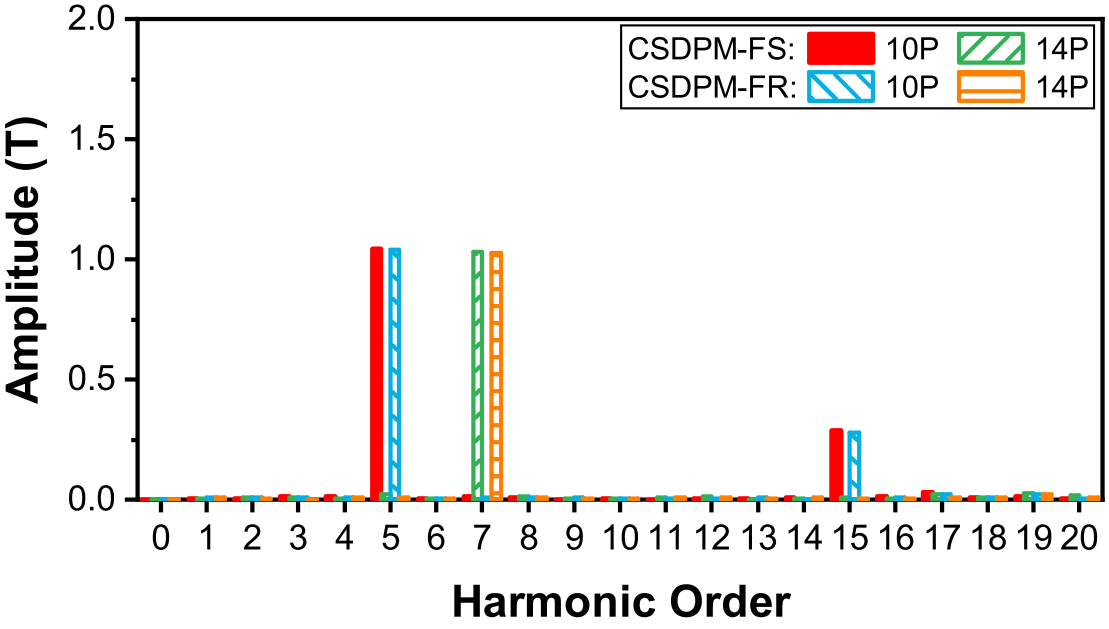

(b) Spectra.

Fig. 5.11. Comparison of air gap flux densities of CSDPM-FS and -FR machines.

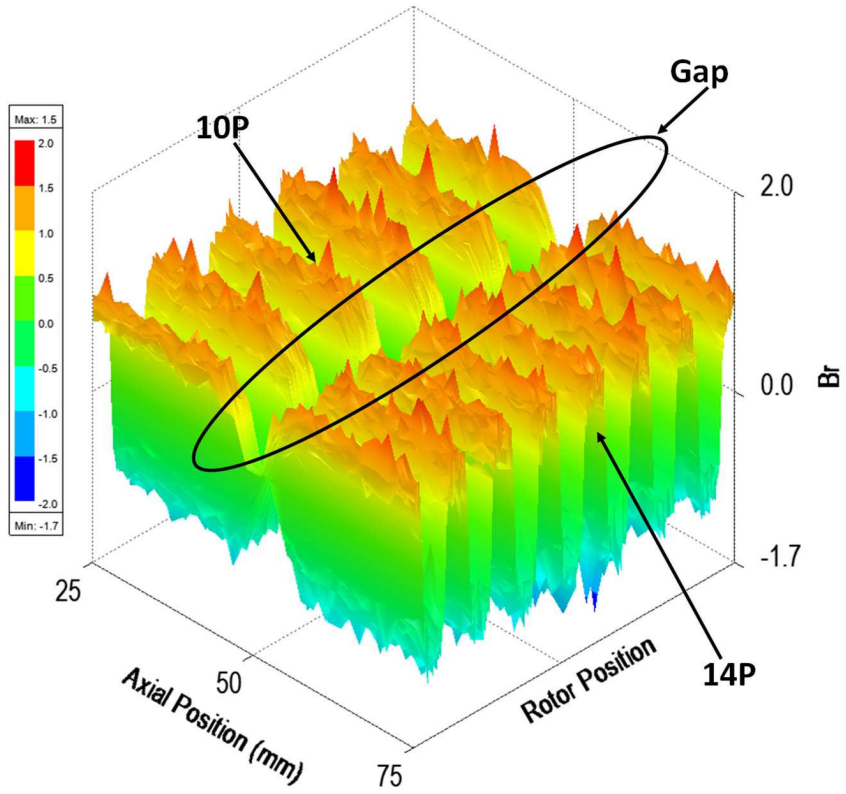

(a) Radial component.

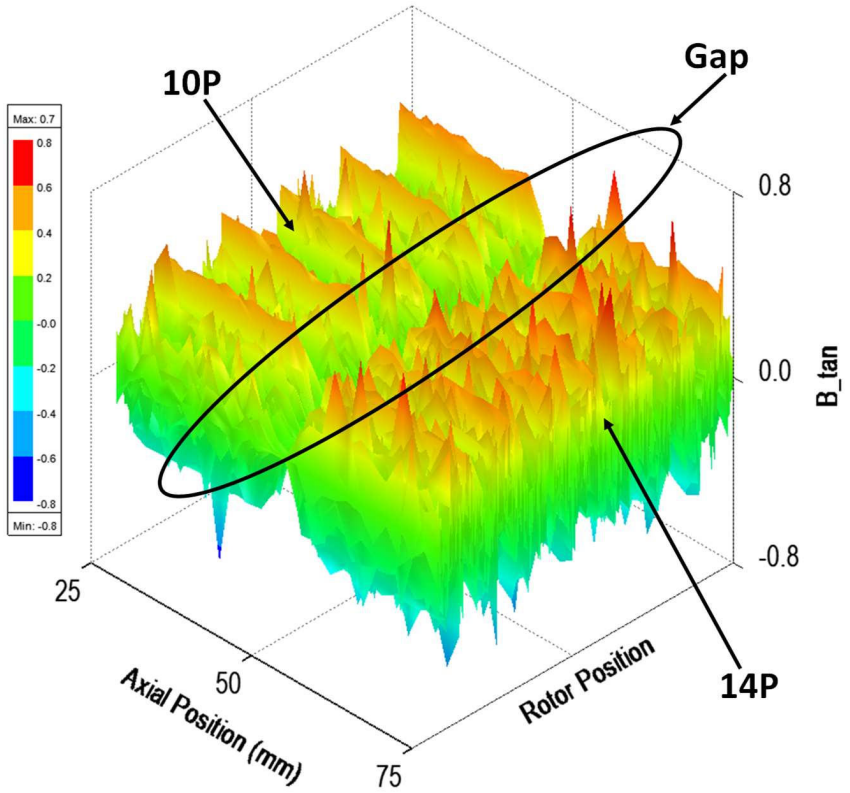

(b) Tangential component.

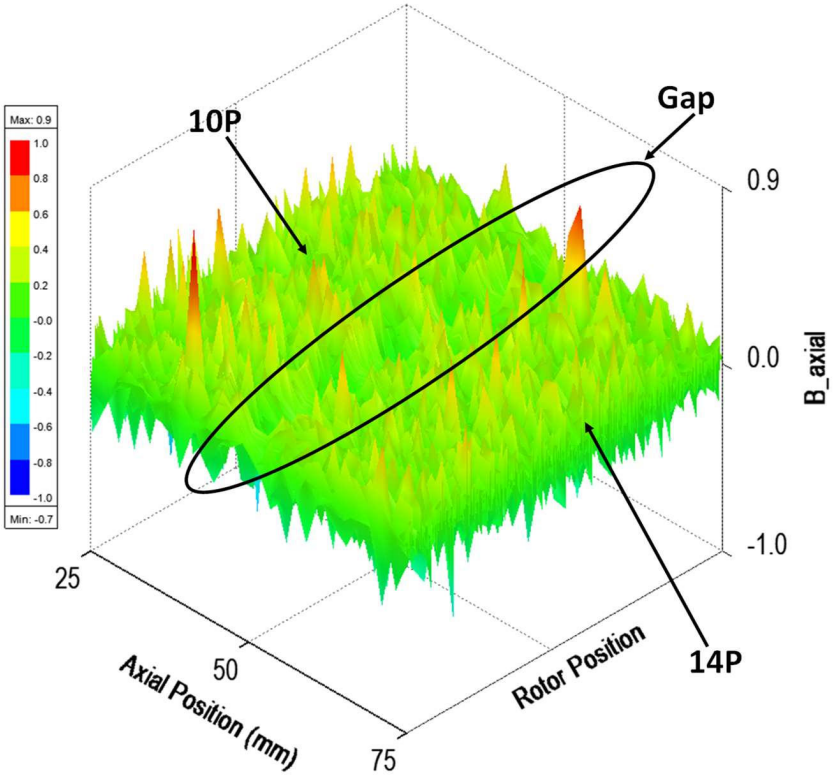

(c) Axial component.

Fig. 5.12. Air gap flux density scanning of CSDPM-FS machine.

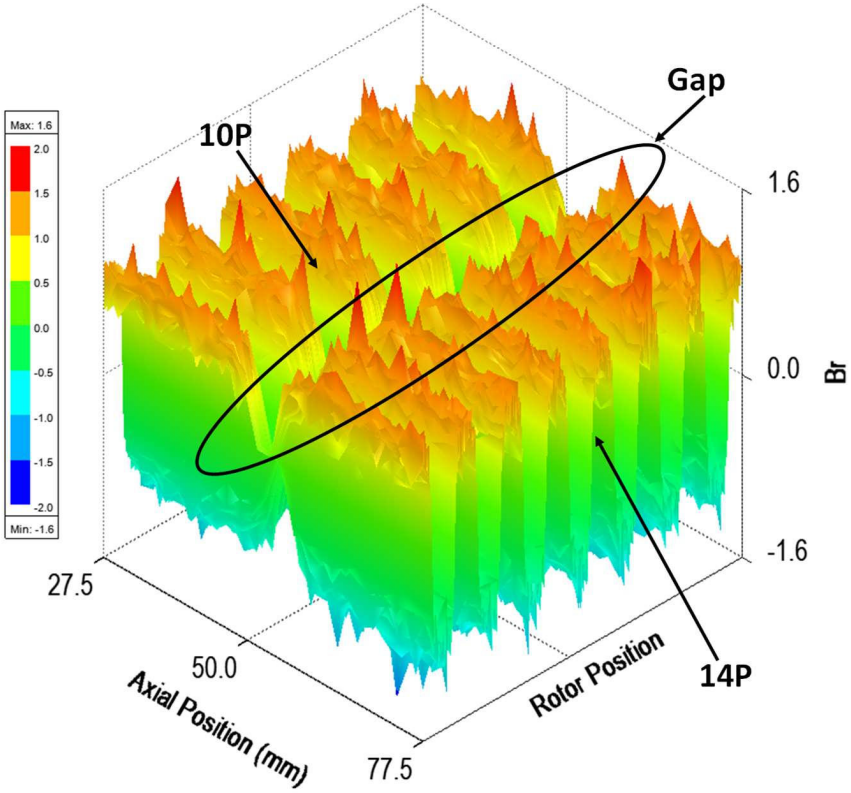

(a) Radial component.

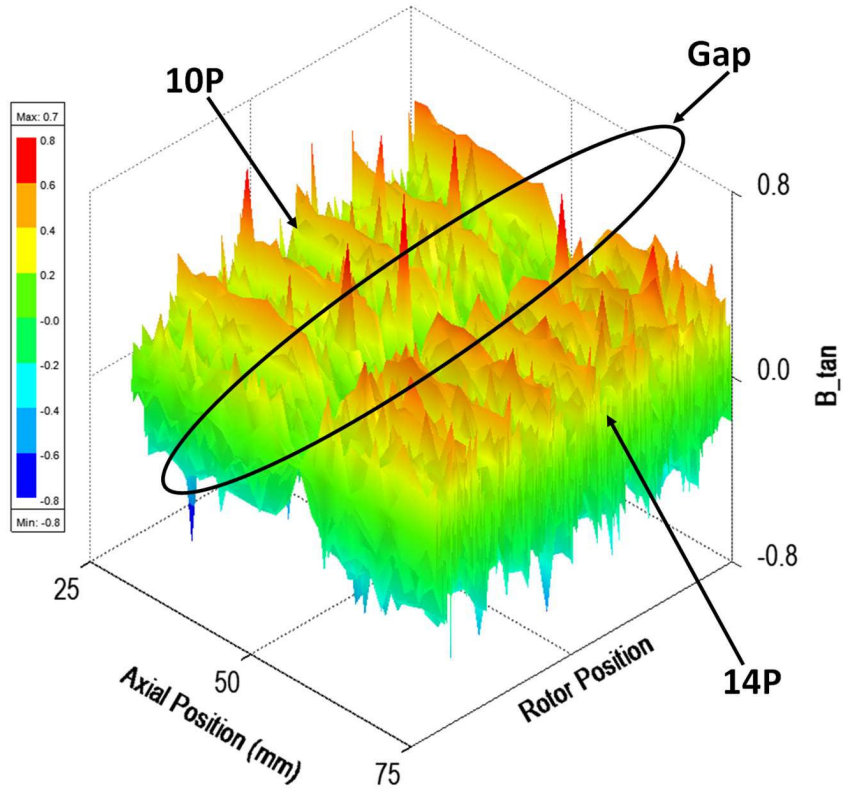

(b) Tangential component.

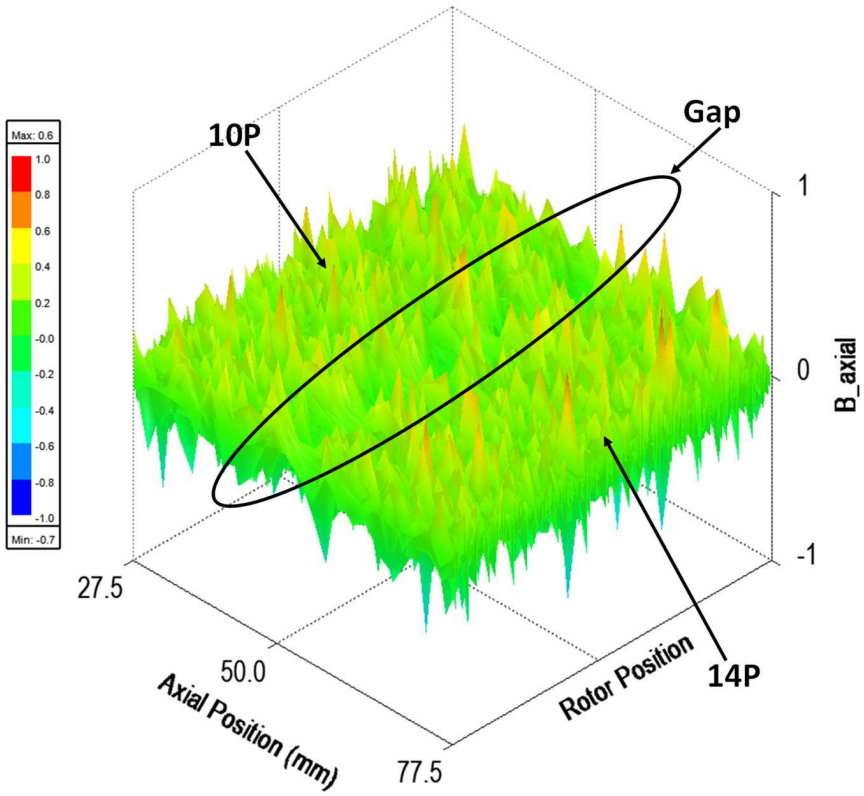

(c) Axial component.

Fig. 5.13. Air gap flux density scanning of CSDPM-FR machine.

Since the air gap flux densities of CSDPM-FS and -FR are similar. The CSDPM-FR machine is selected to analyse the radial, tangential, and axial components of air gap flux densities at the gap between the two rotors in detail, as shown in Fig. 5.14. The spectra show that the air gap flux density in the gap between two rotors mainly contains small 5th and 7th-order components from 10p and 14p rotors due to the end flux leakage.

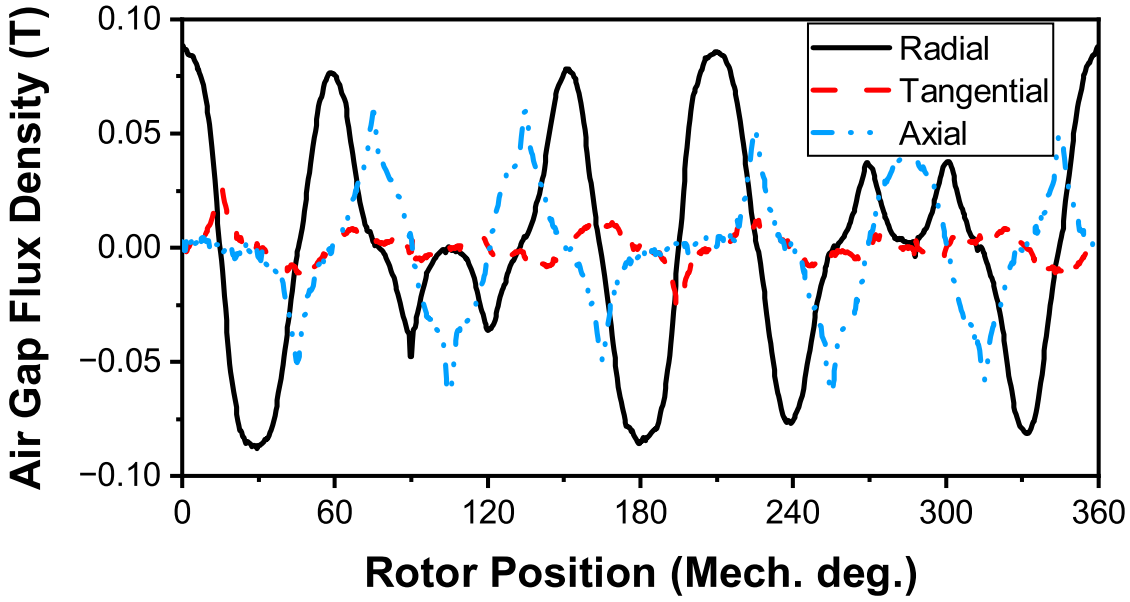

(a) Waveforms.

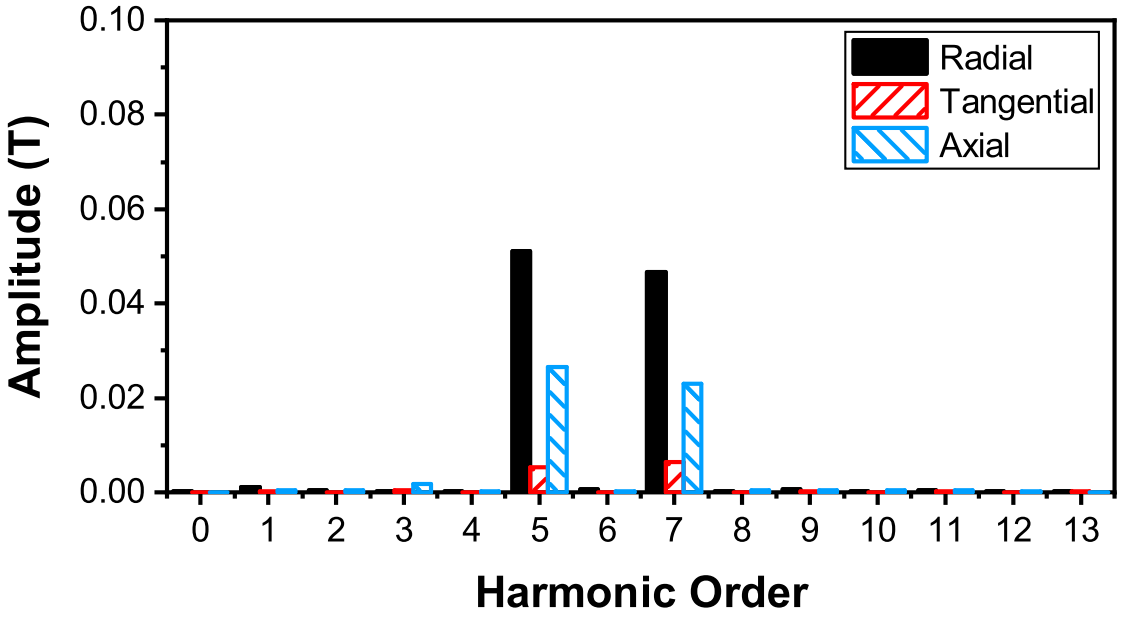

(b) Spectra.

Fig. 5.14. Air gap flux density of CSDPM-FS machine at gap between two rotors.

The flux linkages and back EMFs of CSDPM-FS and -FR machines are shown in Fig. 5.15 and 5.16, respectively. The total flux linkage and back EMF are superimposed by those generated by 10p and 14p rotors separately. In the CSDPM-FR machine, the rotor stack length is fixed at 50mm. The stator stack length of the CSDPM-FR is 105mm, which is longer than that of the CSDPM-FS machine. The flux linkage and related back EMF of the CSDPM-FR machine are higher than those of the CSDPM-FS machine.

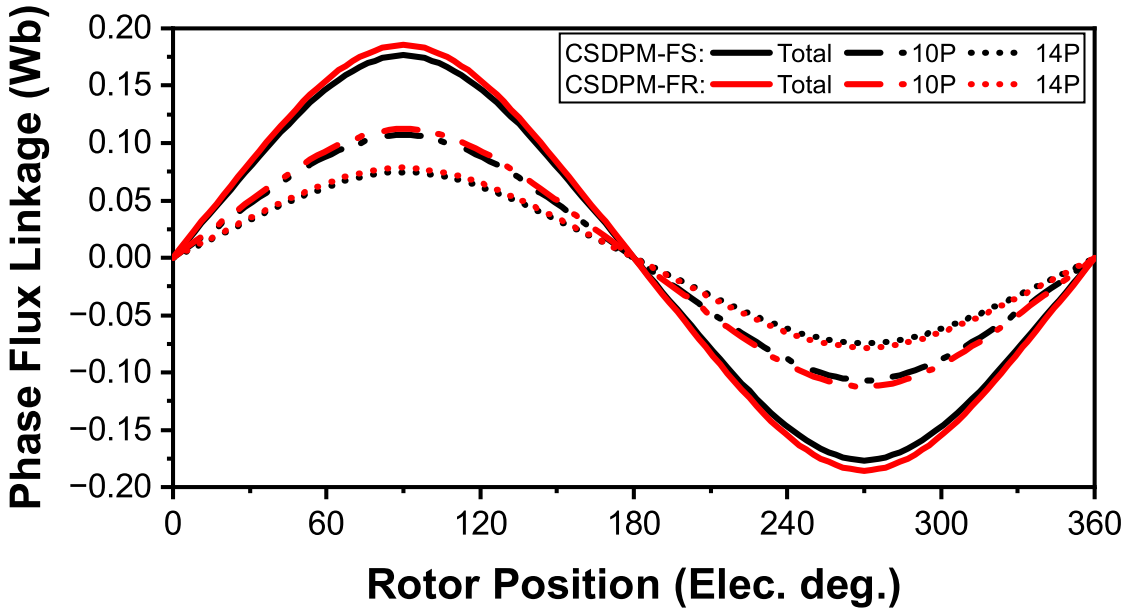

(a) Waveforms.

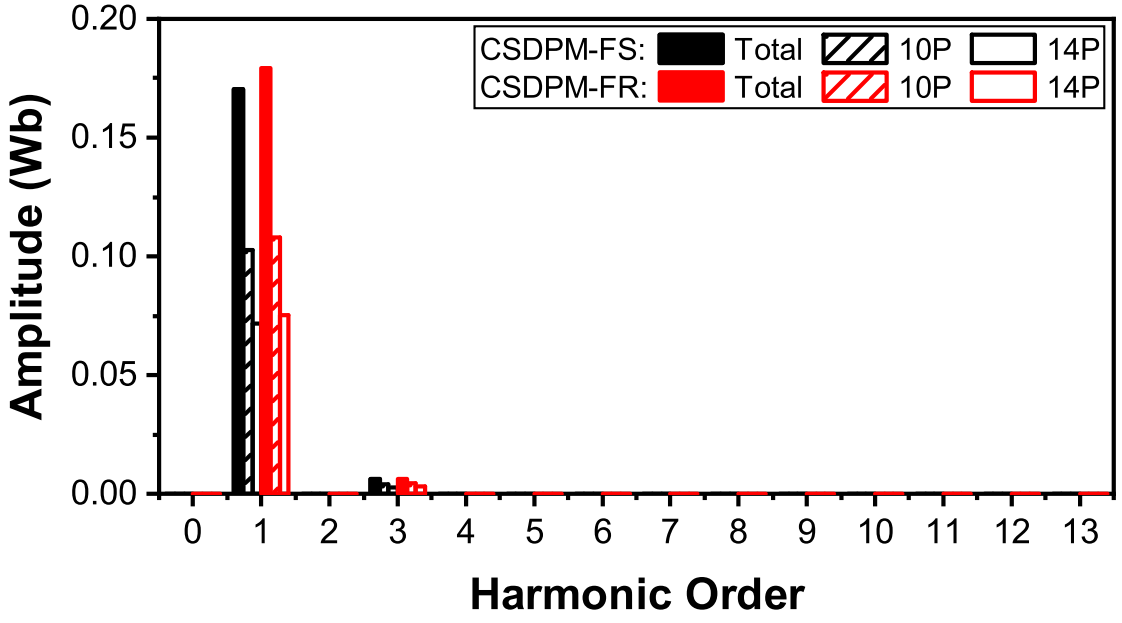

(b) Spectra.

Fig. 5.15. Comparison of phase-A flux linkages of CSDPM-FS and -FR machines.

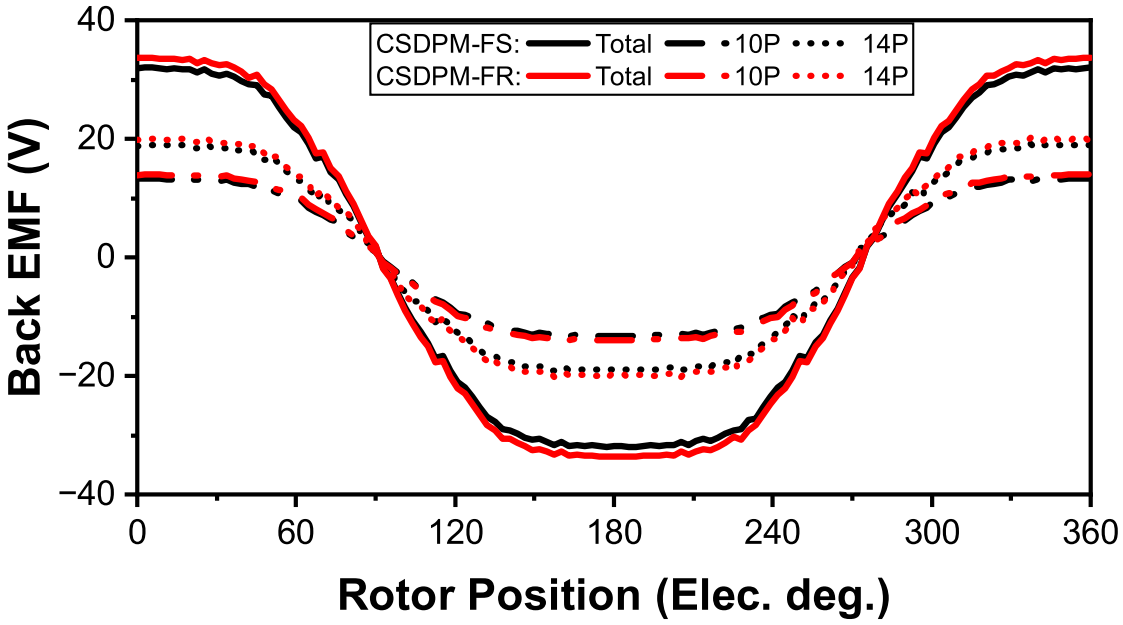

(a) Waveforms.

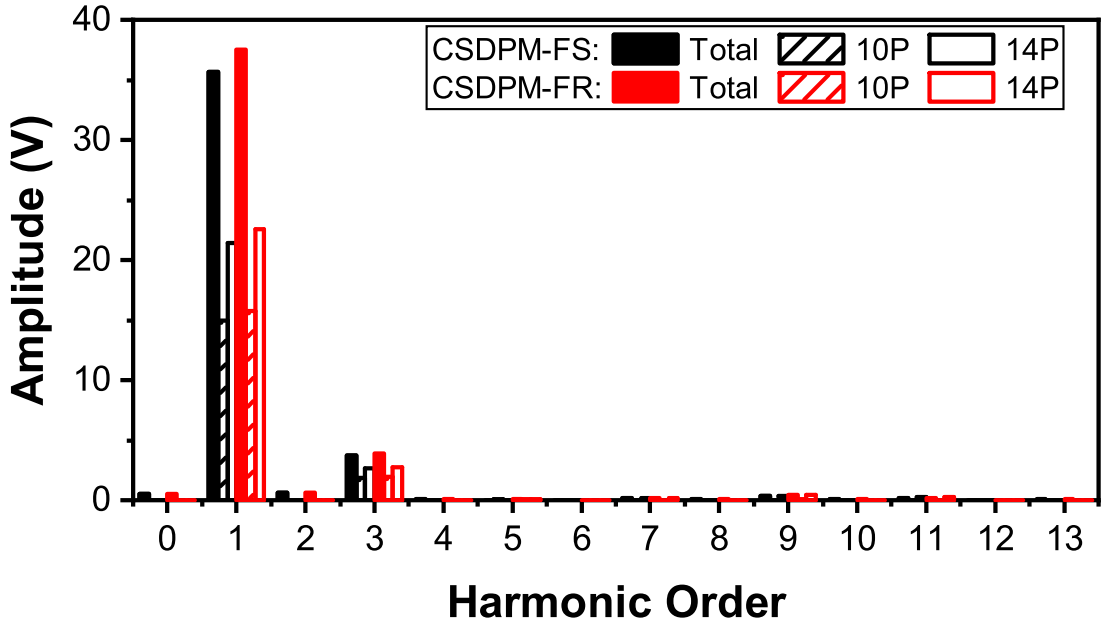

(b) Spectra.

Fig. 5.16. Comparison of back EMFs of CSDPM-FS and -FR machines (n_{10p}=400rpm, n_{14p}=2000/7rpm).

5.5.2 On-load

There are two on-load conditions are considered when the CSDPM machine compared with the SRPM machines.

1) The amplitude of the input current of the CSDPM machine is the same as the optimised SRPM

machine, 5.2A.

2) The copper losses of the CR operation systems using one CSDPM machine or two SRPM machines are the same, 60W.

Fig. 5.17 shows the torques of the CSDPM and SRPM machines. In the first scenario, the machines have the same input current. Since L_{gap}= 5mm, the stack length of each rotor is reduced by 2.5mm in the CSDPM-FS machine. The output torques of the CSDPM-FS machine are smaller than those of the SRPM machines. The torques of the CSDPM-FR machine are similar to those of the SRPM machines.

In the second scenario, the CR operation systems have the same copper losses using one CSDPM machine or two SRPM machines. The CSDPM machine has only one stator armature winding set, which saved one set of end-winding compared with two SRPM machines. Thus, the CSDPM-FR and -FS machines have higher torque compared with SRPM machines in this scenario.

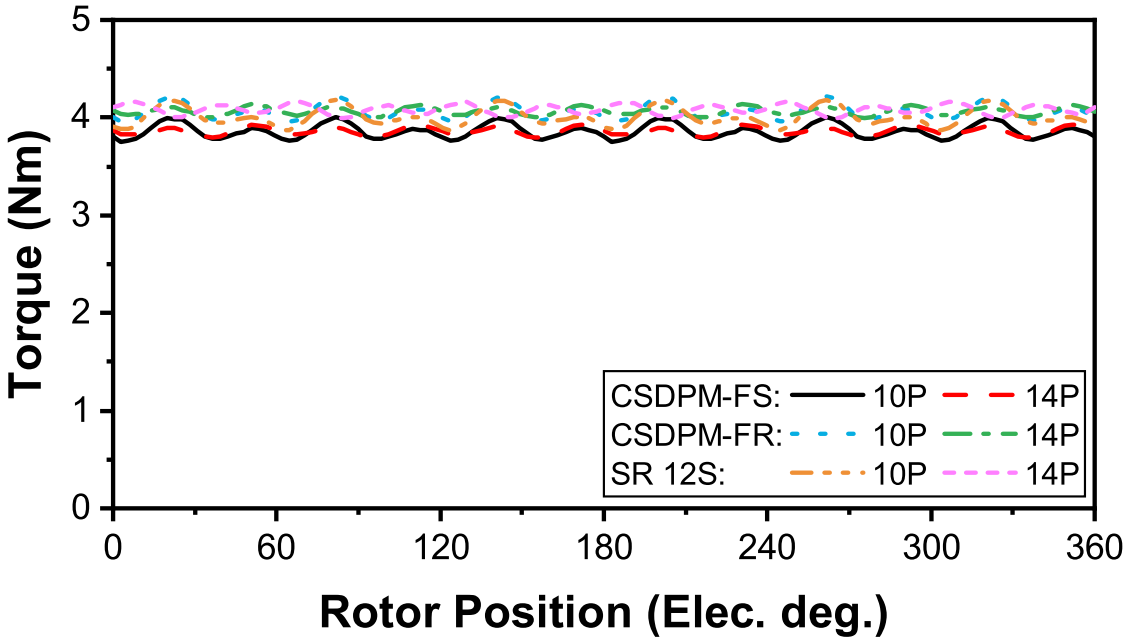

(a) Amplitude of input current=5.2A. Waveforms.

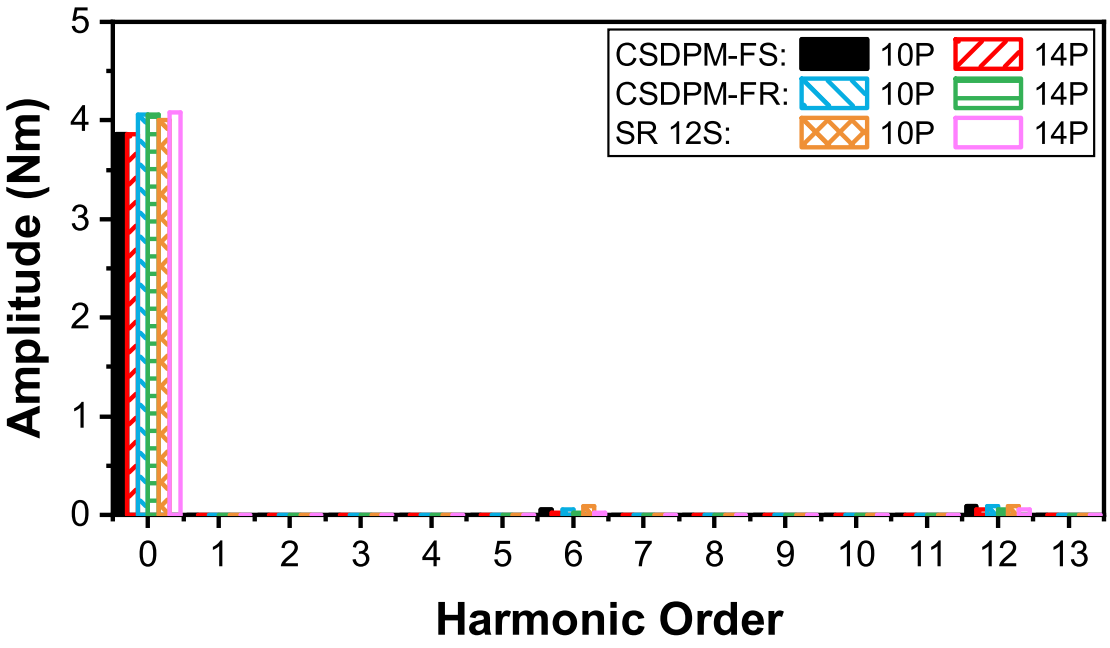

(b) Amplitude of input current=5.2A. Spectra.

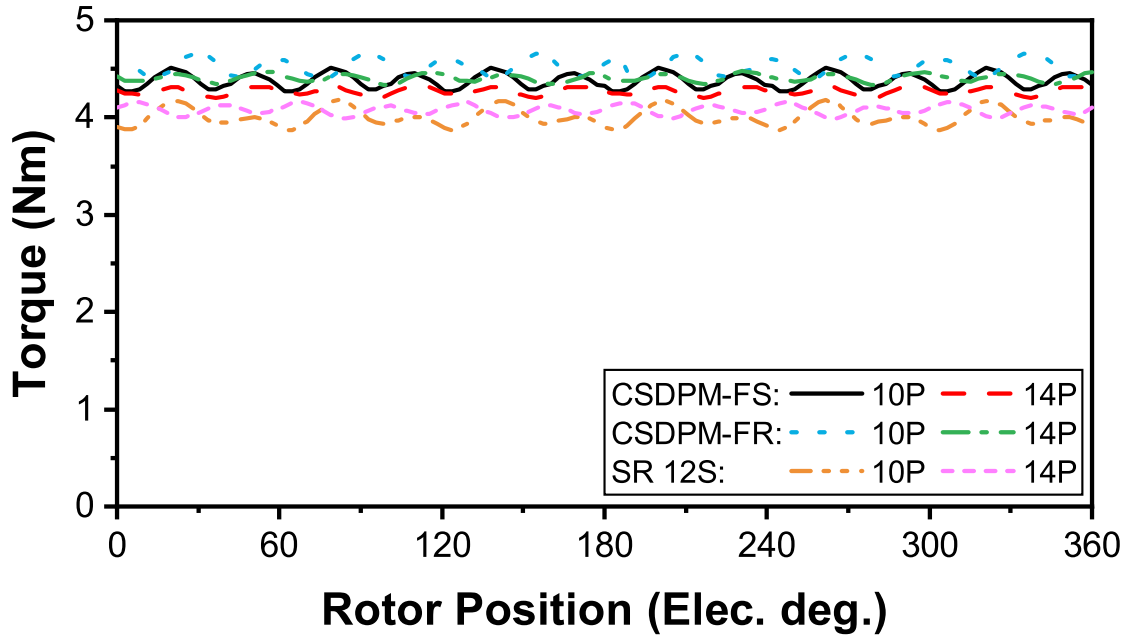

(c) CR system copper loss=60W. Waveforms.

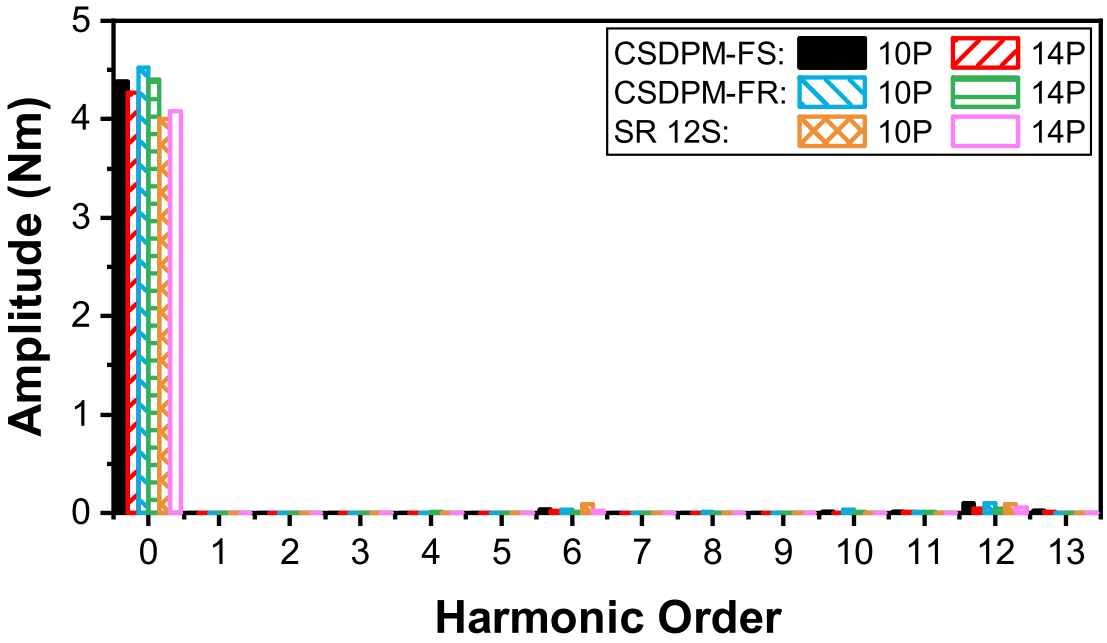

(d) CR system copper loss=60W. Spectra.

Fig. 5.17. Comparison of torques of CSDPM-FS and -FR machines with SRPM machines.

5.5.3 Magnetic coupling

The magnetic coupling between two rotors in CSDPM machines is analysed in this section. The torques of different rotors in CSDPM machines are compared under different magnetising conditions for each rotor when the input current is 5.2A, as shown in Fig. 5.18. It can be seen that the magnetisation state of the PMs on each rotor has no effect on the torque of the other rotor in the CSDPM machine. Since two rotors in the CSDPM machine are axially arranged, there is no overlapped space between the two rotors in the magnetisation direction. Thus, there is no magnetic coupling between the two rotors in the CSDPM machine.

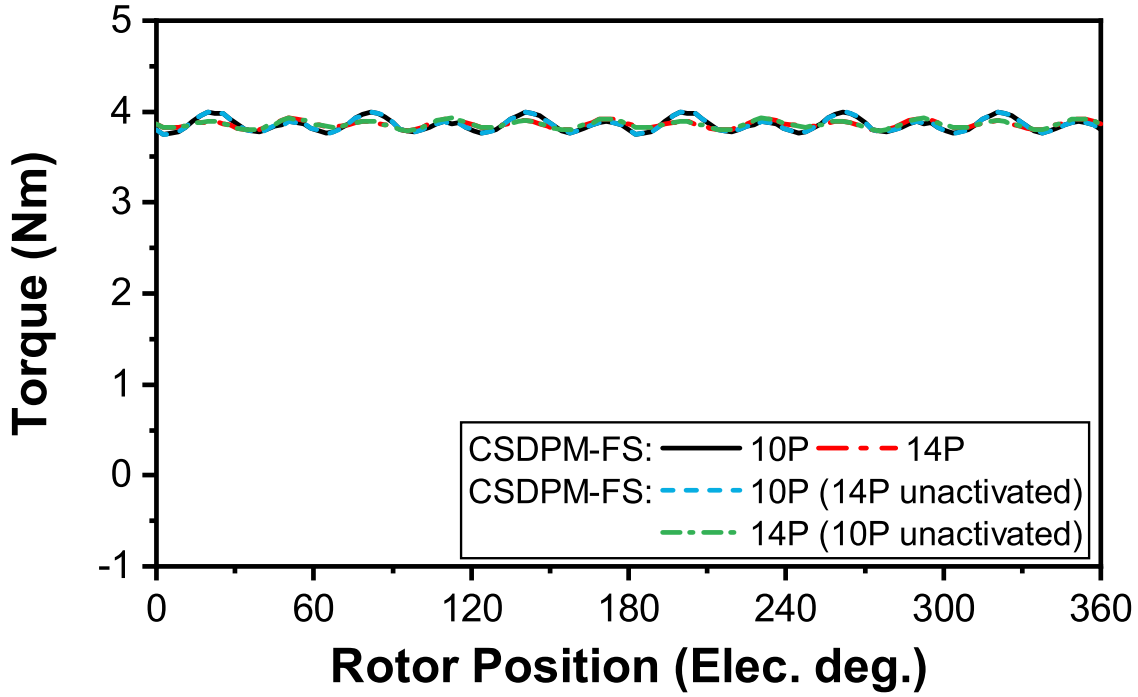

(a) CSDPM-FS. Waveforms.

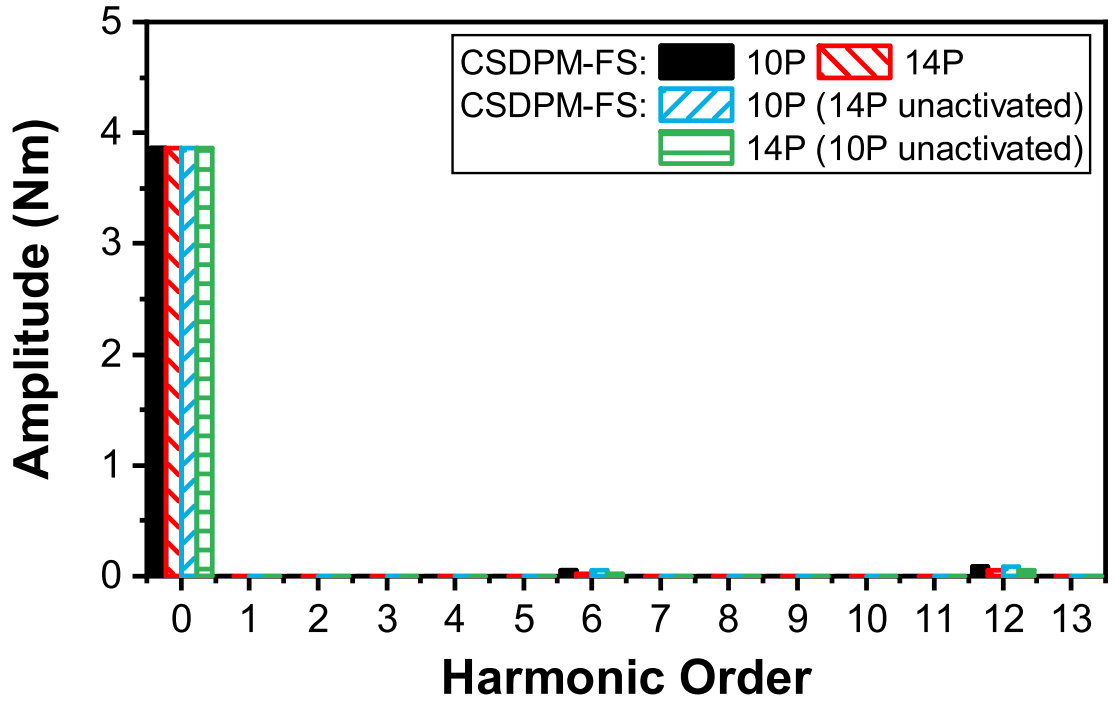

(b) CSDPM-FS. Spectra.

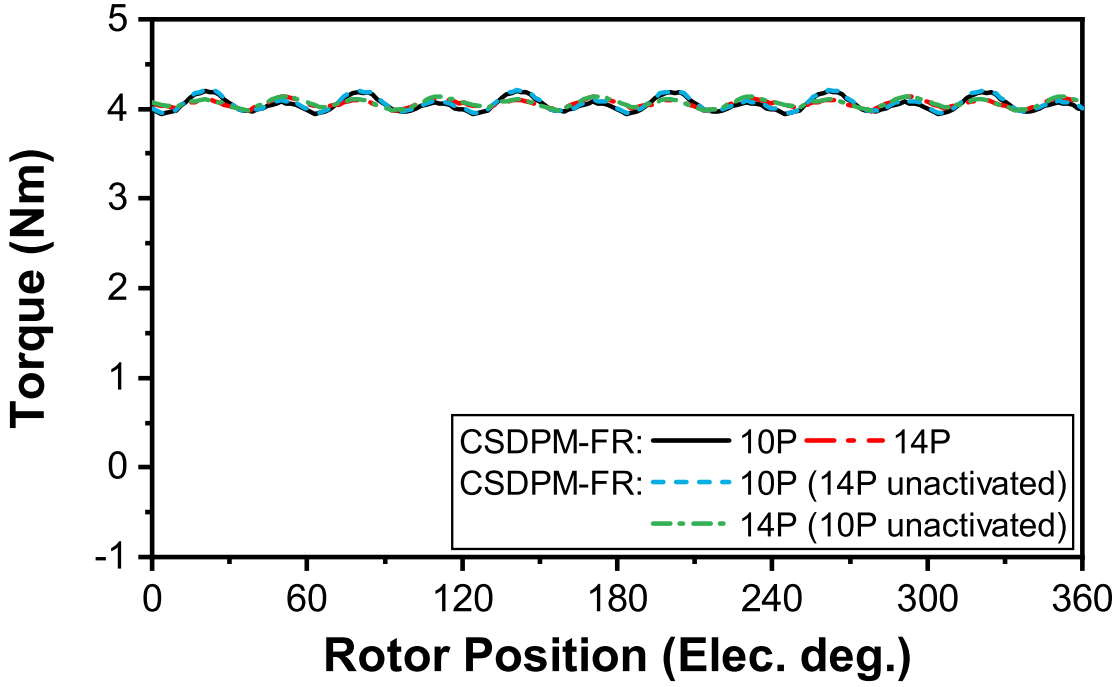

(c) CSDPM-FR. Waveforms.

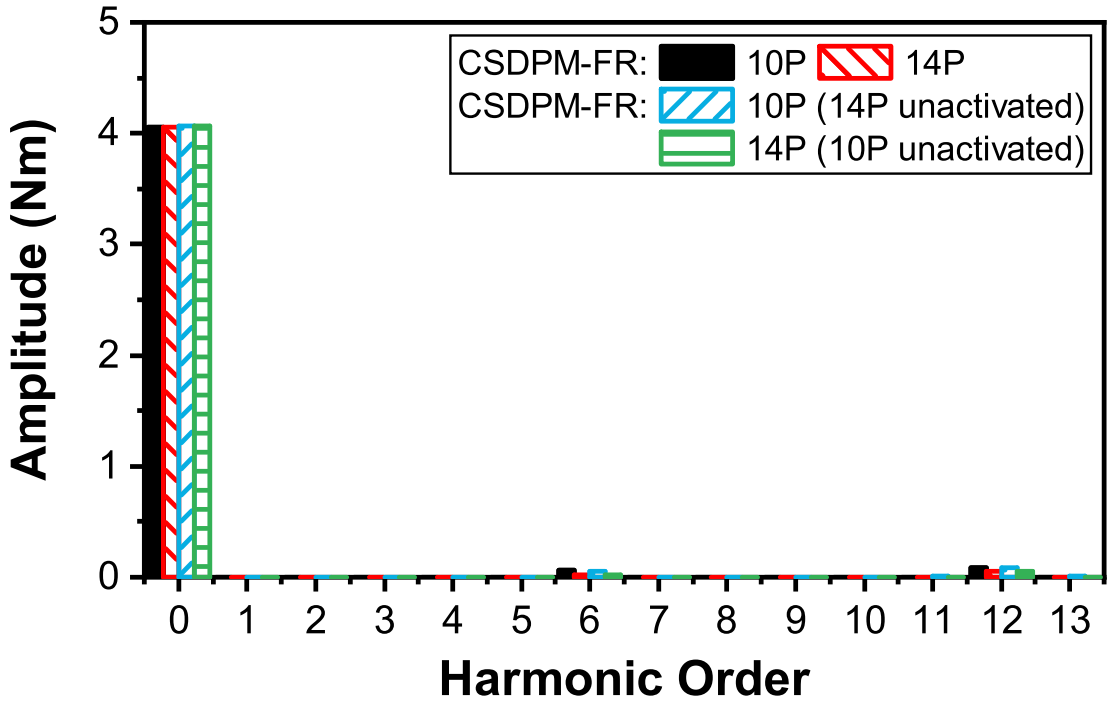

(d) CSDPM-FR. Spectra.

Fig. 5.18. Comparison of torques of CSDPM machines with different magnetisation state.

5.5.4 Torque split

The torque split of two rotors in the CSDPM machine can be easily changed with the stack length of the corresponding rotor, as shown in Fig. 5.19.

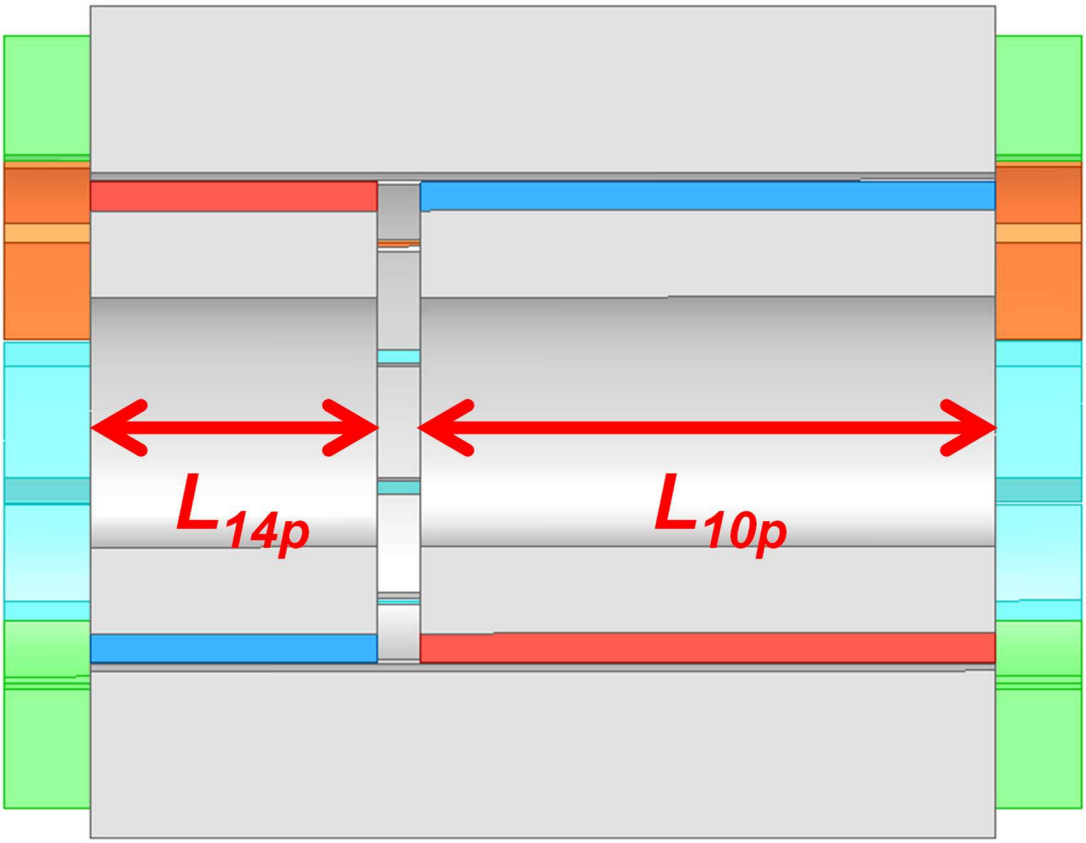

Fig. 5.19. Stack lengths of two rotors in CSDPM machine.

The ratio K_L and K_T between stack lengths and torques of two rotors are defined as:

$$K_L = \frac{L_{10}}{L_{14p}} \tag{5.12}$$

$$K_T = \frac{T_{10p}}{T_{14}} \tag{5.13}$$

where L_{10p} is the stack length of the 10p rotor, L_{14p} is the stack length of the 14p rotor, T_{10p} is the torque of the 10p rotor, and T_{14p} is the torque of the 14p rotor. The torque ratio K_T varied with stack length ratio K_L of the CSDPM machines are shown in Fig. 5.20.

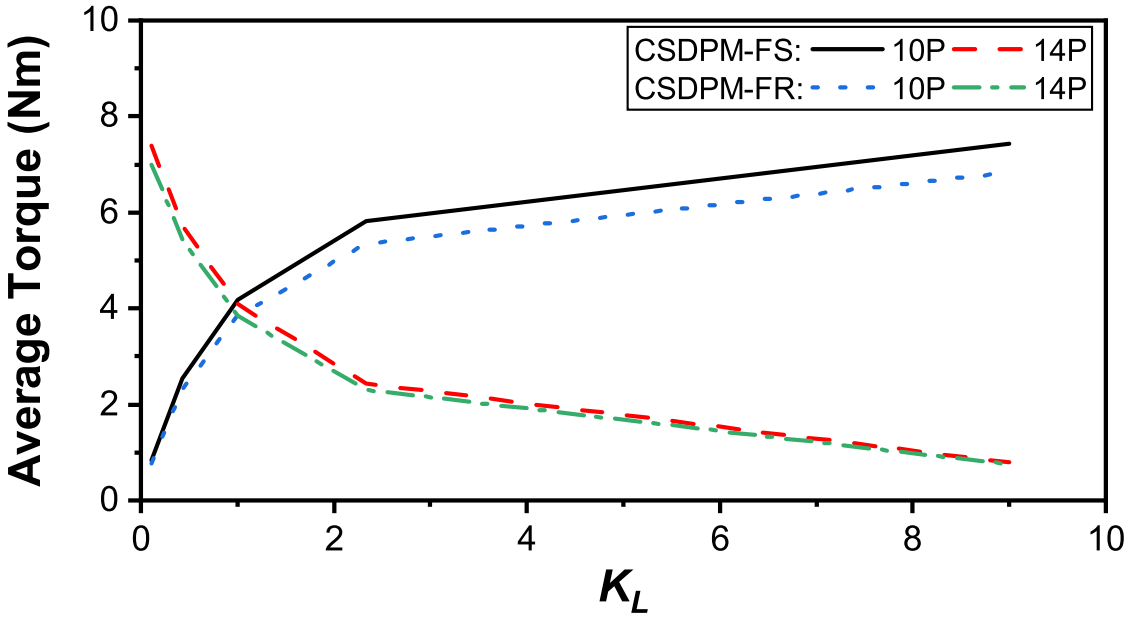

(a) Average torque vs. K_L.

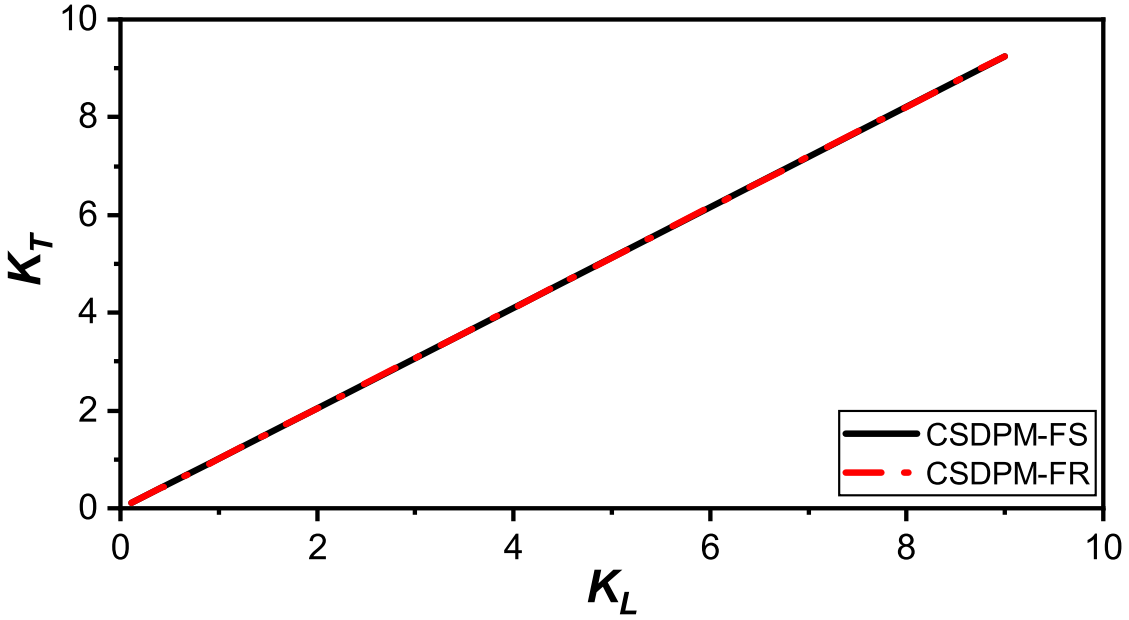

(b) K_T vs. K_L of CSDPM machines.

Fig. 5.20. Torque split.

5.6 Investigation of CSDPM Machine with Different Slot Pole Number Combinations

As mentioned in section 5.3, the slot pole number combination of the proposed CSDPM machine needs to satisfy the relationship as $N_s=p_l+p_h$ to realise the CR operation. Therefore, this section

investigates CDSPM machines with the same slot number, 12 slots, but different pole numbers, i.e., FSCW 12 slots-8/16 poles (12s8/16p) and ISDW 12 slots-4/20 poles (12s4/20p). The CDSPM-FR machine is selected for further analysis because it has higher torque than the CDSPM-FS machine. The 12s8/16p and 12s4/20p CDSPM-FR machines and corresponding coil back EMF phasors are shown in Fig. 5.21 and Fig. 5.22.

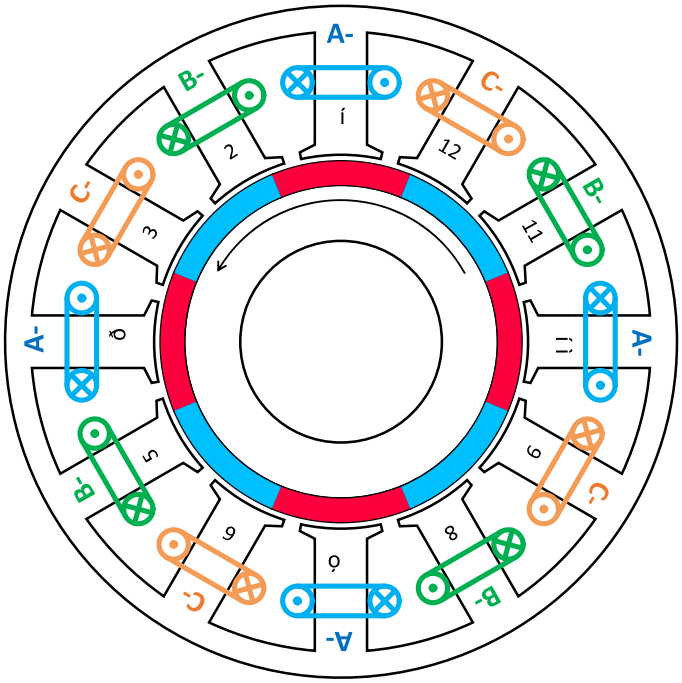

(a) 12s8p.

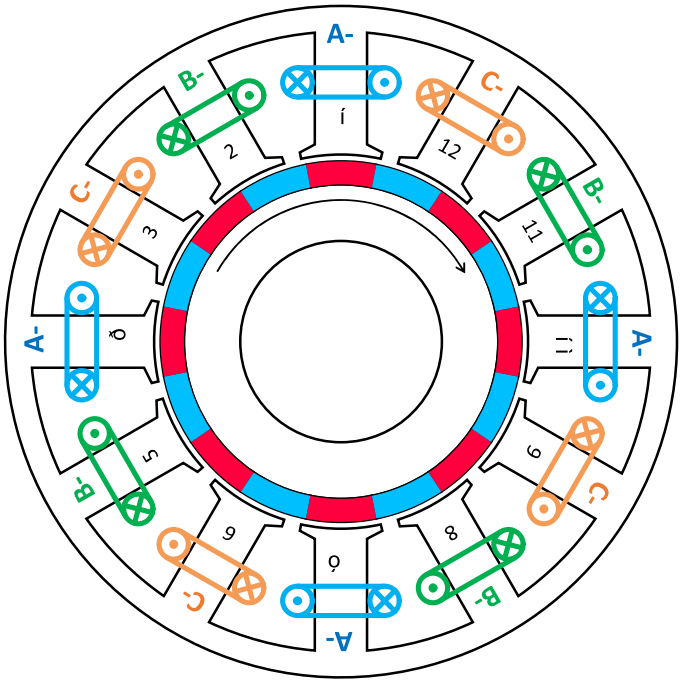

(b) 12s16p.

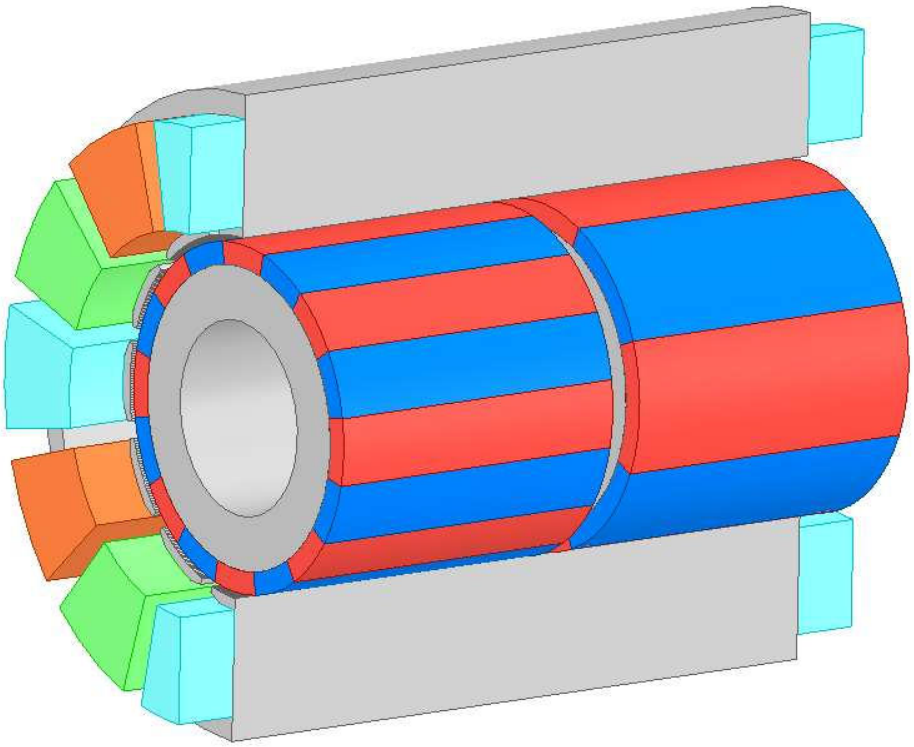

(c) 12s8/16p CSDPM-FR machine.

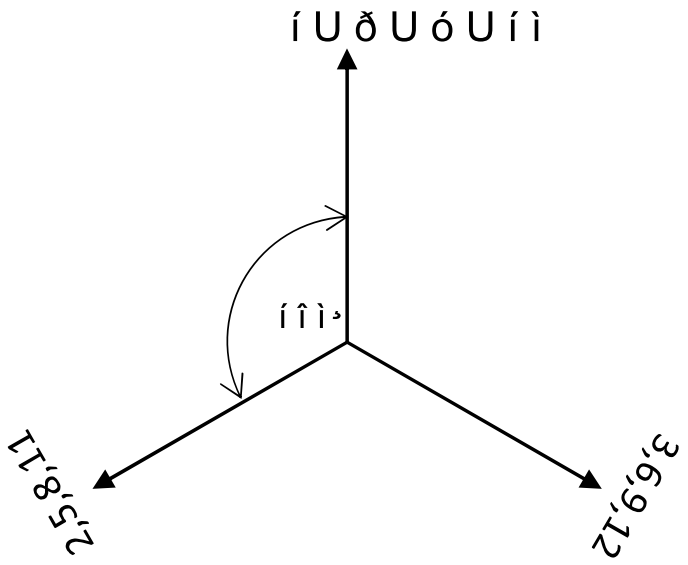

(d) Coil back EMF phasor.

Fig. 5.21. Topologies and coil back EMF phasor.

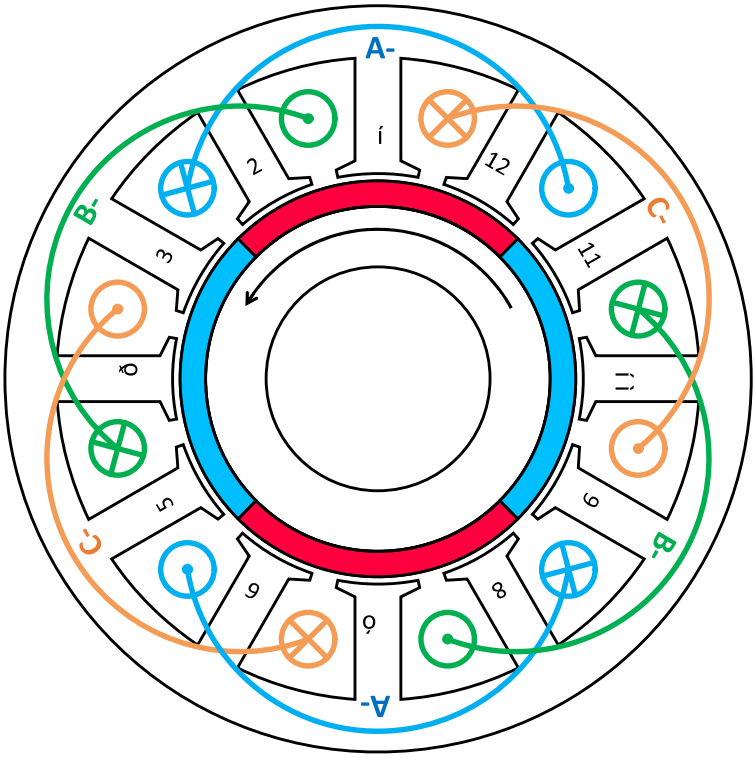

(a) 12s4p.

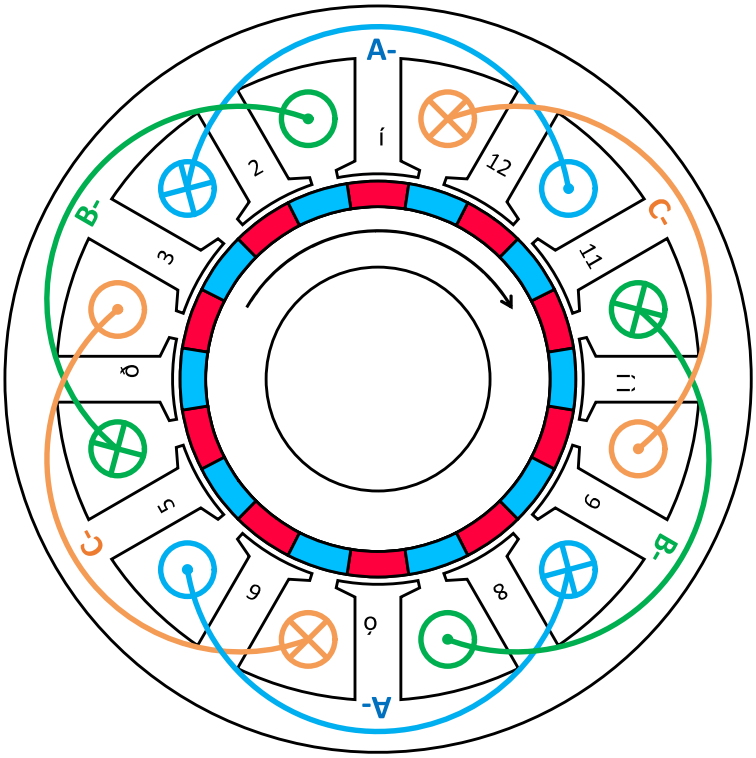

(b) 12s20p.

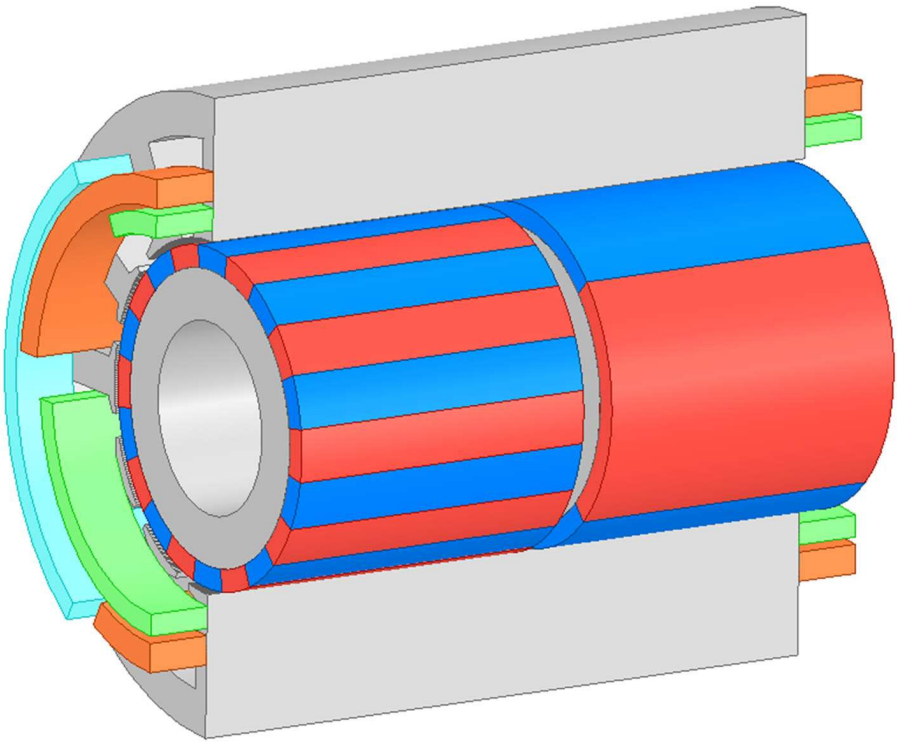

(c) 12s4/20p CSDPM-FR machine.

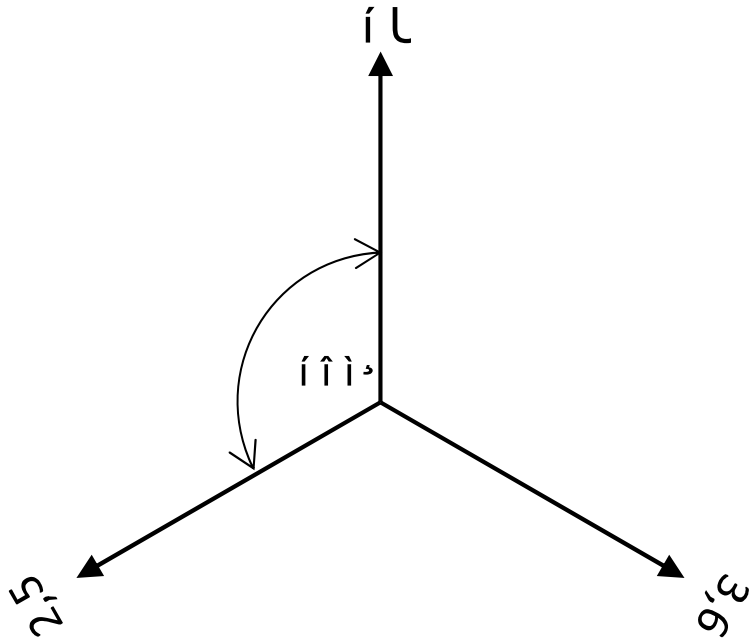

(d) Coil back EMF phasor.

Fig. 5.22. Topologies and coil back EMF phasor.

The CSDPM-FR machines are optimised under conditions in section 5.4 to maximise the torque, but slot opening is also considered in optimisation. The open circuit flux line and flux density distributions of optimised corresponding SRPM machines are shown in Fig. 5.23 and Fig. 5.24. It can be seen that the CSDPM-FR machines use the optimised stator of the low number of pole pair SRPM machine to avoid

oversaturation on the stator when the CSDPM-FR machine is paired with the high number of pole pair rotor.

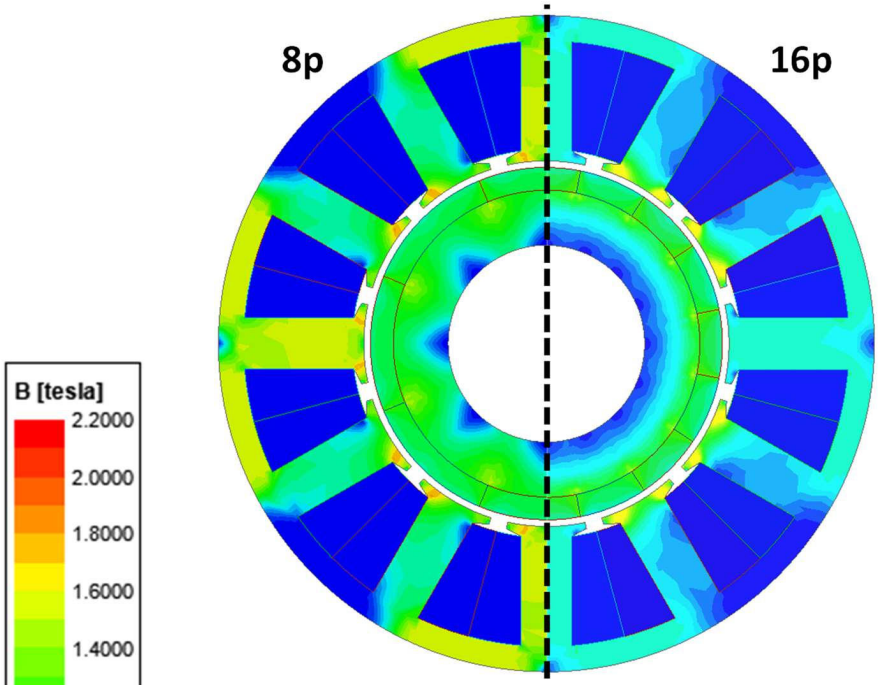

(a) With optimised stator of 8p SRPM machine.

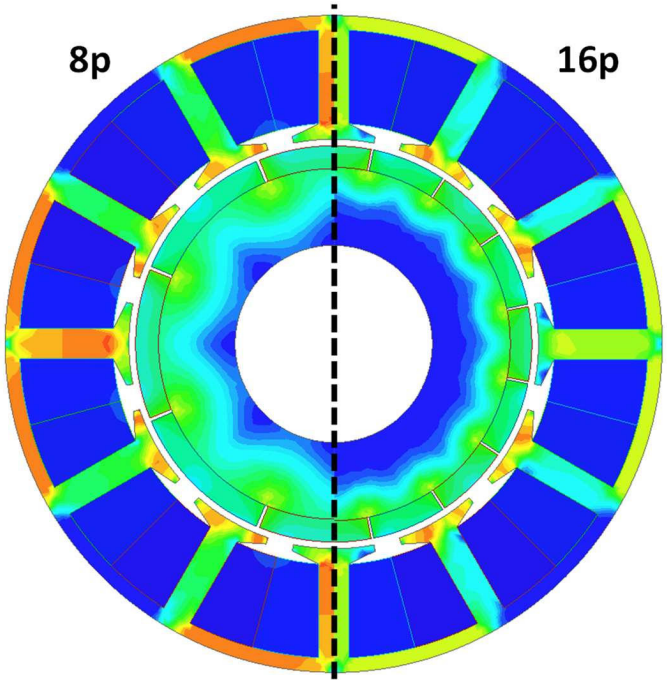

(b) With optimised stator of 16p SRPM machine.

Fig. 5.23. Open circuit flux density and flux line distributions of 12s8p and 12s16p SRPM machines.

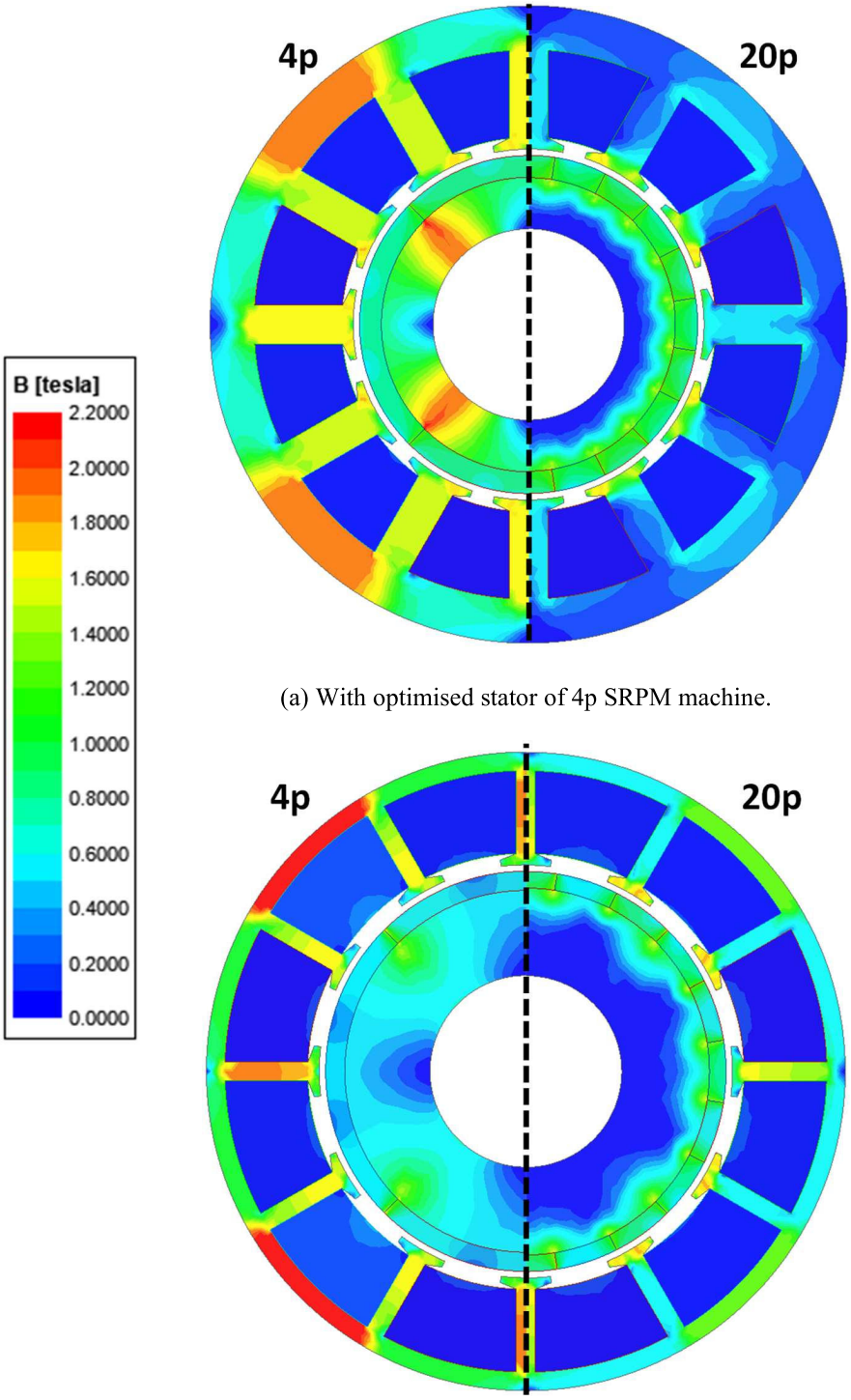

(a) With optimised stator of 4p SRPM machine.

(b) With optimised stator of 20p SRPM machine.

Fig. 5.24. Open circuit flux density and flux line distributions of 12s4p and 12s20p SRPM machines.

The optimised parameters of the CSDPM-FR machines with different slot pole number combinations are listed in Table 5.5. The open circuit flux density distributions of optimised CSDPM-FR machines are shown in Fig. 5.25.

TABLE 5.5
OPTIMISED DESIGN PARAMETERS OF CSDPM-FR MACHINES WITH DIFFERENT SLOT POLE NUMBER COMBINATIONS

Parameter	12s8/16p	12s4/20p
Stator stack length (mm)	105	
Two rotors stack length (mm)	50	
Gap length between two rotors (mm)	5	
Air gap length (mm)	1	
Shaft radius (mm)	15	
Machine outer radius (mm)	50	
Two rotors PM thickness (mm)	3.5	3.5
Two rotors PM pole arc (elec. deg.)	180	180
Split ratio	0.54	0.53
Stator tooth width (mm)	7.8	6
Stator yoke thickness (mm)	3.9	6.9
Stator slot opening (mm)	2.63	3.6

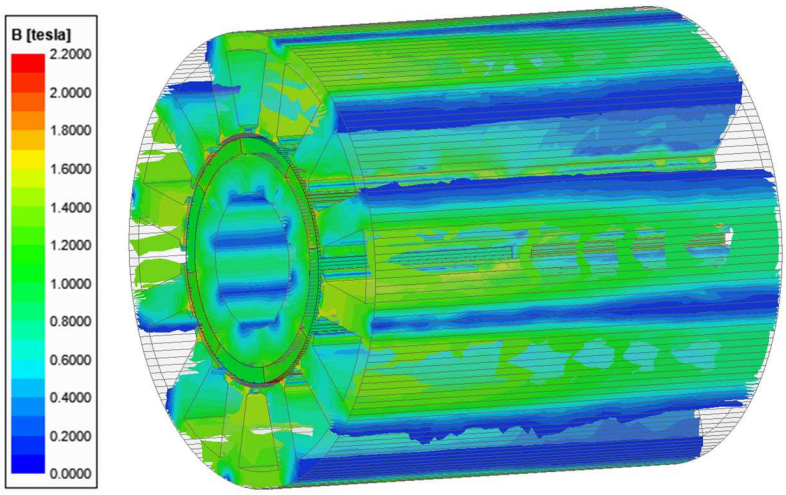

(a) 12s8/16p.

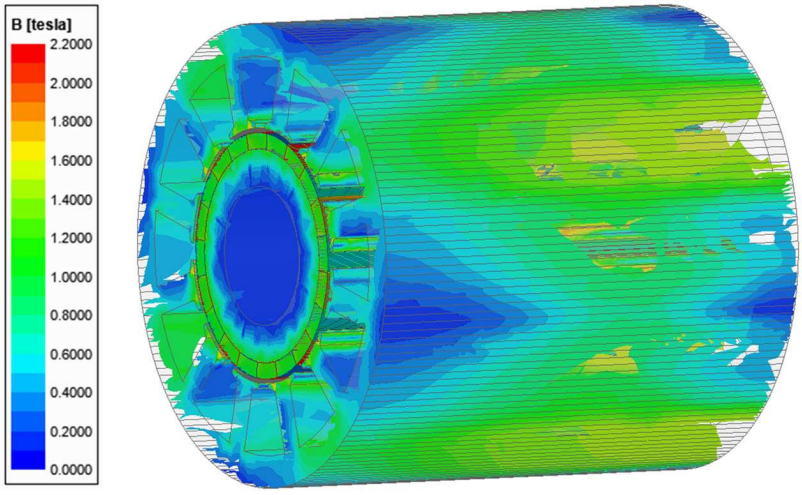

(b) 12s4/20p.

Fig. 5.25. Open circuit flux density distributions of CSDPM-FR machines.

Fig. 5.26 shows the average torques of the CSDPM-FR machines with different slot pole number combinations under the same input current as corresponding optimised SRPM machines. The torque of the CSDPM-FR machine decreases with the increase of the difference in the number of pole pairs of the two corresponding rotors. This is because the CSDPM machine employs the optimised stator of the p_l rotor, which always requires the thicker stator yoke thickness and stator teeth width (Fig. 5.23 and 5.24). The stator structure restricts the torque of the p_h rotor.

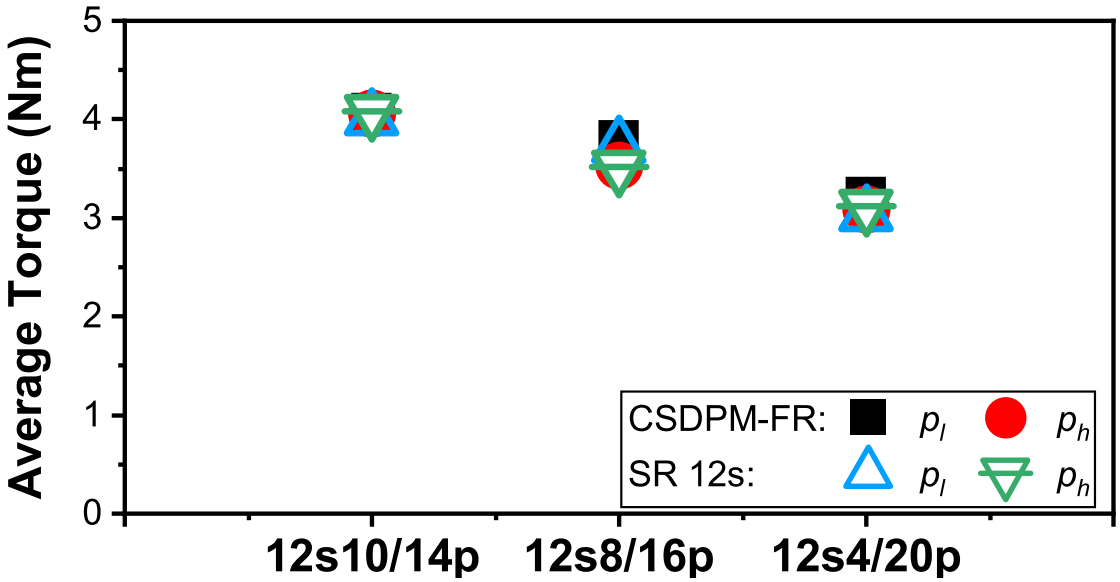

Fig. 5.26. Average torques of CSDPM-FR machines with different slot pole number combinations under same input current as corresponding SRPM machines.

The average torques of the CSDPM-FR machines with different slot pole number combinations under the same copper loss at 60W in the CR system are shown in Fig. 5.27. It can be seen that in a CR system, the CSDPM-FR machines always show higher torque than the two SRPM machines. The ISDW 12s4/20p CSDPM-FR machine shows significantly higher torque than the corresponding ISDW SRPM machines since it saved one set of end-winding of the distributed winding compared with two ISDW SRPM machines in the CR system under the same copper loss condition.

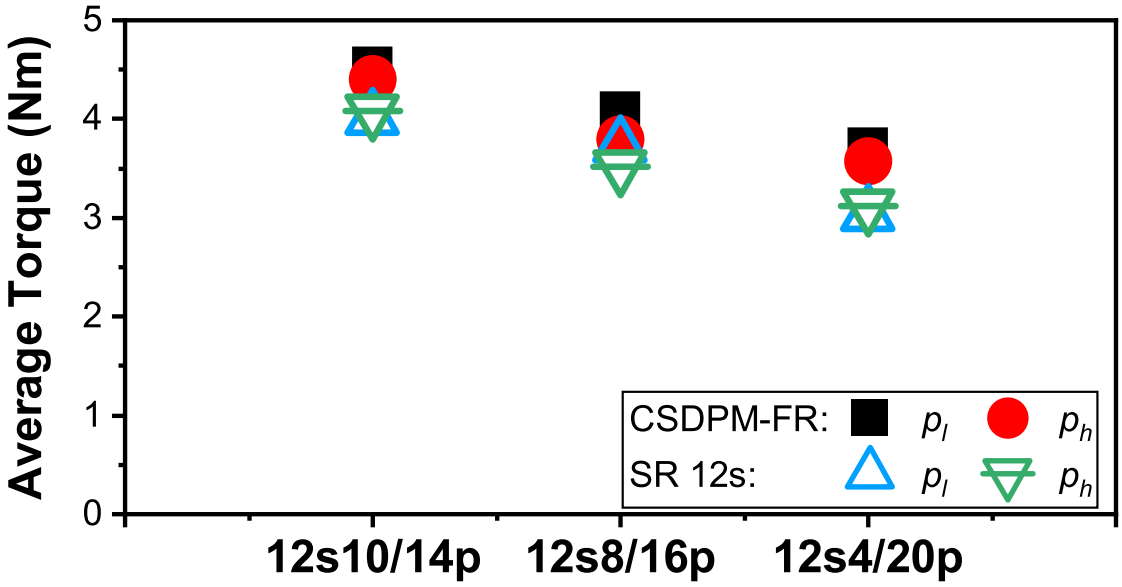

Fig. 5.27. Average torques of CSDPM-FR machines with different slot pole number combinations under same copper loss=60W in CR system.

Consequently, Table 5.6 summarises the comparison of the electromagnetic torques of CSDPM and SRPM machines. In the same input current condition, the CSDPM machines have the same torque as the corresponding SRPM machines since the CSDPM machine can be treated as two SRPM machines combined. In the same copper loss condition, the CSDPM machines have higher torque than the corresponding SRPM machines since the CSDPM machine has saved one set of end-winding compared with the SRPM machine. Thus, the CSDPM machine has advantages in short end-winding and higher torque when the CR system requires ISDW machines.

TABLE 5.6
ELECTROMAGNETIC TORQUES OF CSDPM AND SRPM MACHINES

Slot/Pole			Torque (Nm)	
			Same input current	Same copper loss
12s10/14p	CSDPM	p_l	4.1	4.5
		p_h	4.1	4.4
	SRPM	p_l	4.1	4.1
		p_h	4.1	4.1
12s8/16p	CSDPM	p_l	3.7	4.0
		p_h	3.5	3.7
	SRPM	p_l	3.7	3.7
		p_h	3.5	3.5
12s4/20p	CSDPM	p_l	3.2	3.6
		p_h	3.1	3.5
	SRPM	p_l	3.2	3.2
		p_h	3.1	3.1

As analysed in formula (5.10), the rotational speed ratio of two rotors of the CSDPM machine is adjustable by changing the slot pole number combinations. Under a set frequency of armature current, the rotational speed ratio of two rotors of the CSDPM machine can be defined as:

$$K_s = \frac{n_l}{n_h} = \frac{p_h}{p_l} \tag{5.18}$$

Therefore, the CSDPM machine can satisfy the requirements of the CR wind turbine and CR underwater vehicle propulsion, which needs two rotors not only to rotate in different directions but also at different speeds.

Generally, CR applications require the torques of two rotors to be the same for stability and to avoid the application yawing in one direction. In the CSDPM machine, the torque ratio of two rotors is also adjustable, as mentioned in the previous section.

This CR operation can improve the power capture capability of CR wind turbines by improving the aerodynamic efficiency of CR blades [LIU18] [SHI20] [HOU18] [MAL13] [YAN96] [SAS98], or improve the propulsion efficiency of CR underwater vehicles by recovering the energy loss of one propeller using CR propellers [SHI98] [JUN05] [SAN13] [SHE07]. The design of a CR machine that optimises power capture or improves propulsion efficiency for different applications must consider the specific torque and speed ratio requirements of the two rotors for a specific application. The proposed CSDPM machine can be designed for various torque and speed ratio scenarios, providing design flexibility for different application requirements.

5.7 Experimental Validation

The 12s10/14p CSDPM-FR machine has been prototyped and tested to validate the FEA results. The prototype is made with the same dimensions and parameters as the FEA model, as listed in Tables 5.1 and 5.4. The mechanical structure of the machine prototype is shown in Fig. 5.3 and assembled in Fig. 5.9. The experiments include cogging torque and back EMF at no-load conditions and full and half-load current static torque at on-load conditions.

The cogging torques and static torques of 10p and 14p rotors are measured by using the test method described in [ZHU09]. The test rig is shown in Fig. 5.28. The force produced by the prototype was measured by connecting one rotor shaft to a balance beam and a digital weight scale while the other rotor could rotate freely. The stator was fixed to a lathe machine, allowing rotation to adjust the rotor position. A preload weight was placed on the beam above the scale to ensure continuous contact with the digital scale. The cogging torque at different positions for each rotor was measured by rotating the stator to various angular positions. Fig. 5.29 shows the measured and FEA predicted cogging torque of the 10p and 14p rotors. The measured results meet the FEA results well in both waveforms and harmonics although the amplitudes exhibit some differences.

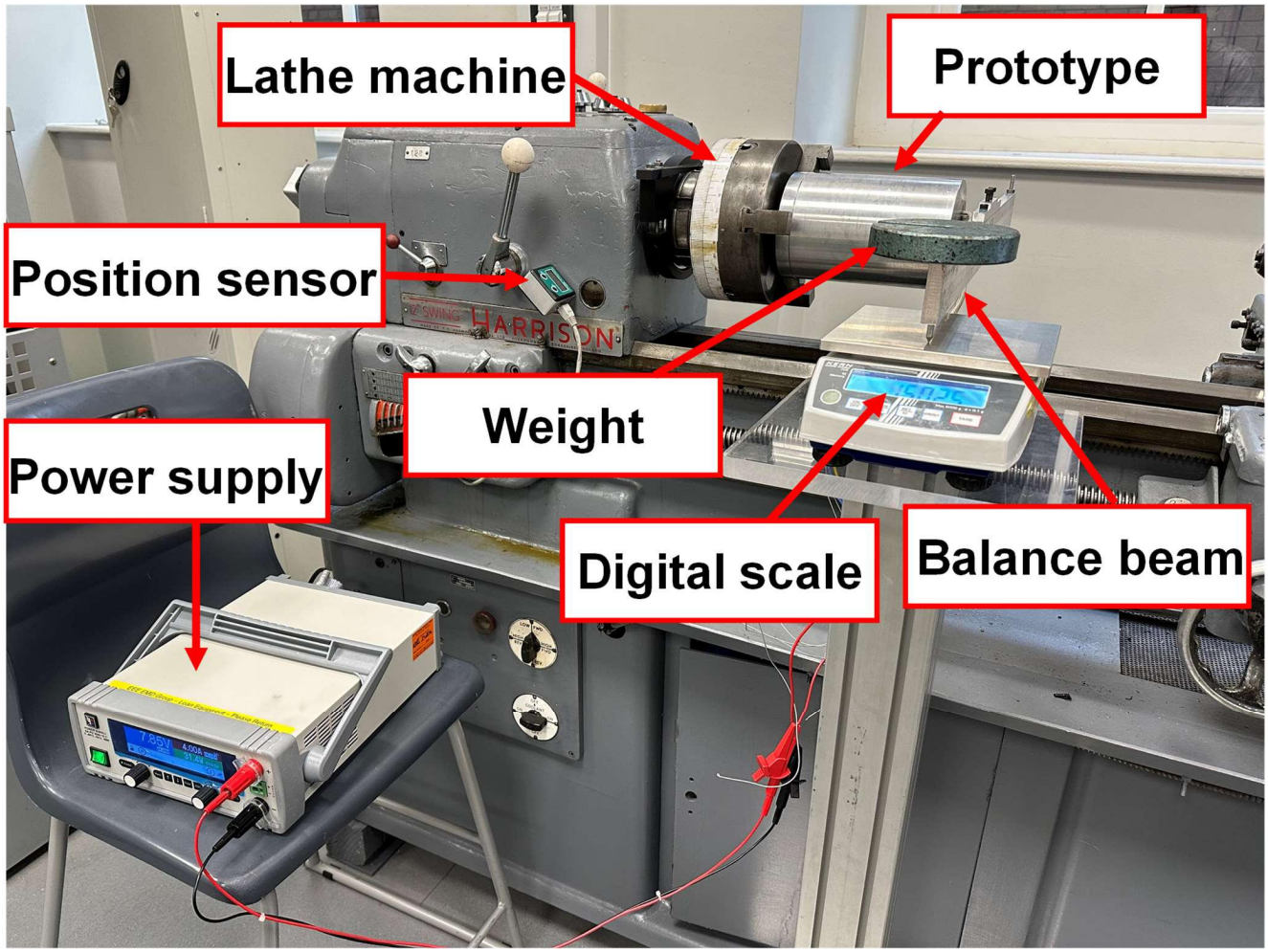

Fig. 5.28. Test rig.

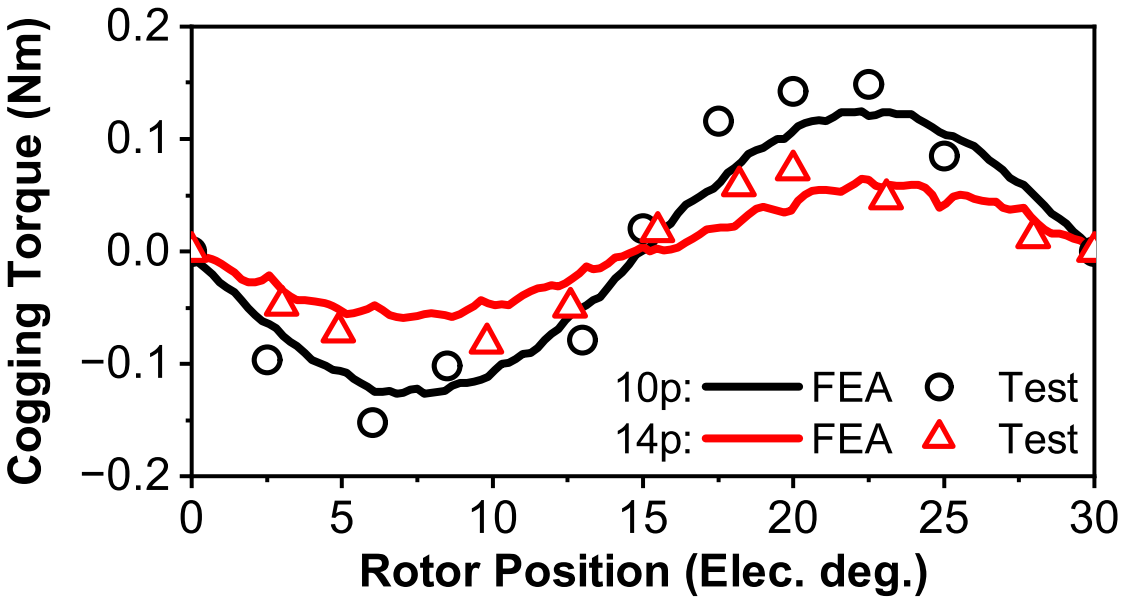

(a) Waveforms.

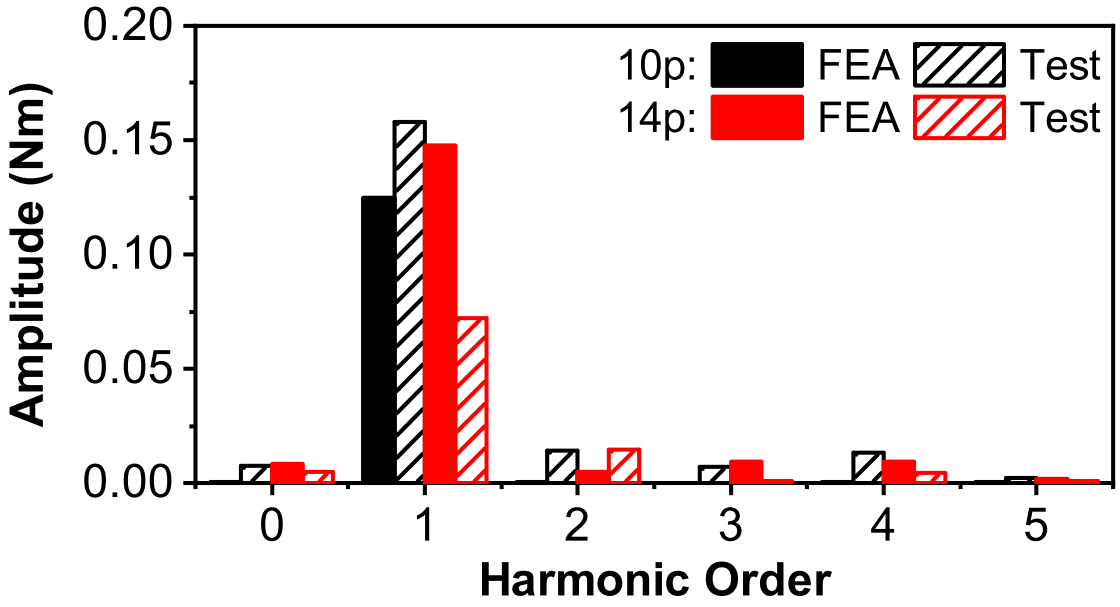

(b) Spectra.

Fig. 5.29. FEA predicted and tested cogging torques.

The phase back EMFs generated by 10p and 14p rotors are measured separately. A 400 r/min prime mover drives each rotor. Since the two rotors have no mechanical coupling and negligible magnetic coupling, the other rotor is stationary when one rotor is driven. Fig. 5.30 shows the measured and FEA predicted back EMFs generated by the 10p and 14p rotors. The test results are in good agreement with the FEA predictions.

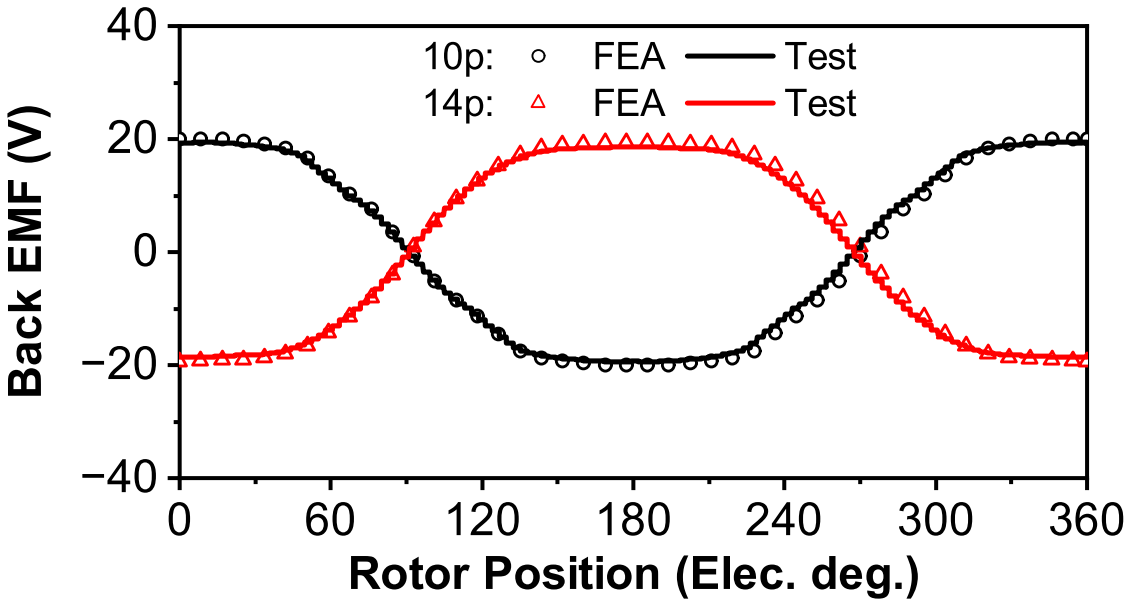

(a) Waveforms.

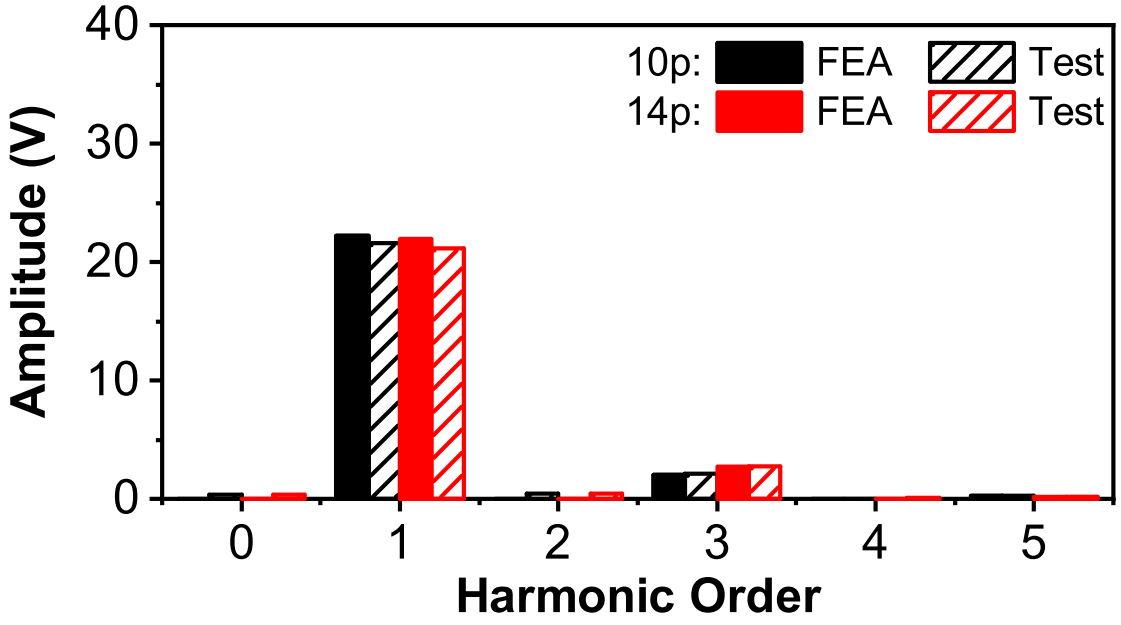

(b) Spectra.

Fig. 5.30. FEA and tested phase back EMFs.

The full and half on-load static torques of 10p and 14p rotors are measured by injecting DC ($I_A = -2I_B = -2I_C = I_{DC}$ for a range of DC values, and the full load current I_{rated} corresponds to the copper loss of 60 W), as shown in Fig. 5.31 (a). Fig. 5.31 (b) shows the variation of average torque with current. It can be seen that the measured torques match well with the FEA results.

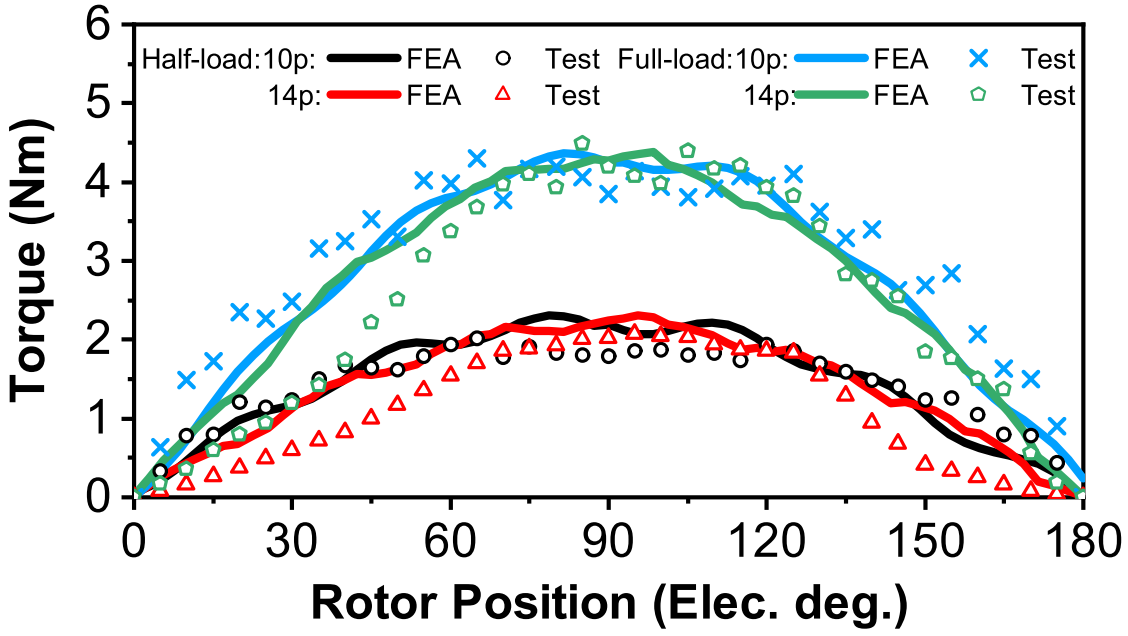

(a) Static torques at full and half-load conditions.

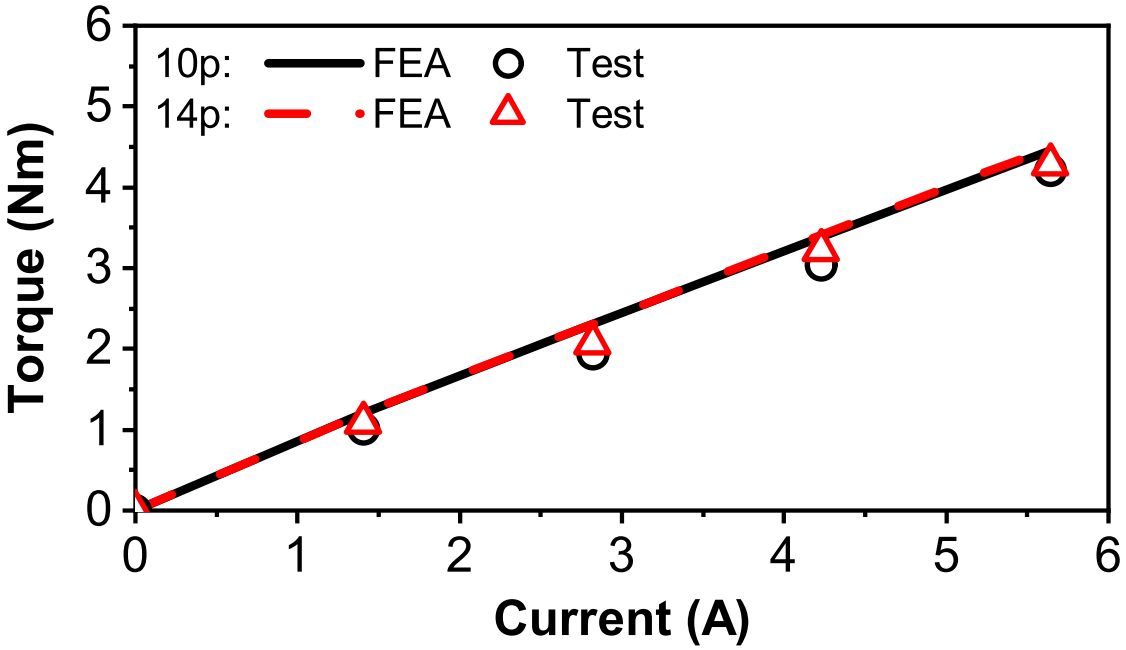

(b) Variation of average torques with currents.

Fig. 5.31. FEA and measured torques.

5.8 Conclusion

This chapter proposes a novel CSDPM machine based on magnetic field modulation for the CR operation system. All feasible slot pole number combinations based on the operation principle are discussed. Moreover, the CSDPM machines with the different pole numbers with the same 12 slots are analysed. The CSDPM machine has one winding set, one shared stator, and two robust rotors to achieve the CR operation. The axially arranged rotors are more accessible to assemble than the conventional radial flux magnetic geared machine. The assembly mechanical structure is presented in the chapter. Compared with the conventional CR operation system achieved by two electrical machines, the proposed CR operation system with the CSDPM machine has higher torque.

CHAPTER 6

GENERAL CONCLUSIONS AND FUTURE WORK

6.1 General Conclusions

This thesis has comprehensively and systematically investigated DRPM machines. Based on the rotational speeds of two rotors, DRPM machines are classified into two categories: two rotors of DRPM machines rotate at the same or different speeds. Additionally, within each category, DRPM machines can be further divided into two types: fluxes in two rotors in series or parallel.

In the scenario that the DRPM machine rotors operate at the same speeds, SDRPM and PDRPM machines with different winding configurations are compared and analysed. The results show that SDRPM machines generally have higher torque performance. Therefore, the SDRPM machine is selected for further comparison with SRPM machines (including ER and IR PM machines). This analysis reveals, for the first time, that although DRPM machines exhibit enhanced overload capabilities, they deliver lower torque and less PM utilisation compared to SRPM machines.

In the scenario that the DRPM machine rotors operate at different speeds, the special case-CR operation is investigated. For the DRPM machine with series magnetic circuits, the YCDRPM machine is investigated by analytical method, FEA, and experiments, and the different operation modes of the YCDRPM machine are analysed. For the DRPM machine with parallel magnetic circuits, a novel CSDPM machine is proposed. The CSDPM machine shows a robust mechanical structure to achieve CR operation. Compared with the conventional CR operation system achieved by two electrical machines, the proposed CR operation system with the CSDPM machine has higher torque.

The relationship between different chapters is shown in Fig. 6.1. Concrete summaries and comparisons will be given in the following sections.

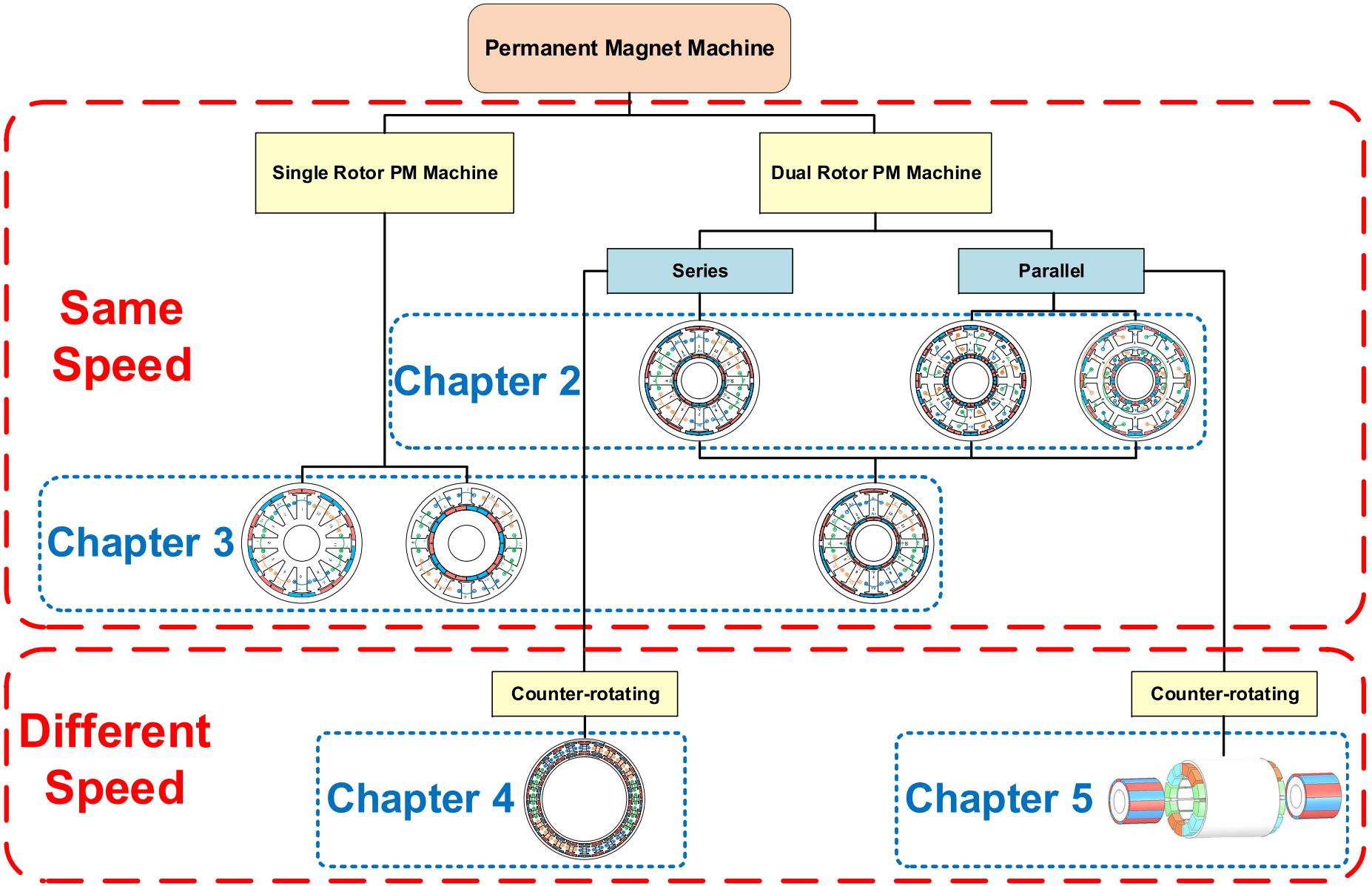

Fig. 6.1 Investigation of DRPM machines.

6.1.1 Dual-rotor PM machines with same speed rotational rotors

In the scenario that the DRPM machines rotors operate at the same speeds is investigated first in Chapter 2 and Chapter 3. The radial flux TC-SDRPM, TC-PDRPM, and TW-PDRPM machines with various slot/pole number combinations and machine sizes are compared. Several key conclusions can be made as follows:

1. In radial structure machines, the inherently larger radius of the outer rotor compared to the inner rotor results in a larger pole arc for the outer rotor PM to produce a higher flux. In this comparative study, the TC-PDRPM demonstrates the highest utilisation of the outer rotor PM, and thus, the highest overall PM utilisation.
2. Regarding scaling effects relative to machine size, the 12s20p TW-PDRPM machine exhibits the highest torque when scaled up radially due to its shorter end-winding. Conversely, the 12s20p TC-PDRPM machine performs better axial scaling since the TC-PDRPM machine has the highest torque, and the end-winding length is negligible with the axial length increase. The TC-SDRPM machine performs better when scaling in both axial and radial dimensions.

The results show the TC-PDRPM machines have the highest PM utilisation, but only the outer rotor contributes the most to the total torque. It shows the SRPM machine has the potential to generate higher torque than the DRPM machine.

Therefore, the SDRPM machine is selected to compare with the SRPM machines in Chapter 3. For the radial-flux SDRPM machine, the different radii of the inner and outer rotors result in different magnetic flux generation between the inner and outer PMs. This discrepancy reduces the resultant magnetic flux due to the series connection of magnetic circuits. Further, comparative studies under various critical parameter conditions reveal that the SDRPM machine has higher torque than the SRPM machines only when the total air gap lengths of the machines are the same. However, variations in the inner bore radius, number of poles, and PM volumes demonstrate that, compared to conventional SRPM machines, the radial-flux SDRPM machine exhibits a more complex structure, lower torque and PM utilisation, and higher costs. The comparisons of performances of different machines are listed in Table 6.1.

Table 6.1 Comparisons of Performances of Different Machines

	Torque density	PM utilisation	Over-load capability	Manufacturing
TW-PDRPM	Δ	Δ	Δ	ΔΔ
TC-PDRPM	ΔΔΔ	ΔΔΔ	ΔΔ	ΔΔ
TC-SDRPM	ΔΔ	ΔΔ	ΔΔΔΔ	Δ
TC-ERPM	ΔΔΔΔ	ΔΔΔΔ	ΔΔΔ	ΔΔΔΔ
TC-IRPM	ΔΔΔ	ΔΔΔΔ	ΔΔΔ	ΔΔΔΔ

Note: Δ to ΔΔΔΔ is from bad to best.

6.1.2 Dual-rotor PM machines with different speed rotational rotors

Although the DRPM machines have lower torque and PM utilisation than the SRPM machines, DRPM machines inherently have an extra rotor compared with SRPM machines. When the two rotors of the DRPM machine operate in different working conditions, the DRPM machine can replace two SRPM machines to meet the requirements of some special applications that require two rotors to reduce the cost and save space. Chapter 4 presents and investigates a radial-flux YCDRPM machine, which integrates a magnetic gear with a PM machine. In this configuration, the TC stator winding is applied to the modulation ring of the magnetic gear, effectively avoiding the mechanical strength limitations typically associated with using the modulation ring as a rotor. This machine employs FSCW in the yokeless structure and induces a CR MMF on opposing sides to achieve the CR operation. This Chapter also discusses various operational modes of the YCDRPM machine, which shows the advantages of the magnetic gear effect. Specifically, under the magnetic geared motor mode, the torque of the YCDRPM machine is significantly enhanced by the synergistic effects of magnetic gearing and armature reaction. Performance evaluations of different slot/pole number configurations reveal that the 24 slots with 26/22 poles configuration have better electromagnetic performance, enhancing output torque and minimizing torque ripple. However, the YCDRPM machine has a sandwiched stator that leads to a complex mechanical structure, and the radial flux structure causes the torques of two rotors of the YCDRPM machine to be modified hard. Therefore, Chapter 5 proposes a novel CSDPM machine based on magnetic field modulation for the CR operation system. The study extensively discusses all feasible slot-pole number combinations applicable to this operation principle. Specifically, CSDPM machines featuring various pole numbers with the same 12-slot configuration are analysed. The design of the CSDPM machine incorporates a single shared winding set, one shared stator, and two robust rotors. Different from conventional radial flux magnetic geared machines, the axially arranged rotors of the CSDPM machine

facilitate easier assembly. This Chapter details the assembly and mechanical structure of the CSDPM machine. Furthermore, comparative analyses reveal that the proposed CR operation system with the CSDPM machine delivers higher torque than conventional systems achieved by two SR electrical machines. The advantages and disadvantages of YCDRPM and CSDPM machines are listed in Table 6.2.

Table 6.2 Advantages and Disadvantages of YCDRPM and CSDPM machines

Chapter	Machine	Advantages	Disadvantages
4	YCDRPM	• One set stator winding, one shared stator, and two rotors to achieve CR operation. • Utilise field modulation between two rotors to operate machine as magnetic gear.	• Sandwiched stator makes mechanical structures difficult and complicated to assemble. • Speed ratio of two rotors is constant and speeds of two rotors cannot be decoupled. • Sandwiched stator hard to cooling.
5	CSDPM	• One set stator winding, one shared stator, and two rotors to achieve CR operation. • Simple mechanical structure and easy to assemble. • Torque split of two rotors is easily modified by changing the rotor stack length.	• Speed ratio of two rotors is constant and speeds of two rotors cannot be decoupled. • Magnetic circuits of two rotors are parallel and cannot utilise field modulation between two rotors.

6.1.3 Research methodologies

Both analytical and FEM are employed in this thesis.

In Chapter 3, the equivalent magnetic circuit method is used to explain the inner and outer PMs of the SDRPM machine hardly generate the same magnetic flux. Thus, the series of connected magnetic circuits decreases the resultant magnetic flux.

In Chapters 4 and 5, the equivalent magnetic circuit method describes the operation principles of the YCDRPM and CSDPM machines. The analytically calculated air gap flux densities, back EMFs, and torques are good to match with the FEA results.

6.2 Future Work

Based on the above analyses and conclusions, some future work are recommended as follows:

1. Investigating the radial flux YCDRPM machine with the consequent pole to improve the PM

utilisation and reduce the cost.

2. Investigating the CSDPM machine with the consequent pole to improve the PM utilisation and reduce the cost.
3. Investigating the electromagnetic performances of the radial flux YCDRPM machine with rotor eccentricity.
4. Investigating the electromagnetic performances of the CSDPM machine with rotor eccentricity.
5. Investigating a novel structure based on the CSDPM machine with split stator teeth to enhance the field modulation effect to increase the torque density of the machine and consider the machine operates at various operation modes.
6. Investigating a novel structure based on the CSDPM machine with axial direction magnetised PM to achieve hybrid magnetic circuits in the CSDPM to utilise the different order MMFs in one air gap.
7. Investigating the thermal management of the YCDRPM and CSDPM machines.

It is important to note that in practical applications, the single shared stator winding of YCDRPM and CSDPM machines introduces control challenges. The control strategy using mono inverter to control multiple induction machines has been extensively studied in [WU88], [KEL94] [BOU94] [LEV03] [JON08]. Similarly, the control strategy utilising mono inverter to control multiple PMSMs is later proposed in [BID11] [LEE15a] [LEE15b].

To ensure the stability of a multi-PMSM system, the synchronism of each machine must be maintained regardless of the load torque variations. In this approach, one machine, referred to as the "master machine," is self-piloted. If the machine with the highest applied load torque is chosen as the master, synchronism is ensured across all machines. This control strategy has been applied to the CR DRPM machine, as detailed in [LUO19] [ZHO18] [CRO23]. The block diagram of the control scheme is shown in Fig. 6.2.

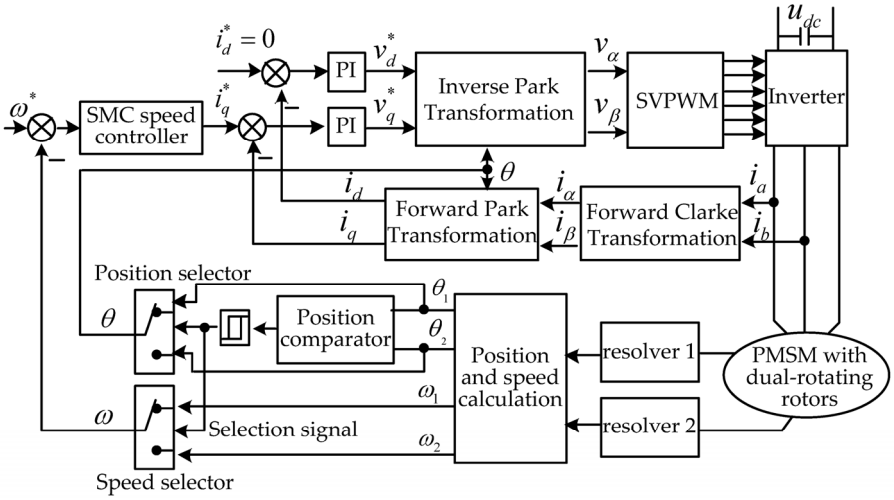

Fig. 6.2 Block diagram of the control scheme of CR DRPM machines [ZHO18].

For the CSDPM machine, the same control strategy can be applied by designating the rotor with the highest load torque as the master rotor and the other as the slave rotor. However, the stability of the slave rotor may not be guaranteed when its load torque exceeds that of the master rotor, which requires further investigation.

In addition, this control strategy cannot be utilised directly on the YCDRPM machine since the magnetic gearing effect causes torque transmission between two rotors of the YCDRPM machine, which should be further analysed in the future.

APPENDIX A END-WINDING CONFIGURATION

The end-winding configurations are illustrated in Fig. A.1. To simplify the calculation of the end-winding length, the end-winding length is determined as a semicircle with a diameter equivalent to the length of the "Arc" [HE21]. Thus, the end-winding length of TC-SDRPM and TC-PDRPM machines $l_{TC\text{-}end}$ in Fig. A.1(b) can be calculated as:

$$l_{TC-end(y=1,3,5)} = \frac{\pi}{2}\left(\frac{(2y-1)(R_3 + h_{is} + R_4 - h_{os})}{2N_s} + \frac{w_{st}}{2}\right) + 2l_{ex} \qquad (A.1)$$

where y is the coil pitch, N_s is the number of stator slots, R_3 and R_4 are the stator inner and outer radii, respectively (Fig. 2.3), h_{is} and h_{os} are the stator inner and outer tooth-tip height, w_{st} is the tooth width, l_{ex} is the extend part as shown in Fig. A.1 (a).

The end-winding length of the TW-PDRPM machine $l_{TW\text{-}end}$ in Fig. A.1 (c) can be calculated as [XU21b]:

$$l_{TW-end} = \frac{\pi}{2}\left(\frac{(R_{syi} - R_{si} - h_{it} + R_{so} - R_{syo} - h_{ot})}{2} + R_{syo} - R_{syi}\right) + 2l_{ex} \qquad (A.2)$$

where R_{syi} and R_{syo} are the stator yoke inner and outer radii, respectively (Fig. 2.3).

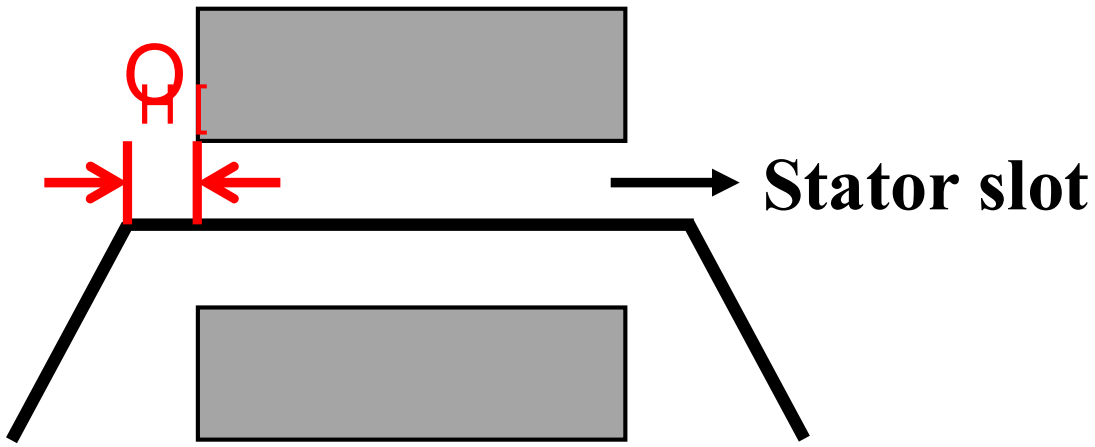

(a) Side view.

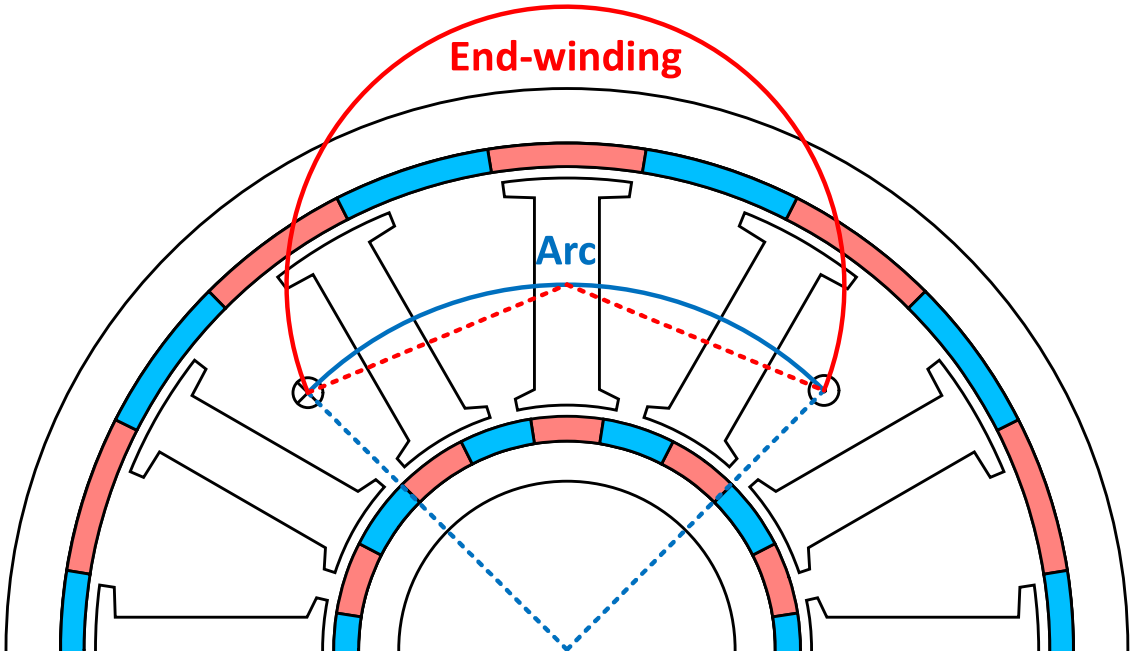

(b) TC.

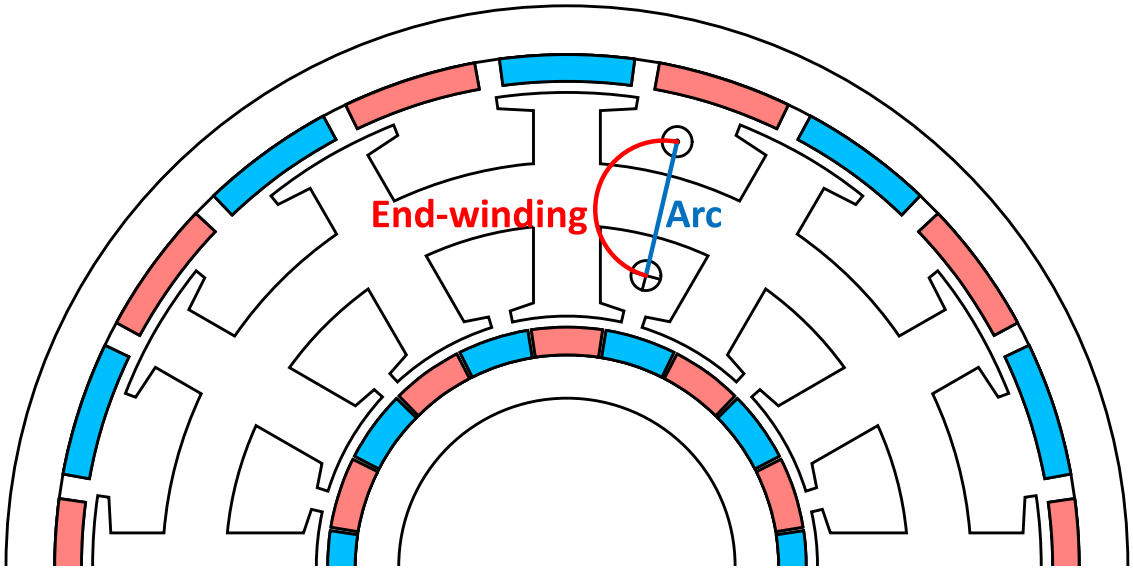

(c) TW.

Fig. A.1. End-winding configuration.

APPENDIX B TC-PDRPM MACHINE WITH SAME INNER AND OUTER SLOT AREAS

Fig. B.1 shows the cross-section of the 12s10p TC-PDRPM machine with the same inner and outer slot areas. The 12s10p TC-PDRPM machine is optimised to maximise the torque under the same conditions as Chapter 2.3, except the inner and outer slot areas are restricted to being the same. The optimised parameters are listed in Table B.1. In this case, the TC-PDRPM machine is named TC-PDRPM-A machine.

TABLE B.1
PARAMETERS OF OPTIMISED OF 12S10P TC-PDRPM-A MACHINE

Parameters	Symbols	TC-PDRPM-A
Stator tooth width (mm)	w_{ist}/w_{ost}	6.8/6.5
Stator yoke position	R_s/R_7	0.51
Stator yoke height (mm)	h_{sy}	5.7
Inner split ratio	R_2/R_7	0.39
Outer split ratio	R_4/R_7	0.83
Inner slot opening (mm)	b_{is}	2.4
Outer slot opening (mm)	b_{os}	6.5
Inner tooth-tip thickness (mm)	h_{is}	1
Outer tooth-tip thickness (mm)	h_{os}	1
Inner tooth-tip slope (deg.)	α_{is}	6
Outer tooth-tip slope (deg.)	α_{os}	11
Inner PM thickness (mm)	R_2-R_1	1.7
Outer PM thickness (mm)	R_6-R_5	2.3
Inner PM pole arc (°elec.)	θ_{im}	142
Outer PM pole arc (°elec.)	θ_{om}	155
Inner PM volume (cm^3)	V_{im}	7.9
Outer PM volume (cm^3)	V_{om}	27
Total PM volume (cm^3)	V_m	34.9
Input current amplitude (A)	I_{amp}	5

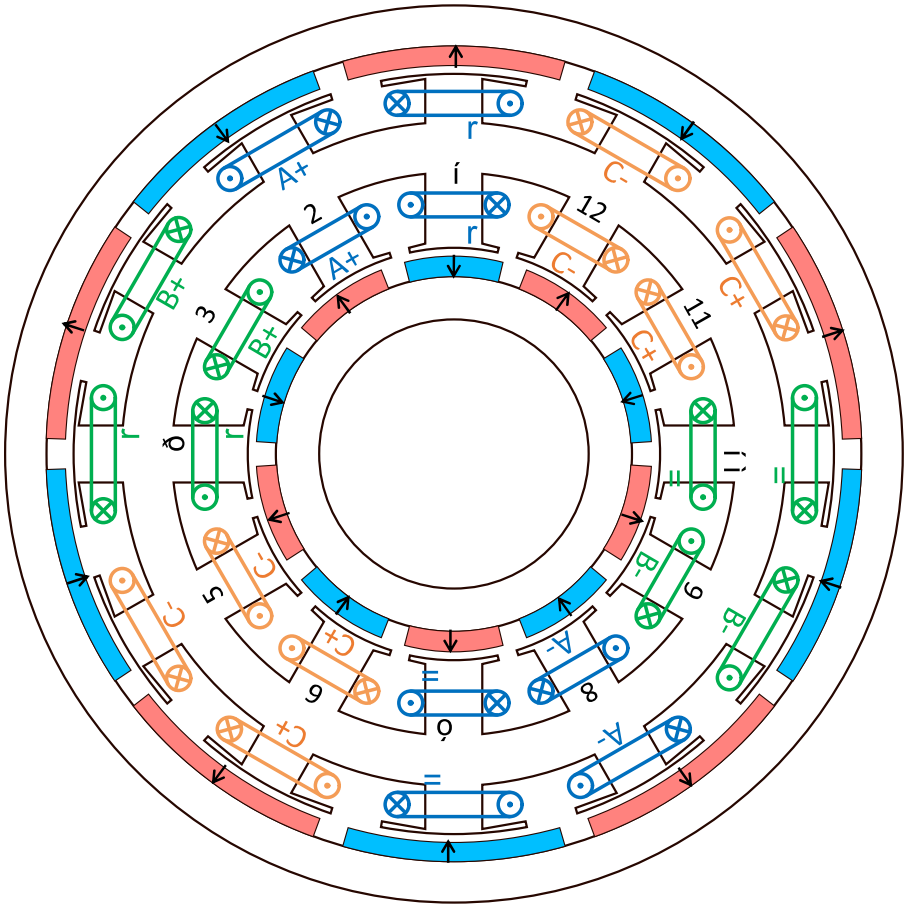

Fig. B.1. Cross section of 12s10p TC-PDRPM-A machine with the same inner and outer slot areas.

The open circuit flux line and flux density distribution of the optimised 12s10p TC-PDRPM-A machine is shown in Fig. B.2. Fig. B.3 compares the electromagnetic performances of the TC-PDRPM and TC-PDRPM-A machines. It can be seen that since the inner and outer stator slot areas of the TC-PDRPM-A machine are restricted, the number of turns in the outer stator slot is restricted. Chapter 2.4 mentions that the outer flux is higher than the inner flux. Thus, the flux linkage generated by the outer rotor is restricted by the number of turns linked to the outer flux. Therefore, the flux linkage, back EMF, and torque of the TC-PDRPM-A machine are lower than those of the TC-PDRPM machine.

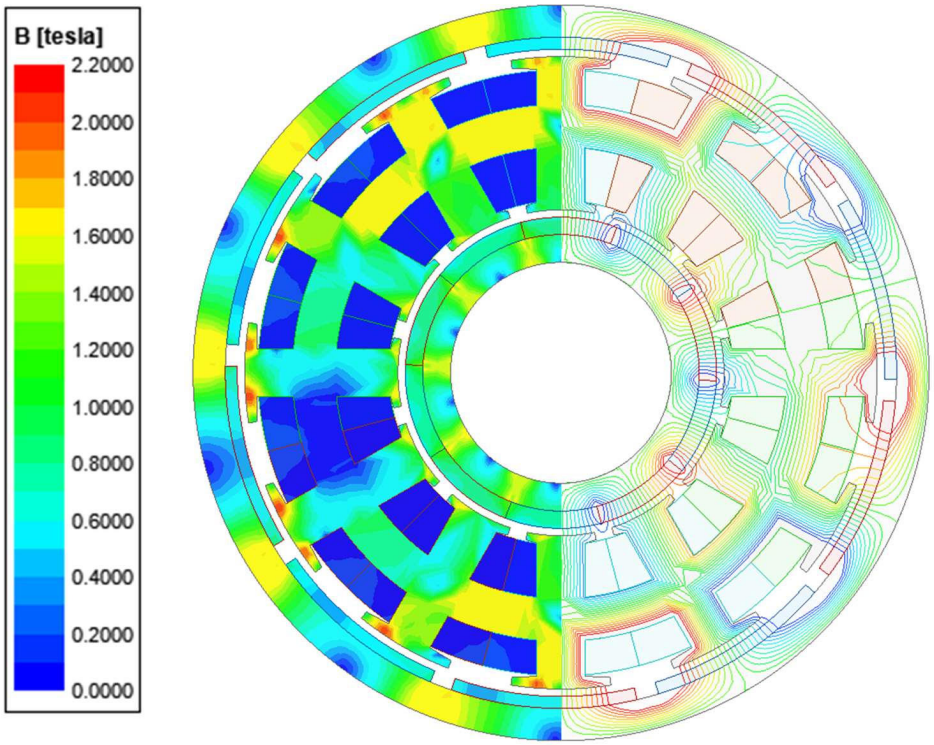

Fig. B.2. Open circuit flux density distribution and flux line of optimised 12s10p TC-PDRPM-A machines.

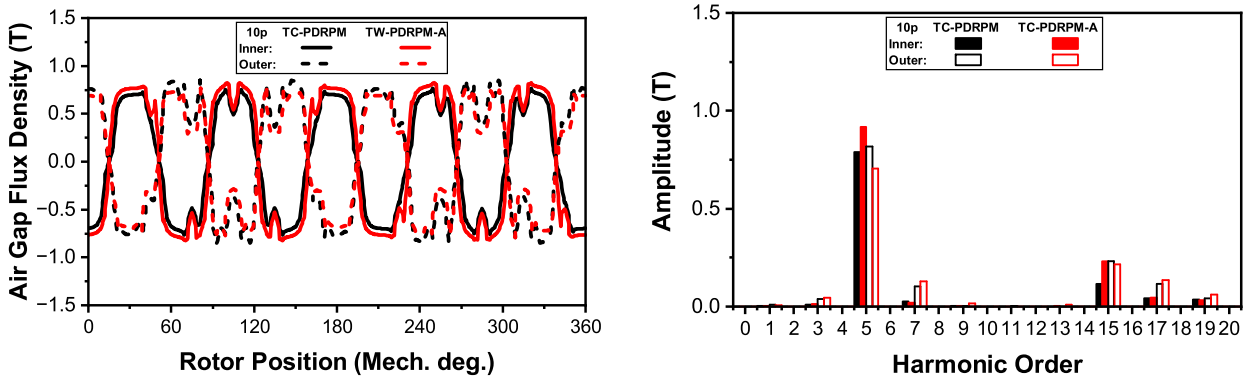

(a) Air gap flux densities.

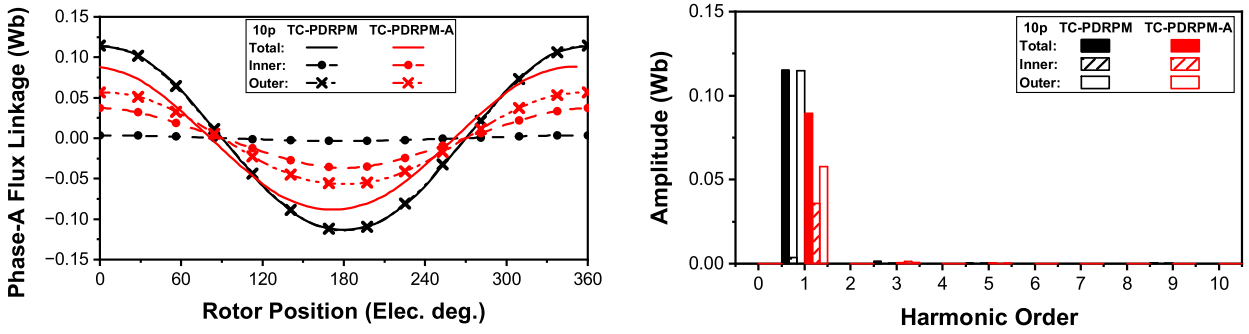

(b) Flux linkages.

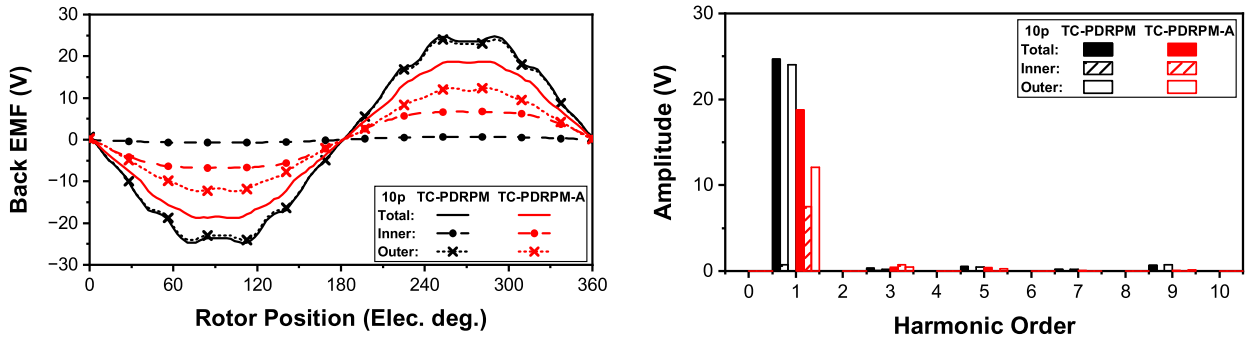

(c) Back EMFs.

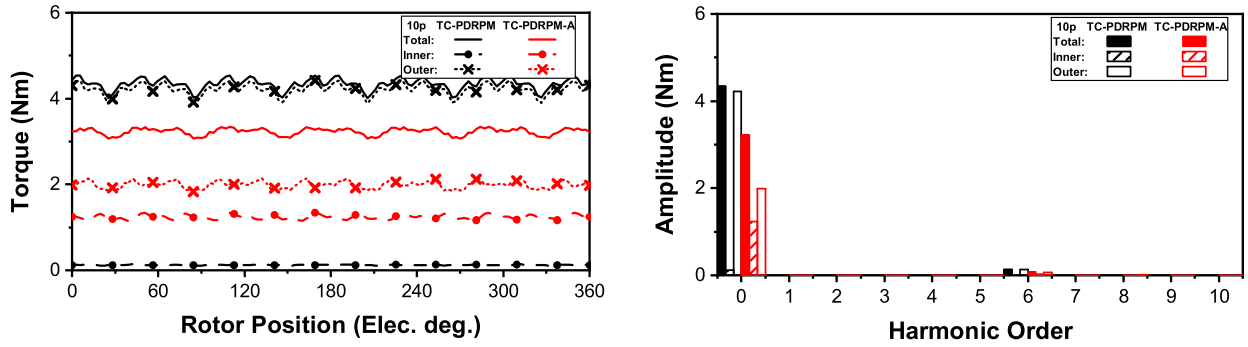

(d) Torques.

Fig. B.3. Comparison of electromagnetic performances of optimised 12s10p TC-PDRPM and TC-PDRPM-A machines.

APPENDIX C 12 SLOTS-10/14 POLES YCDRPM MACHINE

Fig. C.1 depicts the cross-section and corresponding coil-back EMF phasor of the YCDRPM machine with 12s-10p/14p. This machine is optimised under the same conditions as Section 4.4 to maximise the total torque, but the inner bore radius is set to 15mm. The optimised parameters are listed in Table C.1, and the related open circuit flux line and flux density distributions of the machine are shown in Fig. C.2.

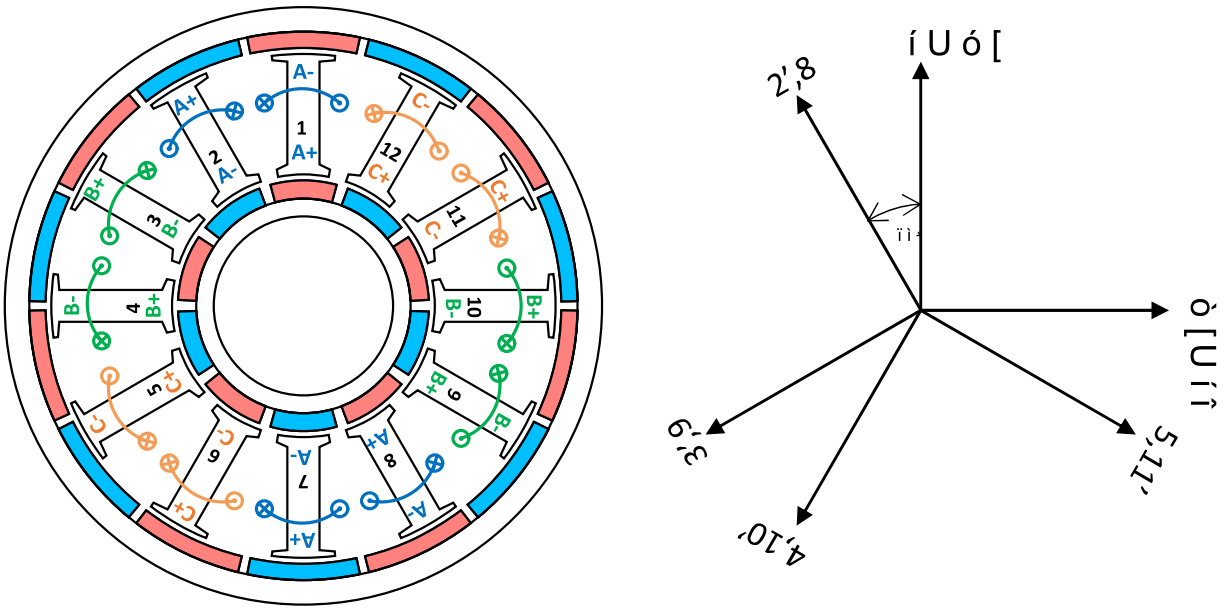

Fig. C.1. 12 slots-10/14 poles YCDRPM machine with. (a) Topology. (b) coil back EMF phasor.

TABLE C.1
DESIGNS OF OPTIMISED 12 SLOTS-10/14 POLES YCDRPM MACHINE WITH 15MM INNER BORE RADIUS

Parameter	12s-10p/14p
Inner bore radius (mm)	15
Outer PM thickness (mm)	2.7
Inner PM thickness (mm)	3.0
Outer PM pole arc (°elec.)	166
Inner PM pole arc (°elec.)	154
PM volume (cm^3)	50.8
Stator outer radius (mm)	42.2
Stator inner radius (mm)	22.0
Stator outer slot opening (mm)	11.4
Stator inner slot opening (mm)	3
Outer tooth-tip height (mm)	0.8
Inner tooth-tip height (mm)	1.3
Outer tooth-tip slope (deg.)	12
Inner tooth-tip slope (deg.)	13
Stator tooth width (mm)	5.4
Slot area (mm^2)	199

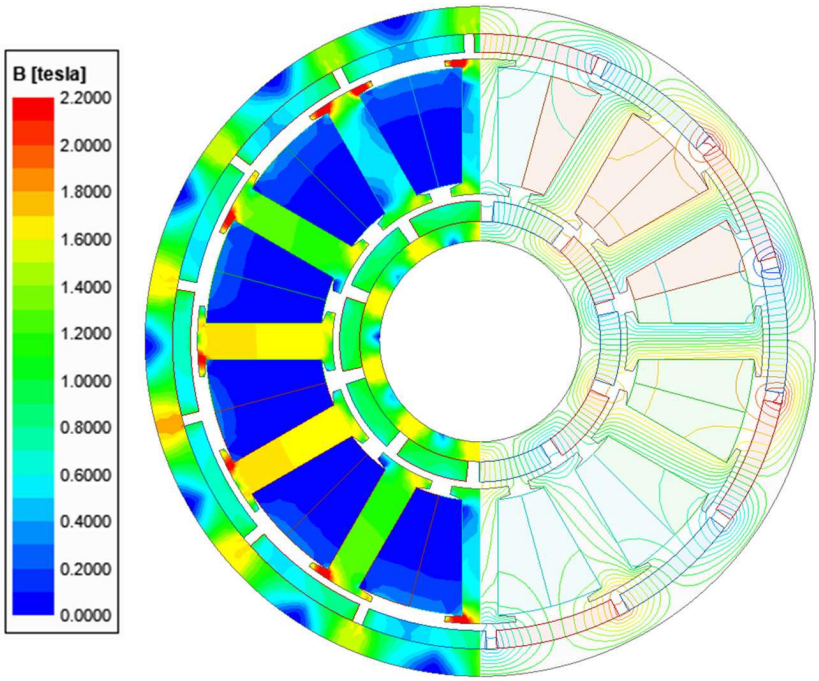

Fig. C.2. Open circuit flux density distributions and flux lines of 12s-10p/14p YCDRPM machine.

The no-load electromagnetic performances, i.e., air gap flux densities, flux linkage, and back EMF are shown in Fig. C.3.

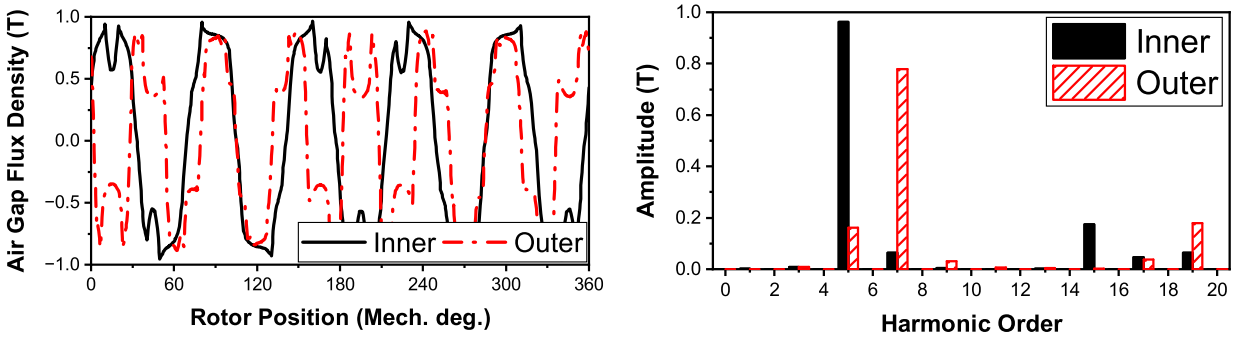

(a) Air gap flux densities.

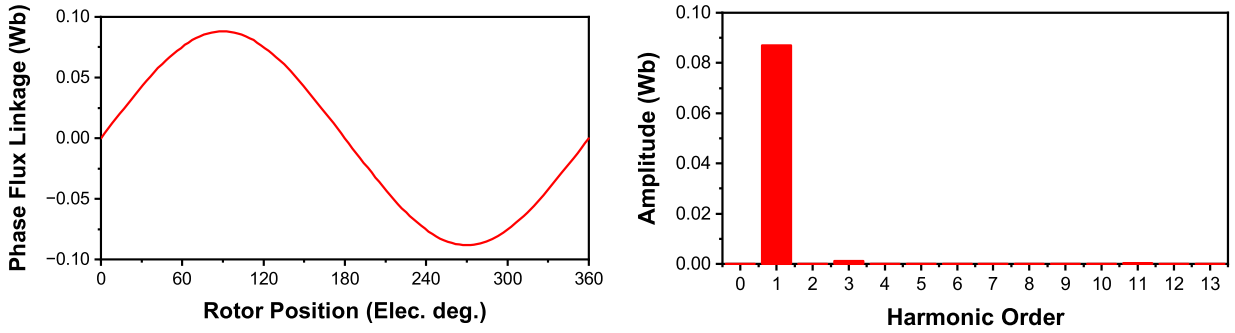

(b) Phase-A flux linkage.

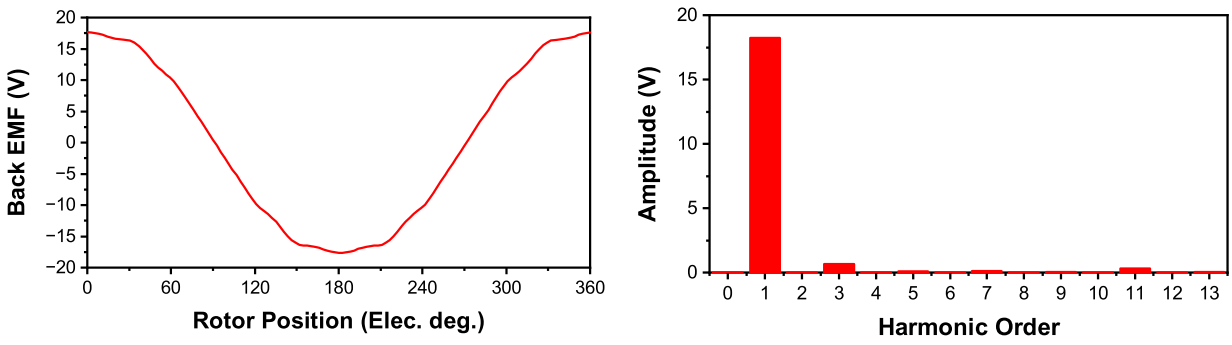

(c) Back EMF.

Fig. C.3. No-load electromagnetic performances of 12s-10p/14p YCDRPM machine.

Fig. C.4 shows the on-load torque of the 12s-10p/14p YCDRPM machine at 30W copper loss. The torque of the outer rotor is significantly higher than that of the inner rotor since the outer rotor radius is much larger than that of the inner rotor. This imbalance in torque between the two rotors does not meet the requirements for counter-rotating applications.

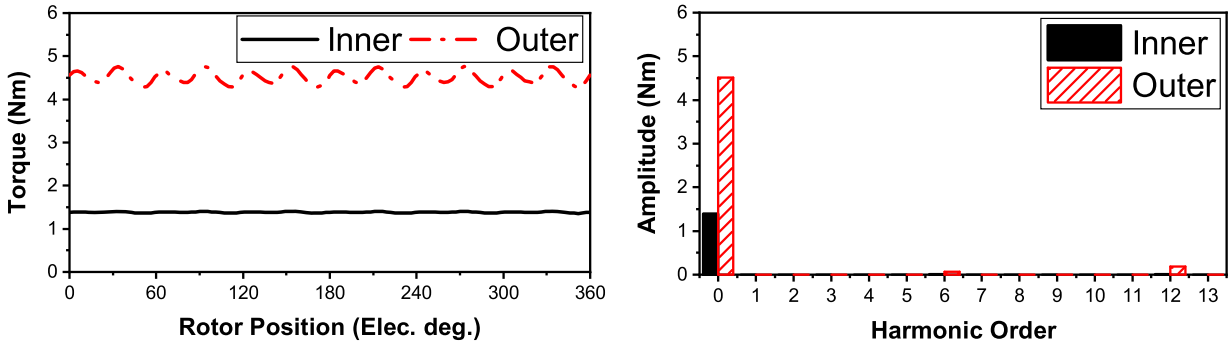

(a) Waveforms.

(b) Spectra.

Fig. C.4. Torque of 12s-10p/14p YCDRPM machine.

Therefore, the 12s-10p/14p YCDRPM machine with a large inner bore radius (35mm) is optimised under the same conditions to maximise the total torque. The inner bore radius is increased from 15mm to 35mm to increase the inner air gap radius, similar to the outer air gap radius. The optimised parameters are listed in Table C.2, and corresponding open circuit flux line and flux density distributions are shown in Fig. C.5. Fig. C.6 shows the electromagnetic performances of the optimised 12s-10p/14p YCDRPM machine with a 35mm inner bore. It can be seen that since the pole arc ratio is small, the magnetic loadings of the 35mm inner bore 12s-10p/14p YCDRPM machine are low, and the back EMF waveform is not sinusoidal. Thus, the high rotor pole numbers for YCDRPM machines with a 35mm inner bore radius are considered to prevent magnetic saturation on the lamination while also improving the magnetic loadings. Since the YCDRPM machine has a yokeless modular stator, only the FSCW machines are considered, and the slot number is doubled from 12 slots to 24 slots in Chapter 4.

TABLE C.2
DESIGNS OF OPTIMISED 12 SLOTS-10/14 POLES YCDRPM MACHINE WITH 35MM INNER BORE RADIUS

Parameter	12s-10p/14p
Inner bore radius (mm)	35
Outer PM thickness (mm)	1.4
Inner PM thickness (mm)	1.5
Outer PM pole arc (°elec.)	19
Inner PM pole arc (°elec.)	14.8
PM volume (cm^3)	22.2
Stator outer radius (mm)	44.8
Stator inner radius (mm)	40
Stator outer slot opening (mm)	9.6
Stator inner slot opening (mm)	5.7
Outer tooth-tip height (mm)	1
Inner tooth-tip height (mm)	0.6
Outer tooth-tip slope (deg.)	10
Inner tooth-tip slope (deg.)	2
Stator tooth width (mm)	9.2
Slot area (mm^2)	33.8

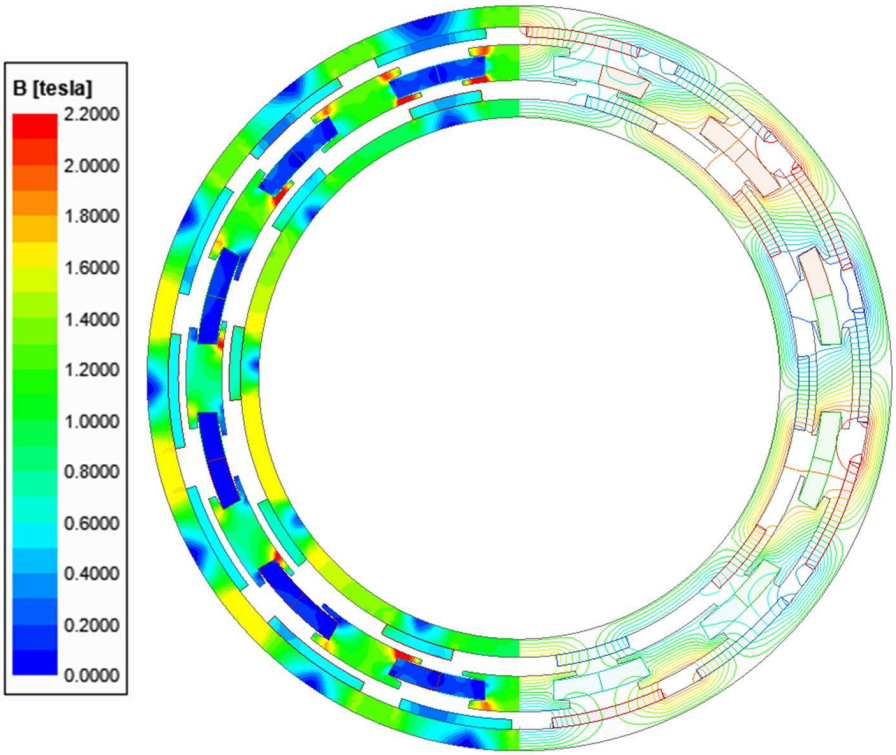

Fig. C.5. Open circuit flux density distributions and flux lines of 35mm inner bore 12s-10p/14p YCDRPM machine.

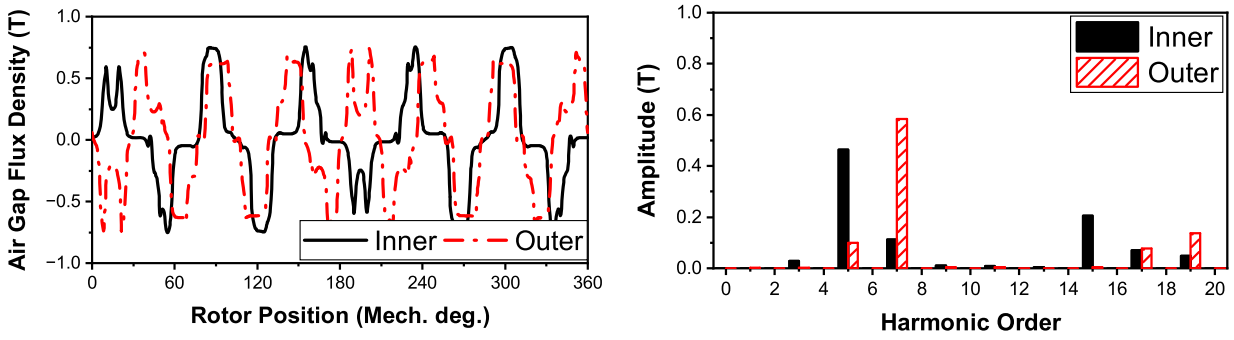

(a) Air gap flux densities.

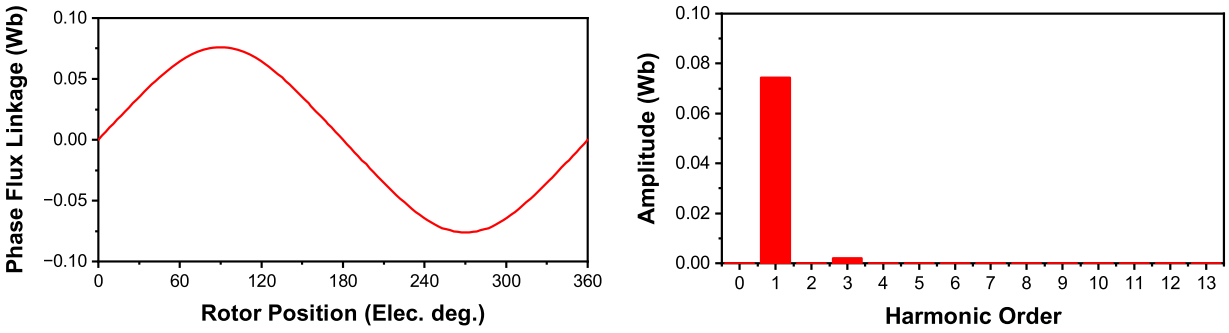

(b) Phase-A flux linkage.

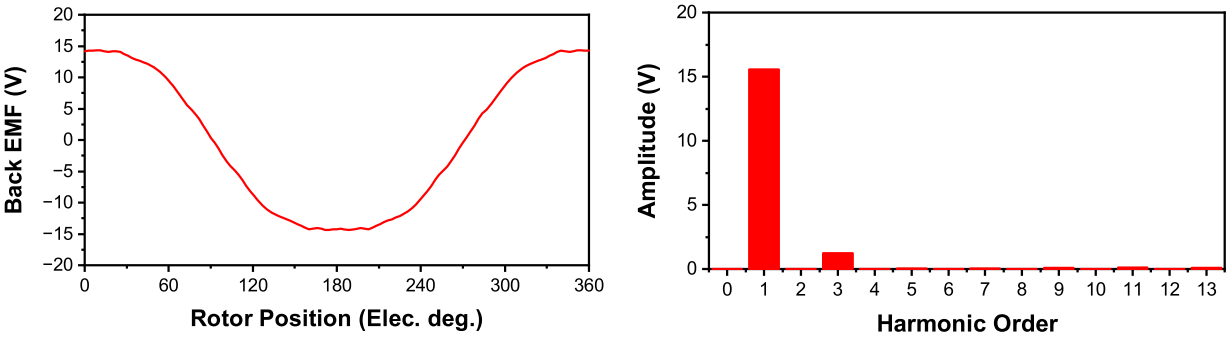

(c) Back EMF.

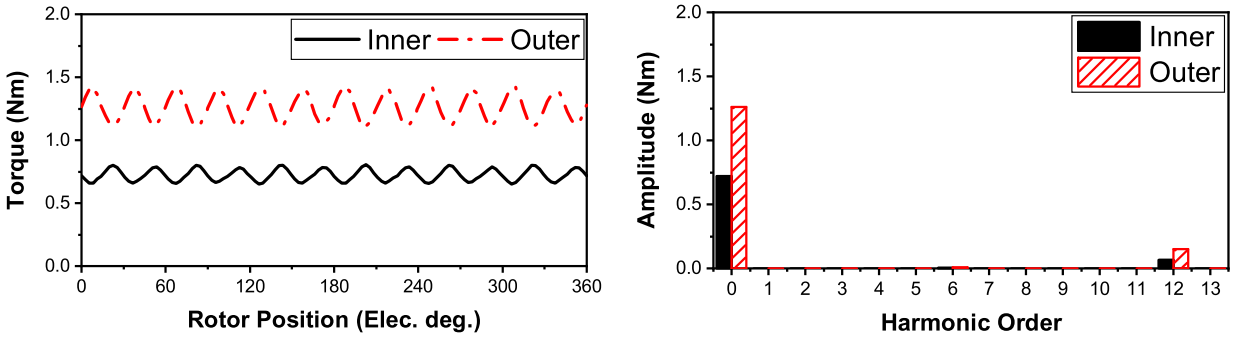

(d) Torques.

Fig. C.6. Electromagnetic performances of 12s-10p/14p YCDRPM machine.

REFERENCES

[ALL20]	A. Allahyari and H. Torkaman, "A novel high-performance consequent pole dual rotor permanent magnet vernier machine," *IEEE Transactions on Energy Conversion*, vol. 35, no. 3, pp. 1238-1246, Sept. 2020.
[ATA01]	K. Atallah and D. Howe, "A novel high-performance magnetic gear," *IEEE Trans. on Mag.*, vol. 37, no. 4, pp. 2844-2846, July 2001.
[ATA04]	K. Atallah, S. D. Calverley, and D. Howe, "Design, analysis and realization of a high-performance magnetic gear," *IEE Proc.—Elect. Power Appl.*, vol. 151, no. 2, pp. 135–143, 2004.
[ATA06]	K. Atallah, S. D. Calverley, and D. Howe, "Design, analysis and realisation of a high-performance magnetic gear," *Proc. Inst. Elect. Eng.-Elect. Power Appl.*, vol. 151, no. 2, pp. 135–143, Feb. 2006.
[ATA08]	K. Atallah, J. Rens, S. Mezani, and D. Howe, "A novel "Pseudo" direct-drive brushless permanent magnet machine," *IEEE Transactions on Magnetics*, vol. 44, no. 11, pp. 4349-4352, Nov. 2008.
[BAI15a]	J. Bai, P. Zheng, B. Yu, L. Cheng, S. Zhang, and Z. Liu, "Investigation of a magnetic-field modulated brushless double-rotor machine with the same polarity of pm rotor," *IEEE Transactions on Magnetics*, vol. 51, no. 11, pp. 1-4, Art no. 8110004, Nov. 2015.
[BAI15b]	J. Bai, P. Zheng, C. Tong, Z. Song, and Q. Zhao, "Characteristic analysis and verification of the magnetic-field-modulated brushless double-rotor machine," *IEEE Trans. Ind. Electron*., vol. 62, no. 7, pp. 4023–4033, Jul. 2015.
[BAI15c]	J. Bai, P. Zheng, L. Cheng, S. Zhang, J. Liu, and Z. Liu, "A new magnetic-field-modulated brushless double-rotor machine," *IEEE Transactions on Magnetics*, vol. 51, no. 11, pp. 1-4, Art no. 8112104, Nov. 2015.
[BAI16]	J. Bai, Y. Liu, C. Tong, Z. Song, and P. Zheng, "Investigation into a magnetic-field-modulated brushless double-rotor machine with the high-strength and low-loss modulating ring rotor," *IEEE Transactions on Magnetics*, vol. 52, no. 7, pp. 1-4, Art no. 8105504, July 2016.

[BIA06]	N. Bianchi, S. Bolognani, and P. Frare, “Design criteria for high-efficiency SPM synchronous motors,” *IEEE Trans. Energy Convers.*, vol. 21, no. 2, pp. 396–404, Jun. 2006.
[BID11]	D. Bidart, M.P. David, P. Maussion, and M. Fadel, "Mono inverter multi-parallel permanent magnet synchronous motor: structure and control strategy", *IET Elec. Power Appl.*, 5, (3), pp. 288–294, 2011.
[BOO10]	J. D. Booker, P. H. Mellor, R. Wrobel, and D. Drury, “A compact, high efficiency contra-rotating generator suitable for wind turbines in the urban environment,” *Renewable energy*, vol. 35, no. 9, pp. 2027–2033, 2010.
[BOU94]	A. Bouscayrol, S. Siala, M. Pietrzak-David and B. deFornel, "Four-legged PWM inverters feeding two induction motors for a vehicle drive application," *1994 Fifth International Conference on Power Electronics and Variable-Speed Drives*, London, UK, pp. 700-705, 1994.
[BOU97]	B.N. Bourtsev, V.N. Kvokov, I.M. Vainstein, and B.A. Petrosian, "Phenomenon of a coaxial helicopter high figure of merit at hover", *Proceedings of 23rd European Rotorcraft Forum*, Dresden, Germany, 16-18 Sept. 1997.
[BOU99]	B.N. Bourtsev, S.V. Selemenev, and V.P.Vagis, "Coaxial helicopter rotor design & aeromechanics", *Proceedings of 25th European Rotorcraft Forum*, Rome, Italy, 14-16 Sept. 1999.
[CAI14]	H. Cai, B. Guan, and L. Xu, "Low-cost ferrite pm-assisted synchronous reluctance machine for electric vehicles," *IEEE Transactions on Industrial Electronics*, vol. 61, no. 10, pp. 5741-5748, Oct. 2014.
[CAO12]	W. P. Cao, B. C. Mecrow, G. J. Atkinson, J. W. Bennett, and D. J. Atkinson, “Overview of electric motor technologies used for more electric aircraft (MEA),” *IEEE Trans. Ind. Electron.*, vol. 59, no. 9, pp. 3523–3531, Sep. 2012.
[CAO21]	L. Cao, K. T. Chau, C. H. T. Lee, and H. Wang, "A double-rotor flux-switching permanent-magnet motor for electric vehicles with magnetic differential," *IEEE Transactions on Industrial Electronics*, vol. 68, no. 2, pp. 1004-1015, Feb. 2021.
[CHA07]	K. T. Chau, D. Zhang, J. Z. Jiang, C. Liu, and Y. Zhang, "Design of a magnetic-geared outer-rotor permanent-magnet brushless motor for electric vehicles," *IEEE*

	Transactions on Magnetics, vol. 43, no. 6, pp. 2504-2506, June 2007.
[CHA08]	K. T. Chau, C. C. Chan, and C. Liu, "Overview of permanent-magnet brushless drives for electric and hybrid electric vehicles," *IEEE Trans. on Ind. Elec.*, vol. 55, no. 6, pp. 2246-2257, June 2008.
[CHE11]	J. Chen, F. Zhang, and W. Zhang, "No-load torque ripple analysis of a novel permanent magnet synchronous motor with anti-rotation dual rotors using finite element method," *2011 International Conference on Electrical Machines and Systems*, pp. 1-5, 2011.
[CHE21]	H. Chen, A. M. EL-Refaie, Y. Zuo, S. Cai, S. Xie, and C. H. T. Lee, "Evaluation of a contra-rotating flux- modulated machine featured with dual flux-modulation for wind power generation," *IEEE Transactions on Industrial Electronics*, vol. 69, no. 9, pp. 8770-8781, Sept. 2022.
[CHE22]	H. Chen, A. M. EL-Refaie, Y. Zuo, S. Cai, S. Xie, and C. H. T. Lee, "Evaluation of a contra-rotating flux- modulated machine featured with dual flux-modulation for wind power generation," *IEEE Trans. on Ind. Elec.*, vol. 69, no. 9, pp. 8770-8781, Sept. 2022.
[COL97]	C. P. Coleman, "A survey of theoretical and experimental coaxial rotor aerodynamic research," *NASA, Ames Research Center Moffett Field*, CA United States, Mar. 1997.
[COR22]	J. K. Cornelius, J. Zhang, S. Schmitz, and E. Smith, "Comprehensive analysis of coaxial rotor dynamics on a support arm," AIAA/AHS VTOL Research, San Diego, CA & Virtual, 3-7 Jan. 2022.
[CRO23]	R. De Croo, T. Van Lierde, and F. De Belie, "Study and validation of a contra-rotating dual rotor switched reluctance machine in marine propulsion," *2023 IEEE International Conference on Electrical Systems for Aircraft, Railway, Ship Propulsion and Road Vehicles & International Transportation Electrification Conference (ESARS-ITEC)*, Venice, Italy, pp. 1-6, 2023.
[DAL18]	A. Dalal and P. Kumar, "Design, prototyping, and testing of a dual-rotor motor for electric vehicle application," *IEEE Transactions on Industrial Electronics*, vol. 65, no. 9, pp. 7185-7192, Sept. 2018.
[DU08]	Shiqin Du, Yuejin Zhang, and Jianzhong Jiang, "Research on a novel combined

	permanent magnet electrical machine," *2008 International Conference on Electrical Machines and Systems*, Wuhan, 2008, pp. 3564-3567.
[DUB16]	Arthur Dubois, Martin van der Geest, JoeBen Bevirt, Robert Christie, Nicholas K. Borer, and Sean C. Clarke, "Design of an electric propulsion system for SCEPTOR," Conference Proceedings, Hampton, NASA CASI, 2016.
[EGU20]	I. Eguren, G. Almandoz, A. Egea, G. Ugalde, and A. J. Escalada, "Linear machines for long stroke applications—a review," IEEE Access, vol. 8, pp. 3960-3979, 2020.
[EL10]	A. M. EL-Refaie, "Fractional-slot concentrated-windings synchronous permanent magnet machines: Opportunities and challenges," *IEEE Trans. Ind. Electron.*, vol. 57, no. 1, pp. 107-121, Jan. 2010.
[FAR21]	M. Faraday, "On some new electro-magnetical motions, and on the theory of magnetism", Quarterly Journal of Science, vol. 12, pp. 74-96, 1821.
[FAR31]	M. Faraday, "Experimental researches in electricity", Philosophical Transactions of the Royal Society of London, vol. 121, pp. 1-300, 1831.
[FRA12]	T. V. Frandsen, P. O. Rasmussen, and K. K. Jensen, "Improved motor intergrated permanent magnet gear for traction applications." *Proceedings Energy Conversion Congress and Exposition* (ECCE), pp. 3332–3339, 2012.
[FRA15]	T. V. Frandsen and P. O. Rasmussen, "Slip torque investigation and magnetic redesign of motor integrated permanent magnet gear*." Proceedings International Conference on Electrical Machines and System* (ICEMS), pp. 929–935, Pattaya, Thailand, 2015.
[FU10]	W. N. Fu and S. L. Ho, "A quantitative comparative analysis of a novel flux-modulated permanent-magnet motor for low-speed drive*," IEEE Transactions on Magnetics*, vol. 46, no. 1, pp. 127-134, Jan. 2010.
[FUJ15]	S. Fujiwara, S. Morimoto, M. Sanada, and Y. Inoue, "Influence of magnet arrangement on torque characteristics of dual-rotor PMSMs," *2015 IEEE 11th International Conference on Power Electronics and Drive Systems*, Sydney, NSW, pp. 816-821, 2015.
[GAN16]	A. Gandhi and L. Parsa, "Double-rotor flux-switching permanent magnet machine with yokeless stator," *IEEE Transactions on Energy Conversion*, vol. 31, no. 4, pp. 1267-1277, Dec. 2016.

[GER13]	S. Gerber and R. -J. Wang, “Torque capability comparison of two magnetically geared PM machine topologies.” *Proceedings International Conference on Industrial Technology* (ICIT), pp. 1915–1920, Cape Town, 2013.
[GER15]	S. Gerber and R. -J. Wang, "Design and evaluation of a magnetically geared PM machine*," IEEE Transactions on Magnetics*, vol. 51, no. 8, pp. 1-10, Aug. 2015.
[GOL18]	D. Golovanov, L. Papini, D. Gerada, Z. Xu, and C. Gerada, "Multidomain optimization of high-power-density PM electrical machines for system architecture selection," *IEEE Transactions on Industrial Electronics*, vol. 65, no. 7, pp. 5302-5312, July 2018.
[GOL19a]	D. Golovanov, A. Galassini, L. Flanagan, D. Gerada, Z. Xu, and C. Gerada, "Dual-rotor permanent magnet motor for electric superbike," *2019 IEEE International Electric Machines & Drives Conference (IEMDC)*, 2019, pp. 951-956.
[GOL19b]	D. Golovanov and C. Gerada, "An analytical subdomain model for dual-rotor permanent magnet motor with Halbach array," *IEEE Transactions on Magnetics*, vol. 55, no. 12, pp. 1-16, Dec. 2019.
[HAG88]	R. Hager and D. Vrabel, "Advanced turboprop project," *NASA*, SP-495, 1988.
[HAN19]	X. Han et al., "Flexible energy conversion control strategy for brushless dual-mechanical-port dual-electrical-port machine in hybrid vehicles," *IEEE Transactions on Power Electronics*, vol. 34, no. 4, pp. 3910-3920, April 2019.
[HAO14]	L. Hao, M. Lin, D. Xu, W. Zhang, and N. Li, "Rotor design techniques for reducing the cogging torque in a novel dual-rotor axial field flux-switching permanent magnet machine," *2014 17th International Conference on Electrical Machines and Systems* (ICEMS), Hangzhou, China, pp. 1581-1586, 2014.
[HAS20]	A. Hassannia, "Conceptual design of fractional slot concentrated winding dual-rotor double-speed synchronous motor," *IEEE Transactions on Energy Conversion*, vol. 35, no. 2, pp. 986-993, June 2020.
[HAY52]	L. H. Hayward, "A review of helicopter patents: a lecture presented to the members of the helicopter association of Great Britain on Friday, January 18, 1952", *Aircraft Engineering and Aerospace Technology*, Vol. 24 No. 4, pp. 92-105, Jan. 1952.
[HE21]	T. R. He, Z. Q. Zhu, F. Xu, H. Bin, D. Wu, L. M. Gong, and J. T. Chen, “Comparative study of 6-slot/2-pole high-speed permanent magnet motors with different winding

	configurations," *IEEE Trans. Ind. Appl.*, vol. 57, no. 6, pp. 5864-5875, Nov.-Dec. 2021.
[HOL04]	B. J. Holmes, M. H. Durham, and S. E. Tarry, "Small aircraft transportation system concept and technologies," *Journal of aircraft*, vol. 41, no. 1, pp. 26–35, 2004.
[HOL94]	J. K. Holt and D. G. White, "High efficiency, counter-rotating ring thruster for underwater vehicles", *Autonomous Underwater Vehicle Technology*, 1994, pp. 337-339.
[HOU18]	L. X. Hou and A. K. Hu, "Energy saving performance analysis of contrarotating azimuth propulsor," *Appl. Ocean Res.*, vol. 72, pp. 12–22, Mar. 2018.
[HUA24]	R. Huang, Z. Dong, Z. Song, and C. Liu, "A novel counter-rotating AFPM machine based on magnetic-field modulation for underwater propulsion system," *IEEE Transactions on Industrial Electronics*, vol. 71, no. 3, pp. 2167-2176, March 2024.
[JAF20]	M. Jafarboland and M. M. Sargazi, "Introducing a novel FSPM motor with double rotor and toroidal windings," *IET Electric Power Applications*, vol. 14, no. 7, pp. 1221-1227, 7 2020.
[JIA08]	L. Jian, K. T. Chau, and J. Z. Jiang, "An integrated magnetic-geared permanent-magnet in-wheel motor drive for electric vehicles," *2008 IEEE Vehicle Power and Propulsion Conference*, Harbin, China, 2008, pp. 1-6.
[JIA09]	L. Jian, K. T. Chau, and J. Z. Jiang, "A magnetic-geared outer-rotor permanent-magnet brushless machine for wind power generation," *IEEE Transactions on Industry Applications*, vol. 45, no. 3, pp. 954-962, May-June 2009.
[JIA11]	Linni Jian, Guoqing Xu, Yu Gong, Jianjian Song, Jianing Liang, and Ming Chang, "Electromagnetic design and analysis of a novel magnetic-gear-integrated wind power generator using time-stepping finite element method," *Progress In Electromagnetics Research*, Vol. 113, 351-367, 2011.
[JIA12]	L. Jian, W. Gong, G. Xu, J. Liang, and W. Zhao, "Integrated magnetic-geared machine with sandwiched armature stator for low-speed large-torque applications," *IEEE Transactions on Magnetics*, vol. 48, no. 11, pp. 4184-4187, Nov. 2012.
[JON08]	M. Jones, S.N. Vukosavic, D. Dujic, E. Levi, and P. Wright, "Five-leg inverter PWM technique for reduced switch count two-motor constant power applications," *IET Elec.*

	Power Appl., 2 (5), pp 257-287, Sept. 2008.
[JUN05]	S. N. Jung, T.-S. No, and K.-W. Ryu, “Aerodynamic performance prediction of a 30 kW counter-rotating wind turbine system,” *Renewable energy*, vol. 30, no. 5, pp. 631–644, 2005.
[KEL69]	D. H. Kelly, "Double-Rotor Induction Motor," *IEEE Transactions on Power Apparatus and Systems*, vol. PAS-88, no. 7, pp. 1086-1092, July 1969.
[KEL94]	P. M. Kelecy and R. D. Lorenz, "Control methodology for single inverter, parallel connected dual induction motor drives for electric vehicles," *Proceedings of 1994 Power Electronics Specialist Conference - PESC'94*, Taipei, Taiwan, pp. 987-991 vol.2, 1994.
[KHA18]	M. F. H. Khatab, Z. Q. Zhu, H. Y. Li, and Y. Liu, "Comparative study of novel axial flux magnetically geared and conventional axial flux permanent magnet machines," *CES Transactions on Electrical Machines and Systems*, vol. 2, no. 4, pp. 392-398, Dec. 2018.
[KUM16]	B. V. R. Kumar and K. S. Kumar, "Design of a new dual rotor radial flux BLDC motor with Halbach array magnets for an electric vehicle," *2016 IEEE International Conference on Power Electronics, Drives and Energy Systems* (PEDES), Trivandrum, pp. 1-5, 2016.
[KWO18]	J. Kwon and B. Kwon, "High-efficiency dual output stator-pm machine for the two-mode operation of washing machines," *IEEE Transactions on Energy Conversion*, vol. 33, no. 4, pp. 2050-2059, Dec. 2018.
[LEE15a]	Y. Lee and J. -I. Ha, "Control method for mono inverter dual parallel interior permanent magnet synchronous machine drive system," *2015 IEEE Energy Conversion Congress and Exposition (ECCE)*, Montreal, QC, Canada, pp. 5256-5262, 2015.
[LEE15b]	Y. Lee and J. -I. Ha, "Control method for mono inverter dual parallel surface-mounted permanent-magnet synchronous machine drive system," *IEEE Transactions on Industrial Electronics*, vol. 62, no. 10, pp. 6096-6107, Oct. 2015.
[LEI06]	J. G. Leishman, "Principles of helicopter aerodynamics, " 2nd ed. Cambridge: Cambridge University Press, 2006.

[LEV03]	E. Levi, M. Jones, and S.N. Vukosavic, "Even-phase multi-motor vector controlled drive with single inverter supply and series connection of stator windings," *IEE Proceedings-Electric Power Application*, 150 (5), pp 580-590, Sept. 2003.
[LI13]	Q. Li, T. Fan, and X. Wen, "Armature-reaction magnetic field analysis for interior permanent magnet motor based on winding function theory," *IEEE Trans. on Mag.*, vol. 49, no. 3, pp. 1193-1201, March 2013.
[LI16a]	D. Li, R. Qu, X. Ren, and Y. Gao, "Brushless dual-electrical-port, dual mechanical port machines based on the flux modulation principle," *2016 IEEE Energy Conversion Congress and Exposition* (ECCE), Milwaukee, WI, USA, pp. 1-8, 2016.
[LI16b]	D. Li, R. Qu, J. Li, L. Xiao, L. Wu, and W. Xu, "Analysis of torque capability and quality in vernier permanent-magnet machines," *IEEE Trans. on Ind. Appl.*, vol. 52, no. 1, pp. 125-135, Jan.-Feb. 2016.
[LI18]	Y. Li, D. Bobba, and B. Sarlioglu, "Design and optimization of a novel dual-rotor hybrid pm machine for traction application," *IEEE Transactions on Industrial Electronics*, vol. 65, no. 2, pp. 1762-1771, Feb. 2018.
[LIA21]	Z. Liang, X. Ren, D. Li, R. Qu, and X. Han, "Analysis of a spoke-array brushless dual-electrical-port dual-mechanical-port machine with reluctance rotor," *IEEE Transactions on Industrial Electronics*, vol. 68, no. 4, pp. 2999-3011, April 2021.
[LIP08]	T. A. Lipo, “Analysis of synchronous machine,” Univ. Wisconsin, Madison, WI, 2008, pp. 53–64.
[LIU12]	C. Liu, K. T. Chau, and Z. Zhang, "Novel design of double-stator single-rotor magnetic-geared machines," *IEEE Transactions on Magnetics*, vol. 48, no. 11, pp. 4180-4183, Nov. 2012
[LIU16]	Y. Liu, S. Niu, and W. Fu, "Design of an electrical continuously variable transmission based wind energy conversion system," *IEEE Transactions on Industrial Electronics*, vol. 63, no. 11, pp. 6745-6755, Nov. 2016.
[LIU18]	G. Liu, G. Qiu, J. Shi, and F. Zhang, "Study on counter-rotating dual-rotor permanent magnet motor for underwater vehicle propulsion," *IEEE Transactions on Applied Superconductivity*, vol. 28, no. 3, pp. 1-5, April 2018.
[LIU19]	Y. Liu, H. Yu, and Y. Wang, "Establishment of a new dual rotor flux switching motor

	magnetic circuit model and optimization of no-load back EMF," *IEEE Transactions on Magnetics*, vol. 55, no. 12, pp. 1-5, Dec. 2019.
[LIU19]	Y. Liu and Z. Q. Zhu, "Influence of gear ratio on the performance of fractional slot concentrated winding permanent magnet machines," *IEEE Trans. on Ind. Elec.*, vol. 66, no. 10, pp. 7593-7602, Oct. 2019.
[LIU21]	J. Liu, J. Bai, G. Liu, Y. Wang, and P. Zheng, "Investigation of an integrated magnetic-field-modulated brushless double-rotor machine with an improved PM rotor," *IEEE Transactions on Magnetics*, vol. 57, no. 2, pp. 1-6, Feb. 2021.
[LIU22a]	G. Liu, P. Zheng, J. Bai, J. Liu, and Y. Wang, "Investigation of a dual-winding dual-flux-concentrated magnetic-field-modulated brushless compound-structure machine," *IEEE Transactions on Magnetics*, vol. 58, no. 2, pp. 1-5, Feb. 2022.
[LIU22b]	J. Liu, J. Bai, P. Zheng, Y. Wang, G. Liu, and J. Lang, "A quasi-sinusoidal concentrated winding used in an integrated magnetic-field-modulated brushless compound-structure machine," *IEEE Transactions on Industrial Electronics*, vol. 69, no. 8, pp. 7675-7684, Aug. 2022.
[LUO17]	X. Luo and S. Niu, "A novel contra-rotating power split transmission system for wind power generation and its dual MPPT control strategy," *IEEE Transactions on Power Electronics*, vol. 32, no. 9, pp. 6924-6935, Sept. 2017.
[LUO17]	X. Luo and S. Niu, "A novel contra-rotating power split transmission system for wind power generation and its dual MPPT control strategy," *IEEE Trans. on Power Elec.*, vol. 32, no. 9, pp. 6924-6935, Sept. 2017.
[LUO19]	D. Luo, R. He, S. Huang, and X. Su, "Optimized vector control strategy for contrarotating permanent magnet synchronous motor under serious unbalanced load adopting torque compensation," *2019 22nd International Conference on Electrical Machines and Systems (ICEMS)*, Harbin, China, pp. 1-6, 2019.
[MAL13]	D. Malgar, N. G. S. Udupa, and N. Venkatram, “Investigation of fatigue behavior of traction gear box gears,” *Proc. Nat. Conf. Challenges Res. Technol. Coming Decades* (CRT 2013), pp. 1–5, Jul. 2013.
[MIR21]	S. A. Mirnikjoo, K. Abbaszadeh, and S. E. Abdollahi, "Multiobjective design optimization of a double-sided flux switching permanent magnet generator for counter-

	rotating wind turbine applications," *IEEE Transactions on Industrial Electronics*, vol. 68, no. 8, pp. 6640-6649, Aug. 2021.
[NIU10]	S. Niu, S. L. Ho, W. N. Fu, and L. L. Wang, "Quantitative comparison of novel vernier permanent magnet machines," *IEEE Transactions on Magnetics*, vol. 46, no. 6, pp. 2032-2035, June 2010.
[NIU13]	S. Niu, S. L. Ho, and W. N. Fu, "Design of a novel electrical continuously variable transmission system based on harmonic spectra analysis of magnetic field," *IEEE Transactions on Magnetics*, vol. 49, no. 5, pp. 2161-2164, May 2013.
[PEL12]	G. Pellegrino, A. Vagati, P. Guglielmi, and B. Boazzo, “Performance comparison between surface-mounted and interior PM motor drives for electric vehicle application,” *IEEE Trans. Ind. Electron.*, vol. 59, no. 2, pp. 803–811, 2012.
[POL13]	H. Polinder, J. A. Ferreira, B. B. Jensen, A. B. Abrahamsen, K. Atallah, and R. A. McMahon, “Trends in wind turbine generator systems,” *IEEE J. Emerg. Sel. Topics Power Electron.*, vol. 1, no. 3, pp. 174–185, Sep. 2013.
[POT15]	J. H. J. Potgieter and M. J. Kamper, "Design optimization of directly grid-connected PM machines for wind energy applications," *IEEE Transactions on Industry Applications*, vol. 51, no. 4, pp. 2949-2958, July-Aug. 2015.
[POT16]	J. H. J. Potgieter and M. J. Kamper, "Double PM-rotor, toothed, toroidal-winding wind generator: a comparison with conventional winding direct-drive PM wind generators over a wide power range," *IEEE Transactions on Industry Applications*, vol. 52, no. 4, pp. 2881-2891, July-Aug. 2016.
[QU03a]	Ronghai Qu and T. A. Lipo, “Dual-rotor, radial-flux, toroidally wound, permanent-magnet machines,” *IEEE Trans. Ind. Appl.*, vol. 39, no. 6, pp. 1665-1673, Nov.-Dec. 2003.
[QU03b]	Ronghai Qu, M. Aydin, and T. A. Lipo, "Performance comparison of dual-rotor radial-flux and axial-flux permanent-magnet BLDC machines," *IEEE International Electric Machines and Drives Conference*, 2003. IEMDC'03., 2003, pp. 1948-1954 vol.3.
[QU04]	Ronghai Qu and T. A. Lipo, "Design and parameter effect analysis of dual-rotor, radial-flux, toroidally wound, permanent-magnet machines," *IEEE Transactions on Industry Applications*, vol. 40, no. 3, pp. 771-779, May-June 2004.

[RAN22a]	Z. T. Ran, Z. Q. Zhu, and D. Liang, “Comparative study of radial-flux dual-rotor fractional-slot permanent magnet machines with series and parallel magnetic circuits,” *25th Inter. Conf. on Elec. Mach. and Sys. (ICEMS)*, Thailand, pp. 1-6, 2022
[RAN22b]	Z. T. Ran, Z. Q. Zhu, F. R. Wei, and E. Cetin, "Comparative study of yokeless dual-rotor and external-rotor radial-flux fractional-slot pm machines," *2022 Inter. Conf. on Elec. Mach. (ICEM)*, Valencia, Spain, pp. 1913-1919, 2022.
[RAS05]	P. O. Rasmussen, T. O. Andersen, F. T. Jorgensen, and O. Nielsen, "Development of a high-performance magnetic gear," *IEEE Transactions on Industry Applications*, vol. 41, no. 3, pp. 764-770, May-June 2005.
[RAS13]	P. O. Rasmussen, T. V. Frandsen, K. K. Jensen, and K. Jessen, "Experimental evaluation of a motor-integrated permanent-magnet gear," *IEEE Transactions on Industry Applications*, vol. 49, no. 2, pp. 850-859, March-April 2013.
[RED12]	P. B. Reddy *et al.*, “Comparison of interior and surface PM machines equipped with fractional-slot concentrated windings for hybrid traction applications,’’ *IEEE Trans. Energy Convers*., vol. 27, no. 3, pp. 593–602, Sep. 2012.
[REH22]	M. Rehan, F. Akram, A. Shahzad, T. A. Shams, and Q. Ali, “Vertical take-off and landing hybrid unmanned aerial vehicles: An overview,” *Aeronautical journal*, vol. 126, no. 1306, pp. 2017–2057, 2022.
[REN17]	X. Ren, D. Li, R. Qu, and T. Zou, "A brushless dual-mechanical-port dual-electrical-port machine with spoke array magnets in flux modulator," *IEEE Transactions on Magnetics*, vol. 53, no. 11, pp. 1-6, Nov. 2017
[REN21]	X. Ren, D. Li, R. Qu, X. Han, and Z. Liang, "A brushless dual-electrical-port dual-mechanical-port machine with integrated winding configuration," *IEEE Transactions on Industrial Electronics*, vol. 68, no. 4, pp. 3022-3032, April 2021.
[SAN13]	P. Santhana Kumar, A. Abraham, R. Joseph Bensingh, and S. Ilangovan, “Computational and experimental analysis of a counter-rotating wind turbine system,” *Journal of scientific & industrial research* (New Delhi, India : 1963), vol. 72, no. 5, pp. 300–306, 2013.
[SAS98]	N. Sasaki et al., “Design system for optimum contra-rotating propellers,” *Journal of marine science and technology*, vol. 3, no. 1, pp. 3–21, 1998.

[SCH12]	R. Schnell, J. Yin, C. Voss, and E. Nicke, "Assessment and optimization of the aerodynamic and acoustic characteristics of a counter rotating open rotor," *Journal of turbomachinery*, vol. 134, no. 6, 2012.
[SHE07]	W Z Shen, V A K Zakkam, J N Sørensen, and K Appa, “Analysis of counter-rotating wind turbines,” *Journal of Physics: Conference Series*, vol. 75, no. 1, p. 012003, 2007.
[SHI20]	H. Shin, J. Chang, and D. Hong, "Design and characteristics analysis of coaxial magnetic gear for contra-rotating propeller in yacht," *IEEE Transactions on Industrial Electronics*, vol. 67, no. 9, pp. 7250-7259, Sept. 2020.
[SHI98]	Shinn C. "The multi-unit rotor blade system integrated wind turbine", US Patent No. 5876181; 1998.
[SI22]	J. Si, T. Zhang, Y. Hu, C. Gan, and Y. Li, "An axial-flux dual-rotor slotless permanent magnet motor with novel equidirectional toroidal winding," *IEEE Trans. Energy Convers.*, vol. 37, no. 3, pp. 1752-1763, Sept. 2022.
[SIN21]	P. Singh and P.P. Friedmann, “Aeromechanics and aeroelastic stability of coaxial rotors,” *Journal of aircraft*, vol. 58, no. 6, pp. 1386–1405, 2021.
[SON14]	S. Song, Y. Xu, H. Tian, and X. Gong, "Design and simulation of dual rotor permanent magnet brushless DC motor," *2014 17th International Conference on Electrical Machines and Systems* (ICEMS), Hangzhou, pp. 1591-1595, 2014.
[SPO88]	E. Spooner and B. J. Chalmers, "Toroidally-wound, slotless, axial-flux, permanent-magnet, brushlessdc motors," *Proc. Int. Conf. Elec. Machines*, Pisa, Vol. 11, p. 81, Sept 1988.
[SPO90]	E. Spooner and B. J. Chalmers, “TORUS, a toroidalstator, permanent-magnet machine for small-scale power generation,” *Proc. Int. Conf. Elec. Machines*, MIT, Cambridge, USA. Vol 111, p. 1053, Aug. 1990.
[STR82]	W.C. Strack, G. Knip, A. L. Weisbrich, J. Godston, and E. Bradley, "Technology and benefits of aircraft counter rotation propellers," *NASA*, Category Aircraft Propulsion and Power, United States, Jan. 1982.
[TAR22]	N. Taran, D. Klink, G. Heins, V. Rallabandi, D. Patterson, and D. M. Ionel, "A comparative study of yokeless and segmented armature versus single sided axial flux pm machine topologies for electric traction," IEEE Transactions on Industry

	Applications, vol. 58, no. 1, pp. 325-335, Jan.-Feb. 2022.
[TOB99]	A. Toba and T. A. Lipo, "Novel dual-excitation permanent magnet Vernier machine," *Conference Record of the 1999 IEEE Industry Applications Conference.* Thirty-Forth IAS Annual Meeting (Cat. No.99CH36370), Phoenix, AZ, USA, pp. 2539-2544 vol.4, 1999.
[UBA17]	C. U. Ubadigha, M. Tsai, and M. Hsieh, "Modulating ring structural configuration influence on the dual air-gap magnetic gear electric machine," *IEEE Transactions on Magnetics*, vol. 53, no. 11, pp. 1-6, Art no. 8207406, Nov. 2017.
[UBA20]	C. U. Ubadigha and M. -C. Tsai, "Analysis of integrated magnetic gear motor with dual mechanical output port: a block diagram approach," *IEEE Transactions on Energy Conversion*, vol. 35, no. 3, pp. 1301-1308, Sept. 2020.
[ULL22a]	W. Ullah, F. Khan, and S. Hussain, "A novel dual rotor permanent magnet flux switching generator for counter rotating wind turbine applications," *IEEE Access*, vol. 10, pp. 16456-16467, 2022.
[ULL22b]	W. Ullah, F. Khan, and S. Hussain, "A comparative study of dual stator with novel dual rotor permanent magnet flux switching generator for counter rotating wind turbine applications," *IEEE Access*, vol. 10, pp. 8243-8261, 2022.
[ULL23a]	W. Ullah, F. Khan, S. Hussain, M. Yousuf, and S. Akbar, "A novel dual port dual rotor wound field flux switching generator with uniform and non-uniform rotor poles for counter-rotating wind power generation," *IEEE Trans. Energy Convers.*, vol. 38, no. 4, pp. 2420-2433, Dec. 2023.
[ULL23b]	W. Ullah, F. Khan, U. B. Akuru, and M. Yousuf, "Magnetic coupling effect and performance analysis of dual rotor permanent magnet flux switching generator for counter rotating wind power generation," *IEEE Trans. Energy Convers.*, vol. 38, no. 4, pp. 2895-2908, Dec. 2023.
[UYG15]	D. Uygun, S. Solmaz, A. Turan, and S. T. Ruzgar, "A new topology for dual rotor/stator BLDC motors applied to marine thrusters," *2015 IEEE 5th International Conference on Power Engineering, Energy and Electrical Drives* (POWERENG), Riga, Latvia, 2015, pp. 353-359.
[VAN13]	J. H. van Wijk and M. J. Kamper, “Double-sided rotor technology for iron-cored

	permanent magnet wind generators: An evaluation," *2013 IEEE Int. Conf. Ind. Tech. (ICIT)*, pp. 1892-1897, 2013.
[WAN09]	L. L. Wang, J. X. Shen, P. C. K. Luk, W. Z. Fei, C. F. Wang, and H. Hao, "Development of a magnetic-geared permanent-magnet brushless motor," *IEEE Transactions on Magnetics*, vol. 45, no. 10, pp. 4578-4581, Oct. 2009.
[WAN12]	J. Wang, R. Qu, and L. Zhou, "Dual-rotor multiphase permanent magnet machine with harmonic injection to enhance torque density," *IEEE Transactions on Applied Superconductivity*, vol. 22, no. 3, pp. 5202204-5202204, June 2012.
[WAN14]	S. Gerber and R. -J. Wang, "Analysis of the end-effects in magnetic gears and magnetically geared machines," 2014 International Conference on Electrical Machines (ICEM), Berlin, Germany, pp. 396-402, 2014.
[WAN17a]	Q. Wang, S. Niu, and S. Yang, "Design Optimization and Comparative Study of Novel Magnetic-Geared Permanent Magnet Machines," *IEEE Transactions on Magnetics*, vol. 53, no. 6, pp. 1-4, June 2017.
[WAN17b]	Y. Wang, S. Niu, and W. Fu, "Electrical-continuously variable transmission system based on doubly fed flux-bidirectional modulation," *IEEE Trans. on Ind. Elec.*, vol. 64, no. 4, pp. 2722-2731, April 2017.
[WAN19]	Y. Wang, S. Niu, and W. Fu, "A novel dual-rotor bidirectional flux-modulation PM generator for stand-alone DC power supply," *IEEE Transactions on Industrial Electronics*, vol. 66, no. 1, pp. 818-828, Jan. 2019.
[WAT04]	J. Watkinson, "Art of the helicopter," 1st ed. Oxford, Burlington, MA: Elsevier Butterworth-Heinemann, 2004.
[WEI22]	Y. Wei, H. Deng, Z. Pan, K. Li, and H. Chen, "Research on a combinatorial control method for coaxial rotor aircraft based on sliding mode," *Defence technology*, vol. 18, no. 2, pp. 280–292, 2022.
[WOO07]	T. J. Woolmer and M. D. McCulloch, "Analysis of the Yokeless And Segmented Armature Machine," *2007 IEEE International Electric Machines & Drives Conference*, Antalya, Turkey, pp. 704-708, 2007.
[WU17]	S. Wu, W. Zhao, S. Wu, and S. Cui, "Design and analysis of counter-rotating dual rotors permanent magnet compensated pulsed alternator," *IEEE Transactions on*

	Plasma Science, vol. 45, no. 7, pp. 1101-1107, July 2017.
[WU88]	B. Wu, S. B. Dewan and P. C. Sen, "A modified current source inverter (MCSI) for a multiple induction motor drive system," *IEEE Transactions on Power Electronics*, vol. 3, no. 1, pp. 10-16, Jan. 1988.
[XIA18]	Z. Xiang, L. Quan, X. Zhu, J. Huang, and D. Fan, "Investigation of optimal split ratio in brushless dual-rotor flux-switching permanent magnet machine considering power allocation," *IEEE Transactions on Magnetics*, vol. 54, no. 3, pp. 1-4, March 2018.
[XIA23]	C. Xia, Y. Feng, M. Jia, Y. Gao, and S. Huang, "A novel counter-rotating axial-flux hybrid-excitation permanent magnet machine with dual-rotor," *IEEE Transactions on Magnetics*, vol. 59, no. 11, pp. 1-5, Art no. 8102605, Nov. 2023.
[XU05]	L. Y. Xu, “Dual-mechanical-port electric machines—A new concept in design and analysis of electric machines,” *Proc. 40th Int. Conf. IEEE Ind. Appl.*, vol. 4, pp. 2828–2834, 2005.
[XU13]	P. Xu, X. Liu, K. Shi, and Y. Du, “Design of dual-rotor radial flux permanent-magnet generator for wind power applications,” *Appl. Mech. Mater.*, vol. 416/417, pp. 9–14, 2013.
[XU17]	P. Xu, K. Shi, Y. Sun, and H. Zhua, “Effect of pole number and slot number on performance of dual rotor permanent magnet wind power generator using ferrite magnets,” *AIP advances*, vol. 7, no. 5, pp. 056631–056631–6, 2017.
[XU21a]	F. Xu et al., “Influence of slot number on electromagnetic performance of 2-pole high-speed permanent magnet motors with toroidal windings,” *IEEE Trans. on Ind. Appl.*, vol. 57, no. 6, pp. 6023-6033, Nov.-Dec. 2021.
[XU21b]	F. Xu *et al*., “Influence of stator gap on electromagnetic performance of 6-slot/2-pole modular high speed permanent magnet motor with toroidal windings,” *IEEE Access*, vol. 9, pp. 94470-94494, 2021.
[Xu24]	H. Xu, Z. Q. Zhu, Y. Zhou, and L. Chen, "Contributions of stator and rotor pms in dual-pm machines with different stator and rotor pole number combinations," IEEE Transactions on Energy Conversion, vol. 39, no. 1, pp. 516-532, March 2024.
[YAN96]	Q. J. Yang, “Fatigue test and reliability design of gears,” *Int. J. Fatigue*, vol. 18, no. 3, pp. 171–177, Apr. 1996.

[YEH12]	Y. Yeh, M. Hsieh, and D. G. Dorrell, "Different arrangements for dual-rotor dual-output radial-flux motors," *IEEE Transactions on Industry Applications*, vol. 48, no. 2, pp. 612-622, March-April 2012.
[YIN17]	X. Yin, Y. Fang, X. Huang, and P. -D. Pfister, "Analytical modeling of a novel vernier pseudo-direct-drive permanent-magnet machine," *IEEE Transactions on Magnetics*, vol. 53, no. 6, pp. 1-4, June 2017.
[ZHA07]	F. Zhang, G. Liu, and X. Wang, "Characteristic simulation of a novel PMSM with opposite-rotation dual rotors," *2007 2nd IEEE Conference on Industrial Electronics and Applications*, Harbin, pp. 618-621, 2007.
[ZHA11]	P. Zhang, G. Sizov, and N. Demerdash, “Comparison of torque ripple minimization control techniques in surface-mounted permanent magnet synchronous machines,” Proc. IEEE IEMDC, pp. 188–193, May 2011.
[ZHA14]	F. Zhang, J. Chen, and G. Liu, "Research on counter-rotating dual rotors permanent-magnet machine for underwater vehicle," *2014 IEEE Conference and Expo Transportation Electrification Asia-Pacific* (ITEC Asia-Pacific), Beijing, pp. 1-7, 2014.
[ZHA17]	W. Zhao, D. Chen, T. A. Lipo, and B. Kwon, "Dual airgap stator- and rotor-permanent magnet machines with spoke-type configurations using phase-group concentrated coil windings," *IEEE Transactions on Industry Applications*, vol. 53, no. 4, pp. 3327-3335, July-Aug. 2017.
[ZHA20a]	Z. Zhang, "Consequent pole toroidal winding dual rotor permanent magnet synchronous machines," *2020 IEEE Energy Conversion Congress and Exposition* (ECCE), Detroit, MI, USA, pp. 2034-2041, 2020.
[ZHA20b]	H. Zhao, C. Liu, Z. Song, W. Wang, and T. Lubin, "A dual-modulator magnetic-geared machine for tidal-power generation," *IEEE Transactions on Magnetics*, vol. 56, no. 8, pp. 1-7, Art no. 6703607, Aug. 2020.
[ZHE13]	P. Zheng, J. Bai, C. Tong, Y. Sui, Z. Song, and Q. Zhao, “Investigation of a novel radial magnetic-field-modulated brushless double-rotor machine used for HEVs,” *IEEE Trans. Magn.*, vol. 49, no. 3, pp. 1231–1241, Mar. 2013.
[ZHO18]	Y.C. Zhong, S.D. Huang, and D.R. Luo, "Stabilization and speed control of a

	permanent magnet synchronous motor with dual-rotating rotors" *Energies*, 11, no. 10: 2786, 2018.
[ZHU00]	Z. Q. Zhu and D. Howe, "Influence of design parameters on cogging torque in permanent magnet machines," IEEE Transactions on Energy Conversion, vol. 15, no. 4, pp. 407-412, Dec. 2000.
[ZHU07]	Z. Q. Zhu and D. Howe, “Electrical machines and drives for electric, hybrid, and fuel cell vehicles,” *Proc. IEEE*, vol. 95, no. 4, pp. 746–765, Apr. 2007.
[ZHU09]	Z. Q. Zhu, “A simple method for measuring cogging torque in permanent magnet machines,” *Proc. IEEE Power Energy Soc. General Meet.*, Calgary, Canada, vols. 26–30, pp. 1–4, Jul. 2009.
[ZHU11]	Z. Q. Zhu, “Fractional slot permanent magnet brush-less machines and drives for electric and hybrid propulsion systems,” Int. J. Compel, vol. 30, no. 1, pp. 9–31, January 2011.
[ZHU14]	Z. Q. Zhu, "Permanent magnet machines for traction applications," Encyclopedia of Automotive Engineering, pp. 1-20, October 2014.
[ZHU18a]	Z. Q. Zhu, M. F. Khatab, H. Li, and Y. Liu, "A novel axial flux magnetically geared machine for power split application," *IEEE Transactions on Industry Applications*, vol. 54, no. 6, pp. 5954-5966, Nov.-Dec. 2018.
[ZHU18b]	Z. Q. Zhu and Y. Liu, "Analysis of air-gap field modulation and magnetic gearing effect in fractional-slot concentrated-winding permanent-magnet synchronous machines," *IEEE Transactions on Industrial Electronics*, vol. 65, no. 5, pp. 3688-3698, May 2018.
[ZHU22]	Z.Q. Zhu, Yinzhao Zheng, Yue Liu, Fangrui Wei, Dawei Liang, Liren Huang, and Hailong Liu, "Effect of end-winding on electromagnetic performance of fractional slot and vernier PM machines with different slot/pole number combinations and winding configurations," *IEEE Access*, vol. 10, pp. 49934-49955, 2022.
[ZHU93]	Z. Q. Zhu and D. Howe, "Instantaneous magnetic field distribution in brushless permanent magnet DC motors. III. Effect of stator slotting," IEEE Transactions on Magnetics, vol. 29, no. 1, pp. 143-151, Jan. 1993.